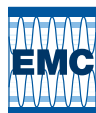


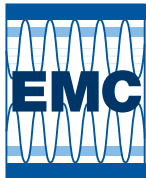


**EMC** 62<sup>ND</sup> ELECTRONIC  
MATERIALS  
CONFERENCE  
Now Virtual

# PROGRAM GUIDE



**62<sup>ND</sup> ELECTRONIC MATERIALS CONFERENCE**  
June 24-26, 2020



# 62<sup>ND</sup> ELECTRONIC MATERIALS CONFERENCE

June 24-26, 2020

## WELCOME TO THE CONFERENCE!

It is with great pleasure that we welcome you to the 62<sup>nd</sup> Electronic Materials Conference (EMC 2020). Though produced this year in a totally virtual format—with both prerecorded and live-streaming presentations—the Conference will continue to follow in EMC’s long tradition of offering premier research on the preparation and characterization of electronic materials. We have a strong community, and we thank those volunteers who have stepped forward to make this Conference happen. We also thank you for choosing to join us!

### Conference Chair

**Kris Bertness** National Institute of Standards and Technology

### Program Chair

**Lisa Porter** Carnegie Mellon University

## CONFERENCE HIGHLIGHTS

### The 62<sup>nd</sup> EMC Program

Scientists from around the world will participate virtually this week to share ideas, present technical information and contribute to the advancement of electronic materials research. Featuring over **350 oral/poster presentations**, the 62<sup>nd</sup> EMC will offer a strong program with **45 technical sessions** focused on: electronic materials science and technology; energy storage and conversion materials; nanoscale science and technology; organic materials, thin films and devices; oxide semiconductors and dielectrics; and wide bandgap semiconductors. Poster Sessions are slated for Wednesday evening and Thursday morning.

### EMC Awards Ceremony & Plenary Session

The 62<sup>nd</sup> EMC kicks off Wednesday morning with the Awards Ceremony & Plenary Session. First, the **2019 Best Student Presentation Award** recipients will be announced and honored. The Plenary lecture follows, with **Joan Redwing**, The Pennsylvania State University, presenting **Epitaxial Growth and Properties of Atomically Thin Semiconductors – Moving Beyond Flakes**. Learn more on page 4.

### Save the Dates

#### 63<sup>rd</sup> Electronic Materials Conference

June 23-25, 2021  
University of California, Santa Barbara  
Santa Barbara, California

#### 64<sup>th</sup> Electronic Materials Conference

June 22-24, 2022  
The Ohio State University  
Columbus, Ohio

## TABLE OF CONTENTS

Committees .....	2	Wednesday Oral Presentations .....	19
EMC Awards Ceremony & Plenary Session ..	4	Poster Presentations .....	43
Daily Schedule of Events.....	5	Thursday Oral Presentations .....	56
Program At-A-Glance.....	6	Friday Oral Presentations .....	89
Poster Sessions.....	9	EMC Index.....	120

## SPECIAL THANKS!



[dimatixmaterialsprinter.com](http://dimatixmaterialsprinter.com)



[ngc.com](http://ngc.com)



**TAIYO NIPPON SANSO**  
The Gas Professionals

[mocvd.jp](http://mocvd.jp)



[tms.org/foundation](http://tms.org/foundation)



## RECORDING/PHOTO POLICY

No photographs/recordings of presentations permitted. Any files temporarily downloaded for viewing will be deleted upon completion of the session unless explicit permission is given by the authors.

EMC is being coordinated with the Device Research Conference, held virtually this year, June 21-24

The 62<sup>nd</sup> EMC has been managed by



**CONFERENCE SERVICES**  
Because the Experience Matters

[mrs.org/conference-services](http://mrs.org/conference-services)

# COMMITTEES

## Executive Committee

<b>Chair</b>	<b>Kris Bertness</b> National Institute of Standards and Technology
<b>Vice-Chair</b>	<b>Lisa Porter</b> Carnegie Mellon University
<b>Secretary</b>	<b>Daniel Wasserman</b> The University of Texas at Austin
<b>Treasurer</b>	<b>Rebecca Peterson</b> University of Michigan

## ELECTRONIC MATERIALS SCIENCE AND TECHNOLOGY

### Contacts to Semiconductor Epilayers, Nanostructures and Organic Films

**Leonard Brillson**, The Ohio State University  
**Shadi Dayeh**, University of California, San Diego  
**Chris Hinkle**, University of Notre Dame  
**Suzanne Mohnney**, The Pennsylvania State University  
**Lisa Porter**, Carnegie Mellon University  
**Tae-Yeon Seong**, Korea University  
**Jerry Woodall**, University of California, Davis

### Embedded Nanoparticles and Nanocomposite Films

**Seth Bank**, The University of Texas at Austin  
**Matt Doty**, University of Delaware  
**Kurt Eyink**, Air Force Research Laboratory  
**Minjoo (Larry) Lee**, University of Illinois at Urbana-Champaign  
**Roberto Myers**, The Ohio State University  
**Joshua Zide**, University of Delaware

### Epitaxial Materials and Devices

**Seth Bank**, The University of Texas at Austin  
**Kurt Eyink**, Air Force Research Laboratory  
**Archie Holmes**, University of Virginia  
**Sriram Krishnamoorthy**, The University of Utah  
**Charles Lutz**, Lumentum Operations LLC  
**Nadeemullah Mahadik**, U.S. Naval Research Laboratory  
**Kyle McNicholas**, Lincoln Laboratory, Massachusetts Institute of Technology  
**Siddharth Rajan**, The Ohio State University  
**Shadi Shahedipour-Sandvik**, State University of New York Polytechnic Institute  
**Stephanie Tomasulo**, U.S. Naval Research Laboratory  
**Christine Wang**, Lincoln Laboratory, Massachusetts Institute of Technology  
**Kin-Man Yu**, City University of Hong Kong

### Materials for Memory and Computation

**Ritesh Agarwal**, University of Pennsylvania  
**Alan Doolittle**, Georgia Institute of Technology  
**Susan Fullerton**, University of Pittsburgh  
**Angel Yanguas-Gil**, Argonne National Laboratory

### Materials Integration

**Daniel Ewing**, Department of Energy's Kansas City National Security Campus  
**Mark Goorsky**, University of California, Los Angeles  
**Doug Hall**, University of Notre Dame  
**Karl Hobart**, U.S. Naval Research Laboratory  
**Rebecca Peterson**, University of Michigan  
**Nate Quitoriano**, McGill University  
**Steve Ringel**, The Ohio State University  
**Patrick Shea**, Northrop Grumman Corporation  
**Jerry Woodall**, University of California, Davis

### Metamaterials and Materials for THz, Plasmonics and Polaritons

**Joshua Caldwell**, Vanderbilt University  
**Kurt Eyink**, Air Force Research Laboratory  
**Rachel Goldman**, University of Michigan  
**Anthony Hoffman**, University of Notre Dame  
**Stephanie Law**, University of Delaware  
**Berardi Sensale Rodriguez**, The University of Utah  
**Jason Valentine**, Vanderbilt University  
**Daniel Wasserman**, The University of Texas at Austin  
**Huili Grace Xing**, Cornell University

### Nano-Magnetic, Magnetic Memory and Spintronic Materials

**Michael Flatte**, The University of Iowa  
**Roland Kawakami**, The Ohio State University  
**Xinyu Liu**, University of Notre Dame  
**Angel Yanguas-Gil**, Argonne National Laboratory

### Nanofabrication and Processing

**Bruno Azeredo**, Arizona State University  
**Kris Bertness**, National Institute of Standards and Technology  
**Mona Ebrish**, U.S. Naval Research Laboratory  
**Xiuling Li**, University of Illinois at Urbana-Champaign  
**Parsian Mohseni**, Rochester Institute of Technology  
**Andre Zeumault**, The University of Tennessee, Knoxville

### Narrow Bandgap Materials and Devices

**Ganesh Balakrishnan**, The University of New Mexico  
**Brian Bennett**, U.S. Naval Research Laboratory  
**Bob Biefeld**, Retired  
**Sanjay Krishna**, The Ohio State University  
**Andrej Lenert**, University of Michigan  
**Kyle McNicholas**, Lincoln Laboratory, Massachusetts Institute of Technology  
**Kunal Mukherjee**, University of California, Santa Barbara  
**Jamie Phillips**, University of Michigan  
**Gregory Triplett**, Virginia Commonwealth University  
**Christine Wang**, Lincoln Laboratory, Massachusetts Institute of Technology  
**Daniel Wasserman**, The University of Texas at Austin  
**Joshua Zide**, University of Delaware

### Point Defects, Doping and Extended Defects

**Andrew Armstrong**, Sandia National Laboratories  
**Ramon Collazo**, North Carolina State University  
**Rachel Goldman**, University of Michigan  
**Lincoln Lauhon**, Northwestern University  
**Kunal Mukherjee**, University of California, Santa Barbara  
**Steve Ringel**, The Ohio State University  
**Shadi Shahedipour-Sandvik**, State University of New York Polytechnic Institute  
**Jun Suda**, Kyoto University  
**Christian Wetzel**, Rensselaer Polytechnic Institute  
**Jerry Woodall**, University of California, Davis

### Quantum Materials

**Matt Doty**, University of Delaware  
**Rachel Goldman**, University of Michigan  
**Anthony Hoffman**, University of Notre Dame  
**Stephanie Law**, University of Delaware  
**Connie Li**, U.S. Naval Research Laboratory  
**Chakrakpani Varanasi**, U.S. Army Research Office

### Transparent Conductors

**Suprem Das**, Kansas State University  
**David Janes**, Purdue University  
**Rebecca Peterson**, University of Michigan  
**Lisa Porter**, Carnegie Mellon University  
**Angel Yanguas-Gil**, Argonne National Laboratory

## ENERGY STORAGE AND CONVERSION MATERIALS

### Electrochemical Energy Storage and Conversion

**Susan Fullerton**, University of Pittsburgh  
**David Gundlach**, National Institute of Standards and Technology  
**Zetian Mi**, University of Michigan  
**Louis Piper**, Binghamton University, The State University of New York  
**Edward Yu**, The University of Texas at Austin

### Energy Harvesting

**Alan Doolittle**, Georgia Institute of Technology  
**Ken Jones**, U.S. Army Research Laboratory  
**Jamie Phillips**, University of Michigan  
**Shadi Shahedipour-Sandvik**, State University of New York Polytechnic Institute

### Solar Cell Materials and Devices

**Geoffrey Bradshaw**, Air Force Research Laboratory  
**Rachel Goldman**, University of Michigan  
**Mark Goorsky**, University of California, Los Angeles  
**Andrej Lenert**, University of Michigan  
**Steve Ringel**, The Ohio State University  
**Oleg Rubel**, McMaster University  
**Jae-Hyun Ryou**, University of Houston  
**Mike Scarpulla**, The University of Utah  
**Christian Wetzel**, Rensselaer Polytechnic Institute  
**Mark Wistey**, Texas State University  
**Jerry Woodall**, University of California, Davis

### Thermoelectrics and Thermal Transport

**Ferdinand Poudeu**, University of Michigan  
**Xiaojia Wang**, University of Minnesota  
**Yaguo Wang**, The University of Texas at Austin  
**Andre Zeumault**, The University of Tennessee, Knoxville  
**Joshua Zide**, University of Delaware

## NANOSCALE SCIENCE AND TECHNOLOGY

### Graphene, BN, MoS<sub>2</sub> and Other 2D Materials and Devices

**Thomas Beechem**, Sandia National Laboratories  
**Kevin Daniels**, University of Maryland  
**Mona Ebrish**, U.S. Naval Research Laboratory  
**Randall Feenstra**, Carnegie Mellon University  
**Susan Fullerton**, University of Pittsburgh  
**Roland Kawakami**, The Ohio State University  
**Manos Kioupakis**, University of Michigan  
**Rachel Koltun**, Guardian Industries  
**Lincoln Lauhon**, Northwestern University  
**Suzanne Mohnney**, The Pennsylvania State University  
**Siddharth Rajan**, The Ohio State University  
**Joan Redwing**, The Pennsylvania State University  
**Joshua Robinson**, The Pennsylvania State University  
**Michael Spencer**, Morgan State University  
**Christine Wang**, Lincoln Laboratory, Massachusetts Institute of Technology  
**Huili Grace Xing**, Cornell University

#### Low-Dimensional Structures— Quantum Dots, Wires and Wells

**Ganesh Balakrishnan**, The University of New Mexico  
**Matthew Doty**, University of Delaware  
**Kurt Eyink**, Air Force Research Laboratory  
**Michael Gerhold**, U.S. Army Research Office  
**Rachel Goldman**, University of Michigan  
**Lincoln Lauhon**, Northwestern University  
**Minjoo (Larry) Lee**, University of Illinois  
at Urbana-Champaign  
**Zetian Mi**, University of Michigan  
**Jamie Phillips**, University of Michigan  
**Paul Simmonds**, Boise State University  
**Daniel Wasserman**, The University of Texas at Austin

#### Materials Integration

**Daniel Ewing**, Department of Energy's Kansas City  
National Security Campus  
**Mark Goorsky**, University of California, Los Angeles  
**Doug Hall**, University of Notre Dame  
**Karl Hobart**, U.S. Naval Research Laboratory  
**Rebecca Peterson**, University of Michigan  
**Nate Quitriano**, McGill University  
**Steve Ringel**, The Ohio State University  
**Patrick Shea**, Northrop Grumman Corporation  
**Jerry Woodall**, University of California, Davis

#### Nanoscale Characterization—Scanning Probes, Electron Microscopy and Other Techniques

**Thomas Beechem**, Sandia National Laboratories  
**Rachel Goldman**, University of Michigan  
**Lincoln Lauhon**, Northwestern University  
**James LeBeau**, Massachusetts Institute of Technology  
**Anders Mikkelsen**, Lund University  
**Jay Mody**, GLOBALFOUNDRIES  
**Volker Rose**, Argonne National Laboratory  
**Rainer Timm**, Lund University  
**Heayoung Yoon**, The University of Utah  
**Edward Yu**, The University of Texas at Austin

#### Nanowires and Nanotubes— Growth, Processing, Characterization and Devices

**Kris Bertness**, National Institute of Standards  
and Technology  
**Matt Brubaker**, National Institute of Standards  
and Technology  
**Xiuling Li**, University of Illinois at Urbana-Champaign  
**Zetian Mi**, University of Michigan  
**Anders Mikkelsen**, Lund University  
**Parsian Mohseni**, Rochester Institute of Technology  
**Roberto Myers**, The Ohio State University  
**Nate Quitriano**, McGill University  
**Rainer Timm**, Lund University  
**George Wang**, Sandia National Laboratories  
**William Wong**, University of Waterloo

## ORGANIC MATERIALS, THIN FILMS AND DEVICES

#### Electronic Materials for Bio

**Francesca Cavallo**, The University of New Mexico  
**Tzahi Cohen-Karni**, Carnegie Mellon University  
**Shadi Dayeh**, University of California, San Diego  
**David Estrada**, Boise State University  
**David Gundlach**, National Institute of Standards  
and Technology  
**Thomas Jackson**, The Pennsylvania State University  
**David Janes**, Purdue University

#### Flexible, Printed and/or Dissolvable Thin Films or Nanomembranes

**Suprem Das**, Kansas State University  
**Daniel Ewing**, Department of Energy's Kansas City  
National Security Campus  
**Gerd Grau**, York University  
**Thomas Jackson**, The Pennsylvania State University  
**Thomas Kuech**, University of Wisconsin  
**Rebecca Peterson**, University of Michigan  
**Jae-Hyun Ryou**, University of Houston  
**Sarah Swisher**, University of Minnesota  
**William Wong**, University of Waterloo

#### Organic and Hybrid Optoelectronic Devices

**Alexander Ayzner**, University of California, Santa Cruz  
**David Gundlach**, National Institute of Standards  
and Technology  
**Tina Ng**, University of California, San Diego  
**Oleg Rubel**, McMaster University  
**Adrienne Stiff-Roberts**, Duke University  
**Wei You**, University of North Carolina

#### Organic Devices and Molecular Electronics

**Gerd Grau**, York University  
**David Gundlach**, National Institute of Standards  
and Technology  
**Thomas Jackson**, The Pennsylvania State University  
**David Janes**, Purdue University  
**Ioannis Kymissis**, Columbia University  
**Takhee Lee**, Seoul National University  
**Francois Leonard**, Sandia National Laboratories  
**Tina Ng**, University of California, San Diego  
**Curt Richter**, National Institute of Standards  
and Technology  
**Adrienne Stiff-Roberts**, Duke University  
**William Wong**, University of Waterloo

## OXIDE SEMICONDUCTORS AND DIELECTRICS

#### Dielectrics and Multifunctional Oxides

**Alan Doolittle**, Georgia Institute of Technology  
**Doug Hall**, University of Notre Dame  
**Anderson Janotti**, University of Delaware  
**David Lederman**, University of California, Santa Cruz  
**Patrick Lenahan**, The Pennsylvania State University  
**Joseph Ngai**, The University of Texas at Arlington  
**Nicholas Strandwitz**, Lehigh University  
**Angel Yanguas-Gil**, Argonne National Laboratory

#### Gallium Oxide

**Elaheh Ahmadi**, University of Michigan  
**Shizuo Fujita**, Kyoto University  
**Masataka Higashiwaki**, National Institute of  
Information and Communications Technology  
**Sriram Krishnamoorthy**, The University of Utah  
**Shin Mou**, Air Force Research Laboratory  
**Rebecca Peterson**, University of Michigan  
**Lisa Porter**, Carnegie Mellon University  
**Siddharth Rajan**, The Ohio State University  
**Marko Tadjer**, U.S. Naval Research Laboratory  
**Hongping Zhao**, The Ohio State University

#### Oxide Semiconductors—Growth, Doping, Defects, Nanostructures and Devices

**Leonard Brillson**, The Ohio State University  
**Steve Durbin**, Western Michigan University  
**Thomas Jackson**, The Pennsylvania State University  
**Anderson Janotti**, University of Delaware  
**Mark Losego**, Georgia Institute of Technology  
**Rebecca Peterson**, University of Michigan  
**Louis Piper**, Binghamton University,  
The State University of New York  
**Shayla Sawyer**, Rensselaer Polytechnic Institute  
**Sarah Swisher**, University of Minnesota

## WIDE BANDGAP SEMICONDUCTORS

#### Diamond and Related Materials

**Mark Goorsky**, University of California, Los Angeles  
**Andrew Koehler**, U.S. Naval Research Laboratory  
**Jung Hun Seo**, University at Buffalo,  
The State University of New York  
**Patrick Shea**, Northrop Grumman Corporation

#### Group III-Nitrides—Growth, Processing, Characterization, Theory and Devices

**Andrew Allerman**, Sandia National Laboratories  
**Zakaria Y. Al Balushi**, University of California,  
Berkeley  
**Srabanti Chowdhury**, Stanford University  
**Theeradetch Detchprohm**, Georgia Institute  
of Technology  
**Alan Doolittle**, Georgia Institute of Technology  
**Russell Dupuis**, Georgia Institute of Technology  
**Daniel Ewing**, Department of Energy's Kansas City  
National Security Campus  
**Qhalid Fareed**, Texas Instruments  
**Daniel Feezell**, The University of New Mexico  
**Hiroshi Fujioka**, The University of Tokyo  
**Jennifer Hite**, U.S. Naval Research Laboratory  
**Andrew Koehler**, U.S. Naval Research Laboratory  
**Xiaohang Li**, King Abdullah University of Science  
and Technology  
**Michael Manfra**, Purdue University  
**Siddharth Rajan**, The Ohio State University  
**Shadi Shahedipour-Sandvik**, State University  
of New York Polytechnic Institute  
**Andrei Vescan**, RWTH Aachen University  
**Christian Wetzel**, Rensselaer Polytechnic Institute  
**Jonathon Wierer**, Lehigh University  
**Huili Grace Xing**, Cornell University

#### Silicon Carbide—Growth, Processing, Characterization, Theory and Devices

**Joshua Caldwell**, Vanderbilt University  
**MVS Chandrashekar**, University of South Carolina  
**Sarit Dhar**, Auburn University  
**Michael Dudley**, Stony Brook University  
**Daniel Ewing**, Department of Energy's Kansas City  
National Security Campus  
**Nadeemullah Mahadik**, U.S. Naval Research  
Laboratory  
**Michael Spencer**, Morgan State University  
**Jun Suda**, Kyoto University

# EMC AWARDS CEREMONY & PLENARY SESSION

Wednesday, 10:00 am – 11:00 am  
Live Plenary Session



## PLENARY SPEAKER

**Joan Redwing**  
The Pennsylvania State University

### *Epitaxial Growth and Properties of Atomically Thin Semiconductors – Moving Beyond Flakes*

**Joan Redwing** is a professor of materials science and engineering at The Pennsylvania State University and serves as director of the 2D Crystal Consortium, an NSF Materials Innovation Platform (MIP) national user facility for the synthesis of 2D chalcogenides. Redwing received her PhD in chemical engineering from the University of Wisconsin-Madison in 1994, and worked at Advanced Technology Materials Inc. (ATMI) for five years prior to joining The Pennsylvania State University in 2000.

Redwing's research focuses on crystal growth and epitaxy of electronic materials with an emphasis on thin-film and nanomaterial synthesis by metalorganic chemical vapor deposition (MOCVD). Her work has influenced a range of materials systems including group III-nitrides,  $MgB_2$  superconductors, Si/SiGe nanowires, and more recently, 2D layered chalcogenides.

Redwing currently serves as vice president of the American Association for Crystal Growth, is an associate editor for Journal of Crystal Growth, and a regional editor for 2D Materials. She is a Fellow of the Materials Research Society, the American Physical Society, and the American Association for the Advancement of Science. She is an author on over 300 publications in refereed journals and holds eight U.S. patents.

## 2019 BEST STUDENT PRESENTATION AWARDS

### ORAL PRESENTATIONS

#### Zixuan Feng

The Ohio State University

*LPCVD Growth of Si Doped B-Ga<sub>2</sub>O<sub>3</sub> Thin Films with Superior Room Temperature Mobilities*

Advisor – Hongping Zhao

#### Anisha Kalra

Centre for Nano Science and Engineering (CeNSE), Indian Institute of Science

*Record High Zero-Bias External Quantum Efficiency of 88% for Al<sub>0.40</sub>Ga<sub>0.60</sub>N-Based p-i-n UV Detectors*

Advisors – Digbijoy N. Nath and Srinivasan Raghavan

#### Debarghya Sarkar

University of Southern California

*Direct Growth of Crystalline III-Vs on Amorphous Dielectrics Using a Combination of Epitaxial and Non-Epitaxial Methods*

Advisor – Rehan Kapadia

### POSTER PRESENTATION

#### Max Kneiß

Universität Leipzig, Faculty of Physics and Earth Sciences, Felix Bloch Institute for Solid State Physics

*Epitaxial Stabilization of  $\kappa$ -Ga<sub>2</sub>O<sub>3</sub> and  $\kappa$ -(Al<sub>x</sub>Ga<sub>1-x</sub>)<sub>2</sub>O<sub>3</sub> Thin Films for Heterostructure Device Applications by Tin-Assisted PLD on Different Substrates*

Advisors – Marius Grundmann and Holger von Wenckstern



Student participation in this Conference is partially supported by a grant from the TMS Foundation

# DAILY SCHEDULE OF EVENTS

## WEDNESDAY

EMC Awards Ceremony and Plenary Session	10:00 am – 11:00 am	Live Plenary Session
Break	11:00 am – 11:30 am	
A: Devices and Materials for Memory Computation	11:30 am – 1:00 pm	ZoomRoom 1
B: Nanowires—Growth, Processing, Characterization and Devices	11:30 am – 12:45 pm	ZoomRoom 2
C: Advanced Design and Processes for III-Nitride Power Electronics	11:30 am – 1:00 pm	ZoomRoom 3
D: 2D Devices	11:30 am – 12:30 pm	ZoomRoom 4
E: Quantum Materials	11:30 am – 12:45 pm	ZoomRoom 5
F: Organic and Hybrid Optoelectronic Devices	11:30 am – 12:30 pm	ZoomRoom 6
Break	1:00 pm – 2:00 pm	
G: Ga <sub>2</sub> O <sub>3</sub> —Growth, Characterization and Defects I	2:00 pm – 4:45 pm	ZoomRoom 1
K: 2D-Materials Applications	2:00 pm – 4:15 pm	ZoomRoom 4
M: Quantum Dots and Wells	2:00 pm – 4:45 pm	ZoomRoom 6
H: Nanoscale Characterization—Scanning Probes, EM and Other Techniques	2:15 pm – 4:45 pm	ZoomRoom 2
I: Materials for III-Nitrides Power Electronics	2:15 pm – 3:15 pm	ZoomRoom 3
L: Silicon Carbide—Materials and Devices	2:15 pm – 5:00 pm	ZoomRoom 5
Break	3:15 pm – 3:45 pm	
J: III-Nitrides—Irradiation and Device Design for Power Electronics	3:45 pm – 4:30 pm	ZoomRoom 3
Break	5:00 pm – 5:30 pm	
PS1: Poster Session I	5:30 pm – 7:00 pm	Poster Session 1

## THURSDAY

PS2: Poster Session II	10:00 am – 11:15 am	Poster Session 2
Break	11:15 am – 11:45 am	
N: Defect and Contacts in WB Semiconductors	11:45 am – 2:45 pm	ZoomRoom 1
O: Fabrication, Processing and Integration	11:45 am – 3:15 pm	ZoomRoom 2
P: III-Nitride Power Devices Utilizing Oxides	11:45 am – 1:00 pm	ZoomRoom 3
R: Metal Dichalcogenides	11:45 am – 3:15 pm	ZoomRoom 4
S: Materials for Memory and Computation	11:45 am – 1:00 pm	ZoomRoom 5
U: Solar Cell Materials and Devices	11:45 am – 3:00 pm	ZoomRoom 6
Break	1:00 pm – 2:00 pm	
Q: III-Nitrides—Photodetectors	2:00 pm – 3:15 pm	ZoomRoom 3
T: Electronic Materials for Bio	2:00 pm – 3:00 pm	ZoomRoom 5
Break	3:15 pm – 3:45 pm	
V: Ga <sub>2</sub> O <sub>3</sub> —Growth, Characterization and Defects II	3:45 pm – 6:45 pm	ZoomRoom 1
W: Electrochemical Energy Storage and Conversion	3:45 pm – 6:00 pm	ZoomRoom 2
X: III-Nitride MBE and Sputtering Growth	3:45 pm – 5:00 pm	ZoomRoom 3
Z: Nanophotonic Materials	3:45 pm – 6:45 pm	ZoomRoom 4
AA: Wide Bandgap Materials—Silicon Carbide and Diamond	3:45 pm – 6:45 pm	ZoomRoom 5
BB: Point Defects, Doping and Extended Defects	4:00 pm – 6:45 pm	ZoomRoom 6
Break	5:00 pm – 5:30 pm	
Y: III-Nitrides—HEMTs	5:30 pm – 6:30 pm	ZoomRoom 3

## FRIDAY

CC: B-Ga <sub>2</sub> O <sub>3</sub> Devices	10:00 am – 1:00 pm	ZoomRoom 1
EE: Hexagonal Boron Nitride and Graphene	10:00 am – 1:00 pm	ZoomRoom 3
FF: Thin Film Devices	10:00 am – 10:15 am	ZoomRoom 4
DD: Thermoelectrics and Energy Harvesting	10:15 am – 1:00 pm	ZoomRoom 2
GG: Oxides Materials and Devices	10:15 am – 11:15 am	ZoomRoom 4
II: Organic Devices and Molecular Electronics	10:15 am – 1:00 pm	ZoomRoom 6
HH: ZnO-Based Contacts, Defects and Devices	10:30 am – 1:00 pm	ZoomRoom 5
Break	11:15 am – 11:45 am	
Break	1:00 pm – 2:00 pm	
JJ: III-Nitrides—Processing	2:00 pm – 3:15 pm	ZoomRoom 1
LL: Narrow Bandgap Materials and Devices	2:00 pm – 5:00 pm	ZoomRoom 2

## FRIDAY

MM: III-Nitrides—Tunnel Junctions and InGaN Growth	2:00 pm – 3:15 pm	ZoomRoom 3
PP: Novel Materials	2:00 pm – 3:15 pm	ZoomRoom 5
RR: Flexible, Printed and/or Dissolvable Thin Films or Nanomembranes	2:00 pm – 4:30 pm	ZoomRoom 6
OO: Spintronic and Magnetic Materials and Devices	2:15 pm – 5:00 pm	ZoomRoom 4
Break	3:15 pm – 3:45 pm	
KK: III-Nitrides—Defects and Characterization	3:45 pm – 5:00 pm	ZoomRoom 1
NN: AlN and AlGaIn Growth	3:45 pm – 5:00 pm	ZoomRoom 3
QQ: Fundamental Issues in Epitaxy	3:45 pm – 5:00 pm	ZoomRoom 5

▲ Plenary Speaker ★ Invited Speaker

EMC Awards Ceremony and Plenary Session			Live Plenary Session
10:00 am			EMC Awards Ceremony
10:10 am	Joan M. Redwing	PL01▲	Epitaxial Growth and Properties of Atomically Thin Semiconductors—Moving Beyond Flakes
11:00 am			BREAK
A: Devices and Materials for Memory Computation			ZoomRoom 1
11:30 am	Vinod K. Sangwan	A01	MoS <sub>2</sub> Memtransistors for Neuromorphic Computing
11:45 am	Jubin Hazra	A02	(Student) Impact of H <sub>2</sub> O Vapor Precursor Pulse Time on 65nm CMOS Integrated Hafnium Dioxide Based Nanoscale RRAM Devices
12:00 pm	Kayla A. Cooley	A03	(Student) A Comprehensive Review of Contact Resistance and Thermal Stability of Metals on GeTe
12:15 pm	Minhyung Ahn	A04	(Student) Resistive Memory Based on (Zr, Hf, Nb, Ta, Mo, W) High Entropy Oxides
12:30 pm	Souvik Mukhopadhyay	A05	(Student) Autonomous Programmable Materials with Embedded Computation, Sensing, Signal Processing and Actuation
12:45 pm	Timothy Michael McCrone	A06	(Student) Heteroepitaxial Thin Film Growth of LiNbO <sub>2</sub> for Rapid Charge Battery, Neuromorphic and Photosynthesis Applications
B: Nanowires—Growth, Processing, Characterization and Devices			ZoomRoom 2
11:30 am	Matt Brubaker	B01	Axial and Radial InGa <sub>N</sub> Quantum Wells in Ordered N-Polar GaN Nanowire Arrays
11:45 am	Alireza Abrand	B02	(Student) Flexible III-V Nanowire-Based Photodetectors via Selective-Area Epitaxy on Reusable Si Substrates
12:00 pm	Quintin Cheek	B03	(Student) <i>In Situ</i> TEM for the Direct Observation and Characterization of Germanium Nanowire Synthesis via the Electrochemical Liquid-Liquid-Solid Crystal Growth Process
12:15 pm	Taoufik Slimani Tlemcani	B04	Influence of Seed Layer on the Performance of ZnO Nanowires-Based Flexible Nanogenerator as Piezoelectric Energy Harvester
12:30 pm	David Magginiti	B05	(Student) Optoelectronic Properties of Red-Luminescent Si Micropillar Arrays Fabricated by Metal-Assisted Chemical Etching
C: Advanced Design and Processes for III-Nitride Power Electronics			ZoomRoom 3
11:30 am	Andrew Binder	C01	Limitations in Impact Ionization Modeling for Predicting Breakdown in Wide Bandgap Power Semiconductors
11:45 am	Alexander Chang	C02	Inverse Proportionality of Dopant Concentration to Growth Speed During Non-Planar Selective Area Regrowth of GaN
12:00 pm	Kai Fu	C03	1.27 kV Etch-then-Regrow GaN p-n Junctions with Low Leakage for GaN Power Electronics
12:15 pm	Vincent E. Meyers	C04	(Student) P-Type Conductivity in Mg-Implanted GaN by Microwave Gyrotron Annealing
12:30 pm	Mona Ebrish	C05	Process Optimization for Selective Area Doping of GaN by Ion Implantation
12:45 pm	Marzieh Bakhtyari-Noodeh	C06	(Student) Growth and Characterization of GaN p-i-n Rectifiers Using Ion-Implantation Isolation
D: 2D Devices			ZoomRoom 4
11:30 am	Yury Illarionov	D01	Low Variability and 10 <sup>10</sup> On/Off Current Ratio in Flexible MoS <sub>2</sub> FETs with Al <sub>2</sub> O <sub>3</sub> Encapsulation Improved by Parylene N
11:45 am	Zhihui Cheng	D02	New Methods and Observations in Contact Scaling for 2D FETs
12:00 pm	Mohammad Nouri	D03	Fabrication of Multilayer MoS <sub>2</sub> Field-Effect Transistor Arrays Using a Modified Exfoliation Method
12:15 pm	Theresa Knobloch	D04	(Student) The Impact of the Graphene Work Function on the Stability of Flexible GFETs
E: Quantum Materials			ZoomRoom 5
11:30 am	Prineha Narang	E01★	Predicting and Controlling the Electronic, Spin and Lattice Degrees of Freedom of Artificial Atoms in Solids
12:00 pm	Steven May	E02★	Probing Electronic Degrees of Freedom at Buried Interfaces in Quantum Heterostructures Using Resonant X-Ray Reflectivity
12:30 pm	Brandi Wooten	E03	(Student) Resonant and Magnetic Doping in Topological Insulator Bi <sub>2</sub> Se <sub>3</sub>
F: Organic and Hybrid Optoelectronic Devices			ZoomRoom 6
11:30 am	Buang Zhang	F01	(Student) LED Performance of PFO/MEH-PPV Blended Polymer Active Regions Deposited by RIR-MAPLE
11:45 am	Bryan Kaehr	F02	Charge-Transfer Liquid Crystals for Re-Writeable Waveguides
12:00 pm	Jacob W. Ciszek	F03	Reduced Metal Penetration of Evaporated Top Contacts on Organic Semiconductors
12:15 pm	Mohamed-amine Guerboukha	F04	(Student) Structural and Electrical Properties of Self-Assembled Molecular Nanodielectrics on Germanium

# PROGRAM AT-A-GLANCE

WEDNESDAY

G: Ga <sub>2</sub> O <sub>3</sub> – Growth, Characterization and Defects I			ZoomRoom 1
2:00 pm	Usman UI Muazzam	G01	(Student) Mist CVD Growth and Optical Studies of $\alpha$ -Ga <sub>2</sub> O <sub>3</sub> on Sapphire
2:15 pm	John Scott Jamison	G02	A New Magnetic Phase of Fe <sub>2</sub> O <sub>3</sub> : Monoclinic $\mu$ -Fe <sub>2</sub> O <sub>3</sub> Epitaxially Stabilized on $\beta$ -Ga <sub>2</sub> O <sub>3</sub>
2:30 pm	Elline Clarissa Hettiaratchy	G03	(Student) Investigating High-Tc Ferromagnetism in $\alpha$ -Fe <sub>2</sub> O <sub>3</sub> / $\beta$ -Ga <sub>2</sub> O <sub>3</sub> Superlattices by Molecular Beam Epitaxy
2:45 pm	Muhammad N Huda	G04	The Mechanism Behind the Easy Exfoliation of Ga <sub>2</sub> O <sub>3</sub> and Prediction of a New Phase
3:00 pm	Michael Evan Liao	G05	(Student) Exfoliation Mechanism Differences between (010) and (-201) $\beta$ -Ga <sub>2</sub> O <sub>3</sub> Substrates Using Helium-Ion Implantation
3:15 pm			BREAK
3:45 pm	Sagar R Bhalerao	G06	(LATE NEWS, Student) Low Temperature-Solution Processed, Gallium Oxide (Ga <sub>2</sub> O <sub>3</sub> ) Thin-Film Transistor Using Anodized high- $\kappa$ Al <sub>2</sub> O <sub>3</sub> Gate Dielectric
4:00 pm	Tal Kasher	G07	Exploration of RF Sputtered Ga <sub>2</sub> O <sub>3</sub> as a Transparent Conductive Oxide for Application to Photovoltaics
4:15 pm	Prashanth Gopalan	G08	(Student) Anisotropic Permittivity of $\beta$ -Ga <sub>2</sub> O <sub>3</sub> in the Terahertz Band
4:30 pm	Marko Tadjer	G09	(LATE NEWS) High Carrier Density Delta-Doped b-(Al <sub>x</sub> Ga <sub>1-x</sub> ) <sub>2</sub> O <sub>3</sub> /Ga <sub>2</sub> O <sub>3</sub> Heterostructure Field-Effect Transistors by Ozone Molecular Beam Epitaxy
H: Nanoscale Characterization – Scanning Probes, EM and Other Techniques			ZoomRoom 2
2:15 pm	Zanlin Qiu	H01	(Student) Nanoscale Polymorph Determination in Functional Metal Oxides Using Convergent Beam Electron Diffraction
2:30 pm	Gabriel Antonio Calderon Ortiz	H02	(Student) Quantification of Ordered Domains in Organic Semiconducting Polymers Using Four-Dimensional Scanning Transmission Electron Microscopy
2:45 pm	Benjamin Klein	H03	Comparative Apex Electrostatics of Atom Probe Tomography Specimens
3:00 pm	Eamonn T Hughes	H04	(Student) Compositional Changes at Dislocations and Interfaces in Heteroepitaxial Semiconductors Studied by Atom Probe
3:15 pm			BREAK
3:45 pm	Jith Sarker	H05	(Student) Atom Probe Tomography Studies to Understand Dopant Interaction in Si-Doped (Al <sub>x</sub> Ga <sub>1-x</sub> ) <sub>2</sub> O <sub>3</sub>
4:00 pm	Rachael Cohn	H06	(Student) Nanosecond Photo-Induced Capacitance and Resistance Measurements in Organic Solar Cell Materials Using Broadband Local Dielectric Spectroscopy and Phase-Kick Electric Force Microscopy
4:15 pm	Thomas Moran	H07	Thickness-Dependent Nanoscale Charge-Discharge Phenomena and AFM-Based Tomography in Dielectric/Piezoelectric Multilayer Thin Films
4:30 pm	Neda Alsadat Aghamiri	H08	Carrier Localization in Perovskite Nickelate from Oxygen Vacancies and Lithium-Ion Doping Imaged Using Near-Field Nano-Imaging at mid-IR and THz Frequencies
I: Materials for III-Nitrides Power Electronics			ZoomRoom 3
2:15 pm	Anisha Kalra	I01	(Student) Polarization-Graded Al <sub>0.40</sub> Ga <sub>0.60</sub> N-on-Sapphire p-i-n Diodes with > 6 MV/cm Breakdown Field
2:30 pm	James C Gallagher	I02	Predicting the Quality of Vertical GaN Devices Using Long-Range Optical Techniques
2:45 pm	Yafei Liu	I03	(Student) X-Ray Topography Characterization of GaN Substrates Used for Power Electronic Devices
3:00 pm	Yuxuan Zhang	I04	(Student) Probing Deep Acceptors in MOCVD GaN-on-GaN—Toward High Power GaN Vertical Devices
3:15 pm			BREAK
J: III-Nitrides – Irradiation and Device Design for Power Electronics			ZoomRoom 3
3:45 pm	Kyle Ahn	J01	(Student) 60Co Gamma Irradiation Effects on IV of GaN Diodes Grown on Sapphire and Freestanding Substrates
4:00 pm	Yu Kee Ooi	J02	Impact of Gamma Irradiation on Interface States in GaN p+n Diodes
4:15 pm	Tsung-Han Yang	J03	(Student) The Investigation of Vertical GaN Schottky Barrier Diode with Floating Metal Guard Rings
K: 2D-Materials Applications			ZoomRoom 4
2:00 pm	Michael Pedowitz	K01	(Student) Layered $\delta$ -phase MnO <sub>2</sub> Nanofibers-Epitaxial Graphene-Silicon Carbide Heterostructures for Fast and Selective Room Temperature Gas Sensing
2:15 pm	Soaram Kim	K02	MoS <sub>2</sub> Nanoflower/Epitaxial Graphene Heterostructure for Chemical Sensing
2:30 pm	Lucas Kyle Beagle	K03	Modular Biomolecule Functionalization of MoS <sub>2</sub> for Selective Sensing
2:45 pm	Lincoln Lauhon	K04	<i>In Situ</i> Transport Measurements Reveal Source of Mobility Enhancement of MoS <sub>2</sub> and MoTe <sub>2</sub> During Dielectric Deposition
3:00 pm	Szu-Chia Chien	K05	Water Absorption in Functionalized Germanane
3:15 pm			BREAK
3:45 pm	Xiaohan Wu	K06	(Student) Non-Volatile Resistance Switching Behavior in Monolayer Two-Dimensional Materials
4:00 pm	Mounika Kotha	K07	(Student) Environmentally Stable Quasi-2D Gallium Telluride for Polarization Sensitive Optoelectronic Applications

L: Silicon Carbide – Materials and Devices			ZoomRoom 5
2:15 pm	Joshua L Justice	L01	Detection and Evolution of Micropipes in SiC Substrates and Epitaxial Layers and Their Impact on MOSFET and Diode Devices
2:30 pm	Nadeemullah Mahadik	L02	Carrier Lifetime Enhancement in Thick 4H-SiC Epilayers Investigated by 2-Photon Absorption
2:45 pm	Brian Robert Manning	L03	(Student) Nitrogen Donor-Deep Level Defect Interactions in 4H-SiC Bipolar Junction Transistors Using Electrically Detected Electron Nuclear Double Resonance
3:00 pm	Nick Yun	L04	(Student) Improved Electrical Characteristics of 4H-SiC JBS Diodes by Applying Post Deposition Annealing (PDA)
3:15 pm			BREAK
3:45 pm	James P. Ashton	L05	(Student) Oxide Leakage Currents and E' Centers in 4H-SiC MOSFETs with Barium Passivation
4:00 pm	Minseok Kang	L06	Body Diode Reliability of Commercially Available 1.7 kV 4H-SiC MOSFETs
4:15 pm	Shengnan Zhu	L07	An Investigation into Anomalous Time-Dependent Dielectric Breakdown Characteristics for 1.2 kV Commercial 4H-SiC Power MOSFETs
4:30 pm	Lu Wang	L08	(Student) Atomistic Study of 4H-SiC/SiO <sub>2</sub> Interfaces—A Systematic Approach
4:45 pm	Isanka Udayani Jayawardhena	L09	(Student) Electrical Characterization of 4H-SiC/ALD-Al <sub>2</sub> O <sub>3</sub> Interface for Different Surface Preparations
M: Quantum Dots and Wells			ZoomRoom 6
2:00 pm	Emily Turner	M01	(Student) Si Quantum Dots and Rings via Rapid Ge Diffusion During High Temperature Oxidation of Si/SiGe Nanostructures
2:15 pm	Lauren McCabe	M02	(Student) Low-Density, Site-Controlled InAs Quantum Dots for Quantum Devices
2:30 pm	Xiongliang Wei	M03	(Student) Controlled Growth of InGaN Quantum Dots on Photoelectrochemically Etched InGaN Quantum Dots Templates
2:45 pm	Flavia P.N. Inbanathan	M04	Microwave-Assisted Synthesis and Characterization of Nitrogen-Doped Graphene Quantum Dots
3:00 pm	Jennifer Selvidge	M05	(Student) Displacing Deleterious Misfit Dislocations from the Active Regions of InAs Quantum Dot Lasers on Si
3:15 pm			BREAK
3:45 pm	Rasha El-Jaroudi	M06	(Student) B-III-V/GaAs Quantum Wells—Towards 1.55 μm Emitters on GaAs
4:00 pm	Rachel Corey White	M07	(Student) Mechanism for Blueshift with Annealing in Near-Infrared B-III-V Alloys on GaAs
4:15 pm	Qian Meng	M08	(Student) Effect of B-In Interactions on the Band Structure and Optical Properties of BGa(In)As
4:30 pm	Jun Tao	M09	(LATE NEWS, Student) Low-Temperature Monolithic InAs Integration on Amorphous Substrates

## Journal of Electronic Materials

A special issue of the *Journal of Electronic Materials* (JEM)\* will be published with peer-reviewed papers from the 62<sup>nd</sup> Electronic Materials Conference.

- Article submission date is **August 31, 2020**.
- Questions? Contact the 2020 Special Issue Editors listed below.

The *Journal of Electronic Materials* reports monthly on the science and technology of electronic materials, while examining new applications for semiconductors, magnetic alloys, dielectrics, nanoscale materials and photonic materials. The *Journal* welcomes articles on methods for preparing and evaluating the chemical, physical, electronic and optical properties of these materials. Specific areas of interest are materials for state-of-the-art transistors, nanotechnology, electronic packaging, detectors, emitters, metallization, superconductivity and energy applications. Review papers on current topics enable individuals in the field of electronics to keep abreast of activities in areas peripheral to their own.

Manuscripts for the EMC 2020 collection will be evaluated according to the same high standards as would be applied to any article submitted to the *Journal*. Authors are encouraged to read carefully and comply with the "Instructions for Authors" on the *JEM website*. Submission of a manuscript implies that the work described has not been previously published and is not under consideration for publication elsewhere.

A FREE Springer book (author's choice, up to \$250 in value) will be awarded for the best paper from this issue!

### 2020 Special Issue Editors

**Joshua Caldwell**  
josh.caldwell@vanderbilt.edu

**Jennifer Hite**  
Jennifer.hite@nrl.navy.mil

**Nadeem Mahadik**  
nadeem.mahadik@nrl.navy.mil

**Parsian Mohseni**  
pkmohseni@rit.edu

**Jamie Phillips**  
jphilli@umich.edu

**Shadi Shahedipour-Sandvik**  
sshahedipour-sandvik@sunypoly.edu

**Randy Tompkins**  
randy.p.tompkins.civ@mail.mil

**Jing Zhang**  
jing.zhang@rit.edu

**TMS**

\* A Journal of The Minerals, Metals & Materials Society (TMS).  
Editor-in-Chief—Shadi Shahedipour-Sandvik

# PS1: POSTER SESSION I

WEDNESDAY PM

5:30 pm - 7:00 pm  
Poster Session 1

Presenter	Paper #	Title
Jian Liu	PS1.01	(Student) <i>In Situ</i> AFM Characterization on Si-Based Anode for Li-Ion Battery
Xinwei Jiao	PS1.02	Cobalt-Free Spinel Cathodes for Next-Generation Lithium-Ion Batteries
Zongjian Fan	PS1.03	(Student) High Brightness Luminescence from Indirect Band Gap AlGaAs Double Heterostructure (DH) Grown by Liquid Phase Epitaxy (LPE)
Hongyu Peng	PS1.04	(Student) Characterization of Hazy Features on AlInP/GaAs Epitaxial Wafers Grown by Organometallic Vapor Phase Epitaxy
Sunghwan Lee	PS1.05	Vapor-Deposited Polymeric Thin Films on Fabrics for Breathable Wearable Device Application
Isaiah Abu Moses	PS1.06	(Student) Structural and Electronic Properties of a New Class of Nanoporous Organic Nanocrystals
Habib Ahmad	PS1.07	(Student) Be Doping of Semi-Insulating GaN without Surface Accumulation Using MME
Ayush Pandey	PS1.08	(Student) On the Origin of Efficiency Droop of AlGaIn Deep Ultraviolet Light Emitting Diodes
Chen Yang	PS1.09	Normally-off GaN Vertical-Channel Junction Field-Effect Transistors with Regrown p-GaN by MOCVD
Mostafa Abdelhamid	PS1.10	(Student) Device Quality $\text{In}_x\text{Ga}_{x-1}\text{N}$ Templates ( $0.07 < x < 0.10$ ) for Optoelectronic Applications
Fiaz Ahmed	PS1.11	(Student) Hybrid QD/Nitride Photo-Detector with Visible/Infrared Response
Alan H Chu	PS1.12	Hybrid Magneto Photonic Material Structure for Plasmon Assisted Magnetic Switching
Michael Barrow	PS1.13	(Student) High Selectivity and High Aspect Ratio GaAs/AlGaAs Reactive Ion Etching with $\text{HBr}/\text{SF}_6/\text{He}$ and $\text{BCl}_3/\text{SF}_6/\text{He}$
Seth Kurfman	PS1.14	(Student) Electric-Field Control of Strain-Driven Tuning of FMR in $\text{V}[\text{TCNE}]_x$
Kevser Sahin Tiras	PS1.15	Identifying the Spin Mixing Mechanisms in Excitonic and Exciplex Organic Light Emitting Diodes
Benard D Kavey	PS1.16	(Student) Synthesis and Structural Characterization of Monodisperse Lanthanide Doped Titanium-Containing Perovskites for Optoelectronic and Thin-Film Applications
Jen-Chun Fang	PS1.17	Micro-/Nano-Voids Guided Two-Stage Film Cracking on Bioinspired Assemblies for High-Performance Electronics
Elena Cimpoiasu	PS1.18	Charge Scattering Mechanisms in Shallow InAs Quantum Wells
Deidra Hodges	PS1.19	Synchrotron and Optical Probing of Mixed Lead Halide Perovskites for Photovoltaics
Thomas Debesay	PS1.20	(Student) I2 Dopant Induced Charge Carrier Mobility Enhancement in Organic Field-Effect Transistors (OFETs)
Wafaa Farag Gebriel	PS1.21	(Student) Colloidal Quantum Dots Photodetectors and their Performance Enhancement with the Plasmonic Effect of Silver Nanoparticles
Benjamin Davis	PS1.22	(Student) Atomic Layer Deposited Metal Oxide Bilayers for Metal-Insulator-Semiconductor Photovoltaics
Ben M Garland	PS1.23	(Student) Exploiting Fixed Charge at Selective Contacts to Control Schottky Barrier Height for Silicon Photovoltaics
Parsian Mohseni	PS1.24	(LATE NEWS) Toward III-V-on-Si Tandem-Junction Solar Cells Using Selective-Area Epitaxial Growth of GaAsP Nanowire Arrays

# PS2: POSTER SESSION II

THURSDAY AM

10:00 am - 11:15 am  
Poster Session 2

Presenter	Paper #	Title
Dawoon Lee	PS2.01	(Student) High Performance Micro-Supercapacitor via Hybrid-Curable Ion-Gel Electrolyte and Laser-Reduced Graphene Electrode for Flexible Energy Storage Devices
Vinamrita Singh	PS2.02	Investigation of Two-Dimensional MoS <sub>2</sub> Based Ultra-Thin Solar Cells
Kishan LAL Kumawat	PS2.03	(Student) Solution Processed SnSe <sub>2</sub> -RGO Composite Hybrid Bulk Heterojunction for Self-Powered Visible IR Broadband Photodetection
Fenghongkang Pan	PS2.04	(Student) Atomic Fe-Ni Bimetallic Sites Boosting Electrocatalytic Oxygen Evolution Reaction
Habib Ahmad	PS2.05	(Student) Extensive Study of Ga-Coverage in UID Regrown GaN by MBE
Masakazu Kobayashi	PS2.06	Orientation Control of ZnTe Epilayers Using the Nano-Faceted and Tilted Sapphire Substrate
Jessica Hendricks	PS2.07	(Student) A Study of Defects in $\beta$ -Ga <sub>2</sub> O <sub>3</sub> Using Admittance Spectroscopy Techniques
Ilgyu Choi	PS2.08	(Student) Spatial Alignment of High-Crystalline InN Nanowires by Applying Magnetic Field
Masamichi Akazawa	PS2.09	Impact of Cap-Layer Materials Used in Long-Term Low-Temperature Annealing on Electrical Properties of Mg-Ion Implanted GaN
Nidhi Puri	PS2.10	(Student) Enhanced Thermoelectric Behavior in Fully Dense Hot Pressed Pellet of Nanostructured Calcium Cobalt Oxide
Alexandra M Boyadzhiev	PS2.11	(Student) High Quality Growth of Magnesium Aluminum Ferrite by Molecular Beam Epitaxy
Youngkyun Kim	PS2.12	(Student) Highly Transparent and Flexible Patterned Ion-Gel Based Triboelectric Nanogenerator for Tactile Sensing Application
Seohyun Maeng	PS2.13	(Student) Large-Area, Free-Standing and Transparent MoS <sub>2</sub> /Ion-Gel Hybrid Films for High-Sensitivity Low-Power Photodetection
Manjri Singh	PS2.14	(Student) Light Sensitive Resistive Memory Behaviour in ZnO/rGO Heterostructure Device
Edward Stockert	PS2.15	Van der Waals Epitaxy of Two-Dimensional Noble Metal Diselenides on III Nitride Semiconductors
Jung Suk Cha	PS2.16	(Student) Electrical Properties of High Barrier-Height Au/NiZn Solid Solution Schottky Contact on Semipolar [20-21] n-GaN for Electronic Devices
Samuel Kim	PS2.17	(Student) Thermal Management of $\beta$ -Ga <sub>2</sub> O <sub>3</sub> Current Aperture Vertical Electron Transistors
Philip M Jean-Remy	PS2.18	(Student) Thermodynamic Phase Diagram Calculations for the Chemical Vapor Deposition of Hexagonal Boron Nitride Using Triethylboron, Ammonia and Hydrogen
Corey L Arnold	PS2.19	(Student) Room Temperature Growth and Investigation of Electrical Properties of Amorphous Boron Nitride
Qi Wang	PS2.20	(Student) Resistive Memory with Perovskite Nickelates
Muhammad Shehzad Sultan	PS2.21	Superparamagnetic Properties of Metal-Free Nitrogen Doped Graphene Quantum Dots Synthesized by Pulsed Laser Ablation
Vamseedhara Vemuri	PS2.22	(Student) Al and Hf Based Metalcones—Inducing Porosity in Nano-Laminate Thin Films
Drake Austin	PS2.23	Laser-Writing of Electronic Circuitry in Thin-Film Molybdenum Disulfide
Makhes Kumar Behera	PS2.24	Low Powered Smart Window Device Based on a Stoichiometrically Downgraded Multi-Layer Structure from VO <sub>2</sub> Thin Films Grown Using Pulsed Laser Deposition

# PROGRAM AT-A-GLANCE

THURSDAY

N: Defect and Contacts in WB Semiconductors			ZoomRoom 1
11:45 am	Niranjan S	N01	(Student) Au-Free Recessed Ohmic Contacts to AlGaIn/GaN HEMT—Study of Etch Chemistry, Metal Schemes and Carrier Transport Mechanism
12:00 pm	Daram N Ramdin	N02	(Student) Ir and Native Deep Level Defects in Fe, Mg, and Si-Doped Edge-Fed Grown Ga <sub>2</sub> O <sub>3</sub>
12:15 pm	Rujun Sun	N03	Chromium Origins of Red Luminescence from Iron-Doped Ga <sub>2</sub> O <sub>3</sub> Bulk Crystals and Its Applications
12:30 pm	Intuon Chatratin	N04	(Student) Optical Properties of Acceptor Impurities in Ga <sub>2</sub> O <sub>3</sub>
12:45 pm	Leila Ghadbeigi	N05	Optical Properties of β-Ga <sub>2</sub> O <sub>3</sub> and Comparison with β-Ga <sub>2</sub> O <sub>3</sub>
1:00 pm			BREAK
2:00 pm	Md Mohsinur Rahman Adnan	N06	(Student) Bias-Dependent Exciton Stark Shift and Franz-Keldysh Effect in β-Ga <sub>2</sub> O <sub>3</sub> Sub-Bandgap Photoresponse
2:15 pm	Ming-Hsun Lee	N07	(Student) Process Influence on the Performance and Aging Stability of Ti/Au Ohmic Contacts to Beta-Phase Gallium Oxide
2:30 pm	Arkka Bhattacharyya	N08	(Student) Selective Area Regrown Low Resistance Ohmic Contacts on β-Ga <sub>2</sub> O <sub>3</sub> Epitaxial Layers Using Metalorganic Vapor Phase Epitaxy
O: Fabrication, Processing and Integration			ZoomRoom 2
11:45 am	Xiuling Li	001	MacEtch Produces Damage-Free High-Aspect-Ratio Semiconductor Nanostructures—Current Status and Future Promise
12:00 pm	Parsian Mohseni	002	Fabrication of Vertical Si Micropillar Arrays by Carbon Nanotube-Assisted Chemical Etching
12:15 pm	Michael Barrow	003	(Student) Through-Wafer GaAs Vias for Heterogeneous Device Integration
12:30 pm	Emine Cagin	004	Ultrahigh-Resolution Nanolithography Using Silicon-Enriched Thermal Resists and Thermal Scanning Probe Lithography
12:45 pm	Robert Coridan	005	Photoelectrochemical Lithography—Spatial Control of Galvanic Replacement Reactions on Photoelectrodeposited Cuprous Oxide
1:00 pm			BREAK
2:00 pm	Brelon James May	006	Molecular Beam Epitaxy of NaCl Layers on GaAs for Substrate Recycling
2:15 pm	Sora Lee	007	(Student) High-Temperature Capable ALD-Based Inorganic Lift-Off Process
2:30 pm	Jideofor A. H. Odoeze	008	High-Quality InP Wet Thermal Oxides Grown Using Dissociation-Suppressing Ultrathin ALD Films
2:45 pm	Emma J. Renteria	009	Interaction of Ammonium Sulfide with the Semiconductor Surfaces of AISb and Related Alloys
3:00 pm	Jihwan Lee	010	(Student) Silicidation—A Low Temperature Route for Vertical Intracellular Nanowire Array Integration on CMOS Devices
P: III-Nitride Power Devices Utilizing Oxides			ZoomRoom 3
11:45 am	Elia Palmese	P01	(Student) AlInN-GaN Based Power Electronic Devices Utilizing AlInO as a Gate Insulator
12:00 pm	Wenjian Liu	P02	Analysis of the Bulk and Interfacial Properties of AlSiO Grown on N-Polar GaN
12:15 pm	Sang-Woo Han	P03	ALD AlON on a-Plane GaN with Extremely Low Interface Trap Density
12:30 pm	Geoffrey Foster	P04	Recovery of Sidewall Etch Damage in p-Type Gallium Nitride
12:45 pm	Mohammad Wahidur Rahman	P05	(Student) Reverse Breakdown Field and Interface Properties of Metal/BaTiO <sub>3</sub> /GaN Junctions
1:00 pm			BREAK
Q: III-Nitrides – Photodetectors			ZoomRoom 3
2:00 pm	Anisha Kalra	Q01	(Student) Microstructure-Defect-Device Performance Correlation for Solar-Blind Al <sub>0.45</sub> Ga <sub>0.55</sub> N Schottky Photodetectors on Sapphire
2:15 pm	Shashwat Rathkanthiwar	Q02	(Student) Evidence of Surface Pits-Induced Photo-Response Enhancement in High Responsivity Al <sub>0.25</sub> Ga <sub>0.75</sub> N UV-B Photodetectors on Si (111)
2:30 pm	Hoon Jeong	Q03	(Student) Geiger-Mode Operation of Gallium Nitride p-i-n Avalanche Photodiodes and Histogram Fitting Measurement
2:45 pm	Emma Rocco	Q04	(Student) Oxygen Impurity Incorporation Due to Growth Interruption and Its Diffusion from These Interfaces in N-Polar GaN:Mg Films Grown by MOCVD and Its Implication in Photocathode Device Characteristics
3:00 pm	Marzieh Bakhtyari-Noodeh	Q05	(Student) Homojunction GaN p-i-n Ultraviolet Avalanche Photodiodes Using Ion-Implantation Isolation

R: Metal Dichalcogenides			ZoomRoom 4
11:45 am	Anil Mane	R01	Growth and Interface Engineering of MoS <sub>2</sub>
12:00 pm	Neha Mohta	R02	Mem-Transistor and Artificial Synapse Based on 2D Ferroelectric $\alpha$ -In <sub>2</sub> Se <sub>3</sub>
12:15 pm	Shahzad Ahmad	R03	Analytical Calculation of Strained Binding Energy in Monolayer MoS <sub>2</sub>
12:30 pm	Corey L Arnold	R04	(Student) Growth and Extrinsic P-Type Doping of Pulsed Laser Deposited Few Layer WS <sub>2</sub> Films
12:45 pm	Neha Mohta	R05	Artificial Synapse Based on Back-Gated MoS <sub>2</sub> FET with High-k Ta <sub>2</sub> O <sub>5</sub> Dielectric
1:00 pm			BREAK
2:00 pm	Martha I Serna	R06	MoS <sub>2</sub> and WS <sub>2</sub> Films Synthesized by One-step Low-Temperature Sulfurization for RRAM Devices Applications
2:15 pm	Sayema Chowdhury	R07	(Student) Large-Area Metal Organic Chemical Vapor Deposition Growth of Few Layer MoS <sub>2</sub> and Its Controlled Sulfurization to Monolayer MoS <sub>2</sub>
2:30 pm	Samuel Berweger	R08	Spatially Resolved Photoconductivity Imaging in MoS <sub>2</sub> /WS <sub>2</sub> Lateral Heterostructures
2:45 pm	Tanushree H. Choudhury	R09	Impact of Plasma Induced Defects in Epitaxial Graphene on Growth of WS <sub>2</sub>
3:00 pm	Ihteyaz Aqaeed Avash	R10	(Student) Growth of Manganese (IV) Selenide on Epitaxial Graphene by Thermal Vapor Selenification of Electrodeposited $\delta$ -Phase Manganese (IV) Oxide
S: Materials for Memory and Computation			ZoomRoom 5
11:45 am	Furqan Mehmood	S01	(Student) Temperature Dependent Wake-Up Effect in Ferroelectric La Doped Hf <sub>0.5</sub> Zr <sub>0.5</sub> O <sub>2</sub> Thin Films
12:00 pm	Aheli Ghosh	S02	(Student) Understanding the Origin of Non-Volatile Programming in LiNbO <sub>2</sub> Memristors via Electrochemical Impedance Spectroscopy (EIS)
12:15 pm	Mark E. Twigg	S03	Reduction Reactions and Phase Transformations in Nb <sub>2</sub> O <sub>5</sub> Films Deposited by Atomic Layer Deposition
12:30 pm	Rafael Jaramillo	S04	Photoconductivity without Photons—Defect Level Switching for Highly-Nonlinear and Hysteretic Electronic Devices
12:45 pm	Maria Patmiou	S05	(Student) Percolation with Plasticity (PWP) Materials for Multi-Valued Memory
1:00 pm			BREAK
T: Electronic Materials for Bio			ZoomRoom 5
2:00 pm	Keundong Lee	T01	A Hybrid Multimodal Surface-Depth Electrode for Electrophysiological and Multi-Photon Brain Activity Mapping
2:15 pm	Paul Bertani	T02	(Student) GaN-Based Immuno-FETs for Cyanobacterial Toxin Detection for Environmental Monitoring and Clinical Applications
2:30 pm	Youngbin Tchoe	T03	Scaling Microelectrode Arrays for Multi-Thousand Channel Human Brain Mapping
2:45 pm	Samantha Maria Russman	T04	(Student) Recording Electrophysiological Activity from the Human Spinal Cord for Neuromonitoring During Surgical Resection
U: Solar Cell Materials and Devices			ZoomRoom 6
11:45 am	Mijung Kim	U01	(Student) Effects of Rapid Thermal Annealing on Metamorphic InGaAs and InGaP Grown by Molecular Beam Epitaxy
12:00 pm	Daniel L Lepkowski	U02	(Student) Theoretical Evaluation of DBR Structures for Improving Tolerance to Threading Dislocations in GaAsP/Si Tandem Solar Cells
12:15 pm	Brian Li	U03	(Student) Control of Te Doping for InGaP Solar Cells Grown by MBE
12:30 pm	Jacob Tyler Boyer	U04	(Student) Development of Low-TDD GaP/Si Virtual Substrates via Correlation of Dislocation Dynamics, Electron Channeling Contrast Imaging and MOCVD Growth
12:45 pm	Sara Pouladi	U05	(Student) Passivation of Low-Angle Grain Boundaries in Single-Crystal-Like GaAs Flexible Thin-Film Solar Cells on Metal Tape for Significant Improvement of Conversion Efficiency
1:00 pm			BREAK
2:00 pm	Barys Korzun	U06	Preparation of Alloys and Investigation of Phase Equilibria in the CuFeS <sub>2</sub> - $\delta$ – CuGaS <sub>2</sub> System
2:15 pm	Michael Francis Miller	U07	(Student) Impact of K-Optimization on Trap Concentrations in ACIGS Solar Cells
2:30 pm	Kaden Powell	U08	(Student) Photovoltaic Response of Thin-Film CdTe Solar Cells under Accelerated Neutron Radiation in a TRIGA Reactor
2:45 pm	Eric Chen	U09	Enhanced Photon Recycling with Energy-Selective Front Reflectors for High-Efficiency GaAs Laser Power Converters

# PROGRAM AT-A-GLANCE

THURSDAY

V: Ga <sub>2</sub> O <sub>3</sub> —Growth, Characterization and Defects II			ZoomRoom 1
3:45 pm	A F M Anhar Uddin Bhuiyan	V01	(Student) MOCVD Growth, Characterization and Phase Transformation of (Al <sub>x</sub> Ga <sub>1-x</sub> ) <sub>2</sub> O <sub>3</sub> Thin Films
4:00 pm	Brian Andrew Eisner	V02	(Student) Characterization of β-Ga <sub>2</sub> O <sub>3</sub> MOVPE Homoepitaxial Thin Films Grown on (-201) and (010) Substrates—Charge Compensation and Depletion in (-201) Films
4:15 pm	Thaddeus James Asel	V03	β-Ga <sub>2</sub> O <sub>3</sub> Films with Low Si Doping Density Grown Via Plasma-Assisted Molecular Beam Epitaxy
4:30 pm	Jacqueline Cooke	V04	(Student) Synthesis and Characterization of Large-Area Nanometer-Thin β-Ga <sub>2</sub> O <sub>3</sub> Films from Oxide Printing of Liquid Metal Gallium
4:45 pm	Zixuan Feng	V05	(Student) Probing Charge Transport and Background Doping in MOCVD Grown (010) β-Ga <sub>2</sub> O <sub>3</sub>
5:00 pm			BREAK
5:30 pm	Rujun Sun	V06	Defects Properties of Czochralski Grown Zr-Doped Ga <sub>2</sub> O <sub>3</sub> by Deep Level Transient Spectroscopy and Photoluminescence
5:45 pm	Elan Weiss	V07	(Student) <i>Ab Initio</i> Computation of Chemical Potentials in β-Ga <sub>2</sub> O <sub>3</sub> for Examining Intrinsic Point Defects, Charge Neutrality and Self-Doping
6:00 pm	Jossue Montes	V08	(Student) Deep Level Transient Spectroscopy Analysis of Ultra-Wide Bandgap β-Ga <sub>2</sub> O <sub>3</sub>
6:15 pm	Hemant Jagannath Ghadi	V09	Growth Temperature Dependence of Electronic Defect States in High-Mobility MOCVD-Grown (010) β-Ga <sub>2</sub> O <sub>3</sub>
6:30 pm	Joe F McGlone	V10	Proton Radiation Effects on Electronic Defect States in High-Mobility MOCVD-Grown (010) β-Ga <sub>2</sub> O <sub>3</sub>
W: Electrochemical Energy Storage and Conversion			ZoomRoom 2
3:45 pm	Lalith Rao	W01	(Student) Development of Thick Cathodes for High-Energy Lithium-Ion Batteries
4:00 pm	Michael Lee	W02	(Student) <i>In Operando</i> AFM Characterization of Mechanical Property Evolution of Si Anode Binders in Liquid Electrolyte
4:15 pm	Eric Wolfson	W03	(Student) Dehydrobenzoannulene-Based Two-Dimensional Covalent Organic Frameworks as an Anode Material for Lithium-Ion Batteries
4:30 pm	Yuanyue Liu	W04	Elucidating the Atomistic Catalytic Mechanism of Single Ni Atom in N-Doped Graphene for CO <sub>2</sub> Reduction
4:45 pm	Chloe Groome	W05	(Student) First Principles Investigation of the Influence of Magnetic Moment for Design of Integrated 3D Graphene Structures with Earth-Abundant Transition Metal Single Atom Catalysts
5:00 pm			BREAK
5:30 pm	Alexander Vaeth	W06	(Student) New Materials for Extreme Environmental Sensors Based on Solid Oxide Fuel Cells
5:45 pm	Christopher Grieco	W07	Eumelanin in a New Light—Biological Pigments with the Excited State Behavior of Graphitic Carbonaceous Nanomaterials
X: III-Nitride MBE and Sputtering Growth			ZoomRoom 3
3:45 pm	Habib Ahmad	X01	(Student) Impact of Substrate Temperature for High Quality Regrown GaN Homoepitaxial Films Grown by Metal Modulated Epitaxy
4:00 pm	Zachary Engel	X02	Advancements in Aluminum Indium Nitride Growth over a Wide Compositional Range—Towards Long Wavelength III-Nitride Optoelectronics
4:15 pm	Ping Wang	X03	Molecular Beam Epitaxy and Characterization of Wurtzite Sc <sub>x</sub> Al <sub>1-x</sub> N
4:30 pm	John Cetnar	X04	Structural, Optical and Electronic Transport Properties of (111) ScN Thin Films Grown on (0001) Fe-Doped GaN, (0001) Al <sub>2</sub> O <sub>3</sub> and (111) MgO
4:45 pm	Kamruzzaman Khan	X05	(LATE NEWS, Student) Epitaxial Growth of III-Nitrides on O-Face ZnO Substrates by Low Temperature RF-Metal Enhanced Epitaxy (MEE)
5:00 pm			BREAK
Y: III-Nitrides—HEMTs			ZoomRoom 3
5:30 pm	Towhidur Razzak	Y01	(Student) Low-Field Transport in High Al-Composition Al <sub>x</sub> Ga <sub>1-x</sub> N Channel High Electron Mobility Transistors
5:45 pm	Sandra M Diez Pinzon	Y02	(Student) N-Polar AlN/GaN Superlattice Heterostructure with Record Electron Mobility of 2050 cm <sup>2</sup> /Vs Grown on GaN Substrate by Plasma-Assisted Molecular Beam Epitaxy
6:00 pm	Weijie Wang	Y03	Active Polarization Engineering in AlGaIn/GaN High-Electron-Mobility Transistors to Modulate Two-Dimensional Electron Gas Density by Piezoelectric Cap Layer and External Bending Strain
6:15 pm	Subhajit Mohanty	Y04	(LATE NEWS, Student) Design of Ultra-Scaled Channel N-Polar GaN HEMTs with High Charge Density Using AlN-GaN Superlattice as the Backbarrier

Z: Nanophotonic Materials			ZoomRoom 4
3:45 pm	Zhengtianye Wang	Z01	(Student) Plasmonic Coupling in Topological Insulator and Band Insulator Layered Structure
4:00 pm	Zuoming Dong	Z02	(Student) Degenerate Semiconductor Interfaces for Electro-Optic Modulation of Mid-IR Surface Plasmons
4:15 pm	Alec Mason Skipper	Z03	(Student) Epitaxially Embedded Mid-Infrared Plasmonic Corrugations
4:30 pm	Yong Wang	Z04	Propagating Dirac Plasmon Polaritons in Topological Insulators
4:45 pm	Hassan Dibaji	Z05	(Student) Self-Winding Helices as Slow-Wave Structures for THz Frequencies
5:00 pm			BREAK
5:30 pm	Yuejing Wang	Z06	(Student) Towards Achieving Self-Assembled Hyperbolic Metamaterials in the Short to Mid-Wave Infrared Spectral Range
5:45 pm	Kurt Eyink	Z07	Controlled Dewetting and Regrowth of Composite ErAs NP–GaAs(001) Interfaces
6:00 pm	Andrej Lenert	Z08	Infrared Plasmonic Oxides for Selectively Transparent Aerogels in High Temperature Solar Receivers
6:15 pm	Irfan Khan	Z09	(Student) Anomalous Mid-Infrared Absorption in Near-Monolayer Films of ZnO Nanoparticles
6:30 pm	W-D. Zhang	Z10	Effect of MBE Growth Conditions on the Resonant-Absorption of ErAs Quantum Dots Near 1550 nm
AA: Wide Bandgap Materials—Silicon Carbide and Diamond			ZoomRoom 5
3:45 pm	Wei Fan	AA01	Improving SiC Crystal Growth and Epitaxial Deposition with Tantalum Carbide Protection Coating
4:00 pm	Tuerxun Ailihumaer	AA02	(Student) Synchrotron X-Ray Topography Study on Dislocation Behavior in Early-Grown 4H-SiC Single Crystals
4:15 pm	Peter L Bonanno	AA03	Double-Sided Half-Loop Arrays Caused by Frank-Read Sources in 4H-SiC
4:30 pm	Qianyu Cheng	AA04	(Student) Characterization of Dislocations on 6H-SiC through X-Ray Topography and Ray-Tracing Simulation
4:45 pm	Michael Spencer	AA05	Growth of High Purity Zone-Refined Boron Carbide Single Crystals by Laser Diode Floating Zone Method
5:00 pm			BREAK
5:30 pm	Tingyu Bai	AA06	Diamond Seed Size and the Impact on the Chemical Vapor Deposition of Diamond Thin-Film Properties
5:45 pm	Lillian Barrett Hughes	AA07	(Student) Understanding the Inhomogeneous Incorporation of Nitrogen in $\delta$ -Doped CVD Diamond Using Spatially Resolved Microanalysis
6:00 pm	A. Glen Birdwell	AA08	Kelvin Probe and Constant Final State Yield Spectroscopy Measurements on Hydrogen Terminated Diamond
6:15 pm	Edward Swinnich	AA09	$\beta$ -Ga <sub>2</sub> O <sub>3</sub> Nanomembrane and Diamond P-N Heterojunction Integrated with Oxide Quantum Tunneling Layer
6:30 pm	Henry Aller	AA10	Thermal Transport across Ga <sub>2</sub> O <sub>3</sub> /Metal Contact Interfaces—Characterization and Time-Evolution
BB: Point Defects, Doping and Extended Defects			ZoomRoom 6
4:00 pm	Hsien-Lien Huang	BB01	(Student) Atomic Distribution of Al and Phase Transformation in $\beta$ -(Al <sub>x</sub> Ga <sub>1-x</sub> ) <sub>2</sub> O <sub>3</sub>
4:15 pm	Chunyi Huang	BB02	(Student) Atom Probe Tomography of Modulation-Doped Branched Nanowires for Quantum Computing
4:30 pm	Ziling Deng	BB03	(Student) Structural and Electronic Properties of Native Point Defects in MoTe <sub>2</sub>
4:45 pm	Sevim Polat Genlik	BB04	(Student) Dislocations as Topological Wires and Magnets
5:00 pm			BREAK
5:30 pm	Shuyan Zhang	BB05	(Student) Structure and Energetics of Point Defects in Titanium Dioxide
5:45 pm	Brenton A Noesges	BB06	(Student) Defects Near Stoichiometric and Non-Stoichiometric Interfaces in Sr <sub>1-x</sub> TiO <sub>3</sub> Homoepitaxial Thin Films
6:00 pm	Hantian Gao	BB07	(Student) Direct, Spatially-Resolved Observation of Defect States with Electromigration and Degradation of Single Crystal SrTiO <sub>3</sub>
6:15 pm	Zhen Zhang	BB08	Oxygen Vacancy Driven Carrier Localization in Strongly Correlated Rare-Earth Nickelates
6:30 pm	Kapil Sharma	BB09	Role of Hydrogen in Wide-Bandgap Oxides— <i>Ab-Initio</i> Study of Crystalline/Amorphous In <sub>2</sub> O <sub>3-x</sub> :H Interfaces

# PROGRAM AT-A-GLANCE

FRIDAY

CC: $\beta$ -Ga <sub>2</sub> O <sub>3</sub> Devices			ZoomRoom 1
10:00 am	Chia-Hung Lin	CC01	Fabrication of Vertical Schottky Barrier Diodes on $\beta$ -Ga <sub>2</sub> O <sub>3</sub> Substrates Prepared by Vertical Bridgman Method
10:15 am	Cheolhee Cho	CC02	(Student) Bias-Temperature Instability Measurement of $\beta$ -Ga <sub>2</sub> O <sub>3</sub> /h-BN MISFETs
10:30 am	Nidhin Kurian Kalarickal	CC03	(Student) $\beta$ -Ga <sub>2</sub> O <sub>3</sub> /BaTiO <sub>3</sub> MESFET with Power Figure of Merit of 376 MW/cm <sup>2</sup>
10:45 am	Praneeth Ranga	CC04	(Student) High-Density Degenerate Electron Gas (10 <sup>13</sup> cm <sup>-2</sup> ) in $\beta$ -(Al <sub>x</sub> Ga <sub>1-x</sub> ) <sub>2</sub> O <sub>3</sub> / $\beta$ -Ga <sub>2</sub> O <sub>3</sub> Heterostructures Grown By Metalorganic Vapor Phase Epitaxy
11:00 am	Evan Michael Cornuelle	CC05	(Student) Exploring Ga <sub>2</sub> O <sub>3</sub> /(Al <sub>x</sub> Ga <sub>1-x</sub> ) <sub>2</sub> O <sub>3</sub> Resonant Tunnel Diode Heterostructures
11:15 am			BREAK
11:45 am	Wenshen Li	CC06	(Student) Observation of Near-Ideal Reverse Leakage Current in $\beta$ -Ga <sub>2</sub> O <sub>3</sub> Schottky Barrier Diodes and Its Implications for High Electric-Field Operation
12:00 pm	Chaker Fares	CC07	(Student) Effect of Annealing on the Band Alignment of ALD SiO <sub>2</sub> on (Al <sub>x</sub> Ga <sub>1-x</sub> ) <sub>2</sub> O <sub>3</sub> for x= 0.2 - 0.65
12:15 pm	Caixia Hou	CC08	Very High Temperature (500 °C) Operating Performance of PtO <sub>x</sub> , IrO <sub>x</sub> , PdO <sub>x</sub> , and RuO <sub>x</sub> Schottky Contacts on $\beta$ -Ga <sub>2</sub> O <sub>3</sub>
12:30 pm	Minghan Xian	CC09	(Student) Effect of Contact Geometry on Forward Bias Failure in $\beta$ -Ga <sub>2</sub> O <sub>3</sub> Schottky Rectifiers
12:45 pm	Luke Andrew McClure Lyle	CC10	Electrical Behavior of Schottky Contacts to (100) $\beta$ -Ga <sub>2</sub> O <sub>3</sub>
DD: Thermoelectrics and Energy Harvesting			ZoomRoom 2
10:30 am	Sho Aonuki	DD01	(Student) Atomic Hydrogen Passivation for Marked Photoresponsivity Improvement of As-Doped n-BaSi <sub>2</sub> Films
10:45 am	Madhubanti Mukherjee	DD02	(Student) High Thermoelectric Figure of Merit via Tunable Valley Convergence Coupled Low Thermal Conductivity in A <sup>II</sup> B <sup>VI</sup> C <sub>2</sub> Chalcopyrites
11:00 am	Madhubanti Mukherjee	DD03	(Student) Strong Chemical Bond Hierarchy Leading to Exceptionally High Thermoelectric Figure of Merit in Oxychalcogenide AgBiTeO
11:15 am			BREAK
11:45 am	Marat Khafizov	DD04	Thermal Transport Measurements and Amorphization Studies in Sapphire Irradiated by Swift Heavy Ions
12:00 pm	Dung Dinh Vu	DD05	(Student) Experimental Techniques to Measure Thermal Hall Effect
12:15 pm	Henry Aller	DD06	Optimizing Top-Side Device Cooling via Metal/Nanocrystalline Diamond Interfaces
12:30 pm	Kasey Hogan	DD07	(Student) <i>In Operando</i> Investigation of GaN PIN Device Characteristics under Electron Irradiation Energies Comparable to Pm-147 Source for Betavoltaic Application
12:45 pm	Jerry M Woodall	DD08	The Al-Si Eutectic as a Phase Change Material for Storing Intermittent Solar Power
EE: Hexagonal Boron Nitride and Graphene			ZoomRoom 3
10:00 am	Jae-Keun Kim	EE01	(Student) Analysis of the Effect of Surface Charge Transfer Doping on Charge Transport of WSe <sub>2</sub>
10:15 am	Samuel T White	EE02	(Student) Modulating hBN and Other 2D Materials with the Vanadium Dioxide Phase Transition
10:30 am	Yanwei He	EE03	Engineering Ni Substrate toward High Quality Two-Dimensional Hexagonal Boron Nitride Films for Metal-Insulator-Metal Devices
10:45 am	Jeffrey Kronz	EE04	(Student) High Temperature Annealing of BN Films Grown from Borazine
11:00 am	Anushka Bansal	EE05	(Student) Impact of Sapphire Surface on High-Temperature CVD Growth of Crystalline Hexagonal Boron Nitride
11:15 am			BREAK
11:45 am	Michael A Susner	EE06	Precision Defect Engineering of Graphene for Applications Using Electron-Beam Chemistry with Radiolyzed Water
12:00 pm	Tawfiqur Rakib	EE07	(Student) An Efficient Electronic Structure Framework for Representing Moiré Patterns in Twisted Bilayer Graphene
12:15 pm	Abhinaba Sinha	EE08	Ballistic Graphene—A High Strain Piezoresistive Material
12:30 pm	Michael A Susner	EE09	Self-Assembled Ferroelectric Heterostructures in a van der Waals Gapped Metal Thiophosphate
12:45 pm	Siavash Rajabpour	EE10	(Student) Realizing Atomically Thin Group-III Metal and Nitride Alloys via Confinement Heteroepitaxy

FF: Thin Film Devices			ZoomRoom 4
10:00 am	Jaeyoung Kim	FF01	(Student) Investigation of Ambipolar Avalanche Breakdown in $\text{WSe}_2$ Field-Effect Transistors
GG: Oxides Materials and Devices			ZoomRoom 4
10:15 am	Jade Cowsky	GG01	(Student) Nanoscale Thickness-Dependent Doping of Indium Tin Oxide (ITO) Quantum Magnetoconductivity Films
10:30 am	Elaheh Kheirandish	GG02	(Student) Free Standing Quasi Two-Dimensional $\gamma\text{-Al}_2\text{O}_3$ Grown by Atomic Layer Deposition
10:45 am	Janine Walker	GG03	(Student) Semiconducting Oxides for Gas Sensing Applications
11:00 am	Sieun Chae	GG04	(Student) Rutile $\text{GeO}_2$ —An Ultra-Wide-Band-Gap Semiconductor for Power Electronics
11:15 am			BREAK
HH: ZnO-Based Contacts, Defects and Devices			ZoomRoom 5
10:30 am	Quark Yungung Chen	HH01	Enhanced Photoconductivity of $\text{ZnO}/\text{In}_2\text{O}_3$ Epitaxial Superlattices—Effects of the Heterojunction Interfaces
10:45 am	Boateng Onwona-Agyeman	HH02	Hydrothermal Synthesis and Characterization of Zinc Oxide Nano-Particles as Photoanode in Dye-Sensitized Solar Cell
11:00 am	Priyanka Karnati	HH03	(Student) Effect of Heterojunction Interface ( $\text{SnO}_2/\text{ZnO}$ ) on Gas Sensing Properties of Core-Shell Nanostructures
11:15 am			BREAK
11:45 am	Micah Haseman	HH04	(Student) Defect Migration and Ohmic to Schottky Contacts in ZnO Nanowires
12:00 pm	Sagar R Bhalerao	HH05	Solution Processed Indium Gallium Zinc Oxide (IGZO) Thin-Film Transistors Operating at 2.0 Volt
12:15 pm	Ritwik Vatsyayan	HH06	(Student) A Comprehensive a-IGZO TFT Device Model and Analog Circuit Validation
12:30 pm	Christopher Allemang	HH07	(Student) Atomic Layer Deposition of Zinc-Tin-Oxide for High Field-Effect Mobility Films
12:45 pm	Jie Zhang	HH08	(LATE NEWS, Student) Ionic Doping of $\text{TiO}_2$ Thin-Film Transistors Using Superacid Treatment
II: Organic Devices and Molecular Electronics			ZoomRoom 6
10:15 am	Nobuo Sasaki	II01	A {100}-Oriented Si Thin-Films Grown on Polyimide by the CW Laser Crystallization
10:30 am	Jaeho Shin	II02	(Student) Highly Tunable Molecular Rectifier Realized by Interfacial Design in Molecular Heterojunction with Two-Dimensional Materials
10:45 am	Heebeom Ahn	II03	(Student) Organo-Metal Halide Perovskite Resistive Memory in a Cross-Bar Array Achieved by Single-Step Solution Process
11:00 am	Fiheon Imroze	II04	(Student) Investigation of the Influence of Cross-Linker of Polymer Dielectric on the Cut-Off Frequency of Organic-Metal-Insulator Semiconductor Capacitors
11:15 am			BREAK
11:45 am	Raj Kishen Radha Krishnan	II05	(Student) Doped Organic Transistors at Ultra-Low Doping Concentrations
12:00 pm	Karla Adriana Gonzalez-Serrano	II06	(Student) Electrical Properties of Spin-Coated Polyethylene Oxide Capacitors as Thin as 8 nm
12:15 pm	Evan K Wujcik	II07	Ultra-Stretchable Conductive Polymer Complex with Excellent Linearity and Repeatable Autonomous Self-Healing Ability
12:30 pm	Joseph Reczek	II08	Direct Re-Writeable Control of Optical Polarization and Functional Properties in Modular Donor-Acceptor Columnar Liquid Crystalline Films
12:45 pm	Sunghwan Lee	II09	Crystallization, Carrier Transport and Device Performance of Vapor-Deposited Conjugated Polymers

## UPDATE YOUR EMAIL PREFERENCES

### DON'T MISS OUT ON:

- ▶ Calls for Papers for EMC, DRC and other Materials-related Conferences
- ▶ Late News Abstract Alerts
- ▶ Exhibit and Sponsorship Opportunities
- ▶ Registration News
- ▶ And More

**OPT IN TODAY!**  
[mrs.org/mymrs](https://mrs.org/mymrs)

# PROGRAM AT-A-GLANCE

FRIDAY

JJ: III-Nitrides – Processing				ZoomRoom 1
2:00 pm	Sai Charan Vanjari	JJ01	(Student) Sc-Based Ohmic Contacts to InAlN/GaN HEMT Structures	
2:15 pm	Clint Frye	JJ02	Ultrahigh GaN:SiO <sub>2</sub> Etch Selectivity by Addition of Al to a Cl <sub>2</sub> /Ar ICP Plasma	
2:30 pm	Emmanuel Kayede	JJ03	(Student) Demonstration of a Wet Etch for N-Polar GaN with >40:1 Selectivity to Al <sub>0.24</sub> Ga <sub>0.76</sub> N	
2:45 pm	Barbara Anna Kazanowska	JJ04	(Student) Chemical Wet Etching of AlGaIn Nanostructures	
3:00 pm	Jacob Leach	JJ05	Low Temperature, Au-Free Ohmic Contacts to n-GaN	
3:15 pm			BREAK	
KK: III-Nitrides – Defects and Characterization				ZoomRoom 1
3:45 pm	Ji Hyun Kim	KK01	(Student) Identification of Point Defects for the Full Compositional Range of Al <sub>x</sub> Ga <sub>1-x</sub> N (0 ≤ x ≤ 1) via Photoluminescence	
4:00 pm	Pegah Bagheri	KK02	(Student) Self-Compensation Management in Ge and Si Doped Al <sub>0.4</sub> Ga <sub>0.6</sub> N by Chemical Potential Control	
4:15 pm	Patrick Howard Carey	KK03	(Student) Improved Irradiation Hardness of High Aluminum Content AlGaIn Polarization Doped Field Effect Transistors	
4:30 pm	Yang Cao	KK04	(Student) Photoluminescence Study of Non-Polar m-Plane InGaIn and Near Strain-Balanced AlGaIn/InGaIn Superlattices	
4:45 pm	Darpan Verma	KK05	(Student) Electric Field Measurement Using Franz-Keldysh Photocurrent Spectroscopy in GaN Devices	
LL: Narrow Bandgap Materials and Devices				ZoomRoom 2
2:00 pm	Stephen D. March	LL01	(Student) Modeling and Measurement of Impact Ionization in Al <sub>x</sub> In <sub>1-x</sub> As <sub>y</sub> Sb <sub>1-y</sub> Digital Alloys	
2:15 pm	Ann Kathryn Rockwell	LL02	(Student) Temperature Stability of III-V Digital Alloy Bandgaps	
2:30 pm	Joshua Andrew McArthur	LL03	(Student) Characterizing the Optical and Electrical Properties of Al <sub>x</sub> In <sub>1-x</sub> As <sub>y</sub> Sb <sub>1-y</sub> Digital Alloys	
2:45 pm	Andrej Lenert	LL04	Leveraging Air-Bridge Architectures for Enhanced Spectral Utilization and Thermophotovoltaic Conversion Efficiency with In <sub>0.53</sub> Ga <sub>0.47</sub> As Cells	
3:00 pm	Patrick Taylor	LL05	MBE Growth of Doped Bi <sub>2</sub> Se <sub>3</sub> —Toward True Topological Insulators	
3:15 pm			BREAK	
3:45 pm	Minjoo Lawrence Lee	LL06	Metamorphic InAs on InP with Low Threading Dislocation Density	
4:00 pm	Ahmad Mansoori	LL07	Interfacial Misfit Dislocation Array Based Metamorphic Antimonide Buffers for Long-Wave IR Detectors	
4:15 pm	Yinan Wang	LL08	(Student) High-Speed Mid-Infrared Detection Using InSb-Pixel-Loaded Microwave Resonators	
4:30 pm	Scott D. Sifferman	LL09	(Student) Highly Strained, High Indium Content III-V Materials toward 4-Micron Type-I Emitters	
4:45 pm	Andrew Frederick Briggs	LL10	Comparison of Auger Recombination Across Material Systems with Externally Applied Biaxial Strain	
MM: III-Nitrides – Tunnel Junctions and InGaIn Growth				ZoomRoom 3
2:00 pm	Syed Mohammad Najib Hasan	MM01	(Student) Monolithic MOCVD-Grown III-Nitride Tunnel Junctions with Ultra-Low Resistance	
2:15 pm	Zane Ali Jamal-Eddine	MM02	(Student) Design of Fully Transparent Tunnel Junctions for Application in III-Nitride Optoelectronics	
2:30 pm	Xuanqi Huang	MM03	(Student) Carrier Localization and Dynamics of Nonpolar m-Plane InGaIn/GaN MQWs at Elevated Temperatures	
2:45 pm	Mostafa Abdelhamid	MM04	(Student) Growth, Characterization and Relaxation of In <sub>x</sub> Ga <sub>1-x</sub> N Templates and Their Impact on Multiple Quantum Wells	
3:00 pm	Zachary Engel	MM05	Al <sub>x</sub> Ga <sub>1-x</sub> N Homo Junction Tunnel Diodes with 0 ≤ x ≤ 58% —First Demonstration of Negative Differential Resistance in Al <sub>x</sub> Ga <sub>1-x</sub> N Homo Junction Tunnel Diodes and 110% Improvement in 275 nm UV-LED Output Power	
3:15 pm			BREAK	
NN: AlN and AlGaIn Growth				ZoomRoom 3
3:45 pm	Yuanpeng Wu	NN01	(Student) Controlling Defect Formation of AlN Nanostructures— Path towards Efficient Current Conduction of Ultrawide Bandgap Semiconductors	
4:00 pm	Shubhra S Pasayat	NN02	(Student) Growth of High Quality Crack-Free Partially Relaxed Thick Al <sub>0.24</sub> Ga <sub>0.76</sub> N on Porous GaN Based Compliant GaN Pseudo-Substrates	
4:15 pm	Yan Guan	NN03	(Student) Plastic Strain Relaxation of Ga-Rich AlGaIn on AlN Single Crystal Substrates	
4:30 pm	Jacob Leach	NN04	Low Temperature Hydride Assisted HVPE Growth of Single Crystal AlN Films	
4:45 pm	Abdullah Mamun	NN05	Crack and Strain Free 16-μm Thick AlN on Sapphire for the Thermal Management of III-N Electronics	

OO: Spintronic and Magnetic Materials and Devices			ZoomRoom 4
2:15 pm	Stephen Ross McMillan	0001	(Student) High-Temperature Probe of Coherent Evolution in Isolated Near-Surface Spin Centers through Resonance in Low-Field DC Magnetoresistance
2:30 pm	Ratnakar Palai	0002	Ferromagnetic Behavior in Rare Earth-Doped III-Nitride Semiconductors Grown by Molecular Beam Epitaxy
2:45 pm	Bradlee K Beauchamp	0003	Temperature-Dependent Magnetic Transitions of a CoCrPt-Ru-CoCrPt Synthetic Ferrimagnet
3:00 pm	Andrew Jacob Franson	0004	(Student) Low-Damping Ferromagnetic Resonance in Electron-Beam Patterned, High-Q Vanadium Tetracyanoethylene Magnon Cavities
3:15 pm			BREAK
3:45 pm	Huma Yusuf	0005	(Student) Tailoring Magnons for Applications in Quantum Information Science
4:00 pm	Yueguang Shi	0006	(Student) First Principles Calculation of the Electronic Structure of V(TCNE) <sub>2</sub>
4:15 pm	Denis R Candido	0007	Analytical Calculation of Fringe Fields and Magnetization Profiles in V(TCNE) <sub>x-2</sub> Cylindrical Disks
4:30 pm	Kwangyul Hu	0008	(Student) Magnon Modes of V(TCNE) <sub>x-2</sub> Magnonic Crystals
4:45 pm	Donley Cormode	0009	(Student) 3D Mode Engineering in Magnon Microresonators
PP: Novel Materials			ZoomRoom 5
2:00 pm	Henrik Sønsteby	PP01	Enabling Low-Temperature Epitaxy of Functional Complex Oxides
2:15 pm	Alexander J Bishop	PP02	(Student) Magnetic and Electronic Characterization of Magnetic Topological Insulator MnBi <sub>2</sub> Se <sub>4</sub>
2:30 pm	Benthara Hewage Dinushi Jayatunga	PP03	MOCVD Growth and Characterization of ZnSnN <sub>2</sub>
2:45 pm	Md Rezaul Karim	PP04	(Student) Metalorganic Chemical Vapor Deposition of ZnGeN <sub>2</sub> Films on GaN—Effects of Cation Stoichiometry on Surface Morphology and Crystallinity
3:00 pm	Brian Bennett Haidet	PP05	(Student) Nucleation of IV-VI Rocksalt PbSe and PbSnSe on (001) and (111) Oriented III-V Zincblende Substrates
3:15 pm			BREAK
QQ: Fundamental Issues in Epitaxy			ZoomRoom 5
3:45 pm	Ashlee Garcia	QQ01	(Student) Optimization of All-MBE Selective Area Epitaxial Overgrowth Method
4:00 pm	Alec Mason Skipper	QQ02	(Student) Monolithic Integration of Patterned Metal-Dielectric Stacks Overgrown with III-V Semiconductors by Molecular Beam Epitaxy
4:15 pm	Krystal Rose York	QQ03	(Student) Tuning Band Gap Energy through Controlled Disorder in Ternary Heterovalent Compounds
4:30 pm	Mark E. Twigg	QQ04	Phase Separation and Surface Diffusion in InGaAs
4:45 pm	Michael Evan Liao	QQ05	(Student) A Refined Model for Epitaxial Tilt of Epilayers Grown on Miscut Substrates
RR: Flexible, Printed and/or Dissolvable Thin Films or Nanomembranes			ZoomRoom 6
2:00 pm	Hongseok Oh	RR01	Scalable Normal and Shear Force Sensing Active-Matrix ZnO Thin-Film Transistors Array on Flexible Substrates for Slip and Grip Feedback in Closed-Loop Robotics
2:15 pm	Hyunwoo Choi	RR02	(Student) MoS <sub>2</sub> Suspended in Polythiophene Semiconductor Solutions for Inkjet-Printed Thin-Film Transistor Device Fabrication
2:30 pm	Andrew Bourhis	RR03	(Student) Leveraging Display IGZO TFT Technologies for High Definition Brain Mapping
2:45 pm	Nam-In Kim	RR04	(Student) Single-Crystalline III-N Thin-Film Piezoelectric Sensors for Various Applications
3:00 pm	Junyu Lai	RR05	(Student) Flexible Solar-Blind Photodetector Based on b-Ga <sub>2</sub> O <sub>3</sub> Nanomembranes
3:15 pm			BREAK
3:45 pm	Yixiong Zheng	RR06	(Student) Thermal Conductivity of b-Ga <sub>2</sub> O <sub>3</sub> Nanomembranes Using a Modified Micro-Raman Spectroscopy
4:00 pm	William Scheideler	RR07	Scalable Strategies for Fabricating Ultrathin Metal Oxides— Synergistic Improvements to Performance and Reliability of Perovskites Solar Cells and Transparent Transistors
4:15 pm	Sejung Kim	RR08	Nanomaterial Based Transparent and Flexible Gas Barrier Film Fabrication by Solution Process



# 62<sup>ND</sup> ELECTRONIC MATERIALS CONFERENCE

June 24-26, 2020

## WEDNESDAY ORAL PRESENTATIONS

# ELECTRONIC MATERIALS CONFERENCE

June 24 - June 26, 2020

\*\* Plenary Presentation

EMC Awards Ceremony and Plenary Session  
Session Chairs: Kris Bertness and Lisa Porter  
Session Hosts: Parsian Mohseni and Daniel Wasserman  
Wednesday Morning, June 24, 2020  
Location: ZoomRoom 1

## 10:00 AM AWARDS CEREMONY

### 10:10 AM \*\*PL01

**Epitaxial Growth and Properties of Atomically Thin Semiconductors—Moving Beyond Flakes** [Joan M. Redwing](#); The Pennsylvania State University, United States

The field of two-dimensional (2D) materials began with the advent of graphene but has expanded to a wide class of materials that occur naturally as van der Waals crystals. Within this class of materials, transition metal dichalcogenides (TMDs) have attracted significant interest in condensed matter physics and next generation electronics and optoelectronics. At the monolayer limit, the semiconducting TMDs (e.g., MX, where M = Mo, W and X = S, Se) exhibit direct band gaps within the visible range, large exciton binding energies and spin-valley polarization. Furthermore, TMD monolayers of different composition and twist angle can be stacked to form heterostructures and moiré superlattices with exotic properties.

The ability to fabricate TMD monolayers by exfoliation of bulk crystals using adhesive tape and stamps has made the field accessible to a wide range of researchers. However, current bulk crystals are limited in size and exfoliation of uniform monolayers is challenging, limiting developments in electronics and optoelectronic applications that require large area monolayers.

In this talk, I will discuss the prospects and challenges associated with the epitaxial growth of TMD monolayers and heterostructures for the development of wafer-scale 2D device technologies. Metalorganic chemical vapor deposition is highlighted as a promising approach which enables growth at high temperatures (>700°C) and large chalcogen overpressures which are needed to obtain stoichiometric epitaxial films. The unique aspects of van der Waals epitaxy of TMDs will be presented including the role of substrate defects, steps and surface passivation. Applications for TMD films in flexible electronics and optoelectronics, monolithic 3D integration and photonics will be reviewed.

## 11:00 AM BREAK

SESSION A: Devices and Materials for Memory Computation  
Session Chair: Angel Yanguas-Gil  
Session Hosts: Lincoln Lauhon and Ke Xu  
Wednesday Morning, June 24, 2020  
Location: ZoomRoom 1

### 11:30 AM A01

**MoS<sub>2</sub> Memtransistors for Neuromorphic Computing** [Vinod K. Sangwan](#), Hong-Sub Lee, Megan E. Beck and Mark C. Hersam; Northwestern University, United States

Advances in silicon-based digital electronics and neuroscience have spurred recent interest in neuromorphic computing. Since logic processing and memory are intimately connected, neuromorphic computing has the potential to overcome the von Neumann bottleneck. Hardware implementations for neuromorphic computing are based on the realization of bio-realistic response functions in solid-state and electrochemical devices. Toward this end, conventional bulk materials have been used extensively as artificial synaptic circuits. However, top-down growth and fabrication approaches have limited control over stoichiometry, architecture, and functionality. Bottom-up approaches in nanomaterials such as quantum dots, nanotubes, and two-dimensional (2D) monolayers enable novel device architectures and functions that better mimic a biological neuron.<sup>1</sup> In particular, 2D materials not only provide unprecedented control over materials stoichiometry and electrostatic control but are also compatible with wafer-scale integration.

In this talk, recent advances in neuromorphic devices based on 2D semiconductors and van der Waals heterojunctions will be discussed. For example, artificial synapses have been realized in multi-terminal

memtransistors (i.e., memristor + transistor) based on polycrystalline, sub-stoichiometric single-layer MoS<sub>2</sub> grown by chemical vapor deposition.<sup>2,4</sup> The internal resistance states of these devices are tuned by both biasing history and the field-effect from the gate terminal. The open channel architecture allows multiple electrodes that enable heterosynaptic plasticity that is a necessary ingredient for hyper-connectivity in neural networks. The operating mechanism is the dynamic tuning of the Schottky barrier height driven by defect-migration or charge trapping near the metal electrodes. Recently, a dual-gated memtransistor has been integrated in a crossbar array architecture where resistive switching is controlled by both bottom-gate and top-gate biases.<sup>5</sup> While the bottom-gate allows Hebbian and non-Hebbian learning responses, the top-gate allows independent addressing of nodes in the crossbar by minimizing the sneak currents that plague conventional memristive crossbar arrays. In this manner, dual-gated memtransistors present favorable pathways to high-density neuromorphic architectures.

## References:

1. Sangwan, V. K.; Hersam, M. C. Nat. Nanotech. (in press).
2. Sangwan, V. K.; Jariwala, D.; Kim, I. S.; Chen, K.-S.; Marks, T. J.; Lauhon, L. J.; Hersam, M. C. Nat. Nanotech. 2015, 10, 403-406.
3. Sangwan, V. K.; Lee, H.-S.; Bergeron, H.; Balla, I.; Beck, M. E.; Chen, K.-S.; Hersam, M. C. Nature 2018, 554, 500-504.
4. Sangwan, V. K.; Lee, H.-S.; Hersam, M. C. IEEE IEDM, 2017, 5.1.1-5.1.4.
5. Lee, H.-S.; Sangwan, V. K.; Bergeron, H.; Jeong, H. Y.; Su, K.; Hersam, M. C. (under review).

### 11:45 AM A02

**(Student) Impact of H<sub>2</sub>O Vapor Precursor Pulse Time on 65nm CMOS Integrated Hafnium Dioxide Based Nanoscale RRAM Devices** [Jubin Hazra](#), Maximilian Liehr, Karsten Beckmann and Nathaniel Cady; SUNY Polytechnic Institute, United States

Hafnium Oxide (HfO<sub>2</sub>) based Resistive Random Access Memory (ReRAM) devices are promising candidates for non-volatile memory, having a wide variety of applications in neuromorphic computing, artificial intelligence and future memory solutions. Stochastic conductive filament (CF) generation and rupture processes, however, contribute to high variability resistive switching in these devices. Addressing this issue requires tuning of device operation parameters that negatively impact the off/on resistance ratio ( $R_{off}/R_{on}$ ) and switching yield, to avoid a major roadblock in reliable RRAM-based designs. This critical reliability aspect was addressed by modifying the H<sub>2</sub>O vapor cycling time during the atomic layer deposition (ALD) step for depositing the HfO<sub>2</sub> switching layer in hafnium oxide-based RRAM devices. The fully integrated nanoscale CMOS/RRAM structures were implemented on a 300 mm wafer platform using a custom RRAM module within SUNY Polytechnic Institute's 65nm CMOS process technology. The RRAM device stack is comprised of a TiN bottom electrode, an HfO<sub>2</sub> mem-resistive switching layer, a Ti oxygen exchange layer (OEL), and a TiN top electrode. This stack is implemented between the M1 and M2 metallization layers, using a FEOL-compatible process flow. A three-wafer process split was executed with standard, 1.5X and 5X H<sub>2</sub>O vapor pulse times for an organic precursor based HfO<sub>2</sub> ALD deposition and the 1T1R performance were evaluated in terms of switching threshold voltages, memory window and switching variability. For electrical characterization, a pulse-based approach was adopted to apply pulses in the orders of tens of microseconds for set/reset operation of ReRAM devices. A read pulse of -0.2 V with a 10 μs pulse width was applied after each set/reset operation, to read out the high resistance state (HRS) and low resistance state (LRS). Based on tested devices across full 300 mm wafers, the 5X pulse time RRAM devices showed higher mean forming voltages attributed to lower leakage current density. Additionally, 1T1R cells fabricated with 5X cycle time showed ~1.5X improvement in memory window with minimal impact on HRS switching variability and thus improving the memory window- HRS switching variability trade-off. We also report an impressive >95% switching yield based on over 450 tested 1T1R devices across full 300 mm wafers, demonstrating the robustness of our process. Ongoing investigation of conduction mechanism and capacitance-voltage measurements are expected to reveal differences in density of trap states in HfO<sub>2</sub> switching layer which contribute to the differences in forming voltage, memory window and switching variability for these different H<sub>2</sub>O vapor cycle time 1T1R wafers.

### 12:00 PM A03

**(Student) A Comprehensive Review of Contact Resistance and Thermal Stability of Metals on GeTe** [Kayla A. Cooley](#) and Suzanne Mohney; The Pennsylvania State University, United States

Germanium telluride is a phase change material that offers a quick and reversible crystalline-to-amorphous phase transition with large contrast in electrical and optical properties. This contrast can be employed for non-volatile memory, radio frequency (RF) switches, or photonic devices. For RF switches, the resistance of ohmic contacts is a significant fraction of the total on-state resistance. Geometries of RF switches and non-volatile memory often place GeTe in direct contact with metal contacts. Therefore, we have examined the role of device processing and contact metallurgy on the resistance of contacts to GeTe and performed a systematic study of reactivity of metal films with GeTe. Contacts with Mo beneath a Ti/Pt/Au cap offer very low contact resistances near 0.004 Ω mm (5 × 10<sup>-9</sup> Ω cm<sup>2</sup>) when *in situ* Ar<sup>+</sup> ion surface treatment is

used. [1] A tin-based contact also provided very low resistance, permitting *ex situ* surfacetreatment but requiring annealing. [2] Its low resistance was ascribed in part to formation of SnTe. Other metallizations with Ti, [2] Cr, Ni, [3] Pt, or Au as the first layer are more resistive, in some cases by a lot (Ni and Pt). Considering the *p*-type conductivity of GeTe, we would predict from the Schottky-Mott model that a metal with a high work function would have the lowest Schottky barrier to GeTe, and therefore lowest contact resistance, in the absence of Fermi level pinning. If there were complete Fermi level pinning, we would expect little dependence on the metal work function. Instead, we see the opposite trend: metals with the highest work functions exhibit the highest contact resistance (0.016  $\Omega$  mm for Ni-based and 0.036  $\Omega$  mm for Pt-based contacts). The explanation for this unexpected trend comes from a study of interfacial reactivity. Our survey of reactivity [4] revealed that Au and Zn thin films are in thermodynamic equilibrium with GeTe in a closed system at room temperature or the mildly elevated temperatures at contact interfaces in remotely heated RF switches. Other metals are also unreactive at 200 °C, likely due to kinetic limitations. From TEM, [2–4] unreactive metals include Mo, Ru, and Re; literature review places W and Ta in the same category. We experimentally observed reactions of Ag, Al, Cu, Fe, Mn, Pd, Ni and Ti on GeTe and identify a driving force for reaction of GeTe with Cd, Co, Hf, Pt, Rh, Sc and Y. We also observed solubility of Cu, Fe, Mn, and Pd in GeTe. Alloying might be used to engineer crystallization speed, power consumption, and endurance of phase change material devices; modify the Seebeck coefficient and conductivity of phase change materials; or create dilute magnetic materials for spintronics. With one exception (Sn/Fe/Au contacts in which SnTe formed), we observed that reactivity was detrimental for low contact resistance. The effect was great in Ni- and Pt-based contacts. For other contacts, detrimental reactions were less extensive; reaction of Ti/Pt/Au contacts was confined to a thin layer of reaction products after annealing for 30 min at 200 °C. Even Au contact metals that were otherwise unreactive were prone to loss of Te due to volatilization, [5] and Te migrated to the Pt layer in a Ti/Pt/Au cap above unreactive Mo contacts. Overall, Mo contacts are particularly promising, with very low resistance as prepared and good thermal stability. With the exchange of a Ti/Pt/Au cap for another metallization during integration, Mo could be the most thermally stable solution for very low resistance contacts to GeTe that can undergo repeated thermal cycling in RF switches. 1. Aldosari *et al.*, *J. Appl. Phys.* **122** (175302) 2017 2. Simchi *et al.*, *ACS Appl. Mater. Interfaces* **10** (1623) 2018 3. Aldosari *et al.*, *ACS Appl. Mater. Interfaces* **8** (34802) 2016 4. Cooley and Mohnney, *J. Vac. Sci. Technol. A* **37** (061510) 2019 5. Aldosari *et al.*, *Thin Solid Films* **621** (145) 2017

#### 12:15 PM A04

**(Student) Resistive Memory Based on (Zr, Hf, Nb, Ta, Mo, W) High Entropy Oxides** Minhyung Ahn<sup>1</sup>, Yongmo P. Ahn<sup>1</sup>, Seung H. Lee<sup>1</sup>, Jihan Lee<sup>2</sup>, John Heron<sup>3</sup>, Wei Lu<sup>1</sup> and Jamie Phillips<sup>1</sup>; <sup>1</sup>University of Michigan, United States; <sup>2</sup>LAM Research Corporation, United States; <sup>3</sup>University of Michigan–Ann Arbor, United States

Demands for computing power and data storage continues to grow with application spaces in artificial intelligence, big data, and the internet of things, requiring electronic devices with new functionality to overcome current bottlenecks in Moore's Law device scaling. Resistive memory (ReRAM, or memristor) is a promising next generation memory based on resistivity modulation by ionics, with a wide range of applications including non-volatile memory, logic switches, neuromorphic computing, and machine learning. However, challenges in retention, reliability and device variability from the random nature of ionic movement limit ReRAM commercialization. In this work, we propose high entropy oxide (HEO) materials as a ReRAM switching medium as a means to increase configurational entropy and to stabilize material properties. We demonstrate an HEO with six transition metals (Zr, Hf, Nb, Ta, Mo, W) deposited by pulsed laser deposition (PLD), with the goal of combining favorable properties of HfO<sub>2</sub>, Ta<sub>2</sub>O<sub>5</sub>, and WO<sub>3</sub> as ReRAM switching materials, while overcoming drawbacks of the binary materials through 'cocktail effect' and HEO formation. PLD targets were synthesized by conventional solid state reaction and sintered by the spark plasma method. Targets with different composition were fabricated to investigate stoichiometric influence on electrical characteristics of HEO ReRAM. To evaluate HEO targets and thin films, material characterization techniques including X-ray fluorescence, X-ray diffraction, X-ray photoelectron spectroscopy, and scanning electron microscopy were used. ReRAM test structures were fabricated using lithographically defined Ta/Pd and Pd as top and bottom electrical contacts, respectively. Current-voltage, resistive switching characteristics, analog switching behavior, and retention measurements were done to evaluate the ReRAM characteristics, demonstrating forming free operation with low SET voltage (<1V), excellent retention in multilevel states with elevated temperature (85°C), cycle to cycle uniformity, and low device variability.

#### 12:30 PM A05

**(Student) Autonomous Programmable Materials with Embedded Computation, Sensing, Signal Processing and Actuation** Souvik Mukhopadhyay, Travis Hery and Sundaresan Vishnu; The Ohio State University, United States

The digital morphing structure is an autonomous programmable structure that can perform self-sensing, actuation and computation (requiring for structural control) and mimic biological systems in function and interaction with their

immediate environment. In an application, a pre-determined shape is programmed and maintained using ionic/electrical signal flow without the need for an external controller. An electronic logic device is defined as a machine that can perform transduction and binary arithmetic using ion transport in ionic electroactive polymers (or) inorganic materials. These logic devices are built from two or more ionic redox transistors (IRT) and the term 'electronic' is a synthesis of 'electronic' and 'ionic' interactions in the IRT. An ionic redox transistor (IRT) is an electrochemical device that regulates ion transport through its bulk as a function of its redox state and was first reported by Hery and Sundaresan. It was shown that the complex impedance for ion transport across PPy(DBS) membranes depends on its redox state. Effectively, ion transport through the polymer due to a transmembrane electrical potential is switched OFF (oxidized) and ON (reduced). The digital morphing structure and the actuators are envisioned to be fabricated from chemomechanical actuators and logic gates formed from IRTs.

The fundamental unit for distributed digital actuation - actuation elements, abbreviated as axels, are classified into two types – extensional and bending axels. Each Axel is fabricated using a combination of computational elements (NAND, NOR gate) and an IRT actuator. The gates are connected electrically in series/parallel for a given mechanical arrangement (series and anti-series) and a morphing panel is fabricated from an array of axels. Each axel will require 2-bits or 4-bits for actuation along an axis depending on its mechanical arrangement. A discrete force or strain is generated from an axel based on the applied digital input. The force generated by an axel element results from ion transport powered by stored electrochemical energy and regulated by the gate input to the ionic redox transistor.

The current demonstration of IRTs use polymeric redox active polymers (PPy(DBS)) and it should be noted that other redox active polymers and inorganic materials (LiNbO<sub>3</sub>, LiFePO<sub>4</sub>(LFP), LiMnCoO<sub>2</sub>, LiNiAlO<sub>2</sub>, etc.) will exhibit transistor-like function for ion transport and fabricated into electronic logic devices. In this paper, we will demonstrate the IRT functionality of partially lithiated LFP, PPy(DBS) with solid state electrolytes (LISICON). The extensional axels will be fabricated into lattice beams to produce linear strain and the bending axels will be fabricated into nodes and planar sheets to produce rotational or bending strains respectively. The bending axels in a planar sheet will produce surface contours and track the deformation of the underlying lattice structure. The stress and strain generated by the chemomechanical actuator will be represented by the constitutive model and characterized using mechano-electrochemistry methods as shown previously by Sundaresan and coworkers.

#### 12:45 PM A06

**(Student) Heteroepitaxial Thin Film Growth of LiNbO<sub>2</sub> for Rapid Charge Battery, Neuromorphic and Photosynthesis Applications** Timothy M. McCrone, Aheli Ghosh, Alex S. Weidenbach, Bill Zivasatienraj and W. Alan Doolittle; Georgia Institute of Technology, United States

Epitaxially grown thin films and bulk crystals of lithium niobate (LiNbO<sub>2</sub>) have been grown using liquid phase electroepitaxy (LPEE). Large volumes of crystal can be grown at a rate of 100s of microns per hour using this technique. By applying a potential, the deposition of suboxides not normally possible without electrical bias can be grown. Previously these materials were grown on a variety of substrates, but by switching the growth substrate to silicon carbide (SiC) an epitaxial thin film was grown. Silicon carbide was chosen as a substrate because of a lattice mismatch of only 5.2%. Growing LiNbO<sub>2</sub> in such a way creates the opportunity to process the material using standard semiconductor processing technology, opening the opportunity to investigate this thin film for neuromorphic computing applications [1]. The bulk crystals grown can be used as a battery cathode material due to the extremely high mobility of lithium ions in the bulk. LiNbO<sub>2</sub> has potential to be studied as a potential complement to LiCoO<sub>2</sub>, a common battery cathode, due to its high conductivity and similar crystal structure. While the theoretical specific capacity of LiNbO<sub>2</sub> is slightly lower than LiCoO<sub>2</sub>, LiNbO<sub>2</sub> provides excellent rate performance of 15mAh/g at 1400mA/g and fully recovers after this extreme discharge, allowing applications requiring extreme discharge rates, such as electric vehicles or rail gun applications [2]. In addition, LiNbO<sub>2</sub> is one of the highest conductivity p-type semiconductors. LiNbO<sub>2</sub>'s high conductivity and 2.04 eV bandgap creates an opportunity for use as a photocatalyst for H<sub>2</sub> evolution [3]. Previous work has explored growth conditions and techniques pertaining to the bulk crystallites where spontaneous nucleation inhibited layer by layer growth. This work shows epitaxially grown LiNbO<sub>2</sub> thin films grown on SiC characterized electrically and by XPS and compared to bulk crystal properties. While material has been grown on SiC before, these previous growths resulted in runaway nucleation due to reaction rate limited growth conditions identified in the in-situ measured voltammogram causing spontaneous nucleation that forces the crystal to leave the plane of the SiC resulting in random bulk crystallite growth. Altering the growth to a lower potential window here the reaction is diffusion limited preventing the spontaneous nucleation allowing the growth of thin films. Thin films were grown on 1x1cm pieces of SiC, though this growth process could be scaled to the any wafer level. The memristive properties of the thin film grown on SiC and the bulk crystals are compared and found to have 4900% resistance changes, more than double the best prior value and among the best in the memristor community of materials. A 125  $\mu$ m long lateral memristors programmed with a mere 500 mV resulting in the lowest programming electric field presently reported, 40 V/cm. XPS investigation revealed a close chemical

match between the thin film and the bulk crystals. XRD characterization of the crystals indicate a large lattice constant shift consistent in direction with strain to the SiC substrate but of a magnitude that would imply significant pliability of the LiNbO<sub>2</sub> film. The use of LPEE to grow bulk crystals and as a thin film material deposition method proves to be a robust, low cost, scalable process for creating high quality thin films. 1. S. A. Howard, "Direct observation of delithiation as the origin of analog memristance in Li<sub>x</sub>NbO<sub>2</sub>," APL Mater. 7, 071103 (2019). 2. Alamgir, Faisal. (2019). Thin-Film Lithium Niobites and their Chemical Properties for Lithium-Ion Storage and Diffusion. ChemElectroChem. 10.1002/celec.201901347R1. 3. Xiaoxiang Xu, "Layered lithium niobium (III)oxide—LiNbO<sub>2</sub> as a visible-light-driven photocatalyst for H<sub>2</sub> evolution", J. Phys. Energy 1 (1) (2018), <https://doi.org/10.1088/2515-7655/aad4be>

SESSION B: Nanowires—Growth, Processing, Characterization and Devices  
Session Chair: Matt Brubaker  
Session Hosts: Parsian Mohseni and Songrui Zhao  
Wednesday Morning, June 24, 2020  
Location: ZoomRoom 2

### 11:30 AM B01

**Axial and Radial InGa<sub>x</sub>N Quantum Wells in Ordered N-Polar GaN Nanowire Arrays** Matt Brubaker, Alexana Roshko, Todd Harvey, Charles Little and Kris Bertness; National Institute of Standards and Technology, United States

Selective area epitaxy of periodic nanowire (NW) arrays has opened new opportunities for wavelength tuning of monolithically integrated light-emitting diodes (LEDs) and for use of resonant effects to enhance light extraction and reduce emission linewidth. In support of these efforts, considerable attention has already been devoted to the facet-dependent growth kinetics of InGa<sub>x</sub>N quantum wells (QWs) and the dependence of their optical characteristics on the NW size and spacing. Previous studies have focused almost exclusively on Ga-polar NWs grown by patterned selective area epitaxy and in this work we examine these effects for core-shell InGa<sub>x</sub>N QWs grown on their ordered N-polar counterparts.

N-polar NW arrays were grown by selective area epitaxy using N-polar GaN-on-silicon(111) wafers with a patterned silicon nitride growth mask. Silicon-doped GaN NWs cores were first grown at high temperature (860 °C) to promote axial growth and then the temperature was lowered to grow three InGa<sub>x</sub>N QWs and a final encapsulating AlGa<sub>x</sub>N shell (700 °C). Samples with different InGa<sub>x</sub>N growth temperatures (480-620 °C) were prepared, leading to varying axial and radial QW growth rates. The overall length of the NWs was approximately 1.3-1.5 μm and the NW arrays had diameters ranging from 140 – 310 nm and pitches ranging from 300 – 3000 nm. Transmission electron microscopy (TEM) and energy-dispersive x-ray spectroscopy (EDS) indicate that the In<sub>x</sub>Ga<sub>1-x</sub>N growth rate and indium mole fraction (x) is higher for the N-face tip facet than for the *m*-plane sidewall facets. *M*-plane growth is completely suppressed for the sample grown at 620 °C and only N-face QWs were observed (thickness~17 nm, x~0.3-0.5). *M*-plane QWs emerged for lower InGa<sub>x</sub>N growth temperatures and were approximately 1 nm thick (x~0.1) at a growth temperature of 530 °C. Interestingly, the lower growth temperatures that supported *m*-plane QW growth caused the N-face QWs and GaN barriers to become intermixed and void regions developed at the expected QW locations. Low-temperature (5 K) photoluminescence (PL) measurements produced strong violet luminescence at wavelengths ranging from 400-410 nm for samples grown at lower temperatures, where *m*-plane QWs were observed by TEM. The approximate *m*-plane indium mole fraction calculated from bandgap bowing parameters was found to correlate well against the EDS-measured mole fraction. Luminescence originating from the N-face tip was potentially related to a broad emission observed at green-to-red wavelengths. However, the PL intensities were substantially lower than those of the *m*-plane QWs and did not vary significantly across the sample set, despite the marked differences in the N-face QW structure. In the sample showing the strongest *m*-plane luminescence, it was found that the peak emission wavelength had only a minor dependence on NW pitch/diameter that is tentatively attributed to shadowing effects in densely-packed arrays. In contrast, the PL intensities exhibit a strong dependence on NW pitch/diameter (that peaks for specific geometries) and likely reflect an interplay between nanowire density, nearest-neighbor shadowing, and optical wave effects.

### 11:45 AM B02

**(Student) Flexible III-V Nanowire-Based Photodetectors via Selective-Area Epitaxy on Reusable Si Substrates** Alireza Abrand, Mohadesch A. Baboli, Thomas S. Wilhelm and Parsian Mohseni; Rochester Institute of Technology, United States

Semiconductor nanowires (NWs) composed of III-V compounds have received considerable attention as novel optoelectronic materials for applications in photodetectors due to their excellent light absorption properties and their ability to enable high carrier collection efficiencies. However, one of the main challenges associated with epitaxially-grown III-V NWs is their manufacturing

cost, which can be attributed to two causes: (1) the cost of III-V wafers used as growth substrates, and (2) the cost of pre-growth nanoscale lithographic processing of selective-area templates that define NW positions. To resolve the first challenge, NWs can be grown on cheaper foreign substrates such as Si, instead of on bulk III-V wafers. To resolve the second challenge, a viable strategy for simultaneously reducing pre-growth fabrication costs and process complexity can be to reuse Si substrates with pre-defined growth templates that have been prepared using conventional, wafer-scale *i*-line lithography. Here, selective-area epitaxy (SAE) of InAs NWs with sub-lithographic dimensions on reusable Si (111) wafers is presented for applications in flexible infrared photodetectors. First, SAE growth masks are prepared by depositing 55 nm-thick SiO<sub>2</sub> layers on Si substrates, followed by conventional *i*-line photolithography and dry-etching to obtain hexagonal arrays of nanopores with 500 nm diameter and 1 μm pitch. Next, InAs NW arrays are grown via the SAE approach using metalorganic chemical vapor deposition. For NW growth, trimethyl-indium (TMIn) and arsine (AsH<sub>3</sub>) are used as precursors for the supply growth species at a growth temperature of 700 °C. For optimization of NW yield, a novel two-step flow-rate modulated growth technique is introduced. During an initial 30 seconds nucleation step, a high TMIn flow rate of 16 μmol/min is used to enhance site-specific heterogeneous nucleation. The nucleation step is followed by a 25 minute crystal growth step at a reduced TMIn flow rate of 1 μmol/min to promote preferential axial extension of the NW lattice. The two-step SAE procedure promotes the enhancement of global NW yield from ~62% to >85%, compared to SAE conditions utilizing a single low-flow growth step. After growth, the NW arrays are embedded in a polymer membrane and mechanically delaminated from their native growth substrate. The backside of the delaminated membranes are dry-etched to expose the NW bases for metal contact deposition. Next, the NW-embedded membranes are bonded to carrier substrates and the encapsulating polymer layers are dissolved. Using this procedure, NW arrays are transferred from their native growth substrate to a new foreign carrier wafer for further device fabrication. In this work, transferring yields of ~100% are realized while preserving the original position and vertical orientation of as-grown NWs. The native SiO<sub>2</sub>-templated Si (111) substrates are then reused for subsequent generations of InAs NW SAE through two different approaches; namely, with and without a citric acid treatment as a means of substrate restoration before regrowth. The best regrowth results with respect to NW verticality, occupation yield, uniformity, and aspect ratio are achieved when native substrates are recycled without any intermediate restoration steps. This is attributed to the delamination process leaving NW bases with heights of ~50 nm on the native substrates that serve as preferential selective-area growth sites. Under the same SAE condition as the primary run, regrowth enables vertical extension of existing NW bases and formation of second-generation InAs NWs with aspect ratios >80 with reproducible global yields of >85% across wafer-scale areas. The performance of flexible InAs NW-based photodetectors will be presented. Emphasis is placed on the Si substrate reuse process for reduction of III-V NW array manufacturing cost toward large-area, flexible, and wearable optoelectronic devices.

### 12:00 PM B03

**(Student) In Situ TEM for the Direct Observation and Characterization of Germanium Nanowire Synthesis via the Electrochemical Liquid-Liquid-Solid Crystal Growth Process** Quintin Check<sup>1</sup>, Eli Fahrenkrug<sup>2</sup> and Stephen Maldonado<sup>2</sup>; <sup>1</sup>University of Michigan–Ann Arbor, United States; <sup>2</sup>Colorado College, United States

The use of liquid transmission electron microscopy (TEM) for the direct visualization and characterization of germanium (Ge) nanowire growth via the electrochemical liquid-liquid-solid (ec-LLS) growth process in water will be discussed. This process has parallels to the more established vapor-liquid-solid (VLS) technique but has the advantage of being compatible with low temperatures and common solvents like water. This work aims to obtain a better understanding of the ec-LLS process, including identifying factors that limit crystalline quality. The focus of this talk will be to demonstrate that electron (e<sup>-</sup>) beam used for imaging can also be used to stimulate the reduction of germanium (IV) oxide at liquid metal nanodroplets suspended in water. Four primary findings from this work will be explained. First, the required conditions for initiating an e<sup>-</sup> beam induced ec-LLS process will be detailed. Second, the role of surface diffusion of Ge adatoms will be discussed. Third, the rate limiting step for Ge nanowire growth, as indicated from a series of in-situ movies, will be presented. Fourth, evidence that shows nanowire growth by low temperature ec-LLS occurs far from thermodynamic equilibrium will be highlighted.

### 12:15 PM B04

**Influence of Seed Layer on the Performance of ZnO Nanowires-Based Flexible Nanogenerator as Piezoelectric Energy Harvester** Taoufik Slimani, Tlemcani, Camille Justeau, Kevin Nadaud, Daniel Alquier and Guylaine Poulin-Vittrant; Université de Tours, CNRS, France

Here we demonstrate the fabrication of a flexible piezoelectric nanogenerator (PENG) based on zinc oxide (ZnO) nanowires (NWs), which were successfully grown by using low temperature hydrothermal method. Three different structures of seed layers like gold (Au)/ZnO, indium tin oxide (ITO)/ZnO and ITO have been deposited onto flexible and transparent poly(dimethylsiloxane) (PDMS) substrates, and then associated to ZnO NWs for the development of

flexible mechanical energy harvesters. The analysis of crystalline quality and growth orientation was studied using X-ray diffraction (XRD) and the morphological properties were investigated using scanning electron microscopy (SEM). The obtained ZnO NWs on ITO seed layer were randomly orientated with a low density, while ZnO NWs grown on Au/ZnO and ITO/ZnO were uniformly distributed and vertically aligned with a high density as evident from SEM images. The fabricated device configuration of the flexible PENG consists in a multilayer structure: PDMS substrate - Au/ZnO or ITO/ZnO or ITO seed layer - ZnO NWs - parylene C matrix - Ti/Al top electrode and PDMS encapsulation layer. The suitability of this structure as a PENG is demonstrated by studying the harvested electrical output under periodic mechanical force. The maximum resulting output open circuit voltage and power were 6.8 V and 407 nW, respectively. The comparison between the different PENG devices performances indicates that a higher electrical power can be harvested when ZnO NWs are deposited on ITO/ZnO seed layer than on Au seed layer. The obtained results from different structures of ZnO NWs PENG offer a flexible, cost-effective and long term stable device for supplying portable electronics.

#### 12:30 PM B05

##### (Student) Optoelectronic Properties of Red-Luminescent Si Micropillar Arrays Fabricated by Metal-Assisted Chemical Etching

Yang Qian<sup>1</sup>, Seokmin Jeon<sup>2</sup>, Yohan Yoon<sup>2</sup>, David J. Maggini<sup>3</sup>, Maoji Wang<sup>3</sup>, Dinorah Segovia<sup>1</sup>, Jordan Gerton<sup>3</sup> and Heayoung P. Yoon<sup>1,3</sup>; <sup>1</sup>The University of Utah, United States; <sup>2</sup>U.S. Naval Research Laboratory, United States; <sup>3</sup>University of Utah, United States

Considerable attention has been devoted to the development of luminescent Si nanomaterials for a wide range of optoelectronic devices, chemical sensors, and biomedical applications. Si is a bio-compatible and non-toxic material, ideal for both in-vitro and in-vivo testing platforms. However, a planar bulk Si (indirect band-gap of 1.12 eV) itself does not display any significant luminescence in the ultraviolet-visible regime. To overcome this limitation, several groups proposed and demonstrated luminescent Si architectures based on a porous Si thin-layer, plasmonic arrays, or engineered dielectric/Si interfaces (e.g., SiO<sub>2</sub>/Si, SiN/Si). In this work, we report well-defined luminescence properties of Si micropillar arrays fabricated by metal-assisted chemical etching (MACE). We use high-resolution photoluminescence (PL) microscopy to map the optical properties of pillar arrays and individual pillars. We present the notably different luminescence properties of the shell and core of the MACE Si micropillars. To fabricate the micropillar arrays, we performed conventional lithography processes on a 3" Si wafer substrate (resistivity < 0.005 ohm-cm). First, double-layer photoresists were spin-coated (LOR10B and S1813) on the substrate and soft-baked. Following an O<sub>2</sub> plasma descum process (75 W for 20 sec), a thin layer of Au film was evaporated ( $\approx 3 \text{ \AA/s}$ ;  $\approx 30 \text{ nm}$  thick) and lifted off. The Au patterned samples were then dipped into a mixed chemical solution (10 M HF and 0.3 M H<sub>2</sub>O<sub>2</sub> in DI water) for 2 hours at 300 K. Each micropillar array (2.5 mm x 2.5 mm) contained  $\approx 105$  pillars. The diameter and height of the pillars were  $\approx 8 \text{ \mu m}$  and  $\approx 20 \text{ \mu m}$ , respectively. We cleaved off each Si micropillar array and placed each on a sample holder for PL microscopy measurements. A 405 nm laser beam source ( $\approx 1.5 \text{ mW}$ ) that was irradiated on the surface of the Si pillar array via an objective lens (air-based 40 X or oil-based 100 X), and the characteristic PL signals were collected by either an avalanche Si photodiode (APD) or a spectrometer (SpectraPro 2300i; Princeton Instruments). For the PL imaging, an area of 35  $\mu\text{m}$  x 35  $\mu\text{m}$  (64-pixel x 64-pixel) was scanned at 0.03 Hz ( $\approx 208 \text{ \mu s}$  per pixel). Each pixel contains a PL spectrum in a wavelength range from 300 nm to 890 nm with a step size of  $\approx 0.43 \text{ nm}$ . The PL datasets were analyzed by MATLAB and Origin programs. Our Si micropillar arrays display distinguished red-luminescent characteristics. The PL images collected with an air-based objective lens (40X; numerical aperture [N.A.] = 0.6) showed a prominent peak at  $\approx 670 \text{ nm}$  (1.65 eV) for each Si pillar. Linescan analysis showed that this intense peak presents near the center of pillars and rapidly decreases at the edge of the pillar. While the luminescence property at  $\approx 670 \text{ nm}$  is evident, it was not possible to resolve the area responsible for the luminescence. To improve the resolution, we performed high-resolution PL imaging using an oil-based objective lens (100X; 1.4 N.A.) that can provide a spatial resolution as high as  $\approx 150 \text{ nm}$ . The PL map clearly showed that the red-luminescence ( $\approx 665 \text{ nm}$ ; 1.86 eV) is mainly attributed to the shell of Si pillars, rather than the interior of pillars. We speculate that the main contribution of the luminescence appears to be associated with the defects in SiO<sub>2</sub>, specifically non-bridging oxygen ( $\equiv \text{Si-O}\bullet$ ). The peak at  $\approx 520 \text{ nm}$  (2.38 eV) is mainly attributed to the luminescence of the oil used to match the refractive indices of glass coverslip and lens for the high-resolution imaging. The shoulder of the peak around 470 nm (2.64 eV) indicates the presence of unrelaxed oxygen vacancies. The sharp peak at 457 nm (2.71 eV) is attributed to the optical component of our PL setup, rather than the luminescence properties of the samples. Currently, we are investigating the electronic properties of the surface and sub-surface of Si micropillars using Kelvin-probe force microscopy to correlate with the observed optical properties.

SESSION C: Advanced Design and Processes for III-Nitride Power Electronics  
Session Chair: Fatemeh (Shadi) Shahedipour-Sandvik  
Session Hosts: Christopher Allemang and Doug Hall  
Wednesday Morning, June 24, 2020  
Location: ZoomRoom 3

#### 11:30 AM C01

##### Limitations in Impact Ionization Modeling for Predicting Breakdown in Wide Bandgap Power Semiconductors

Andrew Binder, Robert Kaplar and Jeramy Dickerson; Sandia National Laboratories, United States

The prediction of breakdown voltage is a critical aspect of modeling for power semiconductor devices. High power devices employ a vertical device architecture to maximize the current carrying capability and breakdown voltage for a given die area. To predict breakdown voltage, impact ionization models such as the one developed by Selberherr can be used to calculate avalanche multiplication given an applied electric field. When the avalanche multiplication factor reaches one, the device is considered to be in breakdown. The inputs to the Selberherr impact ionization model are two coefficients  $\alpha_0$  and  $\epsilon_0$ . From this model the critical electric field can be calculated as a function of doping: this critical electric field is then used to calculate the breakdown voltage.

Impact ionization models, such as Selberherr's model, were created to model ionization in a one-dimensional structure. For this one-dimensional scenario, there are an infinite set of solutions to the ionization model that will yield a specific critical electric field at a given doping level. The ionization coefficients  $\alpha_0$  and  $\epsilon_0$  are exponentially dependent and for any given  $\alpha_0$  there are an infinite number of solutions for  $\epsilon_0$  that will produce an identical solution to the ionization model. As these coefficients increase, critical electric field becomes a stronger function of doping, and as the coefficients decrease the dependency becomes weaker. In a one-dimensional ideal diode, each of these solutions will yield the same breakdown voltage prediction for a given critical electric field at a specified doping level. In addition, the ionization equation will yield the same critical electric field for a range of input coefficients ( $\alpha_0$  and  $\epsilon_0$ ) and these coefficients will trend up together (high ionization coefficients) and trend down together (low ionization coefficients) while still producing the same solution for critical electric field at a given doping. In this way, the solutions are nonunique and the choice of impact ionization coefficients are inconsequential when solving for a critical electric field. When considering a two- or three-dimensional model, the selection of impact ionization coefficients becomes critically important as the infinite set of solutions to the impact ionization model no longer produces a unique breakdown voltage prediction. With a multi-dimensional model, the predicted breakdown voltage can become higher than the ideal breakdown voltage when the ionization coefficients are too low, and the breakdown voltage will drop as the ionization coefficients are increased. In addition, it is noted in simulations that the impact ionization becomes very localized around the point of highest electric field when considering high ionization coefficients, and conversely the ionization becomes very delocalized for low ionization coefficients. A literature review of reported impact ionization coefficients in GaN ( $\alpha_0$  and  $\epsilon_0$ ) yields a vast range of values for critical electric field and a varying dependence on doping. This work demonstrates the impact of ionization coefficients on breakdown and the discrepancy between one-dimensional and two-dimensional models in predicting breakdown voltage. A comparison of impact ionization and breakdown voltage is shown in modeling for an ideal one-dimensional diode and a two-dimensional diode with a step-etched junction termination extension (JTE). Sandia National Laboratories is a multimission laboratory managed and operated by National Technology & Engineering Solutions of Sandia, LLC, a wholly owned subsidiary of Honeywell International Inc., for the U.S. Department of Energy's National Nuclear Security Administration under contract DE-NA0003525.

#### 11:45 AM C02

##### Inverse Proportionality of Dopant Concentration to Growth Speed During Non-Planar Selective Area Regrowth of GaN

Alexander Chang<sup>1</sup>, Bingjun Li<sup>2</sup>, Jung Han<sup>2</sup> and Lincoln Lauhon<sup>1</sup>; <sup>1</sup>Northwestern University, United States; <sup>2</sup>Yale University, United States

GaN is promising for the next generation of power electronics beyond Si. Vertical GaN power devices are preferred over lateral devices due to higher breakdown voltages, better scalability and thermal management. Among different approaches to achieving selective area doping, selective area etching (SAE) and regrowth (SAG) are appealing to avoid high temperature processing steps. However, SAG-grown devices still suffer from premature breakdown and high leakage currents. For example, premature breakdown is often reported to occur at junction edges, where high electric field is routinely present. To improve the device performances, it is essential to quantify the impurity distribution in the active region. Due to the non-planar nature of SAG, different facets evolve with different growth velocities and impurity incorporation rates. Atom probe tomography (APT) was performed on SAG-grown GaN structures to understand how non-planar growth influence dopant incorporation. SAE was used to form trenches on n-GaN surfaces along the a-axis or m-axis, followed by metal-organic chemical vapor deposition of p<sup>+</sup>-GaN by SAG. To trace the

regrowth shape ex-situ at various regions and temporal stages of growth. AlGaIn marker layers were inserted during growth. Indeed, our APT results revealed different facet orientations at trench center versus trench edge as well as different Mg concentrations ( $x_{\text{Mg}}$ ) implying that the doping concentration in the regrown junction is non-uniform. To relate inhomogeneous  $x_{\text{Mg}}$  to processes on growth surfaces (i.e. surface adatom diffusion, adsorption, etc.), spacing between AlGaIn marker layers can be used to calculate the time-dependent facet growth rate. However, there is often an artifact in length-scales of reconstructed APT data due to limitations of the reconstruction procedure. The spacing of atomic planes in the APT reconstruction were analyzed to produce corrected one-dimensional profile of the composition, enabling correlation of  $x_{\text{Mg}}$  to growth rate of facets. We find that dopant concentration varies in inverse proportion to the growth speed of polar and semi-polar facets. We explain the inverse proportionality in terms of difference in diffusion and incorporation rates of Ga and Mg adatoms on polar and semi-polar facets. Finite element modelling (Sentaurus) was used to study the influence of spatially inhomogeneous  $x_{\text{Mg}}$  on p-n junction characteristics. The enhancement/deficit in Mg concentration at different regions of the active junction can locally raise/lower the magnitude of the electric field. With premature breakdown typically occurring at the device edges, a lower  $x_{\text{Mg}}$  at the non-planar device edges are in general favorable for raising the break down voltage of the device. Under reverse bias, simulation results indicate that the lower doping of the semi-polar facet spreads the electric field away from the device edges and lowers the maximum electric field at the device edge, similar to junction termination extensions reported in Si or SiC power devices.

### 12:00 PM C03

**1.27 kV Etch-then-Regrow GaN *p-n* Junctions with Low Leakage for GaN Power Electronics** Kai Fu, Houqiang Fu, Xuanqi Huang, Hong Chen, Tsung-Han Yang, Jossue Montes, Chen Yang, Jingan Zhou, Xin Qi, Xuguang Deng and Yuji Zhao; Arizona State University, United States

Gallium nitride (GaN) power devices have become one of the most promising materials for power electronics, offering remarkable improvements in energy conversion efficiency, switching frequency, and system volume. As one of the most important fundamental building blocks of semiconductor electronic devices, *p-n* junctions, created by doping methods using ion implantation, diffusion of dopants, or epitaxy, are also of great importance in fabricating GaN power devices. Moreover, to fabricate high-performance and flexible GaN power devices, selective-area doping is almost indispensable. However, these methods are still difficult to implement for GaN, especially regarding *p-type* doping. It was found that GaN was not very resistant to ion beam disordering during implantation, which became more severe at higher dose ion implantation. For diffusion of dopants, the high-density dislocations in GaN strongly affect the effective diffusion penetration depth and the surface dissociation becomes significant during high temperature annealing, which makes the diffusion method also difficult for GaN. Therefore, epitaxial regrowth is still regarded as the most feasible method for the selective-area doping for GaN. In each case, dry etching is essential for forming selectively regrown areas prior to regrowth. However, this etch-then-regrow process is very challenging. First, after regrowth, an interface containing a high concentration of contaminants such as silicon (Si), carbon (C), and oxygen (O) is formed even without any etching. Secondly, the dry etching process can introduce surface damage. As a result, very high reverse leakage current has become one of the most serious challenges for regrown *p-n* junctions. In this work, we have investigated the influence of dry etching conditions on the reverse leakage characteristics of GaN *p-n* junctions with *p*-GaN regrown on the etched surface. A combination of low-damage dry etching and wet etching treatments has shown a great potential for producing high-performance regrown *p-n* junctions.

All samples were grown homoepitaxially by metalorganic chemical vapor deposition (MOCVD) on *c*-plane *n*<sup>-</sup>-GaN free-standing substrates. Before regrowth, 9- $\mu\text{m}$ -thick unintentionally doped (UID) GaN drift layers with an electron concentration of  $\sim 10^{16} \text{ cm}^{-3}$  were first grown on the substrates. Then different etching processes were applied to the drift layer, followed by the regrowth process including a thin UID-GaN layer as an insertion layer and a 500 nm *p*-GaN layer. Without any treatment before regrowth, the reverse leakage currents for both samples with and without dry etching are very large, and the breakdown voltages are only about 100 V. Because surface contaminants may cause the leakage, wet etching before the regrowth was then applied to the samples, including UV-ozone to oxidize the surface, and hydrofluoric (HF)-then-hydrochloric (HCl) acids to remove the contaminants. This was found helpful to decrease the leakage of the non-etched sample but no help for the etched sample, which indicates that the dry-etched surface was severely damaged by the plasma etching process. A low-damage ICP etching recipe with a very low RF power was then developed for the etching process. The reverse leakage of the etched sample is dramatically decreased to a level, about  $7.16 \times 10^{-5} \text{ A/cm}^2$  at  $-600 \text{ V}$ , which is even much lower than the non-etched sample and very close to the as-grown sample. To avoid sacrificing the etching rate by using only low power etching, a multiple-RF-power etching recipe was then developed using multiple etching steps with gradually decreased RF powers. The regrown *p-n* diode by the multiple-RF-power etching exhibits a very high breakdown voltage of 1270 V, a low differential on-resistance of  $0.8 \text{ m}\Omega \bullet \text{cm}^2$  and a record low ideality factor of 2. The Baliga's FOM ( $V^2/R_{\text{on}}$ ) for the regrown *p-n* diode is  $2.0 \text{ GW/cm}^2$  which is even comparable to some of as-grown *p-n* diodes.

### 12:15 PM C04

**(Student) P-Type Conductivity in Mg-Implanted GaN by Microwave Gyrotron Annealing** Vincent E. Meyers<sup>1</sup>, Emma Rocco<sup>1</sup>, Kasey Hogan<sup>1</sup>, Benjamin McEwen<sup>1</sup>, Fatemeh (Shadi) Shahedipour-Sandvik<sup>1</sup>, Randy Tomkins<sup>2</sup>, Michael A. Derenge<sup>2</sup>, Kenneth A. Jones<sup>2</sup>, Mike Shevelev<sup>3</sup> and Vlad Sklyar<sup>2</sup>; <sup>1</sup>State University of New York Polytechnic Institute, United States; <sup>2</sup>U.S. Army Research Laboratory, United States; <sup>3</sup>Gyrotron Technology Inc., United States

The wide bandgap and ultra-wide bandgap AlGaIn material system is ideal for applications in high-power, high-frequency, and high-temperature applications due to its diverse and robust material properties. A major challenge facing GaN-based device development is the difficulty of forming highly *p-type*, selectively doped material. Ideally, selective-area doping can be achieved by implantation of an acceptor impurity, the dominant species of which is currently Mg. However, the ion implantation process introduces a large density of defects in the GaN that compensate activated acceptors and inhibit *p-conductivity*. To remove these defects and efficiently activate Mg requires temperatures that are above the decomposition temperature of GaN under equilibrium conditions. Additionally, dopant diffusion at high temperatures may complicate efforts to control doped region boundaries. Methods of nonequilibrium annealing such as symmetric multicycle rapid thermal anneal (SMRTA), microwave annealing, and laser annealing have been reported, but each method faces unique limitations.

In this study we report, for the first time, *p-type* conductivity in implanted GaN by short pulses of gyrotron microwave annealing. Unintentionally doped GaN (u-GaN) samples were implanted with Mg to a uniform concentration of  $10^{19} \text{ cm}^{-3}$  to a depth of 250 nm, capped with a protective AlN layer, and pulse-annealed with a gyrotron microwave source. The gyrotron beam is capable of high power (kW) irradiation of a substrate, rapid heating (up to  $10,000 \text{ }^\circ\text{C/s}$ ), and focused irradiation for selective-area annealing. Annealing was performed at temperatures of  $1250 \text{ }^\circ\text{C}$  or  $1350 \text{ }^\circ\text{C}$  for 10 pulses each, with pulse durations of 1.5–7 s for cumulative soak times of 15–70 s.

Transmission line measurement showed linear current conduction in the sample annealed at  $1350 \text{ }^\circ\text{C}$ , confirming *p-type* conductivity. Samples annealed at  $1250 \text{ }^\circ\text{C}$  remained highly resistive and rectifying. In the measurement range between  $-5 \text{ V}$  and  $5 \text{ V}$ , a contact resistivity of  $\rho_c = 2.53 \text{ } \Omega \text{ cm}^2$  is observed for the  $1350 \text{ }^\circ\text{C}$  annealed sample. We note that the high contact resistivity is partly due to unoptimized *p-metal* contacts, to allow their easy removal for further measurements. Details of the experiments including implantation, annealing, structural, optical and electrical measurements along with detailed SIMS results of dopant distribution will be presented.

The information, data, or work presented herein was funded by the Advanced Research Projects Agency – Energy (ARPA-E), U.S. Department of Energy under the PNDIODES program under the direction of Dr. Isik Kizilyalli.

### 12:30 PM C05

**Process Optimization for Selective Area Doping of GaN by Ion Implantation** Mona Ebrish<sup>1</sup>, Travis J. Anderson<sup>2</sup>, Alan G. Jacobs<sup>3</sup>, Boris Feigelson<sup>2</sup>, Jennifer K. Hite<sup>2</sup>, Michael A. Mastro<sup>2</sup>, Yekan Wang<sup>4</sup>, Mark Goorsky<sup>4</sup> and Karl Hobart<sup>2</sup>; <sup>1</sup>NRC Post Doctoral Fellow Residing at the U.S. Naval Research Laboratory, United States; <sup>2</sup>U.S. Naval Research Laboratory, United States; <sup>3</sup>ASEE Post Doctoral Fellow Residing at the U.S. Naval Research Laboratory, United States; <sup>4</sup>University of California, Los Angeles, United States

Selective doping in GaN is a crucial step to advance GaN power electronic devices to a competitive level by enabling planar process technology. Ion implantation is a common fabrication step for selective area doping to avoid the complications from the etch/regrowth process. Ion-implantation however, is inherently a damaging process to a crystal resulting in the need for annealing to activate dopant species. Annealing is particularly problematic in GaN since the material will decompose to Ga + N<sub>2</sub> at atmospheric pressure for typical implant annealing conditions at  $\sim 2/3$  of the melting point of the crystal. We have previously discussed the symmetric multicycle rapid thermal annealing technique (SMRTA) for implanted dopant activation utilizing AlN capping and overpressure annealing in a metastable pulsed process, but there has not been a comprehensive study on the optimum implant conditions and capping process for dopant activation. In this research high and low temperature MOCVD and sputtered AlN were employed in different stacking arrangements to study the optimum condition for both Si and Mg ion-implantation and activation. The matrix of this study focuses on varying both the cap stack and implantation dose to better understand the activation interface. Each sample has a unique cap stack and three different implant doses; half of the sample was implanted multiple times at 1/3 and 2/3 of the total dose, therefore the total dose for each quadrant will vary from  $2.3\text{E}14 \text{ cm}^{-2}$  to  $7\text{E}14 \text{ cm}^{-2}$ , including a non-implanted reference quadrant. The implant temperature was also varied to distinguish the effect of implant damage mechanisms. Moreover, the implant profile was modified from a flat box to a highly doped surface layer to reduce the contact resistance. The contact and sheet resistances were evaluated electrically by utilizing the circular transmission line measurements (CTLM), and the quality of the interface between the cap and the implanted layer of GaN was assessed through physical characterization using PL, Raman and SEM/TEM techniques. The CTLM structures were patterned with conventional lithography and Pd/Au stack was chosen as the metal contact. In general, we observed better Ohmic contact behavior on the high temperature cap sample than others and less

annealing damage, especially in the non-implanted quadrant. We have also noticed a conspicuous current scaling with the dose in this sample, indicating that active acceptors are contributing to the current transport. We will also investigate the impact of different contact metals on the contact resistance, and analyze the temperature-dependent Hall measurement to verify transport mechanisms.

#### 12:45 PM C06

**(Student) Growth and Characterization of GaN p-i-n Rectifiers Using Ion-Implantation Isolation** Marzieh Bakhtiary-Noodch, Chuan-Wei Tsou, Minkyu Cho, Mi-Hee Ji, Shyh-Chiang Shen, Theeradet Detchprohm and Russell Dupuis; Georgia Institute of Technology, United States

Gallium nitride (GaN) devices are appropriate candidates for high-voltage applications because of their wide bandgap (~3.4 eV) and high breakdown electric-field (~3.3 MV/cm) characteristics. Proper device isolation and field termination are keys to suppressing the leakage current in the fabrication of vertical GaN power devices. Mesa etching is one of the major challenges in the fabrication of these devices, that usually leads to sidewall leakage currents and premature reverse-bias breakdown. Vertical GaN rectifiers using nitrogen-ion implantation as a mean of device isolation, have shown large blocking voltages (BV) and high drive currents and this technique could become an effective approach for the manufacture of high-performance vertical GaN devices. In this study, GaN-based rectifiers were grown by metalorganic chemical vapor deposition (MOCVD) on bulk GaN substrates having a low dislocation density. Vertical GaN power rectifiers grown on bulk GaN substrates having a low dislocation density ( $\sim 10^3 \text{ cm}^{-2}$ ) can be a viable technology for high-power switching applications. In this work, we demonstrate 1130  $\mu\text{m}$  diameter GaN *p-i-n* rectifiers having a blocking voltage (BV) of 1.2 kV and an ON-state current drive of 10 A. Ion implantation using nitrogen ions as used for device definition and electrical isolation. The epitaxial layers for GaN *p-i-n* rectifiers were grown using a close-coupled-showerhead AIXTRON 6x2<sup>TM</sup> MOCVD system on bulk GaN substrates and fabricated using ion-implanted device isolation. The epitaxial layer growth consisted of the following layers: 1.0  $\mu\text{m}$  thick *n*-Ga<sub>0.99</sub>N:Si layer ( $n \sim 7 \times 10^{18} \text{ cm}^{-3}$ ), 4.0  $\mu\text{m}$  thick *n*-Ga<sub>0.99</sub>N:Si layer ( $n \sim 2.5 \times 10^{16} \text{ cm}^{-3}$ ), 6.0  $\mu\text{m}$  thick undoped-GaN, 0.45  $\mu\text{m}$  thick *p*-Ga<sub>0.99</sub>N:Mg layer ( $p \sim 6 \times 10^{17} \text{ cm}^{-3}$ ). This epitaxial structure was designed for a target reverse-bias breakdown voltage of 1.2 kV. The MOCVD growth employed ammonia (NH<sub>3</sub>) and trimethylgallium (TMGa) as primary precursors and biscyclopentadienylmagnesium (Cp<sub>2</sub>Mg) and silane (SiH<sub>4</sub>) as dopants. The free-carrier concentration and resistivity of the doped layers were evaluated by Hall-effect characterization. Secondary ion mass spectrometry (SIMS) measurements were performed to confirm the doping profile of the layers. X-ray diffraction (XRD) was used for the characterization of the crystallographic quality of the PIN structure. The full width at half maximum of the rocking curve derived from (002) and (102) diffraction exhibit values of 90 and 130 arc-sec, respectively, primarily determined by the properties of the GaN substrate. Atomic force microscopy (AFM) was used to study the surface morphology and the corresponding root-mean-square (RMS) of the GaN *p-i-n* rectifier epitaxial structures. The RMS values for scanning area of  $5 \times 5 \mu\text{m}^2$  is  $\sim 2.0 \text{ nm}$  for the typical case. The rectifier device fabrication employed a backside *n*-metal contact formation of a Ti/Al-based metal stack, followed by a Ni/Ag-based *p*-metal contact on the front side of the wafer. Ion implantation of nitrogen ion species were used to provide device isolation. The evaluated devices have the diameters of 280, 830, and 1130  $\mu\text{m}$  and the reverse-biased characteristics of these devices were measured. A BV of 1.2 kV was measured for 1130- $\mu\text{m}$ -dia. devices, defined as the voltage where reverse current density  $J_r = 10^{-2} \text{ A/cm}^2$ . A slightly higher BV was measured for smaller device sizes. A BV of 1.3 kV was observed for devices with 280  $\mu\text{m}$  dia. At a forward bias of 6.2 V, a forward current  $> 11 \text{ A}$  was achieved for 1130- $\mu\text{m}$ -dia. devices. A current drive of 10 A was achieved at a forward bias of  $\sim 7 \text{ V}$  for 830  $\mu\text{m}$  dia. devices. For *p-i-n* rectifiers with 280- $\mu\text{m}$  dia., a value of R-ON of 0.28 m $\Omega$ .  $\text{cm}^2$  was measured at  $I = 3.2 \text{ A}$  ( $J = 5.2 \text{ kA/cm}^2$ ). In this talk, we will further describe the MOCVD growth, device processing, and rectifier electrical characteristics.

SESSION D: 2D Devices

Session Chair: Kevin Daniels

Session Hosts: Qiang Guo and Michael Spencer

Wednesday Morning, June 24, 2020

Location: ZoomRoom 4

#### 11:30 AM D01

**Low Variability and  $10^{10}$  On/Off Current Ratio in Flexible MoS<sub>2</sub> FETs with Al<sub>2</sub>O<sub>3</sub> Encapsulation Improved by Parylene N** Yury Illarionov<sup>1,2</sup>, Theresia Knobloch<sup>1</sup>, Michael Walt<sup>1</sup>, Sayani Majumdar<sup>3</sup>, Miika Soikkeli<sup>3</sup>, Wonjae Kim<sup>3</sup>, Stefan Wachter<sup>4</sup>, Dmitry Polyushkin<sup>4</sup>, Sanna Arpiainen<sup>3</sup>, Mika Prunnila<sup>3</sup>, Thomas Mueller<sup>4</sup> and Tibor Grasser<sup>1</sup>; <sup>1</sup>TU Wien, Austria; <sup>2</sup>Ioffe Institute, Russian Federation; <sup>3</sup>VTT Technical Research Centre, Finland; <sup>4</sup>Institute for Photonics, TU Wien, Austria

**Introduction:** Encapsulation of MoS<sub>2</sub> FETs presents an important step towards top-gated devices which are required for circuit integration. This is because

insulators employed to protect the channel from the ambient can be subsequently scaled and used as top gate insulators. However, encapsulation layers themselves can as a side effect also degrade the device performance. For example, the encapsulation can increase device-to-device variability, reduce the mobility, or cause negative shifts of the threshold voltage which is often observed in MoS<sub>2</sub> FETs protected with Al<sub>2</sub>O<sub>3</sub> [1,2]. Thus, possible limitations of different encapsulation schemes have to be understood prior to the next step, fabricating top-gated devices. **Devices:** We examine flexible CVD-MoS<sub>2</sub> FETs with 30nm thick Al<sub>2</sub>O<sub>3</sub> grown by ALD as a gate insulator. The devices were encapsulated using four different schemes, namely Al<sub>2</sub>O<sub>3</sub>, Al<sub>2</sub>O<sub>3</sub>/Parylene N, Parylene N/Al<sub>2</sub>O<sub>3</sub>/Parylene N and Parylene C/Al<sub>2</sub>O<sub>3</sub>/Parylene N. In all cases the growth of Al<sub>2</sub>O<sub>3</sub> was performed at 200°C, while Parylene N or C was deposited after 3 hours annealing at 130°C followed by 12 hours pumping. **Experimental technique:** We measure static  $I_D$ - $V_G$  characteristics using the autorange mode and the hysteresis using different sweep rates  $S$  and times  $t_{sw}$ . The hysteresis dynamics is expressed by  $\Delta V_{th}(1/t_{sw})$  traces [3], where  $\Delta V_{th}$  is the hysteresis width extracted near the threshold voltage  $V_{th}$ . To verify the stability of our devices, we perform our measurements in the ambient and in vacuum before, during and after annealing at 165°C. For each encapsulation scheme we examine tens of devices to benchmark their variability. **Results:** Similar to previous literature reports [1,2], our results show that the  $I_D$ - $V_G$  characteristics of MoS<sub>2</sub> FETs with Al<sub>2</sub>O<sub>3</sub> encapsulation have a strongly negative  $V_{th}$  due to an n-type doping of the channel by positive charges inside Al<sub>2</sub>O<sub>3</sub>. At these negative  $V_G$  there is a substantial thermionic gate leakage current, which leads to a reduced on/off current ratio of only about  $10^6$ . The use of Parylene N/Al<sub>2</sub>O<sub>3</sub>/Parylene N encapsulation makes  $V_{th}$  considerably more positive and thus allows achieving values up to  $10^{10}$ . A Parylene C layer underneath the Al<sub>2</sub>O<sub>3</sub> also suppresses the negative shift of  $V_{th}$ . However, the ON current is a few orders of magnitude lower as compared to Parylene N devices. Also, the mobility in MoS<sub>2</sub> FETs with Parylene C encapsulation is much smaller than in their counterparts with Parylene N, which is likely due to scattering of carriers at Cl atoms in Parylene C.

We also found that the use of Parylene N/Al<sub>2</sub>O<sub>3</sub>/Parylene N encapsulation makes the  $I_D$ - $V_G$  characteristics of our MoS<sub>2</sub> FETs non-sensitive to the ambient environment and annealing at 165°C, while leading to the smallest device-to-device variability in performance parameters and hysteresis dynamics.

However, the hysteresis in these devices is still sizable, which is caused in part by oxide defects in the Al<sub>2</sub>O<sub>3</sub> and in part by adsorbates introduced during fabrication. The contribution coming from adsorbates is pressure-dependent [4], which results in a decreased hysteresis when measuring in vacuum.

**Conclusions:** We performed a systematic study on the impact of encapsulation on the  $I_D$ - $V_G$  characteristics and hysteresis in flexible MoS<sub>2</sub> FETs. We found that a highly stable Parylene N/Al<sub>2</sub>O<sub>3</sub>/Parylene N encapsulation allows to efficiently suppress the negative shift of  $V_{th}$  and to achieve an on/off current ratio of up to  $10^{10}$ , while maintaining low device-to-device variability. Further steps should be to optimize device processing by avoiding air exposure in between device fabrication and encapsulation, which is expected to reduce the number of adsorbates and further suppress the hysteresis.

**References:** [1] J. Na et al, *Nanoscale*, 6, 433 (2014); [2] N. Liu et al, *ACS Appl. Mater. & Interfaces*, 9, 42943 (2017); [3] Y. Illarionov et al, *2D Mater.*, 3, 035004 (2016); [4] A. Di Bartolomeo et al, *2D Mater.*, 5, 015014 (2017).

#### 11:45 AM D02

**New Methods and Observations in Contact Scaling for 2D FETs** Zhihui Cheng<sup>1,2,3</sup>, Hattan Abuzaid<sup>1</sup>, Yifei Yu<sup>4</sup>, Shreya Singh<sup>1</sup>, Linyou Cao<sup>3</sup>, Curt Richter<sup>2</sup> and Aaron D. Franklin<sup>1,4</sup>; <sup>1</sup>Duke University, United States; <sup>2</sup>National Institute of Standards and Technology, United States; <sup>3</sup>Purdue University, United States; <sup>4</sup>North Carolina State University, United States

**Introduction:** Atomically thin two-dimensional (2D) crystals are promising channel materials for extremely scaled field-effect transistors (FETs). For devices at the sub-10 nm technology nodes, both channel length (distance from source to drain contacts) and contact length (distance that the contacts overlap the 2D channel) must be scaled. However, contacting 2D materials at scaled contact lengths ( $L_c < 30 \text{ nm}$ ) has rarely been pursued or studied in-depth<sup>1</sup>. In this work, we experimentally scaled the  $L_c$  for MoS<sub>2</sub> 2D FETs and found that, contrary to most previous reports, **top contacts can be scaled down to  $\sim 25 \text{ nm}$  without noticeable degradation in contact resistance**. We also observed **significant self-heating in scaled contacts in the saturation regime**. While the first observation is promising for extremely scaled FET technologies, the second illustrates that current crowding in metal-2D contacts is a challenge toward the development for future scaled devices. **Contact scaling:** Ni contacts with  $L_c$  ranging from  $\sim 110 \text{ nm}$  to  $\sim 25 \text{ nm}$  were fabricated on the same bilayer MoS<sub>2</sub>. Note that the channel length,  $\sim 460 \text{ nm}$ , is identical between these devices. The  $I_D$ - $V_{GS}$  curves of the devices show that although they have different threshold voltage ( $V_{th}$ ), their performance is similar after considering the overdrive voltage  $V_{ov} = V_{GS} - V_{th}$ . Since the only difference in the devices is  $L_c$ , the variation in  $V_{th}$  is caused by the change of  $L_c$  and the mechanism behind it merits further investigation. Accounting for the  $V_{th}$  shift, we analyzed the  $I_D$ - $V_{DS}$  curves and confirmed the very similar contact resistance and on-current across different  $L_c$  as the source. A slight negative differential resistance (NDR) is observed for devices with an  $L_c \approx 25 \text{ nm}$  source at a relatively high carrier density of  $7.2 \times 10^{12} \text{ cm}^{-2}$ , suggesting self-heating. **Self-heating and early saturation:** To further explore the self-heating phenomenon, we also fabricated devices with asymmetrical contacts—one side of the contacts with  $L_c \approx 110 \text{ nm}$  and the other side with  $L_c \approx 25 \text{ nm}$ . When the source contact is 25 nm, NDR is

observed, further proving that self-heating in the saturation regime at relatively high carrier density is associated with a small source contact, not the channel region. NDR is not observed when the long  $L_c$  was used as the source. Since the electron injection happens at the source, the  $L_c$  at the drain does not have an impact. Moreover, with the short  $L_c$  (~25 nm) as the source, the same device saturates at  $V_{DS} \approx 2.4$  V, whereas with the large  $L_c$  (~110 nm) as source, the device saturates at  $V_{DS} \approx 4$  V. The early saturation and self-heating are indicative of current crowding at the metal-2D contacts. **Significance:** We experimentally demonstrated new methods to study contact scaling by using progressively scaled contacts and asymmetrical contacts. No degradation of contact resistance was found after contacts were scaled down to ~25 nm; however, early saturation and self-heating behaviors appeared for scaled contacts in the saturation regime. Our new observations suggest that current crowding and self-heating must be considered in the design of future devices with extremely scaled contacts. [1] Zhihui Cheng, et al. IEEE TED., 2018, 65(10), 1-11. [2] Chris English, et al., *Nano Lett.*, 2016, 16(6), 3824-3830. [3] Kirby Smith, et al., *2D Materials*, 2017, 4, 011009. [4] Yao Guo, et al., *ACS Nano*, 2014, 8(8), 7771-7779. [5] Hui Yuan, et al., *Appl. Phys. Lett.*, 2016, 108, 103505. [6] Han Liu, et al., *ACS Nano*, 2014, 8(1), 1031-1038. [7] Arutchelvan G, et al., *Nanoscale*, 2017, 9(30), 10869-10879.

## 12:00 PM D03

### Fabrication of Multilayer MoS<sub>2</sub> Field-Effect Transistor Arrays Using a Modified Exfoliation Method

Mohammad Nourj and William Wong;  
University of Waterloo, Canada

There has been increasing interest in the two-dimensional (2-D) layered transition metal dichalcogenide (TMDC) semiconductor, molybdenum disulfide (MoS<sub>2</sub>), for high-performance large-area electronic applications. A common approach to fabricate MoS<sub>2</sub> field-effect transistor (FET) devices is based on the mechanical exfoliation of thin layers using an adhesive tape to remove and transfer layers of MoS<sub>2</sub> from a bulk substrate. However, this method usually leads to small areas and randomly distributed material, making fabrication of multiple devices difficult. In this investigation, the mechanical exfoliation method is modified through the use of a water-soluble adhesive tape that minimizes the degradation of the MoS<sub>2</sub> layers during the exfoliation process. In this new method, the exfoliation and transfer of the MoS<sub>2</sub> layers are performed similarly to the conventional transfer process but after the layers are transferred onto a process wafer, the tape is removed by simply dissolving it from the wafer with water, leaving the transferred layer intact. While the final shape of the transferred MoS<sub>2</sub> flakes is still random, much larger areas, up to several millimeters, may be transferred at one time. This large-area layer may then be processed using conventional microfabrication techniques to create arrays for MoS<sub>2</sub> devices. An array of 40 nm × 40 nm MoS<sub>2</sub> islands were made on a highly doped Si wafer having a 100 nm thick thermal oxide. The islands, fabricated from a single large flake, were patterned by conventional photolithography and dry etching in a SF<sub>6</sub>/O<sub>2</sub> plasma. Top electrodes consisting of Al/Ti contacts were patterned on top of the patterned array of MoS<sub>2</sub> islands to complete the bottom-gate FET devices. While effective to etch material in the field of the large MoS<sub>2</sub> flake, the dry etch process was also useful to selectively reduce the MoS<sub>2</sub> layer thickness, creating thinner multilayer structures. A threshold voltage shift of > 15 V ( $V_T = -27$  to  $-9$  V) and an increase in the transistor on/off ratio of > 100 was observed when the MoS<sub>2</sub> layers were thinned from 91 nm to 27 nm. These observations are attributed to intrinsic defects that are in the MoS<sub>2</sub> structure. A similar trend in the field-effect mobility and subthreshold swing was also observed. Optimized FETs possessed a typical field-effect mobility of 23 cm<sup>2</sup>/V-s,  $V_T = -9$  V, and a subthreshold swing (S.S.) of 2.75 V/decade for ~ 27 nm thick devices. The fabrication of multiple MoS<sub>2</sub> FETs in an array, which was facilitated by the modified exfoliation method, enabled us to statistically evaluate the exfoliation and thinning process. The performance variations of groups of seven MoS<sub>2</sub> devices had a device-to-device deviation of < 20% in their extracted parameters. The effect of the thinning process revealed that the removal of 1 nm of MoS<sub>2</sub> in the channel region resulted in a measured threshold voltage shift of 0.35 V. Assuming a constant areal density of trap states in the MoS<sub>2</sub>, each layer contains approximately 7.510<sup>10</sup> cm<sup>-2</sup> traps. Furthermore, thinning the channel leads to a S.S. drop rate of 30 mV-dec<sup>-1</sup>nm<sup>-1</sup> and a field-effect mobility change of 0.04 cm<sup>2</sup>-V<sup>-1</sup>s<sup>-1</sup>nm<sup>-1</sup>. These findings suggest a strong correlation to the FET performance as a function of MoS<sub>2</sub> layer thickness for “thin-film” type devices. Finally, the effect of back-channel passivation on the device performance and electrical stability will be presented.

## 12:15 PM D04

### (Student) The Impact of the Graphene Work Function on the Stability of Flexible GFETs

Theresia Knobloch<sup>1</sup>, Yury Illarionov<sup>1,2</sup>, Burkay Uzlu<sup>3</sup>, Michael Waltl<sup>1</sup>, Daniel Neumaier<sup>3</sup>, Max Lemme<sup>2</sup> and Tibor Grasser<sup>1</sup>; <sup>1</sup>TU Wien, Austria; <sup>2</sup>Ioffe Institute, Russian Federation; <sup>3</sup>AMO GmbH, Germany

Graphene field effect transistors (GFETs) are promising for a wide variety of applications, such as Hall sensors [1] and photodetectors [2]. The recent demonstration of flexible GFETs expands the application space towards wearable electronics [3]. However, one of the main obstacles for the commercialization of these devices is the considerable variability and limited long-term stability of the main device parameters. For the first time, we study the stability of flexible GFETs and demonstrate how a small change in the graphene work function, which may be induced by impurities, can considerably

affect stable device operation. Our devices are flexible GFETs with two different types of CVD grown graphene, purchased from Grolltex (Type 1) and Graphenea (Type 2). Both batches use spin-coated polyimide (PI) as a flexible substrate, onto which the graphene monolayer is transferred. In a scalable process the areas of 54 devices per batch are patterned in an oxygen plasma and source and drain contacts of 50nm Ni are sputter-deposited, defining L=80µm and W=50µm. After growing 40nm of Al<sub>2</sub>O<sub>3</sub> by ALD the devices are finalized by sputtering 10nm Ti/ 150nm Al as top gate contact.

We measure the hysteresis of the  $I_D(V_G)$  characteristics at varying sweep times  $t_{sw}$  and sweep ranges  $V_{Gmin}$  to  $V_{Gmax}$ , and calculate the hysteresis width  $\Delta V_H$  as difference between the Dirac point voltage  $V_{Dirac}$  of the forward and the reverse sweep. From the fast  $I_D(V_G)$  characteristics we estimate the field-effect mobility of the two types of graphene to be on average 4000cm<sup>2</sup>/Vs for Type 1 graphene and 1000cm<sup>2</sup>/Vs for Type 2 graphene. The Dirac point voltage  $V_D$  is on average at 0.8V for Type 1 and at 1.3V for Type 2, indicating higher p-type doping and a higher density of intrinsic defects in Type 2 graphene. The high defect density in Type 2 graphene explains the larger device-to-device variability, which becomes apparent from the  $\Delta V_H$  vs.  $1/t_{sw}$  dependences. Despite the higher material quality of Type 1 graphene, the hysteresis width for slow sweeps up to +10V maximum gate voltage is higher. In particular, the Dirac point voltage shift for forward sweeps strongly increases, resulting in a larger hysteresis width. As the voltage shift is related to a charge transfer between the channel and point defects in the insulator, this directly corresponds to more active insulator defects in Type 1 graphene devices. However, the Al<sub>2</sub>O<sub>3</sub> gate insulator is the same for both batches which is why only a work function difference between the two types of graphene can explain the different numbers of active oxide traps. Indeed, the work function of graphene can be adjusted between 3.4eV and 5.1eV by chemical doping [4], [5]. We estimate the work function of higher quality Type 1 graphene at 4.6eV and of Type 2 at 4.9eV, corresponding to a higher density of impurities in the latter case. This results in a more unfavourable energetic alignment for the Type 1 graphene channel to the defect band in Al<sub>2</sub>O<sub>3</sub> at 2.55eV +/-0.3eV below the conduction band edge [6]. During slow sweeps, at negative voltages in Type 1 more defects in Al<sub>2</sub>O<sub>3</sub> can emit electrons, which shifts the forward sweep  $V_{Dirac}$  to more negative voltages and results in a larger hysteresis. Our findings illustrate that the hysteresis width in flexible GFETs depends on the work function of graphene, which determines the energetic barrier for charge trapping by insulator defects in the Al<sub>2</sub>O<sub>3</sub> defect band. Thus, in order to achieve stable operation of flexible GFETs, the graphene work function has to be actively designed to be 5eV or higher, for instance by doping, to match the location of the defect bands in the gate insulator.

[1] B.Uzlu et al., *Sci. Rep.* 9, 18059 (2019). [2] S. Goossens et al, *Nat. Photon.* 11, 366 (2017). [3] T.-H. Han et al, *Mater. Sci. Eng. R* 118, 1 (2017). [4] J.-T. Seo et al., *J.App. Phy.* 116, 084312 (2014). [5] C. Klein et al., *Heliyon* 4, e01030 (2018). [6] Y. Illarionov et al., *2D Mat.* 4, 025108 (2017).

## SESSION E: Quantum Materials

Session Chair: Stephanie Law

Session Hosts: Connie Li and Daniel Wasserman

Wednesday Morning, June 24, 2020

Location: ZoomRoom 5

## 11:30 AM \*E01

### Predicting and Controlling the Electronic, Spin and Lattice Degrees of Freedom of Artificial Atoms in Solids

Princha Narang; Harvard University, United States

Recent work has focused on identifying new defect qubits in 3D and 2D materials with quantum optoelectronic properties that reach beyond the limitations of the well-known nitrogen-vacancy (NV-) center in diamond. Group IV-vacancy centers in diamond have been of particular interest due to their symmetry-protected optical transitions and long-lived spin degree of freedom. In the first part of my talk I will discuss the ground- and excited-state properties of group IV centers in their negative and neutral charge state with a focus on the dynamic and product Jahn-Teller (pJT) effects, including their impact on zero phonon line energetics, spin-orbit coupling and lattice dynamics. From first principles, I will show how we capture the interplay of spin-orbit and electron-phonon coupling in order to accurately describe the pJT-affected excited state manifold, going beyond a perturbative description. In the second part of my talk I will present our recent work on color centers in low dimensional materials in particular the impact of localized strain and strong-spin orbit coupling. I will conclude with discussing schemes for selective control of optically active qubits of differing excitation energies towards creating components for quantum networks.

## 12:00 PM \*E02

### Probing Electronic Degrees of Freedom at Buried Interfaces in Quantum Heterostructures Using Resonant X-Ray Reflectivity

Steven May; Drexel University, United States

A central objective in the study of quantum materials is to control degrees of electronic character such as spin-orbit coupling, orbital polarization, correlations, band inversions, and hybridization to enable new ground

states or physical function. However, the measurement of these quantities remains challenging, particularly if we want quantitative information about how electronic character evolves across buried interfaces. In this talk, I'll discuss how resonant x-ray reflectivity can provide quantitative depth profiles of elemental concentrations, orbital polarization, band hybridization and magnetization in quantum heterostructures. For my first example, I'll show how Fe-O band hybridization and Fe 3d orbital occupancy changes across interfaces in superlattices of correlated SrFeO<sub>3</sub>/CaFeO<sub>3</sub> oxides. In the second example, I'll discuss measurements aimed at understanding how magnetism in Fe is affected when interfaced with the topological insulator Bi<sub>2</sub>Se<sub>3</sub>. Together, these results provide examples of the unique information provided by resonant x-ray reflectivity and illustrate the central role it can play in elucidating interfacial behavior in quantum material heterostructures. This work is supported by the Army Research Office (grant number W911NF-15-1-0133).

### 12:30 PM E03

**(Student) Resonant and Magnetic Doping in Topological Insulator Bi<sub>2</sub>Se<sub>3</sub>** Brandi Wooten<sup>1</sup>, Patrick Taylor<sup>2</sup> and Joseph P. Heremans<sup>1,1,1</sup>; <sup>1</sup>The Ohio State University, United States; <sup>2</sup>U.S. Army Research Laboratory, United States

Topological insulators (TI) are bulk insulators that exhibit topologically protected, spin-locked conducting surface states. While the physics is exotic and has great potential, the materials' properties are not easy to observe nor exploit. Surface electrons have short lifetimes due to interactions with the bulk electrons that result in a dephasing, ruling out applications in quantum computing that require robust states.<sup>1</sup> Here, we seek to overcome this obstacle by using resonant doping to reduce the bulk carrier concentration. This would satisfy the Mott criterion for the metal-insulator transition: the number of electrons due to unintentional doping,  $n_p$ , must be less than the critical carrier concentration,  $n_c$ . In TI Bi<sub>2</sub>Se<sub>3</sub>, the Se vacancies lead to a heavily n-type semiconductor; thus, the Mott Criterion is not reached. Calculations show that by adding resonant dopant, Sn, the density of states in Bi<sub>2</sub>Se<sub>3</sub> is broadened at the top of the valence band. This decreases  $n_c$  by an order of magnitude, allowing for the Mott criterion to be satisfied.<sup>2</sup> Preliminary transport data shows that as the temperature is reduced, Sn-doped Bi<sub>2</sub>Se<sub>3</sub> experiences a change in Seebeck sign, hinting that a truly insulating state is possible. Further, we plan to explore the effects of magnetically doping Bi<sub>2</sub>Se<sub>3</sub> with Mn.

[1] J. Heremans et al., Nat. Rev. Mater. 2 (2017)

[2] C. Jaworski et al. PRB **80**, 233201 (2009); Wiendlocha, J. Electron. Mater. **45**, 3515 (2016)

Funding: Center for Emergent Materials, NSF-DMR-1420451

### SESSION F: Organic and Hybrid Optoelectronic Devices

Session Chair: Adrienne Stiff-Roberts  
Session Hosts: William Wong and Wei You  
Wednesday Morning, June 24, 2020  
Location: ZoomRoom 6

### 11:30 AM F01

**(Student) LED Performance of PFO/MEH-PPV Blended Polymer Active Regions Deposited by RIR-MAPLE** Buang Zhang, Moarabi Kakabalo and Adrienne Stiff-Roberts; Duke University, United States

After the discovery of conjugated polymer electroluminescence by Burroughes et al.[1] in 1989, light-emitting conjugated polymers have received a considerable amount of attention. Brightness, efficiency, and lifetime of polymer light-emitting diodes (LEDs) are being enhanced rapidly.[2] Blue emission polymers receive additional research attention due to lower brightness and efficiency compared to green and red emission polymers.[3] Poly(9,9-di-n-octylfluorenyl-2,7-diyl) (PFO) has been considered as a possible blue-emitting polymer with better emissive properties. Previous work has shown that emulsion-based, resonant infrared, matrix-assisted pulsed laser evaporation (RIR-MAPLE) can deposit PFO with the crystalline beta-phase (b),[4] which exhibits greater charge-carrier mobility. The polymer is dissolved in solvents to form an "oil-in-water" emulsion. The emulsion is instantly frozen into a solid target inside of the deposition chamber. An Er: YAG laser from the RIR-MAPLE system is resonantly absorbed by the hydroxyl bond vibrational mode in the continuous water phase of the emulsion, thereby transferring the polymer onto the substrate without degradation as the water-ice matrix is evaporated.[5] Initial work has shown that LEDs with PFO active regions deposited by RIR-MAPLE have turn-on voltages that are slightly lower compared to some spin-coated devices.[4] From current-voltage measurements, the threshold voltage is as low as 1.7V, whereas comparable spin-coated PFO devices typically have a turn-on voltage ~ 3.4V.[6] Poly[2-methoxy-5-(2'-ethylhexyloxy)-1,4-phenylene vinylene] (MEH-PPV), a conjugated polymer that produces orange-red light, has been shown to affect hole carrier mobility when a small amount is blended with PFO.[7] In addition, the blending of MEH-PPV with PFO at low composition (≤ 2 wt%) was shown to increase the current density in LEDs,[7] yield white light emission,[8] and improve surface quality of deposited films. [9] In this work, the ability to blend MEH-PPV with PFO for a large range of compositions will be investigated to determine the impact on LED performance. It is expected that lower wt% of MEH-PPV in PFO active regions will increase the LED current density and luminance and will result in broad-

band emission, as observed for spin-cast films.[8] However, the film quality and the emission spectra could be different between spin-cast and RIR-MAPLE deposited films, especially as the MEH-PPV wt% increases. Therefore, blended polymer active regions with varying wt% of MEH-PPV in PFO will be deposited by RIR-MAPLE using sequential deposition. Films will be characterized by UV-Vis absorbance (to analyze the blended polymer concentration and bandgap variation) and atomic force microscopy (AFM) (to determine surface morphology). LEDs will be fabricated with the device stack of ITO/PEDOT:PSS/PFO+MEH-PPV/LiF/Al. Current density vs. voltage curves, electroluminescence spectra, brightness measurements, and LED emission spectra will be used to characterize the LED performance. Thus, this work will demonstrate the uniqueness of blended polymer active regions deposited by RIR-MAPLE for application to LEDs. This material is based upon work supported by the National Science Foundation under Grant No. NSF CMMI-1727572. **References:** [1] J. H. Burroughes, et. al., *Nature*, **347**, p. 539 (1990). [2] D. D. C. Bradley, *Curr. Opin. Solid State Mater. Sci.*, **1**, p. 789 (1996). [3] Y. Chen, et. al., *J. Appl. Polym. Sci.*, **134**, p. 6 (2017). [4] S. Ferguson, et. al., *J. Electron. Mat.*, **48**, p. 3388 (2019). [5] W. Ge, et. al., *ACS Appl. Mat. and Inter.*, **8**, p. 19494 (2016). [6] H.-H. Lu, et. al., *Adv. Mat.*, **19**, p. 2574 (2007). [7] M. Redecker, et. al., *Appl. Phys. Lett.*, **73**, p. 1565 (1998). [8] J. Huang, et. al., *Adv. Mat.*, **18**(1), p. 111 (2006). [9] M. Bajpai, et. al., *Synthetic Metals*, **160**, p. 1740 (2010).

### 11:45 AM F02

**Charge-Transfer Liquid Crystals for Re-Writable Waveguides** Michael Wood<sup>1</sup>, Joseph Reczek<sup>2</sup> and Bryan Kaehr<sup>1,3</sup>; <sup>1</sup>Sandia National Laboratories, United States; <sup>2</sup>Denison University, United States; <sup>3</sup>Center for Integrated Nanotechnologies, United States

Field-programmable gate array (FPGA) circuits have widespread utility for prototyping and upgrading electronic integrated circuits. To date, there is no analogous equivalent for photonic integrated circuits. Building upon our recent work showing laser direct write/re-write of donor-acceptor liquid crystals (Adv Mater, 2018), we hypothesized that suitable index contrast for waveguiding could be achieved via patterned orientation of DACLC domains. Indeed, we measured an index contrast of ~0.2 between incident light that is perpendicular versus parallel to patterned LC columns. Next, we built devices guided by modeling that consisted of thin-film LC layers on silicon nitride substrates to confine the mode below the polarized DACLCs. We laser patterned aligned/amorphous 'cladding' against perpendicular LC domains and observed confinement of light through the high index regions (50 micron wide) following edge coupling of 635 and 980 nm laser light. The relatively weak coupling observed was partially due to modal interference and should drastically increase using single mode (5 micron wide) high index regions. Importantly, DACLCs are stable at high temperature (>100C) and samples showed the ability to write and re-write photonic structures without evidence of persistence of prior patterns. Further studies to refine the write process and produce single-mode waveguides with reduced coupling and propagation losses provide a path forward for the development of post-fabrication, re-writable photonic circuits.

### 12:00 PM F03

**Reduced Metal Penetration of Evaporated Top Contacts on Organic Semiconductors** Jacob W. Ciszek; Loyola University Chicago, United States

Organic optoelectronic devices (OLED, OFETs, etc.) are generally configured such that a metal contact must be deposited on top of the organic semiconductor. The degree of damage imparted by the hot (evaporated) or ionized (sputtered) materials ranges from moderate to extreme. Many methods to limit this damage have been examined including inorganic interlayers (e.g. MO<sub>x</sub>), deposition of organic molecules with heteroatoms, LiF, or other barrier layers, each with their own limitations. In the absence of an ideal solution, we instead have developed chemistry to finely alter the surface of the semiconductor to install metal binding groups in sufficient density to prevent metal penetration, all while leaving bulk semiconductor properties intact. In this embodiment, Diels-Alder chemistry is used to install thiols on the surface of a tetracene (a representative example of the acene class of transistor materials) and prevent the penetration of thermally-deposited silver top contacts. Controls (unreacted, non-metal binding molecules) confirm the effect of the thiol or other metal binding functional groups. Spectroscopic evidence and device performance confirms the retention of the bulk semiconductor's properties, while reducing metalation damage. The talk concludes with details on the wide scope of materials which can be reacted and several other examples of device improvement (electrode adhesion in flexible devices, contact uniformity, conductance increases, etc.).

### 12:15 PM F04

**(Student) Structural and Electrical Properties of Self-Assembled Molecular Nanodielectrics on Germanium** Mohamed-amine Guerboukha<sup>1</sup>, Virginie Gadenne<sup>1</sup>, Younal Ksari<sup>1</sup>, David Tomecek<sup>2</sup>, Martin Hruska<sup>2</sup>, Fitl Premysl<sup>2</sup>, Jean-Manuel Raimundo<sup>3</sup> and Lionel Patrone<sup>1</sup>; <sup>1</sup>IM2NP UMR 7334, Aix Marseille Univ, Université de Toulon, France; <sup>2</sup>University of Chemistry and Technology, Czechia; <sup>3</sup>UMR CNRS 7325, Aix-Marseille Université, France

The aim of this work is to design new self-assembled molecular monolayers (SAMs) grafted on Germanium (Ge) exhibiting the best properties of insulation

and passivation as new high-K nanodielectrics for the future generation of transistors (1). We used thiol molecules, with either alkyl/fluorinated/or with specially synthesized bithiophene-based push-pull molecules. Thanks to their dipole that can be aligned by the SAM deposition strategy, such chromophores have been shown to form highly polarizable insulating films (1). We have successfully developed a grafting process without acid treatment, either in one-go (2) or within two steps, that reduces surface roughness. XPS demonstrates the removal of oxide enabling the passivation of Ge surface by dodecanethiol, perfluorodecanethiol, & push-pull thiol SAMs. Good organization of the SAMs is proved by contact angle, AFM & ellipsometry. In relation with the structure, electronic properties (rectification due to dipole, energy levels) and insulation characteristics of the SAMs are investigated by current/capacitance-voltage & impedance measurements at the nanoscale using scanning tunneling microscopy and at the microscale using electrical contacts and analyzed notably by transition voltage spectroscopy(3) and correlated with UPS & IPES spectroscopic analyses. We have reduced current by a factor  $10^5$  compared  $\text{GeO}_x$ . We also investigated a method for recycling Ge substrates by ultraviolet radiation that have been evaluated by atomic force microscopy. Further work will address multilayers of aligned organic molecules. References: 1.A.Facchetti *et al.*, *Adv.Mater.* **17**,1705 (2005). 2.J.N.Hohman *et al.*, *Chem.Sci.* **2**,1334 (2011). 3.X.Lefevre *et al.*, *J.Phys.Chem.* **C119**,5703 (2015). Acknowledgements: Funding from PHC BARRANDE 2018 (40672RL), Campus France, Ministères de l'Europe et des Affaires étrangères (MEAE) et de l'Enseignement Supérieur, de la Recherche et de l'Innovation (MESRI), as well as financial support from Ministry of Education, Youth and Sports, within the projects LTC17058 and 8J18FR011, and by COST Action CA15107 Multi Compare also acknowledged. Equipment was mainly funded by the "Objectif 2" EEC program (FEDER), the "Conseil Général du Var" Council, the PACA Regional Council, Toulon Provence Méditerranée and ISEN-Toulon which are acknowledged.

SESSION G:  $\text{Ga}_2\text{O}_3$ —Growth, Characterization and Defects I  
Session Chair: Sriram Krishnamoorthy  
Session Hosts: Berardi Sensale Rodriguez and Hongping Zhao  
Wednesday Afternoon, June 24, 2020  
Location: ZoomRoom 1

## 2:00 PM G01

**(Student) Mist CVD Growth and Optical Studies of  $\alpha$ - $\text{Ga}_2\text{O}_3$  on Sapphire** Usman U. Muazzam, Prasad Chavan, Muralidharan R, Srinivasan Raghavan and Digbijoy Nath; Indian Institute of Science, India

Among the various polyphases of emerging gallium oxide ( $\text{Ga}_2\text{O}_3$ ) family of materials,  $\alpha$ - $\text{Ga}_2\text{O}_3$  is of particular interest due to its ferroelectric nature and its predicted polarization which could be promising for generating 2DEG and enabling novel device designs. Studies of  $\alpha$ - $\text{Ga}_2\text{O}_3$ , particularly its growth and opto-electronic properties, are however at an embryonic stage. Here, we report on the mist-CVD growth of  $\alpha$ - $\text{Ga}_2\text{O}_3$  and investigation of its optical properties for potential in realizing deep-UV opto-electronic devices.

$\alpha$ - $\text{Ga}_2\text{O}_3$  thin film was hetero-epitaxially grown on sapphire using Mist CVD reactor in fine channel geometry. The in-house Mist CVD consists of two parts, the reactor and mist generator. The precursor used was 5N pure gallium acetylacetonate ( $\text{Ga}(\text{acac})_3$ ) as a source of gallium, 0.33 M of  $\text{Ga}(\text{acac})_3$  and 0.5 ml of HCl was mixed in de-ionised (DI) water. This solution was then ultrasonicated at frequency of 1.6 MHz using mist-generator. The generated mist was directed to the deposition zone using  $\text{N}_2$  as carrier gas. Firstly, 1cm x 1cm of sapphire wafer was solvent cleansed in acetone, isopropyl alcohol and then rinsed with DI water. The cleaned substrate was then placed inside the deposition zone of fine channel mist-CVD. The growth process was carried out for one hour at a temperature of 450 °C and at atmospheric pressure, the dilution and carrier flow rates were maintained at 1.5 SLM and 0.15 SLM respectively, growth rate of 3 nm/min was achieved.

The diffraction peaks in XRD scan were observed at  $19.26^\circ$ ,  $38^\circ$  and  $60^\circ$  corresponding to the (0002), (0004) and (0006) planes respectively of  $\alpha$ - $\text{Ga}_2\text{O}_3$  confirming epitaxial nature of the as deposited film. On-axis rocking curve with full width at half maximum (FWHM) of 99 arcsec shows good quality film with low screw dislocations in the as deposited film. Morphology of as-deposited  $\alpha$ - $\text{Ga}_2\text{O}_3$  thin film was studied using scanning electron microscope (SEM), thickness of the film was measured in cross-sectional SEM to be 187.4 nm. The roughness of the film was found to be 1.85 nm using atomic force microscopy (AFM).

Absorption measurement was done using UV-Visible spectroscopy. The absorption spectrum exhibited two onsets. These features have been studied using Elliott-Toyozaw model.  $\text{Ga}_2\text{O}_3$  has high Fröhlich coupling coefficient owing to its highly polar Ga-O bond which results in enhancement of excitonic binding energy in  $\text{Ga}_2\text{O}_3$ , due to which excitonic signature can be seen in optical measurements even at room temperature. Extracted values of binding energy and direct allowed bandgap was found to be 95 meV and 5.4 eV. Further, to check its potential as an optical material a metal-semiconductor-metal (MSM) photodetector (PD) with lateral inter-digitated geometry was fabricated on  $\alpha$ - $\text{Ga}_2\text{O}_3$ . Interdigitated Ni(20nm)/Au(100nm) fingers were deposited using e-beam evaporator for Schottky contact. Fabricated MSM PD comprises of 17 pairs of interdigitated fingers with a width of 4  $\mu\text{m}$  and spacing

of 6  $\mu\text{m}$ , having an effective active area of 260 x 300  $\mu\text{m}^2$ . UV to visible rejection, peak spectral responsivity (SR) and photo to dark current ratio were found to be 0.12 A/W,  $10^2$ ,  $10^2$  respectively at 8 V. The photocurrent was measured at an illumination of 240 nm. Further, real-time photocurrent transient was studied to determine the response rate of the solar blind photodetector, UV illumination of 240 nm was periodically switched on and off at a bias of 20 V. Rise and fall time of PD are found to be 1.94 s and 0.26 s respectively. In spectral responsivity plot a kink was observed at 310 nm to investigate this kink we have done energy resolved cathodoluminescence (CL) measurements and it was observed that as the beam energy was increased the peaks were getting blue shifted. This type of behaviour could be attributed to donor-acceptor-pair (DAP) transition. Further high temperature measurements of MSM photodetector will be presented.

## 2:15 PM G02

**A New Magnetic Phase of  $\text{Fe}_2\text{O}_3$ : Monoclinic  $\mu$ - $\text{Fe}_2\text{O}_3$  Epitaxially Stabilized on  $\beta$ - $\text{Ga}_2\text{O}_3$**  John S. Jamison, Brélon J. May, Julia Deitz, Szu-Chia Chien, Elline C. Hettiaratchy, Binbin Wang, David McComb, Tyler Grassman, Wolfgang Windl and Roberto C. Myers; The Ohio State University, United States

Here we demonstrate a new monoclinic phase of ferric oxide ( $\mu$ - $\text{Fe}_2\text{O}_3$ ) epitaxially stabilized on (010)  $\beta$ - $\text{Ga}_2\text{O}_3$ . Density functional theory (DFT) calculations predict that the lattice parameters of free standing  $\mu$ - $\text{Fe}_2\text{O}_3$  are within  $\sim 1\%$  of  $\beta$ - $\text{Ga}_2\text{O}_3$ , and that the thermodynamic formation energy of  $\mu$ - $\text{Fe}_2\text{O}_3$  is comparable to that of other naturally occurring polytypes of ferric oxide. Various structures of  $\mu$ - $\text{Fe}_2\text{O}_3/\beta$ - $\text{Ga}_2\text{O}_3$  are grown via plasma assisted molecular beam epitaxy (PAMBÉ). High-resolution x-ray diffraction (XRD) measurements of monoclinic  $\mu$ - $\text{Fe}_2\text{O}_3$  show that the measured out-of-plane (b) lattice parameter, 3.06 Å is in excellent agreement with the predicted lattice constant for relaxed  $\mu$ - $\text{Fe}_2\text{O}_3$  (3.07 Å). Atomic-resolution scanning transmission electron microscopy (STEM) images shows no evidence of other phases of ferric oxide and confirms the complete registry of  $\mu$ - $\text{Fe}_2\text{O}_3$  layers to the underlying  $\beta$ - $\text{Ga}_2\text{O}_3$ . Finally, while DFT modeling predicts antiferromagnetic ordering bulk  $\mu$ - $\text{Fe}_2\text{O}_3$  we observe net magnetic moment in SQUID magnetometry, even up to room temperature, indicating ferro or ferrimagnetic ordering. Further DFT modeling predicts that the interface region between  $\mu$ - $\text{Fe}_2\text{O}_3$  and  $\beta$ - $\text{Ga}_2\text{O}_3$  is responsible for the observed magnetic moment. Antiferromagnetic coupling exists between the octahedral and tetrahedral sites in  $\mu$ - $\text{Fe}_2\text{O}_3$ , cancelling out the magnetic moment in the bulk. At the interface, however, energetics suggest that  $\text{Fe}^{3+}$  will selectively occupy tetrahedral sites which ferromagnetically couple to one another, and the calculated magnetic moment per  $\text{Fe}^{3+}$  ion from SQUID magnetometry is consistent with the DFT modeling supporting the interfacial magnetism hypothesis [1].

[1] J.S. Jamison, B.J. May, J.I. Deitz, S. Chien, D.W. McComb, T.J. Grassman, W. Windl, and R.C. Myers, *Cryst Growth Des.*, **19**, 4205-4211.

## 2:30 PM G03

**(Student) Investigating High-Tc Ferromagnetism in  $\alpha$ - $\text{Fe}_2\text{O}_3/\beta$ - $\text{Ga}_2\text{O}_3$  Superlattices by Molecular Beam Epitaxy** Elline C. Hettiaratchy, John Jamison, Binbin Wang, David McComb and Roberto C. Myers; The Ohio State University, United States

We recently reported on the stabilization of this new  $\mu$ - $\text{Fe}_2\text{O}_3$  exhibiting ferromagnetic response above room temperature [1]. Here we discuss an ongoing growth study involving superlattices composed of the new monoclinic phase of  $\text{Fe}_2\text{O}_3$  with non-magnetic spacers of the ultra-wide band gap semiconductor  $\beta$ - $\text{Ga}_2\text{O}_3$  grown by plasma-assisted molecular beam epitaxy on (010) oriented  $\beta$ - $\text{Ga}_2\text{O}_3$  substrates. The substrate temperatures and the Ga fluxes were varied between 500°C-700°C and  $2.5$ - $6.0 \times 10^{-8}$  Torr, whereas the Fe and  $\text{O}_2$  fluxes and the superlattice periodicity were fixed. Based on atomic force microscopy, the morphology is consistent with island-layer-by-layer growth, i.e. Frank-van der Merwe mechanism. Increasing the substrate temperature from 500°C to 700°C leads to smoother surfaces, with surface roughness decreasing from 1.1 nm to 0.4 nm. Well-defined superlattice peaks are observed using x-ray diffraction (XRD). As previously reported [1], the incorporation of  $\mu$ - $\text{Fe}_2\text{O}_3$ , expected to be antiferromagnetic, into  $\beta$ - $\text{Ga}_2\text{O}_3$ , a diamagnetic material, results in ferromagnetic hysteresis from room temperature to 5 K. The ferromagnetic response apparently emerges from the interface between  $\mu$ - $\text{Fe}_2\text{O}_3$  and  $\beta$ - $\text{Ga}_2\text{O}_3$ . The saturation magnetization for these samples ranges from 400 to 600  $\text{emu}/\text{cm}^3$  at 5K and 70 to 100  $\text{emu}/\text{cm}^3$  at 300K. Ferromagnetic hysteresis is observed up to a temperature of 900 K. We vary the interface quality by forming identical superlattice structures at various growth conditions. We will discuss trends observed in the saturation magnetization, coercivity and Tc with interface quality as determined by scanning tunneling electron microscopy (STEM) and XRD. **Acknowledgment:** This work was supported by the Center for Emergent Materials at The Ohio State University, an NSF MRSEC (DMR-1420451) and by the Army Research Office MURI (W911NF-14-1-0016).

**References:** [1] J. S. Jamison, B. J. May, J. I. Deitz, S.-C. Chien, D. W. McComb, T. J. Grassman, W. Windl and R. C. Myers, "Ferromagnetic Epitaxial  $\mu$ - $\text{Fe}_2\text{O}_3$  on  $\beta$ - $\text{Ga}_2\text{O}_3$ : A New Monoclinic Form of  $\text{Fe}_2\text{O}_3$ ," *Crystal Growth & Design*, **7**, 2019.

## 2:45 PM G04

**The Mechanism Behind the Easy Exfoliation of Ga<sub>2</sub>O<sub>3</sub> and Prediction of a New Phase** Muhammad N. Huda and Sajib K. Barman; The University of Texas at Arlington, United States

The transparent wide band gap semiconductor,  $\beta$ -Ga<sub>2</sub>O<sub>3</sub> has gained wide attention due to its suitability to a wide range of applications. For example, due to its wide band gap and small electron effective masses, it is suitable for power electronic devices. Interestingly, even though this is not a van der Waals material, it can be peeled along (100) surface by a scotch tape method like in graphene, and the resulting ultra-thin layers are used for high power device fabrications.  $\beta$ -Ga<sub>2</sub>O<sub>3</sub> has a monoclinic crystal structure of space group C2/m (space group no. 12). The theoretical calculations have shown that out of the two possible (100) surface-terminations ((100)A and B), (100)B surface is the most stable one, which is also experimentally observed from scanning tunneling microscopy study (STM). One of the interesting properties of this material is that thin layers preserve the pristine bulk-like electronic properties, which makes it even more promising for applications in power devices. However, to the best of our knowledge, there was no study behind the scientific understanding exploring why the exfoliation takes place so easily despite the interlayer interaction in  $\beta$ -Ga<sub>2</sub>O<sub>3</sub> is not van der Waals. In this presentation, we will first show the preferability of the exfoliation phenomenon from thermodynamic total energy calculations, then present our investigations from the first principle calculations on mechanisms behind the easy exfoliation along (100)B surface.

The first principle calculations performed for this work were based on the density functional theory (DFT) as implemented in the Vienna Ab-initio simulation package (VASP). Both generalized gradient approximation functional by Perdew–Burke–Ernzerhof (PBE-GGA) and hybrid functional by Heyd, Scuseria, and Ernzerhof (HSE) have been used. Since PBE-GGA underestimates the fundamental band gaps, and the computational cost for HSE functional calculations are very high, we have used PBE-GGA functional for geometry optimization and total energy calculations, and HSE functional for electronic structure calculations.

Our calculated surface energies for the slabs with (100)A and (100)B surfaces are 0.97 Jm<sup>-2</sup> and 0.49 Jm<sup>-2</sup>, respectively, where the energy for the former is nearly twice. Such higher energy for (100)A surface terminated slab also verifies that exfoliation along (100)B surface is highly preferable. From the charge density plots and Bader charge analyses we found, the octahedrally coordinated Ga-O bonds, perpendicular to the (100)B surface, have more ionic nature. The partial density of states calculations also showed that octahedral Ga-O bonds have a very weak orbital overlap. These bonds break during exfoliation. In contrast, the tetrahedrally coordinated Ga-O bonds, almost in-plane of (100)B, are more covalent. Finally, from bond strength calculation, we have shown that along the surface Ga-O covalent bonds are up to 6 eV per bond stronger than the perpendicular Ga-O bonds which break easily.\* Lastly, we will present hitherto unpublished theoretically predicted a new phase of Ga<sub>2</sub>O<sub>3</sub>. From the stability calculations, such as cohesive energy, this phase is almost as stable as  $\beta$ -Ga<sub>2</sub>O<sub>3</sub>, as well as dynamically stable. Given the configuration of the crystals, we refer to it as the Anatase-like Ga<sub>2</sub>O<sub>3</sub>. The electronic properties of this new phase will be briefly discussed.

\* “Physics behind the easy exfoliation of Ga<sub>2</sub>O<sub>3</sub> ultra-thin film along (100) surface.” S. K. Barman and M. N. Huda; *Physica Status Solidi RRL*, **13**, 1800554 (2019).

## 3:00 PM G05

**(Student) Exfoliation Mechanism Differences between (010) and (-201)  $\beta$ -Ga<sub>2</sub>O<sub>3</sub> Substrates Using Helium-Ion Implantation** Michael E. Liao, Yekan Wang, Tingyu Bai and Mark Goorsky; University of California, Los Angeles, United States

In this study, He<sup>+</sup> ions were implanted into both (010) and (201)  $\beta$ -Ga<sub>2</sub>O<sub>3</sub> substrates simultaneously at -20 °C with an ion energy of 160 keV and a dose of  $5 \times 10^{16}$  cm<sup>-2</sup>. Our previous work successfully demonstrated an important step in controlled-thickness, thin-layer exfoliation of (010)  $\beta$ -Ga<sub>2</sub>O<sub>3</sub> layers on the wafer-scale level.<sup>1</sup> The work presented here leverages on our previous efforts towards exfoliation along another non-cleavage plane: (201). The implanted substrates were first annealed at 200 °C for 12 hours followed by 500 °C for up to 96 hours. The lower temperature step was used to initiate He bubble nucleation, which resulted in no surface blistering in either the (010) or (201) substrates. The subsequent higher temperature step is used to promote He bubble growth at the projected range which produces a buried region with cracks and/or large-scale voids which are necessary for subsequent exfoliation. For the (010) substrate, the first signs of blistering were observed after annealing at 500 °C for 24 hours. Optical Nomarski images showed that the average surface blister diameter was 1.4  $\mu$ m. Upon further annealing up to 96 hours, the surface blisters grew to an average diameter of 4.5  $\mu$ m. On the other hand, even after annealing at 500 °C for 96 hours, the (201) substrate did not show any surface blistering. Scanning transmission electron microscopy images were then taken at the projected range of both the (010) and (201) implanted substrates annealed at 500 °C for 96 hours. The (010) substrates showed large cracks along the projected range, which correspond to where the blisters are directly above the cracks on the surface. On the other hand, the (201) annealed substrate showed only thin, disjointed cracks at the projected range. Interestingly, the cracks in this substrate were all tilted at angles ranging from 0° to 54° from the surface towards the (201) planes; cracks angled

towards the (201) were not observed. Additionally, out of the 136 total cracks observed, 108 cracks were tilted 54°. This angle is special because these cracks are then oriented parallel to the (100) plane, which is the primary cleavage plane in  $\beta$ -Ga<sub>2</sub>O<sub>3</sub>. This directional dependence of the crack formation in the (201) substrate is a consequence of the highly anisotropic properties of the monoclinic structure of  $\beta$ -Ga<sub>2</sub>O<sub>3</sub>. While no surface blistering was observed for the (201) substrate, the presence of these cracks provides a promising pathway towards exfoliating (201)  $\beta$ -Ga<sub>2</sub>O<sub>3</sub>.

References

1. M.E. Liao, et al., *ECS J. Solid State and Tech.*, **8**(11), P673 (2019).

## 3:15 PM BREAK

### 3:45 PM G06

**(LATE NEWS, Student) Low Temperature-Solution Processed, Gallium Oxide (Ga<sub>2</sub>O<sub>3</sub>) Thin-Film Transistor Using Anodized high- $\kappa$  Al<sub>2</sub>O<sub>3</sub> Gate Dielectric** Sagar R. Bhalerao<sup>1</sup>, Paul R. Berger<sup>1,2</sup> and Donald Lupo<sup>1</sup>; <sup>1</sup>Tampere University, Finland; <sup>2</sup>The Ohio State University, United States

Silicon technology and devices have dominated the semiconductor and electronics industries, since the 1960's. However, due to their high process temperatures, there are still a number of applications that are out-of-reach for silicon, namely direct integration into flexible and printed electronics, as opposed to a hybrid integration of adding a pre-fabricated integrated circuit. Direct integration can find usage in low-cost and disposable wearable medical technologies. Therefore, low temperature-solution processed oxide semiconductors that are complimentary to the performance of silicon are a prerequisite for the forthcoming printed, flexible and wearable electronics revolution. Here, in this report first time, solution processed gallium oxide (Ga<sub>2</sub>O<sub>3</sub>) thin film transistors (TFT) are reported. The high- $\kappa$  aluminum oxide (Al<sub>2</sub>O<sub>3</sub>) for the gate dielectric, was deposited with the help of a room temperature anodization process. The Ga<sub>2</sub>O<sub>3</sub> TFTs show high performance, with extracted electron mobility ( $\mu$ ) 2.50 cm<sup>2</sup>/V.s, operating voltage as low as 3V and threshold voltage ( $V_{th}$ ) 0.5 V. Other extracted TFT parameters are the on/off ratio 10<sup>4</sup>, subthreshold swing (SS), 380 mV/dec.; hysteresis 0.12 V, and transconductance ( $g_m$ ), 70  $\mu$ S. TFT fabrication was performed same as previously reported by us [1, 2]. The schematic representation and optical image of fabricated TFT are shown in Fig 1 and 2, respectively.

The transfer (Id vs. Vg) and output (Id vs. Vd) characteristics of the gallium oxide TFTs are represented in the Figs. 3 and 4 respectively. Fig. 5 represents the gate leakage current versus gate voltage along with drain current. The devices shows a quite low threshold voltage,  $V_{th}$ , to be ~0.5V, good on/off ratio ~10<sup>4</sup> with reasonably low hysteresis 0.12 V which is shown in Fig. 6. The electron mobility ( $\mu$ ) was found to be as high as 2.50 cm<sup>2</sup>/V.s, which is very promising in with respect to solution processed gallium oxide at comparatively low processing temperatures. The gate oxide thickness was estimated from the measured MOS capacitance and was found to be ~12 nm, which was further confirmed by cross sectional transmission electron microscopy in our previous report [1,2]. The Al<sub>2</sub>O<sub>3</sub> formed with anodization, exhibits relatively low leakage current in the device operating voltage range as i.e. 3 V, shown Fig. 7. The TFT transconductance ( $g_m$ ) gain is as high as 70  $\mu$ S. Furthermore, the subthreshold swing S was only 0.38 V/dec., which is comparatively quite low compared to the previously report. Furthermore, quality of the gate dielectric, aluminum oxide (Al<sub>2</sub>O<sub>3</sub>) deposited through the anodization process were also investigated with the help of atomic force microscopy (AFM), shown in Fig. 8. The measured average roughness of the aluminum oxide (Al<sub>2</sub>O<sub>3</sub>) was 1.69 nm over the scanning area 5  $\mu$ m.

The electron mobility for the solution process gallium oxide thin film transistor was 2.50 cm<sup>2</sup>/V.s, which is quite encouraging for solution processed low temperature devices. Therefore, this new solution processed gallium oxide deposition approach could be a pioneering pathway for future printed and flexible RF components, such as flexible radios. In this report, we successfully demonstrated a low-voltage, low-temperature and solution-processed gallium oxide TFTs for the first time. **Acknowledgment** The authors would like to extend a special thanks to Business Finland and the Academy of Finland for the financial assistance. **References** [1] Sagar R. Bhalerao, Donald Lupo, Amirali Zangiabadi, Ioannis Kymissis, Jaakko Leppaniemi, Ari Alastalo and Paul R. Berger, “0.6V Threshold Voltage Thin Film Transistors with Solution Processable Indium Oxide (In<sub>2</sub>O<sub>3</sub>) Channel and anodized high- $\kappa$  Al<sub>2</sub>O<sub>3</sub> Dielectric”, *IEEE Electron Device Letters*, May 2019. [2] Sagar R. Bhalerao, Donald Lupo, and Paul R. Berger, “2-volt Solution-Processed, Indium Oxide (In<sub>2</sub>O<sub>3</sub>) Thin Film Transistors on flexible Kapton”, *IEEE International Flexible Electronics Technology Conference (IFETC)*, Aug 2019, Canada.

### 4:00 PM G07

**Exploration of RF Sputtered Ga<sub>2</sub>O<sub>3</sub> as a Transparent Conductive Oxide for Application to Photovoltaics** Tal Kasher, Zak H. Blumer, Jacob T. Boyer, Daniel L. Lepkowski, Tyler Grassman and Steven A. Ringel; The Ohio State University, United States

A major tradeoff in solar cell design is balancing grid metal coverage (shading) with lateral resistance losses. One promising design method to combat this tradeoff is the use of a transparent conductive oxide (TCO), which reduces sheet resistance (and thus resistive losses), while simultaneously avoiding shading. This layer can reduce required grid metal coverage or,

ideally, even the need for a metal grid altogether. Current TCOs, such as Sn-doped  $\text{In}_2\text{O}_3$  (ITO) and Al-doped ZnO (AZO), are not fully transparent and parasitically absorb some of the solar spectrum [1]. A material that has emerged in recent years, gallium oxide ( $\text{Ga}_2\text{O}_3$ ), is an excellent candidate TCO material due to its ultra-wide bandgap of 4.8 eV ( $\beta$  phase) [2], as well as its ability to be doped to very high electron concentrations ( $>10^{20} \text{ cm}^{-3}$ ) [3]; taken together,  $\text{Ga}_2\text{O}_3$  has the potential to be *both* highly transparent *and* highly conductive. Finally,  $\text{Ga}_2\text{O}_3$  has a refractive index of about 2.0 over the solar spectrum [4], suggesting a potential for some efficacy as an anti-reflection coating. One attractive method to deposit  $\text{Ga}_2\text{O}_3$  is RF sputtering, which is amenable to production scaling and affords a high degree of process control. In this work, sputtered  $\text{Ga}_2\text{O}_3$  for use as a TCO is preliminarily explored. A Ge-doped (1 at%) sintered powder  $\text{Ga}_2\text{O}_3$  target was used to deposit thin films on a variety of substrates and/or epilayers, including Si, GaAs, AlInP, and  $\text{Al}_2\text{O}_3$  (sapphire). Initial exploration of deposition process parameters, such as pressure and RF power, resulted in changes to both surface morphology and deposition rate. Preliminary deposition rate studies (at constant RF power) reveal a near-constant bulk deposition rate (following an initial seed layer) of  $\sim 0.8 \text{ nm/min}$ ; work toward optimization/increase of deposition rate is necessary to support the high-volume scaling requirements of the PV industry. The resultant films were found to have good thickness uniformity ( $< 0.5\%$  over  $\sim 1 \text{ cm}^2$ ), an important target to help ensure electrical and optical uniformity. Surface morphologies were analyzed as a function of film thickness, deposition pressure, and deposition power. Surface roughness was found to drastically increase with film thickness. Initial seed layers ( $< 15 \text{ nm}$  film thickness) exhibit smooth morphologies, as determined via atomic force microscopy (AFM), with surface roughness of 0.2 nm RMS, while thicker films ( $> 110 \text{ nm}$ ) exhibit much higher RMS roughness of 4.1 nm. AFM reveals island-like structures that increase in size as film thickness increases. Preliminary experiments suggest that these regions may be the result of localized crystallization and domain ripening, but work is ongoing to elucidate their origin and evolution. Deposition pressure was found to not only have a strong influence on deposition rate, with decreasing pressure leading to faster deposition, but also surface morphology, with smoother morphologies resulting at pressures above 10 mTorr. Even samples with similar thickness exhibit this change in surface roughness, differentiating it from the thickness dependent mechanism noted previously. Additionally, a lower density of island-like structures was observed in samples grown at higher process pressures. Finally, the optical properties of the films were extracted from variable angle spectroscopic ellipsometry. An optical bandgap of 4.8 – 5.1 eV was found for the various films, approximately equal to the expected value of 4.8 eV. This is an important feat as defect states or undesirable phases can result in sub-bandgap absorption, ultimately reducing transparency. The high degree of transparency in the short wavelength range of the solar spectrum should result in nearly zero blue/UV parasitic absorption losses when applied as a TCO, making this material potentially relevant for AM0 applications. Experiments are underway to explore conductivity of these films and the role of various deposition conditions on this key film parameter.

#### 4:15 PM G08

**(Student) Anisotropic Permittivity of  $\beta\text{-Ga}_2\text{O}_3$  in the Terahertz Band** Prashanth Gopalan, Ashish Chanana, Praneeth Ranga, Sriram Krishnamoorthy, Steve Blair and Berardi Sensale Rodriguez; The University of Utah, United States

An integral part of developing  $\beta\text{-Ga}_2\text{O}_3$  based devices is estimating the dielectric permittivity and associated phonon modes at different frequency (wavelength) regions (i.e., optical, infrared, far-IR, THz, microwave and DC). Because of its monoclinic crystal structure,  $\beta\text{-Ga}_2\text{O}_3$  possesses anisotropic permittivity i.e., dependent on crystal directions. Several experimental studies of this anisotropy in optical [1. Bahumik et al., Appl. Opt. 2011], mid- to far-IR [M. Schubert et al., Phys. Rev. B. 2016] and recently in DC [E. Fielder et al., ECS J. Solid State Sci. Technol. 2019] have been reported. In this regard, spectroscopic measurements based on transmission or reflection provide a convenient way to vary the angle between the incident electric field and crystal axis and allow us to extract the (complex) permittivity along any specific direction. In this study, we report the THz dielectric permittivity of  $\beta\text{-Ga}_2\text{O}_3$  substrates of (010) (Synoptics) and (-201) (Tamura Corp.) orientation. Measurement of these orientations provides permittivity along the 'a-', 'c-' (from 010) and 'b-axis' (from -201). Transmission measurements were carried out in a continuous wave THz system (schematic in Figure 1) in the frequency range from 0.15 to 1 THz. Prior to THz measurements, the orientation of 'a' and 'c' axis in the (010) substrate was ascertained via UV-Vis reflection measurements based on the difference in optical bandgaps ( $E_{g(\text{a})} > E_{g(\text{c})}$ ) [F. Ricci et al., J. Phys.: Condens. Matter 2016]. The (transmitted) E-field recorded at the point detector consists of Fabry-Perot fringes (seen in Figure 2) whose amplitude and period depends on the (complex) refractive index and the substrate thickness. Analytically, this response could be described through the ABCD matrix formalism, which accounts for the multiple reflections at two interfaces - Air/GO and GO/Air [L. DuVillaret et al., IEEE J. Sel. Top. Quantum Electron. 1996]. Subsequent fits of the analytical model to the measured data yield  $\epsilon_{r(\text{a-axis})} \sim 9.38 \pm 0.17$  (shown in Figure 2(a)),  $\epsilon_{r(\text{c-axis})} \sim 11.29 \pm 0.21$  (shown in Figure 2(b)) and,  $\epsilon_{r(\text{b-axis})} \sim 9.72 \pm 0.06$  (shown in Figure 2(c)). In all of Figure 2, one can observe a good agreement between the measurement and analytical model for all three axes. Furthermore, in the (010) substrate, we observed a clear difference ( $\Delta n_p \sim 0.29$ ) in the extracted indices along the 'a-' and 'c-' axes. Based on the observed

periodicity of the frequency spectra, modeling was carried out assuming a constant value of refractive index and neglecting losses (the analyzed samples are Fe compensated). Furthermore, no discernible phonon modes were observed in this frequency range as also evidenced with the lack of frequency dispersion (with exception of Fabry Perot resonances). Interestingly, the transmission at any intermediate angle ( $\psi$ ) in the a-c plane can be well described as an angular combination of (complex) transmittance along 'a' and 'c'. This is seen in Figure 2(d) wherein a two-index transmittance model closely follows the trends observed in the measured data. In general, the measurement of angle-dependent THz permittivity of  $\beta\text{-Ga}_2\text{O}_3$  enables us to identify permittivity values along each axis accurately. This study could serve to complement previous far-IR ellipsometry measurements by providing experimental data for a relatively lower frequency region (i.e.,  $10^{12} \text{ Hz}$ ). It is important to note that the THz permittivity values here extracted, as well as the low-frequency permittivity values previously extrapolated from the far-IR [M. Schubert et al., Phys. Rev. B. 2016], would not truly represent static permittivity values as obtained via CV measurements (summarized for comparison in Table I.) but would act as a lower bound for the same. Nevertheless, the data directly measured here could be readily compared with the low-frequency extrapolated from the Far-IR, in which cases it shows several differences. Most notably, our measured data shows the largest permittivity along c-axis.

#### 4:30 PM G09

**(Late News) High Carrier Density Delta-Doped b-(Al<sub>x</sub>Ga<sub>1-x</sub>)<sub>2</sub>O<sub>3</sub>/Ga<sub>2</sub>O<sub>3</sub> Heterostructure Field-Effect Transistors by Ozone Molecular Beam Epitaxy** Marko Tadjer<sup>1</sup>, Kohei Sasaki<sup>2</sup>, Daiki Wakimoto<sup>2</sup>, James C. Gallagher<sup>3</sup>, Alan G. Jacobs<sup>3</sup>, Alyssa L. Mock<sup>4</sup>, Andrew D. Koehler<sup>1</sup>, Mona Ebrish<sup>4</sup>, Travis J. Anderson<sup>1</sup>, Karl Hobart<sup>1</sup> and Akito Kuramata<sup>1</sup>; <sup>1</sup>NRL, United States; <sup>2</sup>Novel Crystal Technology, Japan; <sup>3</sup>American Society for Engineering Education Postdoctoral Fellow, United States; <sup>4</sup>National Research Council Postdoctoral Fellow, United States

The promise of  $\text{Ga}_2\text{O}_3$  to deliver high power, high efficiency, low cost power electronics has advanced significantly in recent years after several breakthroughs were demonstrated [1, 2]. In addition,  $\text{Ga}_2\text{O}_3$  can form ternary alloys with Al and avoid phase separation up to a reasonably high Al mole fraction (about 30 percent at present) to form pseudomorphic b-(Al<sub>x</sub>Ga<sub>1-x</sub>)<sub>2</sub>O<sub>3</sub>/Ga<sub>2</sub>O<sub>3</sub> (a.k.a., AlGO/GO) heterostructures suitable for device applications. Even in the absence of spontaneous polarization in the monoclinic phase, a two-dimensional electron gas (2DEG) has been demonstrated via a delta doping approach, similar to early GaAs heterostructures [3]. In this work, three samples of AlGO/GO were grown on Fe-doped EFG (010)  $\text{Ga}_2\text{O}_3$  substrates at Novel Crystal Technology via O<sub>2</sub>-MBE with the structure. X-Ray diffraction and Rutherford backscattering measurements confirmed Al concentration of  $\sim 24\text{-}25\%$ . Electrochemical C-V measurements yielded a carrier concentration of  $7.9 \times 10^{18} \text{ cm}^{-3}$  for sample 1, and  $3.3\text{-}4.0 \times 10^{19} \text{ cm}^{-3}$  for samples 2 and 3. Mesa regions were etched in BCl<sub>3</sub> plasma and Ti/Au Ohmic contacts were deposited after an additional 20-second BCl<sub>3</sub> plasma etch in the Ohmic regions to improve contact resistance [4]. After a 470°C, 1-min. rapid-thermal anneal, a contact resistance of 93.13  $\Omega\text{-mm}$  was measured on sample 2 using the linear TLM method, indicating that n<sup>-</sup>  $\text{Ga}_2\text{O}_3$  regrowth in the Ohmic regions will be necessary in subsequent process iterations. Room temperature Hall measurements from sample 3 indicated a sheet carrier density ( $N_s$ ) of  $1.12 \times 10^{13} \text{ cm}^{-2}$ , which is the highest reported  $N_s$  for AlGO/GO to-date, Hall mobility  $\mu_H = 95 \text{ cm}^2/\text{V}\cdot\text{s}$ , and a sheet resistance of 5857  $\Omega/\text{sq}$ . Peak Hall mobility of 244  $\text{cm}^2/\text{V}\cdot\text{s}$  was measured at 150 K, and was limited by polar optical phonon scattering at higher temperature and ionized impurity scattering at cryogenic temperature.  $N_s$  decreased to  $6.9 \times 10^{12} \text{ cm}^{-2}$  at 150 K, indicating that the channel was not degenerately doped. Lateral HFETs were processed with a 20 nm thick ALD Al<sub>2</sub>O<sub>3</sub> gate dielectric layer and a 20/200 nm thick Pt/Au gate metal stack. Negative threshold voltage shift was observed as  $N_s$  increased, as well as significant increase in drain current ( $I_{D,\text{SAT}} = 22 \text{ mA/mm}$ ) for samples 2, compared to sample 1. A low contact resistance process is still required to demonstrate record high output current density in these structures. The double peak in the transconductance ( $G_m\text{-}V_{GS}$ ) also indicates the presence of a parasitic channel due to unintentional incorporation of Si at the AlGO/GO interface. In summary, we have presented the first demonstration of a b-(Al<sub>x</sub>Ga<sub>1-x</sub>)<sub>2</sub>O<sub>3</sub>/Ga<sub>2</sub>O<sub>3</sub> HFET device grown via ozone MBE, and have reported a record high sheet carrier concentration in the delta-doped region measured by the Hall and CV techniques. [1] S.J. Pearton et al., Appl. Phys. Rev. 5, 011301 (2018). [2] M. Higashiwaki, G. Jessen, Appl. Phys. Lett. 112, 060401 (2018). [3] S. Krishnamoorthy et al., Appl. Phys. Expr. 10, 051102 (2017). [4] M. Higashiwaki et al., Appl. Phys. Lett. 100, 013504 (2012).

SESSION H: Nanoscale Characterization—Scanning Probes,  
EM and Other Techniques  
Session Chair: Jay Mody  
Session Hosts: Ramón Collazo and Vincent Meyers  
Wednesday Afternoon, June 24, 2020  
Location: ZoomRoom 2

### 2:15 PM H01

**(Student) Nanoscale Polymorph Determination in Functional Metal Oxides Using Convergent Beam Electron Diffraction** [Zanlin Qiu](#), Perena Gouma and Joerg Jinschek; The Ohio State University, United States

In binary metal oxides (BMO), polymorphic transitions lead to materials' structures that could exhibit very different distinct physical and chemical properties. Exact structure determination is essential as these changes in BMO crystal structure offer a fine control over potential properties and, therefore, open up a wide field of applications. However, distinguishing between polymorphs is not trivial. Conventional characterization techniques, such as X-ray diffraction (XRD), Raman and Infrared ray (IR) spectrum, selected area electron diffraction (SAED), nanobeam diffraction (NBE), high-resolution TEM (HRTEM), high-resolution STEM (HRSTEM) as well as thermal analysis, provide information that is not always sufficient for polymorph determination, especially in nanocrystalline BMO. A general way to overcome this and to confirm a specific polymorph structure is performing TEM tilt experiments obtaining data from at least 4-6 zone axis orientation (e.g., using SAED patterns, NBE patterns, HRTEM or HRSTEM images). However, this is complicated and, in case of beam-sensitive materials, this time-consuming approach might not work. Therefore, we propose using Convergent Beam Electron Diffraction (CBED) experiments in one (or a few zone axis orientations) as a direct, easy and universal characterization technique for structure determination of nanocrystalline polymorphic materials. Here, we present results on hafnia ( $\text{HfO}_2$ ) nanoparticles with particle size ranging from 50 nm – 150 nm. There are six published  $\text{HfO}_2$  polymorphs: one cubic, one tetragonal, one monoclinic and three orthorhombic phases. We attempt to identify and distinguish uniquely between the orthorhombic  $\text{HfO}_2$  with space group  $Pca2_1$  and tetragonal  $\text{HfO}_2$  phase with space group  $P4_1/nmc$ . The former one exhibits ferroelectric properties while the latter one is a high-permittivity material [1,2]. In particular, we utilize deficient high order laue zone (HOLZ) lines in CBED patterns, in large-angle CBED (LACBED) patterns and in hollow cone beam CBED (HCB-CBED) patterns for precise determination (with accuracy of 10 pm) for crystal structure determination, such as point group, space group, atomic position [3]. MBFIT [4] is used to simulate all many-beam CBED pattern. CBED experiments are performed using a Tecnai 30 TEM at OSU's Center for Electron Microscopy and Analysis (CEMAS). Our simulation and experimental results show that each of the six  $\text{HfO}_2$  polymorphs has its own unique set of CBED patterns in various zone axis orientation. No two CBED/LACBED/HCB-CBED patterns are identical, enabling a unique phase identification of the various different  $\text{HfO}_2$  polymorphs. [1] Bösecke TS, et al. Ferroelectricity in hafnium oxide thin films. *Applied Physics Letters*. 2011;99(10). [2] Cho D-Y, et al. Stabilization of Tetragonal  $\text{HfO}_2$  under Low Active Oxygen Source Environment in Atomic Layer Deposition. *Chemistry of Materials*. 2012;24(18):3534-3543. [3] Tanaka M. (1997) Convergent-Beam Electron Diffraction. In: Dorset D.L., Hovmöller S., Zou X. (eds) *Electron Crystallography*. NATO ASI Series (Series E: Applied Sciences), vol 347. Springer, Dordrecht [4] Ogata Y, Tsuda K, Kishigoe Y, et al. Refinement of the crystal structural parameters of the intermediate phase of h-BaTiO<sub>3</sub> using convergent-beam electron diffraction. *Acta Crystallographica Section A*. 2004;60(6):525-531.

### 2:30 PM H02

**(Student) Quantification of Ordered Domains in Organic Semiconducting Polymers Using Four-Dimensional Scanning Transmission Electron Microscopy** [Gabriel A. Calderon Ortiz](#)<sup>1</sup>, Menglin Zhu<sup>1</sup>, Letian Dou<sup>2</sup> and Jinwoo Hwang<sup>1</sup>; <sup>1</sup>The Ohio State University, United States; <sup>2</sup>Purdue University, United States

Organic photovoltaics (OPVs) have been widely studied as promising candidates to produce affordable and flexible solar cell devices. The main challenge so far is the relatively low efficiency of these devices compared to their inorganic counterparts. In order to improve their photovoltaic efficiency, a thorough characterization of these materials is required to establish new structure-property relationships and potential ways of improving their performance. Here, we demonstrate a novel characterization and quantification of nanoscale ordered domains in OPVs using 4-dimensional scanning transmission electron microscopy (4D-STEM) based on the new generation fast pixelated STEM detector. Our characterization combines high spatial resolution (~1 nm) and high dynamic range in signal detection, which allow for quantitative determination of the details of the ordering parameters, including the type, size, and volume fraction of the ordered domains with unprecedented precision. We studied Poly(3-hexylthiophene-2,5-diyl) (P3HT) and P3HT: Phenyl-C61-butyric acid methyl ester (PCBM) (P3HT: PCBM). These polymers have been used as one of the standard OPV materials, but their structural ordering is complex and hence not fully understood. We first

calculated the intensity variance among thousands of diffraction patterns, which was found to be correlated to the expected alkyl and  $\pi$ - $\pi$  stackings of P3HT. With the addition of the new generation pixelated detector, real space reconstruction of the nanoscale ordered regions can be achieved at different scattering vectors ( $k$ ), which provides further information of the type of ordering and orientation of the polymer. By measuring each ordered domain reconstructed at every acquired  $k$  value and annular direction ( $\varphi$ ) more detailed information on molecular ordering compared to 1D variance is extracted. Based on the data, we constructed a 2-dimensional histogram showing the average number of the ordered domains as a function of their size and  $k$  value. The map shows a very detailed size distribution of the ordered domains and how they are related to the type of the ordering (which is represented by the  $k$  value). The new detailed information on molecular ordering can be directly compared to theoretical calculations and property data to establish direct structure-property relationships. We have also applied the same method to the P3HT:PCBM blend to investigate the changes in the structure due to the addition of acceptors. For both systems, donor and donor + acceptor blend, our data indicates a general trend showing that bigger particles possess larger spacing between molecules but are slightly less frequent than smaller particles with smaller spacing between molecules. Different accelerating voltage conditions and annealing temperatures have also been studied. In summary, our new analysis provides detailed information on type, size, volume fraction, spatial and orientation distribution of the molecular ordering at the nanoscale. By providing such level of detail our technique can potentially help establish better structure-property relationships and improve the overall understanding of not just P3HT:PCBM systems but other materials that are beam sensitive and/or possess medium range ordering.

### 2:45 PM H03

**(Student) Comparative Apex Electrostatics of Atom Probe Tomography Specimens** [Qihua Zhang](#)<sup>1</sup>, Benjamin Klein<sup>1</sup>, Norman Sanford<sup>2</sup> and Ann Chiaromonte<sup>2</sup>; <sup>1</sup>Georgia Institute of Technology, United States; <sup>2</sup>National Institute of Standards and Technology, United States

Laser-assisted atom probe tomography (APT) is the only known analytical method that can simultaneously provide sub-nm 3D spatial resolution and quantitative sensitivity approaching 1 ppm. APT has been applied with great success to the analysis of metals, semiconductors, dielectrics, and even biological materials [1]; the method is particularly suited to 3D analyses of composite and multilayered nanostructures. In APT, a nano-needle shaped specimen is electrically biased just below the threshold for field evaporation of ions. Field evaporation is then triggered by weak thermal transients imparted by a low-powered pulsed laser. The character of the field-evaporation process is strongly dependent upon the electrostatic environment across the specimen's apex. The electrostatics can be complicated by a 3D or multilayered sample where different constituent materials and interfaces are progressively revealed as ions are field-emitted away and the tip recedes in length. Therefore, rigorous electrostatic analysis is required to help understand the fundamental processes of APT and aid in guiding data analysis. Traditionally, and regardless of the specimen composition, the apex electric field  $E$  has been approximated by the asymptotic relation,  $E = V / (kr)$ , which was originally derived for sharp, metallic conductors [2]. Here,  $V$  is the applied voltage,  $r$  is the radius of curvature of the apex, and  $k$  is a dimensionless fitting parameter with  $1.5 < k < 8.5$ . We have developed a simulation tool that self-consistently solves the nonlinear electrostatic Poisson equation along with the mobile charge carrier concentrations, and provides a detailed picture of the electrostatic environment of APT specimen tips. We consider cases of metals, semiconductors, and dielectrics and compare our Poisson solver to the closed-form, asymptotic solution given above. The solutions compare well, as expected, for metal tips. Surprisingly, the two methods also agree well for semiconductor tips—regardless of the doping level. We ascribe this finding to the fact that even if the tip is fully depleted of majority carriers under the applied bias, an inversion layer will appear at the apex surface. The inversion forms a thin, degenerate, conducting layer that screens the interior of the tip—thus mimicking metallic behavior at the apex surface. A similar phenomenon was previously established to occur in dielectric nanostructures [3]. We will present examples that correlate our Poisson solutions with experimental results collected from complex, multi-constituent APT tips. [1] D. J. Larson, T. J. Prosa, R. M. Ulfig, B. P. Geiser, and T. F. Kelly, *Local Electrode Atom Probe Tomography: A User's Guide*, Springer New York, 2013, ISBN: 978-1-4614-8721-0 (eBook). [2] P. J. Birdseye and D. A. Smith, *Surface Science* 23, 198 (1970). [3] E.P. Silaeva, L. Arnoldi, M.L. Karahka, B. Deconihout, A. Menand, H.J. Kreuzer, and A. Vella, *Nano Letters* 14 (11), 6066 (2014).

### 3:00 PM H04

**(Student) Compositional Changes at Dislocations and Interfaces in Heteroepitaxial Semiconductors Studied by Atom Probe** [Eamonn T. Hughes](#)<sup>1</sup>, Bastien Bonel<sup>1</sup>, Rushabh Shah<sup>2</sup> and Kunal Mukherjee<sup>1</sup>; <sup>1</sup>University of California, Santa Barbara, United States; <sup>2</sup>Massachusetts Institute of Technology, United States

#### Compositional changes at dislocations and interfaces in heteroepitaxial semiconductors studied by atom probe

Heteroepitaxial semiconductor growth allows for the integration of materials with different properties into a single device structure and is key to realizing technologies such as III-V on silicon photonics and III-N light emitters on

sapphire. Threading dislocations, an inevitable consequence of lattice-mismatched heteroepitaxy, are known to be potent centers for non-radiative recombination and often contribute to premature device failure. Although threading dislocation densities can be reduced, they can never be fully eliminated, so understanding how carriers recombine at dislocations and how the chemistry of threading dislocations might alter this behavior is crucial. In working toward this goal, we examine the compositional landscape of individual threading dislocations by atom probe tomography to understand how fast diffusion pathways through threading dislocations can alter the composition of the dislocation itself and of nearby interfaces.

We present two case studies using atom probe tomography to observe altered compositions around threading dislocations in (1) a SnSe/PbSe/GaAs (IV-VI on III-V) heterostructure and (2) an InGaAs/GaAs/Ge/Si (III-V on Si) heterostructure. In both cases we find significant migration of species from one layer into another through a threading dislocation.

In the SnSe/PbSe/GaAs heterostructure, extracting a threading dislocation is made easier by the very high density of threading dislocations in the film which ensures that a randomly selected site will have a significant chance of containing a threading dislocation. We find significant downward diffusion of tin through the dislocation but only slight upward diffusion of lead. This may be due to the threading dislocation gliding to form a misfit dislocation after sufficient SnSe growth, which would halt further upward diffusion of lead at that location. Although Sn is highly soluble in PbSe (up to 21 at.% in the rocksalt phase), its incorporation surrounding the dislocation is only about 5 at.%, possibly a result of limited solubility due to strain. Additionally, after diffusing through the dislocation, tin is seen to accumulate in a narrow band at the PbSe/GaAs interface, likely spreading outward through the high-density misfit dislocation network.

Many of these same features are also observed in the III-V on Si structure. In these lower dislocation density structures, however, extracting a tip containing a threading dislocation is much more challenging since a randomly selected site is very unlikely to contain a threading dislocation. We therefore use electron-channeling contrast imaging (ECCI) to locate a threading dislocation cluster for site-selective tip extraction. We see both upward diffusion of germanium and downward diffusion of indium through the dislocation. The incorporated compositions of germanium (0.3 at.%) and indium (2 at.%) appear to be respectively limited by the solid solubility limit and by strain-limited solubility. Both of these species diffuse orders of magnitude faster through the dislocation than through the bulk lattice. Though there is strong vertical diffusion of species between layers, there is no sign of species accumulation at interfaces or of lateral segregation of indium in the InGaAs layers toward the dislocation core. Even so, very small compositional changes over small regions could be below the sensitivity limit of this technique.

We demonstrate atom probe tomography to be a powerful technique for analyzing local compositional changes around dislocations and interfaces due to interlayer diffusion. Although semiconductors with low threading dislocation densities can make successful extraction and analysis challenging, identifying dislocation cluster sites using ECCI enables much more reliable dislocation extraction.

### 3:15 PM BREAK

#### 3:45 PM H05

**(Student) Atom Probe Tomography Studies to Understand Dopant Interaction in Si-Doped  $(\text{Al}_x\text{Ga}_{1-x})_3\text{O}_3$** , Jith Sarker<sup>1</sup>, A F M Anhar Uddin Bhuiyan<sup>2</sup>, Zixuan Feng<sup>2</sup>, Hongping Zhao<sup>2</sup> and Baishakhi Mazumder<sup>1</sup>; <sup>1</sup>University at Buffalo, The State University of New York, United States; <sup>2</sup>The Ohio State University, United States

In order to realize  $(\text{Al}_x\text{Ga}_{1-x})_3\text{O}_3$  based devices to perform as theoretically predicted, extrinsic doping is necessary to facilitate high mobility. The n-type doping of  $(\text{Al}_x\text{Ga}_{1-x})_3\text{O}_3$  using Si as a dopant is in infancy, it is crucial to understand the dopant interaction in  $(\text{Al}_x\text{Ga}_{1-x})_3\text{O}_3$  matrix to achieve efficient doping for high-efficiency devices. Atom Probe Tomography (APT) is a nanoscale analyzing tool with atomic level mapping capability at high spatial and chemical resolution in three-dimensions [1]. In this work, we employed APT to understand the dopant (Si) interaction in  $(\text{Al}_x\text{Ga}_{1-x})_3\text{O}_3$  with varying Al content. APT analysis was conducted on a Si-doped  $(\text{Al}_x\text{Ga}_{1-x})_3\text{O}_3$  heterostructure with varying  $x = 10\text{-}80\%$  to understand the dopant's behavior in the doped matrix. To investigate the dopant interaction in  $(\text{Al}_x\text{Ga}_{1-x})_3\text{O}_3$ , a statistical analysis method, Radial distribution function (RDF), was conducted on the ions collected during APT experiment. RDF is used to study the affinity between different species which was extended to understand dopant interactions in this case. RDF normalizes the local concentration of a selected species with respect to the overall bulk concentration from the center of each atom of the selected species in a radially outward direction and averaged across the sample using the formula,  $\langle \text{endf} \rangle \rightarrow$ , where  $C_E(r)$  is the concentration of species  $E$ , at a distance  $r$  from the center,  $C_0$  is the average composition of species  $E$  in the analyzed volume. RDF was performed in different regions in each layer considering Si as a species of interest. Considering the center Si atoms position as reference (zero) and RDF provides the normalized concentration of Al and Ga in radially outward direction. At low Al content ( $x = 0.10\text{-}0.20$ ), from the reference Si atom (distance,  $d = 0$ ) towards the 1<sup>st</sup> nearest neighbor location, an increase in Ga concentration is observed while Al concentration remains zero. At reference Si atom position, Ga concentration suddenly drops to zero. This suggests that the dopant Si is occupying Ga sites.

The cation vacancies ( $V_{\text{II}}$ ) are introduced upon Si-doping due to a decrease in their formation energies [2]. Si donors on Ga sites ( $\text{Si}_{\text{Ga}}$ ) are interacting with the  $(\text{Al}_x\text{Ga}_{1-x})_3\text{O}_3$  matrix by forming a defect complex with  $V_{\text{Ga}}$ ,  $(V_{\text{Ga}}-\text{Si}_{\text{Ga}})$  [2]. When Al content varies with  $x = 0.30\text{-}0.50$ , from the RDF of Si-Al and Si-Ga, it was observed that Si is substituting in either Al or Ga site. This is due to the presence of different chemical phases in these  $(\text{Al}_x\text{Ga}_{1-x})_3\text{O}_3$  layers and these phases could be either Ga-rich or Al-rich [3]. At higher Al content ( $x > 0.50$ ), Si is more likely to occupy Al sites, as  $V_{\text{Al}}$  site increases due to lower formation energy with higher Al content, and Si tends to form  $V_{\text{Al}}-\text{Si}_{\text{Al}}$  defect complexes by occupying Al sites [4]. In this work, we investigated how n-type dopant interacts in Si-doped  $(\text{Al}_x\text{Ga}_{1-x})_3\text{O}_3$  films by occupying cationic sites, either Ga or Al, depending on the alloy composition. Since cationic vacancy is created upon doping, dopants tend to occupy cationic sites and likely to form  $V_{\text{III}}-\text{Si}_{\text{III}}$  defect complexes. The information reported here will be highly significant for the wide bandgap semiconductor community to design high performance power and optical devices. References:

- [1] T. F. Kelly *et al.*, *Annu. Rev. Mater. Res.*, **42**, 1 (2012). [2] N. Furuhashi *et al.*, *J. Appl. Phys.* **64**, 4692 (1988). [3] B. Mazumder *et al.*, *Appl. Phys. Lett.* **115**(13), 132105 (2019). [4] S. F. Chichibu *et al.*, *J. Appl. Phys.* **113**, 213506 (2013). [5] Acknowledging Air Force Office of Scientific Research FA9550-18-1-0479 (AFOSR, Dr. Ali Sayir) and National Science Foundation (1810041) for funding support towards the materials growth.

#### 4:00 PM H06

**(Student) Nanosecond Photo-Induced Capacitance and Resistance Measurements in Organic Solar Cell Materials Using Broadband Local Dielectric Spectroscopy and Phase-Kick Electric Force Microscopy** Rachael Cohn and John Marohn; Cornell University, United States

Bulk heterojunction organic solar cells (OSCs) exhibit charge recombination times that are 10s to 1000s of times longer than predicted by Langevin theory. Understanding the mechanism of charge generation and recombination is critical to furthering the development of photoactive materials used in OSCs. We use electric force microscopy (EFM) to better understand the temporal dynamics and spatial distribution of charge generation and recombination in OSCs. Here we report an EFM study of a film of PBDB-T/ITIC, where PBDB-T is a polymer donor and ITIC is a nonfullerene acceptor [1]. The introduction of nonfullerene acceptors has led to recent improvements in OSC efficiency. We begin by using broadband local dielectric spectroscopy (BLDS) [2] to determine the film's charge response time,  $\tau = R_s(C_{\text{tip}} + C_s)$ , where  $R_s$  is the sample resistance,  $C_{\text{tip}}$  is the tip capacitance, and  $C_s$  is the sample capacitance. In BLDS measurements, the tip voltage is amplitude modulated at a fixed frequency, 45 Hz, and sinusoidally modulated at frequencies ranging from 200 Hz to 1.5 MHz at various light intensities. We report the first BLDS measurement on an organic solar cell material. Fitting the BLDS data to an impedance model of the tip-sample interaction, we find that  $\tau \sim R_s C_{\text{tip}}$  and conclude that light changes  $R_s$ , and not  $C_s$ , as is universally assumed in EFM experiments carried out on OSCs. In PBDB-T/ITIC we find that charge recombination is too fast to observe in a real-time time resolved EFM (tr-EFM) experiment. We are working to measure temporal changes in the film's photo-induced capacitance and resistance on the nanosecond timescale using an electrical scanned-probe microscope experiment. Time resolved microwave conductivity is typically used to measure photoinduced changes in the film charge density on the nanosecond time scale, but the technique lacks spatial resolution. Scanning probe microscopy has likewise made significant contributions to our understanding of organic photovoltaics (OPVs). In tr-EFM experiments, the EFM charging rate has been found to correlate with the external quantum efficiency [3]. A time resolution of 10 ns is claimed for the fast-free tr-EFM experiment [4], but this time is shorter than one cantilever oscillation cycle and is therefore unphysical [5,6]. Achieving nanosecond time resolution is required to observe photogenerated charges before they recombine. The phase-kick EFM (pk-EFM) experiment, recently introduced by Dwyer *et al.* [5] measures the photocapacitance and photoresistance charging time,  $\tau_p$ , by measuring the change in cantilever frequency and phase as a function of the delay times  $t_d$  between light and voltage pulses. After performing the experiment at various pulse times  $t_p$ , we plot the total phase shift  $\Delta\phi$  vs.  $t_d$  to obtain the sample's charge recombination transient and the recombination time,  $\tau_r$ . The pk-EFM method has a well-defined theory for both the signal and the signal to noise ratio (SNR) and is capable of achieving sub-cycle, nanosecond time resolution. I will describe our efforts to push pk-EFM's temporal resolution from microseconds to nanoseconds in an OPV film.

#### References

- [1] W. Zhao, D. Qian, S. Zhang, S. Li, O. Inganäs, F. Gao, and J. Hou. *Adv. Mater.*, **2016**, 28, 4734 – 4739. [2] A. M. Tirmizi, R. P. Dwyer, T. Hanrath, and J. A. Marohn. *ACS Energy Lett.*, **2017**, 2, 488 – 496. [3] (a) D. C. Coffey and D. S. Ginger. *Nat. Mater.*, **2006**, 5, 735–740. (b) P. A. Cox, M. S. Glaz, J. S. Harrison, S. R. Peurifoy, D. C. Coffey, and D. S. Ginger. *J. Phys. Chem. Lett.*, **2015**, 6, 2852 – 2858. [4] D. U. Karatay, J. S. Harrison, M. S. Glaz, R. Giridharagopal, and D. S. Ginger. *Rev. Sci. Instrum.*, **2016**, 87, 053702. [5] R. P. Dwyer, S. R. Nathan, and J. A. Marohn. *Sci. Adv.*, **2017**, 3, e1602951. [6] (a) A. Rihaczek and E. Bedrosian. *Proc. IEEE*, **1966**, 54, 434 – 435. (b) B. Boashash. *Proc. IEEE*, **1992**, 80, 520 – 538. (c) B. Boashash. *Proc. IEEE*, **1992**, 80, 540 – 568

#### 4:15 PM H07

**Thickness-Dependent Nanoscale Charge-Discharge Phenomena and AFM-Based Tomography in Dielectric/Piezoelectric Multilayer Thin Films** Thomas Moran<sup>1</sup>, Michael Martin<sup>1</sup>, Jingfeng Song<sup>1</sup>, Keigo Suzuki<sup>2</sup>, Tadasu Hosokura<sup>2</sup>, Koji Murayama<sup>2</sup> and Bryan Huey<sup>1</sup>; <sup>1</sup>University of Connecticut, United States; <sup>2</sup>Murata Manufacturing Co., Ltd., Japan

Multi-layer chip capacitors employing functional ceramic dielectric layers play a vital role in modern electronics for a variety of major industries such as communications and power transportation, among others. Ultimately, the dynamic electrical performance of these devices depends on the nanoscale materials properties of their dielectric/ferroelectric ceramic components in 3-dimensions. Ongoing efforts to maximize charge storage and volume efficiency through the reduction of layer thicknesses have driven these devices into the nanoscale. As such, thickness effects and engineered heterogeneities are of particular interest, requiring advances in nanoscale functional measurements. Accordingly, emerging methods for micromachining and Tomographic AFM, along with Kelvin Probe Force Microscopy (KPFM), Piezo Force Microscopy (PFM), and Conductive AFM (cAFM), are used to study dielectric and ferroelectric heterostructures, both at their surfaces and as a function of thickness. Dynamic charging and discharging processes are notably mapped with KPFM as a function of time and energy, providing novel insight into local dielectric behavior and especially into voltage dependencies of surface or grain boundary defect states. These are related to sub-surface features and thickness dependencies via tomographic PFM and cAFM, volumetrically revealing size effects, 3-dimensional heterogeneities, and charge dissipation pathways in homogenous films and superlattices. By considering in-situ charging and discharging phenomena, the engineered performance for micro- and nano- scale electronic devices such as multi-layer-chip-capacitors can therefore be optimized.

#### 4:30 PM H08

**Carrier Localization in Perovskite Nickelate from Oxygen Vacancies and Lithium-Ion Doping Imaged Using Near-Field Nano-Imaging at mid-IR and THz Frequencies** Neda Alsdad<sup>1</sup>, Aghamiri<sup>1</sup>, Zhen Zhang<sup>2</sup>, Qi Wang<sup>2</sup>, Yifei Sun<sup>2</sup>, Shriram Ramanathan<sup>2</sup> and Yohannes Abate<sup>1</sup>; <sup>1</sup>University of Georgia, United States; <sup>2</sup>Purdue University, United States

We image changes in the electrical conductivity of perovskite nickelate SmNiO<sub>3</sub> (SNO) when the system is driven from pristine to oxygen deficient SNO using scanning near-field optical microscopy in the mid-IR frequencies. We also observe decrease in the electrical conductivity in lithium doped SNO using THz broadband near-field nano-imaging.

SESSION I: Materials for III-Nitrides Power Electronics  
Session Chair: Christian Wetzel  
Session Hosts: Daniel Ewing and Shashwat Rathkanihiwar  
Wednesday Afternoon, June 24, 2020  
Location: ZoomRoom 3

#### 2:15 PM I01

**(Student) Polarization-Graded Al<sub>0.40</sub>Ga<sub>0.60</sub>N-on-Sapphire p-i-n Diodes with > 6 MV/cm Breakdown Field** Anisha Kalra, Shashwat Rathkanihiwar, Muralidharan R., Srinivasan Raghavan and Digbijoy Nath; Indian Institute of Science, India

In this work, we report on quasi-vertical Al<sub>0.40</sub>Ga<sub>0.60</sub>N p-i-n diodes on sapphire with breakdown fields exceeding 6 MV/cm and on-resistance of 6.25 mΩ·cm<sup>2</sup>. The MOCVD-grown epi-stack consisted of a 0.2 μm unintentionally doped Al<sub>0.40</sub>Ga<sub>0.60</sub>N layer sandwiched between a top polarization-graded 0.2 μm Mg-doped AlGaIn layer and a bottom 0.5 μm thick Si-doped Al<sub>0.45</sub>Ga<sub>0.55</sub>N. The p-i-n diodes exhibited a twelve-orders of magnitude rectification and a low reverse leakage current measuring less than 2 nA at 100 V. A turn-on voltage of 4.6 V and a high forward current density exceeding 1 kA/cm<sup>2</sup> at 10 V were observed. An ideality factor of 2.1 was extracted, indicative of generation-recombination processes in the diode. The critical electric field was estimated to be 6.2 MV/cm by considering the voltage at which the reverse current density exceeded 100 μA/cm<sup>2</sup>. This is one of the highest values reported for AlGaIn p-i-n diodes. The state-of-the-art performance parameters can cumulatively be attributed to a low dislocation density in the intrinsic AlGaIn layer owing to the use of a high crystalline quality AlN and AlN/AlGaIn superlattices based buffer and a low resistive polarization graded Mg-doped p-AlGaIn contact layer. Temperature-dependent current-voltage measurements in the 298 to 473 K range revealed hopping conduction along localized trap states as the dominant mechanism contributing to reverse leakage at fields exceeding 2.5 MV/cm. Ultra-wide bandgap (UWBG) semiconductors such as Al-rich AlGaIn and β-Ga<sub>2</sub>O<sub>3</sub> and are attracting interest for beyond-GaN, beyond-SiC, high power electronics due to their ultra-high breakdown fields and hence, their ability to block higher voltages without sacrificing the on-resistance. AlGaIn, in particular, is attractive owing to a technologically mature III-nitride device platform and flexibility in heterostructure band engineering over a 3.4 to 6.1 eV bandgap window. Vertical device architectures, especially p-i-n diodes based on these UWBG semiconductors, are promising since they can enable larger

breakdown voltages in smaller device footprints, support higher power densities, offer lower conduction losses, improved integration flexibility and yield, support high breakdown fields and exhibit low reverse leakage currents. The development of high-performance diodes has, however, been held back because of large dislocation densities in the AlGaIn-layers owing to hetero-epitaxial growth on non-native substrates and due to challenges associated with efficiently doping high Al-mole fraction AlGaIn epi-layers.

We aim to address these challenges by employing growth modifications to realize high crystalline quality AlGaIn epi-layers along with low resistive n-Al<sub>0.45</sub>Ga<sub>0.55</sub>N and p-AlGaIn layers on sapphire. The former was achieved by a careful optimization of nucleation density on the growth surface during AlN growth on sapphire, to minimize the number of coalescence boundaries per unit area to realize state-of-the-art crystalline quality epi-layers, using a two-temperature growth method. The optimized AlN along with dislocation filtering and strain relieving AlN/AlGaIn superlattices has been used as the buffer for the growth of the p-i-n epi-stack to achieve improved carrier concentration and mobility in the Si-doped n-AlGaIn layer. For realization of low resistive, polarization graded p-AlGaIn layers, a combination of Mg-doping and compositional grading of the AlGaIn was utilized. These helped realize quasi-vertical 100 x 100 μm<sup>2</sup> Al<sub>0.40</sub>Ga<sub>0.60</sub>N p-i-n diodes with a breakdown field of 6.2 MV/cm, a low on-resistance of 6.25 mΩ·cm<sup>2</sup>, rectification exceeding 10<sup>12</sup>, a low reverse leakage current of < 2 nA at 100 V, a turn-on voltage of 4.6 V, an ideality factor of 2.1 and a high forward current density exceeding 1 kA/cm<sup>2</sup> at 10 V at room temperature. The results illustrate the promise of AlGaIn p-i-n diodes realized over non-native substrates using simple, cost-effective growth techniques for high power and high field applications.

#### 2:30 PM I02

**Predicting the Quality of Vertical GaN Devices Using Long-Range Optical Techniques** James C. Gallagher<sup>1</sup>, Travis J. Anderson<sup>1</sup>, Andrew D. Koehler<sup>1</sup>, Mona Ebrish<sup>2</sup>, Michael A. Mastro<sup>1</sup>, Jennifer K. Hite<sup>1</sup>, Brendan P. Gunning<sup>3</sup>, Robert Kaplar<sup>3</sup>, Karl Hobart<sup>1</sup> and Fritz J. Kub<sup>1</sup>; <sup>1</sup>U.S. Naval Research Laboratory, United States; <sup>2</sup>National Research Council, United States; <sup>3</sup>Sandia National Laboratories, United States

Present GaN technology consists of heteroepitaxial, lateral devices. It has been predicted that switching to vertical GaN technology would reduce the impurity concentration, raise the critical electric field, and improve the breakdown conditions. This technology has yet to be realized due to the inconsistency of GaN wafer processing. Our previous work [1] has shown that imperfections in GaN wafers can be mapped using long-range non-destructive optical techniques, and surveying many vendors has resulted in a general classification into 2 categories: homogeneous substrates (Type I) and substrates with inhomogeneous distributions of defects (Type II). In this work, we report the results of fabricating vertical Schottky barrier diodes and P-i-N diodes on these different types of GaN wafers to assess the impact on device performance. Homoepitaxial GaN drift layers were grown on select substrates using metal organic chemical vapor deposition. The drift layers were either unintentionally doped (N~4E15 cm<sup>-3</sup>) or intentionally doped (N~1E16 cm<sup>-3</sup>). P-GaN layers were grown on select drift layers by either MBE regrowth or in-situ during the MOCVD growth. Non-destructive techniques (Raman, Photoluminescence, and Optical Profilometry) were used to characterize the Type II wafers and identify regions of high defect density, typically associated with dot-core type wafer production, and a mask layout was designed such that device arrays were aligned to these features. Electrical testing, including current-voltage, capacitance-voltage, and breakdown measurements with electroluminescence, was used to benchmark device performance as a function of distance from a defective region. We have identified that leakage current is particularly sensitive to dislocation density, and the effect is even more pronounced in p-n junctions which have inherently lower leakage current. A comparison to devices on a uniform substrate, statistical analysis of device performance, and temperature-dependent current-voltage to study the mechanisms of current transport will also be discussed to assess the viability of non-uniform substrates for vertical device applications.

SNL is managed and operated by NTESS under DOE NNSA contract DE-NA0003525

[1] J. C. Gallagher *et al.*, "Long range, non-destructive characterization of GaN substrates for power devices," *J. Cryst. Growth*, vol. 506, pp. 178-184, Jan. 2019.

#### 2:45 PM I03

**(Student) X-Ray Topography Characterization of GaN Substrates Used for Power Electronic Devices** Yafei Liu, Hongyu Peng, Tuerxun Ailihumaer, Balaji Raghathamachar and Michael Dudley; Stony Brook University, The State University of New York, United States

Gallium Nitride (GaN), known as one of the most important wide bandgap semiconductors, has many applications in power electronic devices such as inverters and switches, as well as optoelectronic devices like light emitting diodes. However, high-quality bulk GaN growth is still limited by the availability of growth techniques. Two most popular growth method for GaN are hydride vapor phase epitaxy (HVPE) [1, 2] and ammonothermal [3,4] method. HVPE method uses foreign substrates, such as sapphire, gallium arsenide or silicon carbide, which gives a large dislocation density due to significant lattice mismatch and difference in coefficients of thermal expansion. Ammonothermal method gives a much better quality but the crystal size is

limited to 2" in diameter. The presence of defects can limit the performance of devices fabricated on such substrates therefore it is important to understand defect distributions. This information can also be used by crystal growers to devise strategies to eliminate or minimize their impact. In this study, GaN substrates grown by both HVPE (Figure 1) and ammonothermal (Figure 2) methods have been characterized by synchrotron monochromatic beam X-ray topography (SMBXT). The distribution of threading screw/mixed dislocations (TSDs/TMDs), threading edge dislocations (TEDs) and basal plane dislocations (BPDs) is characterized. The Burgers vectors of these dislocations was confirmed by comparing the dislocation images to ray tracing simulated images. X-ray topography enables the comparison of defect distribution between the HVPE and ammonothermal samples. Using High-resolution X-ray Diffraction (HRXRD) measurements, qualitative comparison between the substrates have also been carried out. These results will be correlated with X-ray topography images and discussed with implications for device fabrication. Reference: [1] H.P. Maruska, J.J. Tietjen, Appl. Phys. Lett. 15 (1969) 327. [2] K. Fujito, S. Kubo, H. Nagaoka, T. Mochizuki, H. Namita, S. Nagao, J. Cryst. Growth 311 (2009) 3011. [3] R. Dwilinski, R. Doradzinski, J. Garczynski, L. P. Sierzputowski, A Puchalski, Y. Kanbara, K. Yagi, H. Minakuchi, H. Hayashi, J. Crystal Growth 310 (2008) 3911. [4] T. Hashimoto, F. Wu, J.S. Speck, S. Nakamura, J. Crystal Growth 310 (2008) 3907.

### 3:00 PM 104

**(Student) Probing Deep Acceptors in MOCVD GaN-on-GaN—Toward High Power GaN Vertical Devices** Yuxuan Zhang, Zhaoying Chen, Wenbo Li, Md Rezaul Karim, Adam Arehart, Steven A. Ringel and Hongping Zhao; The Ohio State University, United States

With extraordinary physical properties such as high breakdown field (3.5 MV/cm), high room temperature mobility ( $>1000 \text{ cm}^2/\text{Vs}$ ), and capability of both n-doping and p-doping, GaN represents a promising wide bandgap semiconductor for high power vertical devices. So far, the highest reported breakdown voltage ( $V_{BR}$ ) for vertical GaN power diode is 5 kV [1]. As compared with SiC vertical pn diodes with  $V_{BR}$  of 26.9 kV and drift layer net charge density  $\sim 2 \times 10^{14} \text{ cm}^{-3}$  [2], one key challenge that prevents achieving high performance GaN vertical power devices is from its high background impurity levels at mid- $10^{15}$  to low- $10^{16} \text{ cm}^{-3}$  range. Background Si, C and O are considered as major impurities in MOCVD grown GaN that affect the transport properties. Si and O are known as shallow donors in GaN. It is important to control the background Si and O in order to achieve controllable n-doping in the drift layer. C is a deep acceptor in GaN and C incorporation is strongly influenced by MOCVD growth conditions. Although no direct observation of background Fe in MOCVD grown GaN is reported, defects spectroscopy have observed  $E_c-(0.58 \pm 0.2) \text{ eV}$  defect level in GaN, which could be correlated to Fe impurity [3]. Therefore, Fe impurity in GaN film can serve as strong compensation centers. Minimizing both C and Fe impurity levels in MOCVD GaN drift layer is critical for high performance vertical power devices. In this work, we performed a systematic study on the impurity incorporation in MOCVD grown GaN-on-GaN. The wafer cleaning process was identified as one source of Fe impurities. By using regular solvent and DI water cleaning process, a designed GaN film was grown on free standing GaN substrate. The incorporation of Fe level was studied by both SIMS and deep level transient spectroscopy (DLTS)/deep level optical spectroscopy (DLOS). The DLTS/DLOS measurement revealed a high concentration peak at  $E_c-0.57 \text{ eV}$ , which corresponds to the Fe impurity. The quantitative SIMS measurement also detected high Fe impurity level:  $3 \times 10^{17} \text{ cm}^{-3}$  at the growth interface, which decayed to  $3 \times 10^{16} \text{ cm}^{-3}$  as growth proceeded. A series of cleaning process was designed for GaN-on-GaN MOCVD growth. Depth profile SIMS measurement indicates the solvent cleaning process introduced high level of impurities on the GaN epi surface, while Si contamination at the interface is persistent regardless of the different cleaning processes used. With optimized growth condition and cleaning process without solvent, we are able to achieve background Si at low- $10^{15} \text{ cm}^{-3}$ , and Fe and O concentration below detection limit in SIMS. More sensitive DLTS/DLOS will be performed to identify the Fe impurity level. The effect of MOCVD growth pressure and TMGa flow rate on the incorporation of C was studied. C concentration was measured from quantitative SIMS. From the analysis, C reduces as growth pressure increases. Low C is achieved when growth pressure is greater than 200 Torr. From the analysis, C increases with TMGa flow rate, due to more C impurity from TMGa source. With optimized growth condition, selected GaN sample was evaluated with temperature dependent Hall measurement. Room temperature mobility of  $1007 \text{ cm}^2/\text{Vs}$  and low temperature peak mobility of  $3067 \text{ cm}^2/\text{Vs}$  at 110K were measured, which represents the best reported values. In summary, a systematic study of the MOCVD growth condition and wafer cleaning process was performed to understand and thus minimize impurities incorporation in MOCVD GaN-on-GaN. This work will provide valuable guidance on achieving high purity GaN epilayer for high power vertical devices. [1] H. Ohta et al. JPN. J. APPL. PHYS. 57 04FG09, (2018). [2] N. Kaji, et al. IEEE T ELECTRON DEV 62, 374 (2014). [3] D. Cardwell, et al. Appl. Phys. Lett. 102, 193509 (2013). This work was funded in part by ARPA-E, under Award Number DE-AR0001036, and U.S. DOE's EERE under the Advanced Manufacturing Office, FY18/FY19 Lab Call.

### 3:15 PM BREAK

SESSION J: III-Nitrides—Irradiation and Device Design for Power Electronics  
Session Chair: Christian Wetzel  
Session Hosts: Daniel Ewing and Shashwat Rathkanthiwar  
Wednesday Afternoon, June 24, 2020  
Location: ZoomRoom 3

### 3:45 PM J01

**(Student) 60Co Gamma Irradiation Effects on IV of GaN Diodes Grown on Sapphire and Freestanding Substrates** Kyle Ahn<sup>1</sup>, Yu Kee Ooi<sup>1</sup>, Joshua Gallagher<sup>3</sup>, Farnood Mirkhosravi<sup>2</sup>, Azaree Lintereur<sup>3</sup>, Daniel Feezell<sup>2</sup>, Emily Mace<sup>4</sup> and Michael Scarpulla<sup>1</sup>; <sup>1</sup>The University of Utah, United States; <sup>2</sup>The University of New Mexico, United States; <sup>3</sup>The Pennsylvania State University, United States; <sup>4</sup>Pacific Northwest National Laboratories, United States

III-Nitride based semiconductor devices continue to attract academic and commercial interest for their electronic and optical properties. The wide bandgap allows for more compact high power application, and luminescence at energy levels unattainable by smaller bandgap semiconductors. The high electron mobility permits high bandwidth transistor applications such as high electron mobility transistors (HEMT). Also, high displacement energy and small lattice constant theoretically predict radiation hardness making it possible for electronics fabricated from it to operate in radiation rich environments. Extensive research has been conducted on the effects proton and electron radiation have on GaN. Indeed this work shows GaN has radiation hard properties. However, the effects of gamma radiation are not well understood, and the literature has conflicting results. For example, some publications have reported a reduction in transistor drain current with dose, and others have reported an increase in drain current due to increased mobility. In addition, most of the previously reported work has focused on HEMT structures. Review of the literature suggests that gamma radiation can affect GaN differently depending on substrate and device structure used. We desire to alleviate some of these discrepancies and increase understanding by first studying a simpler device grown on different substrates: a p-n diode. In this work, we investigate the effects of gamma irradiation on the current-voltage (IV) characteristics, specifically the reverse saturation current ( $I_s$ ) and turn on voltage ( $V_{on}$ ), of GaN p-n diodes grown on different substrates: sapphire and freestanding GaN. The samples were irradiated to 2879 kGy and 3937 kGy. IV measurements were taken from six diodes on each sample before and after irradiation.  $I_s$  shows no significant change after irradiation at either dose. After irradiation  $V_{on}$  was calculated and compared to pre-radiation values for individual diodes and then averaged with other diodes on the same sample die. The diodes grown on sapphire show a significant dose-dependent increase in  $V_{on}$  of 27.7% for 2879 kGy and 31.7% for 3937 kGy. We compare this to the diodes grown on freestanding GaN where  $V_{on}$  increased 0.6% for both 2879 kGy and 3937 kGy. We postulate that the differing results for the change in  $V_{on}$  between the substrates could be related to the high dislocation density of the GaN epitaxial layers grown on sapphire as compared to freestanding GaN. These dislocations can act as a sink for point defects induced by irradiation. More experiments and analyses are being done to investigate this. Despite the substantial shift in  $V_{on}$  for the investigated diodes,  $I_s$  shows no significant change after irradiation at either dose. This implies that the defects induced by gamma irradiation do not create a path for leakage current ( $I_s$ ) to flow in diodes on either substrate. In summary, the change in  $V_{on}$  demonstrates that the choice of substrate affects the forward bias IV characteristics of GaN p-n diodes after gamma irradiation. Diodes grown on sapphire substrates have a dose-dependent increase in  $V_{on}$  while diodes grown on freestanding substrates only show a minor shift in  $V_{on}$ .

### 4:00 PM J02

**Impact of Gamma Irradiation on Interface States in GaN p-n Diodes** Yu Kee Ooi<sup>1</sup>, Kyle Ahn<sup>1</sup>, Monica Mahoney<sup>1</sup>, Farnood Mirkhosravi<sup>2</sup>, Daniel Feezell<sup>2</sup> and Michael Scarpulla<sup>1</sup>; <sup>1</sup>University of Utah, United States; <sup>2</sup>The University of New Mexico, United States

III-nitride semiconductors have a broad range of applications: from general illuminations to high power electronics, attributed to their unique properties such as wide bandgap, low thermal carrier generation, and large breakdown field. In particular, the higher energy gap and displacement energy of III-nitride materials as compared to Si and GaAs have enabled the creation of high-voltage, high-current, radiation-tolerant power devices. Studies have shown that the rate of defect creations are primarily influenced by the sample quality, doping level, and radiation type and energy. While previous studies primarily focus on irradiation-induced-defects in the GaN layer that lead to degradation in the device performance, few studies have investigated the impact of gamma irradiation on the III-nitride interface states. In this study, we investigate the effect of gamma irradiation on the interface states for GaN p-n diodes on a sapphire substrate ( $D_s$ ) and free-standing GaN substrate ( $D_{fs}$ ). The diodes were exposed to gamma irradiation of 2879 kGy and 3937 kGy using a <sup>60</sup>Co source under oxygen ambient. Capacitance-voltage (CV) measurements were taken before and after gamma irradiation, and Mott-Schottky analysis has been performed to determine the apparent built-in voltages ( $V_{bi}$ ) and apparent doping densities ( $N_A$ ). The extracted  $V_{bi}$  for  $D_s$  and  $D_{fs}$  before gamma irradiation was  $\sim 9.7 \text{ V}$  and  $\sim 6.7 \text{ V}$ , respectively. This relatively high  $V_{bi}$  was due to the large

Schottky breakdown in the junction between the metal contact and the p-GaN layer. To be more specific, the  $V_{bi}$  can be expressed as the contribution of  $V_{bi, pn} + V_{br, Schottky}$  where  $V_{bi, pn}$  is the built-in voltage for the pn junction and  $V_{br, Schottky}$  is the voltage drop across the Schottky contact to the p-GaN layer. In general, the diodes on both substrates show dose-dependent changes for  $V_{bi}$  and  $N_A$  but with the opposite trend for the two substrates. Specifically, the  $V_{bi}$  for  $D_{FS}$  decrease with increasing irradiation dosage (-0.9% for 2879 kGy and -9.6% for 3937 kGy) while the  $V_{bi}$  for  $D_S$  increase significantly (+20.6% for 2879 kGy, and only 11.6% increase was observed for 3937 kGy. For the  $N_A$ , -5.9% and -17.2% were observed for  $D_{FS}$  exposed to 2879 kGy and 3937 kGy, respectively, while +14.9% and +4.6% were observed for  $D_S$  exposed to 2879 kGy and 3937 kGy, respectively. We attribute the changes of  $V_{bi}$  and  $N_A$  observed in our preliminary results to the interface charges. The interaction of gamma radiation with the semiconductor material mainly occurs through high-energy Compton scattered electrons that dissipate their energy by creating a large number of secondary electron-hole pairs. These secondary electron-hole pairs cause the formation of the displacement that will change the occupancy of surface traps. As a result, the  $V_{bi}$  increases or decreases based on the amount of interaction of the Compton electron-generated secondary electron-hole pairs with the surface traps. The shift in  $V_{bi}$  results in changes in the depletion width, which in turn also leads to changes in the  $N_A$ . We are currently investigating this hypothesis with additional experiments and simulations.

#### 4:15 PM J03

**(Student) The Investigation of Vertical GaN Schottky Barrier Diode with Floating Metal Guard Rings** *Tsung-Han Yang*, Houqiang Fu, Kai Fu, Xuanqi Huang, Chen Yang, Jossue Montes, Hong Chen, Jingan Zhou and Xin Qi; Arizona State University, United States

A vertical GaN Schottky barrier diode with floating metal rings (FMR) as an edge termination structure has been fabricated on bulk GaN substrate. Devices with different geometries including 1) various numbers of rings and 2) various spacing between rings have similar forward electrical characteristics and different reverse breakdown voltage. These devices all have nearly ideal ideality factors around 1.09 and a Schottky barrier height around 1.14V at room temperature. As the temperature increased from 300K to 420 K, the ideality factor slightly decreased and the Schottky barrier height almost remains the same, indicating that these devices have good homogeneity and fit the thermal emission model very well. However, as the number of rings increased from 0 to 5, 10, and 20, the reverse breakdown voltage increased from 223 to 247, 267, and 289V, respectively. In addition, as the distance between the rings and the contact increase from 1.5 to 2, 2.5, 3 and 3.5 um, the reverse breakdown voltage increased from 233 to 247, 260, 271 and 290V, respectively. Overall, the breakdown voltage of devices with more guard rings is generally higher than those with fewer guard rings, indicated that floating metal guard ring structure as an edge termination structure can effectively release the electrical field crowing around the edge of the anode and hence increase the breakdown voltage. In addition, the spacing of the rings also plays an important role that could obviously affect the electric field distribution of the devices. These results could be served as important references for designing vertical GaN electronic devices that can obtain high breakdown capability.

SESSION K: 2D-Materials Applications

Session Chair: Mona Ebrish

Session Hosts: Kevin Daniels and Jamie Phillips

Wednesday Afternoon, June 24, 2020

Location: ZoomRoom 4

#### 2:00 PM K01

**(Student) Layered  $\delta$ -phase MnO<sub>2</sub> Nanofibers-Epitaxial Graphene-Silicon Carbide Heterostructures for Fast and Selective Room Temperature Gas Sensing** *Michael Pedowitz*<sup>1,1</sup>, Soaram Kim<sup>1,1</sup>, Daniel Lewis<sup>1,1</sup>, Balaadithya Uppalapati<sup>2</sup>, Digangana Khan<sup>2</sup>, Ferhat Bayram<sup>2</sup>, Goutam Koley<sup>2</sup>, Rachel Myers-Ward<sup>3</sup> and Kevin Daniels<sup>1,1</sup>; <sup>1</sup>University of Maryland, United States; <sup>2</sup>Clemson University, United States; <sup>3</sup>U.S. Naval Research Laboratory, United States

Transition metal oxides have traditionally seen widespread use as gas sensors due to their low cost and wide range of detectable gases<sup>1</sup>. In recent years the effect of nanostructuring on transition metal oxide gas sensors has been investigated extensively, with the goal of reducing detection limits and improving responsivity<sup>2</sup>. The nanofibers have led to significant increases in responsivity, similar to nanoflowers, due to their high active surface area<sup>3</sup>. However, transition metal oxides' low inherent conductivity severely limits their response time at room temperature, forcing these sensors to be operated at temperatures often exceeding 200°C<sup>4</sup>, which limits their applicability. To overcome this limitation transition metal oxide-graphene heterostructures have been formed, which seek to couple the gas sensing capabilities of transition metal oxides with graphene's inherent conductivity<sup>4</sup>. Among these transition metal oxide-graphene heterostructures manganese dioxide (MnO<sub>2</sub>)-graphene structures provide unique properties that can be exploited to improve gas selectivity. MnO<sub>2</sub>'s rhombohedral birnessite ( $\delta$ ) phase has a layered structure with a well-defined interlayer spacing of 7Å<sup>5</sup>. This allows  $\delta$ -MnO<sub>2</sub> to act as a

molecular sieve, screening gases by their kinetic diameter. In this work we present the growth of  $\delta$ -MnO<sub>2</sub> nanofibers on epitaxial graphene/silicon carbide and demonstrate the gas sensing capabilities of the heterostructure. The  $\delta$ -MnO<sub>2</sub> nanofibers were grown via electrodeposition on epitaxial graphene (EG) synthesized on 6H silicon carbide substrates (SiC) utilizing 0.1M manganese acetate (Mn(CH<sub>3</sub>CO<sub>2</sub>)<sub>2</sub>) solution in a three-electrode electrochemical cell. The resulting MnO<sub>2</sub> deposition was then characterized using Raman spectroscopy, X-ray diffraction spectroscopy (XRD), energy-dispersive X-ray spectroscopy (EDX), atomic force microscopy (AFM), and scanning electron microscopy (SEM) to determine its phase and surface morphology. SEM revealed the film was made up of approximately 30µm x 40µm microplates formed from nanofibrous nanoparticles that had grown together. AFM confirmed this morphology and indicated the fiber thickness was ~10nm. Raman Spectroscopy of the deposition confirmed the formation of  $\delta$ -MnO<sub>2</sub> due to the presence of peaks at 577 cm<sup>-1</sup>, 651cm<sup>-1</sup>, and 133cm<sup>-1</sup><sup>6</sup>. A metal electrode (Ti/Au = 30/120nm) was then deposited on the  $\delta$ -MnO<sub>2</sub> by e-beam evaporation to create a gas sensor. This gas sensor was then tested with 5ppm nitrogen dioxide (NO<sub>2</sub>), 5ppm ammonia (NH<sub>3</sub>), and an ~1000ppm isopropyl alcohol (C<sub>3</sub>H<sub>8</sub>O)/methanol (CH<sub>3</sub>OH) mix, two volatile organic compounds (VOCs), in an environmentally controlled chamber. The device was tested at room temperature and displayed a significant response to NO<sub>2</sub> and NH<sub>3</sub> with ~400ms response times but displayed no response to VOCs. This result is a significant improvement over traditional transition metal oxide gas sensors at room temperature, which struggle to achieve response times less than 30s<sup>4</sup>. The heterostructure also outperformed alternate graphene/metal oxide gas sensors which had response times greater than 10s at gas concentrations of 5ppm<sup>4</sup>. This novel  $\delta$ -MnO<sub>2</sub> nanofiber/EG/SiC heterostructure provides a room temperature gas sensing platform that outperforms alternate transition metal oxide graphene heterostructures. It also has the potential to be extended to alternate application areas, such as energy storage, where high surface area MnO<sub>2</sub> on graphene is desirable. **References:** 1. C. Wang et al. *Sensors* 10, 2088-2106(2010) 2. H. Ji et al. *Nanoscale* 11, 22664-22684(2019) 3. R. C. Pawar et al. *Curr. Appl. Phys.* 12, 778-783(2012) 4. N. Joshi et al. *Microchim. Acta* 185, 213(2018); 5. L. Spinelle et al. *Sensors* 17 (7), 1520(2017); 6. C. Zhu et al. *Mater. Horiz.* 4(3), 415-422(2017)

#### 2:15 PM K02

**MoS<sub>2</sub> Nanoflower/Epitaxial Graphene Heterostructure for Chemical Sensing** *Soaram Kim*<sup>1,1</sup>, Jaeseo Park<sup>2,3</sup>, Michael Pedowitz<sup>1,1</sup>, Daniel Lewis<sup>1,1</sup>, Seunghyun Lee<sup>4</sup>, Balaadithya Uppalapati<sup>2</sup>, Digangana Khan<sup>2</sup>, Ferhat Bayram<sup>2</sup>, Sanjay Krishna<sup>4</sup>, Goutam Koley<sup>2</sup>, Sang-Woo Kang<sup>2,3</sup> and Kevin Daniels<sup>1,1</sup>; <sup>1</sup>University of Maryland, United States; <sup>2</sup>Korea Research Institute of Standards and Science, Korea (the Republic of); <sup>3</sup>University of Science and Technology, Korea (the Republic of); <sup>4</sup>The Ohio State University, United States; <sup>5</sup>Clemson University, United States

Recently, two-dimensional (2D) materials such as graphene and transition metal dichalcogenides (TMDs) are promising for the next generation of electronics, i.e. pressure and chemical sensors in environmental and safety monitoring, batteries and solar cells in energy areas, and medical health care systems [1,2]. In addition, atomically thin 2D graphene and TMD have an extremely high surface-to-volume ratio which is the most vital parameter for chemical sensing applications. Here we have fabricated a heterostructure of molybdenum disulfide (MoS<sub>2</sub>) nanoflower and epitaxial graphene on 6H silicon carbide (SiC) substrate for chemical sensing. We have combined the advantages of high sensitivity and fast response time of graphene with the high surface-to-volume ratio of MoS<sub>2</sub> nanoflower to develop an high sensitivity chemical sensor.

A schematic diagram of the experimental procedure is shown in Fig. 1. To synthesize bilayer epitaxial graphene on 6H SiC, the Si thermal sublimation method was used [3]. After that, nanoflower-structures MoS<sub>2</sub> were grown on graphene/SiC directly using metal organic chemical vapor deposition (MOCVD). Molybdenum hexacarbonyl (Mo(CO)<sub>6</sub>) and hydrogen sulfide (H<sub>2</sub>S) were used as precursor materials, with the partial pressure ratio of 1:1. Carbonaceous impurities were first randomly deposited on graphene/SiC, acting as promoters of nucleation and growth of vertically standing MoS<sub>2</sub> (Stranski-Krastanov growth mode) [4]. The growth of MoS<sub>2</sub> nanoflowers were performed at 350 °C with various chamber pressures and growth times. Samples were investigated by scanning electron microscopy (SEM), atomic force microscopy (AFM), Raman spectroscopy, and photoluminescence (PL). To fabricate the chemical sensor, e-beam lithography and reactive ion etching (RIE, CF<sub>4</sub>) were used to prepare a simple pattern. Finally, the metal electrode (Ti/Au = 30/120 nm) was deposited using an e-beam evaporator. SEM and AFM images of MoS<sub>2</sub> nanoflowers/epitaxial graphene heterostructure on SiC is shown in Fig. 2. The MoS<sub>2</sub> nanoflowers were found to grow well onto the graphene/SiC and withstand repeated cycles of characterization measurements. Figure 3 presents the (a-c) Raman results and (d) PL spectra of the MoS<sub>2</sub> nanoflowers grown on graphene/SiC. These results indicate that the synthesized structures are indeed MoS<sub>2</sub>. The prepared chemical sensor was tested with various gases such as 5 ppm of nitrogen dioxide (NO<sub>2</sub>) and ammonia (NH<sub>3</sub>), and ~1000 ppm of volatile organic compounds (VOCs) and showed superior chemical response and recovery at room temperature as shown in Fig. 4.

It is clearly evident that the MoS<sub>2</sub> nanoflowers were synthesized well on graphene/SiC by MOCVD, which is suitable for gas sensing application due to the synergistic combinations of MoS<sub>2</sub> nanoflowers and epitaxial graphene.

### 2:30 PM K03

**Modular Biomolecule Functionalization of MoS<sub>2</sub> for Selective Sensing** Lucas K. Beagle<sup>1,2,3</sup>, Nicholas Glavin<sup>1</sup> and Christopher Muratore<sup>3</sup>; <sup>1</sup>Air Force Research Laboratory, United States; <sup>2</sup>UES, Inc., United States; <sup>3</sup>University of Dayton, United States

Incorporating transition metal dichalcogenides as active materials in flexible sensors for the detection of specific, desired analytes has recently been an area of intense investigation. The inherent semiconducting properties of molybdenum disulfide (MoS<sub>2</sub>) have previously shown to be effective sensing modalities and much literature has been dedicated to improving the sensitivity of these devices. However, reliability in selectivity while sensing has long been an elusive characteristic among the devices TMD sensing community. We have developed a novel, modular method to functionalize MoS<sub>2</sub> surfaces with custom peptide sequences or amino acid conjugate biomolecules which resulted in an improved selectivity to desired analytes. The backbone of the methodology relies on the use of dual binding domains of which the proximal region is anchored to the surface of the MoS<sub>2</sub> substrate via van der Waals forces, which in contrast to previous methodology required covalent attachment to the surface. The distal end of the biomolecule is designed to have a high binding specificity to the desired analyte based on known interactions.

### 2:45 PM K04

**In Situ Transport Measurements Reveal Source of Mobility Enhancement of MoS<sub>2</sub> and MoTe<sub>2</sub> During Dielectric Deposition** Ju Ying Shang, Michael Moody, Jiazhen Chen, Tobin Marks and Lincoln Lauhon; Northwestern University, United States

Layered transition metal dichalcogenides (TMDs) and two-dimensional (2D) materials are widely studied as complements to Si complementary metal-oxide-semiconductor technology. Field-effect transistors (FETs) made with 2D materials often exhibit mobilities below their theoretical limit, and strategies such as encapsulation with dielectrics grown by atomic layer deposition (ALD) have been explored to tune carrier concentrations and improve mobility. While molecular adsorbates are known to dope 2D materials and influence charge scattering mechanisms, it is not well understood how ALD reactants affect 2D transistors during growth, calling for *in situ* or *operando* methodology. We demonstrate that exposures to the oxidants H<sub>2</sub>O and O<sub>2</sub> at temperatures and pressures relevant to ALD induce reversible electronic changes on MoTe<sub>2</sub> FETs, indicating negligible oxidation takes place during exposure. Furthermore, we report *in situ* electronic measurements on MoS<sub>2</sub> and MoTe<sub>2</sub> FETs during ALD MoO<sub>x</sub> growth, which reveal that significant field-effect mobility improvement occurs within the first five cycles of growth. Further experiments confirm that this mobility enhancement is effected by modulation of the channel, rather than the contacts, and suggest that it is primarily due to screening of charged impurity scattering by the adlayer, rather than a reduction in scattering centers through reactions or an increase in screening by free carriers. Due to the strong influence of the first <2 nm of deposition, when the adlayer may be discontinuous and still evolving in stoichiometry, this work highlights the need for further assessment of nucleation layers and initial deposition chemistry, which may be more important than the bulk composition of the oxide itself in optimizing performance and reproducibility.

### 3:00 PM K05

**Water Absorption in Functionalized Germanane** Thaddeus J. Ase<sup>1,1</sup>, Warren Huey<sup>1</sup>, Brenton A. Noesges<sup>1,1</sup>, Egle Molotokaitė<sup>2</sup>, Szu-Chia Chien<sup>1</sup>, Yaxian Wang<sup>1</sup>, Aldriel Barnum<sup>1,1</sup>, Chris McPherson<sup>1</sup>, Shishi Jiang<sup>1</sup>, Seth Shields<sup>1</sup>, Cosimo D'Andrea<sup>2,3</sup>, Wolfgang Windl<sup>1</sup>, Eugenio Cinquanta<sup>4</sup>, Leonard J. Brillson<sup>1,1</sup> and Joshua Goldberger<sup>1</sup>; <sup>1</sup>The Ohio State University, United States; <sup>2</sup>Istituto Italiano de Tecnologia, Italy; <sup>3</sup>Politecnico di Milano, Italy; <sup>4</sup>Istituto di Fotonica e Nanotecnologie, Italy

Two-dimensional (2D) van der Waals materials such as graphene have been widely studied because of their unique materials properties owing to the single atom thickness of the materials as well as the potential in surface functionalization. Germanane, a germanium analogue to graphene, has recently attracted great attention due to the ability of tuning the electronic structure by changing the terminating ligand on the germanium while the stability of the materials is improved. Therefore in this work we aim to study the effects of functionalized ligands in germanane framework systematically on altering the electronic structure, optical properties, and thermal stability for the purpose of surface functionalization of group 14 graphanes.

Here we study how the surface terminating ligand (-CH<sub>3</sub> and -H) on a Ge framework leads to nonobvious interactions with other chemical species. Here, we show with *ab-initio* molecular dynamics simulations and enthalpy calculations that GeCH<sub>3</sub> reversibly absorbs water into the van der Waals space, whereas GeH does not intercalate water. The intercalated water distorts the surrounding framework, which DFT predicts to result in an unexpected intense above band gap luminescence. Our results are confirmed by a large number of experimental characterization techniques, including XRD, FTIR, TGA, and continuous-wave and time-resolved photoluminescence. This work opens potential applications for surface functionalization of 2D materials in membrane and separation technologies.

### 3:15 PM BREAK

### 3:45 PM K06

**(Student) Non-Volatile Resistance Switching Behavior in Monolayer Two-Dimensional Materials** Xiaohan Wu, Ruijing Ge, Deji Akinwande and Jack C. Lee; The University of Texas at Austin, United States

Over the last two decades, two-dimensional (2D) materials have drawn much attention due to the remarkable electronic, optical, mechanical and thermal properties and a wide range of applications in the next-generation electron devices, optoelectronics and bioelectronics. Recently, researchers have reported the existence of the non-volatile resistance switching (NVRS) behavior in various 2D materials, including graphene oxide, functionalized MoS<sub>2</sub>, partially degraded black phosphorus and multi-layer hexagonal boron nitride (h-BN), etc., where the resistance can be switched between a high-resistance state (HRS) and a low-resistance state (LRS) and sustained for a long time without power supply. Nevertheless, the monolayer 2D materials were believed not to exhibit the NVRS effect in vertical device structure due to excessive leakage current. In our work, we reported the first observation of NVRS phenomenon in a variety of monolayer transition metal dichalcogenide (TMD), including MoS<sub>2</sub>, MoSe<sub>2</sub>, WS<sub>2</sub> and WSe<sub>2</sub>, and monolayer h-BN atomic sheets in vertical metal-insulator-metal (MIM) device configuration, overcoming a fundamental limitation in bulk materials. Compared with traditional metal oxide or other 2D multilayer materials, the single-layer h-BN has only one atomic layer and ~0.33 nm in thickness, featuring the thinnest active layer of NVRS memory devices. The 2D monolayer-based NVRS devices are studied using a crossbar or a litho-free & transfer-free structure, demonstrating stable switching with large on/off resistance ratio (up to > 6 orders of magnitude) and low switching voltage (down to < 1 V). Unlike most of the NVRS devices using metal oxide as the active layer, the 2D monolayer-based devices require no electro-forming step, a prerequisite that initializes a soft breakdown to form a conductive filament for subsequent resistance switching. Moreover, the devices are proved via pulse operation with fast switching speed (< 15 ns), which is comparable to the state-of-the-art speed for 2D memristors. *Ab-initio* simulation was conducted to reveal favorable substitution of metal ions into localized vacancies of the 2D layers, which corresponds to the switching from HRS to LRS, indicating a conductive-bridge-like switching mechanism. Flexible non-volatile memory on soft substrate was fabricated based on monolayer MoS<sub>2</sub> NVRS devices. These memory devices can endure mechanical bending cycling and have stable switching properties with more than 4 weeks retention and more than 150 manual DC cycles. In addition, a new application, zero-static power radio frequency (RF) switch was demonstrated with the monolayer NVRS device. The RF switches using h-BN as the active layer showed great performance with low insertion loss (≤ 0.2 dB) and high isolation (≥ 15 dB) up to 110 GHz. Furthermore, a record cutoff frequency of 70 THz (also known as figure of merit to evaluate the performance of RF switch) was achieved based on MoS<sub>2</sub> switch compared with other switch technologies, such as MEMS, memristor and phase-change memory. The operating frequencies of 2D RF switches cover the RF, 5G and mm-wave bands, making this a promising low-power switch candidate for diverse communication and connectivity systems. The existence of NVRS phenomenon in monolayer TMDs and h-BN indicates fruitful interactions between defects, metal ions and interfaces, and potentially illustrates a universal resistance switching effect in various 2D non-conducting monolayers for applications including ultrathin flexible memory, high-density data storage arrays, neuromorphic computing and zero-power RF switches.

### 4:00 PM K07

**(Student) Environmentally Stable Quasi-2D Gallium Telluride for Polarization Sensitive Optoelectronic Applications** Mounika Kotha, Alex Kaloyeros and Spyros Gallis; SUNY Polytechnic Institute, United States

Gallium telluride (GaTe) is an emerging and promising 2D layered semiconductor that can serve as a vital building block towards the creation of devices within the fields of nanoelectronics, optoelectronics, and quantum photonics. An important obstacle towards practical implementation of quasi-2D gallium chalcogenides for electronic and photonic applications is their surface instability under ambient conditions. Ambient exposure of GaTe leads to significant conduction band restructuring, low photoluminescence (PL) emission yield caused by carrier dissociation via surface states, and an anisotropic to isotropic structural transition. For the as-exfoliated flakes, we observe a significant reduction of the GaTe-related PL (~100×) and Raman (~4×) peak intensities for the few-layered flakes over a time span of few days. We attribute this ambient degradation to the formation of elemental polycrystalline tellurium and gallium oxide through a combination of optical (Raman Spectroscopy) and elemental (Auger and X-ray Photoelectron Spectroscopy) characterization techniques. We have developed a novel chemical passivation technique that results in complete encapsulation of the as-exfoliated GaTe flakes in ultrathin hydrogen-silsesquioxane (HSQ) film. By leveraging our novel passivation method for environmental-stable GaTe flakes, our focus has been to study the anisotropy in the optical properties of GaTe nanomaterials. The anisotropy is caused by the 1D-like nature of the GaTe layer, as the layer comprises of Ga-Ga chains extending along the b-axis crystal direction. The identification of the b-axis in such anisotropic materials is imperative for the fabrication of polarization-dependent devices based on the generation and detection of polarized light, such as polarized photodetectors and light sources.

Our encapsulation process using HSQ serves as a platform for studying the anisotropic properties of pristine GaTe flakes through polarization-dependent

Raman and PL spectroscopy. Although, we observed Raman polarization dependence of different phonon modes from monoclinic GaTe, the selection of the appropriate phonon mode to identify the crystal b-axis is very crucial. We observed that the Raman polarization response for a particular phonon is wavelength and thickness dependent. Conversely, we observed that the GaTe room-temperature PL peak emission (1.66 eV) anisotropy is independent of the excitation wavelength (633 nm, 532 nm, 476 nm and 458 nm) and thickness. We observed a PL polarization anisotropy contrast ( $\rho$ ) of 0.6 calculated using equation (i) for a 40-nm thick GaTe flake using 532 nm excitation wavelength.  $\rho = (I(\parallel) - I(\perp)) / (I(\parallel) + I(\perp))$  (i) where  $I(\parallel)$  and  $I(\perp)$  are the integrated PL intensity along a direction parallel and perpendicular to the b-axis respectively. This value is comparable to other pseudo-1D materials like ZrS<sub>3</sub>. This identification of the crystal b-axis in GaTe through PL spectroscopy was later confirmed using Transmission Electron Microscopy (TEM). Our novel surface-passivation has a dual role, while effectively passivating the flakes, it offers the capability to simplify the integration process for fabricating GaTe-based nanodevices using HSQ, a commonly used resist for electron beam lithography. Our current study of optical and electrical anisotropy in encapsulated GaTe-based nanodevices (photodetectors) is an extension of the exploratory research to study the direction-dependent light-matter interaction in such asymmetric crystal structures.

SESSION L: Silicon Carbide—Materials and Devices  
 Session Chair: Michael Spencer  
 Session Hosts: MVS Chandrashekhar and Patrick Shea  
 Wednesday Afternoon, June 24, 2020  
 Location: ZoomRoom 5

### 2:15 PM L01

**Detection and Evolution of Micropipes in SiC Substrates and Epitaxial Layers and Their Impact on MOSFET and Diode Devices** Joshua L. Justice, Swapna Sunkari and Hrishikesh Das; On Semiconductor, United States

The Silicon Carbide power electronics market is forecasted to surpass 1 billion USD by 2025. This is driving large capacity expansions within the industry, and by extension, the introduction of many new substrate suppliers to the market. To remain competitive, reduce risk and to ensure wafer supply, it becomes necessary to evaluate and qualify as many substrate vendors as possible. In turn, substrates of differing crystal quality need to be accurately characterized for defects. In our previous work, we have examined both crystal defects and killer defects [1-2], we have also quantified the effects of killer defects on both diode and MOSFET products, and we have looked more closely at the effects of non-killer defects [3]. In this work, we look at non-destructive detection of the micropipes in the substrate and epitaxial layers, their evolution to other extended defects in the epitaxial layers and their impact on fabricated diode and MOSFET devices. Traditionally, micropipes in SiC substrates have been characterized by molten KOH etching. The SiC substrate is anisotropically etched around crystal defects and the defects become observable with optical microscopy. These etched pits can be binned and the micropipes can be characterized [4]. This method, however, is destructive and therefore, micropipes in the entire boule are characterized by only one or two wafers (Figure 1a). There has been work done to develop non-destructive methods for detecting and classifying micropipe defects in SiC substrates [5-7]. Even though most substrate manufacturers claim zero micropipe wafers, the reality is that there is a variable presence of micropipes, sometimes even greater than the specified maximum micropipe density (MPD) of 1 cm<sup>-2</sup> in production, prime grade wafers. In this work, a commercially available Lasertec SICA88 metrology tool is used to non-destructively characterize micropipes in both substrates (Figure 1b-d) and epitaxial layers (Figure 1e-f) using multi-channel deep learning algorithms. These results are compared to KOH etch pits on wafers of the same boule (Figure 1a). In addition, the structure of micropipe clusters and dislocations around them can be clearly seen in the photoluminescence (PL) channel. Early detection of these micropipe clusters at incoming inspection is vital to the overall yield of the SiC production line. Micropipe clusters at the edge of the wafer have been shown to cause wafer breakage in a subset of products. Classification of these clusters gives the ability to bin substrates based on breakage risk in the back-end fab. In addition, 100% in-line wafer screening provides insight into the evolution of the micropipes throughout the SiC boule during the crystal growth process (Figure 2), which in turn helps drive crystal quality improvements for future substrate generations. With scans on 100% of substrate and epi wafers, fabricated die can be binned based on the number of micropipes located within the die (Figure 3a). The impact of the micropipes on the electrical yield of 1200V 20A diode die is evaluated (Figure 3b). Though micropipes are present in only a small minority of die, their effects electrically is very clear, especially in the larger densities. The electrical effects on both diodes and MOSFETs will be presented along with the nucleation of extended defects in the epitaxial layers from the substrate micropipes. [1] H. Das, S. Sunkari and H. Naas, ECS Transactions, 75 (12), (2016), pp.233-7 [2] H. Das, S. Sunkari, J. Justice, H. Pham and K.S. Park, Materials Science Forum 963 (2019) pp.284-7 [3] H. Das, S. Sunkari, J. Justice, H. Pham, and G. Park, Proc. ICSCRM (2019), submitted [4] D. Siehe, *et al.*, J. Cryst. Growth., 270 (2004) pp.1-6 [5] T. Kubota, *et al.*, Machine

Vision and Applications (2005) 16: 170 [6] T. Hatakeyama, *et al.*, J. Cryst. Growth., 310 (2008) pp.988-92 [7] S. McGuire, *et al.*, Materials Science Forum, 924 (2018) pp.527-30

### 2:30 PM L02

**Carrier Lifetime Enhancement in Thick 4H-SiC Epilayers Investigated by 2-Photon Absorption** Nadeemullah Mahadik<sup>1</sup>, Peter L. Bonanno<sup>1</sup>, Robert Stahlbush<sup>1</sup> and Daniel J. Lichtenwalner<sup>2</sup>; <sup>1</sup>U.S. Naval Research Laboratory, United States; <sup>2</sup>Wolfspeed, A Cree Company, United States

Bipolar 4H-SiC devices, such as IGBTs, can have low on-state resistance due to conductivity modulation [1] and can also deliver high current with high voltage capacity [2]. High carrier lifetime (~20µs for 20kV [3]) is needed for effective conductivity modulation. Lifetime in as-grown epilayers is in the range of 1-5 µs. Lifetime enhancement techniques were developed to improve it to >25µs [3] by oxidation or implantation/annealing. The enhancement process increases lifetime by reducing the number of Z<sub>1/2</sub> traps, which arise from carbon vacancies, by creation/diffusion of carbon interstitials. Previously, lifetime was measured by time-resolved photoluminescence decay (TRPL) or microwave photo-conductive decay (µWPCD) using UV excitation, which are sensitive to the top 50 µm, and affected by surface recombination (SRV). This is not suitable to investigate lifetime enhancement in 20kV device structures with 130-160µm drift layers. In this work, we use a recently developed 2-photon absorption (TPA)-excited TRPL [4] technique to generate carriers inside the epilayers at varying depths to investigate the effectiveness of lifetime enhancement in thick SiC epilayers. Three commercially-grown samples having 140-190 µm thick SiC epilayers were subjected to thermal oxidation for several hours resulting in 15-30µs carrier lifetime as measured by µWPCD. One similar thickness sample was kept as-grown. Using the TPA-TRPL technique, carriers were generated using a 515 nm pulsed laser within the 3 lifetime enhanced samples and as-grown sample at depths between ~50-160 µm. Photoluminescence from the samples was collected using a fiber coupled to a microscope setup and a photomultiplier tube with a multi-channel scaler to obtain TRPL decay curves up to 20 µs after the laser pulse with good signal-to-noise over 10<sup>10</sup> counts per second after averaging for 90 min per depth. These decay curves were fit to obtain instantaneous inverse slopes of the data, which is analogous to the carrier lifetime at long times. At times over 100ns after the laser pulse, the TRPL decay is influenced mainly by carrier diffusion and bulk recombination, the latter being related to carrier lifetime,  $\tau_{\text{HL}}$ . Initially, diffusion is the dominant mechanism, after which the influence of recombination is observed. We fit the data and extracted the instantaneous inverse slope,  $\tau_{\text{measured}}^{-1}$  of the TRPL decay curves at each depth and compared them to simulated  $\tau_{\text{measured}}^{-1}$  produced by a multiphysics model with an ambipolar diffusion coefficient of 5.5 cm<sup>2</sup>/s, and SRV of 100 cm/s. For the as-grown sample,  $\tau_{\text{measured}}^{-1}$  best matches simulation where  $\tau_{\text{HL}}$  is set to 2µs, which is typical for as-grown epilayers. The simulation was in excellent agreement with the data. For the high lifetime samples, the simulations suggested  $\tau_{\text{HL}} = 25\mu\text{s}$ , which agrees with the µWPCD data. The general shape of the simulations matches the data, but not the magnitude, indicating other unknown contributions that influence the TRPL decay in long lifetime samples. However, the simulations are useful for comparisons of the depth variation of lifetime. We observed that the process used did enhance lifetime throughout the epilayer depth. TPA-TRPL results are being used to optimize the lifetime enhancement process. Details of the results will be presented. Acknowledgement: This work was performed under ONR funding. [1] T. Tamaki, *et al.*, IEEE Trans. Electron Device 55, 1920 (2008) [2] E. van Brunt, *et al.*, Mater. Sci. Forum 821–823, 847 (2015) [3] E. Saito, *et al.*, Appl. Phys. Express 9, 061303 (2016) [4] N. A. Mahadik *et al.*, Appl. Phys. Lett. 111, 221904 (2017)

### 2:45 PM L03

**(Student) Nitrogen Donor-Deep Level Defect Interactions in 4H-SiC Bipolar Junction Transistors Using Electrically Detected Electron Nuclear Double Resonance** Brian R. Manning<sup>1</sup>, Ryan J. Waskiewicz<sup>1</sup>, Patrick M. Lenahan<sup>1</sup> and Duane J. McCrory<sup>2</sup>; <sup>1</sup>The Pennsylvania State University, United States; <sup>2</sup>Keysight, United States

We have developed a sensitive electrically detected electron nuclear double resonance (EDENDOR) spectrometer and demonstrate that it can provide reasonably high signal to noise spectra detecting <sup>14</sup>N nuclear spins at donor sites interacting with deep level defects in the base-emitter junction of a fully processed 4H-SiC bipolar junction transistor at room temperature. Electron paramagnetic resonance (EPR) techniques offer unrivaled analytical power in the identification of the physical and chemical nature of point defects in semiconductors and insulators. However, the sensitivity of conventional EPR is on the order of 10 billion defects. This number greatly exceeds the number of performance-limiting defects in technologically relevant solid-state devices. Electrically detected magnetic resonance (EDMR) is at least 7 orders of magnitude more sensitive than its parent technique, EPR [1,2]. This enormous enhancement in sensitivity makes EDMR a powerful tool in the investigation of point defects in nano-scale electronic device (this sensitivity also makes EDMR potentially useful in various spintronic applications). Although EDMR is a powerful tool, its analytical power could be greatly enhanced with the addition of a nuclear magnetic resonance (NMR) component. The conventional double resonance technique known as electron nuclear double resonance (ENDOR) combines EPR and NMR and has the analytical power to provide detailed atomic scale information about paramagnetic defects in semiconductors and

insulators [3]. The absolute sensitivity of conventional ENDOR is grossly inferior that of classical EPR, making the technique essentially impossible for studies of micro- and nano-scale electronic devices. This also makes the exploitation of long nuclear spin decoherence times quite difficult via classical ENDOR. We show that, by utilizing EDMR detection, ENDOR sensitivity may be enhanced by many orders of magnitude, opening possibilities for electrically EDENDOR to contribute substantially to solid-state device physics, possibly including some spintronic applications. The EDENDOR spectrometer utilizes a single loop non-resonant antenna that is placed within a  $TE_{102}$  microwave cavity adjacent to the transistor to generate the NMR oscillating magnetic field. A frequency sweep is supplied to the NMR coil loop via an arbitrary waveform generator (AWG). To account for impedance mismatch and parasitic electrical effects a proportional-integral-derivative (PID) controller has been implemented to maintain constant power and provide feedback a real time measurement of the power through the loop and adjust the output. The PID controller suppresses the non-resonant background which could otherwise obscure the EDENDOR response. To the best of our knowledge this is the first time ENDOR measurements have ever been made within a fully processed solid state transistor.

[1] D. Kaplan, I. Solomon, and N.F. Mott, *J. Phys. Lett* **39**, L51 (1978).

[2] J. A. Weil, J. R. Bolton, and J. E. Wertz, *Electron Paramagnetic Resonance: Elementary Theory and Practical Applications*. New York: Wiley Interscience, 1994.

[3] L. Kevan, L. D. Kispert, *Electron Spin Double Resonance Spectroscopy*. New York: A Wiley-Interscience Publication, 1976.

### 3:00 PM L04

**(Student) Improved Electrical Characteristics of 4H-SiC JBS Diodes by Applying Post Deposition Annealing (PDA)** Nick Yun, Dongyoung Kim and Woongje Sung; SUNY Polytechnic Institute, United States

#### Summary

Formation of the ohmic metal on the P+ grids in the Junction Barrier Schottky (JBS) diode cell structure is crucial for its surge-capable operation. Patterned oxide is normally used to form self-aligned nickel silicide ( $Ni_2Si$ ) on the P+ grids. After the formation of  $Ni_2Si$ , the patterned oxide needs to be etched to create an opening for the Schottky metal contact. In our investigation, it was observed that reactive ion etching (RIE) introduces plasma damage on the 4H-SiC surface during this oxide opening process, resulting in degradation in the forward and reverse mode of operations for 4H-SiC Titanium (Ti) metal based JBS diode. In this study, a series of post-deposition annealing (PDA) processes were applied to treat the plasma damage, and thereby improving the electrical characteristics of the SiC Ti-JBS diodes. Forward and reverse electrical behaviors of both RIE and wet etched diodes were compared and discussed.

#### Device and Process flow

A  $6\mu m$  thick,  $2.5 \times 10^{16} cm^{-3}$  doped, N- type epitaxial layer on a 6-inch, N+ 4H-SiC substrate was used to fabricate the titanium (Ti) based JBS diodes. A cross-sectional schematic view of the process flow is shown in Fig. 1. The P+ grids as well as the floating field rings in the edge termination were formed by series of high dopant aluminum (Al) implantations. The junction termination extension (JTE) regions were also formed by Al implantation to form Hybrid-JTE (not shown in Fig. 1) [1]. The implantations steps were followed by a  $1650^\circ C$ , 10 minutes activation anneal with a carbon cap to prevent surface lattice damage. A TEOS oxide was deposited and patterned to open the contact for the P+ grids. After deposition of Nickel (Ni), silicidation and ohmic formation processes were conducted. The patterned oxide for this self-aligned  $Ni_2Si$  process was removed by using either 1) wet etchant, Buffered Oxide Etch (BOE), on one wafer, and 2) dry etchant, reactive ion etching (RIE), on the other wafer to create an opening for the Schottky metal contact. The backside metal contact was also formed by Ni with the same RTA process. A  $4\mu m$  thick, Ti/TiN/Al-based metal was deposited and patterned to form the Schottky anode metal. The frontside was passivated by nitride and polyimide. Finally, a solderable metal stack was deposited on the backside.

#### Experimental Results

Fig. 2 shows the typical forward current-voltage (I-V) characteristics of the fabricated RIE and WET etched 4H-SiC Ti-JBS diodes. The inset shows the SEM image of the fabricated diode. As shown, compared with the WET etched reference, RIE etched JBS diode shows higher knee voltage as well as the differential on-resistance, which might be attributed to the plasma damage during the RIE etch process. A systematic experiment was planned and conducted to investigate possible changes in the electrical characteristics by applying various post-deposition annealing (PDA) temperatures and times. Fig. 3 and 4 show the forward and reverse characteristics after applying PDA, respectively. Quarter wafer maps of the diodes after annealing at  $400^\circ C$  and  $500^\circ C$  at various times in a nitrogen ambient are also shown. As can be seen, electrical characteristics were enhanced when PDA was conducted at  $500^\circ C$  up to 4 minutes. It is important to note that the annealing temperature should be kept below  $550^\circ C$  to prevent aluminum diffusion into the Schottky metal. Fig. 5 shows the extracted breakdown voltages of the five optimal diodes from the WET and RIE etched wafers at different PDA splits. Fig. 6 shows cumulative percentage distributions of breakdown voltages for all the diodes from the WET and RIE etched wafers. A full analysis of the RIE induced damage on the 4H-SiC surface and ideality factors after each PDA will be discussed in the full paper. In conclusion, PDA at  $500^\circ C$  for 4 minutes dramatically improved the electrical characteristics of the RIE etched Ti-JBS diode.

### 3:15 PM BREAK

### 3:45 PM L05

**(Student) Oxide Leakage Currents and E' Centers in 4H-SiC MOSFETs with Barium Passivation** James P. Ashton<sup>1</sup>, Patrick M. Lenahan<sup>1</sup>, Daniel J. Lichtenwalner<sup>2</sup> and Aivars Lelis<sup>3</sup>; <sup>1</sup>The Pennsylvania State University, United States; <sup>2</sup>Wolfspeed, A Cree Company, United States; <sup>3</sup>U.S. Army Research Laboratory, United States

The 4H-SiC/SiO<sub>2</sub> interface is a promising system for high-temperature and high-power metal-oxide-semiconductor field-effect transistor (MOSFET) technology. This is so because of the wide bandgap, high critical breakdown field, and high thermal conductivity of 4H-SiC. The advantages of 4H-SiC MOSFETs are overshadowed by the relatively poor quality of the 4H-SiC/SiO<sub>2</sub> interface leading to effective channel mobilities of as little as  $5 cm^2/Vs$  in untreated devices.<sup>1</sup> Annealing in nitric oxide (NO) leads to mobility improvements of over an order of magnitude ( $35 cm^2/Vs$ ).<sup>1</sup> Recently, Lichtenwalner *et al.*<sup>2</sup> showed that the incorporation of a barium (Ba) interface layer (IL) leads to a doubling of the effective channel mobility, with peak value of  $85 cm^2/Vs$ .<sup>2</sup> Studies by Dycus *et al.*<sup>3</sup> showed that strain relief may be one of the factors in the mobility improvement. Recent electrically detected magnetic resonance (EDMR) studies have deduced that the underlying mechanisms behind the improvements are a large reduction in near-interface/interface silicon vacancy defects<sup>4</sup> and a reduction in interface strain with Ba treatment over NO anneals.<sup>4</sup> Lower oxide breakdown fields have also been reported and result in leakage currents through the SiO<sub>2</sub> gate.<sup>5</sup> Chanthaphan *et al.*<sup>5</sup> attributed the degraded insulating properties of the SiO<sub>2</sub> with Ba treatment to intrinsic defects in the metal-enhanced oxidation (MEO) SiO<sub>2</sub> layer. In this work, we utilized EDMR which is based on classical electron paramagnetic resonance (EPR) and, except for the detection scheme, has a very similar response to that of EPR.<sup>6</sup> For this work, the EDMR response consists of two phenomena. The first is spin-dependent recombination (SDR)<sup>7</sup> and the second is spin-dependent trap-assisted tunneling (SDTAT).<sup>8</sup> In the pre-oxide leakage case, the spectrum has an isotropic  $g \approx 2.003$  which is presumably due to SDR involving interface/near-interface silicon vacancy defects.<sup>9</sup> The post-oxide leakage SDTAT response has two overlapping spectra. One spectrum has a  $g \approx 2.0035$  and the other spectrum has  $g \approx 2.0008$ . The spectrum with  $g \approx 2.0008$  is consistent with that of E' centers,<sup>10</sup> silicon dangling bonds back-bonded to three oxygens oftentimes facing into an oxygen vacancy. Thus, it is likely that we are detecting SDTAT of E' centers in the SiO<sub>2</sub> gate via stress induced leakage currents. Our results are consistent with and support the conclusions of Chanthaphan *et al.*<sup>5</sup> and show that leakage currents in the Ba treated 4H-SiC MOSFET gates are caused by intrinsic defects, E' centers. This work at Penn State was supported by the U.S. Army Research Laboratory. Any opinions, findings, conclusions, or other recommendations expressed herein are those of the authors and do not necessarily reflect the views of the U.S. Army Research Laboratory. 1 G.Y. Chung, C.C. Tin, J.R. Williams, K. McDonald, R.K. Chanana, R.A. Weller, S.T. Pantelides, L.C. Feldman, O.W. Holland, M.K. Das, and J.W. Palmour, *IEEE Electron Device Lett.* **22**, 176 (2001). 2 D.J. Lichtenwalner, L. Cheng, S. Dhar, A. Agarwal, and J.W. Palmour, *Appl. Phys. Lett.* **105**, 182107 (2014). 3 J. Houston Dycus, W. Xu, D.J. Lichtenwalner, B. Hull, J.W. Palmour, and J.M. LeBeau, *Appl. Phys. Lett.* **108**, 201607 (2016). 4 J.P. Ashton, P.M. Lenahan, D.J. Lichtenwalner, A.J. Lelis, and M.A. Anders, *J. Appl. Phys.* **126**, 145702 (2019). 5 A. Chanthaphan, Y. Katsu, T. Hosoi, T. Shimura, and H. Watanabe, *Jpn. J. Appl. Phys.* **55**, 1 2016). 6 J.A. Weil, J.R. Bolton, and J.E. Wertz, *Electron Paramagnetic Resonance - Elementary Theory and Practical Applications* (1994). 7 D. Kaplan, I. Solomon, and N.F. Mott, *J. Phys. Lett* **39**, 51 (1978). 8 M.A. Anders, P.M. Lenahan, C.J. Cochrane, and J. Van Tol, *J. Appl. Phys.* **124**, (2018). 9 C.J. Cochrane, P.M. Lenahan, and A.J. Lelis, *Appl. Phys. Lett.* **100**, 023509 (2012). 10 J.P. Campbell, S. Member, P.M. Lenahan, C.J. Cochrane, A.T. Krishnan, and S. Krishnan, *IEEE Trans. Device Mater. Reliab.* **7**, 540 (2007).

### 4:00 PM L06

**Body Diode Reliability of Commercially Available 1.7 kV 4H-SiC MOSFETs** Minseok Kang, Susanna Yu, Tianshi Liu, Diang Xing, Shengnan Zhu, Kristen Booth, Arash Salemi, Marvin White and Anant Agarwal; The Ohio State University, United States

Silicon Carbide (SiC) devices, including MOSFETs, JFETs, and IGBTs, have greatly improved due to improvements in substrate, epitaxy and device processing. Despite the major progress in SiC process technology, unipolar and bipolar SiC devices have yet to be fully implemented in higher voltage applications due to body diode degradation. Basal plane dislocations (BPDs) in epi-layer of SiC MOSFETs result in body diode degradation. The BPDs can transfer from substrate, be formed during epi-layer growth, or be created during subsequent device fabrication processes. Recently published papers showed that BPDs are created by room temperature ion-implantation process. When the internal body diode is forward-biased, the electron-hole pairs recombine within the epi-layer. This recombination provides the energy to expand BPD into stacking fault which cause poor majority carrier conduction in on-state, and high forward leakage current in off-state. Since the stacking fault size depends on the epi-layer thickness, the body diode degradation is more problematic in high-voltage devices. The main objective in this paper is to figure out how stacking faults affect majority carrier conduction and reverse leakage current in commercial SiC MOSFETs. We will also consider re-design of SiC MOSFET

to block the degradation from the body diode. To forward bias the body diode, a negative bias was applied to the drain with respect to source while a bias of  $-5$  V was applied to the gate with respect to source to ensure the complete pinch-off of the MOS channel. The body diode was stressed in forward conduction for 100 hours. The results of forward-bias stress on body diodes are analyzed in commercially available 1.7 kV 4H-SiC MOSFETs from various vendors. Some devices show a significant degradation after forward-bias stress on the internal body diode. These results imply one of three reasons may be responsible for such a high degree of degradation. First, that device may be using room temperature ion-implantation of Aluminum to form  $p^+$  contacts which can create many BPDs. Second, there are significant number of BPDs present from the starting epi-layer. Lastly, some other process may result in the creation of BPDs. These results have significant impact on the design and processing of SiC MOSFETs. If SiC MOSFETs are used without separate freewheeling diode chips in high frequency switching applications, the body diode will conduct during switching cycle of some portions. Alternatively, SiC MOSFETs with built-in or external Schottky diodes are an alternative approach to reducing body diode degradation. In addition, blocking injection of minority carriers in epi-layer by improving design is a good solution. Details will be discussed during the presentation.

#### 4:15 PM L07

**An Investigation into Anomalous Time-Dependent Dielectric Breakdown Characteristics for 1.2 kV Commercial 4H-SiC Power MOSFETs** Shengnan Zhu, Tianshi Liu, Susanna Yu, Diang Xing, Arash Salemi, Minseok Kang, Kristen Booth, Marvin White and Anant Agarwal; The Ohio State University, United States

Due to the higher efficiency and smaller size, 4H-SiC MOSFETs have been rapidly adopted in high-voltage and high-power applications. The automotive industry which demands stringent device reliability and long device operating lifetime is also expected to be the next growth market for SiC power MOSFETs. Therefore, the ruggedness of 4H-SiC power MOSFETs has been extensively examined in recent years. Among the reliability concerns for SiC power MOSFETs, gate oxide reliability is the most critical issue since it relates to the device lifetime, threshold voltage instability, and gate leakage current. This work utilizes Time-Dependent Dielectric Breakdown (TDDB) measurements to evaluate the gate oxide quality and make lifetime predictions for commercial 4H-SiC MOSFETs from several vendors. For vendor E', 110 devices were divided into three groups and tested under several voltages at room temperature, 150°C, and 175°C respectively. By using the thermochemical E-model [1], the extrapolation of the data demonstrated that the predicted lifetime at 150 with  $=20$  V is higher than  $10^6$  hours. Compared with vendor E', the results of TDDB measurements for vendor C indicated an extensive variation of the failure times with each gate bias. This significant variation makes it impractical to predict the device lifetime with normal operating conditions. For vendor D, even with a gate bias close to the breakdown voltage, the devices under test (DUTs) still survived for a surprisingly long time. To investigate the underlying reason, a gate bias of 53 V (about 2 V below the dielectric breakdown voltage) was applied to vendor D devices for over 30 hours. The leakage current reduced significantly in a few minutes after the bias was applied and continued to decrease throughout the stress. This phenomenon indicated that a considerable number of electrons were injected into the near interface gate oxide traps and increased the threshold voltage of the device. Consequently, the electric field in the gate oxide was reduced. The degradation of carrier mobility was also observed due to the stronger surface scattering caused by the interface trapping and the injection of the electron to the near interface oxide traps. Similar measurements have also been conducted with all other vendors. Vendor C and D' showed comparable leakage decrease. The rapid reduction of leakage current and large increase of the threshold voltage didn't show up in results of vendor E' and H. The failure times from TDDB measurements can be prolonged for devices with a significant number of defects in the gate oxide. Consequently, the predicted lifetime under normal operating situation obtained from the extrapolation of TDDB results can be overestimated. The reported results show that the vendors need to keep working on improving the gate oxide quality.

[1] J. W. McPherson, H. C. Mogul, 1998, Underlying physics of the thermochemical E model in describing low-field time-dependent dielectric breakdown in SiO<sub>2</sub> thin films, *Journal of Applied Physics* 84, no. 3 (1998): 1513-1523

#### 4:30 PM L08

**(Student) Atomic Study of 4H-SiC/SiO<sub>2</sub> Interfaces—A Systematic Approach** Lu Wang, Sarit Dhar and Marcelo A. Kuroda; Auburn University, United States

The mechanisms to control the 4H-SiC/SiO<sub>2</sub> interfaces through chemical treatments are instrumental in defining the electronic properties such as the interfacial trap densities and carrier mobilities [1-5]. Hence, understanding interfacial atomic configurations and structure-property relationships are key to improve the performance of power devices. In this study, we produce models of the (0001) Si-face of the 4H-SiC with SiO<sub>2</sub> using first principles calculations within the density functional theory (DFT). Structures are formed using different phases of SiO<sub>2</sub> selected from AFLOW library [6] based on formation energy, electron density, and band gap that are tractable within DFT. An array of realistic atomic configurations is created by adding H, N, O, and Si atoms to

remove dangling bonds. These interfaces are consistent with the chemical bonding revealed by x-ray photoelectron spectroscopy (XPS) and other surface characterization techniques [7-9] and include N areal densities similar to experimental estimates. Large scale first-principles calculations are then carried out to elucidate the relationship between the different interfacial structures and their resulting properties.

The created SiC/SiO<sub>2</sub> interface models are fully relaxed and various properties (e.g. formation energy, electron density, band structure, bond length) are computed. Calculations use the generalized gradient approximation [10] as implemented in the quantum espresso software suite [11]. By comparing the properties of these interfaces to experimental observations, this comprehensive analysis allows to both assess their validity and rationalize the role of nitridation. Electron density profiles matching those obtained by x-ray reflectivity (XRR) [12] suggest that nitridation of the interfaces from NO annealing yields a higher Si density near the interfaces. Moreover, we find that the addition of N stabilizes the interface by reducing strain with no introduction of interfacial gap states. This methodology sheds important insights on the correlation between interface treatments and resulting electronic properties and may be applied to other dielectric-semiconductor structures. The authors gratefully acknowledge the funding support from Army Research Lab grant ARMY-W911NF-18-2-0160, computational resources from AU Hopper HPC, and fruitful discussions with Dr. L. Feldman group in Rutgers University. [1] H. Yano et al., IEEE Trans. Electron Devices 46, 504 (1999). [2] H. Li et al., Appl. Phys. Lett. 70, 2028 (1997). [3] D. Okamoto et al., Phys. Lett. 96, 203508 (2010). [4] L. K. Swanson et al., Appl. Phys. Lett. 101, 193501 (2012). [5] A. Chanthaphan et al., AIP Adv. 5, 097134 (2015). [6] S. Curtarolo et al., Comput. Matter. Sci. 58, 218 (2012). [7] L. I. Johansson et al., Phys. Rev. B53, 13793 (1996). [8] Xu et al., J. Appl. Phys. 115, 033502 (2014). [9] S. Dhar et al., J. Am. Chem. Soc. 131, 46, 16808 (2009). [10] J. P. Perdew et al., Phys. Rev. Lett. 77,3865 (1996). [11] P. Giannozzi et al., J. Phys. Condens. Matter. 21, 395502 (2009). [12] X. Li et al., Appl. Phys Lett. 113, 131601 (2018).

#### 4:45 PM L09

**(Student) Electrical Characterization of 4H-SiC/ALD-Al<sub>2</sub>O<sub>3</sub> Interface for Different Surface Preparations** Isanka Udayani Jayawardhena<sup>1</sup>, Tamara Isaacs-Smith<sup>1</sup>, Ayayi C. Ahyi<sup>1</sup>, Rahul P. Ramamurthy<sup>2</sup>, Koushik Ramadoss<sup>2</sup>, Dallas Morissette<sup>2</sup> and Sarit Dhar<sup>1</sup>; <sup>1</sup>Auburn University, United States; <sup>2</sup>Purdue University, United States

As a wide band gap semiconductor, 4H-SiC has established unique properties with the capability of high power and harsh environmental applications where Si devices cannot exhibit good performance due to its inherent material properties. But, 4H-SiC MOSFET performance is highly affected by the low channel conductance due to trapping of carriers by a high-density of near-interface traps at 4H-SiC/SiO<sub>2</sub> interfaces. These traps are physically located within  $\sim 2$  nm from the semiconductor/dielectric interface and energetically located within the bandgap with an exponentially increasing density near the conduction band-edge of 4H-SiC. Trap passivation using NO[1], PSG[2] or BSG[3]; using different 4H-SiC crystal orientations and depositing high-k dielectrics are alternatives to overcome this limitation. Among the deposited high-k dielectrics approach, ALD Al<sub>2</sub>O<sub>3</sub> is an appropriate candidate for 4H-SiC MOS interfaces due to its materials properties such as good thermal stability, relatively large band gap and high critical electric field. For deposited oxides, it is essential to start deposition on a physically smooth and chemically clean semiconductor surface as that surface will be the semiconductor/dielectric interface after deposition unlike thermally grown oxides, where the interface moves away from the surface as SiC oxidizes. Therefore, appropriate surface preparation is critical for the formation of high-quality interfaces. In this work, we fabricated 4H-SiC/Al<sub>2</sub>O<sub>3</sub> n-MOS capacitors and lateral MOSFETs with different 4H-SiC surface terminations prior to thermal ALD Al<sub>2</sub>O<sub>3</sub> at 200 °C using H<sub>2</sub>O and TMA precursors. Frequency and temperature-dependent capacitance-voltage (CV) measurements and current-voltage measurements were carried out for quantifying trap densities, leakage currents and channel mobilities.

The reference samples received standard RCA clean and HF etch prior to ALD. These samples had high leakage currents and large negative effective charge. A substantial decrease in the effective charge, interface trap density ( $D_{it}$ ) and leakage were observed when sacrificial oxidation (where a high-temperature oxide was grown in O<sub>2</sub> and etched with BOE) was employed prior to ALD. This surface preparation results in an O-terminated surface as Dhar et al. reported[4]. Lateral MOSFETs fabricated by this process had a low peak field-effect mobility ( $\mu_{FE}$ ) of  $\sim 1.5$  cm<sup>2</sup>V<sup>-1</sup>s<sup>-1</sup>. When sacrificial oxide was grown at NO, resulting in a Si-O-N terminated 4H-SiC [1]; further improvement in  $D_{it}$  was observed. Next, H terminated SiC surfaces were formed by etching at 1600 °C in hydrogen gas followed by annealing at 1000 °C in H<sub>2</sub> [5,6]. We observed the lowest  $D_{it}$  in 4H-SiC/Al<sub>2</sub>O<sub>3</sub> capacitors via this termination process[7]. As the H-etch process is difficult to implement in a MOSFET process flow, we replaced it by sacrificial oxidation followed by 1000 °C hydrogen annealing. This process also resulted in a significant reduction of  $D_{it}$  compared to the reference samples, but the  $D_{it}$  was higher than the H etch + H anneal process. Lateral MOSFETs fabricated in parallel had peak  $\mu_{FE}$  of  $\sim 18$  cm<sup>2</sup>V<sup>-1</sup>s<sup>-1</sup>, consistent with the reduction of  $D_{it}$ . It can be concluded that for deposited dielectric/4H-SiC interfaces, the SiC surface termination plays a critical role. Specifically, for ALD of Al<sub>2</sub>O<sub>3</sub> on 4H-SiC, surface termination using H or Si-O-N prior to ALD has a clear benefit over Si-O termination. Further studies

with more results on MOSFETs will be presented at the conference along with surface chemistry models to explain these observations. The authors acknowledge the US Army research laboratory and the II-VI Foundation. [1] G.Y. Chung *et al.*, *Appl. Phys. Lett.* 76.13.1713, 2000. [2] A.U. Jayawardena *et al.*, *Semicond. Sci. Technol.*, 2018. [3] Y. Zheng *et al.*, *IEEE Electron Device Lett.* 38.10.1433, 2017. [4] S. Dhar *et al.*, *J. Am. Chem. Soc.* 131.46.16808, 2009 [5] H. Tsuchida *et al.*, *J. Appl. Phys.* 85.7.3569, 1999. [6] N. Sieber *et al.*, *Appl. Phys. Lett.* 78.9.1216, 2001 [7] J. Jayawardena *et al.*, *MSF*. 963.217, 2019

SESSION M: Quantum Dots and Wells  
 Session Chair: Jonathan Wierer  
 Session Hosts: Seth Bank and Joshua Zide  
 Wednesday Afternoon, June 24, 2020  
 Location: ZoomRoom 6

## 2:00 PM M01

**(Student) Si Quantum Dots and Rings via Rapid Ge Diffusion During High Temperature Oxidation of Si/SiGe Nanostructures** Emily Turner<sup>1</sup>, Keshab R. Sapkota<sup>2</sup>, Christopher Hatem<sup>3</sup>, Ping Lu<sup>2</sup>, George T. Wang<sup>2</sup> and Kevin S. Jones<sup>1</sup>; <sup>1</sup>University of Florida, United States; <sup>2</sup>Sandia National Laboratories, United States; <sup>3</sup>Applied Materials, Inc., United States

Limitations to scaling of Si microelectronics have spurred a wide range of research avenues to continue increasing density and efficiency in devices while maintaining cost effectiveness. Some of these candidates include the integration of new materials such as III-Vs and Ge or fabrication of new geometries for microelectronics. In particular, the incorporation of Ge holds promise due to its proven compatibility with current fabrication methods and its high electron and hole mobility. Si and SiGe quantum dots (QDs) have exciting potential in microelectronics and quantum computing as well as in on-chip optical sources. However, scalable methods for fabricating size-controlled and position-controlled Si/SiGe QDs at dimensions less than 5 nm do not currently exist. To address this, we explore the application of an unusual enhanced Ge diffusion process during the thermal oxidation of Si/SiGe heterostructures as a potential route to create on-chip, position controlled Si/SiGe QDs. High temperature oxidation of Si/SiGe heterostructured fins has been shown to result in the formation of vertically stacked Si nanowires with diameters down to 2 nm. High angle annular dark field scanning transmission electron microscopy (HAADF-STEM) analysis revealed that Ge rapidly diffused along the Si/SiO<sub>2</sub> interface during oxidation, effectively encapsulating the Si layers in defect-free epitaxial strained SiGe. We extend this approach to the oxidation of vertical Si/SiGe axially heterostructured pillars and tubes defined via electron beam lithography and reactive ion etching as a route to create vertically stacked Si quantum-scale structures encapsulated in SiGe nanostructures. The size of the final Si quantum scaled structures is controlled by oxidation time instead of lithography. Results on the formation of QDs within the pillars after oxidation will be presented, including the evolution of the pillars from as-etched pillars to encapsulated Si QDs. In addition, the oxidation of other unique nanostructures inaccessible by other fabrication methods such as Si/SiGe rings will be presented. Finally, a new focused ion beam (FIB) method developed to allow unobstructed, damage free cross sectional TEM analysis of 3-D nanostructures will be briefly discussed. In total, these findings could lead the way to scalable manufacturing of Si/SiGe QDs and other novel quantum scale structures for a variety of microelectronics, quantum information systems, and photonics applications.

## 2:15 PM M02

**(Student) Low-Density, Site-Controlled InAs Quantum Dots for Quantum Devices** Lauren McCabe and Joshua Zide; University of Delaware, United States

We present on low-density, site-controlled InAs quantum dot (QD) growth for integration into quantum devices. InAs QDs have long been considered as possible qubits and the epitaxial formation of these structures is well understood [1]. However, the random nucleation of these self-assembled QDs have made it challenging to produce arrays of QDs desirable for scalable production of devices [2]. It is also a challenge to produce a low enough density of QDs to have single occupancy to integrate into devices, which can be up to tens of microns in size. To overcome these challenges we are engineering a molecular beam epitaxy (MBE) grown III-V QD material platform with low-density arrays of site-controlled growth. While patterning templates [3, 4, 5, 6, 7] is an established method for site controlling QDs, patterns have previously been limited to relatively high density arrays. We have shown by maintaining low arsenic overpressures with higher growth temperatures that the QD occupancy in the patterned array increases with increasing periodicity. Starting with an array of 0.25  $\mu\text{m}$ , a single QD occupancy of less than 30% is observed. Going up to a 10  $\mu\text{m}$  array an 89% occupancy is realized. We are investigating growth parameters for this system to enhance the substrate cleaning, deoxidation, and occupancy of patterned QDs, as well as compare this system to the unpatterned equivalent. Additionally, we are exploring a solution to address the low optical quality typical of patterned quantum dots by growing QD columns over the initially patterned QD array and characterizing the optical quality of the QDs in the columns as they get further from the patterned growth

interface. [1] *Prog. Mater. Sci.* 64, 121-199 (2014) [2] *Adv. Quantum Technol.* 3, 1900034 (2019) [3] *Appl. Phys. Lett.* 92, 183101 (2008) [4] *Appl. Phys. Lett.* 87, 243112 (2005) [5] *Phys. Rev. Lett.* 91, 196103 (2003) [6] *Rep. Prog. Phys.* 72, 046502 (2009) [7] *Materials* 9, 208 (2016)

## 2:30 PM M03

**(Student) Controlled Growth of InGaN Quantum Dots on Photoelectrochemically Etched InGaN Quantum Dots Templates** Xiongliang Wei, Syed Ahmed Al Mueyed, Damir Borovac, Renbo Song, Nelson Tansu and Jonathan J. Wierer; Lehigh University, United States

Quantum dot (QD) light emitters have been intensively researched for over 20 years due to the benefits of strong confinement of carriers in three dimensions. LEDs made with QD active layers should have higher spontaneous emission rates due to higher electron and hole wavefunction overlap, higher radiative efficiency at high carrier densities attributing to reduced Auger recombination, and narrower optical spectrum bandwidth [1]. Significant efficiency improvements could also be realized in QD-based laser diodes (LDs) due to lower current transparency and higher differential gain. However, all these gains can only be realized if there is control of the sizes of the QD ensembles. Although QD-based LEDs and LDs have these theoretical benefits, QDs are not widely used in III-nitride emitters due to the difficulty of fabrication of high density and uniformly sized QDs. Self-assembled (SA) growth such as Stranski-Krastanov growth, is the most popular synthesis method which forms three-dimensional islands due to strain of the epitaxial and underlying layers. III-nitride QDs grown by this method, thus far, are limited in density and uniformity. Therefore, we propose an alternative SA growth method that provides control of the growth of InGaN QDs by using photoelectrochemically (PEC) etched InGaN QD templates layers. The SA InGaN QDs are grown by metal-organic chemical vapor deposition on templates consisting of planar GaN and PEC etched InGaN QDs for comparison [2]. The InGaN QD templates are formed using quantum-size-controlled PEC etching [3,4] of planar InGaN layers on GaN, which produces controlled QD radiuses with a statistical mean,  $\mu$ , of 17.3 nm, a standard deviation,  $\delta$ , of 6.2 nm, and densities of  $1.2 \times 10^{10} \text{ cm}^{-2}$ . The PEC etched QDs are capped with an AlGaN interlayer and GaN barrier layer to recover a planar surface morphology for subsequent SA growth of QDs. The PEC QD templates behave as seeds via localize strain near the PEC QDs which provide improved control of the SA QDs. The SA InGaN QDs are grown at 630 °C with a relatively low V/III of ~4200 and a high In/(In+Ga) molar gas phase ratio of 0.50 for both templates. The SA grown QDs on PEC QD templates are smaller and have controlled radiuses with  $\mu=21.7 \text{ nm}$  and  $\delta=11.7 \text{ nm}$  and emit at ~475 nm. The SA QDs on planar GaN templates are less controlled with radiuses of  $\mu=37.8 \text{ nm}$  and  $\delta=17.8 \text{ nm}$  and emit at ~500 nm. Additionally, the dot densities of the SA QDs on PEC QD templates are ~3 times higher and more closely match the underlying densities ( $8.1 \times 10^9 \text{ cm}^{-2}$ ) and arrangement of the of the template. Multiple quantum dots (MQDs) are also grown on both templates that consist of 4 periods of SA QDs and AlGaN/GaN interlayer/barrier layers. The MQDs grown on PEC QD templates better retain their planarized smooth surfaces after barrier layer growth, and exhibit ~3 times stronger photoluminescence intensity at room temperature compared to MQDs grown on planar GaN. Radiative recombination rates have been measured for both samples using radiative efficiency and differential carrier lifetime measurements [5]. SA QDs grown on PEC QD templates have much higher radiative recombination rates compared to SA QDs grown on planar GaN. We attribute this improvement to the controlled growth of the QDs on PEC etched QD templates. 1. J. J. Wierer, et al. *Lasers and photonics review*, 10, 612-622 (2016). 2. S. A. A. Mueyed, submitted (2020). 3. X. Xiao, et al., *Nanoletters* 14, 5616 (2014). 4. X. Wei, et al. *Appl. Phys. Lett.* 113, 121106 (2018). 5. S. A. A. Mueyed et al., *J. Appl. Phys.* 126, 213106 (2019).

## 2:45 PM M04

**Microwave-Assisted Synthesis and Characterization of Nitrogen-Doped Graphene Quantum Dots** Flavia P.N. Inbanathan<sup>1</sup>, Katherine Leslee A. Cimatu<sup>1</sup>, Payman Sharif Abdar<sup>1</sup>, Uvinduni I. Premadasa<sup>1</sup>, David C. Ingram<sup>1</sup>, Muhammad Shehzad Sultan<sup>2</sup>, Vladimir I. Makarov<sup>2</sup>, Brad R. Weiner<sup>2</sup>, Gerardo Morell<sup>2</sup> and Wojciech M. Jadwisieniczak<sup>1</sup>; <sup>1</sup>Ohio University, United States; <sup>2</sup>University of Puerto Rico at Río Piedras, United States

Graphene quantum dots (GQDs) are metal-free nanoparticles with a wide range of physical and chemical properties. GQDs are easily altered by tuning synthesis conditions. Among others, GQDs have tunable luminescence, low toxicity, bio-compatibility, strong resistance to photobleaching and so on. [1] In the past, GQDs were successfully synthesized by electrochemical approach, organic synthesis, self-catalysis, hydrothermal treatment, microwave-assisted synthesis, etc. [2] The microwave-assisted chemical synthesis is gaining much attention because this method leads to low cost, high yield, and better scalability for commercialization purposes. The prospect of developing magnetically active GQDs apart from known physicochemical properties can make GQD suitable for developing novel nanomaterials for various sensors and device applications. This work presents the results of the microwave-assisted synthesis of nitrogen-doped GQDs (N-GQDs) from glucose and liquid ammonia precursors with a subsequent dialysis filtering process. The resultant N-GQDs were characterized for absorbance, photoluminescence (PL), morphology (atomic force microscopy (AFM)), transmission electron microscopy (TEM)), chemical composition (XPS, C-NMR), and magnetic response. It was found that N-GQDs absorption spectra have three peaks

located at 273 nm (4.54 eV), 302 nm (4.1 eV), and 362nm (3.42 eV) corresponding to the electronic transitions from  $\pi \rightarrow \pi^*$  of C = C, C = N, and C = O respectively.[2] The PL spectra of N-GQDs exhibit emission peak shifts from 420 nm (2.95 eV) to 480 nm (2.58 eV) with the strongest peak at 450 nm (2.76 eV) when excited at 370 nm (3.35 eV). AFM images revealed that N-GQDs have a two-dimensional (2D) lateral shape with a height in the range of 2 nm – 6.8 nm. The high resolution TEM analysis indicated that the N-GQD has a single crystalline structure with a lattice fringe of ~0.24 nm which can be attributed to the (100) graphene plane. The particles are found to be well dispersed and fairly uniform with diameter ranging from 2nm to 6 nm. The elemental composition (XPS) and element-binding configurations (C-NMR) of the N-GQDs composites confirmed the presence of N-doping in QDs. The XPS analysis confirmed the binding energies of C1s (289 eV), N 1s, (402 eV), and O 1s (538.2 eV). The high-resolution XPS C1s peak deconvolution confirmed the presence of the C–O (287.4 eV) and O–C=O (289.2 eV) bonds, respectively. The XPS N 1s peak with a binding energy of 402.51 eV corresponds to a graphitic N-GQDs and the XPS O 1s peak centered at about 538.2 eV proved the existence of oxygenated functional groups which is also verified by C-NMR analysis. The magnetic response of N-GQDs was tested using a vibrating sample magnetometer and indicated its paramagnetic nature. This is in direct contrast to the recently reported superparamagnetic properties of metal-free N-GQDs synthesized by pulsed laser synthesis method [3]. In light of the above experimental observations, we will discuss the role of morphology, nitrogen-content, N- and O-based functional groups in N-GQDs which critically affect the magnetic properties of N-GQDs. References: [1] M. Kaur et.al, Nitrogen-doped graphene and graphene quantum dots: a review on synthesis and applications in energy, sensors and environment, *Adv. Colloid Interf. Sci.*, 259, pp. 44–64 (2018). doi:10.1016/j.cis.2018.07.001. [2] B.Zheng et.al, Ultrafast ammonia-driven microwave-assisted synthesis of nitrogen-doped graphene quantum dots and their optical properties, *Nanophotonics*, 6, pp.259–267 (2017), doi:10.1515/nanoph-2016-0102. [3] Brad R. Weiner et.al, Magnetic properties of metal-free nitrogen-doped graphene quantum dots, 30th Int. Conf. on Diamond and Carbon Materials 8-12, Sep 2019, Melia Lebreros, Seville, Spain.

### 3:00 PM M05

**(Student) Displacing Deleterious Misfit Dislocations from the Active Regions of InAs Quantum Dot Lasers on Si** Jennifer Selvidge<sup>1</sup>, Eamonn T. Hughes<sup>1</sup>, Justin Norman<sup>1</sup>, Chen Shang<sup>1</sup>, Daehwan Jung<sup>2</sup>, Aidan A. Taylor<sup>1</sup>, Robert Herrick<sup>3</sup>, John Bowers<sup>1,4</sup> and Kunal Mukherjee<sup>1</sup>; <sup>1</sup>University of California, Santa Barbara, United States; <sup>2</sup>Korea Institute of Science and Technology, Korea (the Republic of); <sup>3</sup>Intel Corporation, United States; <sup>4</sup>UC Santa Barbara, United States

To realize photonic integrated circuits to their fullest potential requires the development of III-V semiconductor lasers grown heteroepitaxially on silicon chip [1]. Historically, such laser design efforts have been stifled by the presence of high dislocation densities, arising from differences in lattice spacing, thermal expansion coefficients, and polarity between the III-Vs and Si [2]. For this reason, recent heteroepitaxial work has focused on the development of InAs quantum dot (QD) lasers which demonstrate substantially improved performance and reliability over traditional quantum well (QW) based devices [3]. Even so, the lifetimes of experimental heteroepitaxial QD lasers continue to show a strong dependence on threading dislocation (TD) densities [4]. This dependency can be at least partially explained by recent findings demonstrating that, even in high performance experimental InAs QD lasers on Si, a low, but still significant, density of misfit dislocations (MDs) form within the QD active layers as a result of TD glide [5]. Previously, as the origin of these misfits was not well understood, efforts to remove them focused solely on reducing TD density.

Here, we employ a different approach: adding thin quantum well layers above and below the active region to trap the misfits and prevent their formation within the QD layers themselves. We show that these misfit trapping layers are highly successful in forcing TD glide to occur outside the active region by (1) identifying our displaced misfits using cross sectional transmission electron microscopy (STEM) and (2) measuring a 60% increase in room temperature ground state (GS) photoluminescence (PL) emission as compared to a baseline structure. This PL increase, attributable to a reduction in non-radiative recombination losses at defects, suggests improvements to laser performance and lifetimes.

The success of these experiments implies that misfits form in the active region due to two concurrent phenomena: a stress inversion in the film from growth temperature to operating temperature due to differential thermal expansion between the film and substrate and, somewhat counterintuitively, lattice hardening in the QD layers. The indium alloyed QD layers effectively suppress the TD glide during the growth process as we would expect. But as the material attempts to relax the building tensile shear during cool down, the suppression of glide exclusively within these layers causes misfit formation to occur just beyond their upper and lower boundaries.

To characterize the efficacy of the trapping layers and deepen our understanding of the physical processes driving the generation of these misfits, we employed SEM based techniques—cathodoluminescence (CL) spectroscopy and *in situ* electron channeling contrast imaging (ECCI) on model structures. We measure a greater than 90% reduction in the areal density of dark line defects and misfits in our model structure with the addition of a misfit trapping layer in CL and ECCI respectively. Seeing a small number of remaining dark lines, we

then use plan-view STEM tomographic reconstructions on our full laser structure to identify unique behavioral cases of complete and incomplete misfit trapping within the trapping layers. We anticipate that through optimization of these structures and continued examination of the mechanical processes involved, commercially viable silicon-based photonic integrated circuits with heteroepitaxially integrated III-V lasers may finally be within reach.

[1] D. Liang and J.E. Bowers, *Nat Photon* **4**, 511 (2010).

[2] O. Ueda, *Jpn. J. Appl. Phys.* **49**, 090001 (2010).

[3] S. Chen et al., *Nat Photon* **10**, 307 (2016).

[4] D. Jung et al., *Physica Status Solidi (a)* **216**, 1800602 (2019).

[5] A.Y. et al., *IEEE Journal of Selected Topics in Quantum Electronics* **21**, 690 (2015).

### 3:15 PM BREAK

### 3:45 PM M06

**(Student) B-III-V/GaAs Quantum Wells—Towards 1.55  $\mu$ m Emitters on GaAs** Rasha El-Jaroudi<sup>1</sup>, Kyle M. McNicholas<sup>1</sup>, Pankul Dhingra<sup>2</sup>, Rachel C. White<sup>1</sup>, Qian Meng<sup>1</sup>, Mark Wistey<sup>3</sup>, Minjoo L. Lee<sup>2</sup> and Seth R. Bank<sup>1</sup>; <sup>1</sup>The University of Texas at Austin, United States; <sup>2</sup>University of Illinois at Urbana-Champaign, United States; <sup>3</sup>Texas State University, United States

Here we present B GaInAs quantum wells (QWs) grown nearly lattice-matched to GaAs as an approach to realize 1.55  $\mu$ m emitters on GaAs substrates. Telecom wavelength sources on GaAs are of renewed interest, driven by applications ranging from fiber-optic communications, to facial recognition and laser radar. High-quality GaAs-based emitters would enable the fabrication of low-cost, high-power vertical-cavity surface-emitting lasers (VCSELs) due to the availability of AlGaAs/GaAs distributed Bragg reflectors (DBRs) and AlO<sub>x</sub> native oxide layers. In analog to the dilute nitrides, the small atomic size of boron decreases the epitaxial strain when incorporated in high In concentration InGaAs grown on GaAs. In GaInNAs, this strain reduction is ultimately limited by the relatively small amount of N that can be incorporated, typically ~1%, before both the crystalline and optical quality of the material begin to seriously degrade.<sup>1</sup> Conversely, we observe that the addition of boron to B GaInAs does not result in the same level of structural and optical degradation, allowing for wavelength extension from 1.3  $\mu$ m to 1.4  $\mu$ m and demonstrating its potential to strain-engineer emitters on GaAs. B GaInAs and InGaAs QWs were grown by solid-source molecular beam epitaxy (MBE) on (100) semi-insulated GaAs substrates. Samples were characterized by high resolution X-ray diffraction (XRD)  $\omega$ -2 $\theta$  scans and photoluminescence (PL). As expected, the PL intensity decreased rapidly in InGaAs/GaAs QWs with >40% In, indicating a complete loss of optical quality. These changes were mirrored by structural degradation of the QW layers as measured with XRD. However, with the addition of B, both good crystalline quality and strong PL emission were recovered. We previously demonstrated wavelength extension to 1.3  $\mu$ m facilitated by the addition of B to highly compressively strained InGaAs on GaAs.<sup>2</sup> In agreement with Hart and Zunger's theoretical prediction<sup>3</sup> that the solid solubility limit of B substantially exceeds that of N, we now demonstrate further extension of room temperature PL emission wavelength to 1.4  $\mu$ m by simultaneously increasing the concentration of both B and In in B GaInAs QWs. These B GaInAs alloys have the highest simultaneous concentration of B and In yet reported in the literature. Moreover, when compared with the addition of N, the addition of B exhibits significantly less degradation in optical quality with increasing In concentration – even under relatively unoptimized growth conditions – suggesting that B-containing alloys may prove to be a superior approach to reach 1.55  $\mu$ m emission on GaAs. This work was performed in part at the University of Texas Microelectronics Research Center, a member of the National Nanotechnology Coordinated Infrastructure (NNCI), which is supported by the National Science Foundation (No. ECCS-1542159). This work was also supported by the National Science Foundation (Award Nos. ECCS-1838984 and ECCS-1933836). [1] V. F. Gamlin et al. *IEEE J. Selected Topics* (2002); [2] R. H. El-Jaroudi et al. 61<sup>st</sup> Electronic Materials Conference (2019); [3] G. L. W. Hart and A. Zunger. *Phys. Rev. B* (2000)

### 4:00 PM M07

**(Student) Mechanism for Blueshift with Annealing in Near-Infrared B-III-V Alloys on GaAs** Rachel C. White<sup>1</sup>, Rasha El-Jaroudi<sup>1</sup>, Qian Meng<sup>1</sup>, Pankul Dhingra<sup>2</sup>, Minjoo L. Lee<sup>2</sup>, Seth R. Bank<sup>1</sup> and Mark Wistey<sup>3</sup>; <sup>1</sup>The University of Texas at Austin, United States; <sup>2</sup>University of Illinois at Urbana-Champaign, United States; <sup>3</sup>Texas State University, United States

Low-cost GaAs-based near-infrared (NIR) emitters are attractive for applications ranging from LIDAR to fiber-optic communications. The small lattice-constant of boron arsenide (BAs) enables strain-engineering of high In concentration InGaAs telecom-wavelength emitters on GaAs. We have previously demonstrated 1.3  $\mu$ m emission from coherent B GaInAs quantum wells (QWs) on GaAs enabling the first electrically injected emitters with boron-containing active regions.<sup>1,2</sup> When compared to a nominally identical QW active region control sample, an unfavorable blueshift in the emission wavelength was observed in electrically injected emitter structures, which we attribute to unintentional annealing of the active region during the growth of the top contact layer. A similar effect has been observed in several III-V emitter active regions, including highly-strained GaInSb/GaSb QWs and the highly-mismatched alloy GaInNAsSb. In GaInAsSb QWs, this blueshift is attributed to In out-diffusion from the QW;<sup>3</sup> however, in GaInNAsSb this effect has been

attributed to nearest-neighbor rearrangement.<sup>4</sup> As with the dilute nitrides, we also observe an increase in photoluminescence (PL) intensity with annealing, which can be exploited to realize high luminescence efficiency BGaInAs emitters. Here we investigate the mechanism for this blueshift and PL intensity improvement in BGaInAs to facilitate the growth of NIR emitters on GaAs. BGaInAs QWs, BGaInAs films, and InGaAs QWs were grown by solid-source molecular beam epitaxy on (100) semi-insulated GaAs substrates. Samples were progressively annealed by rapid thermal annealing for 1 minute from 550 °C to 900 °C in 50 °C steps. Between annealing steps, the samples were characterized by high resolution x-ray diffraction (XRD)  $\omega$ -2 $\theta$  scans and room temperature photoluminescence (PL). In high In concentration BGaInAs QWs (~ 40% In and 3% B), we observe an obvious blueshift in wavelength of 100 nm, which corresponds to ~ 80meV. A similar blueshift of 60 nm (~ 50meV) has been observed in high In concentration InGaAs QWs (~ 40% In), suggesting that In out-diffusion from the QW is the driving force for the observed wavelength shift. In agreement, we observe no substantial blueshift of emission wavelength (<10 nm or 1 meV) in low In concentration (~ 16%) InGaAs QWs. Conversely, in BGaInAs films of similar In concentration (~ 16% In, 6.4% B) we observe a blueshift of 18 nm, which corresponds to ~ 25 meV, suggesting that nearest-neighbor rearrangement effects may also affect the emission wavelength, as observed in the dilute nitrides. XRD scans of BGaInAs QWs with annealing show the disappearance of QW thickness fringes and a shift of the QW peak towards the substrate peak, which could be indicative of In out-diffusion. Further understanding of the mechanisms for the observed blueshift in BGaInAs is essential for improvement of NIR BGaInAs emitters. Efforts to characterize In out-diffusion using secondary-ion mass-spectrometry (SIMS) and transmission-electron microscopy (TEM) are in progress and will be reported at the conference. This work was performed in part at the University of Texas Microelectronics Research Center, a member of the National Nanotechnology Coordinated Infrastructure (NNCI), which is supported by the NSF (No. ECCS-1542159). This work was also supported by the NSF (Award Nos. EECs-1838984, ECCS-1933836) and a NSF Graduate Fellowship (RCW). [1] R. El-Jaroudi et al, 61<sup>st</sup> Electronic Materials Conference (2019). [2] R. El-Jaroudi et al, 39<sup>th</sup> Conference on Lasers and Electro-Optics (2019). [3] H. Nair, Ph.D Dissertation, University of Texas at Austin (2013). [4] V. Lordi et al, Phys. Review B (2005).

#### 4:15 PM M08

**(Student) Effect of B-In Interactions on the Band Structure and Optical Properties of BGa(In)As** Qian Meng<sup>1</sup>, Rasha El-Jaroudi<sup>1</sup>, Istvan Gulyas<sup>2</sup>, Rachel C. White<sup>1</sup>, Tuhin Dey<sup>2</sup>, Seth R. Bank<sup>1</sup> and Mark Wistey<sup>2</sup>; <sup>1</sup>The University of Texas at Austin, United States; <sup>2</sup>Texas State University, United States

The small lattice constant of boron pnictides provides a method for strain-engineering near-infrared direct-bandgap materials on silicon and GaAs. In other highly mismatched alloy systems, such as the dilute-nitrides, cluster states, and nearest neighbor configurations strongly affect the optical properties.<sup>1,2</sup> Due to the challenging epitaxial growth of BGa(In)As beyond dilute amounts of B, the effects of B incorporation in BGa(In)As on the band structure and optical properties remain relatively unexplored both experimentally and theoretically. We have previously demonstrated high B incorporation in BGaAs, up to 20%, using molecular beam epitaxy (MBE).<sup>3</sup> Here we investigate the effects of B-B clusters and B-In nearest neighbor arrangement on the band structure and optical properties of BGa(In)As. BGa(In)As films were grown on (100) semi-insulated GaAs and GaP by solid-state molecular beam epitaxy (MBE). These films were characterized with high-resolution X-ray diffraction (XRD) and room-temperature photoluminescence. Theoretical calculations of the optical properties were performed using the density function theory (DFT) package Vienna Ab initio Simulation Package (VASP) using HSE06 hybrid functionals. Prior investigations of the BGaAs alloy suggest B cluster states near the conduction band edge may degrade optical quality as the B concentration is increased.<sup>4,5</sup> In our calculations, we find that the interband matrix element strength decreases only modestly with increasing B. However, the matrix element can be increased with the addition of In (3.7%). Calculations show the system energy of B cluster states (B-As-B<sub>n-1</sub>-As-In) and B in nearest neighbor of In (B<sub>n</sub>-As-In) are approximately equal, suggesting both are equally likely to form. While the addition of B in the B-In nearest neighbor configuration increases the bandgap of BGaInAs, the formation of B cluster states reduces both the energy gap and matrix element. This reduction in bandgap and optical quality is likely due to cluster states near the conduction band edge (CBE). Lindsay et al. found that the addition of 6% In to B<sub>0.026</sub>GaAs pushed the CBE away from the B-B cluster pair levels resulting in a strong recovery in dispersion near zone center.<sup>4</sup> Consistent with our calculations showing an increase in matrix element with the addition of In, room temperature PL measurements of BGa(In)As films with ~3% B showed a 2x improvement in PL intensity with the addition of In. Calculations of higher In and B concentrations, towards compositions required for 1eV multi-junction solar cell junctions and telecom-range photodetectors lattice-matched to GaAs and Si are underway and will be reported at the conference. This work was performed in part at the University of Texas Microelectronics Research Center, a member of the National Nanotechnology Coordinated Infrastructure (NNCI), which is supported by the NSF (No. ECCS-1542159). This work was also supported by the National Science Foundation (Award Nos. ECCS-1838984, ECCS-1933836, DMR-1508646, and CBET-1438608). The authors also acknowledge the Learning, Exploration, Analysis,

and Processing (LEAP) cluster at Texas State University for providing HPC resources. [1] K. Osamura et al. J. of Appl. Phys (1975); [2] V. Lordi et al. Phys. Review B (2005); [3] K.M. McNicholas et al. 61<sup>st</sup> Electronic Materials Conference (2019); [4] A. Lindsay and E.P. O'Reilly, Phys. Review B (2007); [5] R. Hamila et al. J. of Appl. Phys. (2012); [6] V. Lordi. PhD dissertation. (2005)

#### 4:30 PM M09

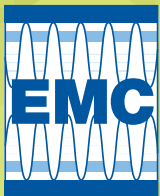
**(LATE NEWS, Student) Low-Temperature Monolithic InAs Integration on Amorphous Substrates** Jun Tao, Debarghya Sarkar and Rehan Kapadia; University of Southern California, United States

Devices built on III-V semiconductor materials have been widely applied in a variety of fields due to their superior optoelectronic properties and high mobilities. However, heterogeneous and scalable BEOL integration of high-quality crystalline III-V semiconductor materials and devices compatible with 3D integrated circuits are fundamentally limited by two factors: (i) the lack of a crystalline growth surface and (ii) the <400°C thermal budget. Here, we demonstrate single-crystalline InAs templated mesas can be directly grown on amorphous Si/SiO<sub>2</sub> substrates at a growth temperature of 300°C by low temperature templated liquid phase (LT-TLP) method, and demonstrate outstanding electron transport and optical properties.

Templated indium (In) mesas capped by silicon dioxide (SiO<sub>2</sub>) were first deposited on Si/SiO<sub>2</sub> substrates through photolithography, thermal or electron beam evaporation, and liftoff process. Then the specimens were heated to growth temperature (300 °C) in the downstream area of the dual-zoom LT-TLP system. The upstream temperature was kept around 600~700 °C to pyrolyze the arsine. After the full growth, SiO<sub>2</sub> capping layers were removed by wet etching (HF:H<sub>2</sub>O=1:10), and electrodes for Hall bar or photoconductive detector structure were fabricated.

To lower the possibility of twinning interfaces and stacking faults commonly observed in III-V semiconductor materials growth, we used the following approaches in our growth: (i) precisely control the flow rate of arsine to obtain a low degree of supersaturation. (ii) reduce the growth rate allowing finer layer-by-layer growth at the solid and liquid interface. (iii) prolong the temperature stabilizing time pre and post the growth window to avoid the temperature fluctuation introduced strain. The single out-of-plane crystal orientation of InAs mesa is indicated by the uniform color in the electron backscattering diffraction (EBSD) image. And the measured Raman spectroscopy is showing a peak at ~218 cm<sup>-1</sup>, which is consistent with the transverse (TO) mode of bulk InAs surface.

Temperature-dependent Hall effect voltages were measured in the physical property measurement system. The peak Hall mobility of 6750 cm<sup>2</sup>/V-s is observed at 50 K, and the room temperature mobility is around 5880 cm<sup>2</sup>/V-s, which is the highest electron mobility from materials grown on non-epitaxial substrates so far. With theoretical calculations, we find that the InAs grown here is not limited by grain boundary scattering but surface roughness scattering. And the projected mobility can reach ~20,000 cm<sup>2</sup>/V-s at 0.5 nm RMS surface roughness. InAs photoconductive detectors were fabricated with interdigitated patterned electrodes. When illuminated by 1550 nm near-infrared (IR) laser at room temperature, the measured photocurrent shows linear dependence to incident power between 7 to 250 μW, and the calculated responsivities reach 171 mA/W at ~ 9.1 μW incident power with 0.3 V bias. The corresponding external quantum efficiency (EQE) is around 13.7 %. The response time estimated by 3 dB cut-off modulation frequency is around 50 μs. Clearly, this work demonstrated the new pathway for BEOL compatible integrations of high mobility and high-performance devices.



# 62<sup>ND</sup> ELECTRONIC MATERIALS CONFERENCE

June 24-26, 2020

## POSTER PRESENTATIONS

**PS1.01**  
**(Student) In Situ AFM Characterization on Si-Based Anode for Li-Ion Battery** Jian Liu; The Ohio State University, United States

Lithium ion battery has been widely used as the energy supply for portable electronic devices because of its superior weight energy density and high voltage output. Plenty of research work has been conducted on exploring advanced electrode materials, among which Si based anode has attracted mass of attention. During Li ion intercalation, more Li can load on Silicon based anode than on conventional layered graphite such that Si anode can reach 4000mAh/g theoretical capacity which is more than ten times to graphite (372mAh/g). Although exhibiting with excellent theoretical capacity, Si based anode suffered from large volume expansion and poor cycle performance. It is essentially important to understand Si particle expansion mechanism and how solid electrolyte interface (SEI) is formed during cycling test for further stabilizing high capacity Si-based anode, and high resolution characterization becomes the most powerful tool to monitor and observe electrode electrochemical and mechanical behavior. However, the barrier for electrode characterization usually lies in the "buried" electrode inside of battery cell, and additionally the difficulty in conducting measurements in in-situ environment. To address these problems, this study proposed an approach to conduct an in-situ high resolution characterization to Si-based anode by using Atomic Force Microscopy (AFM). Atomic Force Microscopy is a type of scanning probe microscopy (SPM), precisely sensing the sample surface 3-D topography and forcing information by employing a mechanically oscillating AFM tip and measure the deflection change due to the interaction between AFM tip and surface features. To fit with AFM test environment, an in-situ sample holder is designed to provide a tightly sealed electrolyte environment while clamping the battery sample and exposing the cross-section area to AFM scanning tip. With the in-situ sample holder, cycle tests are conducted on half cell and full cell samples, which validates the capability of in-situ sample holder loading electrochemical tests. Then the Si-based anode cross-section area is scanned before and after cell cycle test. Focusing on several active material particles, characterize and study the dynamic particle behavior by comparing the AFM scanning results under different state of charge (SOC). Additionally, the SEI layer formation and variation are also studied by observing interface between solid particles and liquid electrolyte.

**PS1.02**  
**Cobalt-Free Spinel Cathodes for Next-Generation Lithium-Ion Batteries** Xinwei Jiao, Tianyang Wang, Lalith Rao and Jung Hyun Kim; The Ohio State University, United States

With the increased adoption of electric vehicles (EVs), the demand for battery materials has increased significantly during the last decade. Among battery cell components, cathode active material occupies a significant portion (> 25 %) of total cell cost. Conventional cathode active materials such as  $\text{LiNi}_{1-x-y}\text{Mn}_x\text{Co}_y\text{O}_2$  (NMC) for EVs consist of cobalt (Co) that is an expensive and critical, foreign sourced material which could pose a supply risk in the future. The objective of this research is to develop and validate  $\text{LiNi}_{0.5}\text{Mn}_{1.5-x}\text{Ti}_x\text{O}_4$  (LNMTO) spinel oxide as a high performance and cobalt-free lithium ion battery (LiB) cathode material. To achieve this goal, we synthesized pilot scale LNMTO material powder and fabricated 2 Ah pouch cells for a performance evaluation. The parent  $\text{LiNi}_{0.5}\text{Mn}_{1.5}\text{O}_4$  (LNMO) cathode has gained great interest due to its high operating voltage ( $\sim 4.7 \text{ V}_{\text{vsLi}}$ ) compared with conventional cathodes ( $\sim 3.8 \text{ V}_{\text{vsLi}}$ ). However, such high voltage led to unwanted parasitic reactions at electrode/electrolyte interfaces and severe capacity fading during cycling of battery full-cells (i.e., LNMO/graphite). To solve this issue, we proposed multiple strategies that can stabilize the electrode/electrolyte interfaces with different improvement mechanisms. Based on the results, we selectively combined them to obtain synergetic improvement; e.g., (1) passivation of spinel oxide surface by employing Ti-substituted LNMTO; (2) passivation of cathode (conducting carbon, in particular) by employing advanced functional binder; (3) strengthen the anode (i.e., graphite)/electrolyte interface by adding electrolyte additives. The experimental data showed that we could only achieve promising battery performances from the high-voltage pouch-cells by combining above improvement parameters. Since the electrolyte oxidation occurring at the cathode surface is catalyzed by carbon conductor (e.g., Super-P Li with 50 nm diameter), passivation of carbon by using functional binder is important. As hydrofluoric acid, a byproduct of electrolyte oxidation, etches the surface of spinel oxide cathode material, using the LNMTO benefits from forming Ti-enriched passivation layer at the particle surface and resisting the etching. Finally, since transition metal migration from cathode leads to a critical failure of anode's existing passivation layer (namely SEI), we strengthen the SEI by employing electrolyte additives. The impact of such multiple improvement mechanism has been carefully examined at various scales of cells: e.g., from coin-type cells to single-layer pouch-type cells to 2 Ah prototype pouch cells. We will also discuss about future strategies to further improve the performance of 2 Ah pouch cells.

**PS1.03**  
**(Student) High Brightness Luminescence from Indirect Band Gap AlGaAs Double Heterostructure (DH) Grown by Liquid Phase Epitaxy (LPE)** Zongjian Fan and Jerry M. Woodall; University of California Davis, United States

Theory would suggest direct band gap materials should be used for efficient light emitter, such that the emission of photons is not reliant on a phonon-assisted transition. But, also theoretically, if a semiconductor's materials quality is good enough, the nonradiative lifetime of carriers will be longer than radiative lifetime, and one could still obtain efficient luminescence from direct band gap transition in indirect materials<sup>1</sup>.

$\text{Al}_x\text{Ga}_{1-x}\text{As}$  compound system achieved great success for high-efficiency red emitters like light emitting diodes (LEDs) and laser over past decades. But because of its indirect bandgap nature after  $x > 0.40$ , it has been superseded by the emergence of AlGaInP system. However, AlGaInP's internal quantum efficiency (IQE) is relatively low, especially for the shorter wavelength yellow-green region<sup>2</sup>. Widely used gas source growth techniques for  $\text{Al}_x\text{Ga}_{1-x}\text{As}$  like Molecular Beam Epitaxy (MBE) usually suffer from oxidation of source materials and defects diffusion from substrate during growth. Therefore, little attention was paid to indirect, usually defective Al-rich  $\text{Al}_x\text{Ga}_{1-x}\text{As}$  compounds. On the other hand, liquid phase epitaxy (LPE) is known for superior materials quality, and has been proven for the successful production of high-efficiency  $\text{Al}_x\text{Ga}_{1-x}\text{As}$  solar cells and LEDs<sup>3-4</sup>.

In this work, we demonstrate bright room temperature photoluminescence (PL) at  $\sim 625 \text{ nm}$  from indirect  $\text{Al}_x\text{Ga}_{1-x}\text{As}$  DH structure grown by LPE pumped by a blue laser diode (450 nm). Comprehensive studies were done in terms of structure and optical characterizations by PL, scanning electron microscopy (SEM) and Energy-dispersive X-ray Spectroscopy (EDX). Extensive effort was made to establish correlation between optical/structure properties and growth procedure/mechanism, to provide deeper understanding of LPE mechanism and related materials physics. The details of the important growth parameters and fabrication procedures will be presented at the conference.

<sup>1</sup>Kyle H. Montgomery, Xin Zhao, and Jerry M. Woodall, *54th Electronic Materials Conference*, State College, PA. (2012).

<sup>2</sup>C. P. Kuo, R. M. Fletcher, T. D. Osentowski, M. C. Lardizabal, M. G. Craford, and V. M. Robbins, *Appl. Phys. Lett.* **57**, 2937 (1990).

<sup>3</sup>J. M. Woodall, and H. J. Hovel, *Appl. Phys. Lett.* **30**, 492 (1977).

<sup>4</sup>H. Rupprecht, J. M. Woodall, and G. D. Pettit, *Appl. Phys. Lett.* **11**, 81 (1967).

**PS1.04**  
**(Student) Characterization of Hazy Features on AlInP/GaAs Epitaxial Wafers Grown by Organometallic Vapor Phase Epitaxy** Hongyu Peng, Tuexun Ailihumaer, Yafei Liu, Balaji Raghothamachar and Michael Dudley; Stony Brook University, The State University of New York, United States

6-inch AlInP/GaAs epitaxial wafers grown by organometallic vapor phase epitaxy (OMVPE) are being developed for light emitting diodes (LEDs) applications [1]. Recently, we reported on the characterization of dislocation configurations in the GaAs substrates and epilayers and analyzed the conditions for relaxation and formation of misfit dislocations [2,3]. Beyond the interface, we have also investigated the changes in epilayer surface morphology under different growth conditions. It is observed that the epilayer surface takes on a hazy morphology, which is rougher compared to regular clear regions as revealed by both optical microscopy and atomic force microscopy. During epitaxial growth, the area of the hazy regions increases with growth pressure but other growth parameters such as growth temperature, V/III ratio, likely influence the onset of hazy morphology. Previous studies on the formation of hazy features report that these can be caused by the deficiency of phosphorus [4], lowered V/III ratio [5] or stacking faults [6]. However, the hazy features in our case, are different from the ones reported. On synchrotron X-ray topographs, the hazy regions have a blurred contrast even though they still diffract X-rays, indicating disordered lattice arrangement. To further understand the structure of the hazy regions and origin of the blurred contrast, we have applied reciprocal space mapping (RSM). Typically, the 004 reciprocal space maps reveal two distinct peaks corresponding to the GaAs substrate and the clear AlInP epilayer, respectively. Weakened and broadened peaks around the clear epilayer peak are also observed, indicating continuously varying strain and tilt between the hazy region and the clear region. By employing the 002 RSM to lower the X-ray penetration depth, the thickness of the hazy regions was analyzed. Comparison of the 002 and 004 RSMs reveals that at the beginning of epitaxial growth, the epilayers do not suffer from lattice distortion and the formation of the hazy morphology occurs when a critical thickness is exceeded. Transmission electron microscopy will be applied to confirm the results exhibited in RSMs and the results discussed with respect to applied growth conditions.

Reference: [1] C. H. Chen, S. A. Stockman, M. J. Peanasky, C. P. Kuo. *Brightness Light Emitting Diodes Semiconductors and Semimetals*, SEMICONDUCT SEMIMET, 48 (1997) pp. 97-144; [2] Hongyu Peng, Tuexun Ailihumaer, Yafei Liu, Balaji Raghothamachar and Michael Dudley, *J. Cryst. Growth*, 533 (2020) 125458; [3] Hongyu Peng, Tuexun Ailihumaer, Balaji Raghothamachar and Michael Dudley, *Ray Tracing Simulation of Images of Dislocations and Inclusions on X-ray Topographs of GaAs Epitaxial Wafers*, *J. Electron. Mater.* Submitted. [4] H. H. Ryu, M. H. Jeon, J. Y. Leem, H. J. Song, L. P. Sadwick, G. B. Stringfellow, *J. Mater. Sci.* (2006) 41:8265-8270; [5] D. S. Cao and G. B. Stringfellow, *Journal of Electronic Materials*, Vol. 20, No. 1, 1991; [6] Yoshihiro Hiraya, Fumiya Ishizaka, Katsuhiko Tomioka and Takashi Fukui, *Applied Physics Express* 9, 035502 (2016)

## PS1.05

**Vapor-Deposited Polymeric Thin Films on Fabrics for Breathable Wearable Device Application** Michael Clevenger, Jung Joo Sohn and Sunghwan Lee; Purdue University, United States

Wearable electronics are electronic devices fabricated on any sort of flexible material that can include rubbers, papers, and fabrics. These devices are a growing branch of technology that can have a large impact on various types of applications. The potential for the creation of new wearable devices from the most important medical applications to ones for novel enjoyment are extreme. In order to develop these wearable electronic devices, traditional inorganic conductive materials do not lend themselves to this type of application due to their mechanically brittle nature. Polymeric materials have superior mechanical flexibility in this type of application and are advantageous to the development of wearable electronic components. This use of a polymeric material can be seen as the application of poly(3,4-ethylenedioxythiophene) (PEDOT) thin films on fabric substrates. PEDOT is one of the most promising conjugated polymers due to its high electrical conductivity and tunable work function as well as stability for potential use in organic electronic and optoelectronic devices, and when applied to a fabric substrate can be utilized in various wearable electronic applications. In order to generate the PEDOT thin film, oxidative chemical vapor deposition (oCVD) will be utilized. oCVD is a deposition process that uses mild thermal energy to generate a chemical reaction between a vaporized source material (in this case EDOT) and an oxidizer in a vacuum chamber. In comparison to more conventional solution-based deposition processes, oCVD lends itself to certain traits that are more beneficial when applied to the creation of wearable electronic devices and thin film deposition on fabric substrates. Films deposited from the use of oCVD better conform to the target substrate, and because of that flexible properties can be maintained. It is also beneficial in that the process can be applicable to almost any type of substrate. Also since no molecules need to be dissolved during the process, solvent use isn't needed, so substrate damage is reduced. This makes the oCVD process extremely versatile and promising for wearable electronic devices: due to its ability to control layer thickness, greater uniformity, enhanced performance, and capability for large area processing with excellent conformality. oCVD polymers can be deposited on fabric substrates where the fabric is still able to maintain its flexible properties as well as breathability, and can effectively be used in next generation devices on fabrics that work as clothing as well as electronics. What will be presented is a comparison of various properties of PEDOT thin films on both glass and fabric substrates. Thin film deposition on a glass substrate is used as a control to compare the performance of oCVD PEDOT on fabrics. Specifically performance in regard to electrical, mechanical, surface, and chemical properties. To mimic daily use in clothing, these properties of oCVD PEDOT on fabrics will be compared before and after undergoing mechanical bending cycles. General electrical properties include an analysis of conductivity, carrier density, and carrier mobility utilizing Hall Effect measurement system and four-point probe. Atomic force microscopy (AFM) and scanning electron microscopy (SEM) are used to determine surface and cross-sectional microstructures and also to compare these between fabric and glass substrates. Fourier-transform infrared spectroscopy (FTIR) and UV-Vis spectroscopy are used to investigate optical properties and chemical element bonding information. Our findings on vapor-processed conjugated polymers on fabrics with high conductivity and mechanical flexibility is expected to significantly contribute to the realization of high performance and sustainable wearable clothing electronic devices that require enhanced uniformity, flexibility, and breathability.

## PS1.06

**(Student) Structural and Electronic Properties of a New Class of Nanoporous Organic Nanocrystals** Isaiah A. Moses and Veronica Barone; Central Michigan University, United States

Graphene exhibits excellent carrier mobility and exotic electronic, mechanical, and thermal properties. It is, however, a gapless semimetal and hence its application in electronics, for instance, in field effect transistors, is a challenge. Besides being gapless, graphene is also poreless. Except for thermal protons, the inter-carbon space in graphene is too small to allow transport of ions, liquid or gas molecules across its layers and hence can not be applied in membrane separations. There is therefore interest in finding 2D materials similar to graphene but with finite band gaps and/or intrinsic porosity. We present new 2D nanoporous organic nanocrystals (NONs). The NONs  $C_{12}H_6-h2D$ ,  $B_6N_6H_6-h2D$  and  $C_6N_6-h2D$  structures – built respectively from organic molecular units benzene, borazine and 1,3,5-triazine – have hexagonal symmetries while  $C_8N_4H_2-o2D$ ,  $C_{10}N_2H_4-o2D$ ,  $C_{10}P_4H_2-o2D$  and  $C_{10}As_2H_4-o2D$  – built respectively from organic molecular units 1,3-diazine, pyridine, phosphine, and arsinine – have oblique symmetries. These stable monolayers have finite band gaps ranging from 2.10 to 6.04 eV and small pores with typical dimensions varying from  $3.1 \text{ \AA}$  to  $5.94 \text{ \AA}$  depending on the molecular unit utilized as a building block[1]. We study the comprehensive stacking energy profile of these NONs and Bernal stacked equilibrium structures similar to graphene are obtained in both the stand-alone and bulk of the symmetric structures ( $C_{12}H_6-h2D$ ,  $B_6N_6H_6-h2D$  and  $C_6N_6-h2D$ ). Our results show that the interlayer interaction energy in graphite is about 55.35 meV/atom in agreement with the experimental value  $52 \pm 5$ [2] while, interestingly, the highest value obtained for the studied NONs is about 59.69 meV/atom for the

$C_{10}As_2H_4-o2D$ . The structural and electronic properties unveiled in these materials point to their potential applications in nanoelectronics, deep ultraviolet optoelectronic and laser devices and membranes for gas separation. References: [1] V. Barone, I. A. Moses, Structure and stability of graphene-like layers built from heterocyclic units, Carbon (152) (2019) 128–133. [2] R. Zacharia, H. Ulbricht, T. Hertel, Interlayer cohesive energy of graphite from thermal desorption of polyaromatic hydrocarbons, Physical Review B 69 (15) (2004) 155406.

## PS1.07

**(Student) Be Doping of Semi-Insulating GaN without Surface Accumulation Using MME** Habib Ahmad<sup>1</sup>, Travis J. Anderson<sup>2</sup>, James C. Gallagher<sup>2</sup>, Evan Clinton<sup>1</sup>, Christopher M. Matthews<sup>1</sup>, Zachary Engel<sup>1</sup> and W. Alan Doolittle<sup>1</sup>; <sup>1</sup>Georgia Institute of Technology, United States; <sup>2</sup>U.S. Naval Research Laboratory, United States

Molecular beam epitaxy (MBE) has been successful in achieving p-type doping using Mg, and, n-type doping by using Ge and Si. However, unintentionally doped (UID) GaN is inherently n-type due to the contaminants such as Oxygen, Si and nitrogen vacancies. There is a huge potential for growing semi-insulating GaN films by using MBE for high power electronics. Fe is one candidate for growing semi-insulating GaN films by using MBE but Fe is difficult to introduce via the MBE process and tends to permanently contaminate MBE systems. Be has a theoretical activation energy in GaN is 60 meV making it a better candidate than Mg for p-type doping of GaN. But MBE grown Be doped GaN has been experimentally shown to not be suitable for p-type doping due to its low solubility limit of low  $10^{17} \text{ cm}^{-3}$  and self-compensation[1]. This self-compensation property of Be doped GaN makes it good for semi-insulating films and devices [2]. However, surface segregation of Be in GaN has been observed which make it difficult to use in device structures requiring precise dopant placement [3]. Step-doped semi-insulating GaN has been achieved in this work without apparent surface accumulation along with a corresponding increased Be incorporation and better doping control. Be doping in GaN has been investigated by low temperature metal modulated epitaxy (MME) and characterized by secondary ion mass spectroscopy (SIMS) and hall effect measurements (HEM). MME has proved to drastically improve p-type GaN by achieving ultra-high doping including hole concentrations in excess of  $2 \times 10^{20} \text{ cm}^{-3}$  [4] and reproducible films. The goal here is to extend this technique to GaN:Be in order to achieve high quality semi-insulating films. 200 nm thick Be doped GaN layers using Be cell temperatures of 706, 729, 760, 786, 813, 850, and 880 °C were grown by MME.  $Al_{0.02}$  GaN layers were employed as marker layers between films and the individual GaN:Be layers were isolated by 200 nm of GaN:Ge films. This sample was characterized by SIMS at Evans Analytical Group (EAG) giving concentrations of  $6 \times 10^{17} \text{ cm}^{-3}$  to  $1.16 \times 10^{20} \text{ cm}^{-3}$ . SIMS showed square step-doping profiles for Be incorporation for these films without any delayed incorporation typical from surface accumulation presumably due to lower growth temperatures and better metals dose control by MME. The squared profile showed a rate of rise of the step edge of  $1.2 \times 10^{18} \text{ cm}^{-3}/\text{nm}$  and a rate of fall of  $2.25 \times 10^{18} \text{ cm}^{-3}/\text{nm}$  for the leading and falling edge of the step-doped Be SIMS profile, essentially at the limit of the SIMS tool. There did appear to be a drop in Be incorporation shortly after shutter opening for the three lowest temperature Be cases, suggesting an effusion cell cooling effect that is well known in low temperature MBE. This drop in doping can easily be compensated by subtle temperature increases on shutter opening. Several individual samples of MME GaN:Be were grown with layer thickness of 100 nm each on semi-insulating HVPE GaN templates using Be doping concentrations of  $4 \times 10^{18}$ ,  $1 \times 10^{19}$ ,  $2 \times 10^{19}$ ,  $5 \times 10^{19}$ ,  $1 \times 10^{20}$ , and  $2 \times 10^{20} \text{ cm}^{-3}$ . Hall measurements were performed by Lakeshore CRX-VF probe station and M91 FastHall Controller at the Naval Research Laboratories (NRL). All these samples showed semi-insulating nature with room temperature measurements impossible to achieve. This result indicates that Be doped GaN layers grown by MME on semi-insulating HVPE GaN could be useful to bury surface contaminants at the growth interface of HVPE GaN and MBE GaN and as resistive current blocking layers in various power diode applications. References: 1. Appl. Phys. Lett. **70** (22), 2 June 1997 2. Appl. Phys. Lett., Vol. 81, No. 20, 11 November 2002 3. Appl. Phys. Lett., Vol. 79, No. 27, 31 December 2001 4. J. Appl. Phys., 117, 045710 (2015)

## PS1.08

**(Student) On the Origin of Efficiency Droop of AlGaIn Deep Ultraviolet Light Emitting Diodes** Ayush Pandey<sup>1</sup>, Anthony Aiello<sup>1</sup>, Jiseok Gim<sup>2</sup>, Robert Hovden<sup>2</sup>, Emmanouil Kioupakis<sup>2</sup>, Pallab Bhattacharya<sup>2</sup> and Zetian Mi<sup>1</sup>; <sup>1</sup>University of Michigan, Ann Arbor, United States; <sup>2</sup>University of Michigan–Ann Arbor, United States

To date, the efficiency of AlGaIn deep UV LEDs is significantly below that of GaN-based blue LEDs. With the use of plasma-assisted MBE, we have demonstrated AlGaIn tunnel junction deep UV LEDs operating at 265 nm with an external quantum efficiency ~11% and wall-plug efficiency ~7.6%. It is also observed that the devices exhibit severe efficiency droop under very low current densities (~1 A/cm<sup>2</sup>). In this study, we have performed a detailed investigation of the underlying cause for the efficiency droop of deep UV LEDs by MBE. The carrier dynamics of AlGaIn quantum well heterostructures were measured using time-resolved photoluminescence spectroscopy. A nearly constant carrier lifetime ~0.3 ns was measured under a wide range of excitation conditions, suggesting that nonradiative Auger recombination plays a small, or negligible

role on the carrier loss process. AlGaIn multiple quantum well heterostructures were grown on AlN on sapphire templates using plasma-assisted MBE. The growth was initiated with a ~160 nm thick AlGaIn buffer layer having the same composition as the barrier. Five quantum wells were grown for each sample, and each AlGaIn quantum well has a thickness ~1.5 nm, with a barrier thickness of ~5 nm. Finally, a ~50 nm thick capping AlGaIn layer with the same composition as the barrier was grown to avoid surface effects. The emission wavelengths were varied in the range of 260 to 300 nm by changing the compositions of well and barrier layers. The epitaxy was performed under slightly metal-rich conditions. Detailed scanning transmission electron microscopy studies indicated that AlGaIn layers of a similar composition to the quantum wells are not compositionally uniform, but with the presence of extensive Ga-rich nanoclusters, which can lead to three-dimensional confinement of charge carriers. The samples were resonantly excited using the third harmonic of a Ti-sapphire laser to avoid generating carriers in the AlGaIn barrier layers, thereby eliminating carrier injection effects present in an electrically injected device. Our preliminary measurements performed on 265 nm AlGaIn quantum well samples showed that the peak emission wavelengths stay constant over a large range of excitation power conditions, suggesting the absence of strong polarization field. This can be explained by the presence of Ga-rich nanoclusters within the AlGaIn quantum wells grown by MBE, which can lead to the strong confinement of charge carriers, thereby minimizing quantum-confined Stark effect. The strong carrier localization also enables more efficient radiative recombination. The measured carrier lifetime stays nearly constant at ~0.3 ns for excitation powers varying from 0.5  $\mu$ W to 10 mW, suggesting that nonradiative Auger recombination plays a very small role in the carrier recombination process. These studies provide strong evidence that the efficiency droop observed at very low current densities (~1 A/cm<sup>2</sup>) in high efficiency AlGaIn deep UV LEDs may not be directly related to Auger recombination, but instead could be due to electron overflow. Due to the large activation energy for Mg dopant in Al-rich AlGaIn, p-type conduction is primarily mediated by hole hopping in the Mg impurity band at room temperature, which has low mobility. The resulting conductivity of the n and p-AlGaIn layers is nearly three orders of magnitude different. As a consequence, even at a small current density of 1 A/cm<sup>2</sup>, the device operates in a regime that severely deviates from the low carrier injection condition. This leads to a significant increase in charge carrier recombination outside of the device active region, i.e., electron overflow to the p-AlGaIn layer. Work is currently in progress to measure the temperature-dependent carrier lifetime and Auger coefficient and to achieve AlGaIn UV-C LEDs with high power operation.

#### PS1.09

**Normally-off GaN Vertical-Channel Junction Field-Effect Transistors with Regrown p-GaN by MOCVD** Chen Yang, Houqiang Fu, Viswanathan N. Kumar, Kai Fu, Hanxiao Liu, Xuanqi Huang, Tsung-Han Yang, Hong Chen, Jingan Zhou, Jossue Montes, Fernando A. Ponce, Dragica Vasileska and Yuji Zhao; Arizona State University, United States

We report the first experimental demonstration of a normally-off GaN-based vertical-channel junction field-effect transistor (VC-JFET). P-GaN regrowth and a subsequent self-planarization process were developed to fabricate the VC-JFETs. The fin-like channel regions were patterned by electron beam lithography (EBL) and aligned to *m*-plane or *a*-plane. The electrical properties of gate-to-source and gate-to-drain p-n junctions were characterized to verify the effectiveness of the p-GaN regrowth. Both VC-JFETs with *m*-plane and *a*-plane channels show decent gate modulation with threshold voltages of 1.4 V and 0.25 V, respectively. The devices exhibited excellent peak transconductances ( $g_m$ ) (over 600 S/cm<sup>2</sup> for *m*-plane or 900 S/cm<sup>2</sup> for *a*-plane). Based on TCAD model, we further discussed the effect of fin geometry on the devices performance. This paper highlights the achievements of normally-off VC-JFETs and lateral p-n junctions by etch-then-regrowth, which has been significantly difficult in GaN devices.

#### PS1.10

**(Student) Device Quality In Ga<sub>x</sub>1-N Templates (0.07 <x <0.10) for Optoelectronic Applications** Evyn L. Routh, Mostafa Abdelhamid, Nadia El-Masry and Salah Bedair; North Carolina State University, United States

The utilization of InGaIn alloys in InGaIn/GaN based multiple quantum wells (MQWs) has shown promise for applications in LEDs and solar cells due to the direct, tunable band gap that spans the visible spectrum. Notably, InGaIn-based LEDs are reported to have achieved an external quantum efficiency (ECE) of 80% [1], which is suitable for use in the blue to ultraviolet range. However, as the emission wavelength increases with nitride-based LEDs, a drop off in ECE is observed in the green to amber range, which has been deemed the "green gap problem" [1]. One such cause of the green gap problem is attributed to lattice mismatch observed in device hetero-structures due to the increased mole fraction of InN necessary for green emission.

In order to minimize the impacts of the lattice mismatch between the GaN underlayer and InGaIn in the InGaIn/GaN MQW, a super-lattice growth technique has been utilized. The In Ga<sub>x</sub>1-N super-lattice, referred to as "semi-bulk" (SB) consists of a period of 20-25 nm In Ga<sub>x</sub>1-N layer and a 1-2 nm GaN interlayer. This periodic growth process allows for a transition from a fully-strained InGaIn layer in the first period to a strain-relaxed surface of the hetero-structure that is suitable for growth of MQW devices, as the lattice parameters of the MQW are closer to the underlying SB [2]. The InGaIn achieves relaxation via the formation of six-faced hexagonal shaped pits (V-pits) that largely originate from dislocations

acquired during the growth process.

The growth parameters of SB have been optimized in order to achieve smooth, step flow growth that minimizes dislocation density and V-pits observed on the surface. The optimized parameters has resulted in device quality morphology of the SB surface with 7-10% indium composition based on prior Secondary Ion Mass Spectrometry (SIMS) measurements [2]. The surface of the SB was studied via atomic force microscopy (AFM), where step-flow terraces are observed. The RMS roughness of the SB with optimized growth conditions is found to be approximately 0.5 nm, compared to an RMS roughness of 1.2 nm across the same area of a SB prior to the new growth approach. Pre-optimization of the SB, large areas of pit coalescence are observed, and step-flow is not evident on the surface. The pit density in the pre-optimized SB growth is estimated to be 4.5 x10<sup>9</sup> cm<sup>-2</sup>. These coalescent areas inhibit the growth of device quality MQW on the SB surface. Utilizing a qualitative technique described elsewhere to estimate pit density via AFM [3], preliminary results have shown pit density to be about 1.6 x10<sup>8</sup> cm<sup>-2</sup> of the new SB approach, which can be attributed to screw dislocations along step-edges.

The SB growth has also resulted in low dislocation density. The impacts of screw-type and edge-type dislocations were characterized using the (00,2) and (10,5) reflections for  $\omega$ -scans, respectively. Notably, we report a dislocation densities of approximately 2x10<sup>8</sup> cm<sup>-2</sup> for screw-type TDs, and 2x10<sup>9</sup> cm<sup>-2</sup> for edge-type TDs. Because of the increasing indium content at different relaxation percentages present in the SB as seen in SIMS measurements, it can be noted that there is a consequential broadening factor in the  $\omega$ -scan. Correcting the broadening due to composition variation deduced edge-type TDs in the mid 10<sup>8</sup> cm<sup>-2</sup>. [1] S. Saito, R. Hashimoto, J. Hwang, and S. Nunoue, Appl. Phys. Express 6, 111004 (2013). [2] M. Abdelhamid, J. G. Reynolds, N. A. El-Masry, and S. M. Bedair, J. Cryst. Growth 520, 18 (2019). [3] R. A. Oliver, M. J. Kappers, J. Sumner, R. Datta, and C. J. Humphreys, J. Cryst. Growth 289, 506 (2006).

#### PS1.11

**(Student) Hybrid QD/Nitride Photo-Detector with Visible/Infrared Response** Fiaz Ahmed, Joshua Letton, Shahab Mollah, Mikhail Gaevski, MVS Chandrashekar, Asif Khan and Andrew Greytak; University of South Carolina, United States

Photo-detecting devices working at room temperature with high speed and high photo-gain in visible and infrared region (IR) region has been elusive. The quest for a sensitizing material and an optimum device design, using solution chemistry and low cost methods is an active area of research in material chemistry.

In this research, we employ a thin layer of PbS QDs prepared through wet chemistry, working as an optical sensitizer on top of a high mobility two-dimensional electron gas (2DEG) HEMT structure. The PbS QD film is the material of choice for this test device due to its wide detection wavelength range, which can in principle be tuned from visible to short-wavelength infrared depending on the size (effective band gap) of the quantum dots. The HEMT enables photoexcited charge transfer from the QD layer to the substrate to be detected with high gain. A similar charge transfer approach was successfully used with indirect band gap semiconductor, SiC. Here, we examine the same hypothesis with a direct gap wide bandgap material.

For this study, an epitaxially grown AlGaIn/GaN HEMT device was fabricated on a sapphire substrate; PbS-QDs were then spin coated on top of the HEMT device after mesa etching and metallization. The completed device was tested for in-plane and vertical conductivity and photo response below and above the band gap of the nitride layers. We observe a significant visible photo response following QD deposition.

#### PS1.12

**Hybrid Magneto Photonic Material Structure for Plasmon Assisted Magnetic Switching** Alan H. Chu, Bradlee K. Beauchamp, Aveck Dutta, Deesha Shah, Alexander Boltasseva, Vlad M. Shalav and Ernesto E. Marinero; Purdue University, United States

All-optical magnetization (AOM) switching is a viable solution for circumventing precession-limited magnetic switching and achieving magnetization reversal in fs time scales. Among the mechanisms involved in such ultrafast, magnetization switching is the generation of large opto-magnetic fields by fs circularly polarized laser pulses. In this work, we seek to exploit plasmonic resonances at the interface between magnetic materials and plasmonic materials to enhance the opto-magnetic field and simultaneously achieve AOM in the nanoscale. The enhancement of the opto-magnetic field is obtained via the excitation of plasmons induced by laser pulses. Ideally, the magneto-plasmonic hybrid structure should comprise a nanomagnet with strong Perpendicular Magnetic Anisotropy (PMA) coupled with the plasmonic resonator. High magnetic anisotropy CoCrPt magnetic films and TiN plasmonic materials are chosen in this work as the thin film components of the magneto-plasmonic nanostructures. However, CoCrPt films grown directly on TiN exhibit in-plane magnetization. To attain the required PMA in CoPtCr whilst ensuring strong magneto-photonic coupling, we have developed nm-thick interlayers grown on TiN to control the magnetization orientation of CoPtCr. We report on the synthesis of these interlayers and examine the effect of interlayer composition and structural characteristics to effectively seed PMA in CoPtCr.

### PS1.13

**(Student) High Selectivity and High Aspect Ratio GaAs/AlGaAs Reactive Ion Etching with HBr/SF<sub>6</sub>/He and BCl<sub>3</sub>/SF<sub>6</sub>/He** Sarah Puzycki, [Michael Barrow](#), Shawn Wright, Fred Terry and Jamie Phillips; University of Michigan–Ann Arbor, United States

Highly anisotropic GaAs etching is needed to fabricate many devices, including high frequency electronics, through-wafer vias, and metamaterials. Standard dry etching processes use a chlorine-based chemistry such as BCl<sub>3</sub> or Cl<sub>2</sub>. Incorporating a fluoride donor, such as SF<sub>6</sub>, results in the formation of a nonvolatile AlF<sub>x</sub> layer on AlGaAs, serving as a passivation layer and etch stop for selective etching of GaAs. In this work, we develop anisotropic GaAs dry etch processes with high selectivity to AlGaAs. The experimental samples consist of epitaxially-grown 500 nm GaAs / 100 nm Al<sub>0.20</sub>Ga<sub>0.80</sub>As/ 206 nm buffer GaAs / GaAs substrate patterned with photoresist etch masks. Etch experiments are performed using a transformer coupled high density plasma etch tool (LAM 9400SE II) with selectivity determined by optical and surface profilometric measurements. For the BCl<sub>3</sub>/SF<sub>6</sub>/He etch chemistry, the RF chuck bias was adjusted to a 20 W bias to obtain the highest GaAs/AlGaAs selectivity of about 22:1 with an etch rate of up to 846 nm/min. The lower chuck biases induced sidewall undercut and higher biases increased AlGaAs surface roughness. For possible improvement in obtaining smooth sidewall profiles, etched surface morphologies, and minimal undercut, we investigated HBr as a replacement for BCl<sub>3</sub>. We demonstrate highly anisotropic GaAs etch profiles for HBr/SF<sub>6</sub>/He with GaAs/AlGaAs selectivity of about 49:1. Details of etch rates, etch profiles, and selectivity will be presented for the BCl<sub>3</sub> and HBr etch chemistries.

### PS1.14

**(Student) Electric-Field Control of Strain-Driven Tuning of FMR in V[TCNE]<sub>x</sub>** [Seth Kurfman](#)<sup>1</sup>, Andrew J. Franson<sup>1</sup>, Piyush Shah<sup>1</sup>, Gopalan Srinivasan<sup>2</sup>, Michael Page<sup>2</sup> and Ezekiel Johnston-Halperin<sup>1</sup>; <sup>1</sup>The Ohio State University, United States; <sup>2</sup>Air Force Research Laboratory, United States

Electric-field control of magnetic resonance has application potential in the design of low-power, compact, high-frequency magnetoelectronic devices, such as microwave filters and circulators. To date, this work has exploited low-loss ferrite materials mechanically coupled to piezoelectric substrates. However, traditional ferrites typically require lattice-matched substrates and extreme growth conditions to produce high-quality material, making on-chip integration while maintaining low damping a significant challenge. Here, we demonstrate electric-field control of the FMR properties of the low-loss ( $\alpha = (3.98 \pm 0.22) \times 10^{-5}$ ), organic-based, room-temperature ferrimagnet vanadium tetracyanoethylene (V[TCNE]<sub>x</sub>) in V[TCNE]<sub>x</sub>/piezoelectric composite heterostructures. These structures show shifts in the resonant frequency position by ~50 MHz, or more than six times the resonant linewidth, which is highly competitive against the best results utilizing YIG or other ferrites in comparable devices. Further studies exploiting piezoelectric materials with higher piezoelectric coefficients, as well as increased mechanical coupling of V[TCNE]<sub>x</sub> to the piezoelectric via direct deposition onto the piezoelectric substrate, may lead to further enhancement of the FMR tuning effects in these devices with V[TCNE]<sub>x</sub>. These results demonstrate the potential of V[TCNE]<sub>x</sub> to complement traditional ferrites in electrically-controlled magnetoelectronic devices. For example, since V[TCNE]<sub>x</sub> can be deposited on a variety of inorganic substrates at ambient pressure and temperature, it has the potential to be directly integrated into magnetoelectric devices without the need for flip-chip fabrication techniques. In this context, we will discuss how this proof-of-principle demonstration of strain-driven FMR effects in V[TCNE]<sub>x</sub> might be extended to phonon-modulated or -driven FMR in magnetoelectric devices. This work supported by NSF Grant No. DMR-1808704

### PS1.15

**Identifying the Spin Mixing Mechanisms in Excitonic and Exciplex Organic Light Emitting Diodes** [Kevser S. Tiras](#)<sup>1,2</sup>; <sup>1</sup>University of Iowa, United States; <sup>2</sup>Nigde Omer Halisdemir University, Turkey

MEH-PPV (a typical excitonic material) based and thermally activated delayed fluorescence (TADF) based devices were studied to identify the spin mixing mechanisms. Magnetic field effect (MFE) measurements are a sensitive tool for investigating the spin-dependent exciton and exciplex physics. In this study, both magneto-conductance and magneto-electroluminescence of the devices were compared. Light efficiency improvement is reported at the presence of an applied magnetic field to certain TADF-based organic light-emitting diodes. We found that hyperfine-field mechanism and delta-g mechanism can explain the MFEs in excitonic and exciplex devices, respectively.

### PS1.16

**(Student) Synthesis and Structural Characterization of Monodisperse Lanthanide Doped Titanium-Containing Perovskites for Optoelectronic and Thin-Film Applications** [Bernard D. Kavey](#) and Gabriel Caruntu; Central Michigan University, United States

Rare-earth doped BaTiO<sub>3</sub> nanocubes have been synthesized using a simple, highly versatile and energy-efficient solvothermal route at temperatures as low as 160 °C. The versatility and flexibility of the proposed synthetic method allowed the rational design of highly crystalline single phase rare-earth doped

BaTiO<sub>3</sub> nanocubes via a simple one-step solvothermal route. Transmission electron microscopy images of the as-synthesized Ba<sub>1-x</sub>Ln<sub>x</sub>TiO<sub>3</sub> (0.01 ≤ x ≤ 0.07; Ln = La<sup>3+</sup>, Ce<sup>3+</sup>, Nd<sup>3+</sup>, Sm<sup>3+</sup>, Gd<sup>3+</sup>, Dy<sup>3+</sup>, Tm<sup>3+</sup>) and the analysis of particle size distribution revealed that the resulting nanocubes are highly monodisperse and self-assembled nanocubes with a mean size of 19 ± 2 nm for all nominal dopant concentrations and compositions. Vibrational spectroscopy and optical measurements were employed to study the surface characteristics, observed narrow band gap energies and the nature of binding that occurs between the oleic acid capping ligand and the surface of the nanocrystals. It was determined that the oleic acid ligand binds to the ions present on the surface of the Ba<sub>1-x</sub>Ln<sub>x</sub>TiO<sub>3</sub> crystal structure via a bidentate coordination mechanism. The powder X-ray diffraction pattern of the as-synthesized nanocrystals showed a single phase highly crystalline diffraction pattern and the crystallite sizes has been estimated using the Williamson-Hall method. Also, dielectric spectroscopy of the as-prepared Ba<sub>0.99</sub>La<sub>0.01</sub>TiO<sub>3</sub> revealed higher permittivity values as compared to the pristine BaTiO<sub>3</sub>.

### PS1.17

**Micro-/Nano-Voids Guided Two-Stage Film Cracking on Bioinspired Assemblies for High-Performance Electronics** [Jen-Chun Fang](#); The Ohio State University, United States

Current metal film-based electronics, while sensitive to external stretching, typically fail via uncontrolled cracking under a relatively small strain (~30%), which restricts their practical applications. To address this, here we report a design approach inspired by the stereocilia bundles of a cochlea that uses a hierarchical assembly of interfacial nanowires to retard penetrating cracking. This structured surface outperforms its flat counterparts in stretchability (130% versus 30% tolerable strain) and maintains high sensitivity (minimum detection of 0.005% strain) in response to external stimuli such as sounds and mechanical forces. The enlarged stretchability is attributed to the two-stage cracking process induced by the synergy of micro-voids and nano-voids. In-situ observation confirms that at low strains micro-voids between nanowire clusters guide the process of crack growth, whereas at large strains new cracks are randomly initiated from nano-voids among individual nanowires.

### PS1.18

**Charge Scattering Mechanisms in Shallow InAs Quantum Wells** [Elena Cimpoiasu](#)<sup>1</sup>, Matthew J. Fox<sup>1</sup>, Benjamin R. Dunphy<sup>1</sup>, Shawn Mack<sup>2</sup>, Joseph A. Christodoulides<sup>2</sup> and Brian R. Bennett<sup>2</sup>; <sup>1</sup>United States Naval Academy, United States; <sup>2</sup>U.S. Naval Research Laboratory, United States

We examined the charge transport in InAs quantum wells with bottom Al<sub>0.8</sub>Ga<sub>0.2</sub>Sb and top In<sub>0.2</sub>Al<sub>0.8</sub>Sb barriers, placed in close proximity to the surface of the heterostructures, at depths from 7 nm to 15 nm. Heterostructures with InAs channels have been the focus of considerable interest because of their potential for novel applications and phenomena. Much research has focused on well designs and growth methods that enhance the electron mobility in InAs quantum wells, which trails the performance of GaAs wells, despite the smaller effective mass of InAs. Most of the studies have focused on channels placed at a safe depth from the surface of the heterostructure in order to remove any, possibly detrimental, surface effects. However, some applications such as down-scaling high-electron mobility transistors or improving the efficiency of spin-injection in devices require that the 2DEG be placed in the proximity of the surface of the heterostructure. Here we identify the dominant scattering mechanisms in shallow heterostructures where the surface states are expected to significantly influence the transport in the channel. We studied five samples, which were either unintentionally doped, doped from below the channel, or doped from above the channel. We measure the longitudinal and transverse resistances of Hall bars in weak and strong magnetic fields to extract the carrier concentration, the mobility, the quantum scattering time, and to observe any fingerprints of spin-orbit coupling, such as beats in the Shubnikov de Haas oscillations. Instead of using gate voltage for the control of the carrier concentration, here we explored the simple use of continuous illumination with variable wavelength from 400 nm up to 1300 nm. The illumination produced an initial increase in the carrier concentration at low photon energy, followed by a decrease upon the further increase of the photon energy. Calculations of the band structure revealed that the band profiles are fairly symmetric for the top-doped samples, but asymmetric for the unintentionally doped and for the bottom-doped samples. As a result, the charge distribution is symmetrically distributed across the well for the top-doped samples and skewed against the bottom interface for unintentionally doped and the bottom-doped samples. The charge density n dependencies of the Hall mobilities and quantum scattering times were used to infer the dominant scattering mechanisms. The n-dependence of the mobility is consistent with scattering of the interface roughness, likely with the bottom barrier interface. The roughness scattering parameters extracted when calculating theoretical values for the mobility that simulated the observed measured dependence indicate increased scattering from the top-doped samples to the bottom-doped ones, consistent with calculations of the charge distributions across the barriers. The n-dependence of the carrier scattering time  $\tau_q$  is less intuitive. While scattering due to interface roughness affects  $\tau_q$ , it is not the dominant mechanism. It is somewhat expected, because mobility is generally limited by large angle scattering mechanisms, while  $\tau_q$  is sensitive to all the scattering mechanisms. We argue that the n-dependence of  $\tau_q$  is a result of scattering of charged donors, remote or close to the interface. In conclusion, symmetric potential profile across the well

has the advantage of reducing the interface scattering, resulting in improved mobility. On the other hand, potential symmetry also means low Rashba spin-orbit coupling, which is not ideal for spintronic applications. An applied gate voltage to such structures would increase the asymmetry, therefore the spin-orbit coupling, at the expense, however, of the mobility values that are limited again by roughness interface scattering. Acknowledgements: This work was partially supported at NRL and USNA by ONR.

#### PS1.19

**Synchrotron and Optical Probing of Mixed Lead Halide Perovskites for Photovoltaics** Deidra Hodges<sup>1</sup>, Angel De La Rosa<sup>1</sup>, Luis Valerio Frias<sup>1</sup> and Xiao Tong<sup>2</sup>; <sup>1</sup>The University of Texas at El Paso, United States; <sup>2</sup>Brookhaven National Laboratory, United States

The methylammonium lead iodide  $\text{CH}_3\text{NH}_3\text{PbI}_3$  (MAPbI<sub>3</sub>) perovskites have attracted a lot of attention as a possible absorber material for thin film solar cells due to their bandgap energy, high optical absorption coefficients and low-cost solution-processing deposition approaches. MAPbI<sub>3</sub> perovskite solar cells have evolved with transformative potential with laboratory efficiencies greater than 20%. Perovskite absorber materials are very inexpensive to synthesize and simple to manufacture, making them an extremely commercially viable option. Perovskites of compositional variations  $\text{ABX}_3$  can yield a range of crystal structures, phases and stabilities. The Goldschmidt's Tolerance Factor is a reliable figure of merit or empirical index to forecast the formation of preferred and stable structures and phases with  $\text{ABX}_3$  hybrid organic-inorganic perovskite tolerance factors in the range of 0.9 to 1. Here, we probe perovskites of compositional variations  $\text{ABX}_3$  with tolerance factors in the range of 0.9 to 1.0, and a large effective ionic radius greater than 200 pm. We report on the structural and optical properties of two hybrid perovskite halides for photovoltaic (PV) applications,  $\text{MAPbI}_3$  and  $\text{FA}_x\text{Cs}_{1-x}\text{Pb}(\text{I}_{1-y}\text{Br}_y)_3$ , with tolerance factors of 0.91 and 0.97 respectively. PV devices were fabricated using these high tolerance factor hybrid perovskite halides. We report we have achieved power conversion efficiencies (PCEs) greater than 21% using the high tolerance factor perovskites investigated. The high tolerance perovskites were also characterized using synchrotron X-ray absorption near edge structure (XANES) spectroscopy at the National Synchrotron Light Source (NSLS) II submicron resolution X-ray (SRX) beamline at Brookhaven National Laboratory (BNL). XANES was used to probe the electronic structure of the high tolerance factor perovskites investigated and here we report on the valency and the localized density of states.

#### PS1.20

**(Student) I2 Dopant Induced Charge Carrier Mobility Enhancement in Organic Field-Effect Transistors (OFETs)** Thomas Debesay and Sam-Shajing Sun; Norfolk State University, United States

Organic/Polymeric semiconductor-based devices have been under extensive studies due to their intrinsic properties, which have tremendous potential to revolutionize the state-of-the-art technology to a more lucrative (by creating a cheaper cost of production) and greener industry. Their inherent advantages include, but not limited to, low cost of processing, lightweight, flexible nature, biocompatibility, material availability, etc. As it is the case in their inorganic counterparts, doping organic semiconductors (OSC) significantly improves the electronic properties, which in turn could result in better device performance. The principal purpose of introducing a minority dopant into a host OSC system is to facilitate the dissociation of the Frenkel excitons (free charge carrier generation). However, there have also been several findings linked to the impact of minority dopants on charge carrier mobility. Thus, in this research work, we have investigated how a small dose of iodine doping enhanced device performance via morphological changes and doping induced charge carrier concentration in a host P3HT OSC. This work will provide valuable scientific findings for further upgrading polymer/organic semiconductor-based technology innovations.

#### PS1.21

**(Student) Colloidal Quantum Dots Photodetectors and Their Performance Enhancement with the Plasmonic Effect of Silver Nanoparticles** Wafaa F. Gebriil and Omar Manasreh; University of Arkansas-Fayetteville, United States

Colloidal nanocrystals (NC) or quantum dots (QDs) have gained a great interest for use in optoelectronic devices since they have shown promising properties. The wet chemical methods that have been used to synthesize nanocrystals are cost-effective and produce high quality crystals. Moreover, the bandgap of the QDs can be tuned over a wide range of wavelengths by changing their size. Another advantage is that colloidal nanocrystals are suspended in a solvent which reduces the complicity and the cost of device fabrication by using free vacuum deposition techniques such as spin coating. Here we investigate photodetectors based on quantum dots with silver nanoparticles integrated to the device. CdSe nanocrystals were synthesized using a wet chemical growth method. A ligand exchange was performed on the synthesized quantum dots for activation. The optical absorbance and photoluminescence spectra at different reaction times were measured. The bandgap of the nanocrystals grown for 1 h is found to be ~ 1.7 eV. Silver nanoparticles were also synthesized via a wet chemical method and their spectral response was measured. Good light absorption enhancement was shown when the quantum dots were coated on a film of the synthesized silver nanoparticles. Photodetectors based on CdSe

quantum dots were fabricated and their conductivity was calculated to be  $6.8254 \times 10^7 \text{ cm Hz}^{0.5} \text{ W}^{-1}$ . After adding a silver nanoparticles layer under the quantum dots film, a conductivity of  $1.49771 \times 10^8 \text{ cm Hz}^{0.5} \text{ W}^{-1}$  was obtained. Also, the photodetector with silver nanoparticles integrated has higher responsivity.

#### PS1.22

**(Student) Atomic Layer Deposited Metal Oxide Bilayers for Metal-Insulator-Semiconductor Photovoltaics** Benjamin Davis and Nicholas C. Strandwitz; Lehigh University, United States

The use of metal-insulator-semiconductor (MIS) tunnel diodes as photovoltaics (PVs) relies on the Schottky barrier between the metal and semiconductor, which induces band bending in the semiconductor absorber allowing for efficient separation of electrons and holes. In the years following early MIS PV research in the 1970s and 1980s, the advent of atomic layer deposition (ALD) has provided a tool for enhanced control of ultrathin film deposition. One method to potentially improve MIS PV performance is the use of ALD oxide bilayers as tunnel insulators. Oxides with different oxygen areal densities have been demonstrated to form interfacial dipoles, manipulating the Schottky barrier. Previous studies have only explored the impact of dipoles between a single ALD oxide and interfacial  $\text{SiO}_x$ . The present work combines two ALD oxides, one ( $\text{AlO}_x$ ) with oxygen areal density higher than that of  $\text{SiO}_x$  and another ( $\text{LaO}_x$ ) with oxygen areal density lower than that of  $\text{SiO}_x$  according to literature. It is hypothesized that the greater oxygen areal density difference will result in a greater impact on the Schottky barrier. Experiments thus far have demonstrated that inserting an ALD  $\text{LaO}_x/\text{AlO}_x$  stack between n-type Si and Ni top contacts increases the average Schottky barrier height to 0.70 eV, compared to 0.63 eV when a similar thickness of only ALD  $\text{AlO}_x$  is used as the tunnel oxide. The findings suggest an interaction between the two oxides that may be utilized to tune the Schottky barrier of MIS PVs and other electronic devices.

#### PS1.23

**(Student) Exploiting Fixed Charge at Selective Contacts to Control Schottky Barrier Height for Silicon Photovoltaics** Ben M. Garland, Benjamin Davis and Nicholas C. Strandwitz; Lehigh University, United States

It is known that a fixed charge ( $N_f$ ) exists at interfaces between alumina ( $\text{Al}_2\text{O}_3$ ) and silicon and this charge can be tuned using thermal processing, even in very thin layers of alumina that allow carrier tunneling. When alumina is deposited on silicon using atomic layer deposition (ALD) and subjected to thermal treatment, excellent hydrogen passivation can be achieved from excess precursor hydrogen migrating to the silicon dioxide surface. When this tunneling alumina layer is utilized in selective contacts involving a metal oxide, hydrogen passivation of interface traps could be achieved while exhibiting a large magnitude of  $N_f$  without the need for heavy doping (n+/p+ a-Si). A low Schottky barrier height ( $SBH$ ) between the metal oxide and silicon would decrease the effective contact resistance and provide a more efficient selective contact. In this work, we investigate insertion of a tunneling layer of alumina deposited by ALD between molybdenum oxide ( $\text{MoO}_x$ ) and p-type Si to allow the  $SBH$  to be controlled using a large negative  $N_f$ , enabling a high efficiency selective contact without the need for heavy doping.

First, we determined the electrical properties (most notably  $N_f$ ) of a n-Si/ $\text{Al}_2\text{O}_3$  stack by making a MOSCAP structure using aluminum contacts and alumina films that are thick enough to preclude electron tunneling (thickness > 3 nm). The growth of alumina on CZ n-Si via ALD utilized trimethylaluminum and  $\text{H}_2\text{O}$  as precursors at 4 deposition temperatures (80°C, 120°C, 200°C, and 300°C). Half of the samples from each deposition temperature were annealed at 425°C in a nitrogen atmosphere for 20 minutes. We conducted capacitance-voltage (C-V) sweep measurements to determine the flat band voltage, which was used to calculate  $N_f$ . The fixed charge varied from  $-0.5\text{E}12 \text{ q/cm}^2$  to  $3.2\text{E}12 \text{ q/cm}^2$  where the samples with alumina grown at 80°C and annealed had the largest magnitude of negative  $N_f$ . Data from Terman method and conductance method interface trapped state density ( $D_{it}$ ) experiments determined that annealed samples had a much lower  $D_{it}$  (approximately  $1.2\text{E}7 \text{ eV}^{-1}\text{cm}^{-2}$ ) compared with as deposited samples (approximately  $6\text{E}12 \text{ eV}^{-1}\text{cm}^{-2}$  at maximum).

$\text{Si}/\text{Al}_2\text{O}_3/\text{MoO}_x/\text{Al}$  structures with thin (< 3 nm) alumina layers were produced to determine  $SBH$ . Sample preparation was identical to the MOSCAPs; however, the alumina layer was thinner to facilitate tunneling. Current density-voltage-temperature ( $J$ - $V$ - $T$ ) sweep and Mott-Schottky ( $MS$ )  $1/C^2$ - $V$  measurements were used in comparison to determine a range for  $SBH$ . The samples with as deposited alumina showed a higher  $SBH$  (~0.22-0.28 eV) compared to annealed samples (~0.17-0.22 eV) from  $J$ - $V$ - $T$  data. In comparison, the samples with as deposited alumina showed a higher  $SBH$  (~0.15-0.27 eV) compared to annealed samples (~0.04-0.12 eV) from  $MS$  data. A trend can be seen when contrasting as deposited/annealed samples and different alumina deposition temperatures from both  $J$ - $V$ - $T$  and  $MS$   $SBH$ . This seems to indicate that this MIS selective contact with tunneling alumina has the lowest  $SBH$  with a deposition temperature of 200°C and post-treatment annealing. Our data indicate that fixed charge does appear to be correlated with  $SBH$  in such a way that decreased barrier heights were found with samples that had a larger negative fixed charge. Further testing is currently underway to confirm this data. Thus, our work shows that manipulation of fixed charge at interfaces may allow for control over barrier heights, which are important for ultimately determining efficiency in Si photovoltaics based on selective contacts.

## PS1.24

**(LATE NEWS) Toward III-V-on-Si Tandem-Junction Solar Cells Using Selective-Area Epitaxial Growth of GaAsP Nanowire Arrays** Mohadeseh A. Baboli, Anastasiia Fedorenko, Stephen Polly, Alireza Abrand, Thomas S. Wilhelm, Seth Hubbard and Parsian Mohseni; Rochester Institute of Technology, United States

Recent efforts toward selective-area epitaxy (SAE) of vertically-aligned GaAs<sub>y</sub>P<sub>1-y</sub> nanowire (NW) arrays on Si substrates using metalorganic chemical vapor deposition (MOCVD) for applications in photovoltaic solar cells are presented. Oxide-based SAE masking templates on n-type Si substrates are patterned with 200 nm-diameter pores for axial growth of n-type GaAsP NW core segments, and subsequent lateral growth of p-type NW shell segments with thickness of 75 nm, to reach a targeted NW diameter of 350 nm. Targeted NW dimensions are extracted from rigorous-coupled wave analysis (RCWA) modeling of optimized geometries for GaAsP NW array-based solar cell. The SAE condition are established for V/III ratios between 500 and 1600 at growth temperatures between 850 °C and 950 °C. The composition of GaAs<sub>y</sub>P<sub>1-y</sub> NWs is tuned toward a targeted value of  $y = 0.73$  by altering the molar flow ratio of hydride precursors. The effect of growth rate on morphology, total yield, and symmetric yield of GaAsP NWs is explored through modulation of the effective local supply of growth species. Nanopore arrays with dimensions of 100 μm × 100 μm are patterned at the center of SiO<sub>2</sub> mesas. Each mesa is surrounded by border regions along which the underlying Si substrate surface is exposed. Thus, the supply of adatoms toward NW growth sites and, consequently, the growth rate and morphology of the resulting SAE NWs is controlled as a function of the masking template geometry. In this work, various SAE template configurations are examined for a constant array size. Under optimized growth conditions, near-unity yield of hexagonally symmetric GaAsP NWs on Si is realized. A process for the fabrication of GaAsP NW array-based solar cells on Si is outlined. Novel strategies for light management using hemispherical back surface reflectors are discussed. Lastly, methods for liftoff of as-grown GaAsP NW arrays, fabrication of flexible NW-based solar cell devices, and reuse of Si substrates for III-V NW SAE are presented.

SESSION PS2: Poster Session II  
Thursday Morning, June 25, 2020  
10:00 AM - 11:15 AM  
Poster Location: ZoomRoom

## PS2.01

**(Student) High Performance Micro-Supercapacitor via Hybrid-Curable Ion-Gel Electrolyte and Laser-Reduced Graphene Electrode for Flexible Energy Storage Devices** Dawoon Lee<sup>1</sup>, Youngkyun Kim<sup>1</sup>, U Hyeok Choi<sup>2</sup> and Jaekyun Kim<sup>1</sup>; <sup>1</sup>Hanyang University, Korea (the Republic of); <sup>2</sup>Pukyong National University, Korea (the Republic of)

To achieve both high mechanical strength and stability, a solid-state electrolyte (SSE) is one of the promising strategies for the next-generation energy storage devices. This approach has attracted significant attention due to the facile fabrication and chemical/mechanical stability of SSE even after severe external damage. However, a relatively low ionic conductivity ( $< 10^{-5}$  S/cm) of SSE, compared to a liquid electrolyte, can limit their actual applications on high performance energy storage devices.

In order to address the trade-off relationship of conductivity and mechanical integrity, a gel polymer electrolyte (GPE), composed of mechanical supporting polymeric matrix and ionic conducting ionic liquid, has been spotlighted as a promising strategy of conventional SSE for next-generation high performance and flexible energy storage component because the unique bicontinuous morphology of GPE. For the perspective of continuous development of high-performance GPE-based devices, designing and optimizing the polymer matrix system with high-conductivity ionic liquid is always demanding.

Arising from the upper mentioned needs, we propose new matrix systems by composing an acrylate monomer (PEGDA), a bisphenol-A diglycidyl ether (DGEBA), and an 1-Ethyl-3-methylimidazolium bis(trifluoromethylsulfonyl) imide (EMIM-TFSI) ionic liquid to fabricate dual-cured ion-gel polymer electrolyte (DIGPE)-based microsupercapacitor for miniaturized energy solution. In particular, this dual-cured approach by sequential thermal and ultraviolet annealing enabled us to accomplish the synergistic benefits of each component as well as the excellent electrochemical performance and stability of device. Also, a large-surface-area graphene electrode onto the flexible substrates via laser reduction method was introduced to ensure the facile fabrication and relatively long cycle life of supercapacitor systems.

Our DIGPE with flexible graphene electrode were systemically investigated to clarify the origin of electrochemical and mechanical improvement of supercapacitor as well as analyze its ionic transport phenomenon within the polymer matrix. Firstly, in order to investigate the movement of ionic liquids, Arrhenius temperature dependence of ionic conductivity was measured via metal-insulator-metal (MIM) structure. The result showed that the room temperature conductivity and specific capacitance of DIGPE is as high as about 4 mS/cm and 46 μF/cm<sup>2</sup>, respectively, suggesting that our strategy can dramatically enhance the electrical performance compared to the general solid-typed electrolytes (~0.23 mS/cm for DGEBA-based SSE). Various deformation tests were conducted to demonstrate the mechanical and electrochemical stability of our DIGPE devices (maintaining the initial performance after 10,000 bending cycle test). Finally, electrochemical performances were measured to evaluate DIGPE-based all-solid-state supercapacitor. Regarding to the high adhesive property from DGEBA epoxy matrix phase, DIGPE-based supercapacitor can effectively reduce the contact resistance between electrode and electrolyte while preventing the peeling-off issue after cycle test. (~88.9 % of capacitance retention value after 10,000 cycle test.)

In conclusion, we successfully fabricate a high conductive and mechanically stable GPE by hybridizing thermal-curable polymer, photo-curable polymer, and ionic liquid. The DIGPE-based supercapacitor exhibits high-performance electrochemical characteristics with mechanical flexibility and corresponding electrochemical stability. Therefore, our method provides valuable insights to design SSE having both high electric properties and mechanical flexibility for the development of next-generation energy storage devices.

## PS2.02

**Investigation of Two-Dimensional MoS<sub>2</sub> Based Ultra-Thin Solar Cells** Vinamrita Singh; Ambedkar Institute of Advanced Communication Technologies and Research, Delhi, India, India

Two-dimensional (2D) materials other than graphene have shown to be promising candidates for hole transporting materials (HTMs), electron transporting materials (ETMs) and as an active layer in solar cells (SC). Due to the suitable work functions, good charge carrier mobilities, stability, and ease of thin film deposition, 2D materials are successfully implemented in SCs. It possesses a high absorption coefficient of  $1.5 \times 10^6$  cm<sup>-1</sup> for a single layer, making it suitable for the realization of ultra-thin SC technology based on only 2D absorbing layers. The efficiency,  $\eta$ , achieved for monolayer MoS<sub>2</sub> SCs is very low, 2.8%, and stability/degradation studies are limited. Due to this, it becomes essential to focus on device engineering and probe into factors which would lead to higher SC performance.

Keeping this in mind, the present work discusses the performance of 2D MoS<sub>2</sub> based SCs. Two device configurations are theoretically analyzed to determine the properties that lead to the highest device efficiency. Firstly, SC of

configuration ITO/2D MoS<sub>2</sub>/Au (Cell 1) was optimized. Using only a single layer of MoS<sub>2</sub> with a thickness of 0.65 nm, resulted in an  $\eta$  of only 0.25%. The  $\eta$  increased with increase in thickness and saturated at 5.38% corresponding to a thickness of 97.5 nm. This is attributed to an increase in current density due to more light absorption by the active layer. The external quantum efficiency (EQE) also increased from ~10% to almost 100% at 97.5 nm thickness, implying that further increase in thickness is not necessary. It has been reported that the thin sheets of MoS<sub>2</sub> tend to bond together leading to bulk-like behavior. Since a thickness of 97.5 nm is sufficiently large compared to monolayer thickness, the bulk material values of band gap (1.5 eV) and dielectric constant (7.2) was used, and an  $\eta$  of 9.09% was obtained. Further, the variation of electron affinity was studied as it determines the carrier transport through the device. As observed an increase in electron affinity led to decrease in  $\eta$ . The lowering of MoS<sub>2</sub> energy levels would reduce the potential barrier for holes and increase in recombination at the ITO/MoS<sub>2</sub> interface. On the other hand, decrease in electron affinity was favorable up to 3.2 eV in terms of electron and hole transport after which the potential barrier between MoS<sub>2</sub>/Au reduced to zero, and the device failed to give SC output. The highest  $\eta$  achieved for Cell 1 was 18.22%, with  $V_{oc}$  =1.47 V,  $J_{sc}$  =17.01 mA/cm<sup>2</sup>, FF =72.92%. However, the performance was much lower after considering realistic series and parallel resistances. The electron affinity of ~3.57 or lower corresponds to p-type MoS<sub>2</sub> semiconductor, which is achievable through plasma treatment and doping MoS<sub>2</sub>. It can be concluded that modifying n-type MoS<sub>2</sub> to p-type is more favorable for SC application.

Thereafter, the p/n junction SC using both n- and p-type MoS<sub>2</sub> was studied. The structure ITO/p-MoS<sub>2</sub>/n-MoS<sub>2</sub>/Au (Cell 2) was optimized. The energy levels of the SCs are such that the electrons can easily transfer from n-MoS<sub>2</sub> to p-MoS<sub>2</sub>. The  $\eta$  of the SC with both p- and n-MoS<sub>2</sub> layer equal to 0.65 nm is 1.82%, with a  $V_{oc}$  of 1.07 V as compared to a very low  $V_{oc}$  = 0.33 V of Cell 1. The higher  $\eta$  may be attributed to the formation of p/n junction leading to lower recombination losses. Upon increasing the active layer thickness of both p and n-MoS<sub>2</sub>, the  $\eta$  saturates to ~24% and falls thereafter. It was further noted that increasing the thickness of n-type layer keeping p-type layer at 0.65 nm led to an increase in  $\eta$ . However, when the p-MoS<sub>2</sub> thickness was increased keeping n-MoS<sub>2</sub> constant, S-kink was observed in the J-V characteristics, drastically reducing the FF. The appearance of such S-kink was attributed to pile up of charge carriers and potential barrier at the electrodes. The highest  $\eta$  obtained for Cell 2 is 30.16%. Hence, it may be concluded that 2D MoS<sub>2</sub> can be successfully used independently as an absorbing layer for SC application.

### PS2.03

**(Student) Solution Processed SnSe<sub>2</sub>-RGO Composite Hybrid Bulk Heterojunction for Self-Powered Visible IR Broadband Photodetection** Kishan L. Kumawat, Deependra K. Singh, Karuna K. Nanda and Saluru B. Krupanidhi; Indian Institute of Science Bangalore, India

Two-dimensional materials such as, SnSe<sub>2</sub>, MoS<sub>2</sub> and RGO have attracted immense attention for various opto-electronic applications. This is because, their band gap is tunable and enables them to absorb a wide range of electromagnetic radiation. Of particular interest is SnSe<sub>2</sub>, its band gap has recently been demonstrated to be tunable, has high absorption coefficient, and an appreciable charge carrier concentration. However, it suffers from low mobility of ~ 1-10 cm<sup>2</sup>/Vs and this limit its response time to optical signal. In the recent study, a heterostructure based on SnSe<sub>2</sub>/PEDOT:PSS was fabricated for self-driven photodetection, and a low responsivity of (1.4 – 2.6) × 10<sup>6</sup> A/W was shown [1], and was mainly attributed to low mobility at the interface of the hetero-structure. In order to improve on the responsivity, here we fabricate a hybrid hetero structure based on SnSe<sub>2</sub> and a high mobility RGO (> 1000 cm<sup>2</sup>/Vs). The device was fabricated by drop-casting solvothermally synthesized SnSe<sub>2</sub>-RGO composite on pulsed laser deposited MoS<sub>2</sub> (thickness ~ 50 nm on Si substrate). A built-in electric potential at the SnSe<sub>2</sub>-RGO/MoS<sub>2</sub> interface drives the device to operate in self power mode. Under IR illumination, the SnSe<sub>2</sub>-RGO/MoS<sub>2</sub> heterostructure shows excellent photoresponse with a responsivity of 12.5 A/W and detectivity 5.22 × 10<sup>12</sup> Jones with no external bias. We estimate the ideality factor of 0.64. The response and recovery rates at zero bias were estimated as 0.10 s. The device also shows excellent photoresponse under visible light illumination. These results suggest a new possible alternative to fabricate fast and highly responsive self-driven photodetectors. [1] Mukhokosi, E. P.; Krupanidhi, S. B.; Nanda, K. K. An Extrinsic Approach Toward Achieving Fast Response and Self-Powered Photodetector. *Phys. Status Solidi* 2018, 215 (21), 1800470.

### PS2.04

**(Student) Atomic Fe-Ni Bimetallic Sites Boosting Electrocatalytic Oxygen Evolution Reaction** Fenghongkang Pan<sup>1</sup>, Tian Jin<sup>2</sup> and Jun Hu<sup>1</sup>; <sup>1</sup>East China University of Science and Technology, China; <sup>2</sup>Xi'an Jiaotong University, China

The sluggish kinetics of electrochemical oxygen evolution reaction (OER) severely restricts the efficiency of energy conversion in power devices. Inspired by recent research focus of single atomic/traditional highly efficient bimetallic catalysts, an in-situ atomic bimetallic coupling approach is developed to create a highly efficient OER catalyst. The atomic bimetallic Fe and Ni are anchored on N, P co-doped carbon matrix through FeNi<sub>6</sub> coordination, the resultant Fe/Ni-N/P-C catalyst exhibits a low overpotential (255 mV @10 mA cm<sup>-2</sup>) and high turnover frequency (0.88 s<sup>-1</sup> @ 350 mV). Meanwhile, the rechargeable

Zn-air battery assembled by Fe/Ni-N/P-C demonstrates high power-density and outstanding durability. DFT calculations reveal that the unique dual-atomic FeNi<sub>6</sub> coordination offers dual active sites to stabilize the OOH\* intermediate, thus synergistically decreases the formation energy barrier of the rate-determining-step for the OER. This work opens up a window for designing and fabrication of highly efficient OER catalysts through the atomic bimetallic approach.

### PS2.05

**(Student) Extensive Study of Ga-Coverage in UID Regrown GaN by MBE** Habib Ahmad, Keisuke Motoki, Evan Clinton, Zachary Engel, Christopher M. Matthews and W. Alan Doolittle; Georgia Institute of Technology, United States

Traditional RF-MBE GaN growth is carried out under Ga-rich conditions to achieve smooth surface morphology and highly crystalline films. It has been found that excess Ga within the droplets regime form large metal droplets which would inhibit growth of the GaN underneath the droplet limiting crystal quality. The effect of Ga-dose (Ga surface coverage) during the metal modulated epitaxy (MME) on the morphological, electronic, structural, and optical properties of the MBE grown films are studied by reflection high energy electron diffraction (RHEED), atomic force microscopy (AFM), hall effect measurements (HEM), X-ray diffraction (XRD), and photoluminescence (PL). The unintentionally doped (UID) GaN were grown on HVPE semi-insulating GaN templates on sapphire. Prior to growth, the substrates were solvent and chemically cleaned. The substrates were outgassed *in situ* for thermal cleaning. Three cycles of Ga flashing were used for reduced oxygen concentration at the growth interface. RHEED showed a marked improvement in the surface of the substrate after three cycles of Ga flashing. From RHEED transient analysis, the time required for the first monolayer coverage was measured to be 0.4 sec and is designated as 1 monolayer open time (MLOT). Similarly, 2 through 64 MLOT doses correspond to MME shutter cycle open time of 0.8 to 25.6 sec samples were grown in order to observe the effect of Ga-dose on the material properties. (a) prior to monolayer coverage, b) in the range of monolayer-to-bilayer coverage, c) at bilayer coverage, d) at the interface of bilayer-to-droplets coverage, e) at droplets regime coverage, and f) deep into the droplets regime coverage. The substrate temperature was kept at 650 °C. RHEED intensity transients for the 1, 2, 2.5, and 3 MLOT samples showed less than bilayer excess Ga coverage during the shutter open cycle leading to a large surface diffusion barrier and resulted in a spotty RHEED pattern which is a characteristic of rough surface morphology. AFM of the 1 MLOT sample exhibited uniformly distributed small hexagonal pits. For the 2, 2.5 and 3 MLOT samples, decreasing densities of both small and large hexagonal pits are observed with increasing Ga coverage due to the island coalescence effect. The streaky RHEED transient of the 4 MLOT sample depicted excess Ga bilayer coverage but its AFM exhibited large flat regions with smooth surface morphology and small regions with pits merging to form larger pits, reminiscent of the intermediate regime in traditional MBE. The streaky RHEED transients of the 8 and 16 MLOT samples showed growth into the droplets regime while the 32 and 64 MLOT samples showed growth deep into the droplets regime. AFM of the droplets regime samples exhibit spiral hillocks-mediated step-flow surface morphology and sub-nanometer root-mean-square (RMS) roughness. The highest hall mobility is observed in the low droplets regime while the 4 MLOT sample showed the worst electrical properties. Symmetric (002) rocking curves and asymmetric (102) rocking curves XRD measurements show optimum crystalline quality in the low droplets regime while the samples in the bilayer-to-droplets transition regime exhibit the worst crystalline quality. Because of the dominance of the thick substrate in the XRD peak heights, full widths were measured at 1/10,000, 1/1000 and 1/100 peak intensity to characterize the MBE grown UID GaN layer. Thus, in cases where the film mimics the substrate quality, these metrics converge toward that of the substrate. The PL measurements confirm the XRD results, showing wide line width for the 4 MLOT sample indicating poor quality GaN. Narrow optical linewidth is observed for the samples grown in the droplets regime. In conclusion, the low droplets regime for excess Ga is observed to be the best Ga-coverage growth condition for UID GaN MME growth while both extreme Ga droplets and Ga deficiencies result in poor quality films.

### PS2.06

**Optimization Control of ZnTe Epilayers Using the Nano-Faceted and Tilted Sapphire Substrate** Masakazu Kobayashi<sup>1,2</sup>; <sup>1</sup>Waseda Univ., Japan; <sup>2</sup>Kagami Memorial Research Institute for Materials Science and Technology, Waseda University, Japan

The Electro-Optic (EO) coefficient of ZnTe is one of the highest among the conventional semiconductor materials with cubic structures. (110) oriented single domain ZnTe layers on heterovalent materials which does not exhibit EO properties is an attractive structure for practical device applications. The transparent substrates are also preferable for the optical alignment tuning when the device structures are emphasized. Sapphire was focused on for the substrate, and (110) oriented ZnTe layer growth was considered for the EO device structure. MBE growth of ZnTe layers have been performed on various surface orientations of sapphire substrates. It was revealed that the high temperature annealing (at 1000 to 1500 °C for ten to forty hours) of the sapphire substrate surface was resulted in the atomically smooth surface. In

addition to the thermal treatment of the substrate surface, the insertion of low temperature grown thin buffer layers was effective in achieving high crystal quality layers of ZnTe. The single domain ZnTe epilayers with the x-ray rocking curve linewidth of about 400 arcsec were achieved on c-plane (0001) sapphire substrates. It was also confirmed that (100) oriented layers were formed on the r-plane substrate while (111) oriented layers were formed on S-plane substrates. Different from c-, r-, S- and a-plane sapphire substrates, the nano-facet formation was observed for the m-plane sapphire substrate after the high temperature annealing. The m-plane was disappeared, and the annealed substrate surface was covered with the periodic nano-facet structure consisting from 5 to 40nm size of alternately appearing facets of r-planes and S-planes. The size of the structure was varied by the annealing condition, and height was about 5 to 10 nm when it was annealed at 1100 °C. The height was increased to 30 nm when the annealing temperature was increased to 1300 °C. Since the (111) layer could be formed on the S-plane substrate, the (110) oriented ZnTe layer from the substrate surface could be formed by using the 20 degree tilted m-plane sapphire with nano-facet structures. In order to obtain highly oriented layers, it is crucial to nucleate ZnTe layers only on the nano-facet of S-plane. It was revealed from previous experiments that the nucleation of ZnTe occurred at around 400 °C on the S-plane sapphire. On the other hand, ZnTe would be sublimated from the r-plane sapphire once the substrate temperature become higher than 350 °C. In this study, the nucleation of ZnTe was carried out at around 400 °C. The nucleation of ZnTe was carried out using the migration enhanced epitaxy (MEE) mode, and Zn beam and Te beam were alternately supplied. Then conventional MBE mode was used to grow about 1 micron of the ZnTe layer at around 350 °C. The orientation profiles were characterized by means of x-ray diffraction pole figure images. When the thickness of the nucleation layer (MEE mode) was about 3 nm, the pole figure image exhibited a mixture of 111 diffraction peaks and 100 diffraction peaks when viewing from the direction normal to the r-plane surface. The obtained layer included domains nucleated on S-plane along with the domain nucleated on the r-plane. When the nucleation layer thickness was about 60 nm, the profile was improved and the domain nucleated on the S-plane was the dominant; the (110) oriented domain normal to the substrate surface was confirmed. It suggested that the substrate surface was mostly covered by the domain nucleated and developed from the S-plane surface after 60 nm of the MEE layer, and this layer has governed the orientation of the successively formed layer. The preferential nucleation on the nano-faceted and tilted substrate would be an effective approach to control the orientation of the epitaxial layer. This work was supported in part by the Waseda University Grant for Special Research Projects.

#### PS2.07

**(Student) A Study of Defects in  $\beta$ -Ga<sub>2</sub>O<sub>3</sub> Using Admittance Spectroscopy Techniques** Jessica Hendricks<sup>1,2</sup>, Mohamed Ahoujja<sup>3</sup>, Adam T. Neal<sup>1</sup> and Shin Moul<sup>1</sup>; <sup>1</sup>Air Force Research Laboratory, United States; <sup>2</sup>Air Force Institute of Technology, United States; <sup>3</sup>University of Dayton, United States

The Ga<sub>2</sub>O<sub>3</sub> semiconductor is receiving great interest due to its potential applications for high power electronics, enabled by its large critical breakdown field. [1] However, in spite of a promising future of Ga<sub>2</sub>O<sub>3</sub> device technology, its electronic properties, in particular deep level defects, are still being explored. [2,3] Along these lines, we investigated deep level defects in Ga<sub>2</sub>O<sub>3</sub> using thermal admittance spectroscopy (TAS) and optical admittance spectroscopy (OAS). An Arrhenius analysis of the TAS and OAS measurements show the energy levels with cross sections. The quantitative characterization of these defects acts as valuable feedback for the optimization of Ga<sub>2</sub>O<sub>3</sub> material growth and devices. [1] M. Higashiwaki et al. Appl. Phys. Lett. **100**, 013504 (2012) [2] K. Irmscher et al. J. App. Phys. **110**, 063720 (2011) [3] Z. Zhang et al. Appl Phys. Lett. **108**, 052105 (2016)

#### PS2.08

**(Student) Spatial Alignment of High-Crystalline InN Nanowires by Applying Magnetic Field** Ilgyu Choi<sup>1</sup>, Sangmoon Han<sup>1</sup>, Hohyun Yang<sup>1</sup>, Siyun Noh<sup>1</sup>, Jin Soo Kim<sup>1</sup> and Mee-Yi Ryu<sup>2</sup>; <sup>1</sup>Jeonbuk National University, Korea (the Republic of); <sup>2</sup>Kangwon National University, Korea (the Republic of)

Recently, InN nanowires (NWs) have been actively studied in terms of both fundamental physics and potential applications to optoelectronic devices because of a high electron mobility, a high saturation velocity, and possibility of wide-range bandgap engineering. However, it is difficult to form high-crystalline InN NWs using conventional growth mode. Consequently, the performances of optical or electronic devices with InN NWs are still limited. Therefore, it is necessary to improve crystal quality of InN NWs to improve device characteristics. It is typically required to control the spatial direction and position of NWs for the fabrication of some optoelectronic devices such as a chip-level nanoscale laser and a field-effect transistor (FET). As an example, for the fabrication of FETs with a few NWs as channel as carriers, the direction and position of the NWs should be precisely manipulated between source and drain electrodes.

In this paper, we report the significant improvement in the crystallinity of InN NWs by controlling initial nucleation characteristics and the manipulation of spatial alignment by applying magnetic field (*B*-field). The InN NWs were grown on a Si substrate using In pre-deposition technique controlling the initial nucleation behavior. After the growth of InN NWs, the NWs were separated from the substrate by a sonication process using isopropyl-alcohol (IPA)

solution. And then, the IPA solution with InN NWs was dispersed on a Si substrate. After a drying process for the solution, the InN NWs were randomly and horizontally distributed on the Si surface. By applying *B*-field, however, the spatial direction of InN NWs was changed during the drying process of the InN-NW-IPA solution. The *B*-field was obtained from a solenoid system by varying voltage and current. With increasing *B*-field, most of the InN NWs became spatially aligned along with the field direction. The minimum (critical) *B*-field required for the change in the direction of the InN NWs was estimated as 6.10 10<sup>-5</sup> T obtained at a voltage of 15 V and a current of 5 A. At a voltage of 16 V, the alignment behavior of InN NWs become more dominant with increasing current. The alignment characteristics of the InN NW depending on the *B*-field will be theoretically discussed by considering magnetic-dipole properties of NW. Also, the fabrication and characterization of FETs with spatially-aligned InN NWs as channels will be discussed.

#### PS2.09

**Impact of Cap-Layer Materials Used in Long-Term Low-Temperature Annealing on Electrical Properties of Mg-Ion Implanted GaN** Masamichi Akazawa<sup>1</sup>, Shunta Murai<sup>1</sup>, Ryo Kamoshida<sup>1</sup>, Encheng Wu<sup>1</sup> and Tetsu Kachi<sup>2</sup>; <sup>1</sup>Hokkaido University, Japan; <sup>2</sup>Nagoya University, Japan

GaN is a promising material for achieving high-power electronic devices because of its wide band gap, high breakdown voltage, and high saturation electron velocity. In fabrication of a power device, ion implantation is a convenient method for selective doping. For GaN, however, ion implantation for forming p-type doping region is difficult. Although Mg-ion implantation is thought to be the most promising way, it is generally difficult to obtain a high activation ratio. To clarify the mechanism of the difficulty in activation of Mg acceptors, study on the defect levels in Mg-ion implanted GaN is necessary. We report here that the cap-layer material during long-term low-temperature annealing affects the behavior of defect levels in Mg-ion implanted GaN. A Si-doped GaN epitaxial layer with the thickness of 3 μm and doping density of 5×10<sup>17</sup> cm<sup>-3</sup> was grown by MOVPE on a free-standing n<sup>+</sup>-GaN substrate. Mg ions were implanted at room temperature with an energy of 50 keV and a dosage of 1.5×10<sup>11</sup> cm<sup>-2</sup>. Subsequently, low-temperature annealing was carried out at 600 °C for 30 h using a cap layer composed of Al<sub>2</sub>O<sub>3</sub> or SiN. After annealing, the cap layers were removed and a new Al<sub>2</sub>O<sub>3</sub> insulating layer and Ni/Au electrode were deposited to complete a MIS structure. Finally, postmetallization annealing was done at 300 °C. A MIS structure enables to study the near-surface region, which is difficult for Schottky barrier diodes. The electrical properties of the Mg-ion implanted GaN were studied by capacitance–voltage (*C*–*V*) measurement of the fabricated MIS diodes. Since the dosage was low and activation annealing was not done, all MIS diodes showed n-type characteristics. Samples without Mg-ion implantation were also prepared for comparison.

The *C*–*V* curve of the as-implanted MIS diode showed an anomalous shape with a wide plateau indicating the existence of the defect levels in GaN, which was improved by cap annealing at 600°C for both cap layers. Nevertheless, the *C*–*V* curve of the Mg-ion implanted sample annealed using the Al<sub>2</sub>O<sub>3</sub> cap layer showed a small bump in the depletion region. The similar curve was also obtained for the sample annealed using the Al<sub>2</sub>O<sub>3</sub> cap layer without Mg-ion implantation. On the other hand, a large bump with a wide plateau was observed in the *C*–*V* curve of the Mg-ion implanted sample annealed using the SiN cap layer. However, only a small bump was observed for the sample annealed using the SiN cap layer without Mg-ion implantation. These results indicate that the behavior of defect levels was affected by the cap-layer material used in low-temperature annealing. The interface state density distribution derived from the *C*–*V* curve showed that a discrete level existed in the band gap of GaN at *E*<sub>c</sub>–0.8 eV for the Mg-ion implanted sample and *E*<sub>c</sub>–0.5 eV for the sample without implantation. Since the energy for detected discrete level was changed by the Mg-ion implantation, the origin of the measured discrete level at *E*<sub>c</sub>–0.8 eV was the defects generated in GaN by Mg-ion implantation. According to the theoretical calculation results [1], the origin of this discrete level can be assigned to the nitrogen interstitial (N<sub>i</sub>) defects. There is possibility that the SiN cap layer blocked the diffusion of N<sub>i</sub> generated by Mg-ion implantation, while the Al<sub>2</sub>O<sub>3</sub> cap layer did not.

This research is supported by MEXT “Program for research and development of next-generation semiconductor to realize an energy-saving society.” The authors appreciate Dr. T. Narita of Toyota Central R&D Labs., Inc. for providing the GaN epitaxial wafers. [1] J. L. Lyons, C. G. Van de Walle, *NPJ Computational Materials* 12, 1 (2017).

#### PS2.10

**(Student) Enhanced Thermoelectric Behavior in Fully Dense Hot Pressed Pellet of Nanostructured Calcium Cobalt Oxide** Nidhi Puri, Ram P. Tandon and Ajit Mahapatro; University of Delhi, India

Thermoelectric (TE) power generation is one of the most motivating environmental friendly course of action for utilizing the waste heat energy using the concept of Seebeck effect. The key TE parameters to gauge the performance of any material are figure-of-merit mathematically defined by  $ZT = S^2/\rho\kappa$  and power factor ( $PF = S^2/\rho$ ), where  $\rho$  is the electrical resistivity,  $S$  is the Seebeck coefficient, and  $\kappa$  is the thermal conductivity of the test material. The essential requirements of a potential TE material include high  $S$  for generation of large voltage from waste heat energy sources, low  $\rho$  to minimize Joule heating, and a low  $\kappa$  to retain heat at the junctions of a TE device. The

oxide materials are adopted by various research groups as active TE materials due to their inherent natural abundance, non-toxicity, thermal and chemical stabilities, and have demonstrated utilization in TE devices operating at high temperatures. Among all the oxide materials, calcium cobalt oxide ( $\text{Ca}_3\text{Co}_4\text{O}_9$ ) possesses a misfit layered structure with high S and low  $\kappa$ , and widely used as promising TE material.

In this work, polycrystalline  $\text{Ca}_3\text{Co}_4\text{O}_9$  powder is synthesized by mixing the precursors, cobalt oxide ( $\text{Co}_3\text{O}_4$ , 3.46 g) and calcium carbonate ( $\text{CaCO}_3$ , 3.33 g) using solid state method of ball-milling (BM). The resulting as-milled slurry is dried on a hot plate at 340 K and further calcined at 1120 K in ambient condition. Further, micro sized particles of  $\text{Ca}_3\text{Co}_4\text{O}_9$  are broken down into nano-scale dimensions by ball-milling the as-synthesized  $\text{Ca}_3\text{Co}_4\text{O}_9$  powder for various time durations of 2, 6, 12, and 24 h. The FESEM images captured for ball-milled micro-powders show homogenous nanostructure formation post BM for 24 h. The as-prepared micro (dimension 400-800 nm) and nano-sized (dimension sub 10 nm)  $\text{Ca}_3\text{Co}_4\text{O}_9$  powders are consolidated by following hot press technique, where the graphite die containing respective sample is placed in vacuum chamber and heated to 1170 K for 25 min with simultaneous application of 200 MPa pressure to achieve highly pure and fully dense pellets with a relative density of  $99.2\pm 0.4\%$ , and are further characterized through spectroscopic, microscopic, thermal, and crystallographic measurements. In X-ray diffraction (XRD) patterns, the most prominent (002) crystallographic plane recorded at  $2\theta=16.5^\circ$  along with other crystallographic planes are observed and agrees with inherent patterns assigned in JCPDS #00-023-0110 for  $\text{Ca}_3\text{Co}_4\text{O}_9$  crystal structure. Also, XRD patterns from both the hot pressed pellets record peaks for (00l) crystallographic planes of  $\text{Ca}_3\text{Co}_4\text{O}_9$ . The estimated Lotgering factor,  $LF=1$  assists the observation of perfectly aligned (00l) XRD planes and reveals achievement of texturing in the pellets that could be attributed to recrystallization during hot pressing due to simultaneous application of high pressure and temperature.

An increment of  $\sim 11\times$  in TE power factor at high temperature of 770 K for bulk nanostructured  $\text{Ca}_3\text{Co}_4\text{O}_9$  pellets prepared using  $\text{Ca}_3\text{Co}_4\text{O}_9$  nanopowders of sub 10 nm dimension that measures  $PF=64.2$  mW/mK compared to 5.8 mW/mK for ceramics of as-synthesized  $\text{Ca}_3\text{Co}_4\text{O}_9$  microstructures. This significant enhancement in PF is attributed to the improvement of S originating from the structural modulation and defects in addition to introduction of increased number of grain boundaries triggered during densification process of hot pressing. The currently prepared bulk nanostructured  $\text{Ca}_3\text{Co}_4\text{O}_9$  could be utilized commercially for mass scale production and this concept of achieving improved PF values due to bulk nanostructuring could be further implemented in enhancing the TE behavior of various other materials.

## PS2.11

**(Student) High Quality Growth of Magnesium Aluminum Ferrite by Molecular Beam Epitaxy** [Alexandra M. Boyadzhiev](#), Michael Newburger, Alexander J. Bishop and Roland Kawakami; The Ohio State University, United States

Magnesium aluminum ferrite (MAFO) has shown potential as an effective low damping material, which results in reduced energy loss in magnetic switching. To date, this material has been grown via pulsed laser deposition. In this work, MAFO has been grown using molecular beam epitaxy (MBE). Flux matched ebeam  $\text{MgO}$ ,  $\text{Al}_2\text{O}_3$ ,  $\text{Fe}_2\text{O}_3$  were grown on both  $\text{MgO}(100)$  and  $\text{MAO}(100)$ . Reflection high-energy electron diffraction was used to observe the diffraction patterns of the material during the growth process. Atomic force microscopy measurements were taken to check surface roughness and uniformity.

## PS2.12

**(Student) Highly Transparent and Flexible Patterned Ion-Gel Based Triboelectric Nanogenerator for Tactile Sensing Application** [Youngkyun Kim](#), Dawoon Lee and Jaekyun Kim; Hanyang University, Korea (the Republic of)

Many studies have been focused on improving the power generation by developing new materials and microstructures for wearable displays and sensor. Remarkable improvement has been made so far to address the issues to replace the traditional battery-based operation of wearable systems. Among them, Triboelectric nanogenerator (TEG) is one of the most popular type of energy harvesting. The triboelectric phenomenon is a contact induced electrification in which a material becomes electrically charged after it is contacted with a different material through friction. It is well studied that triboelectric nanogenerator can be used to convert the mechanical energy into self-powered functional system via triboelectric effect. One can expect that the well-designed TEG and peripheral energy systems will enable to achieve the self-powered flexible electronics, Internet of Things (IoT), health care applications, multifunctional sensor systems and wearable displays.

Here, we introduce the dual cation-containing gel friction layer for high-performance transparent TENG devices and their possible application for high-sensitivity tactile sensor. Instead of using the relatively bulky a 1-ethyl-3-methylimidazolium bis(trifluoromethylsulfonyl)imide ([EMIM]<sup>+</sup>[TFSI]<sup>-</sup>) cation-anion pairs ionic liquid (IL) alone, tetraglyme (or G4) plasticizer and Li salts were added to improve the ionic transport within the bicontinuous polymer matrix while keep the optical transparency. With regard to the improvement and optimization of ionic migration-related triboelectric effect, we incorporated two types of cation movement in the polymer matrix in which EMIM<sup>+</sup> and

Li<sup>+</sup> cations could fulfill each other's shortcomings for the perspective of ionic conductivity. For the systematic investigation of effect on the performance of TENG, transparent dual cation-containing ion-gel was placed on the ITO/PET substrate. The transmittance of ion-gel friction layer was measured and compared according to the content of ionic liquid. The triboelectric performance of TENG as a function of ionic liquid content was investigated from 0% to 40%. Among these, the output voltage of TENG device with an ionic liquid of 20 wt% reached the best values of about 150 V, 40  $\mu\text{A}$  at 20 kPa pressure, which corresponds to 1400 % and 2500 % improvement at the same pressure, respectively, compared to the output of TENG device without IL. It was found that synergistic combination and optimization of Li<sup>+</sup> and EMIM<sup>+</sup> cationic complexes in the transparent polymer matrix plays a harmonized role in boosting the stable output power of TENG up to about 0.3mW/cm<sup>2</sup> in which smaller ionic radius of Li<sup>+</sup> and lower binding energy of EMIM<sup>+</sup> cations become polarized by the surface friction. We also manufactured 20 wt% dual cation-containing ion-gel based TENGs can effectively illuminate 50 green light emitting diodes (LEDs) whose illumination intensity varied depending on the content of the ionic liquid. Using this high-performance dual cation-containing TENG devices, we fabricated the transparent and flexible tactile sensor in which the external pressure of micropatterned friction layer converts into the electrical output voltage and current with the excellent sensitivity and mechanical flexibility. So, we believe that our proposed dual cation-containing ion gel TENG can be a promising energy solution for the wearable electronic functional system and also represents an ideal platform for deformable and pressure-sensitive E-skin.

## PS2.13

**(Student) Large-Area, Free-Standing and Transparent MoS<sub>2</sub>/Ion-Gel Hybrid Films for High-Sensitivity Low-Power Photodetection** [Seohyun Maeng](#)<sup>1</sup>, Dawoon Lee<sup>1</sup>, Dongyun Lee<sup>1</sup>, Seonkyeong Kang<sup>2</sup>, Hyunseok Lee<sup>2</sup> and Jaekyun Kim<sup>1</sup>; <sup>1</sup>Hanyang University, Korea (the Republic of); <sup>2</sup>Chungbuk National University, Korea (the Republic of)

Two dimensional transition metal dichalcogenides (TMDs) has inspired extensive studies in the field of electronic and optoelectronic devices due to their atomically thin layered structure and van der Waals interaction between layers. Among various TMDs, Molybdenum disulfide ( $\text{MoS}_2$ ) has been popular due to the ease of synthesis and the possibility to compensate the weakness of gapless graphene. Also, it is well known that  $\text{MoS}_2$  possesses the tunable bandgap of 1.3 ~ 1.9 eV, depending on the number of stacked layer. For the aspect of tunable bandgap and relevant wide range of controlled absorbance,  $\text{MoS}_2$  materials represents the promising candidate for visible light detection devices. Despite successful demonstration of high-sensitivity  $\text{MoS}_2$ -based photodetector, the performance of the devices continuously needs to be improved for the perspective of low power consumption and ease of fabrication, particularly for the era of ubiquitous electronics. The photodetector devices or phototransistor with low operation voltage commonly employs the thin oxide-based gate insulator for high capacitance. However, the oxide based gate dielectric often requires the expensive vacuum-based equipment and high temperature process, which hinders the flexibility of devices. To lower the operation voltage of phototransistor, high-capacitance electrochemical ion-gel dielectric layer is proposed in which the electrical double layer (EDL) under an applied electric field offers the high area capacitance value of as high as about 10  $\mu\text{F}/\text{cm}^2$ . Solution-processable ion-gel electrolytes are also suitable for facile fabrication and easily applied to large area and polymeric substrate due to the low temperature process. Moreover, its transparency in the visible range is favorable for next-generation wearable photodetector application. Although the hybrid structure of high-capacitance ion-gel and CVD-grown  $\text{MoS}_2$  can enable the large area photodetector with lower operation voltage, it suffers from the absence of large-area process and relatively lower photodetection performance. In order to address the issues regarding the large-area and transparent ion-gel-interfaced  $\text{MoS}_2$  heterostructure as well as high sensitivity photodetection, we propose the adhesive ion-gel stamping method in which the large-area  $\text{MoS}_2$  are released from the growth substrate by the adhesion force of ion-gel. For the ultrathin platform of device fabrication, the PMMA layer was spin-coated on a rigid glass and cured by UV exposure and hotplate annealing. The high-performance  $\text{InSnZnO}$  (ITZO) thin films were deposited on PMMA/glass by RF sputtering at room temperature. After the deposition of the source/drain and side gate electrodes on ITZO film, the ITZO devices is separated from the rigid glass via DI water rinsing process. This ultrathin ITZO devices were aligned and attached to the  $\text{MoS}_2$ /ion-gel heterostructure for the transparent and free-standing photodetectors. ITZO phototransistor with low operation voltage were fully fabricated by attaching the  $\text{MoS}_2$ /ion-gel freestanding film. The Raman spectrum of  $\text{MoS}_2$ /ion-gel freestanding film shows two characteristic wavelength peaks and the offset between the two peaks is 21.1  $\text{cm}^{-1}$ , which indicated the formation of a monolayer  $\text{MoS}_2$ . Also, the ion-gel dielectric exhibited high capacitance with 36  $\mu\text{F}/\text{cm}^2$ , enabling the operation of IZTO transistors with less than 3V gate voltage. The transfer characteristic of the ITZO TFTs with  $\text{MoS}_2$ /ion-gel freestanding film exhibits on/off ratio of  $\sim 10^4$  and the electron mobility of  $\sim 1.1$   $\text{cm}^2/\text{Vs}$ . Therefore, our results suggests that our ion gel stamping method can be used to fabricate the transparent  $\text{MoS}_2$ /ion-gel hybrid films for the flexible oxide semiconductor-based photodetector devices.

## PS2.14

**(Student) Light Sensitive Resistive Memory Behaviour in ZnO/rGO Heterostructure Device** Manjri Singh<sup>1,2</sup> and Surinder P. Singh<sup>1,2</sup>; <sup>1</sup>CSIR-National Physical Laboratory, India; <sup>2</sup>Academy of Scientific and Innovative Research (AcSIR), India

The market driven demand from electronic, optoelectronic, IT, energy, healthcare and environmental sectors are mounting a sustained pressure on researchers for miniaturized and smart futuristic technologies. The materials exhibiting memristive/ resistive switching behaviour have promised to bring out innovative memory devices with high data storage and packing density. Recently, optical resistive memory devices have attracted the attention of researchers because of their promises towards multilevel data storage and applications optoelectronic switches, photonic memory elements, optical fiber telecommunications, neuromorphic computing and artificial intelligence. The choice of appropriate materials exhibiting photo resistive memory effect becomes the foremost priority to be investigated. Graphene, a two-dimensional (2D) material, has got special attention in optoelectronic applications due to its fast carrier dynamics, high packing density and ultra-broadband absorption capabilities ranging from UV to terahertz wavelength. Though the material has already proved its candidature for efficient device designing, but still lacks considerable attention in the field of resistive memory and photodetector due to its band-less and defect-less electronic structure. Graphene oxide (GO), a disordered analogue of graphene, has an eternal broad range bandgap engineering capabilities and vertical conducting pathways that support efficient photogenerated carrier separation and transport which in-turn is beneficial for designing high-performance photodetector and resistive memory devices. In the present work, we have grown zinc oxide (ZnO) nanorods onto indium tin oxide (ITO) coated glass substrate. Further, reduced graphene oxide (rGO) film was deposited over it by spin coating to fabricate rGO/ZnO heterostructure device. The I-V characteristics of rGO/ZnO heterostructure were studied under dark and 376 nm light illumination. Benefiting from the energy band offsets, the device exhibited a light sensitive memristive behavior under voltage sweep cycles of  $0 \rightarrow +V_{\max} \rightarrow 0 \rightarrow -V_{\max} \rightarrow 0$ . The device showed a pinched loop hysteresis with low resistive state (LRS)  $\rightarrow$  high resistive state (HRS)  $\rightarrow$  HRS  $\rightarrow$  LRS transition. The device demonstrated  $\sim 5$  times higher light current compared to dark current in HRS while an overlapping LRS, indicating a multi-level switching which may be utilized for designing short term and long term memory.

## PS2.15

**Van der Waals Epitaxy of Two-Dimensional Noble Metal Diselenides on III Nitride Semiconductors** Edward Stockert, Phoebe Perez, Chien Cheng Kuo, Li Wei Tu, Der-Jun Jang, Quark Y. Chen, Hsuing Chou and Paritosh Wadekar; National Sun Yat Sen University, Taiwan

Two dimensional (2D) noble metal based diselenides such platinum diselenides (PtSe<sub>2</sub>) exhibit a thickness dependent quantum phase transition from an indirect band gap semiconductor ( $\sim 0.3$  eV to 1.4 eV) to a type II Dirac semimetal. High stability against oxidation combined with a high carrier mobility make it an attractive material for integrating onto traditional three dimensional (3D) compound semiconductors such as gallium nitride (GaN), aluminum nitride (AlN), and boron nitride (BN). Such 2D/3D heterostructures can lead to possible applications such as wide band gap sensors, as well as topological field effect transistors (TFET's). Thus, it is imperative to understand the growth mechanism, structural, electrical, optical properties of such heterostructures. In this report, we have used atmospheric pressure chemical vapor deposition (APCVD) method to grow uniform ultrathin PtSe<sub>2</sub> films on the aforementioned substrates. The effect of the deposition parameters, and underlying substrates on the physical properties are investigated using a suite of analytical tools such Raman, x-ray photoelectron spectroscopy (XPS), cathodoluminescence, low energy electron diffraction (LEED), x-ray reflectivity (XRR). These 2D semiconductors are further patterned into Hall bars and characterized for their electrical properties. Our experiments reveal that PtSe<sub>2</sub> can be successfully integrated onto the 3D semiconductors.

## PS2.16

**(Student) Electrical Properties of High Barrier-Height Au/NiZn Solid Solution Schottky Contact on Semipolar [20-21] n-GaN for Electronic Devices** Jung Suk Cha and Tae-Yeon Seong; Korea University, Korea (the Republic of)

III-nitride semiconductor materials are of great importance because of their wide applications in high-efficiency optoelectronic and electronic devices, such as light-emitting diodes (LEDs), metal-semiconductor-metal (MSM) photodetector and metal-semiconductor field effect transistors (MESFETs). However, InGaN/GaN LEDs grown on c-plane (polar) substrates experience a serious decrease in the internal quantum efficiency (IQE) due to the quantum-confined Stark effect. Thus, to resolve such problem, semipolar substrate, such as [20-21] planes, was used for LEDs, whose optical performance was largely improved as compared to polar LEDs. However, semipolar GaN-based optical and electronic devices have not been extensively investigated. This is in part due to the fact that the formation of high-quality Schottky or Ohmic contacts to semipolar GaN have not been extensively investigated. In this study, we investigated the electrical properties of high barrier-height Au/NiZn solid solution Schottky contact on semipolar [20-21] n-GaN for electronic devices.

The SBHs and ideality factors were obtained using current-voltage-temperature (I-V-T), capacitance-voltage (C-V), and barrier inhomogeneity model as a function of annealing temperature. The SBHs and ideality factors estimated using the I-V characteristics were estimated to be in the range of 0.5–0.7 eV and 1.5–2.4 respectively, depending on the annealing temperature. The XPS Ga 2p core levels obtained from the interface regions of the Au/NiZn solid solution/GaN samples shifted toward the lower energies, depending on the annealing temperature. The XPS Ni 2p core level results showed the formation of interfacial NiO and Ni<sub>2</sub>O<sub>3</sub> phases at 650 °C. On the basis of the XPS results, the dependence of the SBH characteristics on the annealing temperature is described and discussed.

## PS2.17

**(Student) Thermal Management of  $\beta$ -Ga<sub>2</sub>O<sub>3</sub> Current Aperture Vertical Electron Transistors** Samuel Kim and Samuel Graham; Georgia Institute of Technology, United States

Beta-gallium oxide ( $\beta$ -Ga<sub>2</sub>O<sub>3</sub>) is a promising semiconductor material for its unique combination of material properties and relevance to many present and future application areas. Ultra-wide bandgap (UWBG) semiconductors (4.5 eV – 4.9 eV) for deep-UV optoelectronics, very high breakdown electric field (8 MV/cm) for high voltage and high power electronics, and outstanding Baliga's figure of merit (BFOM) with superior thermal and chemical stability. Two main shortcomings of  $\beta$ -Ga<sub>2</sub>O<sub>3</sub> are often pointed out, however, in discussions about the material's power device potential. First,  $\beta$ -Ga<sub>2</sub>O<sub>3</sub> has very poor thermal conductivity compare to other wide band gap material, and therefore, poor heat dissipation ability. The experimental thermal conductivity values of  $\beta$ -Ga<sub>2</sub>O<sub>3</sub> fall in the range of  $\approx 10 - 27$  W/m-K at room temperature, which is one or two orders of magnitude lower than those of other UWBG semiconductors. Thermal conductivity of  $\beta$ -Ga<sub>2</sub>O<sub>3</sub> depends on the orientation of material, thickness, and growth method. Therefore, we need to find routes for circumventing the low thermal conductivity of  $\beta$ -Ga<sub>2</sub>O<sub>3</sub>. Second, the critical issue of contacts between metal and Ga<sub>2</sub>O<sub>3</sub> limits the performance of  $\beta$ -Ga<sub>2</sub>O<sub>3</sub> devices. It is important to achieve low-resistance contacts, which contribute to reducing heat generation that could diminish the self-heating effect. Even though, most of the developments of Ga<sub>2</sub>O<sub>3</sub> transistors have been focused on lateral structure, for power switching applications, vertical structure is desirable that can have high current with high breakdown voltage. Therefore, there will be much more heat generation for vertical devices compare to lateral devices. For all these concerns, we investigate thermal conductivity of  $\beta$ -Ga<sub>2</sub>O<sub>3</sub> and thermal boundary conductance between metal and  $\beta$ -Ga<sub>2</sub>O<sub>3</sub> utilizing time domain thermoreflectance (TDTR). In addition, we investigate cooling options for  $\beta$ -Ga<sub>2</sub>O<sub>3</sub> via simulation using COMSOL. We explored top-side cooling, bottom-side cooling, and double-sided cooling that can remove heat from the devices.

## PS2.18

**(Student) Thermodynamic Phase Diagram Calculations for the Chemical Vapor Deposition of Hexagonal Boron Nitride Using Triethylboron, Ammonia and Hydrogen** Philip M. Jean-Remy, Bryan Webler and Robert Davis; Carnegie Mellon University, United States

Hexagonal boron nitride (*h*-BN) is chemically stable, highly thermally conductive and possesses a wide bandgap of  $\sim 6$  eV. Thin films of *h*-BN are candidate materials for optoelectronic applications operative in the deep ultra-violet under harsh conditions. Several boron-containing precursors has been used for the chemical vapor deposition (CVD) synthesis of these films. Specifically, the use of triethylboron (B(C<sub>2</sub>H<sub>5</sub>)<sub>3</sub>) has increased in recent years. However, the presence of C in B(C<sub>2</sub>H<sub>5</sub>)<sub>3</sub> and the reaction between B and C to form B<sub>4</sub>C promote the incorporation of these species in the resulting films under conditions of low total chamber pressure and insufficient partial pressure of NH<sub>3</sub>. As such, a series of CVD phase diagrams that indicate the stability of the phases of BN as well as the occurrence of C and B<sub>4</sub>C as a function of temperature and input precursor concentrations under set chamber pressures and diluent gas concentrations have been calculated and analyzed for the B(C<sub>2</sub>H<sub>5</sub>)<sub>3</sub>/NH<sub>3</sub>/H<sub>2</sub> system. This reaction system was chosen because NH<sub>3</sub> is the commonly used N-source precursor, and H<sub>2</sub> is often used as both the carrier gas for B(C<sub>2</sub>H<sub>5</sub>)<sub>3</sub> and the diluent gas in group III-nitride MOCVD. It was determined that at a (B(C<sub>2</sub>H<sub>5</sub>)<sub>3</sub>/(B(C<sub>2</sub>H<sub>5</sub>)<sub>3</sub> + NH<sub>3</sub>)) composition ratio of 0.001, increasing the H<sub>2</sub> concentration suppresses the stability of C throughout a 400 – 1600 °C range, but it also suppresses the stability of *h*-BN. Further, it was determined that increasing the total system pressure suppresses the occurrence of C while expanding the stability of *h*-BN. These and many additional results of this research will be presented at the conference. These findings will be beneficial for investigators using B(C<sub>2</sub>H<sub>5</sub>)<sub>3</sub> and NH<sub>3</sub> to synthesize *h*-BN via OMVPE. P.M.J. would like to acknowledge the National GEM Consortium for supporting this work.

## PS2.19

**(Student) Room Temperature Growth and Investigation of Electrical Properties of Amorphous Boron Nitride** Corey L. Arnold<sup>1</sup>, Maddox Dockins<sup>1</sup>, Christopher Muratore<sup>2,3</sup>, Nicholas Glavin<sup>3</sup>, Nigel Shepherd<sup>1</sup> and Andrey Voevodin<sup>1</sup>; <sup>1</sup>University of North Texas, United States; <sup>2</sup>University of Dayton, United States; <sup>3</sup>Wright-Patterson Air Force Base, United States

Traditional material and processing techniques for nanoelectronics are approaching a ceiling, requiring a paradigm shift. 2D materials have emerged as leading candidates for next-generation nanoelectronics. Research and development have created numerous conducting and semiconducting 2D materials for futuristic transistors, capacitors, batteries, and memory devices; however, 2D dielectric materials have not received the same attention. Advancement in nanoelectronics based on 2D materials will only occur when matching reliable, high dielectric strength, transparent, and chemically inert 2D dielectric materials are established. Several insulating materials (such as BN, HfO<sub>2</sub>, Al<sub>2</sub>O<sub>3</sub>, etc) are believed to be suitable candidates for transistor gate dielectrics, an environmental passivation layer, and other device elements. However, the obstacle of obtaining required insulating properties at low temperatures constrains the progress of integrating these materials with nanodevices, particularly those on soft or flexible substrates. In this study, we demonstrate the use of pulsed magnetron RF sputtering to grow amorphous boron nitride (a-BN) at room temperature as a possible solution. Film thickness in the range of 10 – 20 nm was determined using a Veeco Dektak 150 stylus profilometer and atomic force microscopy (AFM), and their chemical composition determined using X-ray photoelectron spectroscopy (XPS). Electrical properties such as dielectric constant, leakage current, and breakdown strength were determined using M-I-M structures consisting of W/a-BN/Ti. Exploration of oxide charges at the a-BN interface was achieved using M-I-S structures and frequency-dependent capacitance-voltage (C-V) and conductance-voltage (G-V) measurements to evaluate the potential of a-BN. An understanding of the defect chemistry and their influence on the properties of a-BN is discussed.

## PS2.20

**(Student) Resistive Memory with Perovskite Nickelates** Qi Wang and Shriram Ramanathan; Purdue University, United States

A two-terminal Samarium Nickelate (SmNiO<sub>3</sub>) thin film based memristor device was fabricated by co-sputtering, photo lithography and e-beam lithography. The device had an asymmetrical structure, with patterned palladium (Pd) and gold (Au) electrodes at two terminals, respectively. Optical microscopy as well as scanning electron microscopy (SEM) were used to confirm the structural properties of the device. The resistivity of SmNiO<sub>3</sub> thin film near Pd electrodes, increased up to 10<sup>6</sup> times after it was annealed in a 5% hydrogen (H<sub>2</sub>) / 95% Argon (Ar) gas, due to an electron doping induced metal-insulator transition (MIT). Before and after the device was hydrogenated, measurements of the current-voltage (I-V) characteristics were investigated. After hydrogenation, the I-V curves of the device became non-linear with clear hysteresis loops. Different carrier transport mechanisms based on the IV characteristics were analyzed. Resistance states could be switched by sub-100 ns voltage pulses. It was proposed that the protons in between the two electrodes could redistribute under external electric fields to display high and low resistance states.

## PS2.21

**Superparamagnetic Properties of Metal-Free Nitrogen Doped Graphene Quantum Dots Synthesized by Pulsed Laser Ablation** Muhammad Shehzad Sultan<sup>1</sup>, Vladimir I. Makarov<sup>1</sup>, Wojciech M. Jadwisieniczak<sup>2</sup>, Brad R. Weiner<sup>1</sup> and Gerardo Morell<sup>1</sup>; <sup>1</sup>University of Puerto Rico - Río Piedras, United States; <sup>2</sup>Ohio University, United States

In this study, we developed a novel approach to synthesize high-quality metal-free Nitrogen-doped graphene quantum dots (N-GQDs) with high quantum yield, via irradiation of s-triazene in a solution with benzene by using pulsed laser. The TEM, HRTEM, XPS, XRD, Raman spectroscopy and FTIR were carried out to observe the morphology, size distribution, crystalline structure and to prove successful doping of GQDs with nitrogen atoms. Furthermore, for the first time, to our knowledge, their magnetic properties were investigated. The results indicate that N-GQDs exhibit superparamagnetic behavior. The specific size, shape and zigzag edge structure of N-GQDs were considered to explain the origin of the observed magnetism. The magnetization dependence led to estimating the N-GQD material magnetic permeability for different ambient temperatures. From the zero-field-cooled (ZFC) and field-cooled (FC) magnetization measurements, carried out at 50 Oe magnetic field strength, we estimated the blocking temperature  $T_b$  to be around 300 K. Based on the experimental data analysis, the magnetic permeability, number of correlated spins per single N-GQD, and number density of superparamagnetic N-GQD per gram of material were estimated. The excellent superparamagnetic properties together with optical properties manifested by N-GQDs have the potential to lead to high performance biomedical applications.

## PS2.22

**(Student) Al and Hf Based Metalcones—Inducing Porosity in Nano-Laminate Thin Films** Vamseedhara Vemuri and Nicholas C. Strandwitz; Lehigh University, United States

Molecular layer deposition (MLD) and atomic layer deposition (ALD) are sequential, self limiting thin film deposition techniques, used to fabricate organic, inorganic, and inorganic-organic hybrid thin films. We report the growth of mixed MLD:ALD thin films based on Hf and Al inorganic components (nano-laminates) using trimethylaluminum, tetrakis (dimethyl-amido) hafnium, ethylene glycol as precursors for MLD and water (H<sub>2</sub>O) is used as an oxygen source for ALD reactions. Nano-laminates with different ratios of MLD:ALD (1:0, 1:1, 1:2, 0:1) were examined in effort to tailor film density and porosity. The as-deposited nano-laminate films were subjected to annealing or combined annealing+UV exposure from 150-350 C to induce porosity via removal of the organic component. Positron annihilation lifetime spectroscopy showed that the % porosity in pure MLD films decreases as the annealing temperature increases. In-situ x-ray reflectivity measurements (XRR) indicate that thickness reduction in nano laminate films is relatively low compared to pure MLD films. Incorporation of the organic components and the formation of M-O-C bonding is confirmed using fourier transform infrared spectroscopy (FTIR). By subjecting these nano-laminates to annealing and UV exposure, the decrease in intensity of hydrocarbon bonds compared to pure MLD films can be observed. The capacitance-voltage (C-V) measurements show the relative permittivity values of the as-deposited and processed nanolaminates to be lower compared to the pure oxide films. Hence, the above observations from XRR, FTIR and C-V measurements suggest that the nano-laminate films prevent the structural collapse compared to pure MLD films.

## PS2.23

**Laser-Writing of Electronic Circuitry in Thin-Film Molybdenum Disulfide** Drake Austin<sup>1,2</sup>, Kimberly Gliebe<sup>3</sup>, Paige Look<sup>1,2,4</sup>, David Moore<sup>1,2</sup>, Bryce Boyer<sup>3</sup>, Timothy Fisher<sup>3</sup>, Christopher Muratore<sup>4</sup> and Nicholas Glavin<sup>2</sup>; <sup>1</sup>UES, Inc., United States; <sup>2</sup>Air Force Research Laboratory, United States; <sup>3</sup>Case Western Reserve University, United States; <sup>4</sup>University of Dayton, United States; <sup>5</sup>University of California, Los Angeles, United States

Electronic circuits, the backbone of modern electronic devices, require the precise and tedious integration of conductive, insulative, and semiconductive materials in 2D and 3D space to control the flow of electric current. Strategies to pattern these materials in unique ways outside of a cleanroom environment, such as additive manufacturing, have enabled rapid prototyping and removed many of the design constraints in traditional fabrication. In this work, we implement a manufacturing approach using laser processing in ambient air to directly realize conductive, insulative, and semiconductive phases within a starting amorphous molybdenum disulfide thin film. This is achieved by varying the incident laser intensity and by rastering the a-MoS<sub>2</sub> sample at different speeds, allowing for localized control over the sample's heating in terms of both temperature and duration. The overall result is the ability to locally control the oxidation/crystallization of the sample, allowing for the transformation of select regions of the a-MoS<sub>2</sub> film into MoO<sub>3</sub>, MoO<sub>3</sub>, and 2H-MoS<sub>2</sub>, which respectively exhibit conductive, insulative, and semiconductive properties. The conversion into each of these phases is confirmed through Raman spectroscopy, x-ray photoelectron spectroscopy, and UV-vis spectroscopy, and the electrical properties are characterized using a four-point probe method. An explanation for this conversion is also proposed by using a thermal model together with a description of the reaction kinetics. Finally, by creating these phases in specific patterns, it is shown that electrical devices can be laser-written directly into the a-MoS<sub>2</sub> film. This is demonstrated with a laser-written gas sensor that makes use of the MoO<sub>3</sub>, MoO<sub>3</sub>, and 2H-MoS<sub>2</sub> phases for electrical connections, electrical isolation, and a sensing region, respectively. By exposing the sensor to varying concentrations of NH<sub>3</sub>, the resistance of the sensor is observed to change accordingly due to the modulation of the 2H-MoS<sub>2</sub> conductivity.

## PS2.24

**Low Powered Smart Window Device Based on a Stoichiometrically Downgraded Multi-Layer Structure from VO<sub>2</sub> Thin Films Grown Using Pulsed Laser Deposition** Makhesh K. Behera, Leslie C. Williams, Sangram K. Pradhan and Messaoud Bahoura; Norfolk State University, United States

The need for low powered energy saving devices has increased over the years owing to the impending energy crisis that would be caused by depletion of the conventional energy sources in the near future. While several efforts are being made towards development of alternate energy sources as well as efficient energy storage devices, it still has a long way to go. In the meanwhile, using low powered energy saving devices help us provide the extra time needed for the development and implementation of these new energy sources and storage devices. Low powered smart window device is a part of this class of energy saving devices. Smart windows are essentially IR modulating windows which can modulate the IR rays transmitted through them depending on the temperature they are exposed to, therefore by extension modulating the temperature in the room. VO<sub>2</sub> thin films have been an ideal candidate to be used as a smart window coating. With a metal to insulator transition temperature of 68 °C – closest to RT among all other transition metal oxides, many research

efforts have been focused on using VO<sub>2</sub> as a smart window coating. But, progress in this field has been restricted by the still high transition temperature for practical device applications and the poor metal to insulator transition (MIT) parameters for doped VO<sub>2</sub> thin films. In this work, we present a novel multi-layered structure of VO<sub>2</sub> thin films, stoichiometrically downgraded to serve as a smart window device that can control the % transmission in the IR region. The fabricated multi-layered structure successfully demonstrated the blocking and transmission of the IR rays upon application of voltage less than 15 V reducing the IR transmission by as much as 50%, demonstrating its use as a low powered device. A reduction to the MIT temperature was also seen where the transition temperature was reduced to 48 °C, more than 20 °C less than the theoretical bulk value. An improvement was also seen in the transmission of visible wavelength by over 10% at temperatures above the transition temperature. Moreover, resistive joule heating effect was also investigated during the testing of devices for smart window application

**Acknowledgement**

This work has been supported by NSF-CREST Grant number HRD 1036494 and NSF-CREST Grant number HRD 1547771



# 62<sup>ND</sup> ELECTRONIC MATERIALS CONFERENCE

June 24-26, 2020

## THURSDAY ORAL PRESENTATIONS

11:45 AM N01

**(Student) Au-Free Recessed Ohmic Contacts to AlGaIn/GaN HEMT—Study of Etch Chemistry, Metal Schemes and Carrier Transport Mechanism** Niranjan S<sup>1</sup>, Ivor Guiney<sup>2</sup>, C J Humphreys<sup>3</sup>, Prosenjit Sen<sup>1</sup>, Muralidharan R<sup>1</sup> and Digbijoy Nath<sup>1</sup>; <sup>1</sup>Indian Institute of Science, Bangalore, India; <sup>2</sup>Paragraf, United Kingdom; <sup>3</sup>University of London, United Kingdom

AlGaIn/GaN HEMTs on silicon have been attractive due to economy of scale, better performance at a system level, and very importantly, due to the fact that the existing CMOS foundries can be used for fabricating GaN devices (if the processing technology is also made CMOS compatible) which could significantly bring down the cost of GaN technology. Conventional GaN HEMT's use e-beam evaporated gold-based metal stacks for Source/Drain Ohmic contact fabrication as the Au-based metallization leads to very low values of contact resistance. CMOS compatible fabrication of AlGaIn/GaN HEMT's needs Au-free device processing, since Au acts as a deep-level trap for minority carriers and also has high diffusion rates in Silicon even at moderate temperatures. Among the many Au-free Ohmic metal schemes reported for AlGaIn/GaN hetero-structures, Ti/Al/Ti/W is one of the widely reported metal scheme, since Tungsten is routinely used in CMOS back-end of line processing. However, contact resistance values of  $< 1 \Omega\text{-mm}$  have been rarely reported for AlGaIn/GaN hetero-structures with this metal scheme. Selective recess etching of the AlGaIn barrier below the Ohmic contact areas before metallization is one of the most widely reported methods for obtaining lower values of contact resistance with Au-free CMOS compatible Ohmic metallization schemes. This process of recess etching is especially important when the AlGaIn barrier thickness in the AlGaIn/GaN epi-stack is high. Moreover, sputtering as the metal deposition technique is another important change desired in CMOS compatible processing in contrast to conventional GaN HEMT processing, due to reliability issues caused by X-rays generated during e-beam evaporation. In this work, an effort is made to systematically arrive at contact resistance values of  $< 1 \Omega\text{-mm}$  for AlGaIn/GaN heterostructures on Silicon using sputtered Ti/Al/Ti/W CMOS compatible Ohmic metal stack. Apart from the low Ohmic contact resistance, uniformity of the contact resistance value and surface morphology of the contact pads are the other important characteristics desired in any Ohmic metallization scheme. Trials with  $\text{BCl}_3/\text{O}_2$  recess etch chemistry (widely used for Gate recess etching in e-mode GaN HEMT devices) and  $\text{BCl}_3/\text{Cl}_2$  recess etch chemistry (widely used for GaN etching) were carried out. We obtained good uniformity in electrical characteristics across the AlGaIn/GaN sample with  $\text{BCl}_3/\text{O}_2$  etch chemistry in comparison to  $\text{BCl}_3/\text{Cl}_2$  etch chemistry. Trials with different recess etch depths for AlGaIn before metallization yielded the optimum value of contact resistance for complete recess etch of the AlGaIn barrier. The importance of using the Ti/W cap layer on the Ti/Al contact layers was observed in terms of lower contact surface roughness and lower contact resistance values seen for Ti/Al/Ti/W metal stack in comparison to Ti/Al metal stack. Finally, temperature dependent measurements were carried out on the Ti/Al/Ti/W metal stack for determination of the carrier transport mechanism through the contacts and it was seen that Field emission is the dominant carrier transport mechanism responsible for the Ohmic nature of the contacts described in this work. The obtained contact resistance of  $0.56 \Omega\text{-mm}$  is one of the lowest values of contact resistance reported for this metal stack in literature.

12:00 PM N02

**(Student) Ir and Native Deep Level Defects in Fe, Mg, and Si-Doped Edge-Fed Grown  $\text{Ga}_2\text{O}_3$**  Daram N. Ramdin<sup>1</sup>, Micah Haseman<sup>1</sup>, Hantian Gao<sup>1</sup>, Buguo Wang<sup>2</sup>, David Look<sup>2</sup> and Leonard J. Brillson<sup>1,3</sup>; <sup>1</sup>The Ohio State University, United States; <sup>2</sup>Semiconductor Research Center, Wright State University, United States

$\beta\text{-Ga}_2\text{O}_3$  has attracted considerable interest for next generation high power devices and ultraviolet optoelectronics. Its  $\sim 4.8$  eV wide band gap,  $\sim 8$  MV/cm high breakdown field gradient, ease of n-type doping, and the ability to grow large area, free standing substrates have stimulated rapidly expanding research efforts on both a fundamental and device physics level, including new designs for field effect transistors, Schottky diodes and solar-blind detectors. Integral to these efforts is the control of defects and dopants in  $\text{Ga}_2\text{O}_3$ , both of which will impact the breakdown voltage as well as the charge transport across the device. The energy levels associated with defects and dopants inside  $\beta\text{-Ga}_2\text{O}_3$  are of particular interest for edge-fed-growth (EFG)  $\beta\text{-Ga}_2\text{O}_3$  due to its capacity for high volume manufacturing. Interest in EFG  $\beta\text{-Ga}_2\text{O}_3$  has now extended beyond commercial interests to academic research efforts with particular focus on the unique features of this specific growth technique.

We used depth-resolved cathodoluminescence spectroscopy (DRCLS) to measure the optical emission properties of university-developed EFG  $\beta\text{-Ga}_2\text{O}_3$  both undoped as well as doped with Fe, Mg, and Si. In addition to cathodoluminescence features reported previous [1], we observed pronounced new emissions associated with impurity emission deep within the  $\beta\text{-Ga}_2\text{O}_3$  band

gap. In all four of these EFG  $\beta\text{-Ga}_2\text{O}_3$  crystals, we observed emissions corresponding to an energy level  $\sim 3.2$  eV above the valence band and complementary emissions from the conduction into this level  $\sim 1.6$  eV below, consistent with the 4.8 eV band gap, whose emission we also observe directly. A previous comparison between  $\beta\text{-Ga}_2\text{O}_3$  DRCLS optical transitions and predicted native point defect levels correlated a 3.52 eV oxygen vacancy  $V_{\text{O}}$  energy level with a 3.5 eV transition observed both with DRCLS and surface photovoltage spectroscopy (SPS) [1]. The significant difference between the  $E_{\text{V}} + 3.5$  eV  $V_{\text{O}}$  transition and the 3.2 eV emissions reported here, these energy levels may suggest  $V_{\text{O}}$  - dopant complexes. However, such complexes are not calculated to appear near this energy [3]. Instead, the Ir impurity is calculated to have a Ir<sup>3+</sup> charge state transition under both Ga-rich and O-rich conditions at  $E_{\text{V}} + \sim 3$  eV [3] as indicated in fig. 3. The similarity of dominant deep level emissions for both doped and undoped  $\beta\text{-Ga}_2\text{O}_3$  crystals suggests a defect, defect complex, or impurity common to all four, and the Ir impurity commonly detected in EFG  $\beta\text{-Ga}_2\text{O}_3$  grown from Ir crucibles suggests the presence of this impurity in relative high concentration. Such an impurity-related energy level with a high optical cross section for recombination would pose a significant challenge for both microelectronic and optoelectronic applications. Further studies to determine the comparative Ir densities in crystals grown by different techniques are now underway. DNR, MSH, and LJB acknowledge AFOSR Grant No. FA9550-18-1-0066 (Ali Sayir) 1. H. Gao et al., Appl. Phys. Lett. **112**, 242102 (2018). 2. J.B. Varley et al., Appl. Phys. Lett. **108**, 039901 (2016). 3. H. Peelaers, J.L. Lyons, J.B. Varley, and C.G. Van de Walle, APL Mater. **7**, 022519 (2019).

12:15 PM N03

**Chromium Origins of Red Luminescence from Iron-Doped  $\text{Ga}_2\text{O}_3$  Bulk Crystals and Its Applications** Rujun Sun<sup>1</sup>, Yu Kee Ooi<sup>1</sup>, Dickens T. Dickens<sup>2</sup>, Kelvin Lynn<sup>2</sup> and Michael Scarpulla<sup>1,3</sup>; <sup>1</sup>The University of Utah, United States; <sup>2</sup>Washington State University, United States

Fe doping in the  $\sim 10^{18}$   $\text{cm}^{-3}$  range is the most widely-available method for producing semi-insulating single crystalline  $\text{Ga}_2\text{O}_3$  substrates. Red luminescence features have been reported from multiple types of  $\text{Ga}_2\text{O}_3$  samples and in some cases attributed to Fe or native defects. Herein, however, we demonstrate that the high-intensity red luminescence from Fe-doped  $\text{Ga}_2\text{O}_3$  commercial substrates consisting of two sharp peaks at 689 nm and 697 nm superimposed on a broader peak centered at 710 nm originates from Cr impurities present at concentrations near 2 ppm probably sensitized by the Fe with concentration near 12 ppm. The optical absorption properties of (100)- and (010)-oriented substrates are characterized by transmission. Photoluminescence excitation experiments demonstrate that the red emission intensity is maximized for excitation resonant with the polarization-dependent optical absorption edge while only extremely-weak emission is found for the commonly-reported  $\text{Ga}_2\text{O}_3$  300-600 nm luminescence structure. A consistent picture emerges from these observations combined with Tanabe-Sugano analysis that resonant energy transfer from the  $\text{Ga}_2\text{O}_3$  matrix to octahedrally-coordinated Cr, possibly also sensitized by Fe. This quenches luminescence from the  $\text{Ga}_2\text{O}_3$ -related states while amplifying the luminescence from the Cr. Lastly, we speculate that the source of the unintentional Cr concentration may be Ir components used in bulk crystal growth, which also has implications for unintentional Fe and Si doping in all crystals grown in the same apparatuses. In the other hand, the ratios of blue and green emissions to UV emission of MOCVD film annealed under  $\text{O}_2$  for different temperatures increased exponentially and red peak emerged at elevated temperature. Different films with high resistivity agree well with the feature of increased ratios of blue and green over UV.  $V_{\text{Ga}}$  is proposed as the reason for semi-insulating film at elevated temperature and contributed to blue and green peaks, which is supported by Cr diffusion from substrated evidenced by the emerging red peak.

12:30 PM N04

**(Student) Optical Properties of Acceptor Impurities in  $\text{Ga}_2\text{O}_3$**  Intuon Chatratin<sup>1</sup>, Fernando Sabio<sup>1</sup>, Pakpoom Reunchan<sup>2</sup> and Anderson Janotti<sup>1</sup>; <sup>1</sup>University of Delaware, United States; <sup>2</sup>Kasetsart University, Thailand

$\text{Ga}_2\text{O}_3$  has attracted great attention as a promising material for high power electronic applications due to a very large band gap, high breakdown voltage and ability to be doped n-type. The  $\text{Ga}_2\text{O}_3$  Baliga's figure of merit is only lower than that of diamond. Most importantly, large single crystals of  $\text{Ga}_2\text{O}_3$  are available, facilitating epitaxial growth. Although p-type  $\text{Ga}_2\text{O}_3$  have not been demonstrated as acceptor impurities tend to introduce deep acceptor levels, they can be used to make semi-insulating layers, and that can be useful in device designing. The deep levels of acceptor impurities in ultra-wide-band gap oxides are difficult to often difficult to probe experimentally. To facilitate the experimental characterization of the acceptor impurities, we employed hybrid density-functional calculations to investigate the optical transitions of acceptor impurities in monoclinic  $\text{Ga}_2\text{O}_3$ . We constructed configuration coordinate diagrams to determine the absorption and emission energies that can be compared with the optical absorption and photoluminescence measurements. The results show that all impurities exhibit deep acceptor transitions. The calculated emission energies are compared with the available experiment data. Work supported by the National science Foundation grant No. DMR- 1652994.

## 12:45 PM N05

**Optical Properties of  $\alpha$ -Ga<sub>2</sub>O<sub>3</sub> and Comparison with  $\beta$ -Ga<sub>2</sub>O<sub>3</sub>** Leila Ghadbeigi<sup>1</sup>, Jacqueline Cooke<sup>1</sup>, Giang Dang<sup>2</sup>, Toshiyuki Kawaharamura<sup>2</sup>, Tatsuya Yasuoka<sup>2</sup>, Sriram Krishnamoorthy<sup>1</sup>, Michael Scarpulla<sup>1</sup> and Berardi Sensale Rodriguez<sup>1</sup>; <sup>1</sup>University of Utah, United States; <sup>2</sup>kochi-tech, Japan

$\beta$ -Ga<sub>2</sub>O<sub>3</sub> is a promising candidate for use in high power electronics. Superior characteristics such as large band gap, high electric field breakdown, and large Baliga's figure of merit surpass the application of this material in power rectifiers, field-effect transistors, and solar-blind photodetectors. Ga<sub>2</sub>O<sub>3</sub> is known to have five different crystal structures including monoclinic  $\beta$ , corundum  $\alpha$ , spinel  $\gamma$  and two orthorhombic  $\epsilon$  and  $\delta$  phases. Among different phases,  $\beta$ -Ga<sub>2</sub>O<sub>3</sub> is the most stable phase while  $\alpha$ -Ga<sub>2</sub>O<sub>3</sub> has the same crystal structure as the common  $\alpha$ -Al<sub>2</sub>O<sub>3</sub> (sapphire) however,  $\alpha$ -Ga<sub>2</sub>O<sub>3</sub> is not thermodynamically stable. The synthesis of  $\alpha$ -Ga<sub>2</sub>O<sub>3</sub> is achieved under nonequilibrium conditions such as low temperature heat treatment. Epitaxial films have been synthesized by Molecular beam epitaxy, RF magnetron sputtering, mist chemical vapor deposition and halide vapor phase epitaxy. The optical properties of  $\beta$ -Ga<sub>2</sub>O<sub>3</sub> has been extensively studied. It is known that the monoclinic  $\beta$ -Ga<sub>2</sub>O<sub>3</sub> possess anisotropic characteristics. The bandgap changes according to the incident light polarization where  $E_g$  is 4.57(E||a),  $E_g$  is 4.54(E||c) and  $E_g$  is 4.72(E||b). Also, the photoluminescence of  $\beta$ -Ga<sub>2</sub>O<sub>3</sub> has been the subject of many studies. These studies showed that due to the difference in the absorption edge, photoluminescence excitation changes in different orientations. The photoluminescence excitation is polarization-dependent and it maximizes at the bandgap in each direction. However, the photoluminescence emission is also polarization dependent. This, in particular, is observed from the polarization-dependent of the UV peak. It was shown that holes self-trapped on O| sites are more involved in the creation of the UV peak when the light is polarized in the b direction (E||b). As the electric field is directed to the c direction, both O| and O|| sites are contributing to the creation of UV peak. This phenomenon results in the UV peak shifting up to 160meV. In this study, the optical properties of  $\alpha$ -Ga<sub>2</sub>O<sub>3</sub> grown on a sapphire substrate were investigated. The sample was made using mist chemical vapor deposition.  $\alpha$ -Ga<sub>2</sub>O<sub>3</sub> was formed on c plane double-polished sapphire in the (001) direction. The thickness of the film is 455 nm. Polarization-dependent characteristics were studied through absorbance, photoluminescence, and by varying the excitation wavelength in PL (photoluminescence excitation). Resulting properties were compared with the characteristics of  $\beta$ -Ga<sub>2</sub>O<sub>3</sub> previously reported by us.

Preliminary results show that  $\alpha$ -Ga<sub>2</sub>O<sub>3</sub> has a bandgap of around 5.2 eV, which does not change with polarization. Photoluminescence of  $\alpha$ -Ga<sub>2</sub>O<sub>3</sub> shows similar spectral features than that of  $\beta$ -Ga<sub>2</sub>O<sub>3</sub>. This luminescence can be deconvoluted into four emission bands as UV, UV', Blue, and Green. In  $\beta$ -Ga<sub>2</sub>O<sub>3</sub>, the peak position of the UV emission is polarization-dependent and varies from 360-390 nm, while in  $\alpha$ -Ga<sub>2</sub>O<sub>3</sub>, it is found to be polarization-invariant at the position of 360 nm. On the other hand, the width of the UV band is narrower in  $\alpha$ -Ga<sub>2</sub>O<sub>3</sub> compared to  $\beta$ -Ga<sub>2</sub>O<sub>3</sub>. Based on recent studies, the UV PL in  $\beta$ -Ga<sub>2</sub>O<sub>3</sub> is found to be related to two self-trapped hole levels, which are located 70-160 meV apart and that jointly contribute to the overall UV PL emission. It is thought, however, that in  $\alpha$ -Ga<sub>2</sub>O<sub>3</sub>, holes are self-trapped in only one oxygen site that is tetragonally coordinated. Observing a narrower UV peak in  $\alpha$ -Ga<sub>2</sub>O<sub>3</sub>, which is independent of polarization direction, is consistent with only one self-trapped hole level existing in  $\alpha$ -Ga<sub>2</sub>O<sub>3</sub>. Accordingly,  $\alpha$ -Ga<sub>2</sub>O<sub>3</sub> presents isotropic optical properties in the (001) plane. Photoluminescence excitation was conducted for  $\alpha$ -Ga<sub>2</sub>O<sub>3</sub> and  $\beta$ -Ga<sub>2</sub>O<sub>3</sub> when the incident light was polarized along the major axis. The shape of the PLE provides supporting information enabling to compare these two polymorphs in terms of degree of Stokes shift, electron-phonon coupling, and also position of self-trapped hole levels.

## 1:00 PM BREAK

## 2:00 PM N06

**(Student) Bias-Dependent Exciton Stark Shift and Franz-Keldysh Effect in  $\beta$ -Ga<sub>2</sub>O<sub>3</sub> Sub-Bandgap Photoresponse** Md Mohsinur Rahman Adnan, Darpan Verma, Xia Zhanbo, Nidhin Kurian Kalarickal, Siddharth Rajan and Roberto C. Myers; The Ohio State University, United States

Beta Gallium Oxide ( $\beta$ -Ga<sub>2</sub>O<sub>3</sub>) recently emerged as a central material of interest for high power electronic devices due to its large breakdown field (8MV/cm) and also for designing solar blind UV detectors and gas sensors due to its large bandgap (4.9eV). Here we describe measurements of the Franz-Keldysh (F-K) effect from the sub-band gap photocurrent response in reverse-biased  $\beta$ -Ga<sub>2</sub>O<sub>3</sub> Schottky diodes. Unlike the F-K response observed in other wide band gap semiconductors (SiC and GaN) [1-3], photocurrent spectra of  $\beta$ -Ga<sub>2</sub>O<sub>3</sub> Schottky diodes contain a characteristic peak structure that is qualitatively distinct from the ordinary F-K effect [4]. With an increasing applied field, the  $\beta$ -Ga<sub>2</sub>O<sub>3</sub> spectra show a smooth red shift of this peak structure rather than the typical F-K absorption tail broadening. This peculiar F-K spectral lineshape and field-induced redshift can be understood by considering the strong impact of excitons (electron-hole coupling) on the F-K effect, which dominate the photocurrent spectra in  $\beta$ -Ga<sub>2</sub>O<sub>3</sub> under large reverse bias. Previous ab-initio calculations [4,5] and experimental measurements [6,7] provide a range of exciton binding energy estimates in  $\beta$ -Ga<sub>2</sub>O<sub>3</sub>, all of which are much larger i.e. 0.2 eV (free) – 0.7 eV (self-trapped) than any other wide band gap

semiconductors. The combination of relatively large exciton binding energies [8], light electron effective mass [2, 8], and large electric fields provides a unique situation in which a quadratic Stark shift (electric-field induced exciton binding energy dependence) is observed over a substantial spectral range. Only by including the Stark effect does the F-K model reproduce the peak structure and bias dependent redshifts observed in the measurements. We also consider the exciton formation, recombination, and field-induced dissociation processes and find that the free exciton dissociation dominates the photocurrent response. **Acknowledgment** Funding for this research was provided by the Center for Emergent Materials: an NSF MRSEC under award number DMR-1420451 and by the AFOSR GAME MURI (Grant FA9550-18-1-0479, Program Manager Dr. Ali Sayir). **References** [1] D Verma, M M R Adnan, M W Rahman, S Rajan, R C Myers, arXiv: 2001.03583. [2] T Maeda, T Narita, M Kanekihika, T Uesugi, T Kachi, T Kimoto, M Horita, and J Suda, Appl. Phys. Lett. **112**, 252104 (2018). [3] T Maeda, M Okada, M Ueno, Y Yamamoto, M Horita, and J Suda, Appl. Phys. Express **9**, 91002 (2016). [4] J.B. Varley and A Schleife, Semiconductor Science and Technology, Vol. 30, No. 2, pp. 024010 (2015). [5] A. Mock, R. Korlacki, C. Briley, V. Darakchieva, B. Monemar, Y. Kumagai, K. Goto, M. Higashiwaki, and M. Schubert, Phys. Rev. B **96**, 245205 (2017). [6] S. Yamaoka and M. Nakayama, Phys. Status Solidi C, Vol. 13, No. 2–3, pp. 93–96 (2016). [7] S. Yamaoka, Y. Furukawa and M. Nakayama, Phys. Rev. B **95**, 094304 (2017). [8] F. Bechstedt and J. Furthmuller, Appl. Phys. Lett. **114**, 122101 (2019).

## 2:15 PM N07

**(Student) Process Influence on the Performance and Aging Stability of Ti/Au Ohmic Contacts to Beta-Phase Gallium Oxide** Ming-Hsun Lee and Rebecca L. Peterson; University of Michigan–Ann Arbor, United States

Ga<sub>2</sub>O<sub>3</sub> has attracted significant recent interest for next-generation power electronics owing to its ultra-wide bandgap and the availability of multiple bulk and thin film growth methods. To achieve the full potential of Ga<sub>2</sub>O<sub>3</sub> devices, ohmic contacts with low contact resistance and long-term stability under power device operating conditions are necessary. A typical way to form ohmic contacts is heavily doping the semiconductor to facilitate tunneling across the junction. For the emerging  $\beta$ -Ga<sub>2</sub>O<sub>3</sub> system, this often has been done by Si ion implantation, post-implant anneal, and reactive ion etch (RIE) before Ti/Au metallization.[1] However, the charge transport mechanisms and the stability of Ti/Au – Ga<sub>2</sub>O<sub>3</sub> contacts made with and without ion implant have not received significant attention. Here, we demonstrate the contributions of silicon ion implantation, activation anneals, and the RIE process to contact behavior and stability. In this study, semi-insulating Fe-doped (010) Ga<sub>2</sub>O<sub>3</sub> substrates with a molecular beam epitaxy grown Si-doped conductive epi-layer are used. Some samples are Si-ion implanted followed by activation anneal(s) while others are processed as-received or with RIE treatment only. Circular Transmission Line Model (CTLN) devices are made using Ti/Au metallization followed by 470°C 1-min RTA. Temperature-dependent current-voltage measurements, elevated temperature aging studies, and scanning/transmission electron microscopy (S/TEM) were performed. As expected, the specific contact resistance is significantly reduced by introducing a heavily doped ion-implanted layer, and the contact resistance inversely scales with the post-implant anneal temperature. [2] After aging for > 100 hrs at an elevated temperature, samples with Si-ion implant + RIE show slightly better performance while samples without those processes show an increase in contact resistivity of around 40%. Charge transport mechanisms are analyzed and can be described by thermionic emission (TE) and thermionic-field emission (TFE) models, respectively, for different samples and aging conditions. HAADF STEM images and EDX mappings of different samples show a similar ohmic contact layer structure.[3] [4] However process-dependent features are observed at the interfacial region under HR-TEM. By linking the electrical properties to materials characterization, we will outline possible mechanisms driving the observed changes in contact performance. This work paves the way for future accelerated testing of Ga<sub>2</sub>O<sub>3</sub> test structures and devices under bias and temperature stress. [1] Higashiwaki, M. *et al.* Depletion-mode Ga<sub>2</sub>O<sub>3</sub> metal-oxide-semiconductor field-effect transistors on  $\beta$ -Ga<sub>2</sub>O<sub>3</sub> (010) substrates and temperature dependence of their device characteristics. *Appl. Phys. Lett.* **103**, 123511 (2013). [2] Sasaki, K., Higashiwaki, M., Kuramata, A., Masui, T. & Yamakoshi, S. Si-Ion Implantation Doping in  $\beta$ -Ga<sub>2</sub>O<sub>3</sub> and Its Application to Fabrication of Low-Resistance Ohmic Contacts. *Appl. Phys. Express* **6**, 086502 (2013). [3] Lee, M.-H. & Peterson, R. L. Interfacial reactions of titanium/gold ohmic contacts with Sn-doped  $\beta$ -Ga<sub>2</sub>O<sub>3</sub>. *APL Mater.* **7**, 022524 (2019). [4] Lee, M.-H. & Peterson, R. L. Annealing Induced Interfacial Evolution of Titanium/Gold Metallization on Unintentionally Doped  $\beta$ -Ga<sub>2</sub>O<sub>3</sub>. *ECS J. Solid State Sci. Technol.* **8**, Q3176 (2019).

## 2:30 PM N08

**(Student) Selective Area Regrown Low Resistance Ohmic Contacts on  $\beta$ -Ga<sub>2</sub>O<sub>3</sub> Epitaxial Layers Using Metalorganic Vapor Phase Epitaxy** Arkka Bhattacharyya, Praneeth Ranga, Saurav Roy and Sriram Krishnamoorthy; University of Utah, United States

$\beta$ -Ga<sub>2</sub>O<sub>3</sub> with a wide bandgap of  $E_g \sim 4.6 - 4.9$  eV, has significant potential for high-efficiency power electronics and RF applications mainly due to its high critical breakdown field, good transport properties and availability of high-quality low-cost native single crystal substrates.  $\beta$ -Ga<sub>2</sub>O<sub>3</sub> Schottky diodes, lateral and vertical uniform channel FETs with breakdown voltages exceeding

KVs have already been demonstrated [1].  $\beta$ -Ga<sub>2</sub>O<sub>3</sub> lateral FETs with delta-doped channels exhibiting high drain currents have been demonstrated which not only can achieve high breakdown voltages but also can be promising for RF applications. In order to achieve high drain currents in these delta-doped structures, making good ohmic contacts to the 2DEG channel is critical. The regrown ohmic contacts scheme has been demonstrated using MBE, which avoids the plasma-induced damage in the recess-gate scheme [2]. We have recently demonstrated delta-doping and modulation-doping in the  $\beta$ -Ga<sub>2</sub>O<sub>3</sub> and  $\beta$ -Ga<sub>2</sub>O<sub>3</sub>/ $\beta$ -(AlGa)<sub>2</sub>O<sub>3</sub> heterostructures respectively using metalorganic vapor phase epitaxy (MOVPE) [3,4]. The motivation of this work is to be able to make ohmic contacts to these 2DEG channels using MOVPE. In this contribution, we report the viability of the metalorganic vapor phase epitaxy (MOVPE) technique in demonstrating regrown ohmic contacts to UID/low-doped  $\beta$ -Ga<sub>2</sub>O<sub>3</sub> epilayers. Homoepitaxial  $\beta$ -Ga<sub>2</sub>O<sub>3</sub> thin films were grown on (010)-oriented bulk substrates using a far-injection shower head in a vertical quartz MOVPE reactor (Agnitron Agilis). Triethylgallium (TEGa) and oxygen gas were used as precursors and diluted silane as the dopant gas. In order to avoid material quality degradation due to the regrowth process, we first studied  $\beta$ -Ga<sub>2</sub>O<sub>3</sub> homoepitaxial growth at low temperatures (~700°C and 600°C). Heavily doped  $\beta$ -Ga<sub>2</sub>O<sub>3</sub> thin films were grown on (010)-oriented bulk substrates at 700°C and 600°C to characterize the film quality, growth rate, doping, and mobility. Thin films with superior surface morphology were achieved at low growth temperatures up to 600°C. UID films grown at 600°C exhibited a peak room temperature mobility of 186 cm<sup>2</sup>/Vs for doping density of  $2 \times 10^{16}$  cm<sup>-3</sup> indicative of the high quality films that were attained. The regrowth of n+ Ga<sub>2</sub>O<sub>3</sub> ohmic cap layers was done on a UID ( $2 \times 10^{16}$  cm<sup>-3</sup>) film at 600°C. The selective area regrowth process was achieved using SiO<sub>2</sub> patterned by dry and wet etching. Ti/Au metal stacks were sputter deposited on the n+ layers and annealed to further reduce contact resistance. Circular TLM measurements were used to characterize the regrown ohmic contacts. On the n+ layer, R<sub>c</sub> and  $\rho_s$  were extracted to be 5.3  $\Omega$ .mm and  $9.7 \times 10^{-5}$   $\Omega$ .cm<sup>2</sup> respectively. The total specific contact resistance to the UID film via the regrown n+ layer was extracted to be  $\sim 1.3 \times 10^{-4}$   $\Omega$ .cm<sup>2</sup>. The R<sub>sh</sub> values extracted from Hall measurements before the regrowth process (20.8 k $\Omega$ /sq) and that extracted from the CTLM measurements after the regrowth process (20 k $\Omega$ /sq) matched closely indicating that the material quality of the UID layer was retained after the regrowth process. This initial result of the low-temperature growth and selective area regrowth using MOVPE shows the promise of this approach to realize low resistance contacts for several lateral and vertical device topologies.

SESSION O: Fabrication, Processing and Integration  
 Session Chair: Daniel Ewing  
 Session Hosts: Doug Hall and Sharif Sadaf  
 Thursday Morning, June 25, 2020  
 Location: ZoomRoom 2

#### 11:45 AM O01

**MacEtch Produces Damage-Free High-Aspect-Ratio Semiconductor Nanostructures—Current Status and Future Promise** Xiuling Li; University of Illinois, United States

Metal-assisted chemical etching (MacEtch) defies the isotropic nature of chemical etch by utilizing a patterned metal catalyst for spatially defined etching of semiconductors. MacEtch has been successfully demonstrated for various types of semiconductors, including Si, GaAs, InGaAs, AlGaAs, InP, InGaP, GaN, Ga<sub>2</sub>O<sub>3</sub>, SiC. The metal catalyst type that has been proven to be effective include Au, Pt, Ir, TiN (CMOS compatible), CNTs, and graphene. Aspect ratios produced using MacEtch can readily exceed 100:1 in some cases, while limited in other cases. The resulted tapering and porosity are strong function of the etch kinetics for the particular semiconductor material, metal catalyst type and pattern, and etchant condition. The loading effect is determined by the local carrier generation rate and mass transport rate. Depending on how the etching evolves relative to the catalyst pattern and additional assistance, we classify MacEtch as forward, inverse (i-MacEtch), magnetic-fielded guided (h-MacEtch), self-anchored-catalyst (SAC-MacEtch), vapor-phase (VP-MacEtch) and UV assisted MacEtch. In this presentation, we will report MacEtch of wide and ultra-wide bandgap semiconductors including SiC, GaN, and Ga<sub>2</sub>O<sub>3</sub> and resulted device characteristics, as well as new catalysts enabled MacEtch for beyond CMOS applications. We will discuss the future promise and limitation of MacEtch for applications in photonics, electronics, quantum technologies, and biomedical sciences. Results for SiC, Si, and  $\beta$ -Ga<sub>2</sub>O<sub>3</sub> are shown in Figure 1-3 as examples. The detailed material and structural properties and device characteristics will be discussed. This work was supported in part by a grant from NSF ECCS #18-09946 and ZJUI.

#### 12:00 PM O02

**Fabrication of Vertical Si Micropillar Arrays by Carbon Nanotube-Assisted Chemical Etching** Thomas S. Wilhelm, Ian Kecskes, Mohadeseh A. Baboli, Alireza Abrand, Michael Pierce, Brian Landi, Ivan Puchades and Parsian Mohseni; Rochester Institute of Technology, United States

Metal-assisted chemical etching (MACE or MacEtch) is a simple and cost-effective technique for fabrication of high aspect ratio semiconductor micro-/nano-structures. As an alternative to conventional anisotropic etching methods such as reactive-ion etching (RIE), the MACE approach offers several key advantages, including: (1) operation under room-temperature and atmospheric pressure conditions; (2) mitigation of surface damage and compositional smearing at hetero-interfaces from high-energy ion bombardment; and (3) simultaneous control over both vertical and lateral etch rates. Accordingly, the MACE technique has garnered tremendous research interest, and has been used to fabricate various micro-/nano-scale semiconductor structures for novel device applications in optoelectronics, photonics, nanoelectronics, energy conversion, and energy storage. Although MACE processing has been applied to a broad collection of semiconductor material systems, mostly all common protocols rely on the use of noble metals, predominantly Au, as the catalytic agent. One challenge associated with the use of Au is the potential introduction of deep-level trap defects in Si-based structures. Use of alternative catalysts, such as Ag and Pt, also imposes the challenge of having an optically reflective metallic layer embedded within arrays of nanostructures that may otherwise provide excellent anti-reflective properties. As such, additional wet chemical etching of the catalyst layer is routinely performed after MACE fabrication to mitigate reflection losses; this adds process complexity and may introduce undesirable surface defects.

Here, we demonstrate for the first time that carbon nanotube (CNT) composite membranes can be used as an alternative catalytic medium for MACE-based fabrication of ordered Si micropillar arrays. This so-called carbon nanotube-assisted chemical etching (CNT-ACE) approach overcomes the aforementioned challenges associated with conventional MACE catalysts. Firstly, we show that noble-metal-free CNT films can serve to catalyze oxidant reduction, localized hole-injection, and preferential site-controlled anisotropic etching of Si in room-temperature solutions of H<sub>2</sub>O<sub>2</sub> and HF. Next, we demonstrate that vertical etch rates can be manipulated through KAuBr<sub>4</sub> doping of catalytic CNT membranes. We observe an etch rate enhancement from  $\sim 28$  nm/min to  $\sim 142$  nm/min for KAuBr<sub>4</sub>-doped CNTs compared to undoped films. We attribute the accelerated etch rate to a shift in the aggregate reduction potential of the CNT catalyst film toward that of pure Au. We perform energy-dispersive X-ray spectrometry mapping, Raman scattering spectroscopy, and Auger electron spectroscopy to demonstrate that catalytic CNT films are not degraded, chemically modified, or otherwise damaged as a result of the etching process. We perform UV-Vis-NIR spectrophotometry to quantify the optical absorbance of CNT-ACE-fabricated Si micropillar arrays containing embedded CNT layers, in comparison to Au-MACE-fabricated Si micropillar arrays with embedded Au layers. The CNT-embedded samples show  $\sim 2\%$  solar weighted reflectance, which represents a 33% reduction compared to Au-embedded samples. Lastly, we propose a model for the CNT-ACE mechanism and highlight additional mass transport pathways, in comparison to conventional MACE processes, that enable control over the formation of non-tapered micropillar morphologies. The CNT-ACE method outlined here enables CMOS-compatible fabrication of Si micro-/nano-structures that are particularly useful for photovoltaic and optoelectronic device applications in which non-reflective embedded contacts are desired.

#### 12:15 PM O03

**(Student) Through-Wafer GaAs Vias for Heterogeneous Device Integration** Michael Barrow, Eunseong Moon, Arynn Gallegos, Pilar Herrera-Fierro, David Blaauw and Jamie Phillips; University of Michigan–Ann Arbor, United States

Many applications, such as biological implantables, optoelectronics, photonics, power electronics, high speed communications, and micro-electrical-mechanical systems require diverse material platforms and fabrication processes. Heterogeneous device integration dramatically expands the capabilities of multifunctional microelectronic and photonic systems. Toward this end, through-wafer electrical contacts are vital to enable three dimensional device and system platforms. GaAs and related III-V compounds are established materials for high-quality optoelectronic devices such as infrared LEDs and photovoltaics, though there are few reports of through-wafer vias. We experimentally demonstrate conductive through-wafer GaAs vias, with a specific application to integrate a monolithic microLED and photovoltaic device with a silicon integrated circuit for a highly size constrained biological sensor for neural recording<sup>1</sup>. Via holes are first etched into a semi-insulating GaAs wafer using a chlorine-based transformer coupled high density plasma process optimized to achieve high anisotropy with minimal sidewall roughness. Atomic layer deposition of insulating Al<sub>2</sub>O<sub>3</sub> is used to insulate sidewalls, followed by a subsequent atomic layer deposition of conductive TiN. To meet demands of many heterogeneous microsystems, we used a commercial backgrinding process to thin the wafer to 50  $\mu$ m, including a 20  $\mu$ m layer of parylene to provide mechanical stability and fracture protection. Parylene completely infills the vias, providing a flat surface for contact definition. 500 nm thick Ti/Au contacts are sputtered on the backside of the vias to enable

electrical characterization. We experimentally realize 685  $\Omega$ , 20  $\mu\text{m}$  wide, 50  $\mu\text{m}$  deep GaAs vias. Adjacent vias (50  $\mu\text{m}$  apart) exhibit resistance on the order of  $10^8 \Omega$ , proving that the  $\text{Al}_2\text{O}_3$  layer is highly insulating. To improve conductivity and structural stability, we introduce GaAs vias infilled using pulsed electrochemically deposited copper. Thinned samples with copper-infilled GaAs vias promise high electrical fidelity and a convenient means to contact to components elsewhere on the chip.

[1] J. Lim, E. Moon, M. Barrow, S. R. Nason, P. R. Patel, P. G. Patil, S. Oh, I. Lee, H.S. Kim, D. Sylvestre, D. Blaauw, C. A. Chestek, J. Phillips, and T. Jang, "A 0.19x0.17mm<sup>2</sup> Wireless Neural Recording IC for Motor Prediction with Near-Infrared-Based Power and Data Telemetry", The International Solid-State Circuits Conference, San Francisco (2020).

#### 12:30 PM O04

**Ultrahigh-Resolution Nanolithography Using Silicon-Enriched Thermal Resists and Thermal Scanning Probe Lithography** Tero Kulmala<sup>1</sup>, Samuel Bisig<sup>1</sup>, Jonas Vergés<sup>1</sup>, Emine Cagin<sup>1</sup>, Felix Holzner<sup>1</sup>, Maik Gerngross<sup>2</sup> and Matthias Schirmer<sup>2</sup>; <sup>1</sup>Heidelberg Instruments Nano, Switzerland; <sup>2</sup>Allresist GmbH, Germany

Thermal scanning probe lithography (t-SPL) [1] which relies on the thermal decomposition of polymer resists, such as polyphthalaldehyde (PPA) has recently entered the high-resolution lithography market. T-SPL has enabled both single-digit nanometer patterning and pattern transfer [2] as well as superior alignment accuracy [3] and sub-nanometer accurate 3D patterning [4-5]. The patterning speed is comparable to high-resolution electron beam lithography [6]. As with all lithography processes, patterning high-resolution features with t-SPL requires use of very thin (<10 nm) resist layers, posing challenges to subsequent pattern transfer processes. We have recently demonstrated that silicon-rich, spin-coatable hard masks can be used to transfer the shallow PPA patterns into underlying transfer layers (Figure 1a) thereby amplifying their depth to the desired range for, e.g. lift-off or etching processes. However, due to conical shape of the heatable tips (Figure 1b), the initial PPA thickness remains the main constraint on further improving the resolution of the technique (Figure 1c). Here, we explore the use of PPA functionalized with tetramethylsilane (TMS) side chains (TMS-PPA) as a t-SPL resist. We found that the incorporation of TMS does not significantly affect the patternability of the material but reduces its etch rate by 50 – 60 % as compared to pure PPA. This enables further reduction of the PPA thickness and consequently an enhancement of maximum patterning resolution. We show that ultrahigh-resolution patterns can be written in the thin TMS-PPA films and that these patterns be transferred (Figure 2) using the process described in Figure 1a. [1] R. Garcia et al., *Nature Nanotechnology* **9**, 577-587 (2014). [2] Y. K. R. Cho et al., *ACS Nano* **11** (2017). [3] C. Rawlings et al., *ACS Nano* **9**, 6188 (2015). [4] C. Rawlings et al., *Scientific Reports* **7**, 16502 (2017). [5] T.S. Kulmala et al., *Proc. SPIE* **1058412** (2018). [6] P. Paul et al., *Nanotechnology* **22**, 275306 (2011).

#### 12:45 PM O05

**Photoelectrochemical Lithography—Spatial Control of Galvanic Replacement Reactions on Photoelectrodeposited Cuprous Oxide** Robert Coridan; University of Arkansas—Fayetteville, United States

The synthesis of hierarchically-organized functional interfaces in research-scale systems regularly relies on techniques borrowed from semiconductor fabrication, such as photolithography, electron-beam lithography, reactive ion etching, and metal evaporation. While useful in scientific research, these approaches are generally cost prohibitive for scaling up efficient structural designs and patterning. There is a need for new methods that translate high-precision metallization derived from research prototypes to scalable functional interfaces. Here, we describe our group's recent efforts to pattern  $\text{Cu}_2\text{O}$  films directly by photoelectrodeposition.  $\text{Cu}_2\text{O}$  can act as a photocathode while being electrodeposited, so light can control the local deposition rate. We aim to use this photoelectrochemical lithography of cuprous oxide ( $\text{Cu}_2\text{O}$ ) thin films as a platform for controllable and scalable metallization.  $\text{Cu}_2\text{O}$  can act as a sacrificial intermediate to guide galvanic replacement reactions (GRR) of noble metals such as Au and Ag. This provides a facile, benchtop approach to the fabrication of hierarchically structured, noble metal-based functional interfaces. In this talk, we introduce the process of photoelectrochemical lithography with  $\text{Cu}_2\text{O}$ . We will describe experiments that uncover the chemical mechanism for GRR on  $\text{Cu}_2\text{O}$  and how to exploit it to drive the spontaneous formation of noble metal patterns on electrode surfaces.

#### 1:00 PM BREAK

#### 2:00 PM O06

**Molecular Beam Epitaxy of NaCl Layers on GaAs for Substrate Recycling** Brelon J. May<sup>1</sup>, Jae Jin Kim<sup>1</sup>, Aaron Ptak<sup>1</sup> and David Young<sup>1</sup>; <sup>1</sup>National Renewable Energy Laboratory, United States; <sup>2</sup>Shell International Exploration and Production, United States

Single crystalline III-V materials are at the forefront for many technologies including logic devices, sensors, energy harvesting, and light emitters. Many of these technologies require expensive single crystalline substrates as a starting platform. However, the cost of these substrates inhibits the widespread adoption of some new technologies, specifically cost sensitive devices such as high efficiency photovoltaics. Thus, an efficient method of achieving substrate reuse

is of utmost importance. Several methods have been demonstrated with varying degrees of success via mechanical means or the dissolution of a sacrificial release layer. Many of these techniques require expensive re-polishing steps or hazardous wet etches. The latter is most common but has long release times and relies on the etch-selectivity of Al containing layers in HF, which greatly reduces the ability to design important heterostructures. Here, we report on the investigation of GaAs substrate reuse by means of a water-soluble NaCl layer. NaCl and GaAs are both cubic structures, lattice matched at 100°C, so it is possible that these materials could be integrated without the formation of a high density of extended defects. Molecular beam epitaxy (MBE) is used to deposit NaCl layers on GaAs (001) substrates. Reflection high energy electron diffraction (RHEED) and transmission electron microscopy (TEM) show that the NaCl layer is epitaxial to the underlying GaAs substrate. Subsequent MBE growth of GaAs on NaCl layers is tested over a range of conditions yielding various results. Exclusively low temperature deposition results in amorphous material; heating the sample to higher temperatures prior to GaAs deposition results in desorption of the salt layer. If the overlayer growth is initialized at low temperatures and subsequently heated to typical GaAs growth conditions, a porous and floating polycrystalline structure is obtained. However, by initializing growth at an intermediate temperature, fully dense films on salt are obtained. These films have a range of crystallinity, which is substantially impacted by the presence of the RHEED beam during the initial GaAs deposition. Placement of samples with intermediary NaCl layers in water results in rapid separation of the overlayer from the substrate, causing no obvious surface damage to the parent substrate. These results on the incorporation of heteroionic and heterovalent materials are an important step toward an alternative avenue of rapid, non-hazardous substrate recycling, which could be applied to other rocksalt/III-V systems.

#### 2:15 PM O07

**(Student) High-Temperature Capable ALD-Based Inorganic Lift-Off Process** Sora Lee, Timothy N. Walter, Suzanne Mohney and Thomas N. Jackson; The Pennsylvania State University, United States

Double layer lithography is a well-known patterning process in semiconductor device fabrication. Bilayers of a novolak photoresist and a polymer underlayer of polydimethylglutarimide (PMGI) or poly(methyl methacrylate) (PMMA) are often used. However, polymers must be processed at temperatures below about 300 °C to avoid cross-linking, charring, flow, or other problems. In this work, we developed an inorganic lift-off process using ALD-deposited metal oxide layers and demonstrated successful metal lift-off after annealing the lift-off structure at 500 °C. The inorganic lift-off process uses bilayer stacks of zinc oxide (ZnO) and aluminum oxide ( $\text{Al}_2\text{O}_3$ ) deposited by plasma enhanced atomic layer deposition (PEALD). Trimethylaluminum and carbon dioxide were used as precursors for  $\text{Al}_2\text{O}_3$ , and diethylzinc and nitrous oxide as precursors for ZnO. To create a lift-off profile the layers must be etched selectively and controllably to form a reentrant (that is, bottom layer undercut) profile. For this work we used a pH-controlled selective etch for  $\text{Al}_2\text{O}_3$  [1] and an acidic buffer of acetic acid and sodium acetate for ZnO. Both etches are highly selective with  $\text{Al}_2\text{O}_3/\text{ZnO}$  and  $\text{ZnO}/\text{Al}_2\text{O}_3$  etch ratios >500/1. Depending on the application, either ZnO or  $\text{Al}_2\text{O}_3$  can be used as the bottom layer. For example, ZnO can be easily and selectively etched with respect to many materials, and using ZnO as the bottom layer allows simple residue-free lift-off. In this approach, the  $\text{Al}_2\text{O}_3$  top layer is patterned using conventional photolithography and etching, and the ZnO bottom layer is then etched in the acidic buffer to create the desired reentrant profile. After metal or other deposition, lift-off can be done using dilute mineral acid (for example, HCl) to etch the ZnO layer. Using  $\text{Al}_2\text{O}_3$  as the bottom layer allows a portion of the lift-off stack to be incorporated into the finished device structure. In this approach the ZnO top layer is patterned using conventional photolithography and etching, and the  $\text{Al}_2\text{O}_3$  bottom layer is etched using the pH-controlled etch to form the desired reentrant profile. After metal or other deposition, lift-off can be done by etching the  $\text{Al}_2\text{O}_3$  layer. However, it may be more convenient and more useful to do the lift-off by etching the ZnO (top) layer. The  $\text{Al}_2\text{O}_3$  (bottom) layer will then remain after lift-off between the lift-off patterned regions and can be used, for instance, as a passivation layer.

To demonstrate the high-temperature capability of the inorganic lift-off process we annealed patterned bilayers with reentrant profiles at 500 °C for 30 minutes prior to metal deposition and confirmed that the metal lift-off works with no observed changes compared to the unannealed structures. The high-temperature capability allows elevated temperature processing of material with the lift-off structure in place or high-temperature deposition by techniques such as sputtering or molecular beam epitaxy. Reference: [1] K. G. Sun et al., *ACS Appl. Mater. Interfaces*, 2014, 6, 10, 7028-7031

#### 2:30 PM O08

**High-Quality InP Wet Thermal Oxides Grown Using Dissociation-Suppressing Ultrathin ALD Films** Yuan Tian, Maksym Zhukovskiy, Jideofor A. Odoeze and Doug Hall; University of Notre Dame, United States

InP has long been widely used for both electronic and photonic devices due to its high electron mobility, direct band gap structure, and other favorable properties. Historically, inspired by the great success of the thermal oxide  $\text{SiO}_2$  on Si, many researchers were also very interested in InP oxides. While many tried to form native InP insulators or passivation layers with good chemical stability, dielectric and interface properties for various device

applications [1], none succeeded due to the fundamentally limiting thermal dissociation property of InP material at the high oxidation temperatures required (>500 °C) [2]. Here, we report a promising potential new method for forming useful device quality InP native oxides by using thermal wet oxidation of InP surfaces protected via atomic layer deposition (ALD) of permeable, ultrathin (less than 1 nm) hafnium oxide or aluminum oxide films. The ALD thin film serves as a surface passivation layer which prevents the lighter, more volatile P from evaporating, while also allowing oxidant gases (mixed H<sub>2</sub>O and O<sub>2</sub>) to diffuse into the semiconductor to oxidize the material. The type and the thickness of the ALD layer, the oxidation temperature, the oxidant gas mixture and the oxidation time all have to be properly optimized to achieve InP oxidation without dissociation. Currently, we have demonstrated that both 2 cycles (~1.17 Å/cycle deposition rate) of HfO<sub>2</sub> and 5 cycles (1.01 Å/cycle deposition rate) of Al<sub>2</sub>O<sub>3</sub> from plasma-enhanced ALD (Oxford Instruments FlexAL system) are capable of protecting the surface from dissociation while still allowing sufficient oxidant gases to diffuse through for oxidation to occur. During a 3 hour oxidation in a 2 in. diameter quartz tube furnace at 525 °C (with 0.67 slm N<sub>2</sub> through a 95°C H<sub>2</sub>O bubbler and 5 sccm O<sub>2</sub>), a fairly uniform blueish-green InP oxide film was grown on the protected InP substrates. Scanning electron microscopy (SEM) imaging of the HfO<sub>2</sub> ALD protected oxidation shows dramatically reduced dissociation during the 3 hour oxidation, with growth of a ~104 nm thick InP native oxide. The interface, surface, and oxide homogeneity appear highly uniform. Transmission electron microscopy (TEM) imaging of a different Al<sub>2</sub>O<sub>3</sub> ALD protected sample oxidized 5 hours at 525 °C, also with H<sub>2</sub>O vapor + 5 sccm O<sub>2</sub>, reveals a similarly good quality, uniform, amorphous InP oxide with a low interface roughness on the order of a few atomic monolayers. Chemical analysis using energy-dispersive X-ray spectroscopy used to study the stoichiometry and growth mechanism of the InP oxide will be discussed, along with ongoing experiments to characterize the properties of the InP oxide film. \*Now at Applied Optoelectronics, Inc., Houston, TX [1] J. F. Wager et al., J. Appl. Phys. **51**, 812 (1980). [2] S. Chu et al., J. Electrochem. Soc. **130**, 2398 (1983).

2:45 PM O09

#### Interaction of Ammonium Sulfide with the Semiconductor Surfaces of

**AlSb and Related Alloys** Emma J. Renteria<sup>1</sup>, Connor E. Dix<sup>1</sup>, Subhashree Seth<sup>1</sup>, Ahmad Mansoori<sup>1</sup>, Thomas Rotter<sup>1</sup>, Adam A. Hecht<sup>2</sup>, John Klem<sup>3</sup>, Brianna A. Klein<sup>3</sup>, Anthony Rice<sup>3</sup>, Paul Sharps<sup>3</sup> and Ganesh Balakrishnan<sup>1</sup>; <sup>1</sup>University of New Mexico, United States; <sup>2</sup>The University of New Mexico, United States; <sup>3</sup>Sandia National Laboratories, United States  
Interest in AlSb and related alloys have considerably increased in recent years due to their importance in Type-II superlattice photodiode heterostructures and other optoelectronic devices that operate in the infrared spectrum. More recently, the interest for these materials has expanded to the detection of gamma radiation. AlSb is a promising candidate for high resolution, room temperature gamma detection due to its wide energy bandgap, high carrier mobilities and high atomic number. However, the development of devices based on these materials has been hindered as the surface of these compounds rapidly oxidizes in air due to their high aluminum content and high chemical activity. The conductive oxides, dangling bonds, and surface defects that form on the device sidewalls lead to high levels of reverse leakage current and surface instabilities. To reduce the density of surface states and, consequently, the leakage current of III-V semiconductor devices, sulfur passivation is widely used. In this work, we systematically investigate the impact of ammonium sulfide [(NH<sub>4</sub>)<sub>2</sub>S] based passivation processes on the surface chemical composition and surface morphology of AlSb and related alloys. AlSb devices treated with full-strength (NH<sub>4</sub>)<sub>2</sub>S have shown severe undercut of the detector mesas and spalling of the GaSb top contact layer severely affecting the overall device performance. Therefore, we will conduct a controlled study of the etching phenomena of antimonides with (NH<sub>4</sub>)<sub>2</sub>S at different concentrations and passivation times to find the optimal conditions that can diminish the etching and deleterious effect of full-strength ammonium sulfide on AlSb devices. The surface composition and chemical properties of the material in question will be investigated by energy-dispersive x-ray spectroscopy (EDS) and by x-ray photoelectron spectroscopy (XPS). Characterization of the surface morphology will be studied by scanning electrons microscopy (SEM) and atomic force microscopy (AFM). SNL is managed and operated by NTESS under contract DE-NA0003525. SAND2020-1289 A

3:00 PM O10

#### (Student) Silicidation—A Low Temperature Route for Vertical Intracellular Nanowire Array Integration on CMOS Devices

Jihwan Lee and Shadi Dayeh; University of California, San Diego, United States

Human brain contains billions of neurons that constantly perform mutual communication with each other to form a complex, synaptic network. To discover and develop precise medicines and drugs to treat neurological diseases, there is a critical need to understand the disease models and mechanisms of these neuronal synaptic activities and networks. Fundamentally, one must understand and gain means to interrogate a single neuron, a basic unit that transmits and receives electrical signals. Since neural activity is natively electrochemical, current state-of-the-art neuron sensing technologies perform measurements through electrochemically sensitive interface, including patch clamp electrodes and microelectrode arrays; however, there still exist considerable limitations in scalability, sensitivity, or degree of invasiveness in such devices. On the other hand, nanowires show tremendous potential in

neurointerface applications through their facile incorporation in conventional, scalable nanofabrication processes, integration to CMOS devices for on-chip signal processing, and minimal invasiveness through sub-10 nm tips. Without any additional electroporation pulses, nanowire-based vertical electrode arrays have demonstrated native sensitivity to intracellular potentials and subthreshold postsynaptic potentials that are crucial in analyzing synaptic networks.<sup>[1]</sup> In this work, we report a novel fabrication of platinum silicide nanowire array for the aforementioned electrophysiological interrogation. While silicon-based nanowires are dominant in neurointerface applications, platinum silicide-based nanowires offer combination of major advantages: low temperature (200 to 325°C) to form Pt-Si alloy phase<sup>[2]</sup>, sturdy, poly-crystalline structure to permit nanowire geometry, and low resistivity for electrical connections. We utilize a sputter coater system to perform simultaneous co-sputtering of platinum and silicon to deposit an initial, thick layer of a homogeneous atomic mixture. Rapid thermal annealing at low temperature is subsequently performed to transform the homogeneous solid mixture to Pt-Si alloy phase at proper, desired resistivity range. A nickel dot array mask is patterned on the Pt-Si film via electron-beam lithography and an SF<sub>6</sub> (Sulfur Hexafluoride)/Argon based ICP (inductively coupled plasma)/RIE (reactive ion etch) process is used to form a vertically standing Pt-Si nanowire on the substrate, which in this work, is on the CMOS chip. Ultimately, the achievements in this work will allow integration of individually addressable, platinum silicide nanowire arrays on CMOS devices for interrogation of intracellular electrophysiological signals from networks of cortical and dopaminergic neurons in a single-plane and also 3D tissue-like structures. [1] R. Liu, R. Chen, A. T. Elthakeb, S. H. Lee, S. Hincley, M. L. Khraiche, J. Scott, D. Pre, Y. Hwang, A. Tanaka, Y. G. Ro, A. K. Matsushita, X. Dai, C. Soci, S. Biesmans, A. James, J. Nogan, K. L. Jungjohann, D. V. Pete, D. B. Webb, Y. Zou, A. G. Bang, and S. A. Dayeh. "High Density Individually Addressable Nanowire Arrays Record Intracellular Activity from Primary Rodent and Human Stem Cell Derived Neurons." Nano Letters, no. 17 (2017): 6604752. [2] C. A. Crider, J. M. Poate, J. E. Rowe, and T. T. Sheng. "Platinum Silicide Formation Under Ultrahigh Vacuum and Controlled Impurity Ambients." Journal of Applied Physics, no. 52 (1981): 1329018.

SESSION P: III-Nitride Power Devices Utilizing Oxides

Session Chair: Fatemeh (Shadi) Shahedipour-Sandvik

Session Hosts: Andrew Binder and Matthew Hardy

Thursday Morning, June 25, 2020

Location: ZoomRoom 3

11:45 AM P01

#### (Student) AlInN-GaN Based Power Electronic Devices Utilizing AlInO as a Gate Insulator

Elia Palmese, Matthew R. Peart, Damir Borovac, Xiongliang Wei, Renbo Song, Nelson Tansu and Jonathan J. Wierer; Lehigh University, United States  
To achieve power semiconductor devices with improved efficiency and higher breakdown voltages, wide band gap (WBG) and ultra-wide band gap (UWBG) semiconductors are being researched because of their higher critical electric fields and temperature stability. In recent years, Gallium Nitride (GaN) based power diodes and high electron mobility transistors (HEMTs) have demonstrated kilovolt breakdown voltages and high switching frequencies (>1MHz) [1, 2]. To achieve even higher breakdown voltages ultra-wide bandgap materials such as Ga<sub>2</sub>O<sub>3</sub>, AlGa<sub>2</sub>N, AlInN are being considered. Of these three semiconductors, Al<sub>x</sub>In<sub>1-x</sub>N has intrinsic properties which makes it suitable for a wide range of power devices including having GaN as a latticed matched substrate when x is 0.82, the ability to be both n- an p-type doped, and ability to convert to an oxide [3-6].

This work concentrates on developing a GaN-based metal-oxide-semiconductor field-effect transistors (MOSFETs) with gate oxides formed by oxidizing AlInN. We have shown that AlInN layers grown lattice matched to GaN can be oxidized deeply in wet (H<sub>2</sub>O) or dry (O<sub>2</sub>) atmospheres at elevated temperatures (>800 °C). The resulting AlInO has interesting insulating properties, such as a low leakage currents (highly insulating) and large breakdown field of at least 5 MV/cm [4]. Also, oxidizing an AlInN layer formed on GaN avoids exposing surfaces that make up the eventual MOSFET channel, which is a problem with deposited gate oxides. These favorable properties warrant further research for AlInO as a gate oxide in a power MOSFET.

In this study, AlInO/GaN metal-oxide-semiconductor (MOS) capacitors are fabricated and tested as a precursor to fabricating MOSFETs with AlInO as a gate insulator. The samples are grown on sapphire substrates using MOCVD and consist of a n-type GaN layer (n~2x10<sup>16</sup>/cm<sup>3</sup>) followed by an AlInN layer with variable thicknesses. First, the kinetics of AlInO oxidation process are studied to determine the oxidation rates of AlInN. Oxidation rates are obtained for temperatures ranging from 830 °C to 860 °C in O<sub>2</sub> atmospheres. The rates were determined by measuring the oxide layer thickness using ellipsometry, and they increased with temperature from 0.55 nm/min to 0.96 nm/min. Additionally, the ellipsometry data shows that the refractive index using O<sub>2</sub> are lower at ~1.5 compared to oxidizing with H<sub>2</sub>O ~1.8 [4]. This oxidation rate data is used in the fabrication of the MOS capacitors which are created using standard fabrication procedures. The first processing step is to oxidize the AlInN to form AlInO. After oxidizing a mesa is etched to expose the underlying GaN layer and contacts are formed on the AlInO and outside the mesa. Our

preliminary data show traditional MOS CV characteristics that can be swept from accumulation to depletion. Our best devices thus far result in a relative permittivity for the oxide at  $\sim 5.3$ . This is slightly lower than measured for ALD deposited aluminum oxides ( $\sim 7$ ), and it is possible that InO within the AlInO is lowering that value. This presentation will expand on these results and show how the MOS capacitors behave when changing the oxide thickness, oxidation temperature, and adding post oxidation anneals, and include measurements such as current versus voltage and conductance versus frequency to study the interface charge, breakdown fields, and leakage currents.

[1] Y. Saitoh, et al., *Appl. Phys. Exp.*, 3, 8, (2010). [2] J. L. Hudgins, G. S. Simin, E. Santi and M. A. Khan, 18, 907-914, (2003). [3] M. R. Peart, N. Tansu, and J. J. Wierer, Jr., *IEEE Trans Elec Devs*, 65, 4276-4281, (2018). [4] M. R. Peart, X. Wei, D. Borovac, W. Sun, N. Tansu, and J. J. Wierer, Jr., *ACS Appl. Elec. Mat.*, 1, 1367-1371 (2019). [5] D. Borovac, W. Sun, R. Song, J. J. Wierer Jr., and N. Tansu "submitted (2019). [6] M. Peart et al. "AlInN/GaN diodes for power electronic devices", submitted (2019).

## 12:00 PM P02

**Analysis of the Bulk and Interfacial Properties of AlSiO Grown on N-Polar GaN** Wenjian Liu, Islam Sayed, Jana Georgieva, Silvia Chan, Stacia Keller and Umesh Mishra; University of California, Santa Barbara, United States

N-polar GaN high electron mobility transistors have demonstrated great potentials in power devices and millimeter-wave amplifiers. For high-power and high-frequency applications, dielectrics on N-polar GaN with high break down voltage, low gate leakage and low interface state density ( $D_{it}$ ) are desired [1]. In order to improve the  $D_{it}$  of dielectrics on GaN, an effective method to accurately probe the  $D_{it}$  across whole band gap is critical. Recently, based on the ultraviolet (UV)-assisted Capacitance-Voltage (C-V) methods, we have developed a methodology accounting for the hole traps in bulk dielectrics to accurately extract the interface state density. Through analyzing a series of metal-insulator-semiconductor capacitors (MISCAPs) with different insulator thicknesses, the methodology is applied to the SiN/GaN system which has a negative valence band offset [2].

Here, we expand the same methodology to the AlSiO/GaN system which has a positive valence band offset and illustrate the possible general validity of the methodology. The AlSiO with silicon composition of 37% was grown *in-situ* on N-polar GaN by metal organic chemical vapor deposition. A series of MISCAPs with 9 nm, 17 nm and 25 nm AlSiO have been studied with UV-assisted C-V methods. Two C-V curves were measured prior to and post shining UV, and have been shifted to obtain physical meanings of charge capture and neutralization. The parabolic dependence of the shifted voltage value,  $V_{total}$  on AlSiO thickness can be explained by the existence of  $\sim 6.8 \times 10^{18} \text{ cm}^{-3}$  hole traps uniformly distributed in AlSiO bulk. The extracted  $D_{it}$  at AlSiO/GaN is  $\sim 4.4 \times 10^{11} \text{ cm}^{-2} \text{ eV}^{-1}$ . From the published first principle calculations in a-Al<sub>2</sub>O<sub>3</sub>, the aluminum and oxygen vacancies may potentially act as the structural origin of hole traps [3]. The results and methodology here can provide more insights into understanding and improving dielectric in terms of interface states and bulk traps.

At the conference, a comparison of AlSiO and SiN on N-polar GaN including interface states density, bulk hole trap density, frequency-dependent C-V behavior and I-V curves will also be presented.

References: [1] U. Mishra, et al., *Proceedings of the IEEE* 96, 287-305(2008). [2] W. Liu, et al., *Applied Physics Letters* 116, 022104(2020). [3] M. Choi, et al., *Journal of Applied Physics* 113, 044501(2013).

## 12:15 PM P03

**ALD AION on a-Plane GaN with Extremely Low Interface Trap Density** Sang-Woo Han<sup>1</sup>, Jiansong Song<sup>1</sup>, Rian Guan<sup>1</sup>, Jaime Rumsey<sup>2</sup>, Jacob Leach<sup>2</sup> and Rongming Chu<sup>1</sup>; <sup>1</sup>The Pennsylvania State University, United States; <sup>2</sup>Kyma Technologies Inc, United States

GaN based electronic devices have gained great success in the arena of high-frequency and high-power applications. A high-quality GaN MOS structure has the potential to enable new device designs and higher device performance, thereby bringing the success of GaN electronics to a new level. In this study, we report GaN MOS capacitor made by Atomic-Layer-Deposition (ALD) of AION on a-plane GaN with nearly ideal electrical characteristics, as suggested by bi-directional and frequency-dependent capacitance-voltage measurements. The conductance method was used to evaluate trap density ( $D_{it}$ ). The MOSCAP on a-plane GaN exhibited outstanding performance in comparison with MOSCAP on c-plane GaN. Capacitance vs voltage (C-V) hysteresis values and  $D_{it}$  values were 250 mV and  $8.2 \times 10^{11} \text{ eV}^{-1} \text{ cm}^{-2}$  for c-plane GaN and 50 mV and  $2.74 \times 10^{10} \text{ eV}^{-1} \text{ cm}^{-2}$  for a-plane GaN.

### Experimental Design and Process

The c-plane and a-plane bulk GaN wafers were prepared at Kyma Technologies Inc. The MOSCAP fabrication process started with surface piranha cleaning for 10 min with 1:5 (Hydrogen peroxide:sulfuric acid) ratio. Surface was etched by Cl<sub>2</sub>/BCl<sub>3</sub>-based inductively coupled plasma reactive ion etching (ICP-RIE) followed by 25% TMAH treatment for 70 min at 85 °C. 21.5 nm- thick ALD-AION thin film was deposited at 330 °C. Then, the AION film was annealed in a rapid thermal annealing furnace at 400°C for 10 min in N<sub>2</sub> ambient. Prior to ohmic formation, the backside of the sample was etched by BCl<sub>3</sub>-based ICP-RIE. Ti/Al (200/1000 Å) metal stack was evaporated by e-beam evaporator for the ohmic formation. Top electrodes were made of Ni/Au (200/2000 Å) metal stack.

**Results and Discussion:** Both c-plane and a-plane GaN MOSCAPs exhibited good insulation characteristics. Typical leakage current values at 2.3 MV/cm were 16.4 nA/cm<sup>2</sup> for c-plane GaN MOSCAP and 29.8 nA/cm<sup>2</sup> for a-plane GaN MOSCAP. Typical C-V hysteresis values of c-and a-plane GaN MOSCAPs at 1 MHz were  $\sim 250 \text{ mV}$  and  $\sim 50 \text{ mV}$ , respectively. It should be noted that surface treatment process consisting of ICP-RIE dry etching followed by TMAH wet etching was necessary to improve CV characteristics. The MOSCAP without surface treatment process showed very weak capacitance modulation and exhibited very large hysteresis loop of up to several volts. We employed the conductance method to evaluate Dit. The frequency dependent capacitance and conductance characteristics were obtained in the frequency range from 4 kHz to 1 MHz. A-plane GaN MOSCAP exhibited nearly frequency dispersion free characteristics with extremely low  $D_{it}$  value of  $2.74 \times 10^{10} \text{ eV}^{-1} \text{ cm}^{-2}$  at 0.393 eV. While for c-plane GaN MOSCAP, the extracted  $D_{it}$  value was  $8.2 \times 10^{11} \text{ eV}^{-1} \text{ cm}^{-2}$  at 0.393 eV.

## 12:30 PM P04

**Recovery of Sidewall Etch Damage in p-Type Gallium Nitride** Geoffrey Foster<sup>1</sup>, Andrew D. Koehler<sup>1</sup>, Mona Ebrish<sup>1</sup>, Travis J. Anderson<sup>1</sup>, Brendan P. Gunning<sup>2</sup>, Robert Kaplar<sup>2</sup>, Karl Hobart<sup>1</sup> and Fritz J. Kub<sup>1</sup>; <sup>1</sup>U.S. Naval Research Laboratory, United States; <sup>2</sup>Sandia National Laboratories, United States

The creation of vertical p-n GaN diodes allows for higher breakdown voltage devices than in lateral devices. To accomplish this the top p-region must be isolated. An isolation technique that is used in the creation of trench MOSFET is the chemical etch. This can leave physical damage behind on the p-layer. This is most often seen in the form of nitrogen vacancies, which behave as donors in the lattice<sup>1</sup>. These donors compensate for the Mg acceptors in the lattices and can act as a path for leakage current, diminishing device performance while under reverse bias.

To test the effects of etch damage and recovery, GaN wafers were implanted with  $8 \times 10^{19} \text{ cm}^{-3}$  Mg to make a 500 nm p-type region with  $N_A$  of  $4 \times 10^{17} \text{ cm}^{-3}$ . The N-type region is doped to  $1 \times 10^{16}$  with a thickness of 8  $\mu\text{m}$ . An Ohmic stack of Pd/Pt/Au was deposited on the p+ surface, with a backside contact of Ti/Al/Ni/Au, then a Cl<sub>2</sub>+Ar etch was utilized to form mesas to isolate the p-region in the GaN with several different size mesas. IV measurements were then performed on the etched mesas of 250  $\mu\text{m}$  diameter, looking at turn on characteristics and reverse leakage performance.

To treat the surface damage from the Cl etch, a process of using a UV/Ozone treatment has been developed. After the mesa etch, a UV/Ozone treatment is performed for ten minutes. This is then followed by two minutes in 49% hydrofluoric acid. Without any treatment, at 50 V of reverse bias the leakage current is  $1.8 \times 10^{-9} \text{ A}$ . The first UV/Ozone treatment decreases the leakage current by an order of magnitude, a second treatment decreases this by almost another order of magnitude further, for a final reverse current of  $3.4 \times 10^{-11} \text{ A}$ . The leakage current is likely caused due to the creation of donors on the surface and side walls of the mesa. The observed reduction in the leakage current can be seen as evidence that some of those defects are being removed, or effectively cleaned up. In the forward bias, before treatment there appears to be two turn on regimes. The first is likely due to a shunt resistor like effect from the etch damage on the surface which is causing a short to the n layer beneath. The second is from normal diode behavior. After two clean up treatments are performed, the current in the on regime is now only has one turn on regime. If the ideality factor is plotted as a function of voltage, after treatment, the ideality factor decreases from  $\sim 3.2$  to  $\sim 2.2$ . While both values are above 2, this is likely from residual damage still present on the surface and on the side walls, preventing the device from performing as an ideal diode.

References <sup>1</sup> S.J. Pearton, R.J. Shul, and F. Ren, *MRS Internet J. Nitride Semicond. Res.* 5, e11 (2000).

## 12:45 PM P05

**(Student) Reverse Breakdown Field and Interface Properties of Metal/BaTiO<sub>3</sub>/GaN Junctions** Mohammad Wahidur Rahman, Hareesh Chandrasekar, Towhidur Razzak, Shahadat H. Sohel and Siddharth Rajan; The Ohio State University, United States

**Introduction:** The high breakdown field of wide bandgap semiconductors such as GaN makes them attractive for high-voltage switching applications. The practical realization of such high breakdown fields typically requires the use of p-n junction, which requires a turn-on voltage comparable to the bandgap of GaN. For lower voltage applications, the forward or ON-state power loss due to higher turn-on voltage is typically much larger than the series resistance loss for PN rectifiers. Schottky diodes are desirable due to their low turn voltage but the maximum field achievable is limited by the metal/semiconductor barrier height. A solution to this problem, proposed recently, is to use extreme permittivity dielectrics between the metal-semiconductor junctions [1]. Such high-k/low-k dielectric hetero-junction reduces the field at the metal Schottky barrier, thus increasing the breakdown fields and voltages [2]. In this work, we demonstrate junctions formed by high permittivity BaTiO<sub>3</sub> and n-type GaN and show that breakdown fields up to 2.3 MV/cm can be sustained, while forward conduction can be maintained with a turn-on voltage of 1.5 V. We have also analyzed capacitance-voltage characteristics to elucidate the band offset and fixed charge at the interface. **Experiment:** Four samples with 0 nm (control), 20 nm, 30 nm, and 40 nm BaTiO<sub>3</sub> were prepared. BaTiO<sub>3</sub> was deposited using RF sputtering at 630°C on free-standing n+ GaN templates with a nominal Si doping density of  $1 \times 10^{18} \text{ cm}^{-3}$ . Gate (Ni/Au [30/100 nm]) and ohmic (Al/Ni/

Au [30/30/100 nm]) metals were deposited using e-beam evaporation.

**Results:** The dielectric constant of the BaTiO<sub>3</sub> films was estimated to range from 40–50 using C-V measurements. Rectification of over 8 orders of magnitude was observed on samples with BaTiO<sub>3</sub>, compared to less than 4 orders for the control Schottky samples. The high doping in the sample led to significant reverse leakage and an estimated maximum field of 0.9 MV/cm, as well as premature turn-on of the control Schottky diode. In contrast, the reverse breakdown voltage of the 20 nm BaTiO<sub>3</sub>/GaN diode was significantly higher, 13 V, corresponding to a maximum field in the GaN of 2.3 MV/cm which is minimum assuming non-punch through condition in BaTiO<sub>3</sub> samples. This is significantly higher than the previously reported maximum fields in GaN Schottky diodes, which are generally below 1.5 MV/cm due to Schottky barrier leakage [3]. The dependence of the flat-band voltage of the metal/oxide/semiconductor structure was used to estimate the interface charge at the BaTiO<sub>3</sub>/GaN interface [4]. At equilibrium, GaN was found to be depleted at the surface for all BaTiO<sub>3</sub> samples using C-V measurements. Using at the BaTiO<sub>3</sub>/GaN interface, we estimate a fixed net negative sheet charge density of  $1.38 \times 10^{13} \text{ cm}^{-2}$  which corresponds to  $4.3 \times 10^{12} \text{ cm}^{-2}$  positive fixed charges after accounting the GaN spontaneous polarization charge of  $-1.81 \times 10^{13} \text{ cm}^{-2}$  [5]. The authors acknowledge funding from the DARPA DREAM program (ONR N00014-18-1-2033, Program Manager Dr. Young-Kai Chen, monitored by Office of Naval Research, Program Manager Dr. Paul Maki). **Reference:** [1] Zhanbo Xia, et al. Appl. Phys. Lett. 115, 252104 (2019). [2] Towhidur Razzak, et al. Appl. Phys. Lett. 116, 023507 (2020). [3] Y. Cao, et al. Appl. Phys. Lett. 108, 062103 (2016). [4] Ting-Hsiang Hung, et al. Appl. Phys. Lett. 104, 162106 (2014). [5] Fabio Bernardini, Vincenzo Fiorentini, and David Vanderbilt Phys. Rev. B 56(16), R10024-R10027 (1997)

### 1:00 PM BREAK

SESSION Q: III-Nitrides—Photodetectors  
Session Chair: Theeradetch Detchprohm  
Session Hosts: Andrew Binder and Matthew Hardy  
Thursday Afternoon, June 25, 2020  
Location: ZoomRoom 3

### 2:00 PM Q01

**(Student) Microstructure-Defect-Device Performance Correlation for Solar-Blind Al<sub>0.45</sub>Ga<sub>0.55</sub>N Schottky Photodetectors on Sapphire** Anisha Kalra, Shashwat Rathkanthiwar, Muralidharan R. Srinivasan Raghavan and Digbijoy Nath; Indian Institute of Science, India

In this work, we report on microstructure-defect-device performance correlation for 280 nm, Schottky photodetectors based on hetero-epitaxial Al<sub>0.45</sub>Ga<sub>0.55</sub>N on c-plane sapphire. The growth conditions of the initial AlN nucleation layer were found to significantly impact the density of nuclei on the growth surface and consequently, the density of extended defects in the absorbing AlGa<sub>x</sub>N epi-layers. This had a strong influence on the performance parameters of self-powered Schottky detectors based on these epi-layers. The dark current was found to reduce by ten decades, from 10 mA to 0.6 pA (at -10 V), through a 350 times reduction in the screw dislocation density. Temperature-dependent current-voltage measurements on the high defect density samples revealed carrier tunneling through a thin surface barrier and hopping conduction along localized defect states as dominant transport mechanisms contributing to the dark current under low and high fields, respectively. Dislocation density reduction was associated with a reduction in the density of conducting carriers as well as higher activation energy for hopping, ultimately leading to lower leakage currents. An eight-fold reduction in the edge dislocation density was in turn associated with a 5000-fold enhancement in the zero-bias external quantum efficiency, from 0.01 % to 49 %, when measured under 280 nm front illumination. In addition to dark current and EQE, the impact of growth conditions on the UV-to-visible rejection ratio, detectivity, gain, transient response and linearity with optical power is also discussed. Detectors realized over state-of-the-art quality AlN epi-layers exhibited a peak zero-bias external quantum efficiency of 54 % under 280 nm back illumination, a dark current density below 0.6 nA/cm<sup>2</sup>, a UV-to-visible rejection ratio exceeding six orders of magnitude, a detectivity of  $2.1 \times 10^{14} \text{ cmHz}^{1/2}\text{W}^{-1}$  and a linear response with optical power over three decades. Detectors operating in the sub-290 nm regime of the electromagnetic spectra benefit from a low solar background and find a host of strategic, commercial, astronomical and biological applications. Schottky detectors combine the advantages of both the MSM and p-i-n geometries since they allow a self-powered operation, offer a low background noise, a fast-transient response and benefit from a vertical topology that enables integration into focal plane arrays without the requirement of an ohmic p-contact. Although AlGa<sub>x</sub>N-based Schottky diodes have been studied extensively for high power electronics as well as optoelectronic applications, their performance has been limited by the presence of large densities of point and extended defects in hetero-epitaxially grown AlGa<sub>x</sub>N epi-layers. This makes understanding the correlation between microstructural defects originating during heteroepitaxy and performance of large-area devices quintessential to design epi-stacks with low defect densities and consequently, enable reliable, high-performance devices. The study is based on a series of carefully designed Schottky epi-stacks, with a

variation in the nucleation layer across the samples. The aim of the work was to utilize a template and mask free, scalable, less complicated, relatively low temperature and inexpensive growth technique involving a two-temperature AlN-based buffer. A variation in the crystalline quality of the AlN buffer and consequently, the absorbing AlGa<sub>x</sub>N epi-layers could be achieved by tuning the inter-nucleus distance or the density of nuclei on the growth surface. This was associated with a change in the coalescence boundaries per unit area, and consequently the dislocation densities across the samples. The impact of this crystalline quality change on various detector performance parameters vis-à-vis the dark current, spectral responsivity (or quantum efficiency), detectivity, gain, transient response and linearity is studied through varying structural, optical and electrical characterization techniques.

### 2:15 PM Q02

**(Student) Evidence of Surface Pits-Induced Photo-Response Enhancement in High Responsivity Al<sub>0.25</sub>Ga<sub>0.75</sub>N UV-B Photodetectors on Si (111)** Shashwat Rathkanthiwar, Anisha Kalra, Muralidharan R. Digbijoy Nath and Srinivasan Raghavan; Indian Institute of Science, Bangalore, India, India

We demonstrate the influence of surface pits in tuning dark current and spectral responsivity of Al<sub>0.25</sub>Ga<sub>0.75</sub>N-based ultraviolet B (UV-B) photodetectors with metal-semiconductor-metal (MSM) geometry on Si (111) substrate. Photodetectors fabricated on Al<sub>0.25</sub>Ga<sub>0.75</sub>N epilayers with surface pit density of  $2 \times 10^8 \text{ cm}^{-2}$  exhibited high values of responsivity, photo-to-dark current ratio and visible rejection of 125 A/W,  $1.2 \times 10^4$  and  $2.3 \times 10^3$ , respectively at 5 V. On the contrary, the corresponding values for photodetectors fabricated on epilayers devoid of surface pits were measured to be 17 mA/W,  $6.7 \times 10^2$  and  $6.9 \times 10^3$ , respectively. Localized enhancement of photo-response at surface pits was confirmed by UV-assisted conductive atomic force microscopy. Temperature-dependent carrier transport analysis under dark and UV-illumination revealed the cumulative contribution of pit-induced thermionic field emission and hole trapping induced gain to the observed high responsivity. This work presents the highest values of responsivity for UV-B detectors at a given bias. UV-B (290-320 nm) solar radiation have been proven to affect the Earth's biosystem and human health. The sunburn effect for human skin, a measure of UV index, which is the product of the sunlight radiation intensity and skin sensitivity peaks at ~315 nm. Therefore, a simple, low-cost, reliable, portable and point-of-use UV-B monitoring system operating at 315 nm is of great interest. The tunable direct bandgap of III-nitrides with an intrinsic rejection of visible and infrared wavelengths eliminates the need for filters and operational complexities. High-performance photodetectors require high spectral responsivity and low dark current to enable detection capability of low optical strength signal. While the responsivity dictates the sensitivity i.e. amount of photocurrent generated per unit optical power, the dark current sets the limit on the lowest signal a photodetector can detect. Most of the III-nitride photodetector reports in the literature utilize sapphire substrates for the growth of the active detector epitaxial stack. Although AlGa<sub>x</sub>N-based MSM photodetectors with ultra-low dark current, high responsivity, fast time-response, and good visible rejection have been demonstrated on sapphire substrates, the impact of surface pits on the performance of these detectors has not been reported yet. Compared to sapphire, silicon (111) substrates not only offer scalability, becoming promising towards enabling low-cost solar UV monitoring solutions, but also hold a promise towards the development of transparent and flexible UV detectors by back-side etching of the substrate. In this work, we study the correlation between surface morphology and buffer layer growth conditions of Al<sub>0.25</sub>Ga<sub>0.75</sub>N epilayers on Si (111) vis-à-vis UV-B (315 nm) photodetector performance and carrier transport mechanisms. Compared to the sample with a pit-free surface, the sample with a pit density of  $2 \times 10^8 \text{ cm}^{-2}$  exhibited five orders and four orders of magnitude increase in dark and photocurrent respectively. Using temperature-dependent measurements, the anomalously large dark, and photocurrents were attributed to the thermionic field emission carrier transport mechanism and hole-trapping induced internal gain mechanism respectively at the surface pits. These were corroborated by performing C-AFM measurements under dark and UV-illumination. The pits lead to a significant increase in responsivity with applied bias which measured as high as 6500 A/W at 40 V. This is the highest value reported for III-nitrides based UV-B detectors. This work suggests that surface pits can be controllably incorporated for the realization of high spectral responsivity III-nitride UV photodetectors on Si (111) substrates.

### 2:30 PM Q03

**(Student) Geiger-Mode Operation of Gallium Nitride p-i-n Avalanche Photodiodes and Histogram Fitting Measurement** Hoon Jeong<sup>1</sup>, Eliza A. Gazda<sup>2</sup>, Mi-Hee Ji<sup>3</sup>, Minkyu Cho<sup>1</sup>, Marzieh Bakhtiari-Noodeh<sup>1</sup>, Theeradetch Detchprohm<sup>1</sup>, Shyh-Chiang Shen<sup>1</sup>, Nepomuk A. Otte<sup>2</sup> and Russell Dupuis<sup>1,3</sup>; <sup>1</sup>Georgia Tech, United States; <sup>2</sup>Georgia Institute of Technology, United States; <sup>3</sup>Oak Ridge National Laboratory, United States

III-Nitride (AlGa<sub>x</sub>N) avalanche photodiodes (APDs) have high breakdown field, high electron drift velocity, high thermal conductivity, and low dark current. They also exhibit good UV sensitivity, since the III-nitride material bandgap can be tuned from 3.4 (365nm) to 6.2eV (200nm). With the photon counting technique applied, III-Nitride APDs can operate in Geiger mode, and can be important for numerous applications in UV single photon detection. These applications include quantum key distribution, optical time-domain reflectometry, positron emission tomography, biomedical researches, and

ultraviolet communications.

In this work, we demonstrate Geiger mode operation of GaN *p-i-n* APDs by applying a histogram fitting measurement. The GaN *p-i-n* APD structures were grown by MOCVD in an AIXTRON 6x2 Close-Coupled Showerhead reactor on *c*-plane free-standing (FS) GaN (threading dislocation density of  $\sim 10^6$  cm<sup>-2</sup>). The epitaxial growth starts with 0.6 mm unintentionally doped GaN regrowth, followed by 2.3mm thick Si-doped GaN *n*-layer with a free-electron concentration of  $4 \times 10^{18}$  cm<sup>-3</sup>. The *i*-layer of 280nm thickness is grown on top of the *n*-layer, with a background Si doping of  $2 \times 10^{16}$  cm<sup>-3</sup>. This layer thickness is designed for the breakdown voltage of 95V, i.e., breakdown field of approximately 3.4 MV/cm. The *p*-layer is two stacks of 100nm Mg-doped GaN layer and 15nm highly Mg-doped GaN cap layer. The Mg-doped *p*-layer has a free-hole concentration of  $1 \times 10^{18}$  cm<sup>-3</sup>, and heavily doped *p*-layer has a Mg concentration of  $1 \times 10^{20}$  cm<sup>-3</sup>. The structure is then fabricated into APD devices via the following steps: 1) mesa etching, 2) n-type metal deposition, 3) p-type metal deposition, 4) passivation and via-hole, 5) metal interconnect deposition. In the Geiger-mode operation measurement, a gated quenching circuit was used. Additionally, a noninverting amplifier (buffer) and an inverting amplifier are inserted after the pulse generator and after the GaN APD respectively, to isolate the pulse generator from the rest of the circuit. The computer controlled oscilloscope measures the avalanche current and collects a series of avalanche signals then performs data processing. The APD device is illuminated with the UV light from a Xenon lamp through a monochromator. Using a bifurcated fiber, the UV light is split with one end applying to the APD, and the other end going to a silicon photon counter for reference. The Geiger mode setup is installed in the dark box for an absolute optical isolation. The collected signals are processed through histogram fitting based on Poisson statistics as follows. In the Geiger-mode circuit system, the data-acquisition computer collects the time interval between the rising edge of the pulse and an avalanche event for 10,000 pulse events, then processes this randomly distributed data into one histogram. Finally, the count rate can be obtained by fitting the exponential function  $R = R_0 e^{-t/\tau}$ , in which  $R$  represents count rate. Also by utilizing the silicon photon counter and its single photon detection efficiency (SPDE) characteristic, we were able to estimate SPDE of the GaN APD from  $R$  in the fitting. The dark count rate and SPDE obtain from histogram fitting was  $\sim 20$ MHz and 1% respectively, under 370nm UV light illumination.

#### 2:45 PM Q04

**(Student) Oxygen Impurity Incorporation Due to Growth Interruption and Its Diffusion from These Interfaces in N-Polar GaN:Mg Films Grown by MOCVD and Its Implication in Photocathode Device Characteristics** Emma Rocco<sup>1</sup>, Kasey Hogan<sup>1</sup>, Vincent E. Meyers<sup>1</sup>, Benjamin McEwen<sup>1</sup>, L. Douglas Bell<sup>2</sup> and Fatemeh (Shadi) Shahedipour-Sandvik<sup>1</sup>; <sup>1</sup>SUNY Polytechnic Institute, United States; <sup>2</sup>California Institute of Technology, United States

The lack of centrosymmetric inversion symmetry inherent in the III-nitride system wurtzite crystal structure results in a spontaneous polarization charge along the *c*-direction. Polarization engineered devices employing N-polar III-nitrides, such as LEDs, HEMTs and photodetectors have shown improvement in some specific and important device characteristics over their Ga-polar counterparts by harnessing the polarization charge to reduce efficiency droop, improve channel confinement, and increase quantum efficiency, respectively. In addition to differences in polarization charge directionality, surface atomic configuration of N-polar materials differs compared to III-polar materials, resulting in an increased propensity to incorporate oxygen and other impurities. Incorporation of impurities at interfaces introduced by re-growth processing have been shown to degrade device performance in Ga-polar p-n diodes and photodetectors [1], [2]. Control of donor impurities, such as oxygen, and their diffusion from interfaces is particularly challenging when p-type conductivity is of interest. Here we report our recent results showing oxygen impurity incorporation at interfaces of N-polar GaN:Mg films with u-GaN cap layers [grown by metal organic chemical vapor deposition (MOCVD)] and offer a mechanism for its diffusion. The impact of single and multiple growth interruptions on the specific diffusion mechanism is studied. Oxygen concentration depth profiles measured by secondary ion mass spectroscopy (SIMS) show peaks in oxygen concentration at all interfaces introduced by growth interruption. In samples with a singular growth interruption between the layers, an exponential trend in oxygen concentration is observed, indicative of diffusion through dislocations [3]. Fitting of the experimental (SIMS) data results in a pipe diffusion coefficient of  $\sim 10^{-13}$  cm<sup>2</sup>/s and bulk diffusion coefficient of  $\sim 10^{-16}$  cm<sup>2</sup>/s. These values are in line with reports of Pearton *et al.* and Jakiela *et al.* [4], [5]. Conversely, in samples with multiple growth interruptions, excluding the interface closest to the surface, only a bulk diffusion of oxygen is observed at interfaces – with a sharp peak in concentration with no exponential component. In order to understand the role of dislocation density on the presence of dislocation-mediated diffusion, transmission electron microscopy (TEM) is utilized and reported here. Nominally equivalent dislocation density is observed in all samples. The quantum efficiency (QE) of N-polar GaN photocathodes resulting from the samples reported here is measured by photoemission spectroscopy. The impact of incorporation and diffusion of oxygen impurities in photocathode structures with multiple growth interruptions is reported with degradation of photocathode structures with multiple interruptions achieving maximum QE of 0.27% at 6.1 eV incident photon energy, compared to photocathodes with a singular growth interruption with a maximum QE of 10.79%. [1] A. Aragon *et al.*, “Interfacial

Impurities and Their Electronic Signatures in High-Voltage Regrown Nonpolar m-Plane GaN Vertical p-n Diodes,” *Phys. Status Solidi A*, 1900757 (2019). [2] M. Monavarian *et al.*, “High-Voltage Regrown Nonpolar m-Plane Vertical p-n Diodes: A Step Toward Future Selective-Area-Doped Power Switches,” *IEEE Electron Device Lett.*, vol. 40, no. 3, pp. 387–390, Mar. 2019. [3] J. C. Fisher, “Calculation of Diffusion Penetration Coefficients for Surface and Grain Boundary Diffusion,” *J. Appl. Phys.*, vol. 22, no. 1, pp. 74–77, Jan. 1951. [4] S. J. Pearton, H. Cho, J. R. LaRoche, F. Ren, R. G. Wilson, and J. W. Lee, “Oxygen diffusion into SiO<sub>2</sub>-capped GaN during annealing,” *Appl. Phys. Lett.*, vol. 75, no. 19, pp. 2939–2941, Nov. 1999. [5] R. Jakiela, E. Dumiszewska, P. Caban, A. Stonert, A. Turos, and A. Barez, “Oxygen diffusion into GaN from oxygen implanted GaN or Al<sub>2</sub>O<sub>3</sub>,” *Phys. Status Solidi C*, vol. 8, no. 5, pp. 1513–1515, 2011.

#### 3:00 PM Q05

**(Student) Homo Junction GaN p-i-n Ultraviolet Avalanche Photodiodes Using Ion-Implantation Isolation** Marzieh Bakhtiary-Nooddeh<sup>1</sup>, Minkyu Cho<sup>1</sup>, Chuan-Wei Tsou<sup>1</sup>, Hoon Jeong<sup>1</sup>, Shyh-Chiang Shen<sup>1</sup>, Theeradetch Detchprohm<sup>1</sup>, Ashok K. Sood<sup>2</sup> and Russell Dupuis<sup>1,3</sup>; <sup>1</sup>Georgia Institute of Technology, United States; <sup>2</sup>Magnolia Optical Technologies, Inc., United States

GaN avalanche photodiodes (APDs) with large band gap energy of 3.5 eV have a high sensitivity in the visible-blind region. They are appropriate candidates for operation in many applications because of their capability of operation in the visible-blind spectral region, high detection sensitivity, high breakdown electric field ( $\sim 3.3$  MV/cm), high optical gain, and low dark current. Furthermore, the high structural, chemical and thermal stability, makes GaN APDs attractive for severe environments. Mesa etching is one of the major challenges in the fabrication of these devices. Inductively coupled plasma (ICP) mesa etching creates damage which leads to an increase of the dark current, premature device breakdown, and noise. In this study, front-illuminated GaN-based UV APDs were grown by metalorganic chemical vapor deposition (MOCVD) on free-standing (FS) GaN substrates having a low dislocation density and for the first time processed into APDs using a novel ion-implantation isolation approach to reduce the sidewall leakage current and improve reliability. The epitaxial layers for visible-blind front-illuminated GaN *p-i-n* APDs were grown using a close-coupled-showerhead AIXTRON 6x2” MOCVD system on *n*-type FS-GaN substrates and fabricated using ion-implanted device isolation. The MOCVD growth employed trimethylgallium (TMGa) and ammonia (NH<sub>3</sub>) as primary precursors and silane (SiH<sub>4</sub>), and bis-cyclopentadienylmagnesium (Cp<sub>2</sub>Mg) as dopants. The epitaxial layers consisted of: 1.0 μm thick *n*-Ga<sub>0.99</sub>Si layer ( $n \sim 7 \times 10^{18}$  cm<sup>-3</sup>), 0.2 μm thick *u*-Ga<sub>0.99</sub> undoped layer, 0.1 μm thick *p*-Ga<sub>0.99</sub>Mg layer ( $p \sim 6 \times 10^{17}$  cm<sup>-3</sup>) and 0.02 μm thick *p*<sup>++</sup>-Ga<sub>0.99</sub>Mg layer on the GaN substrates for a target breakdown voltage of 70 V. X-ray diffraction (XRD) was used for the characterization of the crystallographic quality of the APD structure. The full width at half maximum of the rocking curve derived from (002) and (102) diffraction exhibit values of 74 and 55 arc-sec, respectively, primarily determined by the properties of the GaN substrate. The free-carrier concentration and resistivity of the doped layers were measured by Hall-effect characterization of previously grown doping calibration layers. Secondary ion mass spectrometry (SIMS) measurements were performed on the APD device structure to confirm the doping profile of the layers. Atomic force microscopy (AFM) was used to study the surface morphology and the corresponding root-mean-square (RMS) of the GaN *p-i-n* UV-APD epitaxial structures. The RMS values for scanning area of  $1 \times 1 \mu\text{m}^2$ ,  $5 \times 5 \mu\text{m}^2$  and  $20 \times 20 \mu\text{m}^2$  are  $\sim 0.16$  nm,  $\sim 0.31$  nm and  $\sim 0.78$  nm, respectively for the typical case. The reverse-biased *I-V* characteristics of the ion-implanted GaN APDs under dark and illuminated (at  $\lambda = 280$  nm) conditions were evaluated. At the breakdown bias of  $-70$  V, an avalanche gain of  $7 \times 10^5$  was obtained. By using ion implantation for device isolation, the dark current density dropped to below  $10^9$  A/cm<sup>2</sup> at reverse bias up to  $-40$  V. Previously fabricated conventional mesa-etched GaN APDs typically showed up to three orders of magnitude higher dark current density than the ion-implanted devices in the low electric field region. For a typical device, the peak responsivity at  $V = -10$  V is 0.035 A/W and increased to 1 A/W at the avalanche breakdown point. At the break down voltage, a peak responsivity of 1.05 A/W was obtained at  $l = 390$  nm.

SESSION R: Metal Dichalcogenides

Session Chair: Soaram Kim

Session Hosts: Kevin Daniels and Kunyao Jiang

Thursday Morning, June 25, 2020

Location: ZoomRoom 4

#### 11:45 AM R01

**Growth and Interface Engineering of MoS<sub>2</sub>** Anil Manc; Argonne National Laboratory, United States

Thin layer of two dimensional (2D) materials mainly transition metal dichalcogenide (TMD) semiconductor possess exceptional properties such as electrical, optical, magnetic, mechanical and chemical. This allows the exploration of internal quantum degrees of freedom of electrons and their potential for use in optoelectronic, energy, and sensor applications. Although exciting results are being obtained, but all these methods have limitations such

as poor quality of the material, lack of precise control of thickness, interface or ability to integrate them into complex 3D devices. Nevertheless, the biggest challenge in realizing their full potential has been the lack of doable material synthesis methods of such films with high uniformity, conformality and interfacing with other materials such as oxides and metals. Among the various thin film growth methods, atomic layer deposition (ALD) offers the best combination of a controlled layer-by-layer growth of the material with high conformality and suitable integration with other oxides such as dielectrics and metals. At the same time, precisely control thermal-based etching method for 2D-TMD materials are needed. Secondly at present, there are tremendous attention and efforts on development of the thermal vapor based well control etching methods especially on atomic layer etching (ALEt). The successful combination of both ALD and ALEt of 2D-TMDs can pave the way to control the synthesis of 2D-TMD layers over large areas. This interface engineering will be important for 2D-TMD materials integration for future successful large-scale complex device structures fabrication.

Here we will first discuss the ALD growth of 2D-TMDs (e.g. MoS<sub>2</sub>, HfS<sub>2</sub>) and then interface with especially Mo metal and various dielectrics (e.g. Al<sub>2</sub>O<sub>3</sub>, MgO, HfO<sub>2</sub>, TiO<sub>2</sub> and MgS) and vice versa. Then precise control etching processes based on molybdenum hexafluoride (MoF<sub>6</sub>) and H<sub>2</sub>O vapor will be discussed. We have used in-situ quartz crystal microbalance (QCM) and Fourier-transform infrared spectroscopy (FTIR) measurements to monitor the deposition and etching MoS<sub>2</sub> layers. Next, the deposited and etched MoS<sub>2</sub> thin films were analyzed by spectroscopic ellipsometry to determine the thickness and refractive index, and the composition was determined by X-ray photoelectron spectroscopy (XPS). These ex-situ measurements confirmed the MoS<sub>2</sub> deposition and etching behavior findings from our in-situ studies.

#### 12:00 PM R02

**Mem-Transistor and Artificial Synapse Based on 2D Ferroelectric  $\alpha$ -In<sub>2</sub>Se<sub>3</sub>** Neha Mohta, Muralidharan R and Digbijoy Nath; Indian Institute of Science, Bengaluru, India

Two-dimensional layered semiconductors have recently emerged as attractive building blocks for next-generation low-power, non-volatile memories, and synapses for neuromorphic applications. Although ferroelectrics have been widely studied as dielectrics for memristors in metal-dielectric-metal topology, yet, the study of ferroelectrics as the channel material in a transistor architecture for synaptic and memristive applications is still at an embryonic stage.

Here, we demonstrate for the first time, the use of ferroelectric layered 2D  $\alpha$ -In<sub>2</sub>Se<sub>3</sub> as a memristor as well as a synapse by exploiting the hysteresis arising out of in-plane and out-of-plane polarization in it. Various characteristics of an artificial synapse such as excitatory and inhibitory postsynaptic current, long-term potentiation/depression, spike-timing-dependent plasticity (SPDT), etc. are emulated in these devices.

Multi-layer  $\alpha$ -In<sub>2</sub>Se<sub>3</sub> flakes were exfoliated from geological sample using scotch-tape method onto a sputtered Ta<sub>2</sub>O<sub>5</sub>/p-Si platform. E-beam lithography was used to pattern source-drain contact fingers on  $\alpha$ -In<sub>2</sub>Se<sub>3</sub>, and pads on Ta<sub>2</sub>O<sub>5</sub>/p-Si. E-beam evaporated Ni/Au (30 nm/100 nm) stack was used as source-drain contacts while p-silicon was used as the back gate. Measurements were performed using an Agilent B1500 Semiconductor Parameter Analyzer while the pulsing was done by a waveform pattern generator.

Under two-terminal measurements, the devices exhibited significant hysteresis in both forward and reverse biases, the direction of hysteresis being clockwise from low resistive state (LRS) to high resistive state (HRS). The devices were found to exhibit high endurance levels as testified by the repeatability and consistency in the current levels up to 100 sweeps (and beyond). Under 3-terminal measurements, the transfer characteristics (ID-VG) of the devices were also found to exhibit significant hysteresis which can be attributed to the ferroelectric nature of the channel material  $\alpha$ -In<sub>2</sub>Se<sub>3</sub>. Low-temperature measurements are currently being done and will be presented at the conference. Exploiting the hysteresis in the back-gated transistor architecture, synaptic functionalities were realized. Pulses of magnitude  $\pm 2$  V and pulse widths (period) of 20 ms (100 ms) were applied on the gate of the devices. For a series of 40 pulses (-2 V), the postsynaptic current increased with the weight update from 50 to 450 nA emulating potentiation while depression was observed under (+2 V) gate pulses. The PPF index (paired-pulse facilitation) exhibited a range of 0-35% while the spacing between adjacent pulses was varied from 20 to 500 ms. The energy consumption was found to be in the order of hundreds of pico joules. Temperature-dependent STDP/SADP will be presented. This first study of synaptic functionalities in a ferroelectric channel transistor is expected to contribute to the fast-expanding area of hardware neural networks.

#### 12:15 PM R03

**Analytical Calculation of Strained Binding Energy in Monolayer MoS<sub>2</sub>** Shahzad Ahmad<sup>1</sup>, Muhammad Zubair<sup>1</sup>, Osama Jalil<sup>1</sup>, Usman Younis<sup>1,2</sup>, Xinke Liu<sup>2</sup> and Kah-Wee Ang<sup>3</sup>; <sup>1</sup>Information Technology University of Punjab, Pakistan; <sup>2</sup>Shenzhen University, China; <sup>3</sup>National University of Singapore, Singapore

Strain in 2D materials induce band gap shifts with excitonic effects involving binding energy for opto-electronic applications [1-3]. Experimental and numerical studies for strained excitonic effects are reported, where the numerical approaches are computationally expensive and intractable for strained cases [4-6]. We present a screened hydrogen model with fractional Coulomb potential (FCP), to calculate strained binding energies without

numerical excitonic calculations. The FCP model is analogous to an infinite quantum well (IQW), the exploitation of which leads to the calculation of strained binding energies and optical gaps. For monolayer MoS<sub>2</sub>, an unstrained binding energy of  $\approx 0.65$  eV corresponding to a band gap of 2.55eV is calculated. Whereas in-plane and out-of-plane tensile strain alters the binding energy at a rate of 13.866 meV/1% and -12.8 meV/1% of strain, respectively. This results in an optical gap to change at a rate of -124.866 meV/1% of in-plane strain and 128.88 meV/1% of out-of-plane strain. The FCP model is based on the full solution of the screened hydrogen model with Coulomb potential modified as  $V_{\text{fnc}}(r) \propto 1/r^{\beta}$  where  $\beta$  is fractional parameter. The fractional scaling is equivalent to the reduction in IQW width as in Fig. 1. A radial distance of 20 times the Bohr radius with a mesh grid of 300 points emulates the full wave behavior of the FCP model for convergence. The hydrogenic ground states  $E_0$  for  $2 < \beta \leq 3$  are calculated with FCP model to calculate the equivalent reduction in IQW width as  $(\hbar^2/8mE_0)^{1/2}$ , which agrees with the radial distance as in Fig. 2. To calculate binding energy in monolayer MoS<sub>2</sub>, a band gap of  $E_{\text{TB}} = 2.553$  eV is calculated, corresponding to the unstrained lattice constant of 3.162 Å with reported tight binding (TB) model for 2H-MoS<sub>2</sub> [7] as in Fig. 3. FCP based binding energy  $E_{\text{br}} = E_0(\mu/\epsilon^2)$  is computed for  $2 < \beta \leq 3$  to calculate the corresponding band gap as  $E_{\text{FCP}} = E_{\text{br}} + E_g$  where  $E_g \approx 1.9$  eV (Exp.).  $E_{\text{TB}}$  is scanned with  $E_{\text{FCP}}$  to obtain the binding energy of  $E_{\text{br0}} = 0.655$  eV at  $\beta = 2.606$ , in excellent agreement with reported range of 0.5-1.1 eV [8], as in Fig. 4. Finally, strained binding energies are calculated by exploiting the IQW analogy of the FCP model. The calculated reduction in exciton radius  $R_{\text{exc}}$  w.r.t strain is used as IQW width to find the corresponding binding energies  $E_{\text{br}}$  as in Table 1. The  $E_{\text{br}}$  values are mapped to  $E_{\text{TB}}$  w.r.t strain in order to compute the strained optical gaps as  $E_g = E_{\text{TB}} - E_{\text{br}}$ . Here the TB model is exploited for the incorporation of in-plane and out-of-plane tensile strain by accessing the geometrical features of the unit cell as illustrated in the inset of Fig. 3. The result in Fig. 5 confirms a physical relationship of  $\beta$  with the lattice constant as it changes at a rate of 0.666%/1% of in-plane tensile strain. Whereas an in-plane and out-of-plane tensile strain alters the binding energy at a rate of 13.866 meV/1% and -12.8 meV/1% of strain, respectively. This causes the optical gap to change at a rate of -124.866 meV/1% of in-plane and 128.88 meV/1% of out-of-plane strain, respectively. The asymmetric variation in energies highlights a non-linear change in screening due to strain. It also verifies the insensitivity of binding energy in comparison to band gap energy due to strain [8]. Moreover, strain sensitivity increases with structural confinement from bulk to monolayer in MoS<sub>2</sub> as in Fig. 6. In conclusion, the method will potentially allow choosing stable materials insensitive to strain for quantum applications.[1] H. Moon *et al.*, arXiv: 1906.10077 (2019). [2] L. Waldecker *et al.*, *Phys. Rev. Lett.*, **123**, 206403, (2019). [3] T. Mueller *et al.*, *npj 2D Mater Appl* **2**, 29 (2018). [4] W. Song *et al.*, *Phys. Rev. B*, **96**, 235441, (2017). [5] M Feierabend *et al.*, *Phys. Rev. B*, **96**, 045425, (2017). [6] R. Yan *et al.*, *Nano Lett.* **2018**, **18**, 4, 2485-2491. [7] E. Cappelluti *et al.*, *Phys. Rev. B* **88**, 0754094, (2013). [8] H. Shi *et al.*, *Phys. Rev. B* **87**, 155304, (2013).

#### 12:30 PM R04

**(Student) Growth and Extrinsic P-Type Doping of Pulsed Laser Deposited Few Layer WS<sub>2</sub> Films** Corey L. Arnold, Urmilaben Rathod, Chukwudi Iheomare, Andrey Voevodin and Nigel Shepherd; University of North Texas, United States

X-ray photoelectron, Raman and diffraction studies of few-layered pulsed laser deposited (PLD) WS<sub>2</sub> films performed as a function of laser fluence and frequency suggest that Volmer-Weber island growth is dominant for the growth conditions investigated. The correlations between structure, Hall mobility, and Fermi level positions indicate that reducing chalcogen vacancies is critical for optimal mobility in transition metal dichalcogenide (TMD) semiconductors. Extrinsic p-type doping of few-layered TMD WS<sub>2</sub> films with Nb via pulsed laser deposition is demonstrated. Ultraviolet photoelectron spectroscopy (UPS) studies showed a Fermi level of 1.41 eV from the valence band edge for the n-type controls. Films doped at 0.5 and 1.1 atomic percentages niobium were p-type, and characterized by Fermi levels at 0.31 eV and 0.18 eV from the valence band edge. That is, the Fermi level moved closer to the valence band edge with increased doping. With increased Nb doping, the hole concentrations increased from  $3.9 \times 10^{12}$  to  $8.6 \times 10^{13}$  cm<sup>-2</sup>. X-ray photoelectron spectroscopy indicates that Nb substitutes on W lattice sites, and the measured peak shifts toward lower binding energy corresponded well with the UPS data. Schematic energy band diagrams are proposed. The approach demonstrates the potential of PLD for targeted doping of transition metal dichalcogenides, and by extension, its potential for creating p-n junctions.

#### 12:45 PM R05

**Artificial Synapse Based on Back-Gated MoS<sub>2</sub> FET with High-k Ta<sub>2</sub>O<sub>5</sub> Dielectric** Neha Mohta, Roop K. Mech, Sooraj Sanjay, Muralidharan R and Digbijoy Nath; Indian Institute of Science, Bengaluru, India

Artificial neuromorphic computing, which emulates the essential functions of the biological neuron and synapse had led to the development of brain-inspired computational devices, complex algorithms, and operating principles. Two-dimensional (2D) materials have drawn much attention as ideal candidates for ultra-low power devices mimicking synaptic plasticity, future memory and neuromorphic/brain-like computing technologies. While emulating the synaptic plasticity of the neuron, the devices employing conventional oxides such as SiO<sub>2</sub> as the gate dielectric for FET-based synaptic devices suffer from higher

energy consumption and power dissipation [1]. The use of high- $\kappa$  gate dielectric allows the devices to work at lower operating voltages compared with other transistor-like synaptic devices and can well emulate the key synaptic activities including long-term plasticity, spike-amplitude dependent plasticity (SADP), and spike-timing-dependent plasticity (STDP) at a relatively lower energy budget.

In this letter, we report on a multi-layer MoS<sub>2</sub>-based low power synaptic transistor using Ta<sub>2</sub>O<sub>5</sub> as a back-gate dielectric for mimicking the biological neuronal synapse. Exfoliated MoS<sub>2</sub> is utilized as the channel material and the hysteresis in the transfer characteristics of the transistor is exploited to demonstrate Excitatory and Inhibitory postsynaptic currents, long term potentiation and depression (LTP/LTD), indirect Spike Timing Dependent Plasticity (STDP) based on single and sequential gate ( $V_g$ ) pulses respectively. The synapse had achieved a 35% weight change in channel conductance within 15 electrical pulses for negative synaptic gate pulse and 28% change for positive synaptic gate pulse. We also demonstrate complete tunability of amplitude in the synapse by Spike Amplitude dependent plasticity (SADP) at a low voltage of 4V. The use of a high- $\kappa$  dielectric allows for a lower voltage swing and hence lower power compared to using conventional SiO<sub>2</sub> and holds promise for low-power synaptic device architectures. In addition, temperature and light dependence PSC, LTP and LTD are being currently investigated and will be presented.

References:-

A. J. Arnold, A. Razavih, J. R. Nasr, D. S. Schulman, C. M. Eichfeld, and S. Das, "Mimicking Neurotransmitter Release in Chemical Synapses via Hysteresis Engineering in MoS<sub>2</sub> Transistors," ACS Nano, vol. 11, no. 3, pp. 3110–3118, 2017.

### 1:00 PM BREAK

#### 2:00 PM R06

**MoS<sub>2</sub> and WS<sub>2</sub> Films Synthesized by One-step Low-Temperature Sulfurization for RRAM Devices Applications** Martha I. Serna<sup>1</sup>, Yuqian Gu<sup>1</sup>, Taimur Ahmed<sup>2</sup>, Sivasakthya Mohan<sup>1</sup> and Deji Akinwande<sup>1</sup>; <sup>1</sup>The University of Texas at Austin, United States; <sup>2</sup>MIT University, Australia

Recent research in two-dimensional (2D) materials has boosted a renovated interest in new methods to develop large scale TMDS thin films 2D materials offer exceptional versatility to RRAM devices, and electronics structures. However, the application of these designs is limited by the area, geometry, patterning processes, and even synthesis processes that use complex precursors and high temperatures. Consequently, there is a critical need to ensure that two-dimensional 2D materials get integrated into new large area designs, and from that to jump from the laboratory and research facilities to today's electronics user devices. In this work, we developed a one thermal step synthesis strategy for a non-traditional CVD method to synthesize MoS<sub>2</sub> and WS<sub>2</sub> large areas thin films using temperatures below 700°C from metallic thin film precursors with different thicknesses. We evaluated thickness, chemical stoichiometry, and quality of layered structure using transmission electrons microscopy (TEM), X-Ray Photoelectron (XPS), and Raman spectroscopies. Our results demonstrate that the metal precursor thickness and process temperature were the crucial parameters to develop the TMDS patterns. Large scale, MoS<sub>2</sub> and WS<sub>2</sub> memristors were fabricated with a large area transfer technique and show stable nonvolatile switching and satisfying large on/off current ratio (103-105) with a good uniformity.

#### 2:15 PM R07

**(Student) Large-Area Metal Organic Chemical Vapor Deposition Growth of Few Layer MoS<sub>2</sub> and Its Controlled Sulfurization to Monolayer MoS<sub>2</sub>** Sayema Chowdhury, Anupam Roy, Chison Liu, Rudresh Ghosh, Harry Chou and Sanjay K. Banerjee; The University of Texas at Austin, United States

Two-dimensional (2D) transition metal dichalcogenides (TMDs) have garnered immense interest as a channel material for post-Si electronic devices. While currently mechanical exfoliation of tiny flakes produces the best quality crystalline TMD, scaling up to an industrial level requires an optimized growth method. Several bottom up synthesis methods are being explored for some time now, including molecular beam epitaxy (MBE), chemical vapor deposition (CVD) etc. While MBE offers greater control over film thickness and overall homogeneity, small grain size limits practical device applications [1]. The solid precursor-based atmospheric pressure CVD (APCVD) has capabilities to produce considerably larger domains but exhibits inferior control over film thickness. A relatively newer approach to CVD, namely metal organic chemical vapor deposition (MOCVD) uses metal organic precursors in the vapor phase and has successfully compensated for the shortcomings of MBE and APCVD growth, and has demonstrated large-area growth with uniform thicknesses [2]. In this work we demonstrate a two-step growth method to obtain uniform large area growth: MOCVD growth of MoS<sub>2</sub> on Si/SiO<sub>2</sub> substrates and its subsequent sulfurization to monolayer single crystal triangular domains. First, a few layer MoS<sub>2</sub> is grown via MOCVD process using the precursors molyhexacarbonyl (Mo(CO)<sub>6</sub>) and diethyl selenide (C<sub>2</sub>H<sub>5</sub>) under low pressure. The grown film is then sulfurized under ambient pressure for various durations and temperatures. An optimized sulfurization recipe yields monolayer MoS<sub>2</sub> domains with characteristics comparable to APCVD grown MoS<sub>2</sub>, as confirmed by various characterization techniques, e.g., Raman and photoluminescence (PL) spectroscopy, atomic force microscopy (AFM), scanning electron microscopy

(SEM), and X-ray photoelectron spectroscopy (XPS). AFM step height confirms that a few layer MOCVD-grown MoS<sub>2</sub> transforms into monolayer MoS<sub>2</sub> after sulfurization. Monolayer nature of the sulfurized MoS<sub>2</sub> film is further confirmed by corresponding Raman spectra showing a difference of ~20.06 cm<sup>-1</sup> between the A<sub>1g</sub> and E<sub>2g</sub> peaks, characteristic of monolayer MoS<sub>2</sub> [3]. In addition, a sharp PL peak at 1.83 eV corresponds to the direct bandgap of monolayer MoS<sub>2</sub> and a small full width at half maximum (FWHM) of 68 meV is indicative of high crystalline quality. One of the major problems associated with MOCVD growth using diethyl selenide is the presence of carbonaceous species in the resulting film. Raman analysis on an as-grown MOCVD sample shows significant presence of graphene oxide. Our two-step growth helps eradicate carbon contamination which is confirmed from Raman and XPS analyses. Our results suggest that this two-step CVD growth can significantly improve the structural and spectroscopic properties of MOCVD-grown MoS<sub>2</sub> thin films.

This work was supported by the Army Research Office (ARO) Grant # W911NF-17-1-0312 (MURI), and NSF grant ECCS-1542159.

#### References

- [1] A. Roy *et al.*, ACS Appl. Mater. Interfaces, **2016**, *8*, 7396-7402.
- [2] K. Kang *et al.*, Nature **2015**, *520*, 656-660.
- [3] H. Li. *et al.*, Adv. Funct. Mater. **2012**, *22*, 1385-1390

#### 2:30 PM R08

**Spatially Resolved Photoconductivity Imaging in MoS<sub>2</sub>/WS<sub>2</sub> Lateral Heterostructures** Samuel Berweger<sup>1</sup>, Hanyu Zhang<sup>2</sup>, Prasana Sahoo<sup>3</sup>, Benjamin Kupp<sup>1</sup>, Jeffrey Blackburn<sup>2</sup>, Obadiah Reid<sup>2</sup>, Elisa Miller<sup>2</sup>, Thomas M. Wallis<sup>1</sup>, Dmitri Voronine<sup>3</sup>, Pavel Kabos<sup>1</sup> and Sanjini Nanayakkara<sup>2</sup>; <sup>1</sup>National Institute of Standards and Technology, United States; <sup>2</sup>National Renewable Energy Laboratory, United States; <sup>3</sup>University of South Florida, United States

The strong many-body interactions in 2D transition metal dichalcogenides give rise to a rich range of optically excited bound species including excitons and carrier-bound excitons (trions). The optical properties of these materials as well as the associated excited state lifetimes and radiative decay pathways are therefore intrinsically linked to the local free carrier density. Here we map the spatial photoconductivity distribution in MoS<sub>2</sub>/WS<sub>2</sub> lateral heterostructures with spatial resolution of 10s of nm using microwave near-field microscopy (SMM, often called sMIM). Using a continuously tunable optical excitation source we find that the onset of photoconductivity agrees well with established optical bandgaps values and we observe large spatial inhomogeneities throughout the flakes studied. We find that the optoelectronic response of these flakes is dominated by persistent photoconductivity that can remain for days that originates in the MoS<sub>2</sub> regions and can increase the local carrier density by up to three orders of magnitude. We further compare our SMM imaging with spatially PL mapping, where we find excellent correlation between spatial photoconductivity distribution and the competition between trion and neutral exciton species. These results strongly caution that optical measurements of such materials do not simply passively probe their intrinsic properties, but rather can produce a new metastable charged state that is probed instead.

#### 2:45 PM R09

**Impact of Plasma Induced Defects in Epitaxial Graphene on Growth of WS<sub>2</sub>** Tanushree H. Choudhury, Shruti Subramanian, Chowdhury Ashraf, Adri van Duin, Joshua A. Robinson and Joan M. Redwing; The Pennsylvania State University, United States

Layered 2D materials have garnered huge interest due to their inherent chemical, optical and electronic properties. In addition to the individual material property, the weak inter-layer bonding, characteristic of 2D materials allows for variable stacking of a combination of these materials; forming heterostructures. These heterostructures can provide pathways to develop all 2D electronics or enhancing the novel properties of the resultant stack. Current research using transferred exfoliated flakes has demonstrated the rich landscape of possible properties and applications that these heterostructures can exhibit. However, to study these heterostructures without the hindrance of transfer process contaminants, bottom-up growth techniques which can provide pristine interfaces are needed. To understand and control the bottom-up assembly process, it is imperative to investigate the impact of defects in a layered substrate on the growth of other 2D materials. The defects can act as nucleation sites, which in turn can be used to control the density and the domain size of the growing 2D films.

In this work we investigate the effect of defects in epitaxial graphene on the growth of transition metal dichalcogenides like WS<sub>2</sub>. Epitaxial graphene was grown on on-axis 6H (0001) SiC substrate. The defect density of epitaxial graphene was controlled by exposing it to a helium plasma for different durations. The pristine and plasma treated epitaxial graphene was exposed to a H<sub>2</sub>S environment and subsequently to a WS<sub>2</sub> growth environment. The H<sub>2</sub>S treatment and WS<sub>2</sub> growth was carried out at 50 Torr at temperatures ranging between 700-1000°C. The H<sub>2</sub>S and W(CO)<sub>6</sub> precursor flow rate was maintained at 400 sccm and 5.7×10<sup>-4</sup> sccm, respectively. The results show that the defect generation, and subsequent sulfur incorporation was higher when the buffer layer was present between the SiC substrate the graphene layers. The higher defect generation is attributed to the distortion in the bonds of the top graphene layer when the interfacial layer is partially bonded to SiC. In addition, the duration of plasma treatment directly controls the nucleation density of WS<sub>2</sub> domains, which is a crucial factor for controlling the domain size. Another

key observation was that the plasma treatment modified the  $WS_2$  nucleation sites from step edges to terraces. This impact on the nucleation site was, however, temperature dependent. Additional details about the role of the buffer layer, the interaction of the defects with the precursors and the impact on the nucleation site and density will also be presented.

### 3:00 PM R10

**(Student) Growth of Manganese (IV) Selenide on Epitaxial Graphene by Thermal Vapor Selenification of Electrodeposited  $\delta$ -Phase Manganese (IV) Oxide** *Itteyyaz A. Avash*, Michael Pedowitz, Guy D. Cassuto and Kevin Daniels; University of Maryland, United States

Transitional Metal Dichalcogenides (TMD) have been the subject of much intrigue in recent years due to their curious shift of electronic, optical and magnetic properties from bulk to monolayer limit, making them uniquely qualified for various electronic, optical and magnetic applications [1]. Among these TMDs, Manganese (IV) Selenide ( $MnSe_2$ ) is of special interest as its 1T polytype has been found to display long-range magnetic ordering and high magnetic moments ( $3\mu_B$  per unit cell) near room temperature [2]. It also displays a high Curie temperature of 250K, which is tunable up to 375K via 5% biaxial strain, making it an ideal candidate for non-volatile logic data storage, low energy magnetic switching as well as various spintronic applications [3]. In this study, we utilize the chemical vapor deposition (CVD) technique to grow two-dimensional heterostructure of  $MnSe_2$  on few layers epitaxial graphene (EG) synthesized on 6H silicon carbide (SiC) substrate. Here we attempt such growth following two different CVD mechanisms: Thermal Vapor Deposition (TVD) and Thermal Vapor Selenification (TVS); and compare their outcome to choose the optimal growth strategy [4]. The CVD growth was performed in a CVD reactor with a 1" quartz CVD tube and a single heating zone. In our TVD approach, two different sets of reactants were considered. In our first attempt, powdered manganese (IV) oxide ( $MnO_2$ ) and selenium powder (Se) precursors were utilized with EG/SiC heterostructure used as the growth surface. In the second approach,  $MnO_2$  was replaced with the Manganese Acetate ( $Mn(CH_3CO_2)_2$ ) precursor to study the effect of the sublimation temperature of reactants on the growth process. Conversely, in our TVS approach,  $\delta$ -phase  $MnO_2$  is first electrodeposited on epitaxial graphene using a 0.1M solution of manganese acetate in a three-electrode electrochemical cell. This  $MnO_2$ /EG/SiC heterostructure is used as the target growth surface with Se as the lone precursor in the CVD process to bypass the low manganese adhesion issue of the TVD approach. The samples grown were characterized via Raman, SEM, AFM and EDX characterization techniques, all of which demonstrated the presence of  $MnSe_2$  growth for both TVD and TVS mechanisms. For both precursor combinations of the TVD approach, the characteristic A Raman peak of  $MnSe_2$  was visible at  $269\text{ cm}^{-1}$ , although its very low intensity (almost 40-50% of the control FTA peak of the substrate at  $203\text{ cm}^{-1}$ ) indicates extremely low grain size and yield density, a conclusion supported by the SEM and AFM images (around 0.1-0.3 $\mu\text{m}$  diameter grains). The yield was found to be slightly higher (around 300% larger grain size) for manganese Acetate compared to  $MnO_2$ . For the TVS approach, however, both  $E_g$  and  $A_g$  peaks were found to be visible (at  $145\text{ cm}^{-1}$  and  $267\text{ cm}^{-1}$  respectively) with extremely high peak intensity (around 500% of the control peak), implying significantly higher  $MnSe_2$  yield, as also evident in the AFM and SEM data characterized by an elevated deposition density along the graphene step edges. This comparative study of the two approaches clearly shows TVS to be the far superior mechanism compared to TVD for  $MnSe_2$  growth on epitaxial graphene. The TVS approach, once optimized, should result in single-crystal monolayer growth of  $MnSe_2$  heterolayer on the epitaxial graphene substrate, which in turn has the potential to be used in the future wafer-scale synthesis of  $MnSe_2$  based spintronic devices. Reference: [1] Y. Zhang, T. R. Chang, B. Zhou, Y. T. Cui, H. Yan, Z. Liu, F. Schmitt, J. Lee, R. Moore, Y. Chen, H. Lin, H. T. Jeng, S. K. Mo, Z. Hussain, A. Bansil and Z. X. Shen, *Nat. Nanotechnol.*, 2014, 9, 111–115. [2] M. Kan, S. Adhikari and Q. Sun, *Phys. Chem. Chem. Phys.* 16 (2014) 4990. [3] D. O'Hara, T. Zhu, A. Trout, A. Ahmed, Y. Luo, C. Lee, M. Brenner, S. Rajan, J. Gupta, D. McComb, and R. Kawakami, *Nano Letters* 2018 18 (5), 3125-3131. [4] H. F. Liu, S. L. Wong, and D. Z. Chi, *Chem. Vap. Deposition* 2015, 21, 241-259

SESSION S: Materials for Memory and Computation  
Session Chairs: Curt Richter and Angel Yanguas-Gil  
Session Hosts: Ke Xu and Heayoung Yoon  
Thursday Morning, June 25, 2020  
Location: ZoomRoom 5

### 11:45 AM S01

**(Student) Temperature Dependent Wake-Up Effect in Ferroelectric La Doped  $Hf_{0.5}Zr_{0.5}O_2$  Thin Films** *Furqan Mehmood*<sup>1,2</sup>, Jacob L. Jones<sup>3</sup>, Hanan A. Hsain<sup>3</sup>, Pintilie Lucian<sup>4</sup>, Cosmin M. Istrate<sup>4</sup>, Thomas Micolajick<sup>1,2</sup> and Uwe Schroeder<sup>1</sup>; <sup>1</sup>NamLab gGmbH, Germany; <sup>2</sup>TU Dresden, Germany; <sup>3</sup>North Carolina State University, United States; <sup>4</sup>National Institute of Materials Physics, Romania

In recent years ferroelectric hafnium oxide has demonstrated the potential to overcome the integration issues observed with traditional perovskite based

ferroelectric materials [1]. However, the cycling stability of ferroelectric hafnium oxide suffers from the considerably higher coercive field compared to their perovskite counterparts [2]. As a consequence doped  $HfO_2$  based ferroelectric materials suffer from field cycling instabilities. Initially the polarization increases, an effect known as wake-up and for high cycling count the polarization shows a decrease again, which is known as fatigue [3]. The final endurance is typically limited by breakdown. Recently the doping of 10 nm thin mixed  $Hf_{1-x}Zr_xO_2$  film with  $La_2O_3$  (La: HZO) was proposed to reduce leakage current and extend the field cycling endurance. However, the increased endurance was achieved at the price of a pronounced increase of the wake-up effect [4,5]. To reduce the wake-up effect the physical mechanism leading to it must be fully understood. Hence, in this work a comprehensive structural and electrical characterization is performed, and possible mechanisms impacting the wake-up in La doped HZO are discussed. We have examined  $Hf_{0.5}Zr_{0.5}O_2$  films doped with 0- 4.6 mol% of La. Grazing incidence x-ray diffraction (GIXRD) in combination with scanning and tunneling electron microscopy (SEM/TEM), Time of flight secondary ion mass spectroscopy (ToF-SIMS) as well as Piezo response force microscopy (PFM) measurement techniques are used for structural characterization of the films. The films were polycrystalline having a 10-30 nm grain size with similar domain sizes. A stabilization of the non-polar tetragonal phase for increasing La concentration is observed from the GIXRD diffractograms. Moreover, the unit cell aspect ratio extracted from the GIXRD data decreases with increasing La concentration. This is another indication of a non-polar tetragonal phase stabilization.

In general, doped  $HfO_2$  shows a phase change from a non-polar tetragonal to a polar orthorhombic phase ( $Pca2_1$ ) in temperature-dependent GIXRD during cool down. This phase change is connected to an increase in remanent polarization during cool down [6]. Therefore, temperature dependent field cycling measurements were performed from a temperature range from 80-380 K to investigate the correlation between the phase composition of the film and the wake-up effect. The La:HZO showed a strong wake-up effect at room temperature which vanished at 80 K. Accordingly, the magnitude of the wake-up effect is correlated to the amount of the non-polar phase present in the pristine sample. These results suggest a possible phase change during wake-up at room temperature. Recent results show that this would be consistent with the observed de-pinching of the hysteresis loop during the wake-up process. While effects like charge injection and charge motion can also explain the de-pinching of the hysteresis in connection with an increase of the remanent polarization during wake up [7], both phase transformation and charge injection are possible as the cause for the stronger wake-up in La doped HZO at room temperature. Based on above mentioned structural (Fig. 1- Fig. 3) and temperature dependent electrical characterization (Fig. 4 – Fig. 7) the results are summarized in a pictorial model (Fig. 8).

[1]T. S. Böscke et al. *Applied Physics Letters* 2011, 99, 102903.

[2]F. P. G. Fengler, et al. *Conference (ESSDERC)*; 2016; pp. 369–372.

[3]M. Pešić, et al. *Advanced Functional Materials* 2016, 26, 4601.

[4]F. Mehmood, et al. *Advanced Materials Interfaces* 2019, 0, 1901180.

[5]M. G. Kozodaev, et al. *Journal of Applied Physics* 2019, 125, 034101.

[6]M. H. Park, et al. *Advanced Electronic Materials* 2018, 4, 1700489.

[7]Lorenzo P. D. et al. submitted to *Phys Rev B*

### 12:00 PM S02

**(Student) Understanding the Origin of Non-Volatile Programming in  $LiNbO_2$  Memristors via Electrochemical Impedance Spectroscopy (EIS)** *Aheli Ghosh*, Bill Zivasatienraj, Alex S. Weidenbach, Timothy M. McCrone and W. Alan Doolittle; Georgia Tech, United States

The advancement of neuromorphic computing is contingent on the development of nanoscale analog electrical synapses<sup>1</sup> which are power efficient, scalable, and capable of implementing relevant learning rules to facilitate large scale neuromorphic functions. Among contemporary synaptic devices, drift-based intercalation memristors<sup>2-3</sup> have the advantage of inherent analog operation in mimicking biological synapses and achieving adaptive learning. Lithium Niobate ( $LiNbO_3$ ) based memristors have been demonstrated to exhibit conductance changes on the order of 2000% and non-binary operation with a dependence on flux-linkage<sup>4</sup>, enabling analog neuromorphic functions resembling synaptic weight updates in the neuron membrane. It has also been shown that these intercalation based  $LiNbO_3$  memristors are highly scalable with non-volatile operation at voltages as low as 150 mV for a 4  $\mu\text{m}^2$  device<sup>4</sup>.  $LiNbO_3$  based memristors are natively volatile, however, non-volatile resistance changes (programming) are implemented in these devices by using a lithium-absorbing/active contact electrode such as Ag or Al to de-lithiate the  $LiNbO_3$  channel under applied bias. The application of a negative bias on the Li-absorbing electrode moves Li ions under the active electrode and decreases device resistance by Li vacancy generation (programming) and a positive bias on the active electrode increases the device resistance by compensation of vacancies in the  $LiNbO_3$  channel (deprogramming). Electrochemical impedance spectroscopy (EIS) is a powerful characterization technique which can be used to decouple the internal dynamics of electrochemical systems and complex non-linear processes. In this work EIS is used to characterize the Li ion and hole conduction mechanisms in non-volatile  $LiNbO_3$  memristors and their evolution with programming and de-programming in these devices. EIS spectra for  $LiNbO_3$  memristors with one Li blocking Ti/Au electrode and another Li absorbing Al/Au or Ag/Au electrode were measured before and after programming as well as after deprogramming. The impedance spectra were fit

to a circuit model whose components correspond to the ionic and electronic effects in the  $\text{Li}_x\text{NbO}_2$  channel. For the Al active electrode non-volatile memristor, the ionic component of impedance changes by an order of magnitude as the device is programmed and de-programmed, while the electronic component is relatively unchanged. This suggests that the Li ion motion in the device channel and resulting ionic current dominate the resistance modulation mechanism in these devices. For memristors with Ag as active electrode, a five-component circuit is necessary to model the EIS spectra with additional contribution of the ionic effects at the  $\text{Li}_x\text{NbO}_2/\text{Ag}$  interface. The Ag electrode memristors have larger resistance changes indicating the additional change in resistance is dominated by interfacial components not prominent in the Al electrode devices. In both devices, the ionic component in impedance is primarily modified during programming. The previous assumption that channel resistance is modulated by the population of Li vacancies may not apply to these devices because unlike stoichiometric  $\text{LiNbO}_3$  where a small change in %Li vacancies induces a large change in resistivity, significant %Li vacancy changes result in small changes in device resistivity. This study helps gain insight into the electronic and ionic contribution to the non-volatile resistance modulation in  $\text{LiNbO}_3$  memristors and design highly scalable multi-functional memristive systems for future applications in neuromorphic computing. 1. Q. Wan et al., *Adv. Mater. Technol.* **4** 1900037 (2019). 2. Z. Wang, et al., *Nature Mater* **16**, 101–108 (2017). 3. E. J. Fuller et al., *Adv. Mater.*, **29**, 1604310 (2017). 4. B. Zivasatienraj et al., Temporal Versatility from Intercalation-based Neuromorphic Devices Exhibiting 150 millivolt Non-volatile Operation (Under Review). 5. W.E. Henderson et al., *J. Cryst. Growth* **324**, 134 (2011).

### 12:15 PM S03

**Reduction Reactions and Phase Transformations in  $\text{Nb}_2\text{O}_5$  Films Deposited by Atomic Layer Deposition** Mark E. Twigg, Alexander Kozen, Laura Ruppalt, Sharka Prokes and Hans Cho; U.S. Naval Research Laboratory, United States

Phase change materials are of increasing interest, due to their ability to passively change properties when exposed to external stimuli (i.e. temperature, strain, composition changes). Such materials are expected to find applications in next generation sensors and analog neuromorphic computing. Of particular interest are thermochromic phase change materials capable of the insulator-to-metal transition (IMT), an important attribute for components of neuromorphic circuit devices.  $\text{NbO}_2$  undergoes IMT at 808C, thereby enabling stable operation in circuits and devices. The route to achieving a functional  $\text{NbO}_2$  film of suitable crystalline quality, however, is subject to the ability to control film growth and annealing. In order to examine the impact of annealing temperature, duration, and atmospheric chemistry on the phase selectivity of  $\text{NbO}_2$ , thin films of  $\text{Nb}_2\text{O}_5$  have been grown by atomic layer deposition (ALD), subsequently annealed in a reducing atmosphere, and analyzed using transmission electron microscopy (TEM). Films of composition  $\text{Nb}_2\text{O}_5$  were deposited by ALD on (001) Si substrates and were subsequently subjected to 850C and 1000C anneals in forming gas, resulting in polycrystalline films. Subjecting these films to a 850C anneal resulted in the formation of floret-shaped regions within the film. Cross-sectional TEM (XTEM) was then used in order to determine the effect of annealing and reduction on film structure and morphology. This analysis revealed the presence of B- $\text{Nb}_2\text{O}_5$  and T- $\text{Nb}_2\text{O}_5$  phases in the matrix, as well as R- $\text{NbO}_2$  in reduced floret-shaped regions. The 1000C anneal was found to complete the reduction process, resulting in the insulator-to-metal transition (IMT) capable T- $\text{NbO}_2$  phase throughout the film. The crystal phases in the matrix after the 850°C anneal corresponded with large unit cells: T- $\text{Nb}_2\text{O}_5$  phase with space group Pbam (#55) and orthorhombic unit cell with lattice parameters  $a=0.6170$  nm,  $b=2.825$  nm,  $c=0.3928$  nm; the B- $\text{Nb}_2\text{O}_5$  unit cell is monoclinic corresponds to the space group C2/c (#13) with lattice parameters  $a=1.273$  nm,  $b=0.488$  nm,  $c=0.556$  nm, and  $\beta=105.1$  degrees. The R- $\text{NbO}_2$  phase for the florets corresponds to the space group P4/2/mmm (#136) as has a relatively small rutile-type tetragonal unit cell with lattice parameter  $a=0.455$  nm and  $c=0.286$ , and containing 2 formula units. The R- $\text{NbO}_2$  phase is closely related to the B- $\text{Nb}_2\text{O}_5$  phase, which is equivalent to an array of distorted R- $\text{NbO}_2$  subunits translated by crystallographic shear (CS). The phase brought out by the 1000°C anneal, T- $\text{NbO}_2$ , is also closely related to R- $\text{NbO}_2$ , and has the space group I4 $1/a$  (#88) and a large tetragonal unit cell with lattice parameters  $a=0.5981$  and  $c=1.3695$  nm, consisting of 32 formula units, or equivalently, 16 R- $\text{NbO}_2$  unit cells. The crystal phases were determined via the analysis of selected area diffraction patterns (SADPs), in part using the crystallographic relationship between the R- $\text{NbO}_2$  and T- $\text{NbO}_2$  unit cells to determine equivalent zone axes. ALD films of composition  $\text{Nb}_2\text{O}_5$  were also deposited on electron-transparent SiN membranes and then subjected to 550C and 1000C anneals. Here the 550°C anneal induced the B- $\text{Nb}_2\text{O}_5$  and T- $\text{Nb}_2\text{O}_5$  phases without generating the R- $\text{NbO}_2$  phase. The 1000C anneal of the films deposited on SiN membranes retained B- $\text{Nb}_2\text{O}_5$  while generating the R- $\text{NbO}_2$  phase, but without bringing the process to completion and inducing the T- $\text{NbO}_2$  phase. The ability of the reducing annealing treatment to induce the T- $\text{NbO}_2$  phase for  $\text{Nb}_2\text{O}_5$  film deposited on (001) Si substrates, while stopping short of this transition for films deposited on SiN membranes, suggests the importance of the  $\text{SiO}_2$  layer on the Si substrate in contributing to the reduction reaction that results in the technologically important IMT-capable T- $\text{NbO}_2$  phase.

### 12:30 PM S04

**Photoconductivity without Photons—Defect Level Switching for Highly-Nonlinear and Hysteretic Electronic Devices** Rafael Jaramillo; Massachusetts Institute of Technology, United States

Nonlinear and hysteretic electrical devices are needed for applications from circuit protection to next-generation computing. Widely-studied devices for resistive switching are based on mass transport, such as the drift of ions in an electric field, and on collective phenomena, such as insulator-metal transitions. We ask whether the large photoconductive response known in many semiconductors can be stimulated in the dark and harnessed to design electrical devices. We design and test devices based on photoconductive CdS, and our results are consistent with the hypothesis that resistive switching arises from point defects that switch between deep- and shallow-donor configurations: defect level switching (DLS). We demonstrate devices based on the DLS mechanism that are in a high-conductivity state as-fabricated at equilibrium and that switch to a low-conductivity state at forward bias by injecting electrons into the  $n$ -type active layer. We also demonstrate devices using the same active layer but using different contact layers and based on a traditional interface mechanism, that are in a low-conductivity state as-fabricated and that switch to a high-conductivity state at forward bias. This new electronic device design principle - *photoconductivity without photons* - is founded on well-understood semiconductor physics, it leverages decades of research on photoconductivity and defect spectroscopy, and does not rely on mass transport or collective phenomena. It is easily generalized and will enable the rational design of new nonlinear, hysteretic devices for future electronics.

### 12:45 PM S05

**(Student) Percolation with Plasticity (PWP) Materials for Multi-Valued Memory** Victor Karpov, Maria Patmiou, Gursel Serpen and Diana Shvydka; The University of Toledo, United States

Nonvolatile memory cells are often based on disordered materials, noncrystalline or compound, with percolation conduction. Relevant for memory applications are percolation materials with plasticity (PWP), [1] i. e. capable of changing their resistances in response to electric bias. They include metal oxides and chalcogenide compounds used respectively with resistive random-access memory (RRAM)[2] and phase change memory (PCM),[3] granular metals,[4] and nanocomposites.[5] The concept of exponentially strong non-ohmicity earlier known for dc currents in structurally stable percolations systems, is extended in our work over the case of pulse perturbations in PWP materials. The standard treatment (Fig. 1) assumes dc currents continuous through the percolation cluster bonds and resulting in significantly different local electric fields in the local regions of exponentially varying resistivities. The voltage concentrates on most resistive elements producing exponentially strong non-ohmicity. [6] The distinct features introduced here are: (1) Local electric fields in percolation bonds strong enough to structurally modify the underlying material with nonvolatile changes in its local resistivities. (2) Multi-port topology allowing for exponentially large combinatorial number of pathways and possible records in the system (Fig. 2). (3) Pulse-shaped electric bias, which is characteristic of nonvolatile memory operations and qualitatively similar to that of spike-timing-dependent-plasticity (STDP) central to the functionality of neural networks. From the practical standpoint, these features pave a way to multi-valued memory operated in the pulse regime and implementable with a variety of PWP materials. Our analysis is based on the division of all microscopic resistors into two groups: fast and slow relative to the pulse length. The fast group operates like the non-ohmic resistors in dc regime. However slow resistors behave like capacitors and do not accommodate any significant voltages in the pulse regime, which can be illustrated with simplistic models of Fig. 3 and 4 and related PSPICE modeling in Fig. 5. As a result, our theory predicts the non-ohmic currents in pulse regime with current-voltage characteristics analytically described in Fig. 6. The concept of slow resistances operating in capacitive mode will apply to any percolation materials in pulse regime and can be tested experimentally on a variety of systems. As applied to PWP, our consideration predicts that, during pulse time, a significant part of the entire voltage accommodates in the strongest microscopic resistor triggering its switching to the low resistive states thus creating a stepwise change in the bond resistance. The next pulse will similarly switch the second strongest resistor, etc. resulting in a sequence of incremental resistance changes illustrated in Fig. 7. These stepwise changes in the logarithm of macroscopic resistances of PWP materials can be used for multivalued memory. In conclusion, we have developed a theory of pulse nonohmic transport in macro-bonds of percolation with plasticity clusters. We have shown how voltage pulses can trigger subsequent multiple switching events in microscopic regions of those macro-bonds incrementally changing the logarithms of their resistances. The latter prediction paves a way to a class of superior multi-valued memory systems implementable with a variety of materials exhibiting percolation conduction.

#### REFERENCES

- [1] M. Patmiou, et al, *Appl. Phys. Lett.* **115**, 083507 (2019); [2] M. Lanza, , *Materials* **7**, 2155-2182 (2014); [3] A. Sebastian, et al *J. Phys. D: Appl. Phys.* **52**, 44 (2019); [4] I. A. Gladskikh, et al, *Opt. Technol.* **81** 280 (2014). [5] Y. Song, et al, , *Scientific Reports*, **6**, 3967 (2016); [6] B. I. Shklovskii, *Soviet Physics: Semiconductors*, **13**, 53 (1979)

### 1:00 PM BREAK

SESSION T: Electronic Materials for Bio  
Session Chair: Curt Richter  
Session Hosts: Ke Xu and Heayoung Yoon  
Thursday Afternoon, June 25, 2020  
Location: ZoomRoom 5

#### 2:00 PM T01

**A Hybrid Multimodal Surface-Depth Electrode for Electrophysiological and Multi-Photon Brain Activity Mapping** [Keundong Lee](#)<sup>1,2</sup>, Martin Thunemann<sup>1</sup>, Lorraine Hossain<sup>1</sup>, Youngbin Tchae<sup>1</sup>, Jihwan Lee<sup>1</sup>, Sang Heon Lee<sup>1</sup>, Yun Goo Ro<sup>1</sup>, Gyuchul Yi<sup>2</sup>, Anna Devor<sup>3</sup> and Shadi Dayeh<sup>1</sup>; <sup>1</sup>University of California, San Diego, United States; <sup>2</sup>Seoul National University, Korea (the Republic of); <sup>3</sup>Boston University, United States

One of the grand challenges in neuroscience is to understand how neuronal activity is orchestrated to produce function. Single modality technologies offer either high spatial or high temporal resolution and with varied degrees of coverage. Multimodal approaches that can probe the brain's activity from the surface, at depth, and with high spatiotemporal resolution are believed to yield results that may complete our understanding of behavior and function. We report the seamless integration of the electrical and optical modalities for comprehensive and interactive 3D probing and manipulation of cortical neuronal activity and optogenetic (OG) stimulation/inhibition. Our "Windansee" technology, named after the famous Windansea beach in La Jolla, will replace the current cranial glass windows providing measurements of the extracellular local field potential (LFP) and multiunit activity (MUA), as well as a see-through optical access. The Windansee allows us to obtain depth-resolved LFP/MUA information, which can be used for estimation of spiking and synaptic activity in specific cortical neuronal populations, while simultaneously sampling electrical neuronal activity from the cortical surface and implementing single/multiphoton optical imaging and optogenetic stimulation/inhibition in behaving animals.

We leveraged microelectromechanical systems (MEMS) surface micromachining techniques to develop the hybrid surface-depth electrode. The depth electrode is to be maintained inside the cortex chronically and should not block optical access. Therefore, both the depth and surface electrodes need to be flush with the cortical surface: The integrated depth in our device utilizes an inserter with a small neck-region (narrow-constriction) of SU8 that is sheared (thermally or mechanically) to separate the handle from the implanted portion of the depth electrode. The device was implanted chronically in mice for several weeks and we recorded electrophysiological signals and obtained single/multiphoton optical images in awake animals. We will report on recording of brain activity with cellular resolution from the cortical surface to depth in mice. Significantly, strong modulation of single unit activity recordings by whisker and optogenetic stimuli is demonstrated as well as the modulation of local field potential.

#### 2:15 PM T02

**(Student) GaN-Based Immuno-FETs for Cyanobacterial Toxin Detection for Environmental Monitoring and Clinical Applications** [Paul Bertani](#), Seungjun Lee, Hao Yang, Jiyoung Lee and Wu Lu; The Ohio State University, United States

Algal blooms (also known as cyanobacteria) have become a significant problem in the area of environmental health and water safety. Such blooms have caused a great deal of concern due to the increased production of a variety of toxins such as saxitoxins, cylindrospermopsins, anatoxin-a and perhaps the most prevalent, microcystins. Amongst these, microcystin-LR (MC-LR) has been identified as one of the most toxic and the concerning for public health. Conventionally, methods such as ELISA, PCR, and LC-MS are used to evaluate toxin levels in environmental water samples, but while effective, these approaches are imperfect and can be costly, time consuming, and have a limited dynamic range.

To further bolster the information provided by the above methods and improve sampling efficiency, here we present the use of a bio-FET "Lab on Chip" style device based on an AlGaIn/GaN semiconductor platform. Each chip can detect the presence of Microcystin-LR (MC-LR) and other cyanobacterial toxins depending on device functionalization. Each chip is approximately 2 cm x 2 cm and operates by exploiting the intrinsic charge attached to cyanobacterial toxins. Utilizing the field effect, the signal is then proportional to the amount of toxin present in a given sample. Sensor surface functionalization is performed using silane chemistry to link anti-toxin antibodies (such as "ADDA" for MC-LR) to the surface. Following the complete surface functionalization, a "base line" signal is measured to be used as a floor and account for charge unassociated with the analyte (cyanotoxins). Purified toxin is mixed with DI water to evaluate sensing performance for specific concentrations and determination of a dynamic range. Cyanobacterial toxin presence and concentration are typically investigated using water samples, but here we also look at physiological samples such as serum and urine for clinical applications. Samples in spiked water samples and "real" lake water samples with similar concentrations (confirmed by ELISA) are compared to prove device selectivity and ability to separate desired analytes from other elements that might be present and a difference of between 3 and 9% is noted. Real-time tests are also

performed to show sensing time and current saturation is observed after 2-5 minutes. Sensors show the ability to reliably detect toxin as low as 0.05 – 0.1 ng/L. For reference, the EPA health advisory standards, which sets the safety limit of microcystins, anatoxin-a, cylindrospermopsins, and saxitoxin in drinking water at 1.6, 20, 3.0, and 0.2 µg/L for adults respectively<sup>1</sup>. For children under 6 years or age, the limits for microcystins and cylindrospermopsins are considerably lower at 0.3 and 0.7 µg/L respectively. <sup>1</sup> U.S. Environmental Protection Agency Office of Water, Drinking Water Health Advisory for the Cyanobacterial Toxins, June 2015.

#### 2:30 PM T03

**Scaling Microelectrode Arrays for Multi-Thousand Channel Human Brain Mapping** [Youngbin Tchae](#)<sup>1</sup>, Andrew Bourhis<sup>1</sup>, Daniel Cleary<sup>1</sup>, Ahmed Raslan<sup>2</sup> and Shadi Dayeh<sup>1</sup>; <sup>1</sup>University of California, San Diego, United States; <sup>2</sup>Oregon Health & Science University, United States

Clinical mapping of electrophysiological activity in the human brain is routinely used for delineating margins between functional and pathological tissue, for therapeutic applications and brain-machine interfaces. Trade-offs between spatial resolution and cortical coverage, specificity in recording and contact impedance, conformity/compliance to brain curvature/movement and complexity of grid designs often limit the scalability and the potential use of brain mapping electrodes. In this work, we developed a scalable manufacturing process for advanced thin-film microfabrication on 7"×7" square plates to realize human-compatible electrocorticography surface grids with thousands of channels. The 7" long cortical electrodes together with our serializable compact connector overcome challenges associated with the required large separation between the sterile surgical field and the non-sterile acquisition electronics enabling reliable intraoperative recordings from patients undergoing neurosurgical resections. The electrode diameter and pitch were adjustable providing a spatial resolution from micrometer scale to millimeter scale. PEDOT:PSS and Pt nanorod electrodes were used as the contact materials and demonstrated low impedances at frequencies of interest for brain activity mapping.

We demonstrate a few case examples of recording functional and pathological activity from the human brain revealing sub-mm fine functional organization. We recorded from awake patients undergoing tumor resection while performing motor tasks with our grid placed on motor cortex. The geometry of the array included a 32×32 array with multiple 30µm diameter contacts and 1mm spacing extending over a distance of 32mm×32mm. Motion sensors and an accelerometer were attached to a glove worn by the patient who performed a finger flexion/contraction task between thumb and the other four fingers. The motion signals were time-locked to the recordings from the 1024 grids using our custom-made intraoperative monitoring system. Both local field potentials (LFPs) and broadband high gamma activity (HGA) showed distinctive neural correlates of fine-motor movements for different fingers when compared to baseline. These results with our high-density grids offer us glimpse of the functional organization of motor functions in the human cortex.

#### 2:45 PM T04

**(Student) Recording Electrophysiological Activity from the Human Spinal Cord for Neuromonitoring During Surgical Resection** [Samantha M. Russman](#)<sup>1</sup>, Daniel Cleary<sup>2,3</sup>, Joel Martin<sup>2,3</sup>, Youngbin Tchae<sup>2</sup>, Sang Heon Lee<sup>2</sup>, Andrew Bourhis<sup>2</sup>, Jeffrey Gertsch<sup>2</sup>, Sharona Ben-Haim<sup>3</sup>, Joseph Ciacci<sup>3</sup> and Shadi A. Dayeh<sup>2</sup>; <sup>1</sup>University of California, San Diego, United States; <sup>2</sup>Integrated Electronics and Biointerfaces Laboratory, United States; <sup>3</sup>Division of Neurosurgery, United States

Intraoperative neuromonitoring is a standard clinical practice in spinal cord surgeries as it prevents neural injury. Neuromonitoring is conducted by recording motor evoked potentials (MEPs) or somatosensory evoked potentials (SSEPs) in the spinal cord upon either (1) peripheral nerve stimulation or (2) transcranial electrical stimulation<sup>[1]</sup>. Currently, 0.5 mm - 1 mm thick clinical strip electrodes with 6-8 contacts that are 1 cm spaced and are ~3 mm in diameter are used for neuromonitoring. The thick substrate of these electrodes prevents intimate contact with the spinal tissue and reduces recording sensitivity, resulting in high stimulation thresholds. Furthermore, the small number of contacts and their large spacing limits the spatial resolution of these recordings.

Here we report and discuss the applicability of thin-film conformal microelectrodes for neuromonitoring during spinal cord surgical resection. We recorded from the pial surface of the spinal cord of a patient undergoing an intramodular tumor resection during both transcranial and peripheral nerve stimulation. In this experiment, we used a 128-channel array with 4 columns of 32 contacts 30 µm in diameter with 180 µm pitch. Our electrodes recorded evoked potentials at lower threshold currents (2 mA) for peripheral nerve stimulation compared to higher thresholds (16 mA) necessary for the strip clinical electrode. The thin and conformal substrate, along with the low impedance of our electrodes, permitted us to record minute activity from the spinal cord that is otherwise missed with standard clinical electrodes. The successful use of thin-film microelectrode arrays has potential to transform intraoperative neuromonitoring by allowing high resolution recording of SSEPs and MEPs in the spinal cord at lower stimulation thresholds. Moreover, in the future, we envision that our thin-film microelectrode arrays could also be applied to treat spinal cord injury (SCI). Our lab has recently shown that subdural microelectrode arrays overcome the limitations of their epidural

counterparts and also provide additional benefits, including lower initiation thresholds for targeted stimulation. More specifically, not only are stimulation thresholds lowered by submerging the microelectrodes in the subdural space, but also the critical diameter for neurophysiological initiation was found to be smaller, with this critical diameter being for  $\leq 20\mu\text{m}$  ventral stimulation and  $\geq 40\mu\text{m}$  dorsal stimulation. As a result, applying this technology to develop a soft spinal cord implant is within reach and will be discussed in this talk.

[1] Sala, F. et al. Surgery for intramedullary spinal cord tumors: the role of intraoperative (neurophysiological) monitoring. *Eur Spine J* (2007) 16(Suppl 2): 130. [2] Ganji, M. et al. Selective Formation of Porous Pt Nanorods for Highly Electrochemically Efficient Neural Electrode Interfaces. *Nano letters* 19, 6244-6254 (2019).

SESSION U: Solar Cell Materials and Devices  
Session Chair: Mark Wistey  
Session Hosts: Mona Ebrish and Minjoo Lee  
Thursday Morning, June 25, 2020  
Location: ZoomRoom 6

### 11:45 AM U01

**(Student) Effects of Rapid Thermal Annealing on Metamorphic InGaAs and InGaP Grown by Molecular Beam Epitaxy** Mijung Kim<sup>1</sup>, Yukun Sun<sup>1,2</sup>, Brendan Eng<sup>1</sup>, Ryan D. Hool<sup>1</sup> and Minjoo L. Lee<sup>1</sup>; <sup>1</sup>University of Illinois at Urbana-Champaign, United States; <sup>2</sup>Yale University, United States

Metamorphic (MM) III-V junctions serve a critical role in 47%-efficient six-junction (6J) concentrator solar cells, which currently hold the record for highest photovoltaic power conversion efficiency. MM materials are also highly promising for 2J solar cells, and a MM 1.7 eV  $\text{In}_{0.63}\text{Ga}_{0.37}\text{P}/\text{MM}$  1.1 eV  $\text{In}_{0.15}\text{Ga}_{0.85}\text{As}$  tandem has the potential for 37-44% efficiency under the AM1.5G spectrum. Despite the near-optimal spectral matching that can be achieved in MM solar cells, their performance is limited by threading dislocations originating from lattice-mismatched growth. While numerous device studies of MJSCs employing MM junctions have been published, relatively little has been reported on the properties of the individual materials. In this work, we grew MM 1.1 eV  $\text{In}_{0.15}\text{Ga}_{0.85}\text{As}$  (MM InGaAs) and MM 1.7 eV  $\text{In}_{0.63}\text{Ga}_{0.37}\text{P}$  (MM InGaP) on  $\text{In}_{0.49}\text{Ga}_{0.51}\text{P}$  GaAs step-graded buffers (InGaAs GBs) by solid-source molecular beam epitaxy (MBE) and show that the carrier lifetimes of both are significantly improved by rapid thermal annealing (RTA). Remarkably, the lifetime of MM InGaP is shown to exceed that of lattice-matched  $\text{In}_{0.49}\text{Ga}_{0.51}\text{P}$  (LM InGaP) grown in the same MBE system, showing potential for solar cells with improved dislocation tolerance.

InGaAs GBs were grown on GaAs at a substrate temperature ( $T_{\text{sub}}$ ) of 500°C with a grading rate of 0.78%/μm. The InGaAs GBs consisted of 6 compositionally-graded steps from  $x=0.03$  to 0.19, and the final two layers were an  $\text{In}_{0.19}\text{Ga}_{0.81}\text{As}$  overshoot layer and an  $\text{In}_{0.15}\text{Ga}_{0.85}\text{As}$  cap; reciprocal space mapping showed ~95% relaxation for the cap layer. Electron channeling contrast imaging (ECCI) surveys revealed a threading dislocation density (TDD) of  $0.7\text{-}1.0 \times 10^6 \text{ cm}^{-2}$ , which is comparable to the lowest reported values at this lattice constant. Using these low-TDD InGaAs GBs as a platform, we grew a MM  $p$ -InGaAs double heterostructure (DH) at  $T_{\text{sub}} = 500^\circ\text{C}$  and a MM  $p$ -InGaP DH at  $T_{\text{sub}} = 460^\circ\text{C}$  (both with  $p_o \sim 1 \times 10^{17} \text{ cm}^{-3}$ ) to investigate the quality of the 1.1 eV and 1.7 eV materials at the same lattice constant. The nominally lattice-matched barrier layers used for the MM  $p$ -InGaAs and  $p$ -InGaP DHs were  $\text{In}_{0.63}\text{Ga}_{0.37}\text{P}$  and  $\text{Al}_{0.615}\text{In}_{0.385}\text{P}$ , respectively. We then performed steady-state photoluminescence (SSPL) and time-resolved PL (TRPL) studies after different RTA conditions.

The integrated SSPL intensity of MM  $p$ -InGaAs DHs increased up to 2× with annealing at 800°C for 30 s, while TRPL lifetimes ( $\tau_{\text{TRPL}}$ ) were improved 1.3× from 8.5 ns to 11 ns. Although this  $\tau_{\text{TRPL}}$  is 1.7× shorter than that of lattice-matched  $p$ -GaAs DHs grown in our MBE, we expect that efficient MM InGaAs solar cells can nonetheless be realized using these materials. MM  $p$ -InGaP DHs showed dramatic enhancements in SSPL intensity and lifetime after RTA, with an integrated SSPL intensity increase of 23× after a 1000°C 1 s RTA.  $\tau_{\text{TRPL}}$  of the MM  $p$ -InGaP DH increased from 1 ns to 4 ns with RTA, which is 2× longer than the  $\tau_{\text{TRPL}}$  of similarly RTA'd LM  $p$ -InGaP DHs (i.e. nominally dislocation-free) grown in our MBE. Considering that we have recently demonstrated LM InGaP solar cells with open-circuit voltages comparable to the best reported values for any growth technique, the improved lifetime of MM InGaP indicates great potential for dislocation-tolerant solar cells. In conclusion, we showed that the material quality of MBE-grown MM InGaAs and MM InGaP can be greatly improved through RTA, indicating great promise for high-performance solar cells. The relatively long lifetime of MM  $p$ -InGaP warrants further investigation on the combined effects of composition, doping, and annealing on minority carrier lifetime in the presence of dislocations.

### 12:00 PM U02

**(Student) Theoretical Evaluation of DBR Structures for Improving Tolerance to Threading Dislocations in GaAsP/Si Tandem Solar Cells** Daniel L. Lepkowski, Tal Kasher, Tyler Grassman and Steven A. Ringel; The Ohio State University, United States

GaAsP/Si tandem solar cells are a potentially attractive alternative to incumbent Si technologies due to the potential for higher efficiency, while still leveraging existing Si PV manufacturing infrastructure. These devices, at present, are limited in performance by elevated threading dislocation densities (TDD). However, even at target TDD levels of  $\sim 1 \times 10^6 \text{ cm}^{-2}$ , recombination associated with these spatially-localized defects results in a non-negligible reduction of the minority carrier diffusion length ( $L_p$ ) in the GaAsP top cell, which limits both the  $J_{\text{sc}}$  and  $V_{\text{oc}}$  of the cell. Therefore, strategies that improve device performance while working within the constraints placed by undesirable transport properties will likely be required to achieve the highest efficiency cells.

This work computationally explores the efficacy of an epitaxially-integrated distributed Bragg reflector (DBR) behind the GaAsP top cell to improve the optical path length of near band edge photons, thereby allowing for a reduction in the thickness of the GaAsP top cell. A thinner base layer should provide improved minority carrier collection probability by reducing the total width of undepleted material. These effects have been modeled using an optical simulation tool (FilmStar) and an in-house Hovel's model-based quantum efficiency simulator based on separately calculated photogeneration and collection probability profiles. Internal quantum efficiency curves from experimentally demonstrated devices at both  $1\text{-}2 \times 10^7 \text{ cm}^{-2}$  TDD ("high TDD" case) and  $1\text{-}2 \times 10^6 \text{ cm}^{-2}$  TDD ("target TDD" case) were fitted to extract relevant transport properties and used throughout this work.

First, the efficacy of an ideal rear reflector structure, which reflects all in-band photons and transmits all out-of-band photons, was explored. The use of this structure improved  $J_{\text{sc}}$  by 1.25 mA/cm<sup>2</sup> and reduced the optimal base thickness by 0.75 μm for the high TDD case. For the target TDD case, the  $J_{\text{sc}}$  is improved by 0.81 mA/cm<sup>2</sup>, and the base thickness can still be reduced by 0.50 μm. These promising results led to the development of various *practical* DBR structures that attempt to mimic this ideal case.

Initially, 10 and 15 period DBR structures using GaInP/AlInP bilayers were explored. However, the narrow band reflectance profile and high degree of out-of-band reflectance resulted in sub-par results. Instead, the use of combination DBR structures, wherein multiple DBRs with different center wavelengths are stacked upon each other, was more effective. Two such structures were designed and simulated: a stack of three DBRs with 10 periods each (" $3 \times 10$ ") and a stack of two DBRs with 15 periods each (" $2 \times 15$ "). These structures were able to create more broadband reflectance and reduce out of band reflectance due to a reduction in coherence, while maintaining high peak reflectivity (>95%). The thickness of the designed DBR structures was limited to < 3 μm due to the epitaxial thickness constraints present in the GaAsP/Si materials system (~8 μm total). The  $2 \times 15$  DBR resulted in a current improvement of 0.44 mA/cm<sup>2</sup> for the target TDD case, and 0.90 mA/cm<sup>2</sup> for the high TDD case. The  $3 \times 10$  DBR structure performed slightly better than the  $2 \times 15$  in the high TDD case ( $J_{\text{sc}}$  enhancement of 0.92 mA/cm<sup>2</sup>) due to a greater degree of broadband transmission present when using a thinner base. In the target TDD case the  $3 \times 10$  slightly underperformed the  $2 \times 15$ . Nevertheless, while neither of these structures have been largely optimized beyond initial cursory examination, they still exhibit the potential for at least a 1.5% absolute improvement in III-V/Si tandem efficiency in the high TDD case. This value is an underestimate as it does not include potential improvements to fill factor resulting from reduced voltage-dependent collection losses.

Overall, these structures demonstrate promise in providing a methodology for designing around elevated TDD and less than desirable minority carrier transport properties in GaAsP/Si tandems.

### 12:15 PM U03

**(Student) Control of Te Doping for InGaP Solar Cells Grown by MBE** Brian Li<sup>1</sup>, Yukun Sun<sup>2,1</sup>, Ryan D. Hool<sup>3</sup> and Minjoo L. Lee<sup>1</sup>; <sup>1</sup>University of Illinois, Urbana-Champaign, United States; <sup>2</sup>Yale University, United States; <sup>3</sup>University of Illinois at Urbana-Champaign, United States

The use of group-VI dopants is uncommon in III-V solar cells grown by both molecular beam epitaxy (MBE) and metalorganic vapor phase epitaxy (MOVPE) due to complications such as surface segregation and memory effects. However, the highest efficiency (Al)InGaP solar cells reported to date were grown by MOVPE with a Se-doped n-type emitter, suggesting potential advantages over traditional Si doping. To date, there have been no reports on group-VI doping for (Al)InGaP solar cells by MBE; GaTe is a commonly used dopant source in III-V MBE, while Se is typically avoided due to its high vapor pressure. In this work, we investigated Te incorporation in n-InGaP grown by MBE and observed that both Te "pre-dosing" and low substrate temperature ( $T_{\text{sub}}$ ) are important to suppress Te surface segregation and achieve uniform doping. We then demonstrated the first MBE-grown InGaP solar cells with a Te-doped emitter, attaining higher efficiency than cells with a conventional Si-doped emitter due to improved short-circuit current density ( $J_{\text{sc}}$ ). All samples were grown by MBE using a valved cracker cell to supply  $\text{P}_2$  and effusion cells for Ga, In, and Al; Be served as the p-type dopant, and either Si or GaTe served as the n-type dopant. To study Te incorporation, we grew InGaP samples at  $T_{\text{sub}}$  values of 420°C and 460°C with a target doping of  $1.7 \times 10^{18} \text{ cm}^{-3}$  and

inserted a Te pre-dose before growth by depositing  $\sim 0.05$  monolayers of GaTe under  $P_2$  overpressure. Doping profiles were estimated from iterative van der Pauw/Hall effect measurements and HCl etching. InGaP solar cells were grown with n-type emitter regions doped by Si or Te and fabricated using standard procedures. Despite the use of  $T_{\text{sub}} < 500^\circ\text{C}$ , we found that Te segregation in MBE-grown InGaP can be strong and similar to reports of MOVPE-grown InGaP at  $T_{\text{sub}} = 570\text{--}670^\circ\text{C}$ . In a 1000 nm sample grown at  $460^\circ\text{C}$ , initial Hall measurements indicated doping to be 96% of the target value. However, the doping profile was non-uniform, ranging from  $\sim 5 \times 10^{16} \text{ cm}^{-3}$  during initial growth to  $> 6 \times 10^{18} \text{ cm}^{-3}$  near the surface. Next, we grew 500 nm samples at  $460^\circ\text{C}$  and  $420^\circ\text{C}$  to investigate the combined effects of thickness and  $T_{\text{sub}}$  on doping. While the  $460^\circ\text{C}$  sample only reached 14% of the target value, ostensibly due to strong surface segregation, the  $420^\circ\text{C}$  sample reached 75% and exhibited a relatively uniform profile. Photoluminescence (PL) intensity of the  $420^\circ\text{C}$  InGaP:Te sample was comparable to  $460^\circ\text{C}$  InGaP:Si, while mobility improved significantly from 534 to  $695 \text{ cm}^2/\text{Vs}$ . To study the effects of pre-dose on Te incorporation, a 100 nm sample was grown at  $420^\circ\text{C}$  without a pre-dose and compared to a pre-dosed sample etched down to 110 nm. The pre-dose enabled a more abrupt “turn-on” of doping, which is critical for solar cells that employ a thin (50–100 nm) emitter. We grew and characterized three InGaP solar cells: one with an InGaP:Te emitter grown at  $420^\circ\text{C}$ , a second with an InGaP:Te emitter at  $460^\circ\text{C}$ , and a third with an InGaP:Si emitter at  $460^\circ\text{C}$  (control). External quantum efficiency (EQE) of the solar cell with  $420^\circ\text{C}$  InGaP:Te emitter was notably improved at shorter wavelengths compared to the control cell, with a  $\sim 5.4\%$  relative improvement in EQE-derived  $J_{\text{sc}}$  from 9.60 to  $10.15 \text{ mA}/\text{cm}^2$ . The improved short-wavelength response indicates increased minority hole diffusion length in the InGaP:Te emitter, which can be attributed to higher carrier lifetime and/or lower interface recombination velocity. In lighted I-V measurements, the fill factor (FF) and open-circuit voltage ( $V_{\text{oc}}$ ) also improved, enabling the cell with a  $420^\circ\text{C}$  InGaP:Te emitter to attain an efficiency of 10.8% versus 9.8% from the control. In contrast, the cell with InGaP:Te emitter grown at  $460^\circ\text{C}$  exhibited  $< 1\%$  efficiency due to poor n-type doping, showing the importance of managing Te incorporation behavior. Our findings indicate that Te is a promising alternative dopant to Si for higher-efficiency MBE-grown InGaP and AlInGaP solar cells.

#### 12:30 PM U04

**(Student) Development of Low-TDD GaP/Si Virtual Substrates via Correlation of Dislocation Dynamics, Electron Channeling Contrast Imaging and MOCVD Growth** Jacob T. Boyer, Ari N. Blumer, Zak H. Blumer, Daniel L. Lepkowski, Francisco A. Rodriguez, Steven A. Ringel and Tyler Grassman; The Ohio State University, United States

III-V/Si material integration affords device designers access to tunable, high quality III-V alloys on an inexpensive Si platform that can be easily integrated with standard device fabrication techniques. Photovoltaics, photonic-integrated circuits, and optoelectronics stand to benefit strongly from III-V/Si advances. Epitaxially-integrated GaP/Si is a direct bridge between both material systems and has thus received considerable development, especially in recent years. The non-negligible lattice mismatch between GaP and Si, interface heterovalency, and the high potential for the formation of nucleation related defects (e.g. antiphase disorder, stacking faults, etc.) all complicate the production of low defect density GaP/Si virtual substrates that are required for producing high-performing devices. A variety of growth processes have been demonstrated, via MBE and MOCVD, as capable of nucleating and growing and relaxing GaP/Si without nucleation related defects [1], [2] and to result in low threading dislocation density (TDD) [3]. However, across the many available reports, there is little insight regarding the connection of differing epitaxial processes (both at the interface and during bulk growth) and the evolution of the resulting crystal defects.

An extensive study of MOCVD-based GaP/Si growth is underway to address these knowledge gaps. This systemic study considers MOCVD growth conditions near the initial GaP/Si interface (e.g. Si surface pretreatment and layer-by-layer GaP nucleation) and those for ‘bulk’ GaP overgrowth (e.g. temperature, V:III ratio, and doping). Electron channeling contrast imaging (ECCI [4]) is used to image and quantify misfit dislocation arrays at the GaP/Si heterointerface resulting from the different MOCVD process conditions. Using ECCI micrographs, relevant attributes of the misfit dislocation networks are extracted at several stages of GaP film growth and relaxation. Aspects such as average misfit length and effective TDD are found to vary by over an order of magnitude at the onset of critical thickness, depending on MOCVD conditions used for the GaP nucleation stage. In thicker films grown atop GaP nucleated using optimized conditions, relaxation and TDD are found to be strongly affected by bulk growth parameters. This wealth of experimental data has enabled the development of quantitative analytical models to describe and predict dislocation nucleation and glide in such systems.

Through these developments, we have achieved partially-relaxed GaP/Si materials with near-ideal misfit networks and effective TDD of  $7 \times 10^5 \text{ cm}^{-2}$ , as well as fully-relaxed GaP/Si films with TDD  $\sim 4 \times 10^6 \text{ cm}^{-2}$ . These virtual substrates are critical for achieving the integration of low-TDD GaAs<sub>y</sub>P<sub>1-y</sub> materials, and thus high-efficiency photovoltaics, on Si substrates and subcells. Further reductions in TDD are expected with additional tuning of the MOCVD process parameters realized through this characterization-to-growth feedback system.

[1] T. J. Grassman *et al.*, “Nucleation-related defect-free GaP/Si(100) heteroepitaxy via metal-organic chemical vapor deposition,” *Appl. Phys. Lett.*,

vol. 102, no. 14, 2013. [2] K. Yamane *et al.* “Growth of low defect density GaP layers on Si substrates within the critical thickness by optimized shutter sequence and post-growth annealing,” *J. Cryst. Growth*, vol. 312, no. 15, pp. 2179–2184, 2010. [3] K. N. Yaung *et al.* “GaAsP solar cells on GaP/Si with low threading dislocation density,” *Appl. Phys. Lett.*, vol. 109, no. 3, p. 032107, Jul. 2016. [4] S. D. Carnevale *et al.*, “Rapid misfit dislocation characterization in heteroepitaxial III-V/Si thin films by electron channeling contrast imaging,” *Appl. Phys. Lett.*, vol. 104, no. 23, p. 232111, Jun. 2014.

#### 12:45 PM U05

**(Student) Passivation of Low-Angle Grain Boundaries in Single-Crystal-Like GaAs Flexible Thin-Film Solar Cells on Metal Tape for Significant Improvement of Conversion Efficiency** Sara Pouladi, Carlos Favela, Monika Rathi, Jie Chen, Weijie Wang, Venkat Selvamanickam and Jae-Hyun Ryou; University of Houston, United States

We previously developed flexible GaAs single-junction solar cells (SCs) on metal tape to address technical and economic challenges of III-V multi-junction compound semiconductor heterostructures which is the best photovoltaic (PV) materials for high conversion efficiencies. We achieved nearly single-crystalline III-V thin films that are directly grown on inexpensive polycrystalline metal substrates using crystallinity-transformational buffer layers. This PV technology combines the efficiency advantages of high-quality III-V materials with continuous roll-to-roll deposition process of thin film on a low-cost tape substrate to produce flexible, cost-competitive, and high-efficiency SCs with application versatility. While the first demonstrated SC devices showed a promising photon conversion efficiency of  $\sim 7.6\%$ , their performance characteristics were still limited by the presence of low-angle grain boundaries (LA-GBs) causing minority carriers’ recombination and bulk leakage. According to our 2-dimensional modeling, effective passivation of the detrimental effect of LA-GBs is a key pathway to achieve higher efficiencies. The 2D modeling of SCs shows that LA-GBs in the single-crystal-like GaAs limit its performance and effective passivation of these GBs can boost the photo-conversion efficiency remarkably. Therefore, novel passivation treatments using hydrogen and sulfur have been conducted on the single-crystal-like III-V material layers. In the present study, we demonstrate the passivation effect of trioctylphosphine sulfide (TOP:S) solution is particularly effective on the PV performance of newly developed single-crystal-like thin-film GaAs. The effect of TOP:S treatments were characterized by atomic force microscopy (AFM), scanning probe force microscopy (SPFM), and photoluminescence (PL). Surface potential maps of as-grown and TOP:S treated films obtained by SPFM suggest that TOP:S treatment can passivate the energy states at grain boundaries and lower the potential barrier. The enhancement of the PL intensity after TOP:S treatment also reveals the reduction of density of defect states by this treatment. The TOP:S passivation effect on the fabricated GaAs SC was also studied by *I-V* characterization. Dark saturation current after TOP:S treatment decreases from  $J_0 \sim 2 \times 10^{-3} \text{ A}/\text{cm}^2$  to  $\sim 3.5 \times 10^{-4} \text{ A}/\text{cm}^2$  (at  $V = -500 \text{ mV}$ ). Employing TOP:S treatment, the photo-conversion efficiency of GaAs SC increases from 6.1% to 10% by improving  $V_{\text{oc}}$ ,  $J_{\text{sc}}$ , and  $FF$  from 590 mV,  $18 \text{ mA}/\text{cm}^2$  and 62 to 730 mV,  $20.3 \text{ mA}/\text{cm}^2$  and 71, respectively. The final single-crystal-like SC was obtained after deposition of anti-reflection coating (ARC) which delivers an efficiency performance of 13.5%. The efficiency of passivated SCs is about two times of the previous record, 7.6%, for un-passivated devices. A remarkable improvement in efficiency performance of flexible GaAs SCs is achieved with increases of  $\sim 24\%$ , 12.8%, 14.5%, and 64% for  $V_{\text{oc}}$ ,  $J_{\text{sc}}$ ,  $FF$ , and overall efficiency, respectively.

#### 1:00 PM BREAK

#### 2:00 PM U06

**Preparation of Alloys and Investigation of Phase Equilibria in the CuFeS<sub>2-6</sub> – CuGaS<sub>2</sub> System** Barys Korzun<sup>1</sup>, Anatoly Pushkarev<sup>2</sup>, Aliaksandr Zhaludkevich<sup>2</sup> and Joel Hernandez<sup>1</sup>; <sup>1</sup>Borough of Manhattan Community College/ The City University of New York, United States; <sup>2</sup>Scientific-Practical Materials Research Centre of the National Academy of Sciences of Belarus, Belarus

CuGaSe<sub>2</sub> and CuInSe<sub>2</sub> ternary compounds and their solid solutions with the crystal structure of chalcopyrite CuFeS<sub>2</sub>, are used for the fabrication of solar cells with the efficiency exceeding 20.0%. Copper gallium disulfide (CuGaS<sub>2</sub>) is one of the promising chalcopyrite-like compounds that can be used in thin films solar cells but its energy band gap should be adjusted to the optimum value for the photovoltaic conversion, which is approximately 1.35 eV under AM1.5 conditions. An obvious approach for such reduction of the CuGaS<sub>2</sub> band gap consists of combining CuGaS<sub>2</sub> in alloys with other ternary compounds that have a lower band gap, for instance, compound of variable composition of CuFeS<sub>2-6</sub>. The aim of the present paper is to prepare alloys of the CuFeS<sub>2-6</sub> – CuGaS<sub>2</sub> system, investigate phase equilibria and to determine the limits of solubility in this system using X-ray powder diffraction (XRPD), differential thermal analysis (DTA), and scanning electron microscopy (SEM) combined with energy-dispersive X-ray spectroscopy (EDX).

Alloys of the CuFeS<sub>2-6</sub> – CuGaS<sub>2</sub> system were synthesized by solid-state chemical reactions. Samples were powdered, ball milled and the procedure was repeated three times. The starting components were the CuFeS<sub>2-6</sub> and CuGaS<sub>2</sub> ternary compounds prepared by melt of the mixture of the constituent

chemical elements. In addition to the initial ternary compounds  $\text{CuFeS}_{2-\delta}$  with  $\delta = 0.05$  ( $\text{CuFeS}_{1.95}$ ) and  $\text{CuGaS}_2$ , 11 alloys were obtained in the system  $(\text{CuFeS}_{2-\delta})_{1-x} - (\text{CuGaS}_2)_x$ , with a molar part of  $\text{CuGaS}_2$   $x$  equal to 0.05, 0.10, 0.20, 0.30, 0.40, 0.50, 0.60, 0.70, 0.80, 0.90, and 0.95.

The X-ray studies of alloys were carried out using monochromatic  $\text{Cu K}\alpha$  radiation (1.54018 Å, step size  $0.01^\circ$  or  $0.04^\circ$ , counting time 10 s) using diffractometers DRON-4. The Rietveld analysis of the X-ray powder diffraction data was done using the FullProf software. SEM-EDX data were obtained using a Leo 1455VP scanning electron microscope and a Hitachi TM 3000 tabletop scanning electron microscope (Hitachi High-Technologies, Clarksburg MD, USA). The EDX data was processed using Quantax70 X-ray microanalysis software (Bruker, Berlin, Germany). The DTA measurements were performed by means of equipment specially designed and constructed for measurements up to temperatures of 1573 K. The presence of phase transformations and their temperatures were determined with an accuracy of 2 K for the phase transition temperature. Powdered samples (typical mass 1 g) were placed in evacuated silica capsules with  $\text{Al}_2\text{O}_3$  used as a reference material. DTA was run on samples that were heated at the constant rate of 2-3 K/min. The temperatures of the sample and the reference materials were determined with Pt-90%/Rh-10% thermocouples.

It was found that T-x phase diagram of the  $(\text{CuFeS}_{2-\delta})_{1-x} - (\text{CuGaS}_2)_x$  system has a peritectic character with no solubility at room temperature in the composition range  $x = 0.52 - 0.85$ . The lack of complete solubility can be explained by the fact that the crystal structures of the starting ternary compounds  $\text{CuFeS}_{2-\delta}$  and  $\text{CuGaS}_2$  are different. Samples of homogeneous chalcopyrite, having the chemical composition of  $\text{CuFeS}_{2-\delta}$ , possess deficiency of sulfur and exist in the defect chalcopyrite structure at room temperature. The region of existence of  $\text{CuGaS}_2$  compound includes the stoichiometric composition, and the samples crystallize in the ideal crystal structure of chalcopyrite. The transitions from the low temperature defect chalcopyrite structure to the high temperature defect chalcopyrite structure for the  $\text{CuFeS}_{2-\delta}$ -rich alloys were also detected and their temperatures were determined.

## 2:15 PM U07

**(Student) Impact of K-Optimization on Trap Concentrations in ACIGS Solar Cells** Michael F. Miller<sup>1</sup>, Siming Li<sup>2</sup>, Pran K. Paul<sup>1</sup>, Darius Kuciauskas<sup>2</sup>, Rouin Farshchi<sup>3</sup> and Aaron Arehart<sup>1</sup>; <sup>1</sup>The Ohio State University, United States; <sup>2</sup>National Renewable Energy Laboratory, United States; <sup>3</sup>MiaSolé Hi-Tech Corp., United States

Recent progress has been made in improving efficiency in  $\text{Cu}(\text{In,Ga})\text{Se}_2$  (CIGS) absorbers with steady increases in peak efficiency. One way this has been achieved is by adding Ag to CIGS (ACIGS) to achieve higher  $V_{oc}$ . However, these efficiencies are still well below the Shockley-Queisser efficiency limit, and traps acting as recombination centers and compensating centers are one thing limiting the solar efficiency. Past research in CIGS has shown that alkali treatment can improve the efficiency and metastability problems in CIGS, but less is understood about the role of alkali treatments in ACIGS [1]. Here, we investigate the impact of potassium in ACIGS through its impact on trap incorporation and minority carrier lifetime.

The samples in this study were grown in a roll-to-roll coater with Mo, ACIGS, CdS, and ZnO structure. Both cells were grown identically except the second (K-optimized) cell was grown with increased K-doping of the Mo contact and was more Cu-poor near the surface to optimize the K profile. This resulted in an efficiency increase from 16.8% to 18.7% for the K-optimized cell, which was mostly due to a 65 mV  $V_{oc}$  increase. The doping profile showed a 2X increase in acceptor concentration of the K-optimized cell ( $2.5 \times 10^{15} \text{ cm}^{-3}$ ) which suggests that the K was better incorporated into the ACIGS after these optimizations.

To characterize the traps in these cells, deep level transient and optical spectroscopy were used. The DLOS measurements showed an  $E_v + 0.98$  eV trap whose concentration was reduced 10X in the K-optimized cell ( $4 \times 10^{14} \text{ cm}^{-3}$ ). This is consistent with previous results from the alkali treatment in CIGS, which also showed a decrease in near-conduction band trap concentration [1], but the reduction was larger than previous studies possibly indicating the combination of K and Cu-poor surface may both have aided in reducing the  $E_v + 0.98$  eV trap concentration.

The other primary trap is the mid-gap trap ( $E_v + 0.58$  eV), which was quantified using DLTS. Its concentration decreased from  $9 \times 10^{13} \text{ cm}^{-3}$  to  $4 \times 10^{13} \text{ cm}^{-3}$  in the K-optimized sample, which is a 2X reduction. Previous studies have shown this trap is likely an efficient recombination center [2], which makes sense because it is near mid-gap. This trap has also been associated with VOC instability and reduction, so reducing this trap concentration is essential to achieve high VOC and cell efficiency. To help confirm this association, time-resolved photoluminescence measurements have shown in this sample set and a previous study [2] that the minority carrier lifetime (19 ns baseline to 56 ns K-optimized) and this  $E_v + 0.56$  eV trap concentration are inversely proportional, which would be expected for a recombination-limited carrier lifetime.

The K optimization of ACIGS results in significantly improved cell efficiency and reduced trap concentrations that correlate with the improved material and electrical properties. We will report on this and the impact of the K optimization on the cell metastability.

### References:

1. S.Karki et al., *IEEE Journal of Photovoltaics*, 7, 665 (2017).
2. A.J.Ferguson et al., *Journal of Applied Physics*. Manuscript submitted for publication.

## 2:30 PM U08

**(Student) Photovoltaic Response of Thin-Film CdTe Solar Cells under Accelerated Neutron Radiation in a TRIGA Reactor** Kaden Powell<sup>1</sup>, Matthew Lund<sup>1</sup>, Meng-Jen Wang<sup>1</sup>, Yang Qian<sup>1</sup>, David Maggnetti<sup>1</sup>, Matthew O. Reese<sup>2</sup>, Edward Cazalas<sup>1</sup>, Glenn Sjoden<sup>1</sup> and Heayoung P. Yoon<sup>1,2</sup>; <sup>1</sup>The University of Utah, United States; <sup>2</sup>National Renewable Energy Laboratory, United States

Cadmium telluride (CdTe) solar cells are a promising photovoltaic (PV) technology for producing power in space owing to their high-efficiency (> 22.1%), potential for specific power, and cost-effective manufacturing processes. In contrast to traditional space PVs, the high-Z (atomic number) CdTe absorbers can be intrinsically robust under extreme space radiation, offering long-term stability. Despite these advantages, the performance assessment of CdTe solar cells under high-energy particle irradiation (e.g., photons, neutrons, charged particles) is limited in the literature, and their stability is not comprehensively studied. In this work, we present the PV response of  $n$ -CdS /  $p$ -CdTe PVs under accelerated neutron irradiation. We measure PV properties of the devices at different neutron/photon doses. The equivalent dose deposited in the CdTe samples is simulated with deterministic and Monte Carlo radiation transport methods. Thin-film CdTe solar cells were synthesized on a fluorine-doped tin oxide (FTO) coated glass substrate ( $\approx 4 \text{ cm} \times 4 \text{ cm}$ ). CdS:O ( $\approx 100 \text{ nm}$ ) was reactively RF sputtered in an oxygen/argon ambient followed by a close-spaced sublimation deposition of CdTe ( $\approx 3.5 \mu\text{m}$ ) in an oxygen/helium ambient. The sample was exposed to a 10 min vapor  $\text{CdCl}_2$  in oxygen/helium ambient at  $430^\circ\text{C}$ . The samples were exposed to a wet  $\text{CuCl}$  solution prior to anneal  $200^\circ\text{C}$ . A gold back-contact was formed on CdTe via thermal evaporation. The final sample contains 16 CdTe devices. For neutron irradiation, we cleaved the CdTe substrate into four samples and exposed two samples to  $\approx 90 \text{ kW}$  reactor power neutron radiation for 5.5 hours and 8.2 hours, respectively, in our TRIGA (Training, Research, Isotopes, General Atomics) reactor. We observed a noticeable color change of the glass substrates to brown after the neutron/gamma reactor exposure. Presumably, the injected high-energy neutrons caused the breaking of chemical bonds and the displacement of atoms in the glass substrates, creating point defects and color centers. The  $I$ - $V$  characteristics showed noticeable deterioration with over 8 hour radiations. Specifically, the saturation current of the control devices was  $\approx 25 \text{ nA}$  increasing to  $1 \mu\text{A}$  and  $10 \mu\text{A}$  for the 5.5-hour and 8.2-hour radiated samples, respectively. The turn-on voltage of the control devices ( $\approx 0.85 \text{ V}$ ) decreased with the irradiated sample ( $\approx 0.75 \text{ V}$  for 5.5-hour and  $\approx 0.5 \text{ V}$  for 8.2-hour exposures), implying noticeable radiation damage occurred at the heterojunction. The higher values of the ideality factor for irradiated devices ( $n > 2.2$ ) compared to that of the control devices ( $n \approx 1.3$ ) also support the deterioration of the  $p$ - $n$  junction. We observed the notable decrease in shunt resistance ( $R_{sh}$ ) and the increase in series resistance ( $R_s$ ) with the neutron dose. It is possible that Cu ions introduced during the  $\text{CuCl}_2$  treatment may migrate into CdTe grain boundaries (GBs). The presence of Cu ions at GBs can create additional leakage paths for photocarrier transport, deteriorating the overall PV performance. We estimated the radiation dose of CdTe in comparison to Si (conventional PV) using a UTR model (e.g., MCNP6 2D UTR Reactor simulations). In this model, we simulated Si and CdTe at the center point of the triangular fuel lattice and used an "unperturbed flux" tally in the water. Our simulations yielded a dose rate of 6916 Gy/s of neutrons and 16 Gy/s of photons for CdTe, and 1 Gy/s of neutrons and 21 Gy/s of photons for Si (doses +/- <1%). The large dose rate of neutrons in CdTe is mainly attributed to the large thermal neutron absorption cross-section of  $^{113}\text{Cd}$ . Based on this estimation, we calculate that the exposure of our CdTe PVs is equivalent to several million years in LEO (Low-Earth Orbit), or about 10,000 years for Si in LEO. Currently, we are working on a low-dose neutron/photon radiation on CdTe PVs and their light  $I$ - $V$ s and microstructural characterizations to gain better understanding on the degradation of CdTe PVs.

## 2:45 PM U09

**Enhanced Photon Recycling with Energy-Selective Front Reflectors for High-Efficiency GaAs Laser Power Converters** Eric Chen, Sean Babcock, Nicholas Irvin and Richard King; Arizona State University, United States

Recent advancements in photonics and fundamental understanding of photon recycling in solar cells have enabled progress towards achieving solar cell efficiencies near their radiative, Shockley-Queisser limit. Specifically, the addition of a reflective back contact to GaAs solar cells has resulted in performance nearly 87% of the theoretical limit. To perform even closer to their detailed balance limits, solar energy conversion devices such as laser power converters (LPCs) must incorporate more photon recycling architectures that enable high external radiative efficiencies at open circuit conditions and high photocurrent extraction at short circuit conditions. While direct bandgap semiconductors benefit the most from reflective back contacts recently enabled by high material quality resulting in over 99.7% internal radiative efficiencies, they also have demonstrated open-circuit voltage gains when blackbody emission out of the front of the device is restricted. Reduced dark currents of 12% relative to that of a device with an anti-reflection coating have been observed, resulting in 4 mV open-circuit voltage gain. However, the energy selectivity of such a front reflector has not been carefully studied. Furthermore, monochromatic illumination wavelength can be tailored to the energy of the front reflector cut-off to further maximize LPC performance. In this work, a front reflector that maximizes the amount of blackbody restriction is introduced using the Steiner formalism to calculate photovoltaic cell efficiency by

quantifying the energy-, angle-, and volume-dependent photon escape and absorption probabilities through the front and back surfaces under monochromatic light. The lower-energy and higher-energy cut-offs for the front reflector are modeled independently to determine optimal monochromatic illumination wavelength trends in each case. A 3  $\mu\text{m}$  GaAs absorber with a perfect back reflector and ideal internal radiative efficiency of 1.0 is assumed in these models. Varying the front reflector wavelength cut-off from 100 nm shorter than the illumination wavelength to as close as 5 nm shows both a) an increase in maximum LPC efficiency from 74% to over 81% and b) a red-shift of the optimal laser wavelength from 500 nm to 600 nm. This result suggests that the voltage gain from selecting a cut-off energy over 0.6 eV above the absorber bandgap due to sub-reflector-energy photon recycling increases the quasi-Fermi-level splitting and results in an open-circuit voltage gain of 400 mV. The previous calculation assumes no low-energy cut-off energy limit. To explore the effect of selectively reflecting increasing portions of the blackbody emission of the absorber, the range of low-energy cut-offs is varied. Shifting the cut-off wavelength from 5 nm below the laser wavelength to up to 1500 nm shows both a) an increase in maximum LPC efficiency from 75% to over 81% and b) a blue-shift of the optimal wavelength from 870 nm to 600 nm. The main loss in efficiency for shorter illumination wavelengths at smaller  $\Delta\lambda_{\text{reflector}}$  between the reflector and laser wavelengths can be attributed to the lack of blackbody emission restriction. In other words, the highest LPC efficiencies (at higher laser energies) can only be enabled if the reflectance of the spontaneous emission from GaAs can be effectively recycled within the cell. In this calculation the high-energy reflector cut-off is assumed to be the optimal spacing of 5 nm shorter than the laser wavelength. Additional calculations indicate that lower material quality yielding 99% internal radiative efficiency can still retain LPC efficiencies over 60% for laser wavelengths approaching the absorber material bandgap. Preliminary studies show that commercial shortpass filters with  $\Delta\lambda_{\text{laser-reflector}}$  greater than 500 nm are typical and can provide a simple proof-of-principle system for enabling high-efficiency LPCs by enhancing photon recycling effects using an energy-selective front reflector.

SESSION V: Ga<sub>2</sub>O<sub>3</sub>—Growth, Characterization and Defects II  
 Session Chair: Anderson Janotti  
 Session Hosts: Rebecca Peterson and Hongping Zhao  
 Thursday Afternoon, June 25, 2020  
 Location: ZoomRoom 1

### 3:45 PM V01

**(Student) MOCVD Growth, Characterization and Phase Transformation of (Al<sub>x</sub>Ga<sub>1-x</sub>)<sub>2</sub>O<sub>3</sub> Thin Films** A F M Anhar Uddin Bhuiyan<sup>1</sup>, Zixuan Feng<sup>1</sup>, Jared Johnson<sup>1</sup>, Hsien-Lien Huang<sup>1</sup>, Jith Sarker<sup>2</sup>, Menglin Zhu<sup>1</sup>, Md Rezaul Karim<sup>1</sup>, Baishakhi Mazumder<sup>2</sup>, Jinwoo Hwang<sup>1</sup> and Hongping Zhao<sup>1,1</sup>; <sup>1</sup>The Ohio State University, United States; <sup>2</sup>University at Buffalo, The State University of New York, United States

Since the first conceptual device demonstration based on  $\beta$ -Ga<sub>2</sub>O<sub>3</sub>, significant progress has been made for substrate development, epitaxy as well as power and radio frequency electronics. Expanding its bandgap by alloying Ga<sub>2</sub>O<sub>3</sub> with Al<sub>2</sub>O<sub>3</sub> can provide opportunities to achieve high performance power electronic devices with even higher breakdown field strength. In addition, AlGaO/GaO heterostructures can enable the formation of two-dimensional electron gas (2DEG) [1] which can surpass device performance based on Ga<sub>2</sub>O<sub>3</sub> thin films. Development of high quality epitaxy of AlGaO with controllable Al composition and n-type doping can enable AlGaO/GaO 2DEG with high sheet charge density with high mobility through forming high quality AlGaO/GaO interface with large band offset. Currently, the epitaxy of AlGaO is still at an early stage, and the solubility limit of Al<sub>2</sub>O<sub>3</sub> in  $\beta$ -phase Ga<sub>2</sub>O<sub>3</sub> is still unclear. Comprehensive mapping of Al composition in AlGaO and fundamental understanding of material properties are in great need. In this paper, we investigated the MOCVD growth of (Al<sub>x</sub>Ga<sub>1-x</sub>)<sub>2</sub>O<sub>3</sub> on Fe doped semi-insulating (010)  $\beta$ -Ga<sub>2</sub>O<sub>3</sub> substrates over the entire Al composition range (0<x $\leq$ 100%) by systematical tuning of [TMAI]/[TMAI+TEGa] molar flow rate ratio. TEGa, TMAI and pure O<sub>2</sub> were used as Ga, Al and O precursors, respectively. Argon (Ar) was used as the carrier gas [2]. The growth temperature was varied between 825°C and 920°C. For the Al composition x < 27%, high quality single phase  $\beta$ -(Al<sub>x</sub>Ga<sub>1-x</sub>)<sub>2</sub>O<sub>3</sub> was achieved. A mixture of  $\beta$  and  $\gamma$  phases exists in (Al<sub>x</sub>Ga<sub>1-x</sub>)<sub>2</sub>O<sub>3</sub> when Al composition ranges between 27% and 40%, whereas single  $\gamma$ -phase was observed for the films with Al composition x > 40%. The transition from  $\beta$  to  $\gamma$  phase in AlGaO alloys was observed from X-ray diffraction spectra. The growth of  $\gamma$ -phase AlGaO with higher Al content was further confirmed via atomic resolution scanning transmission electron microscopy imaging and nanodiffraction. Compositional and statistical analyses performed on data acquired from atom probe tomography provided insight on the local compositional homogeneity in AlGaO films at different Al compositions. To investigate the crystalline properties at the atomic scale,  $\beta$ -(Al<sub>x</sub>Ga<sub>1-x</sub>)<sub>2</sub>O<sub>3</sub> thin films and AlGaO/GaO superlattice (SL) structures with different Al compositions were characterized using atomic resolution HAADF-STEM. The epilayer displays a uniform cross-section without extended defects or dislocations for 15% Al composition. High resolution STEM imaging of SL structure with 23% Al composition demonstrated uniform Al distribution in the AlGaO sub-layers. The uniformity of the layer structures degraded and the

interfaces between AlGaO/GaO became rougher as the growth proceeded for x=40% although the  $\beta$ -phase AlGaO were found to be maintained in the first few AlGaO layers. N-type doping of  $\beta$ -(Al<sub>x</sub>Ga<sub>1-x</sub>)<sub>2</sub>O<sub>3</sub> film with x varying between 6.3% and 33.4% by using Si as dopant was demonstrated. Controllable n-type doping concentration from low-10<sup>17</sup> cm<sup>-3</sup> to low-10<sup>18</sup> cm<sup>-3</sup> was achieved by systematic tuning of the silane flow rate. A room temperature mobility of 65 cm<sup>2</sup>/Vs and a low temperature peak mobility of ~575 cm<sup>2</sup>/Vs at T = 65K were measured for x= 17.3% with room temperature carrier concentrations of 6.5x10<sup>17</sup> cm<sup>-3</sup>. In summary, we investigated the MOCVD growth of AlGaO films for the entire Al composition range (0<x $\leq$ 100%). Phase segregation and phase transformation were observed in AlGaO films as Al composition increases. Comprehensive material characterization using XRD, AFM, STEM imaging, and atom probe tomography was performed to probe the fundamental material properties of the MOCVD grown AlGaO films. **Acknowledgment:** The authors acknowledge the funding support from the Air Force Office of Scientific Research No. FA9550-18-1-0479 (AFOSR, Dr. Ali Sayir) and NSF (1810041). **References:** 1. Krishnamoorthy et al., Appl. Phys. Lett. 111, 023502 (2017). 2. Bhuiyan et al., Appl. Phys. Lett. 115, 120602 (2019).

### 4:00 PM V02

**(Student) Characterization of  $\beta$ -Ga<sub>2</sub>O<sub>3</sub> MOVPE Homoepitaxial Thin Films Grown on (-201) and (010) Substrates—Charge Compensation and Depletion in (-201) Films** Brian A. Eisner, Praneeth Ranga, Arkka Bhattacharyya, Sriram Krishnamoorthy and Michael Scarpulla; The University of Utah, United States

$\beta$ -Ga<sub>2</sub>O<sub>3</sub> is a wide-bandgap semiconductor with potential applications for high-power electronic devices. Homoepitaxial growth on several different crystal orientations has been performed to varying degrees of success, but growth on the (-201) plane has remained relatively unexplored. We grew UID MOVPE homoepitaxial layers on both (-201) and (010) substrates, electrically and structurally characterizing Schottky diodes on both films. The (010) devices display typical semiconductor behavior in IV and CV, but the (-201) devices showed full sample depletion even at low biases (CV) and significant charge compensation (IV). Specifically, the (-201) IV showed a quadratic Mott-Gurney dependence indicative of space charge transport, with currents orders of magnitude below that of the (010) devices. Heavily-doped (-201) devices did not show this depletion or compensation. The CV data displayed no capacitance variation with voltage, with a constant depletion width on the order of the layer thickness. Structurally, the (-201) layers displayed a terraced morphology under SEM. We put forth three potential explanations for the anomalous IV and CV behavior. A large number of surface states could cause the observed charge compensation and depletion, and DLTS results corroborate their existence. Alternatively, threading dislocations permeating the sample could cause this behavior, and frequent etch pits on the (-201) sample lend credence to this hypothesis. Finally, abundant incoherent stacking faults could lead to the depletion and compensation by impeding charge transport and diffusion, similar to those found in previous studies of (100) homoepitaxy.

### 4:15 PM V03

**$\beta$ -Ga<sub>2</sub>O<sub>3</sub> Films with Low Si Doping Density Grown Via Plasma-Assisted Molecular Beam Epitaxy** Thaddeus J. Aseel<sup>1</sup>, Erich Steinbrunner<sup>1,2</sup>, Jessica Hendricks<sup>1,3</sup>, Adam T. Neal<sup>1</sup> and Shin Mou<sup>1</sup>; <sup>1</sup>Air Force Research Laboratory, United States; <sup>2</sup>Wright State University, United States; <sup>3</sup>Air Force Institute of Technology, United States

In this work, we achieved low unintentional Si doping density in  $\beta$ -Ga<sub>2</sub>O<sub>3</sub> thin films grown via plasma-assisted molecular beam epitaxy (PAMBE).  $\beta$ -Ga<sub>2</sub>O<sub>3</sub> has been of interest due to its large intrinsic breakdown field for high voltage applications. However, a low doping density in the drift region is required to achieve the desired breakdown voltage in a device. Previous analysis has suggested that the total n-type doping density must be equal to or lower than 1x10<sup>16</sup> cm<sup>-3</sup> to achieve a breakdown voltage of 10 kV or greater for an ideal one-sided junction.[1] As such, it is crucial that unintentional doping in the growth of  $\beta$ -Ga<sub>2</sub>O<sub>3</sub> is reduced to achieve the optimal breakdown voltage. We analyzed thin films grown by PAMBE with secondary ion mass spectroscopy (SIMS) and identified two major sources of unintentional Si doping present in the growth chamber, the Si dopant cell and the radio frequency (RF) oxygen plasma source. By adjusting the parameters of these sources we demonstrate the ability to reduce the unintentional doping concentration by two orders of magnitude. A decrease in the Si dopant cell idle temperature during growth resulted in a decrease in the unintentional doping from 2x10<sup>18</sup> cm<sup>-3</sup> to 3x10<sup>17</sup> cm<sup>-3</sup>. Further, decreasing the power of the RF oxygen plasma source yielded in a reduction of unintentional Si doping from 3x10<sup>17</sup> cm<sup>-3</sup> to 1x10<sup>16</sup> cm<sup>-3</sup>. The overall reduction of the unintentional doping allows for the growth of low doping density drift regions for devices grown via PAMBE. [1] A.T. Neal, S. Mou, S. Rafique, H. Zhao, E. Ahmadi, J.S. Speck, K.T. Stevens, J.D. Blevins, D.B. Thompson, N. Moser, K.D. Chabak, and G.H. Jessen, Appl. Phys. Lett. **113**, 062101 (2018).

#### 4:30 PM V04

**(Student) Synthesis and Characterization of Large-Area Nanometer-Thin  $\beta$ -Ga<sub>2</sub>O<sub>3</sub> Films from Oxide Printing of Liquid Metal Gallium** Jacqueline Cooke, Leila Ghadbeigi, Rujun Sun, Arka Bhattacharyya, Michael Scarpulla, Sriram Krishnamoorthy and Berardi Sensale Rodriguez; The University of Utah, United States

Exfoliated gallium oxide (Ga<sub>2</sub>O<sub>3</sub>) has been reported as an ultrathin channel material in field effect transistors. Unlike in 2D materials with van der Waals forces between stacked layers, weak bonding in  $\beta$ -Ga<sub>2</sub>O<sub>3</sub> along the (100) direction enables mechanical exfoliation in a similar manner [1]. To date, the thickness of these exfoliated films has been limited to tens to hundreds of nanometers [1-4]. In this regard, several processes such as plasma etching, have been proposed to attain thinner films [5]. In this work, to reduce the thickness of Ga<sub>2</sub>O<sub>3</sub> films to the nanometer scale, we followed the process developed by Carey *et al.* [6], which enabled us to attain ~2 nm thick Ga<sub>2</sub>O<sub>3</sub> films over a large surface area (> 1 mm<sup>2</sup>). The process for making the ultra-thin films starts with a SiO<sub>2</sub>/Si or sapphire substrate, which is cleaned with acetone, isopropanol, and DI water for 10 min each in an ultrasonic cleaner. Both gallium and the substrate are then heated to 60°C on a hotplate, liquefying the metal. A drop of Ga was applied to the substrate using a syringe, and PDMS was used to wipe off the excess gallium leaving Ga<sub>2</sub>O<sub>3</sub> on the substrate. Because Ga<sub>2</sub>O<sub>3</sub> is a native oxide that naturally forms on the surface of gallium but has a stronger interaction with SiO<sub>2</sub> than to gallium [6], thin films of Ga<sub>2</sub>O<sub>3</sub> remain on the substrate. The sample is then annealed at 1000°C. These films, as deposited and after annealing, were characterized through optical microscopy, AFM, XPS, Raman spectroscopy, PL, and TEM. Optical microscope images showed that upon annealing, the color of the film changes from a light blue to a green transparent color. Through AFM, it is shown that the thickness of the film can be as thin as 2 nm over areas >> 1 mm<sup>2</sup>. XPS indicates the presence of Ga metal residue (of up to 8% wt) in the as-prepared samples. However, after annealing, no traces of this residue are present. The samples were characterized by Raman spectroscopy in order to provide information on its structural properties. For the as-synthesized samples, no Raman signatures were detected, though the crystallinity or amorphous state of the film could not be concluded. However, Raman spectra showed characteristic signatures of  $\beta$ -phase after annealing for samples synthesized on both SiO<sub>2</sub>/Si and sapphire substrates. All samples, before and after annealing, showed the characteristic photoluminescence of Ga<sub>2</sub>O<sub>3</sub> composed of four emission bands at UV, UV', blue, and green wavelengths. After annealing, the overall intensity of luminescence increases which is attributed to an increase in crystallinity and grain size. This enhancement was most strongly observed in samples on sapphire. After annealing, an increase in the green luminescence (with respect to blue) was observed, which is associated with an increase in oxygen interstitials and a decrease in oxygen vacancies in agreement with previous observations reported in the literature. The film was determined to be polycrystalline through TEM imaging where FFT shows a d spacing of 0.210, 0.191, 0.256, 0.301 nm which is consistent with (311), (20-3), (111), and (400) orientations of  $\beta$ -phase Ga<sub>2</sub>O<sub>3</sub>, respectively. Overall, our results demonstrate that annealing of thin films obtained from oxide printing of liquid metal Ga is a non-expensive and straightforward process that can lead to  $\beta$ -Ga<sub>2</sub>O<sub>3</sub> films that are nanometer-thin over wafer-scale areas.

**References:** [1] W.S. Hwang *et al.*, *Applied Physics Letters*, 104(20), 20311 (2014); [2] J. Kim *et al.*, *Physical Chemistry Chemical Physics*, 18, 15760-15764 (2016). [3] H. Zhou *et al.*, *Applied Physics Letters*, 111, 092102 (2017). [4] M. J. Tadjer *et al.*, *ECS Journal of Solid State Science and Technology*, 5, 468-470 (2016). [5] Y. Kwon *et al.*, *Applied Physics Letters*, 110(13), 131901 (2017). [6] B. J. Carey *et al.*, *Nature Communications*, 8, 14482 (2017).

#### 4:45 PM V05

**(Student) Probing Charge Transport and Background Doping in MOCVD Grown (010)  $\beta$ -Ga<sub>2</sub>O<sub>3</sub>** Zixuan Feng<sup>1</sup>, A F M Anhar Uddin Bhuiyan<sup>1</sup>, Zhanbo Xia<sup>1</sup>, Joe F. McGlone<sup>2</sup>, David R. Daughton<sup>2</sup>, Aaron Archart<sup>1</sup>, Steven A. Ringel<sup>1,1</sup>, Siddharth Rajan<sup>1,1</sup> and Hongping Zhao<sup>1,1</sup>; <sup>1</sup>The Ohio State University, United States; <sup>2</sup>Lake Shore Cryotronics, Inc., United States

Metalorganic chemical vapor deposition (MOCVD) of  $\beta$ -Ga<sub>2</sub>O<sub>3</sub> thin films have been demonstrated with record-high room temperature and low temperature mobilities [1, 2]. The extracted low acceptor level ( $N_a < 10^{15}$  cm<sup>-3</sup>) is extremely encouraging for its application in high power electronics. Quantitative defect characterization via DLTS/DLOS also demonstrated one order lower of defects concentration for MOCVD  $\beta$ -Ga<sub>2</sub>O<sub>3</sub> as compared to those grown by other growth techniques [3]. To achieve a controllable doping level as low as mid- $10^{15}$  cm<sup>-3</sup>, one still requires MOCVD  $\beta$ -Ga<sub>2</sub>O<sub>3</sub> with low background doping. In this work, we performed a systematic study on understanding the effect of MOCVD growth condition on the unintentional doping incorporation in (010)  $\beta$ -Ga<sub>2</sub>O<sub>3</sub>. Using a relatively optimized MOCVD growth condition for  $\beta$ -Ga<sub>2</sub>O<sub>3</sub> homoepitaxy on (010) Ga<sub>2</sub>O<sub>3</sub> crystal orientation, we studied the material properties without intentional doping. For unintentionally doped (UID) films grown on semi-insulating Fe doped (010) Ga<sub>2</sub>O<sub>3</sub>, the epi-film exhibited low background doping at 8.5x10<sup>15</sup> cm<sup>-3</sup> with new record room temperature carrier mobility of 194 cm<sup>2</sup>/V s. To enable temperature-dependent Hall measurements especially at low temperatures, the sample was fabricated with n+ Ga<sub>2</sub>O<sub>3</sub> MBE regrowth layer prior to the Ti/Au contact deposition. The same sample demonstrated peak Hall mobility of ~9500 cm<sup>2</sup>/V s at T ~ 45K. The high peak electron mobility occurring at very low temperature indicates a low

compensation concentration ( $N_b$ ) in the MOCVD grown  $\beta$ -Ga<sub>2</sub>O<sub>3</sub> sample. The mobility calculations were performed by considering various scattering mechanisms, including polar optical phonon scattering, acoustic deformation potential scattering, ionized impurity, and neutral impurity scattering. The extracted compensation concentration was at  $N_b \sim 7 \times 10^{14}$  cm<sup>-3</sup>. From secondary ions mass spectroscopy (SIMS) depth profile, the background Si concentration was measured as  $\sim 7 \times 10^{15}$  cm<sup>-3</sup> in the epi-layer, and the Si concentration at the growth interface has 1 order higher of the concentration. This indicates that Si is the main impurity that contributes to the unintentional doping in the film, and the Si contamination at the growth interface is exceptionally high. Capacitance-voltage (C-V) measurement was performed on lateral Schottky diode structures. The carrier depth profile extracted from C-V indicated that charges in the epi-film were depleted, and the measured charge concentration is mostly from the increased Si concentration close to the growth interface.

In order to understand the origin of Si background in the UID  $\beta$ -Ga<sub>2</sub>O<sub>3</sub> films, we performed a series of growth studies by tuning the growth condition and different sample preparation, combined with systematic material characterization. Preliminary results indicate that Si background in MOCVD growth process can be from both surface contamination and incorporation from the growth environment. In summary, we demonstrated superb electrical transport properties from MOCVD grown (010)  $\beta$ -Ga<sub>2</sub>O<sub>3</sub> thin films with high crystalline quality and low charge compensation. Si was identified as the major contributor to the background charge concentration in MOCVD UID  $\beta$ -Ga<sub>2</sub>O<sub>3</sub>. Growth parameters were investigated for further reduction of Si incorporation, which is promising to achieve controllable doping in  $\beta$ -Ga<sub>2</sub>O<sub>3</sub> thin films with an extremely low level. **Acknowledgment:** The authors acknowledge the funding support from the Air Force Office of Scientific Research No. FA9550-18-1-0479 (AFOSR, Dr. Ali Sayir). **References:** [1] Z. Feng, A F M A. U. Bhuiyan, M. R. Karim, H. Zhao, *Appl. Phys. Lett.*, 114, 250601 (2019). [2] F. Alema, Y. Zhang, A. Osinsky, N. Valente, A. Mauze, T. Itoh, J. S. Speck, *APL Materials* 7, 121110 (2019). [3] H. Ghadi, J. F. McGlone, C. M. Jackson, E. Farzana, Z. Feng, A F M A. U. Bhuiyan, H. Zhao, A. R. Archart, S. A. Ringel, *APL Materials* (Accepted, 2020)

#### 5:00 PM BREAK

#### 5:30 PM V06

**Defects Properties of Czochralski Grown Zr-Doped Ga<sub>2</sub>O<sub>3</sub> by Deep Level Transient Spectroscopy and Photoluminescence** Rujun Sun<sup>1</sup>, Yu Kee Ooi<sup>1</sup>, Arka Bhattacharyya<sup>1</sup>, Muad Saleh<sup>2</sup>, Sriram Krishnamoorthy<sup>1</sup>, Kelvin Lynn<sup>2</sup> and Michael Scarpulla<sup>1,1</sup>; <sup>1</sup>The University of Utah, United States; <sup>2</sup>Washington State University, United States

Ultra-wide bandgap  $\beta$ -Ga<sub>2</sub>O<sub>3</sub> attracts significant attention for power electronic applications and developments are accelerated by the availability of single crystals successfully grown by melt methods. Typically, n-type conductivity of  $\beta$ -Ga<sub>2</sub>O<sub>3</sub> crystals grown from the melt is achieved using Sn and Si. Recently, Czochralski grown Zr doped Ga<sub>2</sub>O<sub>3</sub> crystals show an electron mobility 73 ~ 112 cm<sup>2</sup>V<sup>-1</sup>s<sup>-1</sup>, and carrier density of 6.5x10<sup>17</sup> ~ 5x10<sup>18</sup> cm<sup>-3</sup> at room temperature and both experimentally and theoretically confirmed that Zr behaves as a shallow donor with an activation energy about 10 meV. This demonstrates Zr dopant is promising for degenerate doping with promising mobility for Ga<sub>2</sub>O<sub>3</sub> bulk crystal. It is still unclear how the incorporation of Zr affects deep defects, i.e., affect existing intrinsic defects (concentration) or create new defect levels. Hence, we investigate defects in Zr-doped Ga<sub>2</sub>O<sub>3</sub> using deep level transient spectroscopy as well as photoluminescence. CZ (100) UID is investigated as reference for Zr-doped ones. The net free carriers for UID, 1# and 2# Zr-doped Ga<sub>2</sub>O<sub>3</sub> are 1.8x10<sup>17</sup>, 1.5x10<sup>18</sup> and 5.2x10<sup>18</sup>, respectively. The defect energy levels of UID are 0.18, 0.46, **0.86** and 1.03 eV. For 1# Zr-doped Ga<sub>2</sub>O<sub>3</sub>, a new shallow defect of 0.30 eV (4.8 x10<sup>14</sup> cm<sup>-3</sup>) emerged coexisting with 0.71 eV. For 2# Zr doped Ga<sub>2</sub>O<sub>3</sub>, only 0.59 eV is observed. The number of defect decreases with Zr doping increasing. The dominant defects for UID, 1# and 2# Zr-doped Ga<sub>2</sub>O<sub>3</sub> are 0.86 eV, 0.71 eV and 0.59 eV respectively which are believed from intrinsic defects of Ga<sub>2</sub>O<sub>3</sub>; their density decrease slightly but still at a low level of 10<sup>15</sup> cm<sup>-3</sup>, indicating negligible effects on devices built on Zr-doped substrates. With Zr dopants increasing, PL intensity decreased, indicating enhanced non-radiation recombination but the emission peak position remains same, suggesting the radiative defects in Ga<sub>2</sub>O<sub>3</sub> do not change with the incorporation of Zr. This work demonstrates that Zr doped Ga<sub>2</sub>O<sub>3</sub> is a promising for applications in both conducting bulk crystals and epi-layers/transparent films.

#### 5:45 PM V07

**(Student) Ab Initio Computation of Chemical Potentials in  $\beta$ -Ga<sub>2</sub>O<sub>3</sub> for Examining Intrinsic Point Defects, Charge Neutrality and Self-Doping** Elan Weiss, Christian Oberdorfer, Travis Withrow, Roberto C. Myers and Wolfgang Windl; The Ohio State University, United States

$\beta$ -Ga<sub>2</sub>O<sub>3</sub> has quickly emerged as an exceptionally active topic of research. Its large band gap (4.9eV), high breakdown field, and transparent conducting behavior make it a promising material for use in optoelectronics and high frequency and power devices. While the possibility of p-type  $\beta$ -Ga<sub>2</sub>O<sub>3</sub> is still in question, n-type doping has been successfully achieved, and appears to be an inherent property of the material. Here, we examine the self-doping behavior of  $\beta$ -Ga<sub>2</sub>O<sub>3</sub> using a charge and stoichiometry balancing method to holistically describe the intrinsic point defects. Density functional theory studies of

intrinsic point defects in binary semiconductors typically limit themselves to the rich/poor limits of stoichiometry. When it is assumed that the material has a composition at the limit of its stability, the chemical potential of the rich species approaches the bulk energy of that element. This ensures that chemical potentials can be calculated directly. The formation energy of a point defect of given charge becomes linearly dependent on Fermi level with a slope equal to the charge state of the defect. While this provides a convenient and analytically determined value for chemical potential, it fails to provide insight into the energetics of point defects at compositions within the stability limits. In order to better explain the behavior of point defects in  $\beta\text{-Ga}_2\text{O}_3$ , we have derived a system of equations to fully describe the relationships of Fermi level, composition, and charge state to chemical potentials and defect formation energies. There is no analytical solution to this system; however, by employing a numerical solver, the chemical potentials of each element can be determined for any crystal stoichiometry. From this, the defect formation energies, and thus, the equilibrium concentration of each defect at each charge state can be determined as a function of stoichiometry and Fermi level. As excess charges can not exist in nature, for a given stoichiometry, in the absence of extrinsic doping, the material must spontaneously adopt a single well-defined Fermi level determined by charge balancing of the intrinsic impurities. Using hybrid functional based DFT, we examine the tunability of the charge neutrality point, and therefore, the pinned Fermi level with respect to composition. Our results suggest a fundamental thermodynamic explanation for the n-type nature of grown  $\beta\text{-Ga}_2\text{O}_3$  crystals based on the grown stoichiometry and intrinsic point defects. This work was funded in part by a grant from the Air Force Office of Scientific Research under Grant FA9550-14-1-0332. Computational Resources were provided by the Ohio Supercomputer Center under Grant No. PAS0072

#### 6:00 PM V08

**(Student) Deep Level Transient Spectroscopy Analysis of Ultra-Wide Bandgap  $\beta\text{-Ga}_2\text{O}_3$**  *Jossue Montes*, Houqiang Fu, Xuanqi Huang, Xuguang Deng, Hong Chen, Tsung-Han Yang, Jingan Zhou, Chen Yang, Xin Qi and Yuji Zhao; Arizona State University, United States

In recent years, beta-phase gallium oxide ( $\beta\text{-Ga}_2\text{O}_3$ ) has enjoyed a significant interest in research endeavors. With a bandgap between 4.6–4.9 eV, it is an ultra-wide bandgap (UWBG) semiconductor. This introduces a large ensemble of potential applications, particularly relating to power electronics, deep ultra violet (DUV), passivating or transparent conductive oxide for solar cells, etc. There is a wide range of tunability of n-type conductivity across  $10^{16}\text{--}10^{19}\text{ cm}^{-3}$  that is easily attainable in the material using dopants such as Sn or Si. Additionally, large, low-cost single-crystal wafers are readily available commercially. Besides the ultra-wide bandgap,  $\beta\text{-Ga}_2\text{O}_3$  also exhibits a large breakdown electric field ( $\sim 8\text{ MV cm}^{-1}$ ). These qualities result in a very large Baliga's figure of merit ( $\text{BFOM} = \epsilon\mu E_b^3$ ,  $\epsilon$ =relative dielectric constant,  $\mu$ =electron mobility,  $E_b$ =breakdown field) equal to approx.  $50,000\text{ MV}^2/\Omega\text{-cm}^2$ , indicating excellent suitability for  $\beta\text{-Ga}_2\text{O}_3$ -based high power applications. Nascent research into the electrical character of defects throughout the bandgap of  $\beta\text{-Ga}_2\text{O}_3$  has been performed; however, a complete picture has still not yet been realized. Making good devices on a  $\beta\text{-Ga}_2\text{O}_3$  platform necessitates an understanding of both native and impurity-related defects of the material. Deep level transient spectroscopy (DLTS) has been used to survey at least 5 electronic trap states in the upper region of  $\beta\text{-Ga}_2\text{O}_3$  bandgap; however, their origins remain unclear, whether they arise during any of various growth methods, doping, etc. DLTS is a powerful and sophisticated electrical characterization method based on measuring the changing capacitance of the depletion region of a Schottky diode, pn-junction, or MOSCAP. During the DLTS measurement, occupied trap levels are vacated, thus causing the capacitance of the depletion region to change as a function of time due to the emission of trapped electrons to the conduction band. This all-electric, highly sensitive technique is capable of finding and quantifying extremely low defect concentrations in a material. Vertical Schottky barrier diodes (SBDs) were designed and fabricated from bulk (-201)  $\beta\text{-Ga}_2\text{O}_3$  wafers (Sn doping,  $N_t - N_a = 5.2 \times 10^{18}\text{ cm}^{-3}$ ), obtained from Tamura Corp. They were produced by the edge-defined film-fed growth (EFG) method. High resolution x-ray diffraction (HR-XRD) measurements on the as-received samples revealed a full-width at half-maximum (FWHM) value of 43 arcsec, indicating excellent crystal quality. Surface roughness was found to be 0.65 RMS in a  $5 \times 5\text{ }\mu\text{m}^2$  scanning area using atomic force microscopy (AFM). Large Ohmic contacts consisting of metal stacks of Ti (20 nm) / Al (30 nm) / Ni (20 nm) / Au (100 nm) were patterned and deposited using standard lithography and electron beam evaporation. The Schottky contacts were similarly patterned and deposited; a single stack of  $1 \times 1\text{ mm}^2$  Ni was deposited. The DLTS setup used a constant reverse bias of 0.4 V, a positive pulse of 0.5 V, with positive pulse widths lasting 20  $\mu\text{s}$ . The frequency sweep varied between 20-150 Hz at various frequencies (necessarily omitting 60 Hz). The DLTS measurement was carried out from 50 to 300 K at a ramp rate of 30 mK/s. This method revealed 2 clear defects in the spectrum, which at 30 Hz (for example) occurred at temperatures of 187.5 and 229.0 K. A third defect is conceivably lying at 310-320 K, just outside the temperature range used. An Arrhenius plot of the frequency sweep revealed that the 229 K defect is a majority carrier defect i.e. electron trap; its energy level was  $E_c - 0.4\text{ eV}$  with a capture cross-section ( $\sigma$ ) of  $7.86 \times 10^{-15}\text{ cm}^2$ . The second defect revealed using this sweep was a hole trap, occurring at  $E_v + 0.219\text{ eV}$  with a capture cross-section of  $4.23 \times 10^{-19}\text{ cm}^2$ . Further research is currently ongoing, particularly through the use of larger reverse biases ( $\sim 5\text{ V}$ ), longer pulse widths ( $\sim 1\text{ ms}$ ) and higher temperatures ( $\sim 400\text{ K}$ ), to fully sample deeper levels in the materials.

#### 6:15 PM V09

**Growth Temperature Dependence of Electronic Defect States in High-Mobility MOCVD-Grown (010)  $\beta\text{-Ga}_2\text{O}_3$**  *Hemant J. Ghadi*, Joe F. McGlone, Rachel Adams, Zixuan Feng, A F M Anhar Uddin Bhuiyan, Hongping Zhao, Aaron Arehart and Steven A. Ringel; The Ohio State University, United States

Recent work on beta phase gallium oxide ( $\beta\text{-Ga}_2\text{O}_3$ ) grown by metal organic chemical vapor deposition (MOCVD) has demonstrated excellent material quality having high electron mobility of  $184\text{ cm}^2/\text{Vs}$  at 300 K and background acceptor concentration below  $1 \times 10^{15}\text{ cm}^{-3}$  [1]. Our group has previously reported a comprehensive investigation of defect states mapped across the  $\sim 4.8\text{ eV}$  bandgap of MOCVD grown  $\beta\text{-Ga}_2\text{O}_3$ . [2] This work extends that initial study to explore the influence of growth temperature on the distribution (concentrations and energy levels) of individual defect states in MOCVD  $\beta\text{-Ga}_2\text{O}_3$ , using deep level transient/optical spectroscopy (DLTS/DLOS) and admittance spectroscopy measurements. Four samples were grown under nominally identical conditions in Agnitron Agilis R&D MOCVD system using TEGa (triethylgallium) and  $\text{O}_2$  precursors over a range of substrate temperatures - 800, 840, 880 and 920°C. All epi-layers were grown to a target thickness of 1  $\mu\text{m}$  with a target Si doping of  $1 \times 10^{17}\text{ cm}^{-3}$  on commercially available (Tamura) Sn-doped (010) EFG (edge-defined film fed growth) substrates, at constant growth rate of 0.7  $\mu\text{m}/\text{hour}$ . The extracted ionized doping concentration from C-V was close to the target but displayed a small increase with increasing growth temperature. This variation could indicate slight growth temperature-dependent Si incorporation in  $\beta\text{-Ga}_2\text{O}_3$ . Admittance spectroscopy revealed a shallow trap at  $E_c - 0.12\text{ eV}$  and its concentration followed a similar trend to that of the C-V doping. The measured concentrations of this state were  $1.2 \times 10^{14}$ ,  $1.4 \times 10^{14}$ ,  $3.1 \times 10^{15}$  and  $3.6 \times 10^{15}\text{ cm}^{-3}$  for 800, 840, 880 and 920°C grown samples, respectively, with a sharp reduction for the 2 lowest growth temperatures to the point where it is no longer the dominant trap. In contrast, the DLTS-detected state at  $E_c - 0.4\text{ eV}$  was no longer detectable at the highest growth temperature, making an evident opposite trend for these two upper bandgap states. States deeper in the bandgap were detected using DLOS, which revealed three states, each of which have previously studied to varying degrees, at  $E_c - 1.2\text{ eV}$ ,  $E_c - 2.0\text{ eV}$  and  $E_c - 4.4\text{ eV}$ . The  $E_c - 4.4\text{ eV}$  state showed a monotonic concentration reduction with growth temperature, and no real trend for the  $E_c - 2.0\text{ eV}$  state. However, the  $E_c - 1.2\text{ eV}$  trap was only detectable for the 880°C sample. Full details of the dependence of each trap on growth conditions, correlations with transport properties and discussion of possible sources by comparison with theory and SIMS (already underway) will be discussed, with the goal toward continued MOCVD growth optimization. **References:** *Z. Feng, et al., Appl. Phys. Lett., 114, 250601, 2019. H.Ghadi et al., APL Materials., accepted 2020.*

#### 6:30 PM V10

**Proton Radiation Effects on Electronic Defect States in High-Mobility MOCVD-Grown (010)  $\beta\text{-Ga}_2\text{O}_3$**  *Joe F. McGlone*, Hemant J. Ghadi, Zixuan Feng, A F M Anhar Uddin Bhuiyan, Hongping Zhao, Aaron Arehart and Steven A. Ringel; The Ohio State University, United States

Gallium oxide has compelling material properties that have generated a large and growing interest for applications in opto-electronics, power devices, and RF devices. The wide bandgap of  $\sim 4.6\text{--}4.8\text{ eV}$  leads to a large breakdown field that increases the Baliga and Johnson figures of merit, indicating potentially superior performance in high power and high frequency devices. Additionally, the large bandgap has a propensity for better radiation hardness due to higher required displacement energies. An application for  $\beta\text{-Ga}_2\text{O}_3$  based devices is a harsh radiation environment in space applications. There has been significant work to understand the impact of radiation on the GaN based material and devices, which degrades device performance due to the introduction of crystal defects.  $\text{Ga}_2\text{O}_3$  has been shown to have higher displacement energies compared to GaN, so it may have improved radiation tolerance. Recently, beta phase gallium oxide ( $\beta\text{-Ga}_2\text{O}_3$ ) grown by metal organic chemical vapor deposition (MOCVD) has demonstrated excellent material quality having high electron mobility of  $184\text{ cm}^2/\text{Vs}$ . [1] In this work, MOCVD material is exposed to proton radiation at an energy of 1.8 MeV to understand how proton damage will influence the defect spectrum. Since intrinsic defects respond to radiation, radiation can be used to identify if a defect level is intrinsic. The 1  $\mu\text{m}$  thick MOCVD sample was grown in an Agnitron Agilis R&D MOCVD system using TEGa (triethylgallium) and  $\text{O}_2$  precursors at a substrate temperature of 880°C. The doping level was targeted to be  $1 \times 10^{17}\text{ cm}^{-3}$  on a commercially available Sn-doped (010) EFG substrates at constant growth rate of 0.7  $\mu\text{m}/\text{hour}$ . Characterization of the MOCVD grown samples are done through multiple methods, mainly C-V, admittance spectroscopy (AS), and deep level transient and optical spectroscopy (DLTS/DLOS). The electron concentration is extracted from the C-V on the Schottky diodes and monitored for each fluence to determine the carrier removal rate. The carrier removal rate of  $185\text{ cm}^{-1}$  for 1.8 MeV proton radiation in MOCVD  $\text{Ga}_2\text{O}_3$  is significantly lower than published work on the same energy proton radiation in n-type GaN Schottky diodes. [2] There have been other reports on proton radiation in UID EFG  $\beta\text{-Ga}_2\text{O}_3$  and HVPE doped  $\beta\text{-Ga}_2\text{O}_3$  to date which have identified radiation sensitive defects through DLTS. [3], [4] This work uses multiple trap spectroscopy measurements (AS, DLTS and DLOS) to identify the changes in specific defects due to the proton radiation. AS measured a rather shallow trap level in the MOCVD material at  $E_c - 0.12\text{ eV}$  which was unaffected by radiation. DLTS identifies the generation of four new defect states compared to pre-

radiation at  $E_c$ -0.35 eV,  $E_c$ -0.6 eV,  $E_c$ -0.7 eV, and  $E_c$ -1.0 eV, with the  $E_c$ -0.7 eV level showing the highest concentration. Furthermore, DLOS measurements were done to identify levels beyond ~1 eV from the conduction band through an optical excitation process. The DLOS spectrum showed three trap levels with an increase in the concentration of the  $E_c$ -1.2 eV trap and a large increase for the  $E_c$ -2.0 eV trap level, which is the main compensating center. The trap at  $E_c$ -4.4 eV is not sensitive to radiation, which is consistent with our work on neutron radiation on UID EFG  $\beta$ -Ga<sub>2</sub>O<sub>3</sub>. [5] This work will focus on understanding the changes caused by proton radiation for each defect level. With the knowledge of which defects are intrinsic and respond to radiation, theoretical studies for the displacement energies and possible intrinsic defects associated with each level will be discussed. [1] Z. Feng *et al.*, *Appl. Phys. Lett.*, vol. 114, no. 25, p. 250601, Jun. 2019. [2] Z. Zhang *et al.*, *J. Appl. Phys.*, vol. 119, no. 16, p. 165704, Apr. 2016. [3] M. E. Ingebrigtsen *et al.*, *APL Mater.*, vol. 7, no. 2, p. 022510, Dec. 2018. [4] A. Y. Polyakov *et al.*, *Appl. Phys. Lett.*, vol. 112, no. 3, p. 032107, Jan. 2018. [5] E. Farzana *et al.*, *APL Mater.*, vol. 7, no. 2, p. 022502, Dec. 2018

## SESSION W: Electrochemical Energy Storage and Conversion

Session Chair: Zetian Mi

Session Hosts: Louis Piper and Edward Yu

Thursday Afternoon, June 25, 2020

Location: ZoomRoom 2

### 3:45 PM W01

**(Student) Development of Thick Cathodes for High-Energy Lithium-Ion Batteries** [Lalith Rao](#)<sup>1</sup>, Jay R. Sayre<sup>1</sup>, Christopher J. Brooks<sup>2</sup>, Hanna Cho<sup>1</sup>, Marcello Canova<sup>1</sup> and Jung Hyun Kim<sup>1</sup>; <sup>1</sup>The Ohio State University, United States; <sup>2</sup>Honda R&D Americas, United States

Lithium-ion (Li-ion) batteries adopted in electric vehicles (EVs) and grid energy storage systems require significant increase in energy density (> 750 Wh/L) and reduction of costs to enable widespread commercialization. To address these challenges, R&D efforts have been directed towards (a) finding materials with high energy density and (b) improving electrode design. In particular, the latter includes minimizing the use of inactive materials (e.g., current collectors and separators) and increasing the thickness of electrodes (> 250  $\mu$ m), which in turn offers improved energy density with reduced cost. The performance of the thick electrodes is inferior to conventional electrode (i.e., thickness  $\leq$  100  $\mu$ m) due to limited ion and/or electron transports through porous microstructures. It has been believed that a severe capacity fading of thick electrode is associated to a sluggish Li-ion transport via its highly tortuous pore-structure. To solve this issue, some research groups have reported methods to create vertical channels through the thickness of electrode using techniques such as laser-cutting and freeze-casting. However, industry adoption of these techniques can be challenging due to their high processing cost and long processing time.

In this study, we demonstrate in-situ crack formation (also referred to as mud-cracking) as a method to create vertical channels in thick cathodes, which is directly applicable to the conventional manufacturing processes of Li-ion batteries. The method of achieving these cracks significantly depends on the type of active material, solvents, binder combinations and the drying conditions being used. We have explored two different processing routes based on the solvents which are suitable for different active materials.

First, we used aqueous binder for LiFePO<sub>4</sub> cathode based on its good chemical stability in aqueous environment. The crack formation in the thick electrode is achieved by the combination of water-soluble binders, styrene butadiene rubber (SBR) and polyacrylic acid (PAA). Second, we used non-aqueous binder for LiNi<sub>0.6</sub>Mn<sub>0.2</sub>Co<sub>0.2</sub> (NMC) cathode material due to its sensitivity to moisture. We will present the materials and processing parameters that impact the physical properties of the thick cathodes, which includes solid loading and surface energy of slurry, binder composition, types of carbon networks, and drying conditions. Microstructure, physical properties, and electrochemical performances of the thick electrodes were characterized by using SEM, peel-force measurement, electrochemical impedance spectroscopy, four-point dc-probe and cycle life testing. From the results, we have explored the control parameter-electrode microstructure-performance relationship that is critical in understanding how the control parameters can be tuned to achieve the required electrode design.

### 4:00 PM W02

**(Student) In Operando AFM Characterization of Mechanical Property Evolution of Si Anode Binders in Liquid Electrolyte** [Michael Lee](#), Hanna Cho and Jung Hyun Kim; The Ohio State University, United States

Understanding mechano-chemical behaviors of binders facilitates the development of advanced binder materials to accelerate the adoption of Si-based anode materials. We used an approach to characterizing in-operando mechanical behaviors of binders while wetting in electrolyte solvents at nano-scale using atomic force microscopy (AFM). To reproduce Si - binder interfaces in anodes, we designed a model system and measured force spectroscopy between Si micro-cantilevers and binder films made with two representative materials: sodium (Na) alginate and polyvinylidene fluoride

(PVdF). Na-alginate has orders-of-magnitude higher adhesive forces with Si than PVdF after being immersed in dimethyl carbonate (DMC) which can be explained by (i) strong hydrogen bonds between Si surface's oxidation layer and hydroxyl/carboxyl groups in Na-alginate and/or (ii) ion-dipole interactions between these two components. Na-alginate demonstrates a Young's modulus ~56 times greater than that of PVdF after several hours of immersion in DMC and reaching their steady states conditions. The results correlate well with cycle life of Si anodes in battery cells considering that Na-alginate's retention of mechanical strength and higher adhesive forces can help withstand the large volume expansions of Si.

### 4:15 PM W03

**(Student) Dehydrobenzoannulene-Based Two-Dimensional Covalent Organic Frameworks as an Anode Material for Lithium-Ion Batteries** [Eric Wolfson](#), Neng Xiao, Luke Schkeryantz, William K. Haug and Psaras McGrier; The Ohio State University, United States

Developing anode materials with excellent cycling performance and energy capacities for lithium-ion batteries (LIBs) is a challenging task. Covalent organic frameworks (COFs) have gained attention as potential high-performing electrode materials due to their ability to incorporate redox-active monomers directly into their ordered structure. In addition, the use of covalent linkages provides robust electrode materials with high coulombic efficiencies. This presentation will emphasize the synthesis of an imine-linked COF containing redox-active dehydrobenzoannulene (DBA) units for use as an anode material in a lithium-ion battery. The DBA-COF system exhibits a reversible capacity of 207 mA h g<sup>-1</sup> at 50 mA g<sup>-1</sup> after 90 cycles. This work highlights the potential of utilizing DBA units to construct efficient organic-based anode materials for LIBs.

### 4:30 PM W04

**Elucidating the Atomistic Catalytic Mechanism of Single Ni Atom in N-Doped Graphene for CO<sub>2</sub> Reduction** [Yuan Yue Liu](#); The University of Texas at Austin, United States

Single nickel atom embedded in graphene is one of the most representative single atom catalysts, and has a high activity and selectivity for electrochemical CO<sub>2</sub> reduction (CO<sub>2</sub>R) to CO. However, the catalytic origin, especially the coordination structure of Ni, remains highly puzzling, as previous density-functional-theory (DFT) calculations show all the possible structures should be inactive and/or non-selective. Here using ab-initio molecular dynamics (AIMD) and "slow-growth" sampling approach to evaluate the reaction kinetic barriers, we show that the charge capacity (of the site) and hydrogen bonding (with the intermediates), which were neglected/oversimplified in previous DFT calculations, play crucial roles[1,2], and including their effects can resolve the catalytic origin. These factors should also be important to other electrochemical reactions at solid-water interface.

[1] D. Kim, J. Shi, Y. Liu, *JACS*, 2018 DOI: 10.1021/jacs.8b03002

[2] X. Zhao, Y. Liu, submitted

### 4:45 PM W05

**(Student) First Principles Investigation of the Influence of Magnetic Moment for Design of Integrated 3D Graphene Structures with Earth-Abundant Transition Metal Single Atom Catalysts** [Chloe Groome](#); University of California, Irvine, United States

Single atom catalysis (SAC) represents a promising design for the next generation of robust catalysts. These systems, which are commonly single metal atoms stabilized on carbonaceous materials, maximize catalytic performance while simultaneously minimizing the use of expensive and scarce platinum-group metals (PGM). While it is accepted that the molecular environment of a SAC is of crucial consequence to the chemical activity, the exact catalytic sites and chemical pathways responsible have been a matter of some controversy. For industrially practical non-PGM SAC, optimizing the defect environment stabilizing the single metal atom is necessary for enhanced performance. We will present work using a first principles approach for materials discovery to investigate three less studied earth abundant transition metals (V, Mo, Ta) stabilized on single vacancy and pyridinic N-doped defect moieties on graphene substrates to understand the role of electronic transfer, spin state and steric effects on SAC. Our results of all investigated metals demonstrate single atom stability on graphene substrates with both defect moieties. By modeling carbon monoxide oxidation, a common benchmark reaction, facilitated by these defect stabilized SAC with climbing image-nudged elastic band (CI-NEB) calculations, we find that all activation energies for transition metals stabilized on the pyridinic N-doped graphene surface defect are ~0.8 eV or lower. These low activation energy barriers suggest that the CO oxidation reaction would proceed at room temperature with pyridinic N-dopants present in the defect environment. The CI-NEB calculations further illustrate that SAC of Ta and V on pyridinic N doped graphene significantly decrease the activation energy of CO oxidation by 27% and 44%, respectively. Bader charge analysis reveals that the electronic charge transfer is surprisingly similar across the two defect moieties investigated for all four earth-abundant transition metals. However, the pyridinic N-dopant introduces an additional magnetic moment of 0.53  $\mu_B$  on average. Plotting the density of states of CI-NEB transition states shows spin destabilization of O<sub>2</sub> peaks near the Fermi level, suggesting that these imparted magnetic moments could be destabilizing

the O2 bond and hence lowering activation energies for CO oxidation in some cases. We will present results suggesting that magnetic moment could play a significant role in enhancing catalytic performance of SAC on nitrogen doped graphene substrates, as well as more traditionally understood mechanisms such as charge transfer and steric effects. Computational design of materials is used to define processing conditions for three-dimensional porous graphene structures. Fabrication and characterization of macroscopic graphene structures with high surface area and architectures to facilitate mass transport will also be presented.

#### 5:00 PM BREAK

#### 5:30 PM W06

**(Student) New Materials for Extreme Environmental Sensors Based on Solid Oxide Fuel Cells** [Alexander Vaeth](#) and Sheikh Akbar; The Ohio State University, United States

Sensing technology for extreme temperatures and environmental conditions is becoming increasingly important for applications in space travel and hypersonic technology. Solid oxide fuel cells commonly consist of yttria-stabilized zirconia (YSZ), utilizing Pt or perovskite-oxide electrodes. Little work has been completed on the stability or sensitivity of these materials at and near their sintering temperatures (1200-1500°C). In this work, sensors consisting of 8 mol% YSZ with either sputtered or screen-printed platinum electrodes were characterized *in-situ* with electrochemical impedance spectroscopy over temperatures from 800-1400°C with oxygen concentrations ranging from 0.04 to 0.30 atm. It was quickly realized that sensor degradation became present both during a single test and with subsequent testing. The source of the degradation can be found both in electrolyte and electrode. For the electrode morphological, chemical, or diffusion-based reactions with the electrolyte could be the source. The degradation of the electrical conductivity of commonly used 8 mol% YSZ with time at temperatures above 1000°C is likely caused by nano-microstructural changes to the defect structure of the crystal. This leads to the need for new materials for high temperature sensors. These can be split into electrode materials and electrolyte materials. This work focuses on determining the stability of the sensing ability for these new materials. For example, higher doping levels of YSZ have shown negligible conduction loss with time. Also, the electrical stability of other electrolytes like gadolinia-doped ceria (GDC) in these regimes has little documentation and needs explored. Electrode materials will focus on oxide-perovskites like lanthanum-strontium-manganite and platinum alloyed with elements like rhodium and tungsten increasing the melting point of the electrodes. Through this investigation, the chemical, thermal, and electrical stability of these materials alone and with respect to each other will be explored using electrochemical impedance spectroscopy, X-ray diffraction, and electron microscopy. The work done here will guide future work in this subject with respect to material selection for extreme environment sensors.

#### 5:45 PM W07

**Eumelanin in a New Light—Biological Pigments with the Excited State Behavior of Graphitic Carbonaceous Nanomaterials** [Christopher Grieco](#), Forrest R. Kohl and Bern Kohler; The Ohio State University, United States

Eumelanin, the ubiquitous brown biological pigment, possesses sunscreen and redox chemistry functions that are vital to organisms ranging from bacteria to humans. Very recently, eumelanin-based materials have received considerable interest for energy conversion and storage devices. The structure of eumelanin is unknown, but evidence suggests that it contains chemically diverse assemblies of absorbing units, the precise nature of which has eluded researchers for several decades. The inability to study structure-function relationships in eumelanin has limited understanding of the processes that occur following the absorption of solar radiation. In this work, we use a new femtosecond transient absorption spectroscopy approach, previously used to probe the heterogeneous structures in graphene oxide and carbon nanodots, to the study of eumelanin.[1] By tuning the excitation wavelength across the broad absorption spectrum of melanin from the UV to the visible, we address the excited state behavior of the different absorbing units (chromophores) in a synthetic eumelanin. The spectra exhibit transient spectral hole burning, revealing the extreme chemical heterogeneity present in eumelanin. Unexpectedly, a common photoinduced absorption spectrum with virtually identical decay kinetics is seen regardless of which group of chromophores is excited. We assign this to the ultrafast (<200 fs) generation of immobile charge transfer excitons that form and locally decay among the diverse set of chromophores. Raman spectroscopy reveals that structural heterogeneity in eumelanin, like in graphitic carbon materials, arises from different sized domains of sp<sup>2</sup>-hybridized carbon and nitrogen atoms. Our most recent measurements demonstrate strong parallels between the structure and photoproperties of eumelanin and those of graphitic carbonaceous nanomaterials such as graphene oxide and carbon nanodots, suggesting that the latter materials mimic properties that have long been useful to living organisms. Our results encourage multidisciplinary efforts between chemists and materials scientists to uncover the common origins of their photophysical, chemical, and structural properties. [1] F.R. Kohl, C. Grieco, and B. Kohler, Chem. Sci. (2020), DOI: 10.1039/c9sc04527a.

SESSION X: III-Nitride MBE and Sputtering Growth  
Session Chair: Ramón Collazo  
Session Hosts: Russell Dupuis and Brendan Gunning  
Thursday Afternoon, June 25, 2020  
Location: ZoomRoom 3

#### 3:45 PM X01

**(Student) Impact of Substrate Temperature for High Quality Regrown GaN Homoepitaxial Films Grown by Metal Modulated Epitaxy** [Habib Ahmad](#), Keisuke Motoki, Evan Clinton, Christopher M. Matthews, Zachary Engel and W. Alan Doolittle; Georgia Institute of Technology, United States

Metal modulated epitaxy (MME) is a low temperature modified molecular beam epitaxy (MBE) growth technique in which periodic shuttering of the metal fluxes is carried out while keeping the nitrogen plasma constant. MME significantly improves the morphological and structural quality of the epitaxially grown films and enables lower temperature growth for the same crystal quality compared to traditional MBE. The effects of growth temperature on the morphological, structural, electronic, and optical properties of Unintentionally doped (UID) Gallium Nitride (GaN) epitaxial films grown by MME are investigated over a wide temperature range from 500 °C to 750 °C. Most structural properties were found to be improved at intermediate substrate temperatures while optical properties were best at high temperatures. In order to rule out differences in nucleation as a quality modifier, UID GaN epilayers were homoepitaxially grown on c-plane surfaces of semi-insulating hydride vapor phase epitaxy (HVPE) grown GaN on sapphire templates. By examining the surface via *in-situ* reflection high energy electron diffraction (RHEED), it was found that oxide removal from the HVPE substrates was critical to obtain consistent high quality films. Extensive *ex situ* solvent and chemical cleaning, and, *in situ* thermal cleaning and three cycles of Ga flashing were used on all the HVPE GaN templates prior to homoepitaxial UID GaN growth for obtaining an oxide-reduced growth interface. However, this oxide did affect the electrical properties of the grown films. RHEED improved upon each Ga flashing cycle. The UID GaN samples were grown at substrate temperatures from 500 to 750 °C. The samples were grown at a III/V ratio of 1.8 with a total metal dose of 10 seconds open and 10 seconds closed. Growth continued after the shutter was closed for ~8 seconds indicating a significant accumulation of surface Ga in each cycle. In order to achieve this III/V ratio, the Ga flux which was constant at lower temperatures was increased for the sample grown at 750 °C. All the MBE grown GaN were 500 nm thick. Electronic, morphological, structural, and optical characterization of unintentionally doped homoepitaxial GaN samples were measured using hall effect measurement (HEM), atomic force microscopy (AFM), X-ray diffraction (XRD), transmission electron microscopy (TEM), and photoluminescence (PL). RHEED was used for *in situ* monitoring of surface morphology and III/V ratio calculations during growths.

AFM images show large surface pits but also regions of smooth morphology on micrometer scale for the sample grown at 500 °C. AFM images of the sample grown at 550 °C show smooth step-flow growth surface morphology but with scattered Ga droplets accumulation. AFM depicted step flow surface morphology for the samples grown at 600 to 750 °C. From HEM, an optimal mobility was found for intermediate temperatures with the best electrons mobilities achieved at 650 °C. The sample grown at 500 °C was too resistive to measure using hall. Due to homoepitaxy, symmetric and asymmetric rocking curve XRD figures of merit were taken at 1/100, 1/1000 and 1/10, 000 of the peaks in order to majorly probe the MBE grown layer. Defect states and dislocation densities probed by XRD, and TEM indicate the highest crystalline quality of films grown in the temperatures range of 650 to 750 °C. PL was strong in all samples with a full width at half maximum decreasing with increasing temperature. Interestingly, the GaN films grown at 500 and 550 °C show a 6 meV shift in the PL peak position toward lower energy indicating significant strain states in these films. Optimization of the substrate temperature for the MBE grown UID GaN resulted in a set of growth conditions for optimal step-flow surface morphology and high crystalline quality having low threading dislocation densities matching the values found in the substrate.

#### 4:00 PM X02

**Advancements in Aluminum Indium Nitride Growth over a Wide Compositional Range—Towards Long Wavelength III-Nitride Optoelectronics** [Zachary Engel](#), Christopher M. Matthews, Evan Clinton, Habib Ahmad and W. Alan Doolittle; Georgia Tech, United States

AlInN has been a topic of recent study due to its ability to be lattice matched to GaN at a composition of 18% indium, making it a strong candidate for power electronic and optoelectronic applications. An area that has been largely understudied is the growth of AlInN alloys with high indium content. AlInN has a tunable bandgap range from 0.7 to 6.1 eV spanning from the infrared to the ultraviolet range. With high indium content AlInN can achieve multiple important band gap values, such as 2 eV to achieve red light emission in and LED and 1.7 eV, the ideal band gap for a tandem with silicon solar cell. Many challenges exist with the growth of AlInN. As a result of the large lattice parameter mismatch between the binaries AlN and InN a large miscibility gap exists for the ternary. In addition, the growth regimes of InN and AlN are

significantly different in MBE. At the low temperatures required for the growth of AlInN the aluminum adatoms have a low mobility, often leading to lateral phase separation in the film. Metal Modulated Epitaxy (MME) offers a good solution to the growth issues of AlInN. This flux modulated technique allows for growth to proceed under metal rich conditions which increases surface diffusion lengths of the Aluminum even at low temperatures while limiting droplet formation and terminating in a dry surface as is critical for device applications.

AlInN was grown using MME, with a composition of about 70% indium. By optimizing the growth conditions and substrate temperature significant improvements in material parameters were achieved. Improvements were seen in the X-ray Diffraction (XRD) figures of merit, yielding the lowest (0002) rocking curve FWHM ever reported at 135 arcsec, about 12 times lower than previously reported for this composition range. An improvement was also observed in the (10-15) rocking curve FWHM, yielding a low value of 886 arcsec. Smooth surface morphology was also observed in AFM scans, with a low RMS roughness between 0.4 and 0.5nm for the smoothest samples and observation of spiral hillock structures. Photoluminescence measurements yielded promisingly strong emissions that suggested emission from a quantum confined structure. Specifically, four overlapping gaussian peaks were observed with energies that scale quadratically with peak index as expected for a quantum confined structure suggesting a nanostructure that is phase separated. AlInN was also grown via MME in a wide composition range between 90% and 50% Indium. XRD scans of these samples yielded low figures of merit, with (0002) rocking curve FWHM values between 130 and 180 arcsec and (10-15) rocking curve FWHM values between 750 and 1250 arcsec. These promising material advancements will allow for the exploration of optical and photovoltaic devices in the lower bandgap range that is traditionally difficult for the III-Nitride system

#### 4:15 PM X03

**Molecular Beam Epitaxy and Characterization of Wurtzite  $\text{Sc}_x\text{Al}_{1-x}\text{N}$**  Ping Wang, David A. Laleyan, Ayush Pandey, Yi Sun and Zetian Mi; University of Michigan, United States

Recently, Sc-III-N has been theoretically proposed and experimentally demonstrated to satisfy the requirements of the development of next generation wide bandgap applications. As a IIIB element, Sc has the same oxidation state (+3) with IIIA metals, providing an alternate approach to substitute the IIIA elements in conventional III-nitrides. Meanwhile, the substitutional Sc may destabilize the robust wurtzite structure of III-nitrides due to the stable rock-salt structure of ScN. Therefore, the incorporation of Sc offers new opportunities for bandgap, polarization, and piezoelectric engineering in semiconductors. However, the epitaxy of pure wurtzite phase  $\text{Sc}_x\text{Al}_{1-x}\text{N}$  with relatively high Sc composition has remained challenging. Low-temperature sputtering has been used to suppress the phase separation and increase the Sc composition, at the expense of materials quality, which severely limits the potential applications of  $\text{Sc}_x\text{Al}_{1-x}\text{N}$ . Moreover, the fundamental properties of  $\text{Sc}_x\text{Al}_{1-x}\text{N}$ , including variations of bandgap and refractive index with Sc composition, has remained elusive. In this context, we have investigated the epitaxy of  $\text{Sc}_x\text{Al}_{1-x}\text{N}$  on GaN and AlN templates using a Veeco GENxplor molecular beam epitaxial (MBE) growth system. The wurtzite structure is well maintained even at a high growth temperature of 1,000 °C for  $\text{Sc}_{0.2}\text{Al}_{0.8}\text{N}$  without significant degradation of crystal quality. The Sc composition for pure wurtzite phase  $\text{Sc}_x\text{Al}_{1-x}\text{N}$  has been realized in our case is up to 0.34, which is ~14% higher than previous reports. Step-flow growth mode is observed in  $\text{Sc}_x\text{Al}_{1-x}\text{N}$  epilayers with lower Sc ( $x \leq 0.14$ ), while it is superseded by high-density grains for higher Sc layers. The grain size gradually increases with increasing Sc, but the root mean square (RMS) roughness remains lower than 1 nm. The full-width at half maximum (FWHM) of (002) plane X-ray diffraction rocking curve for these  $\text{Sc}_x\text{Al}_{1-x}\text{N}$  epilayers are less than 450 arcsec. Optical absorption studies indicate a decreasing bandgap with increasing Sc with a linear relationship of  $E_g(x) = 6.1 - 3.39x$ , in good agreement with the previous theoretical prediction. A monotonically tunable refractive index between AlN and GaN is further measured for  $\text{Sc}_x\text{Al}_{1-x}\text{N}$  with various Sc compositions. Furthermore, to demonstrate the high-quality of  $\text{Sc}_x\text{Al}_{1-x}\text{N}$ , a high electron mobility transistor (HEMT) structure was grown with a 1 nm GaN capping layer, 20 nm  $\text{Sc}_{0.2}\text{Al}_{0.8}\text{N}$  barrier, 2 nm AlN interlayer, and 100 nm undoped GaN regrowth layer on a Fe-doped insulating GaN/sapphire template. The structure surface has clear spiral atomic steps with a RMS roughness of 0.52 nm for  $3 \times 3 \mu\text{m}^2$ . Room temperature (RT) Hall-effect measurements exhibit a two-dimensional electron gas (2DEG) mobility ( $m$ ) of 970  $\text{cm}^2/\text{Vs}$  and an electron density ( $n_s$ ) of  $3.1 \times 10^{13} \text{ cm}^{-2}$ , resulting in a low sheet resistance ( $R_s$ ) of 206  $\Omega/\square$ . The controlled epitaxy of pure wurtzite phase high-quality  $\text{Sc}_x\text{Al}_{1-x}\text{N}$  with tunable bandgap and refractive index suggests potential applications in optoelectronic, electronic and piezoelectric devices, and integrated photonics.

#### 4:30 PM X04

**Structural, Optical and Electronic Transport Properties of (111) ScN Thin Films Grown on (0001) Fe-Doped GaN, (0001)  $\text{Al}_2\text{O}_3$  and (111) MgO** John Cetnar<sup>1</sup>, Amber Reed<sup>1</sup>, Tobin Muratore<sup>1,2</sup> and David Look<sup>1,3</sup>; <sup>1</sup>Air Force Research Laboratory, United States; <sup>2</sup>University of Dayton, United States; <sup>3</sup>Wright State University, United States

ScN is a degenerate semiconductor with a rocksalt crystal structure which has promising characteristics for integration with other III-nitride compounds. In

the (111) orientation, it has a lattice mismatch of less than 1% with c-plane GaN leading to very low strain across the interface. Over the last few years there has been an increasing interest in ScN as a supplement to GaN technology. The potential uses of ScN in GaN based systems include buffer layers, ohmic contacts, current spreading layers, and polarization-enhancing interlayers for tunnel junctions. Given the requirement for the (111) orientation, it is important to understand how this material behaves when grown in this orientation and how different substrates can influence the growth, crystal quality, and electronic transport properties of ScN.

In this work, we report on the growth and characterization of (111) oriented ScN thin films. The films were grown on (0001) Fe-doped GaN (SI-GaN), (0001)  $\text{Al}_2\text{O}_3$ , and (111) MgO substrates using reactive magnetron sputtering for a range of growth times at 50 W and 200 W power levels. The structure of the samples was characterized using the FWHMs of  $2\theta$ - $\theta$  and rocking curve X-Ray Diffraction measurements. The electronic transport properties (resistivity  $\rho$ , carrier concentration  $n$ , and Hall mobility  $\mu_H$ ) were characterized with Hall-effect measurements using the Van der Pauw configuration, at temperatures ranging from 10 K to 320 K. The temperature dependences of  $n$  and  $\mu$  showed characteristic differences for the ScN films on each type of substrate. Finally, reflectance and transmittance were measured in the energy range  $E = 0.4$  to 6.5 eV, and analyzed to yield absorption ( $\alpha$ ) and reflection ( $R$ ) coefficients, and the real ( $\eta$ ) and imaginary ( $\kappa$ ) parts of the index of refraction. Then a Drude analysis of  $\eta$  and  $\kappa$  vs  $E$  yielded values of the optical carrier concentration  $n_{\text{opt}}$  and mobility  $\mu_{\text{opt}}$  that could be compared with  $n$  and  $\mu_H$ , respectively. The results of these measurements will be presented along with a discussion of the advantages and disadvantages of each substrate material.

#### 4:45 PM X05

**(LATE NEWS, Student) Epitaxial Growth of III-Nitrides on O-Face ZnO Substrates by Low Temperature RF-Metal Enhanced Epitaxy (MEE)** Kamruzzaman Khan, Mahitosh Biswas and Elaheh Ahmadi; University of Michigan-Ann Arbor, United States

III-Nitrides semiconductors have been investigated for optoelectronics devices and high-power microwave devices for the last few decades. The large bandgap and lower effective mass of III-N make this materials system attractive for high-power and high-frequency applications. ZnO can be an alternative substrate for III-N because of its superior lattice match and isomorphous wurtzite crystal structure. Besides, high-quality ZnO substrates can be prepared by hydrothermal methods and are larger than that of the state of the art GaN-bulk substrates.

Matsouka (1992) et al. [1] epitaxially fabricated  $\text{In}_{0.2}\text{Ga}_{0.8}\text{N}$  on ZnO substrates by metal-organic chemical vapor deposition (MOCVD) in the early years of nitride growths. ZnO substrate forms the polycrystalline film when in contact with ammonia in the MOCVD reactor. Additionally, ZnO and  $\text{H}_2$  from ammonia back etch ZnO substrates at high temperatures and ZnO reacts with III-N at high growth temperature forming an interfacial layer. InGaN on ZnO substrates by MOCVD with a low-temperature GaN buffer layer have been explored. Growing good quality GaN buffer layer on the ZnO substrate has always been challenging. MBE is preferred for III-N growths ZnO because of its lower substrate temperature than that of MOCVD for III-N growths. GaN growths on Zn-face and O-face ZnO substrates with substrate treatment by molecular beam epitaxy (MBE) have been demonstrated. InN has been grown on ZnO substrates by MBE as well. Epitaxial growths of different nitrides on ZnO substrates have been studied by pulsed laser deposition [2]. III-N thin films on ZnO substrates showing step flow morphology is crucial to grow high-temperature nitrides on top of the buffer layer. Growing III-N at low temperature decreases the adatom mobility and increases the surface roughness and increases defect formation. in result.

MEE in an MBE system referred to the deposition of metal and nitridation of that metal subsequently. The same process is repeated several times based on the required thickness. In this technique, the group III metal atoms have enough time to diffuse to energetically favorable site in the matrix before nitridation. This can improve quality of the materials grown at low-temperature and decrease the surface roughness. However, there has not been an extensive study comparing low-temperature III-N growths on ZnO substrates by metal-enhance epitaxy growth of with that by MBE.

Here, we have demonstrated GaN, InN growths on O-face ZnO substrates by MEE technique showed drastic improvement in surface morphology with even low substrate temperature in comparison with conventional MBE technique. We studied the GaN and InN growths by MEE with the change in substrate temperature and sample thickness. We have studied the surface morphology during the growths by in-situ RHEED analysis and AFM analysis.

#### References:

[1] T. Matsouka, N. Yoshimoto, T. Sasaki, and A. Katsui, J. Electron. Mater. **21**, 157 (1992). [2] A. Kobayashi, J. Ohta, and H. Fujioka, Sci. Rep. **7**, 1 (2017).

#### 5:00 PM BREAK

### 5:30 PM Y01

**(Student) Low-Field Transport in High Al-Composition Al<sub>x</sub>Ga<sub>1-x</sub>N Channel High Electron Mobility Transistors** Towhidur Razzak<sup>1</sup>, Hao xue<sup>1</sup>, Hareesh Chandrasekar<sup>1</sup>, Mohammad K. Hussain<sup>2</sup>, Shahadat H. Sohel<sup>1</sup>, Mohammad Wahidur Rahman<sup>1</sup>, Sanyam Bajaj<sup>1</sup>, Joe F. McGlone<sup>1</sup>, Steven A. Ringel<sup>1</sup>, Asif Khan<sup>2</sup>, Wu Lu<sup>1</sup> and Siddharth Rajan<sup>1</sup>; <sup>1</sup>The Ohio State University, United States; <sup>2</sup>University of South Carolina, United States

This work reports a detailed characterization and modeling study of low-field transport properties of MOCVD-grown Al<sub>0.70</sub>Ga<sub>0.30</sub>N/Al<sub>0.50</sub>Ga<sub>0.50</sub>N heterostructure field-effect transistors. Mobility is a critical component for high frequency and power transistors. In addition to obvious effects on on-resistance in power devices, mobility also determines the effective velocity in short-channel high-frequency transistors. While high Al composition AlGa<sub>x</sub>N offers high breakdown fields, they also have relatively low mobility compared to GaN-channel HEMTs. However, there has been very little experimental investigation of the scattering mechanisms that limit AlGa<sub>x</sub>N channel devices. A better understanding of the scattering mechanisms limiting high Al composition AlGa<sub>x</sub>N channels may be useful in future device designs and enable higher mobility while maintaining high breakdown electric fields. In this work, we elucidate the principal mobility-limiting mechanisms in high Al composition AlGa<sub>x</sub>N HFETs using theory and experiment and use the framework developed to discuss novel designs that could enable significantly higher mobility while maintaining high breakdown field. The sample consists of a 0.25 μm thick Al<sub>0.5</sub>Ga<sub>0.5</sub>N grown on a 2 μm AlN on sapphire template, followed by a 50 nm thick n-doped ([Si<sup>-</sup>] = 2 × 10<sup>18</sup> cm<sup>-3</sup>) Al<sub>0.70</sub>Ga<sub>0.30</sub>N barrier. The contact layer was a 70 nm n-doped ([Si<sup>-</sup>] = 6 × 10<sup>18</sup> cm<sup>-3</sup>) graded layer with Al composition, x, graded from 0.7 to 0.3. Ohmic contacts were formed using a Ti-based metal stack, RTA annealed at 875°C for 45s. Mesa isolation was performed using Cl<sub>2</sub>-based ICP-RIE etching. Low power gate recess was performed to etch away the graded contact layer with an over-etch of 10 nm of the Al<sub>0.70</sub>Ga<sub>0.30</sub>N barrier layer. Finally, a Ni-based metal stack was used for gate metallization. A schematic structure of the fabricated HEMT and the equilibrium energy-band diagrams under the access regions are shown in Fig. 1. Hall measurements performed on ungated VDP structures showed sheet charge density (n<sub>s</sub>) and electron mobility to be 8.8 × 10<sup>12</sup> cm<sup>-2</sup> and 120 cm<sup>2</sup>/Vs, respectively. TLM measurements showed a contact resistance of 3.9 Ω.mm and sheet resistance of 7 kΩ/sq. n<sub>s</sub> obtained from CV measurement was found to be 5.5 × 10<sup>12</sup> cm<sup>-2</sup> at both room temperature and low-temperature (T = 77 K) which indicates current conduction in the channel is via 2DEG (Fig. 2). Field-effect mobility was measured on FATFET structures (Fig. 3(a)) at very low drain bias using the relationship, μ<sub>FE</sub> = (L · g<sub>m</sub>) / (W · C<sub>gs</sub> · V<sub>DS</sub>), where μ<sub>FE</sub> is field-effect mobility, L is channel length, g<sub>m</sub> is the transconductance, W is the channel width, C<sub>gs</sub> is the gate to source capacitance and V<sub>DS</sub> is the drain voltage. Fig. 3(b) shows the extracted mobility as a function of gate bias while mobility vs n<sub>s</sub> is shown in Fig. 4(a) (FATFET dimensions: L<sub>SD</sub> = 16 μm and L<sub>C</sub> = 14 μm). Analytical models of various scattering mechanisms were used to fit experimentally obtained mobility (Fig. 4(a)). Mobility from individual scattering mechanisms is shown in fig. 4(b). The dominant scattering mechanism was found to be background impurity (5 × 10<sup>17</sup> cm<sup>-3</sup>) scattering for low n<sub>s</sub> while at higher n<sub>s</sub> interface roughness limits the net mobility in the material – both of which can be improved by growth optimization. Remarkably, alloy scattering was not the limiting factor in the samples investigated. This suggests that future improvements in growth could enable significantly higher mobility in high Al composition AlGa<sub>x</sub>N. More significantly, a careful analysis of alloy scattering mechanisms can also enable new channel designs such as multi-channel transistors and ordered alloys, that could enable a reduction in alloy scattering and thereby a significant increase in mobility. **Acknowledgement:** The authors acknowledge funding from AFOSR (Grant FA9550-17-1-0227, Program Manager Kenneth Goretta) and DARPA DREaM program (ONR N00014-18-1-2033, Program Manager Dr. Young-Kai Chen, monitored by ONR, Program Manager Dr. Paul Maki).

### 5:45 PM Y02

**(Student) N-Polar AlN/GaN Superlattice Heterostructure with Record Electron Mobility of 2050 cm<sup>2</sup>/Vs Grown on GaN Substrate by Plasma-Assisted Molecular Beam Epitaxy** Sandra M. Diez Pinzon, Cagliyan Kurdak and Elahieh Ahmadi; University of Michigan, United States

We studied the effect of channel and buffer thickness on the transport properties of N-polar GaN-based high electron mobility transistor (HEMT) structures. Three samples with channel thicknesses of 10 nm, 15 nm and 20 nm were grown by molecular beam epitaxy (MBE) on N-polar Zinc-doped GaN (semi-insulating) substrates with a 100 nm thick C-doped layer and a 200 nm thick buffer layer. The back barrier structure of the samples was formed by an AlN/GaN superlattice with a Si-doped layer (8 × 10<sup>17</sup> cm<sup>-3</sup>) on the back side. Electron transport was studied via Van der Pauw Hall and Shubnikov de Haas

measurements to obtain twodimensional electron gas (2DEG) concentration and mobility of the samples at low temperature (1.7 K). All three samples presented single frequency SdH oscillations at high magnetic fields, confirming the presence of a single level 2-dimensional electron gas (2DEG) on the channel. Similar carrier density (~8 × 10<sup>12</sup> cm<sup>-2</sup>) was extracted from SdH oscillations for the samples with different channel thicknesses. On the contrary, The carrier concentration obtained from Hall measurements at 1.7 K increased by increasing the channel thickness (9.3 × 10<sup>12</sup> cm<sup>-2</sup>, 1 × 10<sup>13</sup> cm<sup>-2</sup>, and 1.3 × 10<sup>13</sup> cm<sup>-2</sup> for the samples with 10 nm, 15 nm, and 20 nm thick channel, respectively). These carrier densities are consistently larger than that obtained from SdH oscillations, indicating the possible presence of a parallel conduction mechanism in addition to the 2DEG. The temperature dependence of the carrier density and mobility was evaluated by magnetotransport measurements between 1.7 K and 300 K. The carrier concentration and mobility for all samples stayed nearly constant for most of the temperature range, up to 200 K. The mobility of the samples at 1.7 K is largest for the sample with 15 nm thick channel, with 5000 cm<sup>2</sup>/Vs and smallest for the sample with 20 nm thick channel, about 3000 cm<sup>2</sup>/Vs. For the sample with 20 nm thick channel, the difference between the carrier concentrations obtained by both methods is the largest. This combined with the lower mobility indicates that this sample is strongly affected by parallel conduction. A second series of samples with buffer layer thickness of 200 nm, 400 nm, and 600 nm was fabricated, all with channel thickness of 10 nm. For the sample with 400 nm thick buffer, the carrier density reduced to 7.9 × 10<sup>12</sup> cm<sup>-2</sup>, which is close to n<sub>s</sub> obtained from SdH on samples with similar epi-structure, suggesting that the parasitic channel with lower electron mobility was eliminated on this sample. The mobility reached a record value of 2050 cm<sup>2</sup>/Vs, never reported before for N-polar GaN-based heterostructures.

### 6:00 PM Y03

**Active Polarization Engineering in AlGa<sub>x</sub>N/GaN High-Electron-Mobility Transistors to Modulate Two-Dimensional Electron Gas Density by Piezoelectric Cap Layer and External Bending Strain** Weijie Wang<sup>1</sup>, Sara Pouladi<sup>1</sup>, Seung Min Lee<sup>2</sup>, James Lundh<sup>3</sup>, Jung Hwan Um<sup>4</sup>, Jie Chen<sup>1</sup>, Shahab Shervin<sup>1</sup>, Jungwoo Oh<sup>2</sup>, Sukwon Choi<sup>3</sup> and Jae-Hyun Ryou<sup>1</sup>; <sup>1</sup>University of Houston, United States; <sup>2</sup>Yonsei University, Korea (the Republic of); <sup>3</sup>The Pennsylvania State University, United States; <sup>4</sup>Ulsan National Institute of Science and Technology, Korea (the Republic of)

Flexible devices made of III-N thin films have implications surpassing merely the ability to fabricate bendable devices. Owing to the unique piezoelectric properties of III-N materials, external strain applied during bending can be exploited to control device characteristics and to provide additional functionality. We investigate the effect of piezoelectric polarization modulation on the 2-dimensional electron gas (2-DEG) channel in Al<sub>0.25</sub>Ga<sub>0.75</sub>N/GaN high-electron-mobility transistor (HEMT) by both BeO cap layer and external strain to prove the concept of active polarization engineering to create multifunctional electronic and photonic devices made of flexible group III-nitride thin films. The multifunctionality of the flexible III-N electronic and photonic devices originates from the electronic band structure modification as a result of changes in piezoelectric charges at the heterostructure interface. Therefore, for the proof of the concept it is necessary to confirm that the electronic band structure and its associated device characteristics are changed according to the controlled strain imposed by external bending. We previously demonstrated that the electronic band structure in AlGa<sub>x</sub>N/GaN HEMTs can be modified by the polarization modulation effect of a single-crystalline piezoelectric BeO cap layer, resulting in a 14% increase of the 2DEG density. This previous report shows the feasibility of polarization engineering in III-N heterostructures, but not specifically for flexible devices. In the present study, we systematically investigate the changes in device characteristics from the band structure modification in flexible AlGa<sub>x</sub>N/GaN HEMTs originating from the strain induced by bending in order to prove the concept of the proposed multifunctional devices enabled by active polarization engineering. We studied the strain effect in a flexible Al<sub>0.25</sub>Ga<sub>0.75</sub>N/GaN HEMT via both numerical simulation and experimental demonstration. The flexible HEMTs were fabricated by a layer-transfer process and integrated with a 150-μm-thick Cu film by electroplating. HR-XRD was used to estimate in-plane strains of ε<sub>xx</sub> = 0.57%, ε<sub>yy</sub> = -0.18% and ε<sub>zz</sub> = -0.59%, ε<sub>xy</sub> = 0.21% for 4-cm bend-down and -4-cm bend-up test conditions, respectively. From the measured output characteristics, current changes of 3.4% and -4.3% were observed in the bend-down and bend-up test conditions, respectively. Threshold voltage shifts were also observed which indicated changes in the 2DEG sheet density in the channel during bending. Computational simulation was performed, where a 4.3% current modulation was demonstrated. The origin of current modulation was discussed and we believe piezoelectric polarization charge induced by the applied strain altered the 2DEG density in the channel and thus resulted in changes of the drain current. Even greater changes in the polarization charge and more current modulation can be expected, if InAlN with larger negative piezoelectric constants is used as the barrier layer. This strain effect of the flexible HEMTs offers the potential for wearable electro-mechanical devices for sensor, transducer, and actuator applications.

6:15 PM Y04

**(LATE NEWS, Student) Design of Ultra-Scaled Channel N-Polar GaN HEMTs with High Charge Density Using AlN-GaN Superlattice as the Backbarrier**

Subhajit Mohanty<sup>1</sup>, Sandra M. Diez Pinzon<sup>2</sup>, Zhe (Ashley) Jian<sup>1</sup> and Elaheh Ahmadi<sup>1</sup>; <sup>1</sup>University of Michigan, United States; <sup>2</sup>University of Michigan–Ann Arbor, United States

GaN-based transistors have demonstrated superior power performance from the S-band to the W-band frequency range compared to alternative device technologies due to high electron velocity and mobility, high 2-D electron gas (2DEG) density and large breakdown field in the III-nitride material system [1]. The enhanced confinement of 2DEG above the natural barrier in N-polar GaN-based HEMTs have several advantages over Ga-polar GaN-based HEMTs which enables them a promising candidate for highly scaled devices. To further enhance operation frequency, GaN channel thickness must be reduced [2], which typically leads to a decrease in both 2DEG density and mobility, and therefore significantly larger sheet resistance. To maintain large 2DEG density while reducing channel thickness, the backbarrier must be modified. One way of modifying the back-barrier is to increase AlN thickness. As a result, valence band (VB) approaches very close to the fermi level due to the polarization field in AlN, and consequently, DC-RF dispersion during large-signal operation due to hole traps present at (Al, Ga) N/GaN negative polarization interface (NPI) if the barrier is not properly Si-doped to compensate these traps [3-4]. In this work, we studied the effects of barrier structure, trap level and density, doping density on 2DEG charge, dispersion, and parasitic channel of heterostructure systematically. A design of a thin channel, high 2DEG and dispersion-free epitaxial structure was also demonstrated which can maintain high 2DEG density in the channel ( $2 \times 10^{13} \text{ cm}^{-2}$ ).

The epitaxial structure comprised of a typical N-polar epi-structure with twelve layers of AlN/GaN (0.5 nm/1.5 nm) superlattice (SL) as back-barrier which is separated from GaN channel by an AlN interlayer (1-4 nm) and GaN/AlN (2/0.5 nm) spacers. The epi-structure was simulated using Silvaco Atlas by varying Si-doping level, AlN interlayer thickness, trap density and energy level to study their impact on 2DEG density, trap ionization and formation of a parasitic channel in the device. In series-A, the entire barrier was doped with Si whereas in the series-B a thin layer (15nm-thick) of Si-doped GaN was doped under the barrier, and in Series-C, both were doped. Simulation results reveal that at low SL doping level (Series-A), the ionized donors cannot neutralize the traps near the GaN channel effectively. As a result, the valence band gets pinned at trap level which hinders any change in the electric field in AlN interlayer resulting in almost constant 2DEG for different AlN thicknesses. As the SL doping level increases, the traps are neutralized sufficiently and excess ionized donor charge enhances 2DEG charge. Furthermore, the doping at the backside (Series-B) is found to be very effective in compensating the traps present at the backside of SL, yet there is little modulation on 2DEG. To suppress the effect of trap both at the backside and near the channel and modulate 2DEG simultaneously, it is imperative to dope both the barrier as well as the backside. In addition, the effect of the AlN interlayer barrier structure was also investigated. Minimum doping required to neutralize all traps increases as we increase AlN thickness. Doping profile, therefore, needs to be carefully tuned for each structure to avoid (i) formation of parasitic channel and (ii) dispersion. An optimized design of epi-structure is demonstrated that enables maintaining a very large 2DEG density ( $\sim 2 \times 10^{13} \text{ cm}^{-2}$ ) in N-polar GaN HEMT with ultra-scaled 5nm-thick channel thickness. This design allows for large 2DEG density in the channel while preventing ionization of hole traps or formation of a parasitic channel.

[1] U. K. Mishra et al., *Proc. IEEE*, vol. 96, 2, pp. 287–305, 2008.

[2] G. H. Jessen et al., *IEEE Trans. Electron Devices*, vol. 54, 10, pp. 2589–2597, 2007.

[3] B. L. Swenson et al., *J. Appl. Phys.*, vol. 106, 6, pp. 1–6, 2009.

[4] C. A. Schaake et al., *Semicond. Sci. Technol.*, vol. 28, 10, p. 105021, 2013.

SESSION Z: Nanophotonic Materials

Session Chair: Seth Bank

Session Hosts: Anthony Hoffman and Parsian Mohseni

Thursday Afternoon, June 25, 2020

Location: ZoomRoom 4

3:45 PM Z01

**(Student) Plasmonic Coupling in Topological Insulator and Band Insulator Layered Structure**

Zhengtianye Wang, Sivakumar V. Wang, Theresa P. Ginley, Greeshma Chandan, Yuying Zhang, Chaoying Ni and Stephanie Law; University of Delaware, United States

Topological insulators (TIs) are quantum materials that exhibit topologically protected helical edge states that arise from strong spin-orbit coupling. These edge states show linear dispersion and cross at the  $\Gamma$  point. Electrons occupying these states are massless Dirac fermions, obeying the Dirac equation for relativistic particles. Therefore, these surface states can house two-dimensional (2D) Dirac plasmons at room temperature similar to other 2D materials like graphene. Moreover, due to the spin-orbit coupling, these TI surface states also demonstrate spin-momentum locking, which limits nonmagnetic scattering. Therefore, Dirac plasmons in TIs are further predicted to be topologically

protected and spin polarized, which could lead to a longer lifetime and the possibility of optical manipulation of a spin wave in a material. Instead of the normal bulk plasmon mode that arises in three-dimensional films, electrostatic coupling between the top and bottom surface states of a single layer of TI thin film gives rise to an optical plasmon mode and an acoustic plasmon mode [1]. However, only the optical mode can be observed by optical methods due to its non-zero dipole [2,3]. Interestingly, the frequency of the optical mode lies in the untapped terahertz (THz) range. A vertically stacked superlattice structure of TIs and normal band insulators (BIs) is expected to result in the coupling of multiple surface states, generating multiple optical modes. These modes are tunable by changing the superlattice crystal structure, which is easy to do with molecular beam epitaxy (MBE). In our system,  $\text{Bi}_2\text{Se}_3$  and  $(\text{Bi}_{1-x}\text{In}_x)_2\text{Se}_3$  (BIS) were used as the TI and BI materials, respectively. BIS is a topologically trivial alloy of  $\text{Bi}_2\text{Se}_3$  and  $\beta\text{-In}_2\text{Se}_3$ , both of which belong to the group and share close lattice constants: 2.866nm and 2.823nm, respectively. Using BIS, indium diffusion into the TI layers is less of a concern than it would be with pure  $\beta\text{-In}_2\text{Se}_3$  as the BI layer [5].

We demonstrated experimental evidence of multiple Dirac plasmon coupling in BIS/ $\text{Bi}_2\text{Se}_3$ /BIS/ $\text{Bi}_2\text{Se}_3$ /BIS stacked layers grown on sapphire (0001). The films were patterned into microribbon arrays with varying widths to excite localized plasmon modes. Fano-shape extinction spectra containing two distinct plasmon modes were observed with all samples in the range of 1.5THz-8THz through Fourier-transformed Infrared (FTIR) spectroscopy measurements. A three-oscillator, double-Fano-resonance model was adopted to extract parameters of the high/low frequency plasmon mode and to model the quantum interference between the surface plasmons and the bulk phonon ( $\alpha$  phonon=2.01THz). A blueshift in frequency was observed for both the high/low frequency modes as the microribbon width narrows, similar to what has been observed in the single optical plasmon mode in a single layer  $\text{Bi}_2\text{Se}_3$  [2,3]. A coupling of the two plasmon modes was observed with increasing wavevector. The tunability of the plasmon frequencies via changing the thickness of BI and TI layer were also shown. Understanding plasmon coupling across the multilayer TI/BI structure will provide a deep insight to the many-body interaction in low-dimensional strong spin-orbit coupling systems. It also lays the foundation for future tunable THz devices for detection, security screening and advanced communication.

**Reference**

[1] R. E. V Profumo, R. Asgari, M. Polini, and A. H. Macdonald, *Phys. Rev. B* **85**, 085443 (2012).

[2] T. P. Ginley and S. Law, *Adv. Opt. Mater.* **1800113** (2018).

[3] P. Di Pietro, M. Ortolani, O. Limaj, A. Di Gaspare, V. Giliberti, F. Giorgianni, M. Brahlek, N. Bansal, N. Koirala, S. Oh, P. Calvani, and S. Lupi, *Nat. Nanotechnol.* **8**, 556 (2013).

[4] Y. Wang and S. Law, *Opt. Mater. Express* **8**, 2570 (2018).

[5] Y. Wang, T. P. Ginley, S. Law, Y. Wang, T. P. Ginley, and S. Law, *J. Vacu. Sci. Technol. B* **36**(2), 02D101 (2018).

4:00 PM Z02

**(Student) Degenerate Semiconductor Interfaces for Electro-Optic**

**Modulation of Mid-IR Surface Plasmons** Zuoming Dong<sup>1</sup>, Raj Vinnakota<sup>2</sup>, Andrew F. Briggs<sup>1</sup>, Seth R. Bank<sup>1</sup>, Dentcho Genov<sup>3</sup> and Daniel Wasserman<sup>1</sup>; <sup>1</sup>University of Texas at Austin, United States; <sup>2</sup>Troy University, United States; <sup>3</sup>Louisiana Tech University, United States

The field of plasmonics has been of particular interest for next generation photonic devices due to the potential for subwavelength confinement of optical modes, offering new approaches for sub-diffraction limit imaging, sensing and waveguiding. At short wavelengths (near-IR and visible), plasmonic structures typically utilize traditional noble metals which, at longer wavelengths, behave more like perfect conductors than plasmonic metals [1]. At these longer wavelengths, plasmonic behavior can be achieved with highly doped semiconductors [2], offering the opportunity for monolithically integration of plasmonic media with semiconductor devices in a single material system. Such a hybrid semiconductor-plasmonic device architecture offers the potential for a new class of dynamic, electrically-controlled mid-IR optoelectronic devices. One such example is the proposed surface plasmon polariton diode (SPPD) [3], an optoelectronic switch in which a surface plasmon polariton can be supported (and dynamically tuned) at the interface of an electrically controlled p-n<sup>+</sup> junction.

Here we present a mid-IR optoelectronic switch based on an InGaAs p-n<sup>+</sup> junction diode grown by molecular beam epitaxy (MBE) on (100) InP and consisting of 1  $\mu\text{m}$  of n<sup>+</sup>-InGaAs () followed by 750 nm of p-InGaAs (). Optical coupling to the SPP modes is achieved using a grating structure etched into the p-InGaAs, and electrical contact is achieved with a Ti/Au top contact along the unetched portion of the p-InGaAs as shown in Fig. 1 (a). Thus, our device's grating structure serves to both couple light into the SPP mode at the p-n<sup>+</sup> interface and as a top electrode for carrier injection. We demonstrate SPP coupling into the degenerate plasmonic interface at (Fig. 1(b)) and electrical modulation of the device's reflectivity at the SPP coupling wavelength using a mid-IR reflection set-up based on a Fourier transform infrared (FTIR) spectrometer and mid-IR microscope. First we measured the reflection of a planar Au surface (Fig. 2(a)), which serves as the reference for the device's modulated reflectivity measurements. Next, we measured the electrically modulated change in reflection of the device using the setup shown in Fig. 2(b) which is similar to Fig. 2(a) except that the light is now modulated electrically by biasing the device electrically (using a 10 kHz square wave signal). The MCT detector output was fed into a lock-in amplifier (LIA), synchronized to

the pulse generator. The demodulated output of the LIA gives the reflection change spectra from the modulated device which was then normalized to the reflection from the Au surface, giving the absolute change in reflectivity ( $\Delta R/R$ ) under different biases. A multi-physics finite-element model was developed to simulate the change in reflectivity as a function of applied bias to the device. We achieve 1.4% reflectivity modulation amplitude with 1.41V forward bias, as shown in Fig. 3. In summary, we have fabricated and characterized a mid-IR optoelectronic switch based on an InGaAs p-n<sup>+</sup> diode. We can modulate the coupling to SPP modes supported at the p-n<sup>+</sup> interface by controlling electrical injection of charge into the p-type InGaAs. A finite-element model is also developed to simulate the observed modulation, and shows good agreement with our experimental results. ZD and DW gratefully acknowledge funding from the National Science Foundation (Award No. ECCS-1611231). AB and SB gratefully acknowledge support from the National Science Foundation (Award No. DMR 1508603 and 1508783). RV and DG gratefully acknowledge funding from the National Science Foundation (Award No. ECCS-1610200) and NSF EPSCoR CIMM project (Award No. OIA-1541079). [1] S. Law, V. Podolskiy, D. Wasserman, *Nanophotonics* 2 (2), 103-130 (2013). [2] S. Law, D.C. Adams, A.M. Taylor, and D. Wasserman, *Optics Express*, 20, 12155 (2012). [3] R.K. Vinnakota, D. A. Genov, *Sci. Rep.* 4 (2014).

#### 4:15 PM Z03

##### (Student) Epitaxially Embedded Mid-Infrared Plasmonic

**Corrugations** Alec M. Skipper, Priyanka Petluru, Ashlee Garcia, Daniel Ironside, Aaron J. Muhowski, Daniel Wasserman and Seth R. Bank; The University of Texas at Austin, United States

Plasmonic emission enhancement has emerged as a potential solution for improving the efficiency of mid-infrared devices [1]. The mid-infrared possesses a wealth of molecular “fingerprints” and atmospheric absorption windows, necessitating the development of robust devices for applications in sensing, defense, and communication [2]. However, materials in the mid-IR are plagued by Auger and Shockley-Read-Hall recombination, limiting device performance [3]. Plasmonics are ideal for overcoming these limitations due to the strong optical field enhancement at the interface of metallic nanostructures that allow for increased light-matter interaction in absorbers and emitters [4]. Highly n-doped InAs possesses a tunable plasma wavelength and compatibility with typical mid-IR optoelectronic materials [5]. By adjusting the doping concentration, the plasma wavelength of molecular beam epitaxy (MBE) grown InAs can be tailored to minimize loss and maximize field enhancement at a target mid-IR wavelength. While typical plasmonic materials can be patterned to engineer strong localized resonances, the lack of lateral control in conventional MBE makes it challenging to create similar structures compatible with monolithically-grown plasmonic InAs. To this end, we report the epitaxial growth of highly doped InAs plasmonic ridges and progress towards strong localized resonant enhancement of mid-IR emitters and absorbers. Windows were etched in a SiO<sub>2</sub> film deposited on (001) InAs wafers to act as seed crystals to nucleate epitaxial growth. By using periodic supply epitaxy (PSE), a technique that cycles the supply of group-III atoms with a constant group-V overpressure, III-V growth can occur on the semiconductor substrate without polycrystalline deposition on the SiO<sub>2</sub> film. The enhanced adatom mobility of PSE results in highly faceted crystalline semiconductor material above the SiO<sub>2</sub> film which can subsequently be planarized by continuous growth [6]. By growing highly-doped InAs at the beginning of the planarization step, the plasmonic InAs matches the contour of the faceted ridges produced by PSE. This results in a fully-epitaxially integrated textured metal for mid-IR plasmonics. Results were confirmed using scanning electron microscopy (SEM) and Fourier transform infrared (FTIR) spectroscopy to verify the structure and plasma wavelength of the material. Experiments to model and integrate these structures with mid-IR absorbers and emitters are underway and will be reported at the conference. This research was partially supported by the National Science Foundation through the Center for Dynamics and Control of Materials: an NSF MRSEC under Cooperative Agreement No. DMR-1720595, as well as DMR-1839175 and ECCS-1926187. [1] L. Nordin et al., “Enhanced emission from ultra-thin long wavelength infrared superlattices on epitaxial plasmonic materials,” *Appl. Phys. Lett.* (2020) [2] F. Tittel et al., “Mid-Infrared Laser Applications in Spectroscopy” in *Solid-State Mid-Infrared Laser Sources* (2003) [3] B. Olson et al., “Auger recombination in long-wave infrared InAs/InAsSb type-II superlattices,” *Appl. Phys. Lett.* (2015) [4] R. Stanley, “Plasmonics in the mid-infrared,” *Nature Photonics* (2012) [5] S. Law et al., “Mid-infrared designer metals,” *Optics Express* (2012) [6] D. Ironside et al., “High-Quality GaAs Planar Coalescence over Embedded Dielectric Microstructures Using an All-MBE Approach,” *ACS Cryst. Growth Des.* (2019)

#### 4:30 PM Z04

**Propagating Dirac Plasmon Polaritons in Topological Insulators** Yong Wang and Stephanie Law; University of Delaware, United States

The properties of topological insulators (TIs) have been widely explored due to their unique band structure. The energy states at the TI surfaces exhibit linear dispersion and spin-momentum locking. Carriers occupying these states are therefore two-dimensional, massless, and spin-polarized. Dirac plasmons in TIs, which are comprised of Dirac carriers in TI surface states, are predicted to be both carrier density waves as well as spin density waves. Since most TI films are much thinner than the wavelength of light, plasmons excited on the top and bottom surfaces couple, resulting in an acoustic and an

optical plasmon mode. Due to the spin-momentum locking characteristics of the TI surfaces, the optical mode is predicted to be spin-polarized. Before the spin properties of TI plasmons can be measured, propagating plasmons must first be excited. There are a variety of ways to excite plasmons in TI thin films. The most common way is to etch the film into an array of stripes to create localized plasmons. Although this technique has been highly effective, these localized modes cannot easily be used to understand the spin properties of TI plasmons. To excite propagating plasmons, we instead choose to use a grating coupler fabricated on the surface of the TI film.

We first grew a series of 50nm Bi<sub>2</sub>Se<sub>3</sub> films using a molecular beam epitaxy (MBE) system. The TI films had the following structure: a layer of 5nm BiInSe<sub>3</sub> (BIS) on the top, 50nm Bi<sub>2</sub>Se<sub>3</sub> TI in the middle, and 50nm BIS between the TI and the Al<sub>2</sub>O<sub>3</sub>(0001) substrate. The BIS layer on the top serves as a protection layer to prevent surface degradation and charge redistribution caused by the grating metal. The BIS layer on the bottom serves as a buffer layer to optimize the quality of the TI growth. After growth, 100nm gold/10nm titanium gratings with different grating periodicity are lifted off of the surface of the film. The periodicity of the gratings ranges from 100nm to 700nm. TM polarized transmission spectra are then taken in a Fourier Transform Infrared Spectroscopy (FTIR) system. From the extinction spectra, we observe a series of absorbing peaks that shift with the grating periodicity. We have ruled out any source other than the plasmons that could have possibly caused the peaks to show up in the range. TM transmission spectra were taken on a bare sapphire substrate, a single layer TI film directly grown on sapphire, a single layer BIS film grown on sapphire, and a sapphire substrate with gratings on top. None of the spectra shows the same peaks as those we see in TI films with top gratings. Hence, we have successfully demonstrated the existence of the propagating Dirac plasmons in the TI Bi<sub>2</sub>Se<sub>3</sub> and the tunability of the plasmon frequency with grating period. We simulated the plasmon frequency as a function of momentum using the coupled Dirac plasmon model, which further proves the excitation of the Dirac plasmons.

Our next steps will be to launch the plasmon and detect the spin wave dynamically. TIs are the only known single-material system where such spin-polarized plasmons can be observed. The observation of propagating Dirac plasmons in TI is significant not only because it proves the theoretical predictions of TI Dirac plasmons, but also creates possibilities in developing future technology. A frequency-tunable propagating spin-density wave could be feasible for better memory or computing systems.

#### 4:45 PM Z05

##### (Student) Self-Winding Helices as Slow-Wave Structures for THz

**Frequency** Hassan Dibaji<sup>1</sup>, Divya Prakash<sup>1</sup>, Matthew Dwyer<sup>2</sup>, Shelley Scott<sup>2</sup>, Danier van der Weide<sup>2</sup>, Max G. Lagally<sup>2</sup> and Francesca Cavallo<sup>1</sup>; <sup>1</sup>University of New Mexico, United States; <sup>2</sup>University of Wisconsin–Madison, United States

We demonstrate a transformative path to miniaturize helical slow-wave structures (SWSs) for operation at THz frequencies. SWSs are central to the operation of travelling wave tubes that can potentially provide higher gain and bandwidth than any solid-state device at THz frequencies. Several processing techniques have been proposed to reduce the size of the SWSs to the required (micro- and sub-microscale) dimensions for operation at mm and sub-mm frequencies. However, a scalable, rapid, and high-yield process to build helical SWSs for THz frequencies is not available.

Our approach relies on using self-assembly of metal nanomembrane (NM) strips into helices and subsequent electroplating of the helical strips. The structure is unique in that it has microscale diameter, a helical geometry, and potentially high electrical/thermal conductivity. An additional advantage of self-winding SWSs is that they can be fabricated via processing techniques analogous to the ones conventionally used for microelectronic devices.

Here we present a combined theoretical and experimental effort that focuses on parametric design and fabrication of these novel SWSs for high-power THz sources. We coordinate simulations of cold helices and beam-wave interaction to determine a useful range of design parameters for the SWSs. These parameters include diameter, pitch, tape width (width of the NM strips), and surface finish. Based on our simulation results we design and fabricate prototype helices that promise to operate as SWSs at THz frequencies. Fabrication of microscale SWSs begins with defining NMs strips by optical lithography, metal evaporation, and lift-off. In our work we use Cr/Au NMs that have an inherent stress gradient across their thickness. We define the metal strips onto a bulk semiconductor substrate (e.g., Si or Ge) coated with a sacrificial or release layer. Ge, GeO<sub>2</sub>, and SiO<sub>2</sub> sacrificial layers have all been used in our experiments. NM strips self-assemble into helices with a diameter ranging from ~5 to 40 μm upon selective wet etching of the sacrificial layer. These precisely defined helices are generated by control of the material properties, including thickness, elastic modulus, and built-in strain. Electroplating of self-assembled helices increases the thickness of the Au layer to a few micrometers, while at the same time preserving the microscale helical geometry of the SWSs.

Work supported by U.S. AFOSR-Award No. FA9550-19-1-0086

#### 5:00 PM BREAK

### 5:30 PM Z06

**(Student) Towards Achieving Self-Assembled Hyperbolic Metamaterials in the Short to Mid-Wave Infrared Spectral Range** Yuejing Wang, Joshua Zide and Stephanie Law; University of Delaware, United States

We present our ongoing efforts towards achieving self-assembled hyperbolic metamaterials (HMMs). HMMs are interesting for many applications including enhanced sensing, subwavelength imaging, radiative decay engineering, and so forth. There are two common ways to create an HMM: embedding an array of subwavelength metallic rods within a dielectric matrix or building a subwavelength metal/dielectric superlattice. By engineering the subwavelength structure, the real part of the permittivities in the parallel and perpendicular directions can have opposite signs, resulting in an open hyperbolic photonic dispersion surface in  $k$ -space. By far, most research of HMMs has been focused on visible wavelengths using traditional metals and dielectrics. Fabricating a short- to mid-wave infrared (IR) HMM would be useful for a wide range of applications. However, there is a lack of a practical metallic component in these wavelengths. Traditional metals like gold and silver cannot be used due to their large and negative permittivities in the IR range. Heavily-doped III-V semiconductors have been demonstrated as excellent mid-IR plasmonic materials, but so far their shortest plasma wavelengths are limited to  $\sim 5.5 \mu\text{m}$ . The semi-metallic nature of many lanthanide mononitrides (e.g. ErAs) provides a material choice to overcome this challenge. The common group V lattice sites and the similar lattice constant between lanthanide mononitrides and traditional III-V semiconductors allow the epitaxial integration of these two components. More interestingly, previous study suggested ErAs lamellars or ErAs rods are likely to self-assemble in (In)GaAs matrices by engineering the growth parameters. This indicates the possible one-step growth of a self-assembled HMM where (In)GaAs is the dielectric component and ErAs is the metallic component.

Preliminary molecular beam epitaxy (MBE) growth and Fourier transform infrared spectroscopy (FTIR) characterization of an ErAs:InGaAs sample containing  $\sim 38\%$  ErAs was conducted. Growth was conducted in a co-deposition mode, allowing the ErAs inclusions to self-assemble. The discontinuity of the Brewster angle at  $\sim 2.3 \mu\text{m}$  in the TM polarized reflection spectrum was observed; this occurs when  $\epsilon_{\parallel}$  crosses zero while  $\epsilon_{\perp}$  is positive, suggesting the onset of type I HMM behavior. However, the bandwidth of this type I HMM behavior is very narrow. Type II HMM behavior was also observed at longer wavelengths. Such type I behavior at short wavelengths and type II behavior at long wavelengths indicated the formation of a multilayered HMM. This demonstrates great potential for creating a novel self-assembled metamaterial for many short- to mid- wave infrared applications. Future work includes optimizing the growth parameters of this multilayered HMM to increase its bandwidth and also explore the suitability of self-assembled ErAs nanorods (e.g. grown within a (111)A GaAs matrix) as another type of HMM.

### 5:45 PM Z07

**Controlled Dewetting and Regrowth of Composite ErAs NP-GaAs(001) Interfaces** Kurt Evinck, Yuanchang Zhang, Madelyn J. Hill, Brittany Urwin and Mahalingam Krishnamurthy; Air Force Research Laboratory, United States

ErAs is a semimetallic rare earth mononitride which has a plasmonic response in the IR-region. ErAs has a rock salt crystal structure and is known to grow epitaxially in zinc-blende GaAs. This ability has led to numerous potential application such as thermoelectrics, plasmonics, and photonics. In the case of plasmonics, patterning the ErAs is required in order to design particular resonances in a metasurface. However, Er oxidizes extremely easily in air which has prevented ErAs use in these application. Due to the difference in crystal structure of ErAs and GaAs, a high energy interface exists between ErAs and GaAs. ErAs nanoparticles form on the GaAs surface via an embedded growth mode in which the ErAs NP are partially buried in the GaAs surface. We recently observed a dewetting of GaAs films from the ErAs NP-GaAs composite interface. In this presentation we study this phenomena as a vehicle for the formation of tunable plasmonic structures. Previously we have shown that the dewetting process depends on several variable such as ErAs NP concentration, the dewetting temperature, dewetting time, and the thickness of the GaAs cap. We explore the ability to form a patterned surface by controlling the thickness of the GaAs. Specifically we produce a cap covering an ErAs NP growth (0.5 monolayers) which is sufficiently thick to prevent the surface from dewetting. By ex-situ etching we thinned the GaAs cap back to a thickness between 2 and 5nm which will allow dewetting. We then perform in-situ cleaning followed by dewetting of the structure in an MBE chamber. We dewet at a temperature greater than  $550^{\circ}\text{C}$  for at least 15 min. We show that we can form dewetted regions of exposed ErAs NPs. Using a low flux growth process, we control the ErAs growth to only the exposed region and produce large areas with continuous ErAs. This demonstration is a first step in producing definable resonances in a metasurface composed of ErAs using this approach.

### 6:00 PM Z08

**Infrared Plasmonic Oxides for Selectively Transparent Aerogels in High Temperature Solar Receivers** Zachary Berquist, Kevin Turaczy and Andrej Lenert; University of Michigan-Ann Arbor, United States

Visibly-transparent silica aerogels are a promising alternative to vacuum insulation in next-generation concentrated solar power (CSP) applications. However, they are characterized by undesirable thermal radiative transmission

in the mid-wave infrared (MWIR) that accounts for most of the energy losses. Here, we experimentally and computationally investigate multicomponent aerogels which selectively enhance MWIR absorption and thus suppress outgoing radiative losses at high temperatures. We incorporated transparent conducting oxide (TCO) nanoparticles (NP) into silica aerogels and characterized the effect of the TCO NPs on the optical and thermal properties of the aerogels. We demonstrate a significant enhancement of MWIR absorption in these multicomponent aerogels relative to silica aerogels. The TCO NPs exhibit a strong plasmonic absorption peak around  $4.5 \mu\text{m}$  – within the transparency window of silica aerogels. We also experimentally demonstrate an increase in solar thermal conversion efficiency with the use of multicomponent aerogels using elevated temperature ( $>400^{\circ}\text{C}$ ) heat flux measurements. The experimental results agree with our simulations of coupled radiative and conductive heat transfer. These results suggest that plasmonic multicomponent aerogels have the potential to improve the performance of low-irradiance, high-temperature CSP receivers.

### 6:15 PM Z09

**(Student) Anomalous Mid-Infrared Absorption in Near-Monolayer Films of ZnO Nanoparticles** Irfan Khan, Caroline Howell, Tracie McGinnity, Ryan K. Roeder and Anthony Hoffman; University of Notre Dame, United States

The interaction of mid- and far-infrared light with optical phonons presents opportunities for novel applications in enhanced spectroscopy, selective absorption and emission, and highly sensitive detectors. The vast majority of this work has been carried out using nano-patterned materials, stacked layers of dielectric materials, or doped materials to engineer the dielectric response. Recently, there have been demonstrations of controlling the mid-infrared permittivity via optical pumping to dynamically tune optical modes. In this work, we present evidence of a new approach to modify the dielectric response of ZnO nanoparticles (NPs) by coupling to an optical phonon mode that is normally not infrared active. We demonstrate anomalous absorption in ZnO NPs at energies very close to an optical phonon mode that is Raman-active only in bulk ZnO. This work opens up new opportunities for engineering the optical properties of mid-infrared materials and long-wavelength light-matter interactions.

ZnO is a II-VI semiconductor material with hexagonal wurtzite crystal structure and 6 optical phonon modes. From Group theory analysis, these modes at the  $\Gamma$ -point have the irreducible representation of  $1A_1 + 2B_1 + 1E_1 + 2E_2$ . The  $A_1$  and  $E_1$  modes are both IR and Raman active. The two  $B_2$  modes are both IR and Raman silent, whereas, the two  $E_2$  modes are Raman active only. Modes that are Raman active only exhibit non-centrosymmetric vibrations without a strong optical dipole moment. Therefore, such modes should not couple to infrared optical fields. However, our optical measurements show strong absorption at the energy of this mode, even as we tune the temperature of the system, shifting the  $E_2$  frequency.

ZnO NPs with a mean diameter of  $\sim 100$  nm were prepared by a solvothermal synthesis adapted from previously published methods. For transmission measurements, pellets were prepared by mixing ZnO:KBr in 1:300 concentration by mass and pressed at 525 MPa using a hydraulic press. Transmission measurements were performed using a Bruker Vertex 80v Fourier transform infrared spectrometer and a room temperature DTGS detector. The transmission spectrum was calculated by taking the ratio of the sample spectrum to the spectrum of a blank KBr pellet. For Raman measurements, we use a Jasco NRS-5100 micro-Raman system with 532 nm excitation laser, 100x objective, and a custom made temperature controlled sample heater.

To identify the spectral positions of the various modes, we perform a multi-peak fit to the measured FTIR spectra using Voigt functions. In the IR absorption data we observe peaks/shoulders at 411, 445, 508, and 535  $\text{cm}^{-1}$ . The 508 and 535  $\text{cm}^{-1}$  peaks agree well with surface phonon polariton modes that are predicted by Mie scattering theory for anisotropic polar NPs. The 411  $\text{cm}^{-1}$  peak corresponds to the TO phonon frequency. The 445  $\text{cm}^{-1}$  peak in the IR data is at the same frequency as the  $E_2^{\text{high}}$  phonon mode which we also measure using Raman spectroscopy. We perform temperature-dependent FTIR and Raman measurements to observe the shift and broadening of this anomalous absorption peak and correlate those changes with the measured  $E_2^{\text{high}}$  phonon mode. Though FTIR and Raman spectroscopy are fundamentally different physical processes, we see qualitative agreement between the two measurements. Both measurements indicates a red shift and broadening of the peak with increasing temperature. The  $E_2^{\text{high}}$  phonon mode is predicted to be infrared-silent for crystals. However, we believe that symmetry-disruption due to the small size of the NPs, small crystallite size, or defects can activate the mode, resulting in the strong absorption observed in our measurements.

### 6:30 PM Z10

**Effect of MBE Growth Conditions on the Resonant-Absorption of ErAs Quantum Dots Near 1550 nm** W-D. Zhang<sup>1,2</sup>, Elliott Brown<sup>3</sup> and Richard Mirin<sup>3</sup>; <sup>1</sup>Wright State University, United States; <sup>2</sup>Terapico LLC, United States; <sup>3</sup>National Institute of Standards and Technology, United States

Recently we have discovered a new way to produce relatively high levels of THz radiation ( $>0.1$  mW average) using a dense array of ErAs quantum dots in a GaAs matrix and pumping with 1550-nm femtosecond pulses [1]. The mechanism appears to be extrinsic photoconductivity mediated by super-radiance [2]. ErAs quantum dots are known to form spontaneously in GaAs when the doping is greater than  $\approx 7 \times 10^{17} \text{ cm}^{-3}$ . For these devices to

become practical, it is important that the ErAs quantum dots have the appropriate size to contain two bound energy levels separated by the 1550 nm pump photon of  $\sim 0.80$  eV. Here, we present studies on optimum growth conditions for producing dense arrays of quantum dots having resonant absorption centered around 1550 nm. We primarily focus on two parameters: substrate temperature and erbium doping density. Eight 3-inch wafers were grown [Table 1], and characterized with TEM, SIMS, SEM, surface profilometry and infrared (IR) spectroscopy. For example, the TEM images on wafer ASP-537 (Fig. 1) showed the presence of ErAs quantum dots, and a “most likely” diameter of 1.9 nm. The corresponding near IR attenuation spectrum (Fig. 2) mapped from the center to edge of the wafer showed a peak attenuation around 1300 nm – shy of the desired 1550 nm. The SIMS of wafer ASP537 was conducted and yielded an average Er concentration of  $5.5 \times 10^{20} \text{ cm}^{-3}$ , just 25% greater than the MBE-calibrated value of  $4.4 \times 10^{20}$  carried out at NIST. Near-IR on the other seven wafers was also carried out and the peak wavelength at five points between center and edge is shown in Fig. 3. We were able to rule out a growth temperature of 590°C since both wafers grown at that temperature (labeled as ASP-535 and -541) displayed poor material quality overall, and displayed resonant absorption peaks well beyond 1900 nm. The closest three wafers to the desired 1550 nm peak were identified as ASP-536, -543 and -554, the first was grown at 560°C and doped to  $4.4 \times 10^{20} \text{ cm}^{-3}$ ; the second grown at 530°C and doped to  $8.0 \times 10^{20} \text{ cm}^{-3}$ ; and the third grown at 545°C and doped to  $8.0 \times 10^{20} \text{ cm}^{-3}$ . However, they all suffer from poor uniformity as shown in Fig. 3. On the other hand, two other wafers, ASP-537 and 553 both doped to  $4.4 \times 10^{20} \text{ cm}^{-3}$ , have better uniformity, but display resonances mostly around  $\sim 1250$  nm. The former was grown at 530°C, the latter grown at 545°C. A Dektak analysis on ASP-553 yields a root mean square deviation of  $\sim 125$  Ang, showing smooth surface morphology that is suitable for planar device fabrication, and has insignificant effect on the attenuation through scattering.

[1] “High power generation of THz from 1550-nm photoconductive emitters”, A. Mingardi, W-D. Zhang, E. R. Brown, A. D. Feldman, T. E. Harvey, and R. P. Mirin, Optics Express, Vol. 26, Issue 11, pp. 14472-14478 (2018).

[2] “THz Superradiance from a GaAs: ErAs Quantum Dot Array at Room Temperature,” W-D. Zhang, E. R. Brown, A. Mingardi, R. P. Mirin, N. Jahed, and D. Saadekia, Applied Sciences, 9(15):3014, July 2019.

SESSION AA: Wide Bandgap Materials—Silicon Carbide and Diamond  
 Session Chair: Nadeemullah Mahadik  
 Session Hosts: Jennifer Hite and Vincent Meyers  
 Thursday Afternoon, June 25, 2020  
 Location: ZoomRoom 5

### 3:45 PM AA01

**Improving SiC Crystal Growth and Epitaxial Deposition with Tantalum Carbide Protection Coating** Wei Fan, Hao Qu, Jeffery Lernnartz, Creighton Tomek, Peter Schmidt-Sane, Xiang Liu, Brian Kozak and Gregory Shaffer; Momentive Quartz Technologies, United States

Fabricating Silicon Carbide (SiC) devices requires high quality SiC wafer substrates and SiC epitaxial layers with low defect densities and low impurities. SiC crystal growth usually takes place in a high temperature physical vapor transport (PVT) by sublimation of SiC source over 2200°C. Chemical vapor deposition (CVD) of SiC epitaxial layer on wafers also operates at relatively high temperature ( $>=1600^\circ\text{C}$ ) with Si and H presence. Graphite is the construction material for PVT furnace components and CVD wafer carriers due to its high temperature stability and electrical conductivity needed for inductive heating. However, Si and H species can aggressively attack bare graphite at those operating temperatures. Graphite also releases carbon particulates and metal contamination, which can be incorporated into the SiC crystal growth or epi deposition as defects. Tantalum carbide (TaC), on the other hand, with its high temperature stability, high purity and high chemical resistance, can be a perfect coating material to protect graphite reactor components from the corrosive environment and to suppress contamination in contact with graphite. In this study, we demonstrated the key TaC coating properties and performances that can benefit both SiC crystal and wafer productions. TaC coating was generated through a proprietary high temperature CVD process. Coating with average thickness of 35  $\mu\text{m}$ , grain size of 20  $\mu\text{m}$  and roughness of 1.50  $\mu\text{m}$  was deposited on graphite substrates with various shapes such as plate, disc and rod. Cross section SEM also revealed a dense and conformal coating was achieved on all surfaces, including sharp inner corners. XRD and XPS analyses indicated as deposited TaC layer is highly crystalline and has a Ta to C ratio of 1:1. We developed accelerated etching test with corrosive gases, such Si, H<sub>2</sub>, SiH<sub>4</sub> and CH<sub>4</sub>, which are precursors in SiC crystal and epitaxial growth. These tests were systematically carried out on graphite, SiC and TaC coated samples. Their testing conditions simulated the PVT or CVD application environments. It was found that the etch rates of graphite and SiC coating was at least  $>10$  times those of TaC. Surface morphology of TaC remained unchanged before and after all the tests. The etching study demonstrated that TaC remained inert to Si, C, and H species and acted as an passivation layer to protect graphite substrate from being attacked. Impurities of TaC was measured via GDMS and compared to chlorine purified research grade graphite. Significant amount of nitrogen and oxygen can be found in graphite substrate,

together with traceable boron, silicon, and sulfur, while TaC coating provides a much cleaner surface that seals the impurities in the graphite substrate from the SiC crystal or wafer processing. SiC crystal grown with TaC coated crucible showed much higher bulk resistivity and mobility due to less impurity incorporation. TaC produced in this study exhibited excellent coating uniformity, high thermal and chemical stabilities, and high purity. TaC coating can extend graphite component life, and maintain SiC sublimation stoichiometry, suppress impurity migration, and potentially reduce energy consumption as well. Ultimately TaC coated graphite component is expected to improve the process yield and the product quality in SiC crystal growth and SiC epitaxial deposition.

### 4:00 PM AA02

**(Student) Synchrotron X-Ray Topography Study on Dislocation Behavior in Early-Grown 4H-SiC Single Crystals** Tuerxun Ailihumacr, Hongyu Peng, Yafei Liu, Balaji Raghothamachar and Michael Dudley; Stony Brook University, United States

Silicon carbide (SiC), particularly 4H-SiC has been attracting significant attention for high-power device applications. Due to its many excellent physical properties, 4H-SiC-based devices are able to achieve high voltage and high switching operations at high temperatures. However, the crystal quality of 4H-SiC substrates is one of the most vital issues that need to be improved. Over the past few decades, the effect of various defects existing in the crystals such as threading screw/mixed dislocations (TSD/TMDs), threading edge dislocations (TEDs) and basal plane dislocations (BPDs) has been studied and revealed to be detrimental to the reliability of SiC power devices[1-2]. Recently, initial stages of physical vapor transport (PVT) growth of SiC has been a major focus to study the step morphology and defect formation during the early growth stage [3-5]. However, formation mechanism of dislocations at the initial growth stage is yet to be studied in detail.

This paper describes a study on dislocation behavior of large diameter 4H-SiC crystals at the early stages of PVT growth, particularly nucleation and multiplication of dislocations which forms the basis for subsequent growth of the full crystal boule. Synchrotron x-ray topography technique was applied to multiple 6-inch PVT-grown layers with thickness of several hundred microns. Grazing-incidence topographs in  $g=11-28$  and  $g=1-109$  recorded from both the back side (seed) and newly-grown layer shows the presence of screw type BPDs with  $b=\pm 1/3[11-20]$  at the inner region of the wafers, which was further confirmed by comparing with ray tracing simulated images of these dislocations. Their origins are likely from deflection of TEDs onto the basal plane by the overgrowth of macro-steps. Pairs of TSDs/TMDs were found to be newly generated at the initial growth stage and some are deflected onto the basal plane. High density of newly generated TEDs were also observed in the early-grown layers. Furthermore, dislocations with unique shapes were observed and found to be associated with deflection of TMDs and TEDs, which became the major source for BPD generation. Possible models to explain their formation mechanism were proposed. Additional studies of the step morphology on the 4H-SiC facet region are currently being carried out. [1] St. G. Muller, J. J. Sumakeris, M. F. Brady, R. C. Glass, H. M. Hobgood, J. R. Jenny, R. Leonard, D. P. Malta, M. J. Paisley, A. R. Powell, V. F. Tsvetkov, S. T. Allen, M. K. Das, J. W. Palmour, and C. H. Carter, Jr., Eur. Phys. J. Appl. Phys. 27, 29 (2004). [2] R. Singh and M. Pecht, IEEE Ind Electron M 2, 19 (2008). [3] E.K. Sanchez, J.Q. Lin, M. De. Graef, M. Skowronski, W.M. Vetter, M. Dudley, J. Appl. Phys. 91 (3) (2002) 1143. [4] N. Ohtani, C. Ohshige, M. Katsuno, T. Fujimoto, S. Sato, H. Tsuge, W. Ohashi, T. Yano, H. Matsuhata, M. Kitabatake, J. Cryst. Growth 386 (2014) 9. [5] C. Ohshige, T. Takahashi, N. Ohtani, M. Katsuno, T. Fujimoto, S. Sato, H. Tsuge, T. Yano, H. Matsuhata, M. Kitabatake, J. Cryst. Growth 408 (2014) 1-6.

### 4:15 PM AA03

**Double-Sided Half-Loop Arrays Caused by Frank-Read Sources in 4H-SiC** Peter L. Bonanno, Nadeemullah Mahadik and Robert E. Stahlbush; U.S. Naval Research Laboratory, United States

SiC-based power devices have crucial advantages compared to their Si-based counterparts for high-power applications where SiC's 3-times higher bandgap and thermal conductivity allows for greater breakdown voltages, faster switching, lower switching losses, lower on-resistance, and easier cooling. Device reliability depends on minimizing extended defects in the epitaxial layer of the wafer, especially basal plane dislocations (BPDs), which form Shockley stacking faults (SSFs) during forward bias operation. SSFs can expand to cover large areas of the active layer, which increases on-state resistance and often causes increased off-state leakage. The problem is especially pronounced in thick epitaxial layers for high-voltage devices, where the long growth times allow BPDs to glide many millimeters and create long half-loop arrays (HLAs) that will degrade any devices along their path.

Lowering BPD density in epitaxial layers with thicknesses below 20  $\mu\text{m}$  has been very effective. To continue progress for thicker layers needed for higher voltage devices, it's important to understand new sources of BPDs in thicker epitaxial layers. In this study, we identify a never-before reported double-sided HLA structure and propose a formation mechanism based on shear stress and Frank-Read sources.

A commercial 6" 4H-SiC sample with 4 degree offcut was obtained with a 20 micron n<sup>+</sup> buffer layer, followed by a 120 micron n<sup>+</sup> active layer. Ultraviolet photoluminescence (UVPL) was used to image the BPDs. We excited the

epilayer with 355 nm (above band-gap) light and collected the defect luminescence through a 655 nm long-pass filter, which filtered the band-edge luminescence and showed BPDs as bright lines. In this wafer, we identified a dozen double-sided HLAs. The same UV excitation was applied repeatedly to cause the BPD segments in the HLAs to fault. The faulted area between the partials expanded and eventually combined into one large stacking fault spanning the entire double-sided HLA structure. This shows that the entire structure inhabits the same basal plane and thus originates from the same source. Previous work has established that the cross product between the line direction of the partial dislocation and its Burgers vector points to the Si-face for Si-core partials. This allowed us to determine the Burgers vectors and line directions all of the partials in the double-sided HLA. From this analysis we conclude that the entire structure originates from a single BPD. Its Burgers vector is  $\frac{1}{2} \langle 11\bar{2}0 \rangle$  (parallel with offset direction), its line direction is perpendicular to the Burgers vector and it is terminated by threading dislocations on both ends. This structure has been observed in the literature, and is believed to develop spontaneously at the growth front during epitaxy [1]. We show that with a combination of compressive and shear stress, the structure behaves as a Frank-Read source that interacts with the growth surface to produce the observed double-sided HLA structure. In the case of slightly less local shear stress and/or slightly faster growth rate, it behaves as a more classical Frank-Read source, resulting in dislocation loop pileups that are also observed in the sample. [1] Zhang, J. Appl. Phys. 101, 053517 (2007)

#### 4:30 PM AA04

**(Student) Characterization of Dislocations on 6H-SiC through X-Ray Topography and Ray-Tracing Simulation** Qianyu Cheng, Tuexun Ailihumaer, Yafei Liu, Hongyu Peng, Zeyu Chen, Balaji Raghothamachar and Michael Dudley; Stony Brook University, The State University of New York, United States

Silicon carbide (SiC) is a promising semiconducting material owing to its superior characteristics such as wide band-gap, high saturated electron velocity, high breakdown electric field strength, and high thermal conductivity.<sup>[1]</sup> This combination of advanced electronic and physical properties fulfills the requirement of high power, high frequency, and high temperature operation for modern power electronic devices.<sup>[2]</sup> In order to overcome limitations to growth and continuously pursue the quality improvement of the crystal, obtaining a clear understanding of the nature and behavior of different dislocations is of great importance. Synchrotron X-ray topography<sup>[3]</sup> is a powerful characterization tool for imaging dislocations and other defects. Similar to PVT-grown 4H-SiC wafers, synchrotron X-ray topographic images of PVT-grown 6H-SiC wafers reveal the existence of threading screw dislocations (TSDs) as well as other types of threading edge dislocations (TEDs) and basal plane dislocations (BPDs). However, recent research in 4H-SiC has shown the majority of threading dislocations with screw components are actually mixed-type dislocations with Burgers vectors  $nc+ma$  (where  $m$  and  $n$  are integers), which are known as threading mixed dislocations (TMDs).<sup>[4]</sup> Direct TMDs observation methods such as transmission electron microscopy (TEM) and synchrotron white-beam X-ray topography (SWBXT) are only suitable for axial sliced samples slated for research purposes as the wafers are cut parallel to the growth axis, which is destructive to the boule. Therefore, in order to investigate dislocations in commercially preferred offset  $c$ -plane-oriented wafers, comparison to ray-tracing simulated images of possible dislocation types is preferable. In addition to 4H-SiC<sup>[4]</sup>, this technique has been successfully implemented to characterize dislocations in GaN<sup>[5]</sup>, ZnO<sup>[6]</sup>, and AlN<sup>[7]</sup>. In this study, the same principle will be followed to investigate dislocations in 6H-SiC wafers. PVT grown 6H-SiC wafers have been characterized by synchrotron monochromatic beam X-ray topography (SMBXT) in the grazing-incidence geometry to record all six different reflections (Fig. 1). The distribution of TSDs, TMDs, threading edge dislocations (TEDs), and basal plane dislocations (BPDs) are characterized, and their Burgers vectors determined by correlation between real topographic observations and simulated results obtained through ray-tracing simulation (Fig. 2). This study can provide a clear understanding of dislocations in 6H-SiC, which is crucial for achieving further enhancement on crystal quality. Reference: [1]: C. Codreanu, et al, Comparison of 3C-SiC, 6H-SiC and 4H-SiC MESFETs Performances, *Materials Science in Semiconductor Processing* 3 137 (2000). [2]: J. W. Sun, et al, Shockley-Frank Stacking Faults in 6H-SiC, *Journal of Applied Physics* 111, 113527 (2012). [3]: M. Dudley, X. R. Huang, X-ray Topography, *Materials Research Society Symposium Proceedings* 307, 213 (1993). [4]: J. Q. Guo, et al, Direct Determination of Burgers Vectors of Threading Mixed Dislocations in 4H-SiC Grown by PVT Method, *Journal of Electronic Materials* 45, 4 (2016). [5]: B. Raghothamachar, et al, X-ray Topography Characterization of Gallium Nitride Substrates for Power Device Applications, submitted for publication. [6]: T. Y. Zhou, "Threading Dislocation Characterization and Stress Mapping Depth Profiling via Ray Tracing Technique," Ph.D. Thesis, SUNY Stony Brook, Advisor: Michael Dudley (2015). [7]: T. Y. Zhou, et al, Characterization of Threading Dislocations in PVT-Grown AlN Substrates via X-Ray Topography and Ray Tracing Simulation, *Journal of Electronic Materials* 43, 838 (2014).

#### 4:45 PM AA05

**Growth of High Purity Zone-Refined Boron Carbide Single Crystals by Laser Diode Floating Zone Method** Michael Straker<sup>1</sup>, MVS Chandrashekhar<sup>2</sup>, Ankur Chauhan<sup>3</sup>, Mekhola Sinha<sup>3</sup>, W. Adam Phelan<sup>3</sup>, Kevin Hemker<sup>3</sup> and Michael Spencer<sup>1</sup>; <sup>1</sup>Morgan State University, United States; <sup>2</sup>University of South Carolina, United States; <sup>3</sup>Johns Hopkins University, United States

Boron carbide is an ultra-hard refractory material (2400C melting point) used in ceramics for ballistic armor applications. It also has remarkable thermoelectric properties, and its icosahedral structure is unique among carbon-based materials. Its lattice constant on various planes is close to that of many wide bandgap materials, including SiC, GaN, and Diamond, while being able to melt. This makes it an attractive substrate material that can be synthesized using techniques compatible with the silicon industry for vertical device architectures, owing in part to its high electrical conductivity. We report on the growth and characterization of 4mm diameter x50mm long boron carbide (B<sub>4</sub>C) single crystals using a laser diode floating zone (LD-FZ) method at 5-20mm/hr growth rates, resulting in a graphitic skin being formed on the surface during growth. Electron microstructure analysis shows the presence of a significant number of twinning-boundaries along the growth direction ( $\langle 001 \rangle_h$ ) oriented in the  $\langle 1210 \rangle_h$  plane. At growth rates  $< 10$ mm/hr, the crystal orientation was not reproducible, suggesting a critical rate for twin-plane mediated growth to dominate. [CM1] Zone refinement of these crystals led to a significant reduction of trace impurities to better than 99.999 wt % purity, at the expense of increased twinning. Powder x-ray diffraction confirms that the bulk is rhombohedral B<sub>4</sub>C, consistent with the microstructure. The x-ray reciprocal space maps reveal the growth direction to be close to the  $\langle 001 \rangle_h$  direction, and the corresponding w-rocking curve width is  $\sim 530$ arcsec. The rocking curve consisted of 3 distinct peaks, indicating in-plane mosaicity, consistent with the twinning observed. Berkovich nano-indentation of the key  $\langle 001 \rangle_h$  plane showed  $41 \pm 1$  GPa hardness, with a Young's modulus of  $520 \pm 14$  GPa, comparable to the literature. These crystals demonstrated p-type conductivity as measured by capacitance-voltage, and I-V characterization revealed defect mediated conduction.

#### 5:00 PM BREAK

#### 5:30 PM AA06

**Diamond Seed Size and the Impact on the Chemical Vapor Deposition of Diamond Thin-Film Properties** Tingyu Bai<sup>1</sup>, Yekan Wang<sup>1</sup>, Tatyana Feygelson<sup>2</sup>, Marko Tadjer<sup>2</sup>, Karl Hobart<sup>2</sup>, Nicholas Hines<sup>3</sup>, Luke Yates<sup>3</sup>, Samuel Graham<sup>3</sup>, Julian Anaya<sup>4</sup>, Martin Kuball<sup>4</sup> and Mark Goorsky<sup>1</sup>; <sup>1</sup>University of California, Los Angeles, United States; <sup>2</sup>U.S. Naval Research Laboratory, United States; <sup>3</sup>Georgia Institute of Technology, United States; <sup>4</sup>University of Bristol, United Kingdom

Diamond is known to be a promising material for thermal management in high power devices due to its high thermal conductivity. Chemical vapor deposition (CVD) of the diamond film can be integrated near the device hot spot to help dissipate heat. Diamond deposition requires conditions that are not harmful to the device layer structure and nucleation is a key issue. In order to improve the nucleation conditions, the surface is usually seeded with nanocrystalline diamond, which leads to coalesce of diamond grains and growth into a continuous polycrystalline film. The diamond grains should be as large as possible to reduce the impact of phonon scattering at grain boundaries, especially for the nano-scale crystallites near the growth interface. In this study, the seeding condition has been studied to help improve the thermal conductivity of diamond films by increasing the grain size near the growth interface. In this research, diamond seeds were assessed for their role in the heterogeneous nucleation for diamond films deposited on silicon. Two diamond seed sizes  $\sim 4$  nm and  $\sim 20$  nm – were studied. Samples were examined after 15 minutes of deposition and after deposition of a one  $\mu$ m layer. For the as-seeded Si wafers, scanning electron microscopy (SEM) has been used to measure the seeding density and distribution. Then, cross-section Transmission Electron Microscopy (TEM) samples were prepared and examined for accurate seed size measurement. After one  $\mu$ m growth, TEM was used to access the crystalline size accurately at 50 nm – 300 nm above the interface. The study revealed that the larger seed size, even when with a smaller seeding density, produces a larger grain size ( $\sim 39\%$  difference at 50 nm above the interface) near the interface region. Raman thermography was used to determine the in-plane thermal conductivity of the one  $\mu$ m thick diamond layers. Several positions were measured across the wafers and the average value was  $\sim 91$  W/mK when the 4 nm seed size was used and  $\sim 110$  W/mK when the 20 nm seed size was used. This shows that using larger seed size leads to a higher in-plane thermal conductivity (19% difference) as measured by Raman thermography. By fine control of the seed size and density, thermal conductivity near the nucleation region can therefore be improved. This confirms that the seeding condition is critical to diamond film growth for thermal applications in electronic devices.

5:45 PM AA07

**(Student) Understanding the Inhomogeneous Incorporation of Nitrogen in  $\beta$ -Doped CVD Diamond Using Spatially Resolved Microanalysis** Lillian B. Hughes<sup>1</sup>, Simon Meynell<sup>2</sup>, Claire McClellan<sup>2</sup>, Tom Mates<sup>1</sup>, Kunal Mukherjee<sup>1</sup> and Ania B. Jayich<sup>2</sup>; <sup>1</sup>University of California Santa Barbara, United States; <sup>2</sup>University of California, Santa Barbara, United States

Nitrogen-vacancy (NV) centers in diamond are known for their spin-dependent fluorescence and long quantum coherence times, making them suitable for applications in quantum sensing. The controlled engineering of NV centers into a high crystalline quality diamond matrix can be achieved via nitrogen d-doping during plasma-enhanced chemical vapor deposition (CVD), followed by subsequent vacancy creation and annealing processes. Surface defects that arise during CVD growth are well known, however, and have been shown to affect NV coherence times [1]. A better understanding of diamond growth and nitrogen incorporation mechanisms as well as their relation to surface morphology will enable the creation of more sensitive quantum technology. We present the CVD growth of isotopically purified  $^{12}\text{C}$  (99.999%) (100) diamond films d-doped with  $^{15}\text{N}_2$  (> 98%) at a pressure of 25 Torr and substrate temperature of 800°C and systematically investigate the role of step-edge density in the growth. This is controlled through the selective miscut of the seed substrate ranging over angles from 0.16 to 1.66 degrees. We demonstrate that both nitrogen and defect density vary with the miscut and determine an optimal angle for incorporation. Using spatially resolved secondary ion mass spectrometry (SIMS) employing a  $\text{Cs}^+$  ion beam of 30 nA, 15 keV, and a mass resolving power of 6000 (M/DM), we further report that nitrogen preferentially incorporates within hillock-type defects, suggesting a step-edge-dependent mechanism of nitrogen doping in the crystal. Fine-tuning of the SIMS spatial resolution and quantifying the nitrogen density as well as site-specific microstructural characterization of hillocks using transmission electron microscopy (TEM) will supplement our understanding of the defect incorporation and nucleation mechanisms. Scanning confocal and electron spin resonance (ESR) measurements also confirm the nitrogen enrichment in hillocks and show that the hillocks exhibit similar linewidths to single NV centers as compared to other defect types, suggesting that hillocks may not compromise NV quality. Altogether, the localized incorporation of nitrogen at hillock sites could be used to preferentially pattern and control NV centers within the diamond film, providing an exciting method of engineering NV centers for more sensitive and robust quantum applications. [1] J. Achard, V. Jacques, and A. Tallaire, ArXiv:1912.09749, [Cond-Mat, Physics:Physics], (2019).

6:00 PM AA08

**Kelvin Probe and Constant Final State Yield Spectroscopy Measurements on Hydrogen Terminated Diamond** A. G. Birdwell, Dmitry Ruzmetov, Mahesh R. Neupane, James D. Weil, Kevin G. Crawford, Pankaj B. Shah and Tony G. Ivanov; U.S. Army Combat Capabilities Development Command-Army Research Laboratory, United States

Diamond has exceptional thermal properties, a large bandgap and high breakdown strength. These materials properties make diamond very attractive as a potential next generation semiconductor electronics material. As a result, the U.S. Army Combat Capabilities Development Command's Army Research Laboratory has an in-house program to develop radio-frequency field-effect transistors on single crystal diamond substrates. These devices are fabricated on hydrogen terminated diamond (H-D) surfaces, and employ both atmospheric adsorbates and transition metal oxides as the transfer-doping electron acceptor layers leading to a two-dimensional hole gas (2DHG) current channel. Our presentation will review how the nondestructive metrologies of Kelvin Probe (KP) and Constant Final State Yield Spectroscopy (CFSYS) can be used to characterize the robustness and charge-transferring efficiency of the H-D surface by quantifying the density of the 2DHG. The results obtained by KP and CFSYS will be compared to those obtained by Hall measurements.

6:15 PM AA09

**$\beta$ -Ga<sub>2</sub>O<sub>3</sub> Nanomembrane and Diamond P-N Heterojunction Integrated with Oxide Quantum Tunneling Layer** Edward Swinnich and Jung-Hun Seo; University at Buffalo, The State University of New York, United States

Power electronics is a key component in everyday life for managing and transforming electric power. Semiconductor power switching devices play an important role in enabling such electronics. As future power electronics require improved electrical property, better heat handling capability, and smaller footprint, the development of another class of wide bandgap (WBG) materials and structure are urgently needed to fulfill such needs. As an emerging WBG semiconductor, beta-phase gallium oxide ( $\beta$ -Ga<sub>2</sub>O<sub>3</sub>) has been intensively researched in recent years due to its large bandgap ( $E_g \sim 4.9$  eV) and high electron mobility, making it a potential WBG semiconductor for next-generation power electronics and optoelectronics. Despite promising material properties of  $\beta$ -Ga<sub>2</sub>O<sub>3</sub>, the well-known deficiency of  $\beta$ -Ga<sub>2</sub>O<sub>3</sub>, the lack of an efficient p-type dopant, largely prohibits the use of  $\beta$ -Ga<sub>2</sub>O<sub>3</sub> toward a wider spectrum of power electronics. In fact, this is the common deficiency in all WBG semiconductors, namely, the lack of one or the other type of efficient dopant. For example, ZnO, SiC, GaN, and  $\beta$ -Ga<sub>2</sub>O<sub>3</sub> lack or do not have an efficient p-type dopant. This deficiency reversely happens to n-type diamond. While p-type doping in diamond is easy and well-known, the effective n-type doping in diamond is known to be challenging, due to the small lattice constant of diamond compared with potential n-type dopants.

In order to overcome aforementioned material challenges, we have developed a new way to heterogeneously integrate two dissimilar single-crystalline semiconductors using an ultra-thin oxide quantum tunneling interface layer. As shown in Figure 1(a) and (b), our new heterogeneous integration method between two dissimilar semiconductors is enabled by employing novel single crystal nanomembrane (NM) and an ultra-thin oxide as a quantum tunneling layer that is formed by atomic layer deposition (ALD), and a reliable micro-transfer printing method.

In this work, we have heterogeneously integrated  $\beta$ -Ga<sub>2</sub>O<sub>3</sub> NM with diamond to form an ultra WBG p-n diode (Figure 1(c) and (d)). To understand the band-alignment of the heterostructure, ultraviolet photoelectron spectroscopy (UPS) and X-ray photoelectron spectroscopy (XPS) was performed and determined their conduction band offset and valence band offset (Figure 1(e) and (f)). Furthermore, we have developed an in-situ electron affinity tuning method from +2eV to -1eV by the excessive hydrogenation of the diamond surface in the ALD chamber, thus it is possible to adjust band offset of  $\beta$ -Ga<sub>2</sub>O<sub>3</sub>/diamond heterojunction and perform oxide deposition in a single process step which ensures the stability of the diamond surface chemistry. As shown in Figure 1(d), the fabricated  $\beta$ -Ga<sub>2</sub>O<sub>3</sub>/diamond p-n heterojunction shows excellent rectifying behavior with extremely low reverse current (below 1pA) and relatively low ideality factor ( $n \sim 2$ ). The excellent electrical property together with a large tunability of band-offset suggest that our method can offer a customized solution depending on the application as shown in Figure 1(g); namely, we can intentionally increase the band offset (i.e., the built-in potential of the p-n junction), when the device needs low leakage current or high breakdown. We can also reduce it when we want to enhance the recombination or generation of the device.

In summary, a seamless ultra WBG heterojunction p-n diode between  $\beta$ -Ga<sub>2</sub>O<sub>3</sub> NM/diamond was successfully demonstrated. The capability of tuning the band offset of the heterojunction provides a great degree of freedom to customize the device performance. Our research can be widely applied to any other of the WBG semiconductors which suffer from unbalanced material properties. For example, unique heterostructures such as AlGaIn/Diamond, Boron nitride(BN)/AlN, and  $\beta$ -Ga<sub>2</sub>O<sub>3</sub>/GaN are possible which conventional method cannot offer, thus this method will enable us to fully utilize each material's unique property and feature.

6:30 PM AA10

**Thermal Transport across Ga<sub>2</sub>O<sub>3</sub>/Metal Contact Interfaces—Characterization and Time-Evolution** Henry Aller<sup>1</sup>, Xiaoxiao Yu<sup>1</sup>, Chabak Kelson<sup>2</sup>, Adam Wise<sup>1</sup>, Robert Howell<sup>3</sup>, Andrew Gellman<sup>1</sup>, Alan McGaughey<sup>1</sup> and Jonathan A. Malen<sup>1</sup>; <sup>1</sup>Carnegie Mellon University, United States; <sup>2</sup>Air Force Research Laboratory, United States; <sup>3</sup>Northrop Grumman Electronic Systems, United States

Topside heat removal in Ga<sub>2</sub>O<sub>3</sub> devices is largely dependent on the thermal boundary conductance of the metal/ Ga<sub>2</sub>O<sub>3</sub> interfaces. During device operation, temperatures rises can permanently alter the interface structure. We examine the thermal boundary conductance of (i) Au/(Cr, Ni, or Ti contact)/ Ga<sub>2</sub>O<sub>3</sub> interfaces for contact thicknesses between 0-10 nm and (ii) the Ohmic and Schottky contacts of a prototype Ga<sub>2</sub>O<sub>3</sub> device. For all samples, the thermal boundary conductance was measured using the non-destructive pump-probe optical technique, frequency domain thermoreflectance. For (i), while the thermal boundary conductance increases monotonically with increasing thickness for Ni, a maximum is observed for Cr and Ti. These maxima are the result of the formation of a thin oxide layer on the  $\beta$ -Ga<sub>2</sub>O<sub>3</sub> substrate during the contact growth. The structure of the Cr-based sample is analyzed using TEM imaging, confirming the existence of a crystalline Cr<sub>2</sub>O<sub>3</sub> layer. We determine that grown oxide layers ultimately lower thermal boundary conductance and become thicker as more metal is deposited. To examine the impact of these findings on device performance, in (ii), a prototype device is measured/heated multiple times. Device temperature rises could lead to further oxide layer growth and/or the alloying of the metal stacks. Our results suggest that chemical reactions and annealing due to normal heating during device operation may cyclically degrade the thermal conductivity/conductance of films/interfaces within devices, further promoting device temperature rise (i.e., thermal wind up). We suggest approaches for slowing reactions and alloying so as to increase device lifetimes.

SESSION BB: Point Defects, Doping and Extended Defects

Session Chair: Rachel Goldman

Session Hosts: Emma Rocco and Sharif Sadaf

Thursday Afternoon, June 25, 2020

Location: ZoomRoom 6

4:00 PM BB01

**(Student) Atomic Distribution of Al and Phase Transformation in  $\beta$ -(Al<sub>x</sub>Ga<sub>1-x</sub>)<sub>2</sub>O<sub>3</sub>** Hsien-Lien Huang, Jared Johnson, A F M Anhar Uddin Bhuiyan, Zixuan Feng, Hongping Zhao and Jinwoo Hwang; The Ohio State University, United States

$\beta$ -Ga<sub>2</sub>O<sub>3</sub> has gained tremendous attention as a promising transparent conductive oxide, ultra-wide band material due to its unique advantages including a large

band gap energy (~ 4.8eV), high breakdown voltage, and its availability as high quality bulk grown single crystals [1]. However, realizing its full potential as a semiconductor material requires the manipulation and control of its band gap, which could enable novel heterostructure designs for carrier confinement and field effect transistors or deep UV optoelectronic devices. Recent efforts have indicated that the bandgap of  $\beta$ -Ga<sub>2</sub>O<sub>3</sub> can be engineered through the incorporation of Al [2], forming  $\beta$ -(Al<sub>x</sub>Ga<sub>1-x</sub>)<sub>2</sub>O<sub>3</sub> with a band gap up to 8.8 eV. High crystalline quality  $\beta$ -(Al<sub>x</sub>Ga<sub>1-x</sub>)<sub>2</sub>O<sub>3</sub> structures with Al composition up to  $x=40\%$  have been achieved using metalorganic chemical vapor deposition (MOCVD) [1] and a high mobility two-dimensional electron gas has been demonstrated to form at a  $\beta$ -(Al<sub>x</sub>Ga<sub>1-x</sub>)<sub>2</sub>O<sub>3</sub>/Ga<sub>2</sub>O<sub>3</sub> interface [2]. Ultimately, advancing these alloyed  $\beta$ -Ga<sub>2</sub>O<sub>3</sub> epitaxial films requires the precise control of the point defects that critically influence their important properties. And their exact control requires attaining the essential detailed atomic scale structural information, which will provide key information on their formation during growth and their impact on properties. Here, we present the atomic scale characterization of Al-alloyed  $\beta$ -Ga<sub>2</sub>O<sub>3</sub> and the observation of phase transformation in (Al<sub>x</sub>Ga<sub>1-x</sub>)<sub>2</sub>O<sub>3</sub> thin films. Employing the unprecedented resolution and chemical sensitivity generated by scanning transmission electron microscopy (STEM), we specified the exact substitutional positions of the alloying-element Al in molecular beam epitaxy (MBE) and MOCVD grown  $\beta$ -(Al<sub>x</sub>Ga<sub>1-x</sub>)<sub>2</sub>O<sub>3</sub> films (Fig. 1). The exact composition and distribution of Al at each substitutional cation position were analyzed utilizing quantitative STEM. In addition, the mixture of  $\beta$  and  $\gamma$  phases in higher composition (Al<sub>x</sub>Ga<sub>1-x</sub>)<sub>2</sub>O<sub>3</sub> thin films were investigated using STEM imaging and nanodiffraction (Fig. 2). Driven by the strain induced from the configurational relaxation during Al incorporation, the rotations of the  $\beta$  phase and introduction of the defective spinel structure were verified using the nanodiffraction patterns. Identification of structural change in the (Al<sub>x</sub>Ga<sub>1-x</sub>)<sub>2</sub>O<sub>3</sub> films has significant implications on the future growth of (Al<sub>x</sub>Ga<sub>1-x</sub>)<sub>2</sub>O<sub>3</sub> films. Additionally, the recently discovered divacancy-cation interstitial complexes were discerned in  $\beta$ -(Al<sub>x</sub>Ga<sub>1-x</sub>)<sub>2</sub>O<sub>3</sub> films [3]. Our atomic scale STEM investigation not only provides new crucial information that can be advantageous to the growth of  $\beta$ -(Al<sub>x</sub>Ga<sub>1-x</sub>)<sub>2</sub>O<sub>3</sub> films but also opens a viable path for future atomic scale studies of ultra-wide band gap semiconductors. We acknowledge support by the Department of Defense, Air Force Office of Scientific Research GAME MURI Program (Grant No. FA9550-18-1-0479).

**References:** [1] A. F. M. Anhar Uddin Bhuiyan et al., *Appl. Phys. Lett.* 115(12), 120602 (2019) [2] Y. Zhang et al., *Appl. Phys. Lett.* 112, 173502 (2018) [3] J.M. Johnson et al., *Appl. Phys. X* 9, 041027 (2019)

#### 4:15 PM BB02

**(Student) Atom Probe Tomography of Modulation-Doped Branched Nanowires for Quantum Computing** Chunyi Huang<sup>1</sup>, Megan O. Hill<sup>1</sup>, Martin Friedl<sup>2</sup>, Anna F. Morral<sup>2</sup> and Lincoln Lauhon<sup>1</sup>; <sup>1</sup>Northwestern University, United States; <sup>2</sup>École Polytechnique Fédérale de Lausanne, Switzerland

Branched In(Ga)As nanowires were grown at a wafer scale with GaAs nanomembranes as templates by molecular beam epitaxy (MBE) (Fig. 1(a)). These gold-free and defect-free III-V nanowires have been proposed as a host for Majorana Fermions in quantum computing schemes. Previously,<sup>[1]</sup> we used atom probe tomography (APT) to analyse the distribution of Si dopants in similar nanowires and found that they segregated preferentially towards the growing In(Ga)As nanowire surface, rather than incorporating into the supporting GaAs membrane. In the present work, we aimed to incorporate Si dopants inside the supporting GaAs membrane (Fig. 1(b)) to increase the nanowire free carrier concentration while preserving mobility. To test the nature and extent of dopant segregation in GaAs nanomembranes, low concentration Al marker layers were introduced at various stages during growth, enabling atom probe measurements to analyze the dopant location relative to the position of the growth interface. Si dopants were introduced at the mid-point between the first two Al markers (the bottom of Fig. 2(a)). After the second Al marker, a low temperature GaAs capping layer was added over the whole structure. Two dimensional concentration maps of Al and Si show a large Si peak close at the top of the second marker layer, rather than in between the two layers (Fig. 2(b)). A one-dimensional profile along the growth direction shows that Si concentration increases halfway between the two Al marker layers, as expected, but peaks near the upper Al marker (Fig. 2(c)), indicating that Si accumulates on the GaAs surface during nanomembrane growth. Furthermore, the segregation is on a (111) facet, consistent with prior work.<sup>[1]</sup> Growth conditions were then developed to find a regime that both promoted nanomembrane growth and inhibit segregation to enable delta-doping. The atom probe reconstruction in Fig. 3(a) shows a portion of a modulation doped In(Ga)As nanowire supported on a GaAs membrane. Due to the finite field of view defined by the instrument and the sample preparation, the full structure cross section is not visible in the reconstruction (Fig. 3(a)), but the location of In(Ga)As/GaAs interface is readily identified. Analysis of the sub-region indicated in the dashed black line, extracted in Fig. 3(b), reveals a high density of Si near the GaAs-InGaAs interface (Fig. 3(c)). To accurately measure the Si dopant distribution, a proximity histogram was generated (Fig. 3(d)) on either side of a 16% In mole fraction isosurface. The Si concentration peaks below the nanomembrane/nanowire interface, demonstrating the localization of Si dopants to a region below the In(Ga)As nanowire. Low temperature electrical transport measurements confirm the remote doping of the nanowires, demonstrating an important step towards the realization of branched nanowire networks that enable manipulation of Majorana zero modes for quantum

computing. **References:** [1] Friedl, M., et al. Template-assisted scalable nanowire networks. *Nano Lett.* **2018**, *18*, 2666-2671.

#### 4:30 PM BB03

**(Student) Structural and Electronic Properties of Native Point Defects in MoTe<sub>2</sub>** Ziling Deng, Sara Mueller, Wolfgang Windl and Jay Gupta; The Ohio State University, United States

MoTe<sub>2</sub>, a two-dimensional(2D) layered material[1], has recently attracted much attention due to its excellent electronic properties, e.g. sizable band gap[2], high photoresponsivity[3] and fast response[4]. Intrinsic defects are commonly observed in MoTe<sub>2</sub> growth[5], which would have a significant impact on the physical, optical, thermal, and electrical properties of the material. However, studying the atomic structure of intrinsic defects in this 2D materials is difficult since they damage quickly under the intense electron irradiation in transmission electron microscopy (TEM)[6]. To overcome this, we have performed a joint study between STM measurements and DFT calculations to identify the atomic structure and electronic nature of native point defects in MoTe<sub>2</sub>. We constructed analytical model from DFT and studied the structural and electronic properties of those defects. The two major intrinsic defects in 2D transition-metal dichalcogenide (TMD) materials are metal vacancies and chalcogen antisites[7], therefore, in this work we will mainly study these two defects with different charge states. In order to understand the formation of defects and their atom-scale dynamics in MoTe<sub>2</sub>, we will use DFT to predict the constitutional defects with the lowest formation energies as well as their dominated charge states in Mo-rich, Te-rich and stoichiometric conditions to determine the necessary chemical potentials for all systems of MoTe<sub>2</sub>. Additionally, theoretically simulated scanning tunneling microscopy (STM) images generated by density functional theory were used to compare with experimental STM data to enable us to assign structure of a number of defects observed during experiments.

This study provides an effective method to study the defects in MoTe<sub>2</sub> systems by presenting results for the energetics of native point defects in MoTe<sub>2</sub>. Base on our calculation, the formation energies and charged states of the vacancies and antisites will be determined, moreover, the simulated simulated STM images allow for the identification of structural defects of MoTe<sub>2</sub> observed in the experiment.

[1]Wang, Q. H.; Kalantar-Zadeh, K.; Kis, A.; Coleman, J. N.; Strano, M. S. *Nat. Nanotechnol.* **2012**, *7*, 699–712. [2]Lezama, I. G.; Arora, A.; Ubaldini, A.; Barreateau, C.; Giannini, E.; Potemski, M.; Morpurgo, A. F. *Nano Lett.* **2015**, *15*, 2336–2342. [3]Yin, L.; Zhan, X.; Xu, K.; Wang, F.; Wang, Z.; Huang, Y.; Wang, Q.; Jiang, C.; He, J. *Appl. Phys. Lett.* **2016**, *108*, 043503. [4]Oton, T. J.; Nagareddy, V. K.; Russo, S.; Craciun, M. F.; Wright, C. D. *Adv. Opt. Mater.* **2016**, *4*, 1750–1754. [5]Yi Li, Yaqiang Ma, Mingyu Zhao, Qian Sun, Yawei Dai, Jing Liu, Huiting Li, Xianqi Dai. *J. Alloy Compd.* **2018**, *735*, 2363-2372. [6]Kenan Elibol1, Toma Susi1, Giacomo Argentero1, Mohammad Reza Ahmadpour Monazam1, Timothy John Pennycook1, Jannik C. Meyer1, and Jani Kotakoski1. *Chem. Mater.* **2018**, *30*, 1230-1238. [7]Edelberg, D.; Rhodes, D.; Kerelsky, A.; Kim, B.; Wang, J.; Zangiabadi, A.; Kim, C.; Abhinandan, A.; Ardelean, J.; Scully, M.; Scullion, D. arXiv:1805.00127.

#### 4:45 PM BB04

**(Student) Dislocations as Topological Wires and Magnets** Sevim Polat Genlik and Maryam Ghazisaeidi; The Ohio State University, United States

Dislocations —one dimensional topological defects—in electronic materials, are considered to have a negative influence on electronic properties; their presence is thought to cause non-radiative recombination of charge carriers which lead to overheating of the crystal and malfunction of the device. Therefore, great effort has been made to produce dislocation-free crystals. However, recent studies show that dislocations can also be turned into useful functional features. For instance, it is reported that magnetic properties of dislocations differ from the lattice due to broken symmetry of the magnetic order and local non-stoichiometry of the dislocation core [1][2]. In another study, it is shown that inherent screw dislocations in certain elemental and compound semiconductors generate coherent spin currents through spin orbit coupling effect [3]. Thus, dislocations, with unique and localized magnetic and electronic properties, as well as their interactions in attracting point defects could be engineered to designing next generation technological devices and there is need for a thorough theoretical understanding of their influence on electronic and magnetic properties by means of atomic scale modelling which provide a predictive way to model strongly distorted dislocation core region. We present a systematic study of the core structure and electronic and magnetic properties of various dislocations in diamond using density functional theory (DFT). DFT calculations are performed with the Vienna ab initio Simulation Package (VASP), using norm-conserving pseudopotentials. Exchange and correlation contributions are treated within both the generalized gradient approximation and hybrid HSE06 (Heyd-Scuseria-Ernzerhof) functionals. To be able to satisfy periodic boundary conditions and to minimize long range elastic field interactions, supercells with two dislocations having opposite sign Burgers vectors (i.e. dislocation dipole) are used, which result in an infinite quadrupolar array of dislocations. The analysis of the electronic band structure along the dislocation line together with band decomposed charge density distributions reveal mid-gap energy states induced by broken atomic bonds in the dislocation core. Deep levels associated with dislocations are found to be donor type (n-type) charged dislocations. In addition, we compute the

interaction of dislocations with nitrogen-vacancy centers. These results have a strong potential for tailoring the functionality of dislocations in various elemental and compound semiconductors for future electronic devices.

[1] Shimada, T., Xu, T., Araki, Y., Wang, J., & Kitamura, T. (2017). Multiferroic dislocations in ferroelectric PbTiO<sub>3</sub>. *Nano letters*, 17(4), 2674-2680.

[2] Sugiyama, I., Shibata, N., Wang, Z., Kobayashi, S., Yamamoto, T., & Ikuhara, Y. (2013). Ferromagnetic dislocations in antiferromagnetic NiO. *Nature nanotechnology*, 8(4), 266.

[3] L. Hu, H. Huang, Z. Wang, W. Jiang, X. Ni, Y. Zhou, V. Zielasek, M. G. Lagally, B. Huang, F. Liu, "Ubiquitous Spin-Orbit Coupling in a Screw Dislocation with High Spin Coherency" *Phys. Rev. Lett.* 121, 066401 (2018).

#### 5:00 PM BREAK

#### 5:30 PM BB05

**(Student) Structure and Energetics of Point Defects in Titanium Dioxide** Shuyan Zhang, Alan McGaughey and Reeya Jayan; Carnegie Mellon University, United States

We apply molecular dynamics (MD) simulations to study the role of point defects, which can be induced during microwave radiation (MWR) assisted processing, on the structure of the rutile and anatase phases of titanium dioxide (TiO<sub>2</sub>). MWR is known to lower the TiO<sub>2</sub> synthesis temperature and to generate mixed amorphous-crystalline phase compositions. Despite the extensive use of MWR in TiO<sub>2</sub> processing and experimental evidence demonstrating its effects, the underlying mechanisms that lead to the resulting structures remain unknown. Understanding such non-thermal, field-driven processes has implications in engineering low-temperature processes for integrating ceramics with delicate polymeric materials for flexible electronics, energy harnessing, and energy storage applications.

To probe defect TiO<sub>2</sub> phases, a variable-charge force field is selected based on its transferability and its ability to predict material properties and defect formation energies. The lattice constant, elastic constants, and dielectric constants are predicted with good accuracy compared to experimental measurements. The mean square displacements of the ions are calculated for structures initialized with different concentrations of titanium Frenkel defects, oxygen Frenkel defects, or oxygen vacancies. The ionic translational mobility as the structures move toward equilibrium is enhanced as the defect concentration increases. Pair distribution function (PDF) analysis is applied to characterize the equilibrium structures and to allow for comparison to experimental measurements. Our findings provide insight into the formation and structure of defect TiO<sub>2</sub> phases.

#### 5:45 PM BB06

**(Student) Defects Near Stoichiometric and Non-Stoichiometric Interfaces in Sr<sub>1-x</sub>TiO<sub>3</sub> Homoepitaxial Thin Films** Brenton A. Noesges<sup>1</sup>, Daesu Lee<sup>2</sup>, Hongwei Wang<sup>3</sup>, Thaddeus J. Asel<sup>1</sup>, Jinbo Pan<sup>2</sup>, Jung-woo Lee<sup>2</sup>, Qimin Yan<sup>3</sup>, Xifan Wu<sup>3</sup>, Chang-Beom Eom<sup>2</sup> and Leonard J. Brillson<sup>1,1</sup>; <sup>1</sup>The Ohio State University, United States; <sup>2</sup>University of Wisconsin-Madison, United States; <sup>3</sup>Temple University, United States

SrTiO<sub>3</sub> (STO), integral to growth of many perovskite oxides, has many applications involving interfaces with other materials. However, defects which affect the properties of STO films can also play a significant role at an interface with another material or even STO with a different stoichiometry. With depth-resolved cathodoluminescence spectroscopy (DRCLS), we determined how systematically reducing Sr content in Sr<sub>1-x</sub>TiO<sub>3</sub> thin films grown on STO impacted the defects and electronic structure within the Sr-deficient film as well the effect non-stoichiometry has on the Sr<sub>1-x</sub>TiO<sub>3</sub>/STO interface. Understanding the formation of defects and how defects can impact electronic structure at an interface is crucial to improving complex oxide devices. We used pulsed laser deposition (PLD) to systematically decrease Sr content to control defect formation in 10 nm Sr<sub>1-x</sub>TiO<sub>3</sub> (0 < x < 0.02) films while DRCLS tracked defects through the Sr-deficient film, across the interface and into the near-interface substrate. We observed multiple electronic defects with optical transitions corresponding to Sr vacancies (V<sub>Sr</sub>), oxygen vacancies (V<sub>O</sub>), Ti on Sr anti-site defects (Ti<sub>Sr</sub>) and a feature related to Ti<sup>3+</sup>. Changes in the electronic structure of the substrate near the interface are also observed as Sr concentration in the overlayer is varied. Within the Sr-deficient Sr<sub>1-x</sub>TiO<sub>3</sub> film, we observe that the relative density of V<sub>Sr</sub> increases as Sr concentration decreases. As more of these V<sub>Sr</sub> sites are created, our results also show the creation of Ti<sub>Sr</sub> anti-sites as Ti fills in this Sr vacancy [1]. An increase in the acceptor-type V<sub>Sr</sub> density also correlates with suppression of Ti<sup>3+</sup> emission since excess electrons that would reduce Ti<sup>4+</sup> to Ti<sup>3+</sup> are compensated by excess holes. Increasing the beam voltage to probe across the film-substrate interface into the near-interface STO substrate reveals Sr concentration & depth-dependent behavior of the Ti<sup>3+</sup> state. This transition appears in all substrates with intensity correlated to Sr-concentration of the epilayer even if the Ti<sup>3+</sup> transition was suppressed in the deposited STO. Other defect-related transitions in the substrate spectra appear virtually identical, indicating that changes in the Ti<sup>3+</sup> substrate luminescence are related to changes in the Sr<sub>1-x</sub>TiO<sub>3</sub> layer. DRCLS is a powerful tool for studying defect distributions within ultra-thin films and near interfaces to understand the impact of defects on electronic structure. DRCLS can identify the interplay of specific defects in epitaxially deposited overlayers to enable design and growth of device structures with controlled defect densities and distributions in complex oxide heterostructures as well as other semiconductor systems. The

authors gratefully acknowledge support from NSF grant DMR-18-00130. [1] D. Lee, H. Wang, B.A. Noesges, T.J. Asel, J. Pan, J.W. Lee, Q. Yan, L.J. Brillson, X. Wu, and C.B. Eom. Identification of a functional point defect in SrTiO<sub>3</sub>. *Phys. Rev. Materials* 2, 060403(R) (2018)

#### 6:00 PM BB07

**(Student) Direct, Spatially-Resolved Observation of Defect States with Electromigration and Degradation of Single Crystal SrTiO<sub>3</sub>** Hantian Gao<sup>1</sup>, Sulata Sahu<sup>2</sup>, Clive Randall<sup>2</sup> and Leonard J. Brillson<sup>1,1</sup>; <sup>1</sup>The Ohio State University, United States; <sup>2</sup>The Pennsylvania State University, United States

Complex oxides such as SrTiO<sub>3</sub> have attracted considerable attention for a broad range of potential applications, especially as capacitor dielectrics for microelectronics. Key to their performance is their stability at elevated temperature and under high electric field stress which is limited by resistance degradation. The mechanism of such degradation has been investigated extensively, where electromigration of oxygen vacancies that build ionic space charge regions within the dielectric is a major concern<sup>1,2</sup>. However the direct observation of these defect distribution spatially on a macroscopic scale, together with the defects' changes in physical nature and electronic energies on a nanoscale with applied electric fields at elevated temperatures has until now not been fully reported. Complementary electrical measurements, spatially- and depth-resolved cathodoluminescence spectroscopy (DRCLS) provides direct microscopic evidence for the mechanism of resistance degradation in both Fe-doped and undoped SrTiO<sub>3</sub>. Laterally and depth-resolved cathodoluminescence spectroscopy (DRCLS) provided direct, nanoscale measurements of oxygen vacancy and oxygen vacancy complex distributions in undoped and Fe-doped SrTiO<sub>3</sub> with high temperature electric field stress associated with dielectric resistance degradation. DRCLS provided direct and spatially resolved observation of oxygen vacancy migration driven by external electric fields from anode to cathode in undoped SrTiO<sub>3</sub> between laterally separated electrodes, resulting in increased current leakage and lower thermal breakdown strength. DRCLS measurements through planar Pt electrodes after high temperature electric field cycling reveal pronounced oxygen vacancy depletion within the surface space region of the Pt/SrTiO<sub>3</sub> Schottky barrier as predicted theoretically. These results provide a direct insight into the transient states impacting the conduction during the electromigration of the oxygen vacancies. The deconvolution of different peaks and their intensity variations relative to the direct band gap provide methods to gauge the relative defect energetics of these gap states. This data is discussed in relation to providing a tool to further understand conduction in mixed ionic conductors. The authors gratefully acknowledge support from AFOSR Grant No. FA9550-18-1-0066 (A. Sayir) <sup>[1]</sup> R. Waser, *et al.*, *J. Am. Ceram. Soc.* **73** 1645 (1990). <sup>[2]</sup> T. J. M. Bayer, *et al.*, *J. Appl. Phys.* **122**, 244101 (2017). <sup>[3]</sup> F. J. Morin and J. R. Oliver, *Phys. Rev. B* **8**, 5847 (1973). <sup>[4]</sup> A. Klein, *J. Am. Ceram. Soc.*, **99**, 369 (2016). <sup>[5]</sup> R. Giesecke, R. Hertwig, T. H. M. Bayer, C. A. Randall, and A. Klein, *J. Am. Ceram. Soc.* **100**, 4590 (2017).

#### 6:15 PM BB08

**Oxygen Vacancy Driven Carrier Localization in Strongly Correlated Rare-Earth Nickelates** Zhen Zhang and Shriram Ramanathan; Purdue University, United States

Oxygen vacancies are found to manipulate strongly the electromagnetic and electronic structure behavior of oxide semiconductors. The electron doping, associated with oxygen vacancy formation, generally elevate the carrier concentration of the system, which then leads to increase of electrical conductivity. In this work, we will discuss the observation of an entirely opposite behavior in perovskite rare-earth nickelates upon introducing oxygen vacancy. By creating an extreme oxygen starvation environment, we incorporate oxygen vacancies into perovskite nickelates reversibly and results in a phase transition where the charge carriers become localized within the unit cell. As a result, their electrical conductivity decreases by more than six orders of magnitudes. Utilizing advanced characterization techniques such as x-ray absorption spectroscopy, x-ray photoemission, and mid-IR infrared nano-imaging as well as first principle calculations, the underlying mechanism of carrier localization is found as a combination of appearance of on-site electron-electron correlation in Ni 3d orbital upon charge filling and oxygen vacancies induced crystal field splitting. We further control the distribution of oxygen vacancies in the solid-state devices by voltage and find a multilevel resistance switching behavior with endurance over ten thousand cycles.

#### 6:30 PM BB09

**Role of Hydrogen in Wide-Bandgap Oxides—Ab-Initio Study of Crystalline/Amorphous In<sub>0.33</sub>:H Interfaces** Kapil Sharma and Julia Medvedeva; Missouri University of Science and Technology, United States

The role of hydrogen cannot be ignored because of its unavoidable presence during deposition, processing, and/or operation of semiconductor devices [1]. Furthermore, Koida in 2007 showed that hydrogen-doped indium oxide (IO:H) exhibits excellent carrier mobility (>100 cm<sup>2</sup>/Vs) in combination with tunable carrier density (10<sup>18</sup>-10<sup>20</sup> cm<sup>-3</sup>) and optical transparency in the visible and near-infrared regions, outperforming commercially-employed tin-doped indium oxide, ITO [2]. Since then, IO:H has attracted a great attention of scientific communities striving to understand the underlying behavior of hydrogen in semiconducting materials and to determine ways to enhance the overall device

performance. Based on the results of first-principles density-functional calculations, it was found that hydrogen is a shallow donor in crystalline  $\text{In}_2\text{O}_3$ , regardless of its particular location within the ordered lattice, whereas oxygen vacancies are deep defects [3,4]. The results may not be applicable to amorphous In-based oxides, currently preferred in state-of-the-art display technologies owing to their high carrier mobilities ( $\gg a\text{-Si:H}$ ); low-temperature, low-cost, large-area deposition; and smooth surfaces. In contrast to crystalline oxides, lack of periodicity; strong local (nearest-neighbor) and medium-range distortions in the Metal-Oxygen (M-O) polyhedral network; coordination morphology; and an increased number of degrees of freedom in amorphous materials are likely to result in a wide distribution of the binding energy and localization of M-OH and M-H defects and also affect thermal stability of the corresponding hydrogen bonds. In addition, the nanostructure of amorphous oxide materials is complex: it may feature large structural voids in low-density materials or a significant fraction of nanocrystallites when the density is close to that of the crystalline oxide. In indium oxide, nanocrystallites with sizes of 1-4 nm were observed by HRTEM below the so-called X-ray amorphous transition [5]. While the density and distribution of such nanocrystallites affects the crystallization process, it may also have a significant effect on the carrier transport. Indeed, both the grain size upon crystallization and the temperature behavior of the electron mobility were found to have an intricate dependence on the hydrogen content in sputtered IO:H suggesting that several carrier scattering mechanisms are likely to be simultaneously at play [6]. In this work, to understand the fundamental role of hydrogen on the structural and electronic properties of amorphous indium oxide, we studied a crystalline/amorphous interface before and after H-doping using ab-initio molecular dynamics and density-functional electronic structure calculations. To understand the bonding preferences of H, i.e., to predict possible local structural characteristics in the In-O coordination, bond length, and distortion distributions that would attract H, over 100 different locations of H radical in the crystalline/amorphous interfaces with three different oxygen stoichiometries were investigated. Based on a thorough analysis of the calculated total energy, structural changes, and the conduction charge density distribution before and after H-doping in the relaxed interfaces, we determine the resulting electronic and optical properties for the most energetically favorable site locations of H at the amorphous-crystalline interface and further investigate the stability of the H bonds to shed light on possible H mobility at room temperature and its effect on crystallization. [1]: J. Weber, *Phys. Stat. Solidi (c)*, vol. 5, pp. 535-538, 2008. [2]: T. Koida et al., *JPN. J. Appl. Phys.*, vol. 46, pp. L685-L687, 2007. [3]: S. Limpijumnong et al., *Phys. Rev. B.*, vol. 80, p. 193202, 2009. [4]: J. J. Melendez et al., *J. Phys. Chem. C*, vol. 120(7), pp. 4007-4015, 2016. [5]: D. B. Buchholz et al., *Chem. Mater.*, vol. 26, pp. 5401-5411, 2014. [6]: S. Husein et al., *J. Appl. Phys.*, vol. 123, p. 245102, 2018.



# 62<sup>ND</sup> ELECTRONIC MATERIALS CONFERENCE

June 24-26, 2020

## FRIDAY ORAL PRESENTATIONS

#### 10:00 AM CC01

**Fabrication of Vertical Schottky Barrier Diodes on  $\beta$ -Ga<sub>2</sub>O<sub>3</sub> Substrates Prepared by Vertical Bridgman Method** Chia-Hung Lin<sup>1</sup>, Keigo Hoshikawa<sup>2,3</sup>, Atsushi Kajikura<sup>3</sup>, Kimiyoshi Koshi<sup>1</sup>, Yu Yamaoka<sup>1</sup>, Kazuhito Fujii<sup>1</sup>, Masanori Yokoo<sup>1</sup>, Hirofumi Wada<sup>1</sup>, Quang Tu Thieu<sup>1</sup>, Amutha Thangaraja<sup>1</sup>, Yuki Uchida<sup>1</sup>, Yuki Koishikawa<sup>1</sup>, Fumio Otsuka<sup>1</sup>, Shinya Watanabe<sup>1</sup>, Kohei Sasaki<sup>1</sup> and Akito Kuramata<sup>1</sup>; <sup>1</sup>Novel Crystal Technology, Japan; <sup>2</sup>Shinshu University, Japan; <sup>3</sup>Fujikoshi Machinery Corp., Japan

Ga<sub>2</sub>O<sub>3</sub> possesses an ultrawide bandgap of 4.5 eV, namely a large prospective breakdown electric field of 7-8 MV/cm, and the commercial Ga<sub>2</sub>O<sub>3</sub> bulk substrates with high crystal quality are available. Therefore, Ga<sub>2</sub>O<sub>3</sub> facilitates the development of high-power, low energy-consumption electronic devices. Our group have manufactured 2-inch  $\beta$ -Ga<sub>2</sub>O<sub>3</sub> (001) bulk substrates by using the Edge-defined Film-fed Growth (EFG) method and recently, 4-inch substrates with the full width at half maximum of X-ray rocking curve (FWHM-XRC) of around 25 arcsec are provided. The vertical Bridgman (VB) method is also one of the promising candidates for producing high-crystallinity  $\beta$ -Ga<sub>2</sub>O<sub>3</sub> substrates and can further lower the cost owing to free of using iridium, which allows substrates to be prepared even in air [1]. In this work, we compared the performance of  $\beta$ -Ga<sub>2</sub>O<sub>3</sub> vertical Schottky barrier diodes (SBDs) fabricated on the  $n^+$ -Ga<sub>2</sub>O<sub>3</sub> substrates by using the EFG and VB methods. The net donor concentrations ( $N_d - N_a$ ) and FWHM-XRCs of the Sn-doped EFG-grown and VB-grown  $n^+$ -Ga<sub>2</sub>O<sub>3</sub> (001) substrates were [6.7 $\times$ 10<sup>18</sup> cm<sup>-3</sup>, 27 arcsec] and [3.4 $\times$ 10<sup>18</sup> cm<sup>-3</sup>, 28 arcsec], respectively. Vertical Ga<sub>2</sub>O<sub>3</sub> SBDs with 9.9- $\mu$ m-thick and 9.6- $\mu$ m-thick  $n$ -Ga<sub>2</sub>O<sub>3</sub> drift layers were individually grown on the EFG-grown and VB-grown substrates by halide vapor phase epitaxy. The  $N_d - N_a$  in drift layers grown on the EFG-grown substrate were 1.6 $\times$ 10<sup>16</sup> cm<sup>-3</sup>, and those on the VB-grown substrate were 2.0 $\times$ 10<sup>16</sup> cm<sup>-3</sup>. Ni/Au Schottky anode electrodes with a diameter of 1 mm and Ti/Au ohmic cathode electrodes were fabricated on the drift layers and blanket evaporated onto the back side of the  $n^+$ -Ga<sub>2</sub>O<sub>3</sub> substrates, respectively.

The specific on-resistances ( $R_{on}$ ) were extracted from linear fits to the forward current density-voltage ( $J$ - $V$ ) characteristics of the SBDs in linear scale. The average  $R_{on}$  were estimated to be 9.3 and 8.5 m $\Omega$ ·cm<sup>2</sup> for the SBDs fabricated on the EFG-grown and VB-grown substrates, respectively. The average ideality factors ( $\eta$ ) of 1.04 and 1.01 were extracted from linear fits to the semi-logarithmic  $J$ - $V$  plots for the SBDs fabricated on the EFG-grown and VB-grown substrates, respectively. The reverse  $J$ - $V$  characteristics of the SBDs were also carried out to determine the maximum reverse biases ( $V_{r,max}$ ), which were defined as the maximum set value of 200 V if the  $J$  has not limited by the compliance  $J=10^{-4}$  A/cm<sup>2</sup> or those when the  $J$  reached to the compliance value. The average  $V_{r,max}$  of 174 V and 191 V were estimated for the SBDs fabricated on the EFG-grown and VB-grown substrates, respectively. The SBDs fabricated on the VB-grown substrates showed larger  $V_{r,max}$  values and closer near unity of  $\eta$  than those on the EFG-grown substrates, demonstrating that the VB method offers comparable or even better potential to the EFG one for producing high-crystallinity  $\beta$ -Ga<sub>2</sub>O<sub>3</sub> (001) bulk substrates.

Part of this work was supported by the New Energy and Industrial Technology Development Organization (NEDO).

I. K. Hoshikawa *et al.*, J. Cryst. Growth, **447**, 36 (2016).

#### 10:15 AM CC02

**(Student) Bias-Temperature Instability Measurement of  $\beta$ -Ga<sub>2</sub>O<sub>3</sub>/h-BN MISFETs** Cheolhee Cho<sup>1</sup>, Janghyuk Kim<sup>1</sup>, Jinho Bae<sup>1</sup>, Marko Tadjer<sup>2</sup> and Jihyun Kim<sup>1</sup>; <sup>1</sup>Korea University, Korea (the Republic of); <sup>2</sup>U.S. Naval Research Laboratory, United States

$\beta$ -gallium oxide ( $\beta$ -Ga<sub>2</sub>O<sub>3</sub>) is a promising material for post power electronics owing to its wide bandgap of 4.8 eV, high breakdown electric field (8 MV/cm), and good thermal stability. It is known that  $\beta$ -Ga<sub>2</sub>O<sub>3</sub> with a monolithic structure can be exfoliated into ultra-thin flakes because of weak out-of-plane force along the (100) plane, being integrated with van der Waals materials easily. Hexagonal boron nitride (h-BN) attracts great attention as an alternative material because of its atomically sharp interface and low density of charged impurity, which increases the electrical properties of the semiconductor device. Moreover, the thermal conductivity of h-BN (50 W/m.K) is higher than that of other dielectric materials such as SiO<sub>2</sub> (1.4 W/m.K) and Al<sub>2</sub>O<sub>3</sub> (35 W/m.K). Therefore, metal-insulator-semiconductor field-effect transistors (MISFETs) having a configuration of  $\beta$ -Ga<sub>2</sub>O<sub>3</sub>/h-BN heterostructure are expected to increase the enhance device performance with the synergetic effect of both materials. However, there are few studies about the bias and temperature stability of  $\beta$ -Ga<sub>2</sub>O<sub>3</sub>/h-BN MISFETs. In this study, we systematically investigated the bias-temperature threshold voltage instability (BTI) of  $\beta$ -Ga<sub>2</sub>O<sub>3</sub>/h-BN MISFETs.  $\beta$ -Ga<sub>2</sub>O<sub>3</sub> (200-300 nm) and h-BN (20-40 nm) flakes were mechanically exfoliated and dry-transferred onto SiO<sub>2</sub>/Si substrate using a micromanipulator. After that source, drain, and gate electrodes (Ti/Au 50/100

nm) were defined by e-beam evaporation. The optical characteristics, surface morphology, and structural properties of the  $\beta$ -Ga<sub>2</sub>O<sub>3</sub> and h-BN flakes was examined via Raman spectroscopy, photoluminescence spectroscopy (PL), atomic force microscopy (AFM), and transmission electron microscopy (TEM). BTI measurement of MISFETs was carried out in the following sequence varying bias stress time and temperature; drain-to-source current ( $I_D$ )-gate bias ( $V_{GS}$ ) sweep, gate bias stress,  $I_D$ - $V_{GS}$  sweep (backward), and repeating stress and sweep. This work showed a great potential of van der Waals heterostructure of  $\beta$ -Ga<sub>2</sub>O<sub>3</sub>/2D materials on future nanoscale power devices. Details of the measurement procedure and results will be presented at the conference.

#### 10:30 AM CC03

**(Student)  $\beta$ -Ga<sub>2</sub>O<sub>3</sub>/BaTiO<sub>3</sub> MESFET with Power Figure of Merit of 376 MW/cm<sup>2</sup>** Nidhin Kurian Kalarickal, Zixuan Feng, Xia Zhanbo, A F M Anhar Uddin Bhuiyan, Wyatt Moore, Joe F. McGlone, Aaron Arehart, Steven A. Ringel, Hongping Zhao and Siddharth Rajan; The Ohio State University, United States

We report on the design and demonstration of BaTiO<sub>3</sub>/ $\beta$ -Ga<sub>2</sub>O<sub>3</sub> based MESFETs with state-of-art power figure of merit ( $V_{BR}^2/R_{ON}$ ) of 376 MW/cm<sup>2</sup>. Such high performance was achieved using MOCVD grown  $\beta$ -Ga<sub>2</sub>O<sub>3</sub> epilayers with a high channel sheet charge density of 2 $\times$ 10<sup>13</sup> cm<sup>-2</sup> and a thick (73 nm) high-k BaTiO<sub>3</sub> gate dielectric deposited ex-situ using RF sputtering. The device represents the highest reported power figure of merit to date for  $\beta$ -Ga<sub>2</sub>O<sub>3</sub> lateral devices. With a theoretical breakdown field of 8 MV/cm,  $\beta$ -Ga<sub>2</sub>O<sub>3</sub> provides a new material platform for improving performance metrics of high voltage switching devices. The availability of bulk substrates enables low defect density material and high quality homoepitaxial  $\beta$ -Ga<sub>2</sub>O<sub>3</sub> thin films using various techniques like MBE, MOCVD, HVPE and PLD. Both vertical and lateral high voltage devices previously demonstrated on  $\beta$ -Ga<sub>2</sub>O<sub>3</sub> show excellent performance [1] but are limited due to two main factors - the lack of a suitable dielectric to support electric fields in excess of 8 MV/cm and, the high sheet resistance of  $\beta$ -Ga<sub>2</sub>O<sub>3</sub> channels. In this report we demonstrate the use of high permittivity sputtered BaTiO<sub>3</sub> as a suitable gate dielectric for  $\beta$ -Ga<sub>2</sub>O<sub>3</sub> which can simultaneously enable higher sheet charge density and high breakdown voltage. 2D device simulations were used to understand the effect of high-k ( $\epsilon_r=300$ ) gate dielectric thickness (20 nm to 80 nm) on the electric field profile in the gate-drain region. Thicker high-k layers suppress non-uniformity in electric field along the channel and lower the field in the growth direction. (Al<sub>1-x</sub>Ga<sub>x</sub>)<sub>2</sub>O<sub>3</sub>/Ga<sub>2</sub>O<sub>3</sub> heterostructures were grown by MOCVD (Agnitron Agilis R&D oxide system) with 500 nm of unintentionally doped (UID) buffer layer, followed by 30 nm of doped Ga<sub>2</sub>O<sub>3</sub>, 5 nm doped (Al<sub>0.25</sub>Ga<sub>0.75</sub>)<sub>2</sub>O<sub>3</sub> layer and 15 nm UID (Al<sub>0.25</sub>Ga<sub>0.75</sub>)<sub>2</sub>O<sub>3</sub> cap layer. Ohmic contacts were defined using stepper lithography followed by Si ion implantation (Leonard Krokco, inc) to form heavily doped regions. A Ti/Au/Ni (40/60/40 nm) metal stack was then deposited and annealed for 2 min at 470 (N<sub>2</sub> ambient) to form source and drain ohmic contacts. 73 nm thick BaTiO<sub>3</sub> layer was then sputtered to form the gate dielectric. C-V and TLM measurements were performed before depositing the BaTiO<sub>3</sub> gate dielectric, and a sheet charge density of 2 $\times$ 10<sup>13</sup> cm<sup>-2</sup>, sheet resistance of 3.4 K $\Omega$ /sq and contact resistance of 1.4  $\Omega$ .mm were obtained. After deposition of BaTiO<sub>3</sub> the measured values were sheet charge density of 2 $\times$ 10<sup>13</sup> cm<sup>-2</sup>, sheet resistance of 5.4 K $\Omega$ /sq and contact resistance of 4.1  $\Omega$ .mm indicating that the sputtering process impacts the channel mobility and the ohmic contact resistance. DC I-V and breakdown voltages were measured to estimate the on-resistance and the breakdown voltage. The measured on-resistance varies from 13.6  $\Omega$ .mm to 42.8  $\Omega$ .mm as the source-drain spacing is increased from 1.5  $\mu$ m ( $L_{GD}=0.5 \mu$ m) to 7.5  $\mu$ m ( $L_{GD}=6 \mu$ m). The corresponding breakdown voltage ( $V_{DG}$ ) increases from 201 V (4 MV/cm) to 918 V (1.5 MV/cm). Such high breakdown voltages are significant considering the high sheet charge density in the MESFET channel (2 $\times$ 10<sup>13</sup> cm<sup>-2</sup>). The power figure of merit ( $V_{BR}^2/R_{ON}$ ) at a breakdown voltage of 640 V ( $L_{GD}=4.2 \mu$ m,  $R_{ON}=25.9 \Omega$ .mm), was calculated to be 376 MW/cm<sup>2</sup> which is the highest reported for any  $\beta$ -Ga<sub>2</sub>O<sub>3</sub> lateral device. In summary we have demonstrated BaTiO<sub>3</sub>/ $\beta$ -Ga<sub>2</sub>O<sub>3</sub> based MESFETs with superior power figure of merit performance of 376 MW/cm<sup>2</sup> by utilizing a thick high-k BaTiO<sub>3</sub> gate dielectric. The integration of high permittivity dielectrics with Ga<sub>2</sub>O<sub>3</sub> could provide a promising direction for future material and device research. This work was funded by AFOSR GAME MURI (Grant FA9550-18-1-0479, Program Manager Dr. Ali Sayir). **References** [1] Li, Wenshen, et al. *IEEE Electron Device Letters* 41.1 (2019): 107-110.

#### 10:45 AM CC04

**(Student) High-Density Degenerate Electron Gas (1013 cm<sup>-2</sup>) in  $\beta$ -(Al<sub>x</sub>Ga<sub>1-x</sub>)<sub>2</sub>O<sub>3</sub>/ $\beta$ -Ga<sub>2</sub>O<sub>3</sub> Heterostructures Grown by Metalorganic Vapor Phase Epitaxy** Praneeth Ranga<sup>1</sup>, Arka Bhattacharyya<sup>1</sup>, Saurav Roy<sup>1</sup>, Yu Kee Ooi<sup>1</sup>, Michael Scarpulla<sup>1</sup>, Daniel Feezell<sup>2</sup> and Sriram Krishnamoorthy<sup>1</sup>; <sup>1</sup>The University of Utah, United States; <sup>2</sup>The University of New Mexico, United States

We demonstrate a high-density electron sheet charge in MOVPE-grown  $\beta$ -(Al<sub>0.26</sub>Ga<sub>0.74</sub>)<sub>2</sub>O<sub>3</sub>/ $\beta$ -Ga<sub>2</sub>O<sub>3</sub> heterojunction. Also, we show a very narrow FWHM (full width at half-maximum) in MOVPE-grown delta-doped Ga<sub>2</sub>O<sub>3</sub>,  $\beta$ -Ga<sub>2</sub>O<sub>3</sub> is an ultra-wide bandgap(UWBG) material with a high critical breakdown field of 6-8 MV/cm.  $\beta$ -Ga<sub>2</sub>O<sub>3</sub> suffers from severe polar optical phonon scattering which limits the expected maximum room temperature mobility to  $\sim$ 200 cm<sup>2</sup>/V. s in uniformly-doped thin films. Alternate doping

strategies such as delta and modulation doping can potentially reduce the amount of impurity scattering in the channel. Delta-doped  $\beta$ -Ga<sub>2</sub>O<sub>3</sub> films are expected to show reduced scattering in the channel due to the spreading of the electron wavefunction into the regions outside the location of the sheet of ionized donor atoms. Delta-doped MESFETs with a gate to channel distance of ~20 nm and short gate lengths have been used to realize  $f_t$  of 27 GHz [1], indicating the potential for RF device applications. Ab initio transport studies indicate that the enhanced screening of optical phonons at high 2DEG charge densities leads to increase in 2DEG mobility. Channel mobility as high as 1000 cm<sup>2</sup>/V.s can be potentially attained by realizing a high-density 2DEG at modulation-doped AlGaO/GaO heterointerface [2]. Recently, a 2DEG sheet charge density exceeding  $6 \times 10^{12}$  cm<sup>-2</sup> has been reported in both MBE and MOVPE-grown delta-doped  $\beta$ -(Al<sub>x</sub>Ga<sub>1-x</sub>)<sub>2</sub>O<sub>3</sub>/ $\beta$ -Ga<sub>2</sub>O<sub>3</sub> heterojunctions [3,4]. High Al content  $\beta$ -(Al<sub>x</sub>Ga<sub>1-x</sub>)<sub>2</sub>O<sub>3</sub> and abrupt dopant profiles are critical for obtaining a high-density 2DEG. Growth of  $\beta$ -(Al<sub>x</sub>Ga<sub>1-x</sub>)<sub>2</sub>O<sub>3</sub> has been limited to 20-25% Al content using MBE, largely because of issues associated with Ga incorporation at high growth temperatures. Higher Al content in  $\beta$ -(Al<sub>x</sub>Ga<sub>1-x</sub>)<sub>2</sub>O<sub>3</sub> films can be potentially attained by MOVPE growth technique owing to its ability to grow at high temperatures. N-type doping of high Al-content  $\beta$ -(Al<sub>x</sub>Ga<sub>1-x</sub>)<sub>2</sub>O<sub>3</sub> thin films is already demonstrated using MOVPE growth technique [5,6].

Growth of delta-doped (010)  $\beta$ -Ga<sub>2</sub>O<sub>3</sub> films is performed by using Agnitron Agilis MOVPE reactor with TEGa<sub>2</sub>O<sub>3</sub> and silane(SiH<sub>4</sub>) as precursors and argon as the carrier gas. Delta doping of  $\beta$ -Ga<sub>2</sub>O<sub>3</sub> is achieved by interrupting the growth of  $\beta$ -Ga<sub>2</sub>O<sub>3</sub> and supplying silane to the reactor with purge steps before and after silicon incorporation. Multiple samples are grown under different growth conditions to study silicon incorporation in  $\beta$ -Ga<sub>2</sub>O<sub>3</sub> films. CV/SIMS measurements are used to characterize the sheet charge density/Si atom density and FWHM of the silicon delta sheet. Sheet charge density extracted from CV measurements is between  $2 \times 10^{12}$  cm<sup>-2</sup> and  $9 \times 10^{12}$  cm<sup>-2</sup>. CV extracted charge density deviated from SIMS measured silicon concentration at high silane flows. By further optimizing the growth conditions, FWHM as low as 3.5 nm is realized in delta-doped thin film. Using a delta-doped  $\beta$ -(AlGa)<sub>2</sub>O<sub>3</sub> barrier layer, a room temperature electron sheet charge density of  $1 \times 10^{13}$  cm<sup>-2</sup> is realized at  $\beta$ -(AlGa)<sub>2</sub>O<sub>3</sub>/ $\beta$ -Ga<sub>2</sub>O<sub>3</sub> interface. RT CV extracted sheet charge density was identical to the lower temperature(90 K) value, confirming the degenerate nature of the electron gas. This value is the highest reported electron gas density in  $\beta$ -(Al<sub>x</sub>Ga<sub>1-x</sub>)<sub>2</sub>O<sub>3</sub>/ $\beta$ -Ga<sub>2</sub>O<sub>3</sub> material system for a single electron channel. Transport characterization of the high-density electron gas will be reported.

**References:** [1] Xia Z. et al IEEE Electron Device Lett. 40 1052 (2019); [2] Ghosh K. and Singiseti U. J. Mater. Res. 32 4142 (2017); [3] N.K Kalarickal et. al. arXiv:1910.11521 (2019); [4] P.Ranga, et al. arXiv:1910.12432 (2019); [5] P.Ranga et. al. Appl. Phys. Express 12 111004 (2019); [6] Anhar Uddin Bhuiyan, A F M et al Appl. Phys. Lett. 115. 120602 (2019).

**Acknowledgement:** This material is based upon work supported by the Air Force Office of Scientific Research under award number FA9550-18-1-0507 monitored by Dr Ali Sayir. We thank Air Force Research Laboratory, Sensors Directorate for discussions.

#### 11:00 AM CC05

**(Student) Exploring Ga<sub>2</sub>O<sub>3</sub>/(Al<sub>x</sub>Ga<sub>1-x</sub>)<sub>2</sub>O<sub>3</sub> Resonant Tunnel Diode Heterostructures** Evan M. Cornuelle, A F M Anhar Uddin Bhuiyan, Zixuan Feng, Jared Johnson, Hsien-Lien Huang, Jinwoo Hwang and Hongping Zhao; The Ohio State University, United States

High-power terahertz and millimeter-wave devices have ubiquitous application in imaging, security, and medicine. Fast electronic transport via quantum mechanical tunneling make resonant tunneling diodes (RTDs) prime candidates to fill this device space. Fundamental oscillations up to 1.92 THz [1] at room temperature have been reported in InGaAs/AIAs based RTDs but lacked significant output power. Wide band-gap material systems have the potential to increase output power due to increased operating voltage. The GaN/AlN material system has drawn considerable interest over the past decade with great progress; however, oscillation frequencies have not yet surpassed 1 GHz. One key challenge in III-N based RTDs is the lack of high-quality low dislocation density native substrates. Recently, Ga<sub>2</sub>O<sub>3</sub> has attracted growing interests for power electronics application. Considering the following advantages, this emerging ultra-wide bandgap material system has a great potential for RTDs: (i) the stable b-phase Ga<sub>2</sub>O<sub>3</sub> and (Al<sub>x</sub>Ga<sub>1-x</sub>)<sub>2</sub>O<sub>3</sub> are polarization-free materials, which reduces complexity for electron confinement in the well region (ii) there exists a large band offset at the Ga<sub>2</sub>O<sub>3</sub>/(Al<sub>x</sub>Ga<sub>1-x</sub>)<sub>2</sub>O<sub>3</sub> heterostructure interface as Al composition increase subsequently reducing non-tunneling current mechanisms; and (iii) the availability of high quality low dislocation density free-standing Ga<sub>2</sub>O<sub>3</sub> substrates produced by thermal based growth techniques can enable high quality Ga<sub>2</sub>O<sub>3</sub>/(Al<sub>x</sub>Ga<sub>1-x</sub>)<sub>2</sub>O<sub>3</sub> heterostructure epitaxy on economies of scale. The equilibrium band diagrams and bound state energy levels for a series of Ga<sub>2</sub>O<sub>3</sub>/Al<sub>2</sub>O<sub>3</sub> RTDs were calculated using a Schrödinger-Poisson solver. The structures simulated had the barrier thicknesses of 1.5nm, 2.0nm, and 2.5nm; well thicknesses between 2.0nm and 3.5nm; and spacer of 5 nm and 12nm. Increasing well thickness increased the number of bound states (from 3 to 6) in the QW and reduced the energy separation. The barrier thickness had minimal effect on the number of energy states and energy level in the well. Structures with the same well thickness followed nearly identical energy level vs. state number trends independent of the barrier thickness. The small separation in energy between the structures with varying spacer thickness

is due to an energy shift relative to the Fermi-level and was explained from energy state differences. These simulation results provide a design space and growth requirements for achieving high quality and high performance Ga<sub>2</sub>O<sub>3</sub> RTDs. Preliminary growth studies of Ga<sub>2</sub>O<sub>3</sub>/(Al<sub>x</sub>Ga<sub>1-x</sub>)<sub>2</sub>O<sub>3</sub> superlattices grown via MOCVD provided efficacy for Ga<sub>2</sub>O<sub>3</sub> RTD devices. Two eight-period superlattices were grown with Al composition of 23% and 40%. The sample with 23% Al composition demonstrated high quality material with uniform and sharp heterointerfaces throughout. When Al composition increased to 40%, high quality heterointerfaces were demonstrated for the first 2 periods. We expect high quality Ga<sub>2</sub>O<sub>3</sub>/(Al<sub>x</sub>Ga<sub>1-x</sub>)<sub>2</sub>O<sub>3</sub> RTD structures can be achieved with higher Al composition, since very thin (Al<sub>x</sub>Ga<sub>1-x</sub>)<sub>2</sub>O<sub>3</sub> barrier layer thickness (1.5-2.5 nm) are required. In this work, we will investigate a series of RTD device structures by modifying the well and barrier thicknesses in addition to tuning Al composition in the (Al<sub>x</sub>Ga<sub>1-x</sub>)<sub>2</sub>O<sub>3</sub> barriers. Material characterization using STEM imaging will probe the interface quality and layer thickness. RTD devices will be fabricated into devices and characterized by dc I-V measurements

In summary, Schrödinger-Poisson simulations of different Ga<sub>2</sub>O<sub>3</sub>/(Al<sub>x</sub>Ga<sub>1-x</sub>)<sub>2</sub>O<sub>3</sub> RTDs were performed to observe the relationship between critical device dimensions and number and location of bound energy states. MOCVD growth of Ga<sub>2</sub>O<sub>3</sub>/(Al<sub>x</sub>Ga<sub>1-x</sub>)<sub>2</sub>O<sub>3</sub> superlattice were performed and characterized by STEM imaging displaying high quality material and heterointerfaces in thicknesses greater than required for RTDs. I. T. Maekawa, et al., *Appl. Phys. Express*, **9**, 024101 (2016)

#### 11:15 AM BREAK

#### 11:45 AM CC06

**(Student) Observation of Near-Ideal Reverse Leakage Current in  $\beta$ -Ga<sub>2</sub>O<sub>3</sub> Schottky Barrier Diodes and Its Implications for High Electric-Field Operation** Wenshen Li, Devansh Saraswat, Yaoyao Long, Kazuki Nomoto, Debdeep Jena and Huili Grace Xing; Cornell University, United States

$\beta$ -Ga<sub>2</sub>O<sub>3</sub> is a promising ultra-wide bandgap semiconductor material for high power device applications because of the high breakdown electric field of up to 8 MV/cm and the availability of melt-grown substrates. Due to the difficulty in native p-type doping, Schottky barrier diodes (SBDs) are the most important rectifiers in Ga<sub>2</sub>O<sub>3</sub>. In addition, SBDs allow for sensitive probing of the surface and material properties. In recent year, promising performance in Ga<sub>2</sub>O<sub>3</sub> SBDs has been demonstrated. However, there have been only a few reports on the reverse leakage mechanisms in Ga<sub>2</sub>O<sub>3</sub> SBDs. This subject is of high importance, since the breakdown voltage of SBDs based on wide-bandgap semiconductors is typically limited by the leakage current, rather than the intrinsic breakdown electric field. Previous studies on the leakage mechanisms have been carried out only under relatively low surface electric field ( $E$ ) below 2 MV/cm, where thermionic emission (TE) or thermionic-field emission (TFE) process dominates [1][2]. In this work, we investigate the intrinsic leakage mechanisms of Ga<sub>2</sub>O<sub>3</sub> SBDs up to a surface electric field of 3.4 MV/cm, which allows for the revelation of the field emission (FE) process for the first time. The Ni-Schottky barrier diodes (SBDs) under study were fabricated on a Sn-doped (-201)  $\beta$ -Ga<sub>2</sub>O<sub>3</sub> substrate ( $N_b - N_a = 1.45 \times 10^{18}$  cm<sup>-3</sup>). Ga<sub>2</sub>O<sub>3</sub> is prone to plasma-induced damage [3], thus the Schottky contact surface was not exposed to any plasma process throughout the entire fabrication process.

Temperature-dependent forward  $I$ - $V$  characteristics was analyzed using the TE model. The ideality factor is 1.14 at 23°C and decreases to 1.05 at 200°C. The extracted barrier height after image-force correction is ~1.35 eV. We have verified that the leakage current density ( $J$ ) has no dependence on the device size, indicating that edge leakage is sufficiently suppressed with our mesa edge termination. At room temperature, the reverse current can be well-fitted with the field-emission model alone, indicating that barrier tunneling process dominates. To further verify the barrier tunneling process, Fowler-Nordheim (F-N) plot was generated from the temperature-dependent reverse  $I$ - $V$  characteristics. The curve at room temperature shows good linearity in the F-N plot, which is a strong indication of the FE process. Furthermore, throughout the entire electric-field range and under each temperature, the reverse  $J$ - $E$  characteristics can be well-fitted with our numerical barrier tunneling model, with the barrier height as the only fitting parameter. The  $J$ - $E$  characteristics transitions from a TFE-dominated regime at lower electric field to a FE-dominated regime at higher surface electric field. The barrier height values extracted from the reverse  $J$ - $E$  characteristics is consistent with the values extracted from the forward  $I$ - $V$  characteristics and  $C$ - $V$  measurements, with a maximum difference of only 0.06 eV. This further supports the validity of the reverse leakage modeling. Using the numerical tunneling model, we calculate the maximum practical surface electric field in Ga<sub>2</sub>O<sub>3</sub> SBDs defined at a maximum reverse leakage current density of 1 mA/cm<sup>2</sup> or 100 mA/cm<sup>2</sup>, as a function of the barrier height. The results suggest that it is possible to reach a maximum surface electric field close to breakdown electric field of  $\beta$ -Ga<sub>2</sub>O<sub>3</sub> (6-8 MV/cm) as long as a sufficiently high barrier height (>2.2 eV) is realized. In conclusion, near-ideal reverse leakage current is observed in  $\beta$ -Ga<sub>2</sub>O<sub>3</sub> SBDs up to a surface electric field of 3.4 MV/cm, suggesting excellent surface and material quality. Both TFE- and FE-dominated regimes are identified. The calculation of the maximum practical surface electric field suggests the possibility of approaching the breakdown electric field in Ga<sub>2</sub>O<sub>3</sub> SBDs.

[1] M. Higashiwaki et al., *Appl. Phys. Lett.* **108**, 133503 (2016). [2] K. Konishi et al., *Appl. Phys. Lett.* **110**, 103506 (2017). [3] J. Yang et al., *Appl. Phys. Lett.* **110**, 142101 (2017).

## 12:00 PM CC07

**(Student) Effect of Annealing on the Band Alignment of ALD SiO<sub>2</sub> on (Al<sub>x</sub>Ga<sub>1-x</sub>)<sub>2</sub>O<sub>3</sub> for x= 0.2 - 0.65** Chaker Fares<sup>1</sup>, Zahabul Islam<sup>2</sup>, Aman Haque<sup>2</sup>, Max Kneiß<sup>3</sup>, Holger v. Wenckstern<sup>3</sup>, Marius Grundmann<sup>3</sup>, Marko Tadjer<sup>4</sup>, Fan Ren<sup>1</sup> and Stephen J. Pearton<sup>1</sup>; <sup>1</sup>University of Florida, United States; <sup>2</sup>The Pennsylvania State University, United States; <sup>3</sup>Universität Leipzig, Felix-Bloch-Institut für Festkörperphysik, Germany; <sup>4</sup>U.S. Naval Research Laboratory, United States

There is a great current interest in the development of Ga<sub>2</sub>O<sub>3</sub>-based heterostructures for power electronics and solar-blind UV photodetectors. In particular, (Al<sub>x</sub>Ga<sub>1-x</sub>)<sub>2</sub>O<sub>3</sub>/Ga<sub>2</sub>O<sub>3</sub> is being used in heterostructure field-effect transistors with promising and improving performance. Additionally, the bandgap of this alloy can be tuned by varying the Al content allowing for the growth conditions to be varied based on the needed application. Recent reports on the (Al<sub>x</sub>Ga<sub>1-x</sub>)<sub>2</sub>O<sub>3</sub>/Ga<sub>2</sub>O<sub>3</sub> structure have shown good device operation fabricated using single-phase layers with x values up to ~0.25 and single-crystal quality up to ~40%. It is of interest to measure the band alignments for common dielectrics on (Al<sub>x</sub>Ga<sub>1-x</sub>)<sub>2</sub>O<sub>3</sub>, as these will be used in MOS transistors. Given the large bandgap of (Al<sub>x</sub>Ga<sub>1-x</sub>)<sub>2</sub>O<sub>3</sub> alloys there are a limited number of options for dielectrics that might have adequate valence and conduction band offsets. During the formation of Ohmic contacts or annealing of implant isolation regions in MOS transistors based on (Al<sub>x</sub>Ga<sub>1-x</sub>)<sub>2</sub>O<sub>3</sub>, it is necessary to anneal at temperatures of 500-600°C. There has, as of yet, been no examination of how high temperatures affect the band offsets between SiO<sub>2</sub> and (Al<sub>x</sub>Ga<sub>1-x</sub>)<sub>2</sub>O<sub>3</sub>. In this study, we utilize x-ray photoelectron spectroscopy (XPS) to report on the determination of the band alignment of atomic layer deposited SiO<sub>2</sub> onto (Al<sub>x</sub>Ga<sub>1-x</sub>)<sub>2</sub>O<sub>3</sub> at compositions ranging from (Al<sub>0.2</sub>Ga<sub>0.8</sub>)<sub>2</sub>O<sub>3</sub> to (Al<sub>0.65</sub>Ga<sub>0.35</sub>)<sub>2</sub>O<sub>3</sub>. After measuring the initial band alignment of the SiO<sub>2</sub>/(Al<sub>x</sub>Ga<sub>1-x</sub>)<sub>2</sub>O<sub>3</sub> heterostructures, we also investigate the influence of post-deposition annealing at 600°C on the heterostructure's band offsets. The valence band offset is found to decrease significantly as a result of this annealing, by amounts of 0.65 eV for (Al<sub>0.2</sub>Ga<sub>0.8</sub>)<sub>2</sub>O<sub>3</sub> to 1.75 eV for (Al<sub>0.65</sub>Ga<sub>0.35</sub>)<sub>2</sub>O<sub>3</sub>. Clearly, the thermal budget during device processing must be considered when making MOS structures on (Al<sub>x</sub>Ga<sub>1-x</sub>)<sub>2</sub>O<sub>3</sub>. The valence band offsets decrease significantly as a result of this annealing, with the change dependent on the initial Al composition. The decrease ranges from 0.65 eV for (Al<sub>0.2</sub>Ga<sub>0.8</sub>)<sub>2</sub>O<sub>3</sub> to 1.75 eV for (Al<sub>0.65</sub>Ga<sub>0.35</sub>)<sub>2</sub>O<sub>3</sub> and is likely due to an increase in interfacial disorder as a result of annealing. Concurrently, the conduction band offsets increase, improving carrier confinement for electrons within the heterostructure. The band alignment remains type I (nested gap) across the entire composition range examined.

## 12:15 PM CC08

**Very High Temperature (500 °C) Operating Performance of PtO<sub>x</sub>, IrO<sub>x</sub>, PdO<sub>x</sub>, and RuO<sub>x</sub> Schottky Contacts on β-Ga<sub>2</sub>O<sub>3</sub>** Caixia Hou<sup>1,2</sup> and Martin Allen<sup>1,2</sup>; <sup>1</sup>University of Canterbury, New Zealand; <sup>2</sup>MacDiarmid Institute for Advanced Materials and Nanotechnology, New Zealand

Monoclinic beta-phase gallium oxide (β-Ga<sub>2</sub>O<sub>3</sub>) is currently the subject of very strong research interest for high-efficiency power electronics and deep UV photodetectors due to its ultra-wide band gap (4.85 eV) and very high breakdown strength (~8 MV/cm). One of the important challenges to unlocking the potential of β-Ga<sub>2</sub>O<sub>3</sub> for power electronics devices, is the production of robust thermally-stable Schottky contacts, as these form the key component in high-speed rectifying diodes and metal-semiconductor field effect transistors. In the work presented here, very high temperature β-Ga<sub>2</sub>O<sub>3</sub> Schottky contacts were fabricated on β-Ga<sub>2</sub>O<sub>3</sub> single crystal substrates using intentionally-oxidized platinum group metal (PGM) Schottky contacts (SCs), i.e. PtO<sub>x</sub>, IrO<sub>x</sub>, PdO<sub>x</sub>, and RuO<sub>x</sub>, fabricated via the reactive rf sputtering of plain PGM targets using an oxygen-containing plasma. All four types of oxidized PGM SCs showed rectification ratios of at least 10 orders of magnitude at temperatures up to 350 °C, significantly higher than their plain metal counterparts, with reverse leakage current densities (at -3 V) of less than ~2 × 10<sup>-8</sup> Acm<sup>-2</sup>, the measuring limit of the Semiconductor Parameter Analyzer. At temperatures above 350 °C, measurable increases in reverse leakage current were observed, due to increasing thermionic emission over the respective Schottky barriers. However, the PtO<sub>x</sub>, IrO<sub>x</sub>, PdO<sub>x</sub>, RuO<sub>x</sub> SCs still showed rectification ratios of approximately 7, 6, 5, 4 orders of magnitude at an operating temperature of 500 °C. This remarkable high temperature SC performance is due to the thermal stability of these PGM oxides and their high work functions, that increase with increasing oxygen content resulting in effective Schottky barriers in excess of 2.0 eV at 500 °C. These results show that intentionally-oxidized PGM SCs to β-Ga<sub>2</sub>O<sub>3</sub> have significant potential for the fabrication of high temperature β-Ga<sub>2</sub>O<sub>3</sub> rectifying diodes, UV photodetectors, and metal-semiconductor field effect transistors.

## 12:30 PM CC09

**(Student) Effect of Contact Geometry on Forward Bias Failure in β-Ga<sub>2</sub>O<sub>3</sub> Schottky Rectifiers** Minghan Xian<sup>1</sup>, Chaker Fares<sup>1</sup>, Fan Ren<sup>1</sup>, Zahabul Islam<sup>2</sup>, Aman Haque<sup>2</sup>, Marko Tadjer<sup>3</sup> and Stephen J. Pearton<sup>1</sup>; <sup>1</sup>University of Florida, United States; <sup>2</sup>The Pennsylvania State University, United States; <sup>3</sup>U.S. Naval Research Laboratories, United States

β-Ga<sub>2</sub>O<sub>3</sub> has recently attracted a tremendous amount of attention due to its ultra-wide bandgap and potential application in the power electronics sector.

Compared to other commercially applicable wide bandgap materials, Ga<sub>2</sub>O<sub>3</sub> is notable due to its large theoretical breakdown field (8MV/cm), wide bandgap (4.6-4.9 eV), and ability to be bulk grown which allows for cheap manufacturing. Even in the early stages of Ga<sub>2</sub>O<sub>3</sub> material development, reported milestones for Schottky rectifiers include switching currents larger than 1 A in one study, absolute forward currents greater than 30 A in a different study, and devices holding a reverse breakdown voltage larger than 2.8 kV. Despite Ga<sub>2</sub>O<sub>3</sub>'s many advantages, its thermal conductivity is an order of magnitude lower than its GaN and SiC counterparts. Furthermore, large differences in anisotropic thermal conductivity have been reported along different crystallographic directions, namely 27 W/m-K in the [010] plane and 11W/m-K in [100] plane. In addition to empirical data, previous reports have utilized thermal imaging and modeling to visualize and predict this phenomenon. These challenges for Ga<sub>2</sub>O<sub>3</sub> require that proper thermal management must be utilized to develop devices able to operate while mitigating heating effects. In this work, we have investigated the impact of Schottky diode geometry and crystal orientation on the maximum achievable forward current before thermally induced failure. The fabrication sequence starts with 650 μm β-phase Sn-doped Ga<sub>2</sub>O<sub>3</sub> substrate with a 10 μm Si-doped epitaxial layer grown by Halide Vapor Epitaxy. Backside ohmic contact (Ti/Au) was deposited by electron beam (e-beam) evaporation and annealed for 30 s at 550°C in N<sub>2</sub> ambient. 40 nm Al<sub>2</sub>O<sub>3</sub> and 360 nm SiNx dielectric were deposited as field plated dielectric. Buffered Oxide Etchant (BOE) was used for wet etching to open dielectric windows of various geometries. Subsequently, the sample surface was treated in ozone for 20 minutes to remove hydrocarbon and other contaminants, followed with Ni/Au deposition using e-beam evaporation and standard solvent lift-off. For diode stress measurement, a pulse generator was used to apply continuous voltage bias at 95% duty cycle for 1 min at various voltage levels up to the point of device failure. After Schottky diodes of square and rectangular were fabricated along the [010] and [100] direction, the diodes were increasingly biased to determine which orientation could dissipate heat more effectively, which leads to a larger forward current before degradation in reverse breakdown. Plastic deformation on Schottky metal and epitaxial layer had also been observed. Diode with long side perpendicular to [010] direction was shown to be able to handle higher forward current before degradation, while square geometry and diode long side perpendicular to [100] direction fails at subsequently lower bias voltage. Diodes with optimized geometry are expected to provide 25% more forward current prior to the onset of diode failure, which shows greater resistance to thermal stress. This work has served as a fundamental investigation on the correlation between diode geometry/orientation and degree of thermally induced diode failure. Further optimization of diode design and homoepitaxial growth method is still needed to realize its theoretical capabilities.

## 12:45 PM CC10

**Electrical Behavior of Schottky Contacts to (100) β-Ga<sub>2</sub>O<sub>3</sub>** Luke A. Lyle<sup>1</sup>, Lisa Porter<sup>1</sup>, Kumar Das<sup>2</sup>, Zbigniew Galazka<sup>2</sup>, Andreas Popp<sup>3</sup>, Diamond Moody<sup>1</sup>, Kunyao Jiang<sup>1</sup>, Elizabeth Favela<sup>1</sup>, Tianxiang Lin<sup>1</sup> and Guenter Wagner<sup>2</sup>; <sup>1</sup>Carnegie Mellon University, United States; <sup>2</sup>North Carolina State University, United States; <sup>3</sup>Leibniz-Institut für Kristallzüchtung, Germany

Over the past decade beta-gallium oxide (β-Ga<sub>2</sub>O<sub>3</sub>) has accrued increased interest due to its ultrawide bandgap of ~4.8 eV, superior figure of merit for numerous electronic and optoelectronic applications, and the availability of single-crystal melt-grown substrates. Considering these factors, β-Ga<sub>2</sub>O<sub>3</sub> has been primarily pursued for applications as high-power electronics and UV photodetectors. In this study we report the electrical behavior of Au, Mo, Ni, Ti, Co, and Pd Schottky contacts on (100) Ga<sub>2</sub>O<sub>3</sub> substrates. The unintentionally-doped, n-type substrates were grown by the Czochralski method at the Leibniz-Institute for Crystal Growth (IKZ) in Berlin, Germany. Current-voltage (I-V) measurements of these diodes yield low ideality factors (n~1.0-1.3) for all metals and Schottky barrier heights ranging from 0.6 eV to 1.45 eV. Capacitance-voltage (C-V) measurements of these diodes reveal Schottky barriers heights ranging from 0.75 eV to 1.90 eV. I-V-T measurements conducted on Ti, Co, and Pd reveal inhomogeneous barriers that follow the model proposed by Werner et al. [1] and yield Schottky barrier heights of 0.73 eV, 1.24 eV, and 2.2 eV, respectively. Corresponding σ values of the proposed spatial Gaussian distribution of the barrier is obtained to be 0.092 eV, 0.72 eV, and 0.197 eV, respectively. The voltage dependence of the Schottky barrier was also examined. Taken together, the results indicate a strong dependence of the Schottky barrier height on metal workfunction: the slope S (also known as the index of interface behavior) was 0.96 and 0.61 for the C-V and I-V determined Schottky barrier heights, respectively. [1] Werner, J. and Guttler, H. "Barrier inhomogeneities at Schottky contacts". J. Appl. Phys., Vol. 69, No. 3, (1990).

#### 10:30 AM DD01

**(Student) Atomic Hydrogen Passivation for Marked Photoresponsivity Improvement of As-Doped n-BaSi<sub>2</sub> Films** Sho Aonuki<sup>1</sup>, Yudai Yamashita<sup>1</sup>, Takuma Sato<sup>1,2</sup>, Zhihao Xu<sup>1</sup>, Kaoru Toko<sup>1</sup>, Yoshikazu Terai<sup>3</sup>, Noritaka Usami<sup>4</sup> and Takashi Suemasu<sup>1</sup>; <sup>1</sup>University of Tsukuba, Japan; <sup>2</sup>Université Grenoble Alpes, France; <sup>3</sup>Kyushu Institute of Technology, Japan; <sup>4</sup>Nagoya University, Japan

Barium silicide (BaSi<sub>2</sub>) has been attracting considerable attention as a new candidate for thin-film solar cell applications. Its band gap is 1.3 eV, suitable for a single-junction solar cell. Furthermore, both a large absorption coefficient ( $3 \times 10^4 \text{ cm}^{-1}$  at 1.5 eV) and a large minority-carrier diffusion length ( $\sim 10 \mu\text{m}$ ) can be utilized in BaSi<sub>2</sub>. Very recently, we demonstrated the operation of a BaSi<sub>2</sub> homojunction solar cell for the first time<sup>[1]</sup>. We are now focusing on further improvement of BaSi<sub>2</sub> light-absorbing layers with fewer defects. According to the first-principles calculation<sup>[2]</sup>, Si vacancy ( $V_{\text{Si}}$ ) is most likely to occur in BaSi<sub>2</sub> films, generating defect levels within the band gap. Therefore, passivation of the Si dangling bonds in BaSi<sub>2</sub> films is very important for their use in solar cell applications. We have used the photoresponsivity as a measure to investigate the optical properties of BaSi<sub>2</sub> films, and obtained the highest photoresponsivity ever reported for undoped BaSi<sub>2</sub> films after supplying atomic hydrogen (H) for 15 min<sup>[3]</sup>. H atoms are considered to occupy  $V_{\text{Si}}$  and passivate point defects in BaSi<sub>2</sub>. The basic structure of a solar cell is a pn junction.

Therefore, it is important to make defects inactivated in impurities-doped BaSi<sub>2</sub> as a next step. In this study, we focus on the effect of atomic H supply on the photoresponsivity enhancement of As-doped n-BaSi<sub>2</sub> films. 500-nm-thick lightly As-doped BaSi<sub>2</sub> epitaxial films were formed on Si(111) substrates by molecular beam epitaxy (MBE). The electron concentration was around  $7 \times 10^{16} \text{ cm}^{-3}$  at room temperature. Next, H atoms were supplied to As-doped n-BaSi<sub>2</sub> films *in-situ* by an RF plasma gun with different supply durations  $t_{\text{BaSi}_2\text{H}} = 1 - 30$  min. Then, a 3-nm-thick a-Si capping layer was formed to prevent oxidation. Finally, 1-mm-diameter ITO electrodes with the thickness of 80 nm on the surface and Al electrodes with the thickness of 150 nm on the whole back side were formed by sputtering. The photoresponsivity increased for wavelengths shorter than approximately 1000 nm, corresponding to the band gap of BaSi<sub>2</sub>, showing that the photogenerated carriers in the BaSi<sub>2</sub> films contributed to the measured photoresponsivity. The photoresponsivity increased with  $t_{\text{BaSi}_2\text{H}}$  and reached a maximum of about 3.0 A/W for samples at  $t_{\text{BaSi}_2\text{H}} = 1, 10$  min under a bias voltage of  $-0.3$  V between top and bottom electrodes, which is 6 times higher than that of As-doped BaSi<sub>2</sub> films without H supply. This result demonstrated that the atomic H supply is a very effective means to passivate As-doped n-BaSi<sub>2</sub> films. At  $t_{\text{BaSi}_2\text{H}} \geq 15$  min, however, the photoresponsivity degraded significantly. In undoped BaSi<sub>2</sub> films, the optimum  $t_{\text{BaSi}_2\text{H}}$  was 15 min and the photoresponsivity decreased at  $t_{\text{BaSi}_2\text{H}} \geq 20$  min. We speculate that excess H atoms degrade the optical properties of BaSi<sub>2</sub> films, and that As occupied  $V_{\text{Si}}$  and inactivated them like H, leading to a shorter  $t_{\text{BaSi}_2\text{H}}$  for passivation than that of undoped BaSi<sub>2</sub>. To confirm the increase of carrier lifetime in As-doped n-BaSi<sub>2</sub> films by H passivation, we performed  $\mu$ -PCD measurements and measured  $\tau_{1/e}$ , which is the time when the reflected microwave intensity decreases by  $\exp(-1)$  of the initial value after the excitation laser was turned off.  $\tau_{1/e}$  was determined to be approximately 0.1, 0.8, 2.7, 1.0, 2.8, 1.6  $\mu\text{s}$  at  $t_{\text{BaSi}_2\text{H}} = 0, 1, 10, 15, 20,$  and 30 min, respectively. These results show that the carrier lifetime was surely improved by H passivation and saturated at  $t_{\text{H}} \geq 10$  min. On the basis of these results, we conclude that an atomic H supply is also beneficial for n-type BaSi<sub>2</sub> films.

[1] K. Kodama *et al.*, Appl. Phys. Express **12**, 041005 (2019).

[2] M. Kumar *et al.*, J. Mater. Chem. A **5**, 25293 (2017).

[3] Z. Xu *et al.*, Phys. Rev. Mater. **3**, 065403 (2019).

#### 10:45 AM DD02

**(Student) High Thermoelectric Figure of Merit via Tunable Valley Convergence Coupled Low Thermal Conductivity in A1B1VC2V Chalcopyrites** Madhubanti Mukherjee<sup>1</sup>, George Yumnam<sup>2</sup> and Abhishek Singh<sup>1</sup>; <sup>1</sup>Indian Institute of Science, India; <sup>2</sup>The University of Missouri, United States

Development of high performance thermoelectric materials requires a designing approach which will result into excellent electronic and poor phononic transport properties. Tetragonal chalcopyrites have recently attracted significant attention due to their complex and unusual electronic structures, which may influence the transport properties. The conflicting requirements of achieving simultaneously high Seebeck coefficient and high electrical conductivity are achieved in this class of materials, by tuning crystal and electronic structural parameters through isoelectronic substitution, which leads to unprecedented enhancement in electronic transport properties of A<sup>1</sup>B<sup>1</sup>C<sup>2</sup>V (group II = Be, Mg, Zn, and Cd; group IV = Si, Ge, and Sn; and group V = P and As). Multiple valleys in conduction bands, present in these

compounds, are tuned to converge by substitution of group IV dopant, which offer enhanced powerfactors for n-type carriers. Additionally, these substitutions improve the convergence of valence bands, which is found to have a direct correlation with the tetragonal distortion ( $\eta$ ) of these chalcopyrites. Complete convergence of the bands is achieved with  $\eta \approx 0.99$ , indicating a smaller distortion in the system. Enhanced p-type powerfactors are thus realized as a result of this band convergence, arising from smaller tetragonal distortion. Furthermore, several chalcopyrite compounds with heavy elements such as Zn, Cd, and As possess low phonon group velocities and large Grüneisen parameters that lead to low lattice thermal conductivities. Combination of optimized electronic transport properties and low thermal conductivity results in maximum ZT of 1.67 in CdGeAs<sub>2</sub> at moderate n-type doping. The approach developed here to enhance the thermoelectric efficiency does not involve doping, alloying, or any kind of structural engineering, thus can be realized readily and can be a useful strategy of designing new thermoelectric materials.

#### 11:00 AM DD03

**(Student) Strong Chemical Bond Hierarchy Leading to Exceptionally High Thermoelectric Figure of Merit in Oxychalcogenide AgBiTeO** Madhubanti Mukherjee and Abhishek Singh; Indian Institute of Science, India

The chemical bond hierarchy (CBH) in typical cage structures are considered as the key parameter for realizing high thermoelectric performance. Using first principles calculations and lattice dynamics, we demonstrate CBH hosted unique rattling motion in a non-caged oxychalcogenide AgBiTeO, causing ultralow lattice thermal conductivity of 0.9 W/m-K at room temperature. The CBH in this compound leads to a distinct structural bonding, wherein Ag and Te atoms are loosely bonded to the rigid framework of the lattice. These form distorted four-centered Ag-Te tetrahedra. These loosely bound clusters exhibit large amplitude atomic vibrational motions with a very shallow potential energy surface, leading to rattling motion. The rattling induced thermal damping is further confirmed by the presence of several avoided-crossing points of low lying optical phonon mode with longitudinal acoustic mode in the phonon dispersion. In addition to that, unique in-plane off phase collective vibrations of Ag-Te tetrahedra introduce localized flat phonon dispersions that lower the group velocity and significantly reduce the lattice thermal conductivity. Additionally, unique in-plane collective vibrations of Ag-Te tetrahedra provide localized flat phonon dispersions that lower the group velocity, hence, significantly reduce the  $\kappa_l$ . Most importantly, this phenomenon prevents carrier-phonon scattering, resulting into a high electrical conductivity in AgBiTeO. Combination of ultralow lattice thermal conductivity and exceptional electronic transport properties give an unprecedented range of ZT from 1.00 to 1.99 in a large temperature range of 700-1200K, for n-type charge carriers.

ACS Appl. Mater. Interfaces, 2020 (<https://doi.org/10.1021/acsmi.9b21358>)

#### 11:15 AM BREAK

#### 11:45 AM DD04

**Thermal Transport Measurements and Amorphization Studies in Sapphire Irradiated by Swift Heavy Ions** Vinay S. Chauhan<sup>1</sup>, Azat Abdullaev<sup>2</sup>, Zhandos Utegulov<sup>2</sup> and Marat Khafizov<sup>1</sup>; <sup>1</sup>The Ohio State University, United States; <sup>2</sup>Nazarbayev University, Kazakhstan

Sapphire ( $\alpha\text{-Al}_2\text{O}_3$ ) has been investigated as radiation-resistant material for fusion reactors, outer space exploration applications and as a substrate material in transistors and sensors. Ionizing radiation, when employed in a device in the radiation environment, can cause single event effects, total ionizing dose effect, displacement damage, and amorphization. The overall effect of these defects is degradation performance characteristics and catastrophic failure of the device. Thermal management of electronics is of the prime focus in packaging design. The fundamental action of thermal dissipation in the active region of electronic devices is of foremost importance, as the major part of the energy consumed appears as heat there. This heat generated, if not removed, leads to the creation of hot spots in the devices which have detrimental effects on device performance. Heat transfer is usually restricted due to intrinsic and extrinsic defects or due to thermal interfaces. On the other hand, there are devices especially thermoelectrics and heat sinks where heat flow in a preferential direction increases the effectiveness of the device. The heat flow in a specific direction is governed by the intrinsic or induced thermal transport anisotropy and this calls for the materials and methods where the heat transfer characteristics of the material can be tailored as per the needs.

The impact of accelerated particles causing displacement damage on structural and electronic properties have been extensively studied. Very few studies have considered the impact of the radiation damage on thermal conductivity primarily due to difficulty in measuring thermal conductivity in thin damaged layers limited to few hundreds of nanometers if the energy of the implanted particle is below 1 MeV. In this work, we have studied the thermal conductivity degradation and microstructure evolution of sapphire when irradiated by swift heavy ions (SHI).

We studied the thermal transport in a single crystal sapphire patterned by vertically aligned a few-nanometer diameter and several micrometer long cylindrical ion tracks. These ion tracks were introduced by exposing sapphire to energetic ions of xenon accelerated to 167 MeV with fluences ranging from  $10^{12}$  to  $10^{14}$  ions/cm<sup>2</sup>. We employed thermoreflectance techniques such as time-

domain thermoreflectance (TDTR) and modulated thermoreflectance (MTR) to measure the thermal conductivity of sapphire in cross- and in-plane directions. We observed the differences in the variation of conductivities in different directions and attribute it to the aligned nature of tracks that effectively reduce the mean free path of phonons traveling in-plane direction. The cross-plane conductivity reduction is owed to the anisotropic reduction of acoustic velocity caused by phonon confinement.

We further demonstrated the applicability of TDTR to resolve thermal transport behavior in SHI irradiated oxides having a nonhomogeneous damage profile on a nanometer scale and also in microstructure characterization. We measured the thickness of the amorphous layer in sapphire due to SHI and compared it with the TEM results. The thickness measurement results were found to be in good agreement. We modeled the experimental results using the classical thermal transport model to understand the impact of ion-tracks on thermal transport. The presented approach facilitates future studies aiming at resolving the impact of distinct damage resulting from electronic and nuclear stopping regimes under irradiation. We have successfully shown in this work that the SHI irradiation is an effective avenue to tailor anisotropic thermal conductivity of insulating materials and enables studies of nanoscale thermal transport.

#### 12:00 PM DD05

**(Student) Experimental Techniques to Measure Thermal Hall Effect** Dung D. Vu and Joseph P. Heremans; The Ohio State University, United States

As the thermal analog of the Hall effect, the thermal Hall effect (THE) measures the resultant transverse thermal gradient when a longitudinal thermal gradient is applied along a sample in an orthogonal magnetic field. Since electrons, phonons, and magnons all carry entropy, their currents transport heat, and they do so both in the sample being measured and in the instrumentation used to execute the measurements. Therefore, the THE is not only extremely challenging to measure, but challenging to interpret, as the data contain contributions from all sources. For example, it is difficult to isolate the contributions of dissipationless edge-state electron currents in topological materials and the anisotropy in both phonon and magnon currents from all the other, more trivial, effects in the samples. In this talk, we introduce the experimental techniques to measure the THE and the characteristics of a THE signal that is intrinsic to a given sample. The common problems encountered while conducting THE experiment and the methods to verify the validity of experimental data also will be discussed in detail.

#### 12:15 PM DD06

**Optimizing Top-Side Device Cooling via Metal/Nanocrystalline Diamond Interfaces** Henry Aller<sup>1</sup>, Nick Golio<sup>1</sup>, Karl Hobart<sup>2</sup>, Tatyana Feygelson<sup>2</sup>, Alan McGaughey<sup>1</sup>, Andrew Gellman<sup>1</sup> and Jonathan A. Malen<sup>1</sup>; <sup>1</sup>Carnegie Mellon University, United States; <sup>2</sup>U.S. Naval Research Laboratory, United States

Top-side device cooling methods, e.g., diamond heat sinks on top of the metal contacts, facilitate heat removal from hot spots near the gate, directly lowering local and global temperature rises. Because the top-side surface of modern devices is often complex and rarely flat, conformal nanocrystalline diamond (NCD) growth techniques are critical to maximize the contact area between the device and the heat sink. The effectiveness of these heat sinks strongly depends on the thermal boundary conductance of the metal/NCD interface. In this study, we seek to optimize thermal transport across Au/Cr/Pd/NCD substrate stacks. Cr was chosen for its thermal merits. Excellent adhesive properties and high maximum phonon frequencies has enabled Cr to produce some of the largest thermal boundary conductance interfaces for materials like Diamond, Al<sub>2</sub>O<sub>3</sub>, and AlN. Despite this, Cr is predicted to react with NCD to form enthalpically favorable carbides, which will lower the thermal boundary conductance. We hypothesize that a thin non-reactive Pd layer can eliminate these reactions and preserve the metal/NCD thermal boundary conductance in heated conditions. Pd and then Cr layers are deposited as perpendicular wedges with thickness of 0 to 20 nm on a single NCD sample, allowing us to test all thickness combinations of Pd and Cr. The thermal boundary conductance is measured using a non-destructive pump-probe optical technique, frequency domain thermoreflectance (FDTR). By scanning the FDTR across the sample surface, a 2D map of thermal boundary conductance is created for all Pd/Cr thickness combinations. A local maximum in thermal boundary conductance is observed for a specific Cr/Pd thickness combination, providing evidence that our hypothesis is correct. The sample was then annealed and remeasured multiple times. Changes in the 2D thermal boundary conductance map are used to quantify the ability for thin Pd layers to improve the thermal stability of metal contacts throughout a device's lifetime.

#### 12:30 PM DD07

**(Student) In Operando Investigation of GaN PIN Device Characteristics under Electron Irradiation Energies Comparable to Pm-147 Source for Betavoltaic Application** Kasey Hogan, Miguel Rodriguez, Emma Rocco, Vincent E. Meyers, Benjamin McEwen and Fatemeh (Shadi) Shahedipour-Sandvik; Colleges of Nanoscale Science and Engineering, SUNY Polytechnic Institute, United States

Betavoltaic (BV) micro-batteries have characteristically high energy density, relatively low mass and long lifetime. The (Al)GaN material system in particular shows promise for use in a BV configuration due to its desirable properties including wide and tunable bandgap, radiation hardness, chemical

inertness, and physical hardness. Current state-of-the-art GaN based devices suffer from low conversion efficiency (<1%) and limited output power as a result of limited minority carrier diffusion length within the material and availability of low energy beta sources, respectively. To improve device performance, it is necessary to both optimize the device design for a higher collection efficiency of generated electron-hole-pairs (EHPs) that also employs higher surface area, as well as selection of appropriate higher energy emitting sources such as Pm-147 (62 kV avg. energy).

Here we report on application of an electron source with high accelerating voltage (62-200 kV) and development of *in-situ* electrical characterization capability in order to enable detailed study of new device designs and performance comparison against conventional device configurations. Specifically, *in-operando* investigation of a GaN PIN device using a modified transmission electron microscope (TEM) electron flood technique is being reported here for the first time, to the best of the author's knowledge. A large-area planar GaN PIN (0.04 cm<sup>2</sup>, 17.8 nA/cm<sup>2</sup> at -5 V) was irradiated with an electron beam of approximately equivalent area. A parametric study of electron beam accelerating voltage and input beam current was performed. In order to tune the input beam current to the device surface, control of the source emission current, choice of selective area apertures, and condenser lens configuration were made. At an approximate input current density of 5 nA/cm<sup>2</sup>, the maximum power produced (MPP) decreases from 2.45 μW/cm<sup>2</sup> to 0.45 μW/cm<sup>2</sup> when increasing the beam voltage from 62 kV to 200 kV. This reduction in power corresponds to reduced EHP generation/capture within the active regions of the device. The reduction in power observed, as the beam voltage is increased, is modeled by CASINO2 Monte Carlo simulations. At 62 kV beam voltage, the MPP is shown to increase with increased beam current (up to 48.2 μW/cm<sup>2</sup> at 177 nA/cm<sup>2</sup>), where no observable degradation of the device occurs at any input beam current, confirmed by repeated device dark current measurements following the irradiations. Results of the time-dependent irradiation will be presented along with a detailed discussion on the electron beam parameter settings.

#### 12:45 PM DD08

**The Al-Si Eutectic as a Phase Change Material for Storing Intermittent Solar Power** Jerry M. Woodall; University of California, Davis, United States

Using the average 1 kW/m<sup>2</sup> of terrestrial solar irradiance as source of global scale alternative power on earth is a very compelling way to reduce the planet's dependence on fossil sources to meet the 10<sup>17</sup> watt hours of energy annually consumed on earth. However, this power density is not available 24/7 at the same geographical location. Currently, this limitation is being partially mitigated via utility company buy-back of customer generated solar electricity. However, it is patently obvious that if, for example, all PG&E customers in California produced solar cell power during the day and the government required PG&E to buy it back, even at a discounted rate, this power distribution system would be unsustainable.

This presentation will describe our experimental data using the Al-Si eutectic alloy as an economically and technically viable phase change material (PCM) that could be used to store solar irradiance and thus enable a 24/7 global scale solar energy economy. The composition of Al-Si eutectic is 12.4% Si with a melting point of 577 C, and a heat of fusion of 154 watt-hours/kg of alloy. To simulate solar melting during daytime and nighttime loads, we used 400-minute melting and freezing cycles by varying the temperature of a furnace to cause melting and freezing. Our experimental results showed a constant alloy temperature of 577 ± 2 C over a 24-hour period with no degradation of the alloy. Thus, we believe we have developed a possible global scale storage technology that will enable intermittent solar power to provide 24/7 terrestrial power.

SESSION EE: Hexagonal Boron Nitride and Graphene

Session Chair: Isaac Ruiz

Session Hosts: Huili Grace Xing and Hongping Zhao

Friday Morning, June 26, 2020

Location: ZoomRoom 3

#### 10:00 AM EE01

**(Student) Analysis of the Effect of Surface Charge Transfer Doping on Charge Transport of WSe<sub>2</sub>** Jae-Keun Kim<sup>1</sup>, Kyungjune Cho<sup>1,2</sup>, Youngrok Kim<sup>1</sup>, Junseok Seo<sup>1</sup>, Jiwon Shin<sup>1</sup>, Jaeyoung Kim<sup>1</sup>, Keehoon Kang<sup>1</sup> and Takhee Lee<sup>1</sup>; <sup>1</sup>Seoul National University, Korea (the Republic of); <sup>2</sup>Max Planck Institute of Microstructure Physics, Germany

Transition metal dichalcogenides (TMDCs) has attracted remarkable attention as a promising semiconductor of next generation nanoelectronics because of unique properties such as atomically flat nature, tunable band gap depending on their thickness. Due to their large surface area to volume ratio, these materials are sensitive to environmental conditions. This property makes surface charge transfer doping an effective method to control the carrier density of TMDCs [1]. However, there have been only a few studies which have shown the effect of surface charge transfer doping on charge transport properties of TMDCs. Here, we report the effect of surface charge transfer doping on charge transport properties of tungsten diselenide (WSe<sub>2</sub>) by using various p-type molecular dopants, 2,3,5,6-tetrafluoro-7,7,8,8-tetracyanoquinodimethane (F<sub>4</sub>-TCNQ),

molybdenum tris(1,2-bis(trifluoromethyl)ethane-1,2-dithiolene) (Mo(tfd)), and magic blue. These strong molecular acceptors have different electron affinities, and thus the doping strengths between the dopants vary significantly, which we characterized with WSe<sub>2</sub> field-effect transistors (FETs). We also measured 4-point probe FET mobility to investigate the doping effect on the intrinsic charge transport of WSe<sub>2</sub>. This study can help developing suitable molecular dopants for controlling electrical properties in TMDC devices by understanding dopant-induced effects on charge transport.

References 1. K. Cho et al, ACS Nano, 13, 9713 (2019).

#### 10:15 AM EE02

**(Student) Modulating hBN and Other 2D Materials with the Vanadium Dioxide Phase Transition** Samuel T. White<sup>1</sup>, Thomas G. Folland<sup>1</sup>, Alireza Fali<sup>2</sup>, Yohannes Abate<sup>2</sup>, Joshua Caldwell<sup>1</sup> and Richard F. Haglund<sup>1</sup>; <sup>1</sup>Vanderbilt University, United States; <sup>2</sup>University of Georgia, United States

Two-dimensional materials, with their flexibility, transparency, and range of electrical properties (spanning conductors, semiconductors, and insulators), hold great promise for electrical and optical applications. Highly sensitive to the surrounding environment due to their extreme thinness, and transferrable onto arbitrary substrates due to their Van der Waal's nature, they are excellent building blocks for heterostructure stacks. By incorporating a phase-change material (PCM) as a substrate, switchable or reconfigurable behavior can be added to make functional devices. Vanadium dioxide (VO<sub>2</sub>) is a representative, widely-studied PCM with excellent properties. It undergoes an insulator-to-metal transition at the easily-accessible temperature of ~68°C, accompanied by an orders-of-magnitude change in resistivity and large changes in optical constants. This transition can also be stimulated optically on a femtosecond timescale. VO<sub>2</sub> is a strongly-correlated material, and its properties near the phase transition are strongly sensitive to many factors, notably temperature, doping, and strain. We have advanced the growth and processing of VO<sub>2</sub>, and explore its use as an active substrate for hexagonal boron nitride (hBN) and other 2D materials.

First, we systematically investigate the effect of substrate on phonon polaritons (PhPs) in hBN. The PhP modes in hBN, sustained in its upper and lower Reststrahlen bands (~1365-1610 cm<sup>-1</sup> and ~760-820 cm<sup>-1</sup>, respectively), are hyperbolic, allowing for strong wavelength compression and the possibility of hyperlensing. These modes extend outside the hBN far enough to interact with the local dielectric environment, yet are sufficiently contained within the material to minimize loss when the surrounding material is absorbing, as in the case of VO<sub>2</sub>. We use isotopically pure hBN, in which the PhPs are extremely long-lived. We employ scattering scanning near-field optical microscopy (s-SNOM) and nano-FTIR spectroscopy to measure the dispersion of PhPs in hBN atop a variety of substrates. The wavelength and propagation figure of merit can be tuned via the complex dielectric function of the substrate, and these results match well with theoretical calculations. Furthermore, higher-order modes show a smaller relative change in wavevector, suggesting a possible scheme for refractively separating different-order modes.

Based on these behaviors, we demonstrate a reconfigurable hyperbolic metasurface consisting of multilayer hBN on single crystals of VO<sub>2</sub>. As strained single crystals of VO<sub>2</sub> are heated through the phase transition, the metallic phase nucleates at defect sites and grows as temperature increases, leading to spatially distinct metallic and insulating domains with sharp boundaries. As PhPs in hBN propagate across the insulator-metal domain boundaries, the change in substrate dielectric function causes a ~1.6X decrease in PhP wavelength. Despite the increased loss, the PhPs retain a long propagation length. The wavelength change leads to refraction of the PhPs in accordance with a generalized form of Snell's Law, in addition to reflection, at the domain boundaries. By patterning the metal-insulator domains of the PCM substrate, it would be possible to design reconfigurable planar optics—such as in-plane lenses or waveguides—which could be erased and re-written by cycling the phase transition. We present simulations demonstrating some such devices. Though patterning metallic domains in VO<sub>2</sub> is still a challenge, the location and pattern of metallic domains can be influenced by strain, local heating, or area selective doping.

Going forward, we will investigate the use of VO<sub>2</sub> single crystal substrates to modulate other 2D material properties, such as photoluminescence in the transition metal dichalcogenide WSe<sub>2</sub>, and ways to incorporate other forms of VO<sub>2</sub>, such as nanoparticle arrays, into 2D material heterostructures.

#### 10:30 AM EE03

**Engineering Ni Substrate toward High Quality Two-Dimensional Hexagonal Boron Nitride Films for Metal-Insulator-Metal Devices** Yanwei He, Zhenjun Cui, Hao Tian, Ivan Chiang, Wenhao Shi, Long Xu, Yuan Li and Jianlin Liu; University of California, Riverside, United States

Two-dimensional hexagonal boron nitride (h-BN) plays a significant role in nanoscale electrical and optical devices because of its superior properties. However, the difficulties in the controllable growth of high-quality films have limited its application and performance. One of the crucial factors that influences the quality of h-BN films obtained via molecular beam epitaxy is the metal substrate property. Here we report our comprehensive study of h-BN growth on poly- and single- crystalline Ni(100) and Ni(111) substrates with and without carburization treatment. We demonstrated that Ni(100) with carburization is a better substrate for h-BN growth considering the growth speed and coverage. While the carburization is essential to h-BN growth on

Ni(100), it adversely affects the growth on Ni(111). Nevertheless, the pristine Ni(111) substrate can be a good candidate for single-crystalline h-BN film growth as the epitaxial flakes on top are well aligned. As-grown continuous single-layer h-BN films achieved on Ni(100) substrates were used to fabricate Ni/h-BN/Ni metal-insulator-metal (MIM) devices. Direct tunneling, dielectric breakdown, and recovery of MIM devices were studied. The MIM devices fabricated can sustain repeated DC voltage sweeping stresses up to 85 times under a high compliance current of 100 mA, and the critical electric field is determined to be around 11.8 MV/cm.

#### 10:45 AM EE04

**(Student) High Temperature Annealing of BN Films Grown from Borazine** Jeffrey Kronz, Joan M. Redwing and David Snyder; The Pennsylvania State University, United States

Hexagonal boron nitride (hBN) is a wide bandgap layered material that has garnered much attention in the 2D scientific community due to its atomic flatness and use as an encapsulating dielectric layer for graphene and the transition metal dichalcogenides (TMDs) such as MoS<sub>2</sub> and WSe<sub>2</sub>. In addition, there is interest to use hBN as a substrate for vapor phase growth of TMDs, however, this requires large area, high crystal quality hBN beyond that achievable with exfoliation.

BN films are traditionally grown by chemical vapor deposition (CVD) on transition metal or insulating substrates such as sapphire by a direct deposition from vapor phase sources. An alternative approach employs a two-step process whereby a borazine film is initially deposited at low temperature (400 °C) on a substrate followed by high temperature annealing to crystallize the layer. Sapphire and silicon are both desirable substrate choices due to their integration into current manufacturing processes. However, sapphire also has the benefit of high melting temperature allowing for higher temperature anneals and matching crystal structure so it has been selected as the substrate for growth in this work. Borazine follows a direct reaction path to form a BN film through a dehydrogenation restructuring once deposited. The initial restructuring is seen as a polymerization that results in an amorphous network of B-N hexagon rings linked as chains with hydrogen terminations. These hydrogens are then removed and the chains all align and connect to form the BN film. This reaction is initiated as the film is heated and has several well-studied dehydrogenation regimes that ultimately yield the hBN film. However, this process ends at 1100 °C and typically yields an amorphous or turbostratic BN (tBN) film. Further investigations of the phase diagram of BN reveal that hBN is not the thermodynamically stable phase until temperatures exceeding 1300 °C. This suggests that while the borazine films may finish the dehydrogenation reactions by 1100 °C, the hBN left still requires additional thermal energy to fully reorder and crystallize as hBN.

In this study, the effects of annealing temperature, time and pressure on borazine conversion to BN were investigated. Borazine is generated by sublimation of ammonia borane at 130 °C after which it is deposited at 400 °C under 100 Torr of a N<sub>2</sub>/H<sub>2</sub> (85%/15%) mixture. Annealing was first carried out from 1200 °C and 1600 °C in a high vacuum environment of 5x10<sup>-5</sup> Torr. These films were found to be completely evaporated, and preliminary thermodynamic calculations indicated that hBN could destabilize at these low pressures and high temperatures. To confirm, the anneals were repeated in 700 Torr of N<sub>2</sub>. The borazine films annealed at this pressure with temperatures up to 1600 °C were still intact. Raman spectroscopy demonstrated that the hBN E<sub>2g</sub> mode at 1367 cm<sup>-1</sup> increased in intensity and decreased in full-width half maximum (FWHM) at 1600 °C compared to the films annealed at 1000 °C and 1100 °C. However, there was still material loss from both the film and substrate, suggesting that annealing the borazine films at 1600 °C without fully completing the dehydrogenation process at 1100 °C will cause the residual hydrogen in the film to react and etch both the BN film and sapphire substrate underneath. Scanning electron microscopy (SEM) images revealed this etching as hexagonal pits in the sapphire substrate which were found only where the film was present on the sapphire substrate and not on bare sapphire that was annealed at the same time. This further supports that the residual hydrogen in the borazine films is reacting to cause this etching and should be addressed prior to annealing above 1100 °C.

#### 11:00 AM EE05

**(Student) Impact of Sapphire Surface on High-Temperature CVD Growth of Crystalline Hexagonal Boron Nitride** Anushka Bansal, Maria Hilse, Roman Engel-Herbert and Joan M. Redwing; The Pennsylvania State University, United States

Hexagonal Boron Nitride (hBN) is a 2D, III-nitride wide bandgap semiconductor that has a structure very similar to graphene. Due to its extraordinary physical properties, such as high resistivity, high thermal conductivity, stability in the air up to 1000°C and large bandgap (E<sub>g</sub> ~ 5.9 eV), hBN appears to be a promising material for emerging applications, including deep UV (DUV) optoelectronics, single-photon emitters, and neutron detectors. There is also significant interest in monolayer and few-layer hBN as an encapsulating layer for 2D devices based on graphene and transition metal dichalcogenides. While high-quality hBN bulk crystals are available for exfoliation, the size of the crystals is limited, consequently, there is continued interest in the epitaxial growth of large-area hBN films using chemical vapor deposition (CVD). However, high-quality hBN film growth typically requires high growth temperatures (1100°C-1500°C). It has been reported that this temperature range alters the sapphire surface under ultra-high vacuum (UHV)

conditions. In the case of chemical vapor deposition (CVD), the presence of hydrogen in the growth ambient is expected to also modify the sapphire surface. However, its impact on hBN growth has not yet been explored. In this work, we studied the growth of crystalline and epitaxial hBN in a vertical cold wall MOCVD reactor using diborane ( $B_2H_6$ ) and ammonia ( $NH_3$ ) as precursors for B and N, respectively using  $H_2$  as a carrier gas. The growths were performed on c-plane sapphire substrates at a growth temperature of  $1350^\circ C$  under a pressure of 50 Torr.  $B_2H_6$  reacts with  $NH_3$  at temperatures as low as room temperature to form  $H_3N-BH_3$  and other volatile B-N species, consequently, gas-phase chemistry plays an important role in this deposition process. Therefore, the influence of the precursor flow method (pulsed versus continuous) on the deposition rate were studied in order to understand the extent of gas-phase chemistry/ parasitic reactions. Stoichiometric hBN films were obtained on sapphire using N/B ratio of  $\sim 7500$  under continuous precursor flow giving a growth rate of  $\sim 12$  nm/hr. However, the sequential pulsing of the  $B_2H_6$  (2 sec) and  $NH_3$  (1 sec) precursors using the same N/B ratio resulted in a significant increase in the growth rate ( $\sim 300$  nm/hr) due to reduction in the extent of parasitic reactions. Using the pulsed mode of growth, continuous thin films of hBN were obtained along with wrinkles due to thermal expansion coefficient (CTE) difference between sapphire and hBN. The  $E_{2g}$  Raman active mode of hBN was observed at  $1368.8$   $cm^{-1}$  with a FWHM of  $27.6$   $cm^{-1}$ . Also, pre-growth  $H_2$  annealing of sapphire at the growth temperature alters the surface lattice parameter as confirmed by RHEED and is believed to induce a chemical change as well. RHEED pattern of the obtained hBN film suggests rotationally oriented, crystalline hBN film with  $[11-20]_{hBN} \parallel [1-100]_{sapphire}$  epitaxial relation. In order to further understand the impact of surface preparation on the growth of hBN, pre-nitridation of the substrate was introduced pre-growth after  $H_2$  annealing to convert top layers into AlN. The  $E_{2g}$  mode FWHM reduced from  $27.6$   $cm^{-1}$  to  $21.1$   $cm^{-1}$  after surface nitridation for 90 sec. The results indicate that the pre-nitridation of the sapphire surface may help in converting top layers into crystalline AlN to provide a better surface for BN growth. In summary, we report continuous, rotationally oriented, crystalline h-BN films obtained using CVD with  $E_{2g}$  FWHM of  $21.1$   $cm^{-1}$  (previous reports:  $20$   $cm^{-1}$  -  $35$   $cm^{-1}$ ). Further studies are underway to provide additional insights into the role of gas-phase chemistry and surface preparation on the properties of highly crystalline hBN films on sapphire.

#### 11:15 AM BREAK

#### 11:45 AM EE06

**Precision Defect Engineering of Graphene for Applications Using Electron-Beam Chemistry with Radiolyzed Water** Michael A. Susner<sup>1</sup>, Ahmad E. Islam<sup>2</sup>, Jennifer Carpena-Nunez<sup>1</sup>, Rahul S. Rao<sup>1</sup>, Tyson Back<sup>3</sup>, Jie Jiang<sup>4</sup>, Ruth Pachter<sup>5</sup> and Benji Maruyama<sup>2</sup>; <sup>1</sup>UES, Inc., United States; <sup>2</sup>KBR, Inc., United States; <sup>3</sup>AFRL/RXAN, United States; <sup>4</sup>AFRL/RXAP, United States; <sup>5</sup>Air Force Research Laboratory, United States

Defect engineering of graphene is attractive for a wide range of applications. Here, we present a mask-less, resist-free, and fully reversible process to engineer defects in graphene using electron-beam (e-beam) chemistry with radiolyzed water. The process was performed inside a variable pressure scanning electron microscope by generating radiolysis products using reactions between the e-beam and water vapor, which in turn reacted with the graphene at the location of the probe. These reactions enabled controlled chemistry on the graphene surface at a resolution of  $\sim 60$  nm and hence created defects in precise locations defined by the e-beam. Detailed characterization and theoretical analyses suggested the presence of  $sp^3$ -type defects, the density of which was tuned by varying the e-beam dose. In addition, these  $sp^3$ -type defects were cycled in and out of graphene by alternating e-beam chemistry and thermal annealing. This reversibility promises future applications of e-beam chemistry in reconfigurable plasmonics and electronics.

#### 12:00 PM EE07

**(Student) An Efficient Electronic Structure Framework for Representing Moiré Patterns in Twisted Bilayer Graphene** Tawfiqur Rakib<sup>1</sup>, Elif Ertekin<sup>1</sup>, Pascal Pochet<sup>2</sup> and Harley Johnson<sup>1,3</sup>; <sup>1</sup>University of Illinois at Urbana-Champaign, United States; <sup>2</sup>Univ. Grenoble-Alpes and CEA, France

Electronic structure theory reveals the possibility of tuning exotic properties such as magnetism and superconductivity in bilayer graphene (BLG) by controlling misalignment between layers. This misalignment between layers results in moiré patterns that reflect the superstructure within the bilayers. Low twist angle moiré patterns in particular, which have long wavelengths, have shown remarkable electronic properties, but these patterns are computationally very costly to study. One recently proposed method provides a qualitative description of electronic contributions to moiré patterns. [1] But to better understand twisted bilayer graphene (tBLG) electronic structure, one needs a more physically motivated model for the charge density. Here, we present a framework that allows us to study the electronic structure of tBLG moiré patterns in a computationally efficient way, relying on density functional theory (DFT) calculations of larger angle tBLG. We use these results, with local weighting derived from the mechanics of the interlayer structure, to train a procedure that creates charge densities and related properties of lower angle tBLG. This procedure allows us to simulate charge density distributions in tBLG at a reasonable computational cost. With this method, we can generate a better description of scanning tunneling microscopy (STM) results for tBLG,

allowing us to study the connection between electronic structure and moiré patterns in small twist-angle tBLG.

[1] "Toward Moiré engineering in 2D materials via dislocation theory"; P Pochet, BC McGuigan, J Coraux, and HT Johnson; Applied Materials Today 9, 240-250 (2017)

#### 12:15 PM EE08

**Ballistic Graphene—A High Strain Piezoresistive Material** Abhinaba Sinha, Abhishek Sharma, Ashwin Tulapurkar, V Ramgopal Rao and Bhaskaran Muralidharan; Indian Institute of Technology Bombay, India

Graphene is known as a wonder material due to its unique properties [1]. Owing to its exceptional electro-mechanical properties, graphene is seen as a promising material for straintronics. A deeper understanding of ballistic transport in graphene will be necessary for miniaturized electro-mechanical systems. In this paper, we investigate the piezoresistance of ballistic graphene for potential applications in nano-electro-mechanical systems and flexible electronics. We develop a generalized model to compute the piezoresistance effect in ballistic graphene using a parametrized tight-binding Hamiltonian coupled with the Landauer quantum transport formalism [2]. Using our developed computational framework, we evaluate the longitudinal, transverse and angular gauge factors of ballistic graphene along armchair and zigzag directions. We predict a significant enhancement ( $\sim 1000\%$ ) in the value of transverse gauge factor compared to longitudinal gauge factor. This anomalous variation in gauge factor is rationalized by deformation of Dirac cones and change in separation between transverse modes due to strain. We also evaluate the angular piezoresistance with respect to the direction of electron transport and strain. The value of angular gauge factor oscillates between the longitudinal gauge factor and transverse gauge factor. The angular gauge factor plot has a periodicity of 180 degree due to two fold symmetry of the strained Dirac cones. The angular gauge factor vanishes at  $\theta=20$  degree. Besides, the piezoresistance behaviour along armchair and zigzag directions are identical due to similar deformation of Dirac cones for same strain. The results obtained in this paper could be useful for future straintronics and flexible electronics devices.

#### References:

1. A. K. Geim, Science 324, 1530 (2009). 2. A. Sinha, A. Sharma, A. Tulapurkar, V.R. Rao, & B. Muralidharan Piezoresistance in ballistic graphene, Physical Review Materials, 3(12), 124005 (2019).

#### 12:30 PM EE09

**Self-Assembled Ferroelectric Heterostructures in a van der Waals Gapped Metal Thiophosphate** Michael A. Susner; UES, Inc., United States

Single crystals of the van der Waals layered ferroelectric material  $CuInP_2S_6$ , when synthesized with Cu deficiency, spontaneously phase separate into paraelectric  $In_{4-x}P_2S_6$  domains embedded within a ferroelectric  $CuInP_2S_6$  matrix. The interfacial strain between these two chemical domains within the single crystal increases the Curie Temperature ( $T_c$ ) of the ferroelectric phase. Here we identify a route to form and tune these intralayer heterostructures between these phases through control of chemical phase separation. We conclusively demonstrate that Cu-deficient  $Cu_{1-x}In_{1+x}P_2S_6$  forms a single phase at high temperature. We also identify the mechanism by which the phase separation proceeds upon cooling. Above 500 K both  $Cu^+$  and  $In^{3+}$  become mobile, while  $P_2S_6^{4-}$  anions maintain their structure. We therefore propose that this transition can be understood as eutectic melting on the cation sublattice. Such a model suggests that the transition temperature for the melting process is relatively low because it requires only a partial reorganization of the crystal lattice. As a result, varying the cooling rate through the phase transition controls the lateral extent of chemical domains over several decades in size. At the fastest cooling rate, the dimensional confinement of the ferroelectric  $CuInP_2S_6$  phase to nanoscale dimensions suppresses ferroelectric ordering due to the intrinsic ferroelectric size effect. Intralayer heterostructures can be formed, destroyed, and re-formed by thermal cycling, thus enabling the possibility of finely tuned ferro structures that can potentially be optimized for specific device architectures.

#### 12:45 PM EE10

**(Student) Realizing Atomically Thin Group-III Metal and Nitride Alloys via Confinement Heteroepitaxy** Siavash Rajabpour<sup>1</sup>, Natalie Briggs<sup>1</sup>, Hesham Elsharif<sup>1</sup>, Yanfu Lu<sup>1</sup>, Stephen W. Holovick<sup>1</sup>, Timothy Bowen<sup>1</sup>, Alexander Vera<sup>1</sup>, Susan B. Sinnott<sup>2</sup>, Nabil D. Bassim<sup>2</sup>, Adri van Duin<sup>1</sup> and Joshua A. Robinson<sup>1</sup>; <sup>1</sup>The Pennsylvania State University, United States; <sup>2</sup>McMaster University, Canada

Confinement heteroepitaxy (CHet)<sup>1,2</sup> exploits the epitaxial graphene (EG)/SiC interface as a platform to realize 2D allotropes of traditionally 3D materials that could have significant technological impacts on next generation technologies such as topological quantum computing, sensing and high frequency electronics. Atomically thin, air stable metals, metal-alloys, oxides, and nitrides have been realized by CHet. Unique properties, such as non-centrosymmetric bonding, novel atomic structures, enhanced superconductivity, extreme optical properties, and long-term stability make such systems highly attractive for device applications.

In this talk, we will discuss atomically thin  $In_xGa_{1-x}$  metal and nitride alloys and how quantization impacts physical, electronic, and optical properties. CHet is a thermal vaporization process in which plasma-treated EG/SiC are placed over

elemental(s) precursors and heated in a low vacuum argon atmosphere in a tube furnace from 600–1100°C. X-ray photoelectron spectroscopy (XPS) and Auger electron spectroscopy (AES) suggest the presence of intercalant layers at the EG/SiC interface and indicates that the alloy composition can be controlled by precursor ratios. Cross-sectional scanning transmission electron microscopy (STEM) allows for direct imaging of the graphene/intercalant/SiC heterostructures. STEM images alongside with Electron energy loss spectroscopy (EELS) and Auger electron spectroscopy (AES) mapping depicts uniform dispersity of gallium/indium alloys. Furthermore, impacts of nitridation on structural, electronic and optical properties of  $\text{In}_x\text{Ga}_{1-x}$  alloys will be discussed. Tunability of  $\text{In}_x\text{Ga}_{1-x}$  composition and the atomic thickness of 2D nitrides leading to tunable band gaps with higher energies compared to bulk and can be used in electronic and optical applications such as a tunnel barrier for hot electron transistors.

1. <http://arxiv.org/abs/1905.09962> 2. *Nanoscale*, 11 (33) (2019) 15440–15447

SESSION FF: Thin Film Devices  
Session Chair: Emmanouil Kioupakis  
Session Hosts: Vincent Meyers and Emma Rocco  
Friday Morning, June 26, 2020  
Location: ZoomRoom 4

#### 10:00 AM FF01

**(Student) Investigation of Ambipolar Avalanche Breakdown in WSe<sub>2</sub> Field-Effect Transistors** Jaeyoung Kim, Jinsu Pak, Kyungjune Cho, Jae-Keun Kim, Jiwon Shin, Woocheol Lee, Keehoon Kang and Takhee Lee; Seoul National University, Korea (the Republic of)

Transition metal dichalcogenides (TMDCs) are promising candidates as post-silicon semiconductor materials in nanoscale electronic devices due to their good electric properties as well as thickness-dependent tunable band gap and facile device fabrication. As electronic devices are scaled down to sub-micrometer sizes, the active layers of these two-dimensional (2D) semiconductor materials experience high electric field upon operation, resulting in electrical breakdown. Hence understanding the behaviors of 2D semiconducting materials under high voltage bias is important for their reliable device application. Although the avalanche breakdown effect has been studied extensively in 3D semiconductors, only recently there has been reports on the avalanche breakdown in atomically thin TMDC materials. Extending from our previous report on avalanche breakdown in n-type MoS<sub>2</sub> [1], we explored and compared hole and electron avalanche breakdown effects in a single device, using an ambipolar semiconducting material, tungsten diselenide (WSe<sub>2</sub>). The critical electric field for both carriers followed the known power dependence to the band gap energy. We also conducted measurements on the impact ionization rate, and observed its relationship to the applied lateral electric field. Some factors unique to WSe<sub>2</sub>, such as its structure and defects that may influence the impact ionization parameters are discussed. Our study will help understanding of the electron and hole avalanche multiplication phenomena of 2D TMDC semiconductors.

**References** [1] Jinsu Pak et al., *ACS Nano*, **12**, 7109 (2018).

SESSION GG: Oxides Materials and Devices  
Session Chair: Emmanouil Kioupakis  
Session Hosts: Vincent Meyers and Emma Rocco  
Friday Morning, June 26, 2020  
Location: ZoomRoom 4

#### 10:15 AM GG01

**(Student) Nanoscale Thickness-Dependent Doping of Indium Tin Oxide (ITO) Quantum Magnetoconductivity Films** Jade Cowsky<sup>1</sup>, Daram N. Ramdin<sup>1</sup>, Hantian Gao<sup>1</sup>, Kevin Leedy<sup>2</sup>, David Look<sup>3</sup> and Leonard J. Brillson<sup>1,1</sup>; <sup>1</sup>The Ohio State University, United States; <sup>2</sup>Air Force Research Laboratory, United States; <sup>3</sup>Wright State University, United States

The alloy indium tin oxide (ITO) is widely used as a transparent conducting oxide in optoelectronic applications because of its electrical conductivity and optical transparency as well as its ease of deposition as a thin film. Polycrystalline ITO films have exhibited quantum interference effects on a nanoscale associated with variable-range-hopping transport, that is, phonon-assisted tunneling between localized states in the disordered material. 1 Recent theoretical calculations using the framework of quantum magnetoconductivity (QMC) have addressed the effects of ionized impurity and lattice vibrational scattering on electron concentration and mobility in ITO films created by pulsed laser deposition (PLD). 2 Hall-effect and QMC measurements of these films reveal QMC in the thinnest sample (13 nm) that is more than ten times stronger than in the thickest (292 nm) despite nearly the same phonon information. We have used nanoscale depth-resolved cathodoluminescence spectroscopy (DRCLS) to measure the depth-dependent Burstein-Moss band gaps and defects in the full range of film thickness in order to identify physical mechanisms that account for this nanoscale thickness dependence.

Figure 1 illustrates Monte Carlo rates of electron-hole pair creation inside In<sub>2</sub>O<sub>3</sub>:10%SnO<sub>2</sub> films on fused silica as a function of incident electron beam energy EB showing that 0.5 keV to several keV controls excitation on a near-nanometer scale. Figure 2 illustrates significant defect and band gap changes vs. depth within the outer 30 nm for a 242 nm thick ITO film while Fig. 3 shows relatively low defect emissions and only gradual changes from the 13 nm film through the interface. No interface-specific features are evident (Fig. 6). Deconvolution of the 13 nm film's CL spectrum (Fig. 4) reveals a dominant, Burstein-Moss shifted band gap feature at 4.1 eV corresponding to an  $n = 7.5 \times 10^{14} \text{ cm}^{-2}$  sheet carrier density and 2% Sn density, whereas Fig. 5 illustrates band gap peaks at 3.64, 3.9, and 4.2 eV typical of thicker films suggesting multiple Sn and doping densities. Since variable-range hopping is sensitive to point defects and domain boundaries, the near-nanoscale DRCLS detection of higher carrier density uniformity and lower relative defect densities can account for the relatively high QMC measured for the thinnest ITO films. These results highlight the role of nanoscale variations in carrier density and defects inside ultrathin deposited QMC films. LJB, JC, and DCL gratefully acknowledge National Science Foundation Grant no. DMR-18-00130. W. Schirmacher, *Phys. Rev. B* **41**, 2461 (1990). J.W. Cleary, E.M. Smith, K.D. Leedy, G. Grzybowski, and J. Guo, *Opt. Mat. Express* **8**, 1231 (2018).

#### 10:30 AM GG02

**(Student) Free Standing Quasi Two-Dimensional  $\gamma$ -Al<sub>2</sub>O<sub>3</sub> Grown by Atomic Layer Deposition** Elaheh Kheirandish, Marvin Schofield, Marija Gajdardziska-Josifovska and Nikolai Kouklin; University of Wisconsin-Milwaukee, United States

In this study we present details of a two-step synthesis and related structural characterizations of free standing quasi-2D nanosheets of  $\gamma$ -Alumina, a bulk non van der Waals compound. The nanosheets were realized using a high yield non-exfoliating strategy that utilizes a graphene scaffold. As first step ~10 nm amorphous Alumina was deposited using a multi-cycle Atomic Layer Deposition (ALD) followed by an air anneal at 800 °C to remove the graphene scaffold and promote the crystal order. HRTEM, X-ray and electron diffraction analysis reveal the samples are polycrystalline cubic spinel  $\gamma$ -Alumina with a close packed cubic texture in the  $\langle 111 \rangle$  ALD induced growth direction. The network resembles the graphene scaffold with the crystal growth direction remaining entirely morphologically controlled. At the same time, the surface of the  $\gamma$ -Alumina nanosheets are not atomically smooth and exhibit characteristic ripples formed as a result of the post growth strain relaxation. Thickness profiling <sup>[1]</sup> using bright field TEM imaging point to existence of steps on the order of 10 nm whereas SEM crosssectional investigations indicate the overall thickness of the flakes of ~35-192 nm attributed to folding and sintering of 2D nanosheets. Photoluminescence (PL) spectroscopy reveals a medium strength defect-assisted light emission that peaks at ~387 nm, with the excitation mechanism involving multi-defect bands within the band gap of 2D  $\gamma$ -Alumina. SEM-based inspections combined with the direct, two-terminal electrical transport measurements confirm that the flakes remain mechanically and electrically interconnected with the metal-alumina flake and the flake-flake junctions remaining Ohmic at the temperature range of 223-373 K. The RT conductivity is further found to be ~23 nS/m which is four orders of magnitude higher than that of ~99.5% pure  $\alpha$ -Alumina studied by Morell. <sup>[2]</sup> Reduction in the band gap energy of  $\gamma$ -Alumina due to formation of defect bands <sup>[3]</sup> as well as presence of texture <sup>[4]</sup> are among factors contributing to the increase in the conductivity of the 2D  $\gamma$ -Alumina. The newly-developed approach presents a low-cost high-yield synthesis of a variety of quasi-2D metal oxides for applications in next-generation nano-electronic, sensing and photonic devices. The texture-effected structural anisotropy is another critical attribute of the samples that can open a door to future deployment of the crystallographically textured  $\gamma$ -Alumina in high performance nanoelectronic devices.

Ref. [1] R. F. Egerton, *Electron Energy-Loss Spectroscopy in the Electron Microscopy*, 2nd Edition, Plenum Press, 1996; [2] R. Morell, *Handbook properties of Technical Engineering Ceramics*, Part 2, Data Reviews, Section I, High Alumina Ceramics, London, p.255, 1987; [3] B. Ealet, M. Elyakhloufi, E. Gillet, M. Ricci, *Thin Solid Films*, 250, 90-100 (1994); [4] A.Tan, C.K. Kuo and P.S. Nicholson, *Solid State Ionics*, 42, 233-241 (1990)

#### 10:45 AM GG03

**(Student) Semiconducting Oxides for Gas Sensing Applications** Janine Walker, Sheikh Akbar and Patricia Morris; The Ohio State University, United States

Semiconducting metal oxides have been investigated since the 1960's for highly sensitive conductometric gas sensing applications. These sensors operate based on modulating bulk conduction via the exchange of electrons between a gas analyte and the sensing material. Size reduction of these materials has shown to increase sensitivity by reaching a complete depletion conditions due to this electronic exchange. For this reason, nanotechnology has been utilized to further improve the performance of these sensors leading to sensors exhibiting high gas sensitivity. Increased understanding of selectivity observed for this class of sensor technology has been difficult to achieve due to the wide range of parameters utilized in fabricating these materials. To improve selective sensing, heterostructural sensing devices have been investigated. Tin dioxide nanowires functionalized with copper oxide have been fabricated and their sensing capabilities have been tested. The response towards hydrogen and

carbon monoxide have been compared between pristine nanowire sensors and the same sensors after deposition of copper oxide. This study demonstrated different response towards each gas between the unfunctionalized and functionalized sensing material. Tin dioxide nanowires were synthesized via a vapor-liquid-solid (VLS) method. Tests were performed for this device then a  $\text{Cu}(\text{NO}_3)_2$  precursor solution was deposited onto the sensor and repeated testing was performed. The gas tests were performed for unfunctionalized tin dioxide nanowires and tin dioxide nanowires functionalized with copper oxide for hydrogen and carbon monoxide gas. Response was calculated by taking the ratio of sensor resistance in air to the resistance in the gas analyte. It was observed that the response towards hydrogen and carbon monoxide for the unfunctionalized tin dioxide sensor was approximately 2.24 and 1.13, respectively. After functionalization, the response was approximately 1.68 and 4.50 for hydrogen and carbon monoxide, respectively. The decreased response towards hydrogen and increased response towards carbon monoxide showed that copper oxide functionalization resulted in improved selectivity for carbon monoxide over hydrogen. Furthermore, the increased baseline resistance in air of the functionalized tin dioxide sensor indicated charge carrier depletion in the tin dioxide nanowires due to the formation of a heterojunction between the tin dioxide and copper oxide. It is expected that charge carrier depletion would result in an overall improved response towards either gas tested. Therefore, a surface chemistry effect between the gas analytes and the copper oxide is expected to be the cause for the observed changes in response. Studies to characterize these gas-surface interactions should be carried out in the future.

#### 11:00 AM GG04

**(Student) Rutile  $\text{GeO}_2$ —An Ultra-Wide-Band-Gap Semiconductor for Power Electronics** Sieun Chae<sup>1</sup>, Kelsey A. Mingle<sup>1</sup>, Hanjong Paik<sup>2</sup>, Nguyen Vu<sup>1</sup>, John Heron<sup>1</sup> and Emmanouil Kioupakis<sup>1</sup>; <sup>1</sup>University of Michigan, United States; <sup>2</sup>Cornell University, United States

Ultra-wide-band-gap (UWBG) semiconductors have tantalizing advantages for power electronics as the wider band gap allows the larger breakdown strength. A few materials have been discovered for UWBG semiconductors (e.g., AlN/AlGaIn,  $\beta$ - $\text{Ga}_2\text{O}_3$ , and diamond), however, they are still facing many challenges, such as doping asymmetry or inefficient thermal conduction, which limit their adoption in devices. We identified rutile germanium oxide ( $r\text{-GeO}_2$ ) to be a promising, yet unexplored UWBG (4.68 eV) material. From the first-principles calculations, we calculate the electron mobility of  $153.6 \text{ cm}^2 \text{ V}^{-1} \text{ s}^{-1}$  and the breakdown electric field of  $7.0 \text{ MV cm}^{-1}$ , which leads to the Baliga figure of merit of  $r\text{-GeO}_2$  to be  $\sim 3$  times larger than that of  $\beta\text{-Ga}_2\text{O}_3$ . We also determine  $r\text{-GeO}_2$  has superior thermal conductivity ( $45 \text{ W m}^{-1} \text{ K}^{-1}$  (calculated) and  $49 \text{ W m}^{-1} \text{ K}^{-1}$  (experiment)) and dopability (shallow ionization energies are predicted for donors and a 0.45 eV ionization energy is predicted for Al acceptor) relative to  $\beta\text{-Ga}_2\text{O}_3$ . Though thin film synthesis of  $r\text{-GeO}_2$  has remained challenging due to a highly-metastable amorphous phase, we, for the first time, synthesized epitaxial thin film of  $r\text{-GeO}_2$  on a sapphire substrate using ozone-assisted molecular beam epitaxy and an oxidized source. Our work motivates further exploration of  $r\text{-GeO}_2$  as an alternative UWBG semiconductor that can compete with the state-of-the-art UWBG materials.

SESSION HH: ZnO-Based Contacts, Defects and Devices  
 Session Chair: Rebecca Peterson  
 Session Hosts: Leonard Brillson and Jamie Phillips  
 Friday Morning, June 26, 2020  
 Location: ZoomRoom 5

#### 10:30 AM HH01

**Enhanced Photoconductivity of ZnO/In<sub>2</sub>O<sub>3</sub> Epitaxial Superlattices—Effects of the Heterojunction Interfaces** Tai-Siang Lin<sup>1</sup>, C.M. Lin<sup>1</sup>, Yu-Ling Kuo<sup>1</sup>, Paritosh Wadekar<sup>1</sup>, Chih-Hsiung Liao<sup>2</sup>, Sung-Wei Yeh<sup>3</sup>, Ching-Wen Chang<sup>1</sup>, Chi-Chung Kei<sup>4</sup>, Li Wei Tu<sup>1</sup>, Di Chen<sup>5</sup>, Quark Y. Chen<sup>1,5</sup> and Wei-Kan Chu<sup>2</sup>; <sup>1</sup>National Sun Yat-Sen University, Taiwan; <sup>2</sup>ROC Military Academy, Taiwan; <sup>3</sup>National Kaohsiung University of Science and Technology, Taiwan; <sup>4</sup>Taiwan Instrument Research Institute, Taiwan; <sup>5</sup>University of Houston, United States

Temperature-dependent photoconductive behaviors of epitaxial superlattices, specifically those of ZnO/In<sub>2</sub>O<sub>3</sub>, were studied between 10K and 300K under intense illuminations of the 633 nm, 514 nm, and 454 nm EM radiations separately from an Ar-laser. The photoconductive mechanism was analyzed in the context of thermally assisted processes in association with the interface states believed to be originated from the epitaxial heterojunction interfaces. The samples were fabricated by RF magnetron sputtering on c-sapphire. When the initial layer is In<sub>2</sub>O<sub>3</sub>, the samples are smooth and of excellent epitaxy. The epitaxial relations can be described as (111)In<sub>2</sub>O<sub>3</sub> // (0001)ZnO with the a-axis of the substrate points in two orthogonal directions [110] and [112] of In<sub>2</sub>O<sub>3</sub> and a- or m-axis of the ZnO, largely representative of two twinned structural phases of perpendicularly twinned domain boundaries. However, as the growth periods increased from three to six periods, the existence of stacking faults becomes severe and photo-excitation efficiency becomes poor. The impurity or defect related electronic states, which are largely localized, led the mechanism of conduction to be mainly through charge hopping, in contrast to

the band conduction for doped single component thin films. Variable range hopping dominates the conductive mechanism in the lower temperature regions, while fixed range hopping becomes significant as the temperature increases, with both playing a role near room temperature. The effect of photo-assisted hopping may occur when the SLs sample is illuminated by the Ar-laser of a specific line. The presence of higher energy photons corresponds to an increased probability of absorptions of phonons, or quantized atomic vibrations, in the thermally-activated process and the resulted phenomena of variable-temperature data of the photoconductivity are interpreted in such context.

#### 10:45 AM HH02

**Hydrothermal Synthesis and Characterization of Zinc Oxide Nanoparticles as Photoanode in Dye-Sensitized Solar Cell** Boateng Onwona-Agyeman; University of Ghana, Ghana

Solar cells are generally classified into three (3) generations; the first generation is based on silicon crystals such as monocrystalline silicon and polycrystalline silicon. The second generation of solar cell are thin films. These cells are made from amorphous silicon, copper-indium-gallium-selenide (CIGS) and cadmium telluride (CdTe). Dye Sensitized Solar Cells (DSC) is the most common type of third generation of solar cells. The low production cost and ease of production of the DSC has attracted a lot of research interest. The DSC is made up of a transparent n-type semiconductor as an electrode on which a porous wide bandgap semiconductor is deposited. The specific surface area of this porous semiconductor is designed to be large, in order to accommodate monolayer of dye on its surface. ZnO has similar properties but it's more readily available, cheaper, non-toxic and has excellent chemical and thermal stability. In this work, a hydrothermal synthesis technique is used to produce nano-sized ZnO particles. A zinc acetate solution of 0.5 M was prepared in 50 ml of methanol under stirring. To this solution, 25 ml of 1 M NaOH was added drop-wise under continuous stirring at room temperature forming transparent white solution which then turns milky. Hydrothermal temperatures (90, 100, 110 and 120°C) were used. The functional groups of the synthesized ZnO nanoparticles were characterized by Fourier transform infrared (FTIR) spectroscopy in the range of 4,000 – 500  $\text{cm}^{-1}$ . The morphology and the elemental composition of the samples were examined by using Field Emission Scanning Electron microscope fitted with an EDX acquisition detector. The thermal properties of the samples were determined using differential scanning calorimetry and thermal gravimetric analysis instrument. 22.3 mg of the sample was heated in air in an alumina crucible up to 800°C at a heating rate of 10 K/min. The XRD peaks formed in the as-prepared samples became sharp with increasing hydrothermal temperatures whilst the crystallinity of the samples also improved with increasing hydrothermal temperatures with (101) being the dominant peak in the samples prepared at 110 and 120°C. The crystallite sizes of the samples were calculated by the Derby-Scherer equation. The FTIR analysis was conducted on the samples to identify the organic and inorganic functional groups present in the samples prepared. The peak corresponding to the Zn-O bond vibration at 531  $\text{cm}^{-1}$  wave number is observed. It can also be observed that annealing the samples removed all the organic compounds and the molecules of water present. This is in line with the observation made by XRD as the samples became more crystalline with sharper peaks. The results from the XRD and FTIR confirmed the synthesis of high purity ZnO nanoparticles. The surface morphology of the samples was determined using an SEM and the images show the formation of spherical nanoparticles. The spherical morphology of the particles became distinct after annealing. The elemental compositions of the ZnO nanoparticles were observed using energy dispersive x-ray spectroscopy. The same peaks (for Zn and O) for all samples were observed in the EDX data confirming the formation of ZnO. Based on the results from our characterizations, we have obtained pure ZnO nanoparticles that can be used as porous photoanode in a porous-structured solar cell such as DSC. The synthesized nanoparticles were characterized by XRD, SEM, EDX, DRS, FTIR and TGA. The XRD and EDX results confirm the crystalline nature, hexagonal wurtzite structure and the elemental composition of the ZnO NPs. In particular, ZnO NPs prepared by the hydrothermal treatment at 120°C and annealing at 500°C for 30 minutes showed the highest (002) diffraction peak as required for optoelectronic devices such as in nanostructured solar cell. The synthesized materials can be potentially used as key components in porous-structured opto-electronic devices such as solar cells.

#### 11:00 AM HH03

**(Student) Effect of Heterojunction Interface (SnO<sub>2</sub>/ZnO) on Gas Sensing Properties of Core-Shell Nanostructures** Priyanka Karnati, Sheikh Akbar and Patricia Morris; The Ohio State University, United States

Metal oxide-based core-shell (C-S) nanostructures have been studied for gas sensing applications to eliminate poor selectivity [1]. When designing core-shell nanostructures with n-n, p-n and n-p junctions, an equalization of the Fermi level induces the formation of accumulation and depletion layers at the interface through charge redistribution, modifying the conduction channel. The selection of the core and the shell material is important as it would affect the properties of the heterojunction interface. Parameters such as the thickness of the shell layer, type of sensing material and working temperature have been studied for C-S nanostructure-based gas sensors. However, less attention has been given to factors affecting the conduction mechanisms in C-S nanostructures.

In C-S nanostructures optimizing the shell layer thickness to the Debye length

range of the material has proven to enhance the sensor performance. Mechanisms such as potential barrier carrier transport and surface depletion layer formation play important roles in enhancing the gas sensing performance [2]. Understanding the gas sensing mechanism is not straightforward due to the presence of the heterojunction interface. Therefore, there is a need to understand the sensing mechanism in C-S nanostructures. One way to determine the role of the heterojunction is by exchanging the core and shell layers in C-S nanostructures and analyzing the gas sensing properties. Metal oxides such as Tin dioxide (SnO<sub>2</sub>) and Zinc oxide (ZnO) are chosen to synthesize C-S nanostructures. SnO<sub>2</sub> nanowires were synthesized by using the VLS (Vapor-liquid- Solid) process with Au as the catalyst. The ZnO layer was deposited by using a sputtering technique. The thickness of the ZnO shell layer can be varied by changing the deposition time. To study the effect of exchanging the core and shell layer, ZnO nanorods were synthesized by using the hydrothermal process. The Sn layer was deposited on ZnO nanorods by using a sputtering technique and annealed in air to form the SnO<sub>2</sub> layer. X-ray diffraction (XRD), Scanning electron microscopy (SEM) and Transmission electron microscopy (TEM) characterizations are used to confirm the phase, morphology, and dimensions of the synthesized C-S nanostructures. Kelvin probe force microscopy is used to calculate the work function of C-S nanostructures to determine the formation of the heterojunction. Response curves are measured in a custom built probe station towards 1000 ppm of H<sub>2</sub> gas. Impedance spectroscopy (AC) measurements are performed to determine the contribution from different parts of C-S nanostructures towards the gas sensing response. This study that is ongoing will help in the understanding of the gas sensing mechanism and the role of heterojunction in C-S nanostructures.

ZnO was sputtered on SnO<sub>2</sub> nanowires grown through the VLS process for 30 seconds. Response curve towards 1000 ppm hydrogen gas at 300°C for ZnO decorated SnO<sub>2</sub> nanowires and pristine SnO<sub>2</sub> nanowires have been compared. Response is calculated as the ratio between resistance in air and resistance in hydrogen gas. The response of ZnO decorated SnO<sub>2</sub> nanowires (11) is enhanced when compared to the pristine SnO<sub>2</sub> nanowires (7.39). The enhanced response proves the formation of a heterojunction between ZnO and SnO<sub>2</sub>. The impedance curves for ZnO decorated SnO<sub>2</sub> nanowires in nitrogen gas at different temperatures have been measured. The ability to measure impedance curves also proves the stability of the hetero-nanostructures. Future work involves measuring response and fitting impedance curves for SnO<sub>2</sub> decorated ZnO nanorods towards 1000 ppm hydrogen gas.

[1] P. Karnati, S.A. Akbar, P.A. Morris, Conduction mechanisms in one dimensional core-shell nanostructures for gas sensing: A review, *Sensors Actuators, B Chem.* 295 (2019) 127–143.

[2] D.R. Miller, S.A. Akbar, P.A. Morris, Nanoscale metal oxide-based heterojunctions for gas sensing: A review, *Sensors Actuators, B Chem.* 204 (2014) 250–272.

## 11:15 AM BREAK

### 11:45 AM HH04

**(Student) Defect Migration and Ohmic to Schottky Contacts in ZnO Nanowires** Micah Haseman<sup>1</sup>, Hantian Gao<sup>1</sup>, Daram N. Ramdin<sup>1</sup>, Holger v. Wenckstern<sup>2</sup>, Marius Grundmann<sup>2</sup> and Leonard J. Brillson<sup>1</sup>; <sup>1</sup>The Ohio State University, United States; <sup>2</sup>Universität Leipzig, Germany

ZnO and other II-VI compound semiconducting nanowires have sparked considerable interest in next generation optoelectronics. This is primarily due to the large surface to volume ratio which makes these nanowires and similar nanomaterials prime candidates for gas sensing and high efficiency nanoscale photovoltaics. Central in the application of these nanoelectronics is understanding and controlling the native point defects which can affect both carrier transport and recombination and are mobile under applied electric fields. Furthermore, device integration largely depends on the nature of metal-semiconductor interfaces and whether the resultant contacts are ohmic or rectifying (Schottky). We used nanoscale lateral and depth-resolved cathodoluminescence spectroscopy (DRCLS) along with hyperspectral imaging (HSI) via scanning electron microscope (SEM) to directly observe the redistribution and migration of native point defects in ZnO nanowires under an applied electric field. We measure in an ultra-high vacuum environment the current-voltage (I-V) behavior of Pt contacts deposited via focused ion beam (FIB) as a function of native point defect migration under an increasing electrical bias up to 3x10<sup>15</sup> V/cm. HSI maps allow us to observe lateral intensity distributions of specific point defect features, normalized to the near band edge emission, acquired pixel by pixel over SEM scanning region. Similarly, DRCLS from 0.5 – 15 kV enables probing through the Pt contacts, across the metal semiconductor interface, and into the nanowire bulk. Optical signatures at 2.0 eV (V<sub>zn</sub> clustering), 2.35 eV (Cu<sub>zn</sub>), 2.7 and 2.9 eV (V<sub>zn</sub>) in PLD grown ZnO nanowires exhibit homogeneous distributions that then segregate along the length of the nanowire under applied bias, moving directly underneath one contact and away from the other with a sufficiently intense electrical field. As the defect density is depleted near the ZnO surface/Pt contact interface, the current voltage curves exhibit the onset of rectifying behavior. This is likely due to a decrease in the probability of defect-assisted tunneling<sup>1</sup> as the number of available states diminishes with defect migration. This is the first direct observation of controlling Schottky rectification at a metal-nanowire contact by electrically manipulating native point defects. The change from ohmic to rectifying contacts due to defect migration under an applied electric field is of

general significance as nanoscale materials move into the device and application stages.

### 12:00 PM HH05

**Solution Processed Indium Gallium Zinc Oxide (IGZO) Thin-Film Transistors Operating at 2.0 Volt** Sagar R. Bhalerao<sup>1</sup>, Jari Keskinen<sup>1</sup>, Anna Railanmaa<sup>1</sup>, Matti Mäntysalo<sup>1</sup>, Donald Lupo<sup>1</sup> and Paul R. Berger<sup>1,2</sup>; <sup>1</sup>Tampere University, Finland, Finland; <sup>2</sup>The Ohio State University, United States

Over the past decade, extensive efforts have been made to develop thin film transistors (TFT) for potential applications in microelectronics, such as Internet of Things (IoT), radio frequency identification tags (RFID) and flexible active-matrix organic light emitting diodes (AMOLED), following the increased demand for the flexible, wearable and ultra-thin electronics [1]. To meet the demand for the future electronic application, especially printed and flexible electronics that can be autonomously powered, energy thrifty, metal oxide semiconductors can be seen as potential replacement candidate for amorphous or polycrystalline silicon. Recently, TFTs based on solution-processed metal oxides have received much attention due to the advantages of low cost and scalable processing compared to high temperature and/or high vacuum, vapor deposition techniques. Amongst all other metal oxides, indium gallium zinc oxide (IGZO) is the most popular and widely studied due to its superior optoelectronic properties, such as uniformity, transmittance, low temperature processing, high mobility etc. [2]. Thin film transistors with indium gallium zinc oxide semiconductor have been already reported in the past; however, the device operating voltage and processing temperature are still present major challenges for flexible and printed electronics [3]. Here, we report low voltage (2.0 V) thin film transistors with solution processed, high quality IGZO semiconductor film and room temperature deposited anodized aluminum oxide Al<sub>2</sub>O<sub>3</sub> dielectric. By uniting the device fabrication with ultra-thin (~10 nm) room temperature deposited anodic Al<sub>2</sub>O<sub>3</sub> gate oxide and comparatively low temperature (300°C) annealed IGZO film, we reduced the operating voltage below the 2 volts. The fabricated TFTs reported here exhibits excellent field effect electron mobility as high as  $\mu_{\text{eff}} = 2.82 \text{ cm}^2/\text{V}^2\text{s}^{-1}$ , on-off ratio (Ion/Ioff) 10<sup>4</sup>, threshold voltage (V<sub>th</sub>) 0.75 V, transconductance (g<sub>m</sub>) 73 uS and subthreshold swing (SS) 270 mV/dec, with effective operation at 2.0 V. These values are quite promising in the regard to solution processing and low temperature device fabrication. The indium gallium zinc oxide ink was formed by dissolving the indium nitrate hydrate (In(NO<sub>3</sub>)<sub>3</sub>·xH<sub>2</sub>O), gallium nitrate hydrate (Ga(NO<sub>3</sub>)<sub>3</sub>·xH<sub>2</sub>O), and zinc nitrate hydrate (Zn(NO<sub>3</sub>)<sub>2</sub>·xH<sub>2</sub>O) in 2-methoxyethanol with a proportion of 0.085 : 0.0125 : 0.0275 M respectively [4]. The thin film transistor fabrication procedures were the same as previously reported by us [5]. A Keysight B1500A semiconductor device parameter analyzer connected to a Cascade Microtech probe station via tri-axial cables was used to measure the electrical performance of the fabricated IGZO TFTs.

ACKNOWLEDGMENT: The authors would like to extend a special thanks to Business Finland and the Academy of Finland for the financial assistance.

### REFERENCES

- Street, R. A. Thin-Film Transistors. *Adv. Mater.* 2009, 21, 2007– 2022.
- Fortunato, E.; Barquinha, P.; Martins, R. Oxide Semiconductor Thin-Film Transistors: A Review of Recent Advances. *Adv. Mater.* 2012, 24, 2945–2986.
- X Xiao, L Zhang, Y Shao, X Zhou, H He and S Zhang, Room-Temperature-Processed Flexible Amorphous InGaZnO Thin Film Transistor, *ACS Appl. Mater. Interfaces* 2018, 10, 31, 25850-25857.
- J-W Jo, K-T Kim, H-H Park and S K Park, High-Speed and Low-Temperature Atmospheric Photo-Annealing of Large-Area Solution-Processed IGZO Thin-Film Transistors by Using Programmable Pulsed Operation of Xenon Flash Lamp, *Journal of the Korean Physical Society*, Vol. 74, No. 11, June 2019, pp. 1052~1058.
- S R Bhalerao , D Lupo, A Zangiabadi, I Kymissis , J Leppäniemi, A Alastalo and P R Berger, 0.6 V threshold voltage Thin film transistors with solution processable (In<sub>2</sub>O<sub>3</sub>) channel and anodized high-κ Al<sub>2</sub>O<sub>3</sub> dielectric, *IEEE electron device letters*, vol. 40, no. 7, July 2019.

### 12:15 PM HH06

**(Student) A Comprehensive a-IGZO TFT Device Model and Analog Circuit Validation** Ritwik Vatsyayan, Andrew Bourhis, Hongseok Oh and Shadi Dayeh; University of California, San Diego, United States

Amorphous Indium Gallium Zinc Oxide (a-IGZO) thin film transistors (TFTs) were first implemented in 2004 [1], and have developed over the last decade to disrupt the display industry[2]. a-IGZO can be deposited on flexible and glass substrates at low temperature without degrading its mobility and as a result, it is favored for applications with low thermal budget. Our group is leveraging the a-IGZO TFT processing for acquisition electronics integrated on thin-film polymer substrates for brain mapping applications. To measure minute potentials down to a few microvolts and to switch rapidly for scanning over larger numbers of contacts, a more complete a-IGZO model that captures all modes of operating regimes (subthreshold, linear and saturation), the AC characteristics and noise properties is needed. Existing device models for TFTs that are applied to a-IGZO TFTs do not empirically match the measured device characteristics. Specifically, these models do not include important parameters such as contact resistance, sub-threshold, noise, and gate leakage currents. In this work, we report the development and verification of a new model for a double-gate a-IGZO thin film transistors (TFTs) based on empirical data collected from a large number of devices fabricated on flexible polyimide substrates. The parametric study consisted of arrays of a-IGZO TFTs with gate

widths in the range of (100  $\mu\text{m}$ -1000  $\mu\text{m}$ ) and gate length in the range of (5  $\mu\text{m}$ -50  $\mu\text{m}$ ), transmission-line-measurement (TLM) patterns, ground-signal-ground (GSG) RF patterns and verification circuits. The fabricated devices have a measured electron mobility of (11-15)  $\text{cm}^2/\text{Vs}$ , Hooge's parameter as low as 1.4e-3, an OFF current of  $\sim 1\text{e-}14$  A and a tunable threshold voltage (negative, normally-on) with deposition conditions. This is a major gain compared to the mobility and noise performance of polycrystalline Silicon TFTs (which show mobility of 1-4  $\text{cm}^2/\text{Vs}$  and Hooge's parameter of  $3\text{e-}3 - 2.2\text{e-}2$ ) and great promise for use in highly sensitive applications. The model shows good agreement with the experimentally measured data on over a wide frequency range (from 10Hz-10MHz). The device performance was verified for the DC, small signal and noise performance. After verifying the accuracy of the model, we constructed amplifier and oscillator circuits in Cadence and performed circuit simulations to validate their operation and then implemented these circuits experimentally on polyimide substrates. We will report the model and circuit results, compare with simulations, and benchmark against other TFT models.

[1] Nomura, K. et al., "Room-temperature fabrication of transparent flexible thin-film transistors using amorphous oxide semiconductors", *Nature* 432, 488-492 (2004).

[2] Lee, J. H. et al., "World's Largest XGA AMLCD Panel Using IGZO Oxide TFT", *SID Symposium Digest of Technical Papers*, Vol.39, 625-628 (2008).

### 12:30 PM HH07

**(Student) Atomic Layer Deposition of Zinc-Tin-Oxide for High Field-Effect Mobility Films** Christopher Allemang, Tae Cho, Orlando Trajo, Shantam Ravan, Neil P. Dasgupta and Rebecca L. Peterson; University of Michigan-Ann Arbor, United States

Fabrication of thin-film electronics for 3D monolithic integration on top of complementary metal oxide semiconductor integrated circuits (CMOS ICs) requires materials with high field-effect mobilities,  $\mu_{FE}$ , and deposition techniques compatible with the silicon back end of line manufacturing thermal budget of  $\sim 450^\circ\text{C}$ .<sup>1</sup> Transparent amorphous oxide semiconductors (TAOS) are well-suited for 3D monolithic integration because of their superior electron transport, compared to amorphous-Si and organic semiconductors, and their amorphous morphology allows for large-area process uniformity.<sup>2</sup> While indium-gallium-zinc-oxide (IGZO) has been widely studied as a TAOS and manufactured commercially, zinc-tin-oxide (ZTO) is being studied as an alternative TAOS to IGZO because zinc and tin are more earth-abundant than indium and gallium and therefore are less expensive materials.<sup>3</sup> Vacuum-based processes already used in CMOS processing, like sputtering and atomic layer deposition (ALD), have been studied as deposition techniques for ZTO. Here, ALD is studied as the thin film deposition technique because it is a low-temperature process that allows precise control of film interfaces, stoichiometry, and thickness. Previous studies on ALD ZTO thin-film transistor (TFTs) using  $\text{H}_2\text{O}_2$  as the oxidant resulted in as-deposited films that are highly conductive due to a high number of oxygen vacancies and post-deposition anneals at  $350^\circ\text{C}$  or above were necessary for  $\mu_{FE} > 11 \text{ cm}^2\text{V}^{-1}\text{s}^{-1}$ .<sup>4,5</sup> Here, several ALD processes are studied to deposit ZTO as the channel material for bottom-gate, top-contact TFTs. The resulting ZTO thin films were analyzed using ellipsometry, X-ray photoelectron spectroscopy (XPS), grazing incidence X-ray diffraction, and X-ray reflectivity (XRR). As-deposited ZTO films deposited using these processes exhibit semiconducting behavior due to a low density of oxygen-related defects, confirmed by XPS. ZTO deposited at  $150^\circ\text{C}$  using a thermal process with optimized tin composition and  $500^\circ\text{C}$  post-deposition anneal show good transistor performance with  $\mu_{FE} = 5.4 \text{ cm}^2\text{V}^{-1}\text{s}^{-1}$ . In this talk, we will describe further improvements in performance made possible by adding plasma to the ALD ZTO process to increase the  $\mu_{FE}$  to greater than  $15 \text{ cm}^2\text{V}^{-1}\text{s}^{-1}$ . We furthermore will explain the improvements by linking materials characterization to electrical behavior. The work presented here moves us closer to future monolithic integration of ZTO thin-film electronics on top of CMOS ICs. This work was supported by the National Science Foundation grant CMMI-1727918. Portions of this work were performed using the LNF, (MC)<sup>2</sup>, and J. D. Hanawat X-Ray MicroAnalysis Laboratory, which are supported by the College of Engineering at the University of Michigan. <sup>1</sup> S. Sedky, A. Witvrouw, H. Bender, and K. Baert, *IEEE Transactions on Electron Devices* 48, 377 (2001). <sup>2</sup> K. Nomura, H. Ohta, A. Takagi, T. Kamiya, M. Hirano, and H. Hosono, *Nature* 432, 488 (2004). <sup>3</sup> P. Schlupp, F.-L. Schein, H. von Wenckstern, and M. Grundmann, *Advanced Electronic Materials* 1, 1400023 (2015). <sup>4</sup> B.D. Ahn, D. Choi, C. Choi, and J.-S. Park, *Appl. Phys. Lett.* 105, 092103 (2014). <sup>5</sup> J. Heo, S. Bok Kim, and R.G. Gordon, *Applied Physics Letters* 101, 113507 (2012).

### 12:45 PM HH08

**(LATE NEWS, Student) Ionic Doping of  $\text{TiO}_2$  Thin-Film Transistors Using Superacid Treatment** Jie Zhang, Meng Jia, Guangyang Lin, Peng Cui and Yuping Zeng; University of Delaware, United States

Metal oxide thin film transistors (TFTs) promise to enable a wide range of applications, such as high-resolution display and RF identification tags. To meet the requirements of these applications, TFTs with enhanced current drivability are highly desirable. Herein, we report for the first time on a simple, equipment-free, solution-based superacid (SA) treatment to enhance the current drivability of  $\text{TiO}_2$  TFTs. The on-current is found to be enhanced by nearly  $2\times$  via a quick dip in SA solution. The mechanism is investigated by using an

ionic liquid with the same anion and solvent for control experiment. It is believed that the protons from SA are doped into the offset region of  $\text{TiO}_2$  TFTs, forming an electron-double-layer (EDL) and thus boosting the on-current. These  $\text{TiO}_2$  TFTs are formed in a top-gate structure with source/drain offsets. The gate width ( $W_G$ ), gate-drain offset ( $L_{GD}$ ), gate-source offset ( $L_{GS}$ ) and gate length ( $L_G$ ) of  $\text{TiO}_2$  TFTs is 70, 1.5, 1.5 and 2.5  $\mu\text{m}$ , respectively. The channel material, gate dielectric, S/D metal and gate metal are respectively 15 nm  $\text{TiO}_2$ , 10 nm  $\text{ZrO}_2$ , 250 nm Al and 170 nm Ni/80 nm Au. Two samples with  $\text{TiO}_2$  TFTs of same dimensions are prepared and dipped into 0.2 mg/mL bis(trifluoromethane) sulfonamide (TFSI) solution (so called 'SA') and 1-ethyl-3-methylimidazolium bis(trifluoromethylsulfonyl)imide (EMIm TFSI) solution, respectively. The samples were dipped for 20 s at room temperature with air ambient and blow dried with  $\text{N}_2$  right after being removed from solutions. It is noted that two solutions are of the same concentration, anion and solvents with the only difference in the cations. The electrical properties of  $\text{TiO}_2$  TFTs before and after treatments were measured. It is shown that SA-treated TFTs exhibit an enhanced on-current in contrast to that a decrease in on-current can be observed in the EMIm TFSI-treated TFTs. Both treated-TFTs show similar fast switching behaviors with subthreshold swing of  $\sim 120$ -130 mV/dec and the same gate leakage current level (at  $\sim 10^{-12}$ A) as the as-fabricated TFTs. This may be due to the fact that, the  $\text{ZrO}_2/\text{TiO}_2$  channel interface is mostly encapsulated by top-gate metal, leading to the less influence by the post-treatment. The Schottky contact behaviors can also be observed in the output characteristics of both TFTs, possibly due to that the Al metals are attacked by treatments arising from the acid nature of both solutions. The statistical results of current change, defined as the current ratio before and after treatment at  $V_{DS} = 10$  V and  $V_{GS} = 4$  V biasing condition, demonstrate that SA treatment enhance the TFT on-current by nearly  $2\times$  in contrast to that of a  $\sim 20\%$  current decrease for EMIm TFSI treatment. The current drop in the EMIm TFSI-treated TFTs can be explained by the formation of the Schottky barrier between S/D metal and  $\text{TiO}_2$ , which would hinder the electron injection and extraction process. Despite of Schottky behaviors observed in both TFTs, the current increase after SA treatment indicates the existing of a strong current boosting mechanism, covering the detrimental effects from Schottky contacts. SA is a well-known protonating agent with abundant labile hydrogen [1]. It is believed the current enhancements originate from the protons in SA solutions. Protons, with small ionic radius of 25 pm, may penetrate the  $\text{ZrO}_2$  in the TFT offset region and accumulate at the  $\text{ZrO}_2/\text{TiO}_2$  interface, forming an EDL and n-doping the offset region in TFTs [2]. In contrast, the TFSI anion and EMIm cations, with large ionic radius of 0.9 nm and 0.8 nm, respectively [3], may be blocked by  $\text{ZrO}_2$  and thus have less influences on the TFT performance. In summary, SA treatment is shown as effective method to enhance the current drivability of  $\text{TiO}_2$  TFTs by ionic doping of the offset region.

[1] M. Amani et al., *Science*, vol. 305, p. 1065-1068, (2015). [2] S. Fathipour et al., *J. Appl Phys*, vol. 120, p. 234902, (2016). [3] A. Elbourne et al., *ACS Nano*, vol. 10, p. 1021, (2015).

SESSION II: Organic Devices and Molecular Electronics  
Session Chair: David Janes

Session Hosts: Benjamin McEwen and Heayoung Yoon  
Friday Morning, June 26, 2020  
Location: ZoomRoom 6

### 10:15 AM II01

**A {100}-Oriented Si Thin-Films Grown on Polyimide by the CW Laser Crystallization** Nobuo Sasaki<sup>1,2,3</sup>, Muhammad Arif<sup>2</sup>, Yukiharu Uraoka<sup>2</sup>, Jun Gotoh<sup>3</sup> and Shigeto Sugimoto<sup>3</sup>; <sup>1</sup>Sasaki Consulting, Japan; <sup>2</sup>NAIST, Japan; <sup>3</sup>V-Technology, Japan

This paper demonstrates crystal growth of {100}-oriented Si thin films on polyimide by an unseeded single scan of the green continuous wave (CW) laser crystallization. We fabricated the second a-Si layer sandwiched by two  $\text{SiO}_2$  layers as an underlying buffer layer to prevent the damage to polyimide by thermal diffusion of the absorbed laser power. Si films on polyimide are required for the applications of flexible flat panel displays (FPDs) and flexible electronics.

A {100}-oriented grain-boundary free Si thin film on quartz has been grown by a single scan of the green CW laser unseeded crystallization with a  $\text{SiO}_2$  cap [1-3]. Surface crystal orientation control is required to improve the uniformity of the electrical characteristics of TFT, because the surface orientation affects effective mass [4] and Si-SiO<sub>2</sub> interface charge [5]. The surface orientations of the grains in the crystallized film by the commercially available pulse excimer laser annealing (ELA) are random.

The CW laser heats the Si layer to be crystallized for a longer time than that of pulse laser by a factor of  $\sim 1000$  and tends to increase the temperature of the underlying layer by the vertical thermal diffusion. In this study, we made the second a-Si layer to enhance lateral thermal diffusion. If the absorbed power in a-Si to be crystallized diffuse mainly vertically, the polyimide is easily heated up and damaged because of the low thermal conductivity and low thermal resistance of polyimide. A preliminary study shows that the optical effect to polyimide by the transparent light going through the Si layer is negligible at the laser power for crystallization because less than 30 % irradiated power goes through the 60 nm Si layer in the green laser irradiation and this value does not

damage the polyimide.

A 60 nm-thick a-Si film to be crystallized with a 123-nm SiO<sub>2</sub> cap and an underlying buffer layer was deposited by PECVD on polyimide coated glass. The buffer layer consisted of the second a-Si of 150 nm-thickness sandwiched by two 700 nm-thick SiO<sub>2</sub> layers. The polyimide layer was made by spin coating of varnish on glass and cured for 10 min. at 450 °C. The thickness of polyimide was 2 μm. After the de-hydrogenation annealing at 430 °C for 1 hour, the a-Si was crystallized by the unseeded CW laser lateral crystallization with a DPSS Nd:YVO<sub>4</sub> laser at a 532-nm wave-length and a 15 mm/s scan velocity keeping the substrate at room temperature in air. A highly-uniform top-flat line beam was used [1-3]. The beam shape was a 492 μm × 8 μm line beam. The beam profile was top flat for the long axis and Gaussian for the short axis. The crystal quality was investigated by EBSD (Electron Back-Scatter Diffraction).

The preferential {100} surface-orientation is confirmed by IPF (inverse pole figure) map in ND (surface normal direction) of the crystallized film at 0.8 W laser power and 15 mm/s scan velocity. A larger melted width of 300 μm is obtained than that of Si on quartz of 200 μm due to the enhanced lateral temperature distribution. The crystallized region shows 88.3% occupancy of the {100} surface-orientation within 15°. The necessary crystallization power decreases in the Si on polyimide structure than that in the Si on quartz structure by a factor of 0.3-0.6.

In conclusion, it is verified that {100} oriented Si thin-films on polyimide can be produced by a single scan of the unseeded green CW laser crystallization by utilizing a cap SiO<sub>2</sub> and a buried a-Si lateral heat dissipation layer sandwiched by two SiO<sub>2</sub> layers. The crystallized film showed 88.3% occupancy of the {100} orientation within 15°.

#### References

[1] N. Sasaki, Y. Nieda, D. Hishitani, and Y. Uraoka, *Thin Solid Films* **631**, 112 (2017). [2] N. Sasaki, M. Arif, and Y. Uraoka, *Jpn. J. Appl. Phys.* **58**, SBBJ02 (2019). [3] N. Sasaki, M. Arif, and Y. Uraoka, *Appl. Phys. Express* **12**, 055508 (2019). [4] T. Sato, Y. Takeishi, and H. Hara, *Phys. Rev. B*, **4**, 1950 (1971). [5] N. Sasaki, *Jpn. J. Appl. Phys.* **12**, 1458 (1973).

#### 10:30 AM II02

**(Student) Highly Tunable Molecular Rectifier Realized by Interfacial Design in Molecular Heterojunction with Two-Dimensional Materials** Jaehoo Shin<sup>1</sup>, Seunghoon Yang<sup>1</sup>, Yeonsik Jang<sup>2</sup>, Jung Sun Eo<sup>1</sup>, Tae-Wook Kim<sup>3</sup>, Takhee Lee<sup>2</sup>, Chul-Ho Lee<sup>1</sup> and Gunuk Wang<sup>1</sup>; <sup>1</sup>Korea University, Korea (the Republic of); <sup>2</sup>Seoul National University, Korea (the Republic of); <sup>3</sup>Korea Institute of Science and Technology, Korea (the Republic of)

Until now, a specifically designed functional molecular species has been recognized as an absolute necessity for realizing the diode's behavior in molecular electronic junctions.<sup>[1-4]</sup> However, even non-functional molecules can be served for the implementation of molecular diode with employing appropriate energy band alignment in heterostructure molecular junctions. Here, we suggest a facile approach for the implementation of a tailored diode in a molecular junction based on non-functionalized alkyl and conjugated molecular monolayers. A two-dimensional (2D) semiconductor (MoS<sub>2</sub> and WSe<sub>2</sub>) was used as a rectifying designer at the alkyl or conjugated molecule/Au interface. From the adjustment of band alignment at molecules/2D semiconductor interface that can activate different transport pathways depending on the voltage polarity, the rectifying characteristics can be implemented and controlled. The rectification ratio could be widely tuned from 1.24 to 1.83 × 10<sup>4</sup> by changing the molecular species and type and the number of layers of the 2D semiconductors in the heterostructure molecular junction. Our work sets a design rule for implementing tailored-diode function in a molecular heterojunction structure with non-functionalized molecular systems. [1] Díez-Pérez, I. *et al.* Rectification and stability of a single molecular diode with controlled orientation. *Nat. Chem.* **1**, 635 (2009). [2] Van Dyck, C. & Ratner, M. A. Molecular rectifiers: a new design based on asymmetric anchoring moieties. *Nano Lett.* **15**, 1577-1584 (2015). [3] Yuan, L., Breuer, R., Jiang, L., Schmittel, M. & Nijhuis, C. A. A molecular diode with a statistically robust rectification ratio of three orders of magnitude. *Nano Lett.* **15**, 5506-5512 (2015). [4] Chen, X. *et al.* Molecular diodes with rectification ratios exceeding 10<sup>5</sup> driven by electrostatic interactions. *Nat. Nanotechnol.* **12**, 797 (2017).

#### 10:45 AM II03

**(Student) Organo-Metal Halide Perovskite Resistive Memory in a Cross-Bar Array Achieved by Single-Step Solution Process** Heebeom Ahn, Keehoon Kang, Woocheol Lee, Junwoo Kim, Youngrok Kim, Daekyoung Yoo and Takhee Lee; Seoul National University, Korea (the Republic of)

Resistive random access memory (RRAM) has been widely studied as a next-generation memory candidate due to its low power consumption, low manufacturing costs, and scalability. A broad range of solution-processable materials are available as active layer of the device. Among them, RRAM based on organo-metal halide perovskite materials have been reported to show outstanding resistive switching characteristics such as a low switching field and high ON/OFF ratio. However, fabrication of high-yield, high-density perovskite memory device still remains as a main challenge since obtaining pinhole-free and uniform perovskite thin films is difficult due to their sensitive deposition conditions. In this presentation, 8 × 8 cross-bar array perovskite unipolar memory device with maximum device yield of 94% is demonstrated, based on

nearly pinhole-free perovskite thin films. High-quality perovskite thin films were obtained by employing one-step spin coating process with a non-halide lead source. The memory device has exhibited a unipolar switching behavior with a relatively low operation voltage and high ON/OFF ratio up to 10<sup>8</sup>. Other memory characteristics including endurance and retention time were also comparable to other reported perovskite RRAMs. Furthermore, we showed that one diode-one resistor (1D-1R) scheme for reducing cross-talk interference in a high density array can be achieved with our unipolar perovskite RRAM devices. In addition, the scaling analysis of current noise and reset current for each resistance state was performed, from which we could infer that the unipolar resistance switching is due to the formation and rupture of a percolation network by defects in the material. This research shows potential for low-cost and high-density practical organo-metal halide perovskite memory devices [1]. Reference [1] K. Kang, H. Ahn et al., *Adv. Mater.* **31**, 1804841 (2019).

#### 11:00 AM II04

**(Student) Investigation of the Influence of Cross-Linker of Polymer Dielectric on the Cut-Off Frequency of Organic-Metal-Insulator Semiconductor Capacitors** Fiheon Imroze<sup>1</sup>, C.A. Mithun<sup>1</sup>, P.K. Manda<sup>1</sup>, Karunakaran Logesh<sup>1</sup>, Soumya Dutta<sup>1</sup> and P. Venkatakrishnan<sup>2</sup>; <sup>1</sup>Indian Institute of Technology Madras, India; <sup>2</sup>Indian Institute of Technology, Madras, India

Organic metal-insulator-semiconductor capacitor (OMISCAP) has been considered to be a fundamental device structure to study the interfacial properties of metal-semiconductor and semiconductor-dielectric interfaces in organic thin-film transistors (OTFTs)<sup>[1]</sup>. Apart from these, MISCAP can also be an indispensable component in circuit applications such as tunable low pass filter, amplifiers etc. One of the major requirements for circuit applications is the frequency limit up to which the device can be operated without any performance degradation. Typically organic field-effect devices are restricted to low frequency operating range due to their low mobility of organic semiconductor, as discussed extensively by various research groups<sup>[2][3][4]</sup>. At higher frequencies, the frequency dispersion would limit the device operating range. The cut-off (f<sub>c</sub>) frequency up to which there is no capacitance dispersion decides the operating range of MISCAP. However, while using polymer dielectrics as the insulator in MISCAP, dielectric relaxation may interfere with the semiconductor relaxation that can cause a further decrease in f<sub>c</sub><sup>[5]</sup>. One of the widely used polymer dielectrics in organic thin-film devices is poly(4-vinylphenol) (PVP), which has a relatively high k-value, low leakage current and larger relaxation bandwidth (> 500 kHz) as per our findings using Metal-Insulator-Metal (MIM) devices. However, the presence of hydroxyl groups in pristine PVP results in device instability at the semiconductor/dielectric interface and increases gate leakage. Upon adding poly(melamine-co-formaldehyde) (PMCFD) cross-linker to the PVP, the free hydroxyl groups are suppressed by the cross-linker chain reducing the interfacial trap density as well as leakage current<sup>[6]</sup>. In this work, the influence of the cross-linker concentration in pristine PVP on f<sub>c</sub> is thoroughly investigated. Organic MISCAP devices consisting of a high mobility poly[2,5-bis(3-tetradecylthiophen-2-yl)thieno[3,2-b]thiophene](PBTTT-C14) as an active layer, PVP as the dielectric and a hole injecting metal were fabricated. The cross-linker concentration in pristine PVP was varied in order to study its effect on f<sub>c</sub>. The devices were characterized inside a vacuum probe station using Agilent E4980A precision LCR meter. The f<sub>c</sub> is calculated by taking 10% of the flat portion of the capacitance vs. frequency (C-f) plot in the strong accumulation region. A decrease in f<sub>c</sub> upon increasing the concentration of the crosslinker was observed. Thus for circuit applications it is important to choose the concentration of the crosslinker to make a trade-off between device stability and frequency limit. **References:** [1] Manda, Prashanth Kumar et al., *IEEE Transactions on Electron Devices* **66.9** (2019): 3967-3972. [2] Meijer, E. J., et al., *Applied Physics Letters* **78.24** (2001): 3902-3904. [3] Ullah, Mujeeb, et al., *Journal of Applied Physics* **106.11** (2009): 114505. [4] Maddalena, Francesco, et al., *Organic Electronics* **17** (2015): 304-318. [5] Manda, Prashanth Kumar et al., *Materials Today: Proceedings* **19** (2019): 53-57. [6] Karunakaran, Logesh et al., *Organic Electronics* **65** (2019): 15-18.

#### 11:15 AM BREAK

#### 11:45 AM II05

**(Student) Doped Organic Transistors at Ultra-Low Doping Concentrations** Raj Kishen Radha Krishnan, Shiyi Liu and Bjorn Lussem; Kent State University, United States

Organic transistors have been proposed for a number of applications like flexible displays, gas sensors, smart cards, low cost RFID tags etc<sup>1</sup>. Over the years the performance of organic transistors has improved tremendously, and organic semiconductors have reached mobility values similar to amorphous silicon. However, there are still significant hurdles to the large-scale commercial use of organic transistors. Specific issues that need to be addressed include - improving mobility, reducing contact resistance<sup>2</sup>, controlling the majority/minority carriers, stability and reproducibility<sup>3</sup>. Doping has been used very effectively as a strategy to address a number of these issues and achieve high performance and reproducibility in inorganic devices. In particular, doping has been used successfully in organic opto-electronic devices to improve their performance, but the doping concentrations used are large (in the range of several wt.%). Doping at such large concentrations significantly alters the morphology of the thin films and their electrical properties, hiding interesting

physical processes in the doped film. Most importantly, minority charge carrier generation is suppressed at these high doping concentrations, which suppresses the formation of an inversion channel in most transistors. Therefore, doping OFETs is often restricted to contact doping or interface doping<sup>4</sup>. Studying the effect of channel doping requires the use of ultra-low doping concentrations. To achieve low doping concentrations, we use co-evaporation of host and dopant material with a rotational shutter to cut the ratio of dopant that is mixed with host. The rotational shutter consists of a rotating metal disc with slits that sits above the evaporative dopant source and cuts the rate at which the dopant is co-deposited with the host. In our lab we have used this to achieve doping of the order of 100ppm. This has enabled us to systematically study the effect of doping in a number of systems- C60:O-MeO-DMBI-I, Pentacene:C60F36, Pentacene:F6TCNNQ and DNTT: F6TCCNQ. The effect of doping is studied in Organic Field-Effect Transistors and MOS devices. The effect of doping on threshold voltage, mobility, contact resistance, hysteresis has been studied in detail in doped C60 MOS devices. With the help of a numerical model, key insights into the doping mechanisms at ultra-low doping concentrations are reached. In addition, doped Dinaphthothienothiophene (DNTT) based ambipolar OFETs with comparable hole and electron mobility have been achieved. Although, inversion is typically not observed in organic MOS devices in low frequency capacitance measurements, doped DNTT MOS devices show clear accumulation, depletion and inversion at low frequencies. The results indicate that doping can be used effectively to tune transistor properties. Inversion and ambipolar transport in DNTT provide hope for implementing an organic complementary circuit with the same material. **References** 1. Tang, W. & Huang, Y. Recent progress in printable organic field. *J. Mater. Chem. C* 7,709- 808(2019) 2. Klauk, H. Will We See Gigahertz Organic Transistors? *Adv. Electron. Mater.* 4, 1–8 (2018). 3. Ahmed, R. *et al.* Reproducibility and stability of C 60 based organic field effect transistor. *Synth. Met.* 161, 2562–2565 (2012). 4. Xu, Y. *et al.* Doping : A Key Enabler for Organic Transistors. *Adv. Mater.* 30, 13–19 (2018).

#### 12:00 PM II06

**(Student) Electrical Properties of Spin-Coated Polyethylene Oxide Capacitors as Thin as 8 nm** Karla A. Gonzalez-Serrano and Alan C. Seabaugh; University of Notre Dame, United States

Polyethylene oxide (PEO) containing an alkali perchlorate has been widely used to electrolytically gate bulk and two-dimensional semiconductors [1–3]. Considering the use of PEO at the limits of device scaling, we report the properties of metal/PEO/Si (MPS) capacitors at the limits of thickness scaling, obtained by spin coating in an Ar ambient. Thicknesses were measured by ellipsometry, accumulation capacitance measurements, and transmission electron microscopy (TEM) with a minimum thickness of ~8 nm observed by TEM. In an argon glovebox (99.999% Ar, H<sub>2</sub>O <0.1 ppm, O<sub>2</sub> <0.1 ppm), PEO (Mw=110,000 g/mol, Polymer Standards Service) was dissolved in acetonitrile at room temperature to form a 1% wt. solution. CsClO<sub>4</sub> was added in an ether oxygen to Cs<sup>+</sup> ratio of 76:1. In the glovebox, pure-PEO or PEO:CsClO<sub>4</sub> was coated on 3.5×3.5 cm<sup>2</sup> Si wafers (n-type: Sb (100), 0.01–0.02 Ω-cm; p-type: B, 0.01–0.02 Ω-cm) that were MOS cleaned and HF dipped (50:1 DI:HF, 5 s). Wafers were spun at spin speeds of 2, 4, 6, 8, or 10 krpm for 30 s, then baked at 50 °C for 10 minutes to evaporate the solvent. Finally, capacitor top-electrodes were formed by shadow mask evaporation (1 nm Ti / 180 nm Pd, diameters 20, 45, and 63 μm). When not under test in an N<sub>2</sub> ambient, the capacitors were stored in an Ar glovebox to minimize water absorption. Variable angle spectroscopic ellipsometry (VASE, J. A. Woollam Co.) measurements in air were used to fit the frequency (1/λ) dependence of PEO's index of refraction *n* using a Cauchy formula,  $n(\lambda) = A + B/\lambda$  (fitting parameters: *A*, *B*). This was then used to determine the thickness of PEO on Si vs. spin speed. Thickness was also measured from accumulation capacitance measurements and the thinnest PEO capacitor corresponding to the 8 krpm spin was also measured by transmission electron microscopy (TEM). The electrical and TEM measurements were in agreement, but the ellipsometric thicknesses were larger by approximately 3×, perhaps indicating a shrinkage of the film over time. The frequency dependence of the impedance (*Z*-*f*) was measured in capacitors of various thicknesses biased in accumulation (with the top contact *V<sub>G</sub>* = 2 V). The impedance magnitude was well behaved, decreasing inversely with frequency while the phase remained around -90°, as expected for a simple capacitor. This ideal frequency dependence was also observed for bias conditions spanning the range of voltage used in subsequent *C*-*V* measurements. Pure-PEO capacitors were simulated in BandPro (W.R. Frensley, UT Dallas) to obtain band diagrams and simulated *C*-*V* characteristics. The modeled device was n-Si (*N<sub>D</sub>* = 110<sup>18</sup> cm<sup>-3</sup>), thickness *t<sub>PEO</sub>* = 7.4 nm, dielectric constant  $\epsilon_{PEO}$  = 1.5, band gap = 4.5 eV [4], with a metal/PEO Schottky barrier of 2.2 eV, and PEO/Si  $\Delta E_g$  of 1.2 eV. The measured *C*-*V* was in agreement with minimum and maximum (accumulation) capacitance, deviating in the depletion capacitance transition. The capacitance vs.  $1/t_{PEO}$  dependence was used to extract the dielectric constant of PEO,  $\epsilon_{PEO} \sim 1.6 \pm 0.1$ , which is consistent with a prior report for thick PEO films, ~0.25–0.40 μm [5]. PEO:CsClO<sub>4</sub> on p<sup>+</sup>-Si was ~8 nm thicker than pure-PEO when measured by ellipsometry before gate evaporation. *Z*-*f* showed that capacitors with CsClO<sub>4</sub> had a lower impedance magnitude than pure PEO and a less ideal phase between -50° and -80°. However, the accumulation capacitance at -1.6 V was only ~10% lower. [1] D. K. Efetov and P. Kim, *Phys. Rev. Lett.* 105, p. 256805 (2010). [2] K. Ueno, H. Shimotani, H. Yuan, J. Ye, M. Kawasaki, and Y. Iwasa, *J. Phys. Soc. Jpn.* 83, p. 032001 (2014). [3] C. Alessandri, S. Fathipour, H. Li, I. Kwak, A. Kummel, M.

Remškar, and A. C. Seabaugh, *IEEE Trans. Electron Dev.* 64, pp. 5217–5222 (2017). [4] V. M. Mohan, V. Raja, P. B. Bhargava, A. K. Sharma, and V. V. R. N. Rao, *J. Polymer Research* 14, pp. 283-290 (2007). [5] N. H. A. Nasir, C. H. Chan, H.-W. Kammer, L. H. Sim, and M. Z. A. Yahya, *Macromolecular Symposia* 290, pp. 46-55 (2010).

#### 12:15 PM II07

**Ultra-Stretchable Conductive Polymer Complex with Excellent Linearity and Repeatable Autonomous Self-Healing Ability** Evan K. Wujcik<sup>1</sup>, Yang Lu<sup>1</sup>, Lauren McLoughlin<sup>1</sup>, Dajung Hong<sup>2,1</sup>, Sang Gyu Yim<sup>2</sup> and Ju-Won Jeon<sup>2</sup>; <sup>1</sup>The University of Alabama, United States; <sup>2</sup>Kookmin University, Korea (the Republic of)

Wearable strain sensors are essential for the realization of applications in the broad fields of remote healthcare monitoring, soft robots, immersive gaming, among many others. These flexible sensors should be comfortably adhered to skin and capable of monitoring human motions with high accuracy, as well as exhibiting excellent durability. However, it is challenging to develop electronic materials that possess the properties of skin—compliant, elastic, stretchable, and self-healable. This work demonstrates a new regenerative polymer complex composed of poly(2-acrylamido-2-methyl-1-propanesulfonic acid) (PAAMPSA), polyaniline (PANI) and phytic acid (PA) as a skin-like electronic material. It exhibits ultrahigh stretchability (1935%), excellent repeatable autonomous self-healing ability (repeating healing efficiency > 98%), and exceptional linearity (*R*<sup>2</sup> > 0.995) — outperforming current reported wearable strain sensors. The deprotonated polyelectrolyte, multivalent anion, and doped conductive polymer, under ambient conditions, synergistically construct a regenerative dynamic network of polymer complex crosslinked by hydrogen bonds and electrostatic interactions, which enables ultrahigh stretchability and repeatable self-healing. Sensitive strain-responsive geometric and piezoresistive mechanisms of the material owing to the homogenous and viscoelastic nature provide excellent linear responses to omnidirectional tensile strain and bending deformations. Furthermore, this material is scalable and simple to process in an environmentally-friendly manner, paving the way for the next generation flexible electronics.

#### 12:30 PM II08

**Direct Re-Writeable Control of Optical Polarization and Functional Properties in Modular Donor-Acceptor Columnar Liquid Crystalline Films** Joseph Reczek; Denison University, United States

Principles of organic supramolecular chemistry offer creative design strategies for the generation of materials with tunable properties and novel functionality. Donor-acceptor columnar liquid crystals (DACLCs) are a class of supramolecular materials that self-assemble from the straight-forward mixing of two complementary aromatic components, an electron-rich donor (D) and an electron-poor acceptor (A). The alternating assembly of molecular components in DACLCs leads to an intense charge-transfer (CT) absorption band in the Vis-NIR region. The photoexcitation of CT absorption can only occur in the direction of columnar stacking, causing highly-oriented DACLC films to be strongly dichroic — essentially serving as optical polarizers in the CT region. Recently, we have achieved exquisite control over the columnar alignment and resulting optical properties of DACLC films through a method of laser-induced thermal gradient. DACLC regions can be aligned according to the direction and rate of laser writing, allowing for re-writable control of optical polarization in DACLC films down to the micron scale. We have established the angular resolution of DACLC alignment with respect to transmitted linearly polarized light (LPL) to be better than 10 degrees (> 90% confidence level). This allows for the practical “writing” of at least 18 independently discernable polarizations (0–170 degrees) thereby affording high-density encoding of images and information in films. High transmittance in the CT region of DACLCs aligned orthogonally to incoming LPL provides for additional functionality from the overlay of complementary films, offering additional applications in cryptography that span a broad range of sophistications. In this talk we will discuss the developing optical and material properties of DACLCs, as well as the mechanism and fidelity of thermal-gradient induced molecular alignment. We will also demonstrate current examples of image and data encoding and overlay cryptography using DACLC films.

#### 12:45 PM II09

**Crystallization, Carrier Transport and Device Performance of Vapor-Deposited Conjugated Polymers** Sunghwan Lee and Michael Clevenger; Purdue University, United States

Conjugated polymers have been extensively considered for use in next generation electronic and optoelectronic devices due to their cost effectiveness, mechanical flexibility, material abundance and low-thermal budget processing. Particularly, thiophene and its derivatives have been widely investigated as semiconducting active layers in organic solar cells<sup>1</sup> and organic field effect transistors<sup>2</sup>; as sensing materials in volatile organic compound sensors<sup>3</sup>; as electrochromic layers<sup>4</sup> in smart windows. Further, this class of materials have been considered as organic electrodes as well in those devices to enhance chemical compatibility with organic active layers and also to provide full mechanical flexibility compared to that of inorganic counterpart electrodes. In the field of organic electronics and optoelectronics, however, there have been long time challenging issues including: (1) achieving highly crystalline polymer

films which provides greater carrier transport and hence enhanced device performance<sup>5</sup>, and (2) air stability over time for the implementation in real-world device applications. Enhancing fundamental understanding of the intrinsic nature and structure properties of materials may lead to the establishment of strategies to address these challenging issues<sup>6</sup>. Oxidative chemical vapor deposition (oCVD) is an emerging technique to synthesize, deposit and dope conjugated polymers in a single step process at low temperatures (20-150 °C). The main advantages of the vapor phase oCVD technique include: (1) no requirements for monomer solubility in solvents; (2) no wetting issues between processed materials and underlying substrates, which is frequently reported for conventional solution-process polymers; (3) ability to coat films over large area; (4) compatibility with other current standard mass production processes. Particularly, the oCVD process that exclude any solvents during thin film growth allows for exploring polymers that have been challenging to process due to their insoluble nature such as unsubstituted polythiophene<sup>6</sup>, PEDOT (without PSS)<sup>7</sup>, polyselenophene<sup>8</sup> and polyisothianaphthene<sup>9</sup>. In this presentation, two oCVD processed conjugated polymers of unsubstituted polythiophene (PT) and PEDOT, a widely used thiophene derivative, are selected. Their amorphous/crystalline structures, valence states and chemical environments, air stability and field effect transistor (FET) device performance will be compared. Through glancing incident angle x-ray diffraction analysis, we found that oCVD PEDOT shows crystalline structures and the crystalline orientation is controlled with processing temperature and thickness of the resulting films, while PT films are in the amorphous state. It should also be noted that PT demonstrates superior air stability compared to oCVD PEDOT, solution processed PEDOT:PSS and other conjugated polymers. In addition, the carrier transport behaviors of the polymers are significantly different: PEDOT follows semi-metallic transport mechanisms; however, the transport of PT is governed by hopping conduction mechanisms. We will relate the differences in amorphous/crystalline structure, carrier transport, micro-structures to their substitution or unsubstitution in their monomer position. These findings will contribute to establishing strategies to achieve air-stability and crystallization of conjugated polymeric materials for high performance organic electronic and optoelectronic applications. <sup>1</sup> E. Bundgaard et al., Sol. Energy Mater. Sol. Cells **91** (11), 954 (2007). <sup>2</sup> S. R. Forrest, Nature **428** (6986), 911 (2004). <sup>3</sup> X. Wang et al., ACS Appl. Mater. Interfaces **7** (30), 16213 (2015). <sup>4</sup> Y. Tao et al., Electrochimica Acta **77** (0), 157 (2012). <sup>5</sup> X. Wang et al., Sci. Adv. **4** (9), eaat5780 (2018). <sup>6</sup> S. Lee et al., Org. Electron. **33**, 253 (2016). <sup>7</sup> S. Lee et al., Adv. Funct. Mater. **24** (45), 7187 (2014). <sup>8</sup> W. Jo et al., Org. Electron. **26**, 55 (2015). <sup>9</sup> D. Borrelli et al., Macromolecules **46** (15), 6169 (2013).

SESSION JJ: III-Nitrides—Processing  
 Session Chairs: Mark Goorsky and Doug Hall  
 Session Hosts: Jung-Hun Seo and Christian Wetzel  
 Friday Afternoon, June 26, 2020  
 Location: ZoomRoom 1

#### 2:00 PM JJ01

**(Student) Sc-Based Ohmic Contacts to InAlN/GaN HEMT Structures** Sai Charan Yanjari, Sandeep Vura, Muralidharan R, Srinivasan Raghavan and Digbijoy Nath; Indian Institute of Science, India

GaN HEMTs have seen rapid advancements over the past two decades because of their suitability for high-frequency and high-power applications. Contact resistance is one of the key parameters that decides the cut-off frequency of a transistor. To achieve very high cut-off frequencies, ohmic regrowth [1][2] is generally adopted not just to lower the contact resistance but also to enable deep scaling in these devices. Owing to its high surface roughness, traditional Ti/Al/Ni/Au metal stack, though capable of delivering low contact resistance is not widely preferred as ohmic stack for deeply scaled GaN HEMTs. *The objective of this work is to demonstrate an alternative Sc/Al/Ni/Au metal stack that can form a better ohmic contact with reduced surface roughness to InAlN/GaN HEMT structures.*

The InAlN/GaN HEMT structure used in this work was a MOCVD grown commercial epitaxial stack that comprised of 10 nm  $\text{In}_{0.17}\text{Al}_{0.83}\text{N}$  barrier, a 0.8 nm AlN spacer, 1  $\mu\text{m}$  thick GaN and a 300 nm buffer layer grown on HR-Si (111). The fabrication process started with mesa isolation using reactive ion etching with  $\text{BCl}_3/\text{Cl}_2$  etch chemistry. Sc (20 nm)/Al (120 nm)/Ni (30 nm)/Au (50 nm) was deposited for ohmic contacts on these samples. The samples were then subjected to different annealing conditions with temperature ranging from 700 °C to 825 °C for 60 seconds in  $\text{N}_2$  ambient using RTA. For comparison, a reference sample was processed with standard Ti (20 nm)/Al (120 nm)/Ni (30 nm)/Au (50 nm) contact scheme annealed at 780 °C for 60 seconds in  $\text{N}_2$  ambient.

For samples annealed at 780 °C, the contact resistance measured using TLM structures turned out to be 0.4-0.5  $\Omega\text{-mm}$  for both Ti/Al/Ni/Au and Sc/Al/Ni/Au metal stacks. The surface roughness measured using AFM for Ti/Al/Ni/Au was found to be 73 nm while that of Sc/Al/Ni/Au was about 38 nm. The surface morphology of the contacts became better with reduction in annealing temperature. The variation of contact resistance and surface roughness as a function of annealing temperature revealed an optimum temperature of 780 °C – 790 °C for formation of ohmic contacts (for Sc-based metal stack) with

relatively low surface roughness as compared to Ti-based contacts. EDXS analysis for the sample with Sc contact annealed at 780 °C shows partial inter-diffusion of Sc from the contact region into the GaN through the dislocations, leading to the formation of ScGaN inclusions with Sc in the immediate proximity to the InAlN barrier resulting in formation ohmic contact. Mechanism of ohmic contact formation with the Sc-based contacts will be discussed in greater detail.

References:

- [1]. Tang, Yan, et al. IEEE Electron Device Letters 36.6 (2015): 549-551.
- [2]. Shinohara, K., et al. 2012 International Electron Devices Meeting. IEEE, 2012.

#### 2:15 PM JJ02

**Ultrahigh GaN:SiO<sub>2</sub> Etch Selectivity by Addition of Al to a Cl<sub>2</sub>/Ar ICP Plasma** Clint Frye, Scott Donald, Catherine Reinhardt, Lars Voss and Sara Harrison; Lawrence Livermore National Laboratory, United States

The choice of carrier wafer was found to significantly influence etch rates, selectivity, and morphology in GaN micropillar etching in a Cl<sub>2</sub>/Ar high density ICP plasma. 4-inch fused silica, silicon, silicon carbide, sapphire, aluminum nitride, and high purity aluminum carriers were investigated. 7x7 mm<sup>2</sup> GaN on sapphire chips with a PECVD SiO<sub>2</sub> hard mask were used. The etch was performed at 2 mTorr for 10 min using Cl<sub>2</sub> and Ar gas flow rates of 28 sccm and 3.5 sccm, respectively. The table temperature was set to 200 °C and the ICP power was as maintained at 1000 W. Two RF powers (25 W and 75 W) were used to test the effects of ion bombardment. The GaN etch rate when using a sapphire carrier was the highest at 0.536  $\mu\text{m}/\text{min}$  for an RF power of 75 W. The aluminum carrier produced the slowest GaN etch rates, presumably due to the sinking of Cl<sub>2</sub> as it reacted with the aluminum. Aluminum nitride and high purity aluminum carriers yielded the highest GaN:SiO<sub>2</sub> selectivities, reaching 44:1 using aluminum nitride at 25W RF power due to significant suppression of the SiO<sub>2</sub> etch rate. It is hypothesized that the large selectivity is a result of AlCl<sub>3</sub> reacting with the SiO<sub>2</sub> mask to form a hardened aluminum silicate layer on the mask surface that is more resistant to etching. AlCl<sub>3</sub> is produced by etching the aluminum nitride carrier as confirmed by optical emission spectroscopy of the plasma. Auger electron spectroscopy (AES) obtained on the mask after etching confirms that a surface layer of the mask is composed of Al, Si, and O when using an aluminum nitride wafer. AES shows that the mask is composed of Si and O after etching when using fused silica, silicon carbide, silicon, and sapphire wafers. The aluminum carrier coated the mask, etched floor, and pillar sidewall surfaces with Al and C. Introducing Al into the plasma enhances the etch selectivity of an SiO<sub>2</sub> mask likely due to the formation of a robust surface layer of an aluminum silicate, thereby enabling deeper GaN etching without the use of a nickel hard mask. Al may also be potentially used as a passivation material during GaN etching as vertical profiles were achieved for the aluminum carrier. AES indicated a significant amount of Al on the etched sidewall. Floor pitting and trenching, sidewall roughness, and faceting were all influenced by carrier wafer type and will be discussed. Prepared by LLNL under Contract DE-AC52-07NA27344. ABS-803641

#### 2:30 PM JJ03

**(Student) Demonstration of a Wet Etch for N-Polar GaN with >40:1 Selectivity to Al<sub>0.24</sub>Ga<sub>0.76</sub>N** Emmanuel Kayede, Brian Romanczyk, Nirupam Hatui, Islam Sayed, Stacia Keller and Umesh Mishra; University of California, Santa Barbara, United States

Gallium nitride high electron mobility transistors (GaN HEMTs) are proven to be well suited devices for highly efficient solid-state radio frequency and mm-wave power amplification, especially when high output power is desired. Up to 9.4 W/mm output power density at 94 GHz has now been realized using N-polar GaN deep recess HEMTs with peak PAE exceeding 30%. During the fabrication of these, and other GaN transistors, plasma etches have been exclusively used to etch III-N layers. Relative to the Ga-polar surface, the N-polar surface offers enhanced chemical reactivity allowing for III-N layers to be etched in wet etches. Others have shown that N-polar GaN is etched with a rough surface morphology in many acidic and basic solutions. However, to date, the demonstration of a smooth etched surface that can be applied to N-polar HEMT fabrication has yet to be shown. In this work we present a selective wet etch wherein N-polar GaN is shown to etch preferentially over Al<sub>0.24</sub>Ga<sub>0.76</sub>N with a selectivity exceeding 40:1 and by utilizing the high selectivity a smooth surface can be obtained.

This study explored the etching characteristics of UID N-polar GaN, UID Al<sub>0.24</sub>Ga<sub>0.76</sub>N, and a N-polar deep recess HEMT structure. The three samples were grown on miscut sapphire substrates using established MOCVD techniques. The AlGa<sub>0.24</sub>Ga<sub>0.76</sub>N sample consisted of 20 nm of Al<sub>0.24</sub>Ga<sub>0.76</sub>N grown on a GaN template and capped by 2 nm of GaN prevent cracking. The HEMT sample is a deep recess HEMT structure with a 12 nm GaN channel, 2.6 nm Al<sub>0.24</sub>Ga<sub>0.76</sub>N cap, and 15 nm GaN cap. The samples were etched in an acidic aqueous solution at room temperature for times varying between 15 and 60 min using a patterned PECVD SiO<sub>2</sub> etch mask which was stripped in HF following the etch to evaluate the etch depth. It was observed that the GaN etched with a rate of 42 nm/hr while the AlGa<sub>0.24</sub>Ga<sub>0.76</sub>N sample etched at a rate of 1 nm/hr after accounting for the removal of the 2 nm GaN capping layer resulting in a selectivity exceeding 40:1. During the etch, no degradation in surface roughness was observed for the AlGa<sub>0.24</sub>Ga<sub>0.76</sub>N sample. On the other hand, the UID GaN sample was observed to have pyramidal structures. However, when

applied to a HEMT sample and utilizing an over etch, the size and density of these structures was shown to be reduced for longer etch times. These results demonstrate the feasibility of a wet etch that can be used to replace the traditional dry etch processes. For instance, this selectivity of this wet etch is significantly greater than the 15:1 selectivity observed in our normal  $\text{BCl}_3/\text{SF}_6$  ICP etch used to recess the GaN cap. This process of wet etching N-polar GaN has the potential for reducing fabrication costs and increasing process margin of GaN HEMTs.

#### 2:45 PM JJ04

**(Student) Chemical Wet Etching of AlGaIn Nanostructures** Barbara A. Kazanowska<sup>1</sup>, Keshab R. Sapkota<sup>2</sup>, Andrew Allerman<sup>2</sup>, Brendan P. Gunning<sup>2</sup>, Kevin S. Jones<sup>1</sup> and George T. Wang<sup>2</sup>; <sup>1</sup>University of Florida, United States; <sup>2</sup>Sandia National Laboratories, United States

AlGaIn is a leading candidate for current and future ultra-wide bandgap electronic (e.g. power electronics and sensors) and optoelectronic (e.g. deep-UV light emitting diodes (LEDs) and lasers) applications. However, three-dimensional (3D) etch technologies for AlGaIn remain immature compared to both silicon and even GaN, limiting the full potential for novel devices. A more robust development of three-dimensional top-down etch techniques is required as current chemical wet etch processes are significantly underdeveloped due to a substantial chemical inertness of Ga-polar surfaces to common industry etchants. It has been previously reported that strong acids ( $\text{H}_3\text{PO}_4$ ) and molten salts (KOH) can be used to smoothly etch non-polar and semi-polar facets in GaN. Here, we build from the foundation of anisotropic KOH-based wet etchants for GaN nanostructures and explore AlGaIn alloys. We perform the first nonpolar orientation-dependent etch rate measurements for AlGaIn as a function of Al content. Additionally, in conjunction with a two-step top-down fabrication process developed at Sandia National Laboratories, we investigate here the effect of  $\text{H}_3\text{PO}_4$  etching on high aspect ratio GaN and AlGaIn nanowires. We present the time dependent etch evolution as a function of temperature leading to tapered nanowires with sharp tips measured on the order of 10 nm in diameter. Sandia National Laboratories is a multi-program laboratory managed and operated by NTESS Corporation, a wholly owned subsidiary of Honeywell Corporation, for the U.S. Department of Energy's National Nuclear Security Administration under contract DE-NA0003525.

#### 3:00 PM JJ05

**Low Temperature, Au-Free Ohmic Contacts to n-GaN** Jacob Leach and Jaime Rumsey; Kyma Technologies, United States

GaN-based electronic devices have made great headway in the arena of MMICs for RF applications and switching elements for power electronics applications. The ability to make low resistance Ohmic contacts to GaN is of critical importance to realizing highly efficient devices, and such contacts typically make use of a high temperature annealing process in order to realize the lowest resistivities. The use of such high temperature processes for Ohmic contacts thus constrains the overall process order that can be used for device fabrication since gate metallization and dielectric layers typically cannot be subjected to such high temperatures for Ohmic contact annealing (typical temperatures are 800C or above). In this work, we outline our progress toward the development of an Ohmic contact process that does not require a high temperature anneal and thus is suitable for use in a gate-first transistor fabrication process. We employed a metal stack consisting of AlSi/Ti/AlSi/W and anneal in the range of 350-550C under  $\text{N}_2$  at atmospheric pressure to realize Ohmic contacts with specific contact resistivities as low as  $2 \times 10^{-3} \Omega \text{cm}^2$  on bulk GaN substrates with carrier concentrations of  $3 \times 10^{17} \text{cm}^{-3}$  for an annealing temperature of 450°C. Preliminary results exhibit lower values when utilizing this scheme on more heavily doped GaN layers. In addition to this, the metal remains very smooth after annealing, which is beneficial for applying this scheme to GaN-based nanostructured devices. Furthermore, our AlSi/Ti/AlSi/W stack is Au-free, which is of potential interest for GaN processing being performed in Si foundries.

#### 3:15 PM BREAK

SESSION KK: III-Nitrides—Defects and Characterization  
Session Chairs: Mark Goorsky and Doug Hall  
Session Hosts: Jung-Hun Seo and Christian Wetzel  
Friday Afternoon, June 26, 2020  
Location: ZoomRoom 1

#### 3:45 PM KK01

**(Student) Identification of Point Defects for the Full Compositional Range of  $\text{Al}_x\text{Ga}_{1-x}\text{N}$  (0 ≤ x ≤ 1) via Photoluminescence** Ji Hyun Kim<sup>1</sup>, Isaac Bryan<sup>1</sup>, Ronny Kirste<sup>2</sup>, Zachary Bryan<sup>1</sup>, Pramod Reddy<sup>2</sup>, Doug Irving<sup>1</sup>, Ramón Collazo<sup>1</sup> and Zlatko Sitar<sup>1</sup>; <sup>1</sup>North Carolina State University, United States; <sup>2</sup>Adroit Materials, United States

GaN, AlN, and its ternary alloy have had significant development and implementation in devices due to its wide range of applications in UV optoelectronics and power devices. However, it is subject to various point

defects that can severely limit their electrical and optical properties. Therefore, the correct identification and understanding of such point defects is imperative for developing methods to reduce or eliminate undesirable defects while promoting the right defect configurations that will lead to the properties needed for the devices. The defects discussed in this work include self-compensating native defects, unintentional impurities, and various defect complexes. For example, the widely discussed  $\text{C}_{\text{N}}$  defect,  $\text{V}_{\text{N}}$  defect, and  $\text{V}_{\text{III}}$  related complexes are included. These are mainly point defects that are commonly present in undoped and doped  $\text{Al}_{1-x}\text{Ga}_x\text{N}$  of different compositions with various doping levels of n and p-type dopants such as Si, Ge, and Mg.

The main characterization technique utilized is Photoluminescence (PL) for the identification of point defects in GaN, AlN, and its ternary alloy. While PL is a commonly used technique, analyses of the spectra are a major topic of debate in the community. Point defect identification has been based on the iteration between DFT studies, evolving based on availability of new computational methods, and characterization, with higher accuracy possible due to sample quality improvements. However, hybrid functional DFT models, expected to provide accurate point defect energetic models, still have limitations with estimations for ternary alloys. This study utilizes defect transition energy values of GaN and AlN as suggested by hybrid functional models but confirmed by PL measurements on systematically grown samples with controlled point defect configurations as end points to experimentally identify the defect transition energy values in AlGaIn. The measured PL spectra of the samples grown with known growth parameters to produce the defect of interest helps trace the transition energy of the defect over the entire Al composition of AlGaIn. Based on these observations, it is established that the defect energies increase with the increase of Al content. However, the transition energy values of the point defects do not exhibit a linear trend, but rather follow the similar AlGaIn bandgap trend as a function of Al content as described by Vegard's law with a bowing parameter. With this defined relationship, this work aims to provide up-to-date identifications of common point defects and their energies for the entire Al composition range for the future development of AlGaIn based technologies.

#### 4:00 PM KK02

**(Student) Self-Compensation Management in Ge and Si Doped  $\text{Al}_{0.4}\text{Ga}_{0.6}\text{N}$  by Chemical Potential Control** Pegah Bagheri<sup>1</sup>, Shun Washiyama<sup>1</sup>, Ji Hyun Kim<sup>1</sup>, Ronny Kirste<sup>2</sup>, Pramod Reddy<sup>2</sup>, Yan Guan<sup>1</sup>, Andrew J. Klump<sup>1</sup>, Ramón Collazo<sup>1</sup> and Zlatko Sitar<sup>1</sup>; <sup>1</sup>North Carolina State University, United States; <sup>2</sup>Adroit Materials, United States

Significant challenges in point defect control in AlGaIn epitaxy has complicated the realization of AlGaIn based devices. Si and recently Ge are typically employed as n-type dopant in AlGaIn which exhibit a low activation energy (<50 meV) in  $\text{Al}_{1-x}\text{Ga}_x\text{N}$  with  $x < 0.8$  and  $x < 0.5$ , respectively. However, Si and Ge doped AlGaIn exhibits a “knee behavior” resulting in a conductivity and carrier concentration maxima at a specific dopant concentration. Hence a high doping limit exists for n-AlGaIn that lowers the maximum achievable carrier concentrations.

In this work, we demonstrate a systematic chemical potential control (CPC) based point defect control (PDC) where we relate the growth environment variables to the defect formation energy. This is realized by determining and controlling the impurity chemical potentials through the growth environment to achieve minimal point defect incorporation or generation. Here, we employed this framework to provide a quantitative relationship between point defect formation energies and growth process parameters for the case of Si and Ge doping in  $\text{Al}_{0.4}\text{Ga}_{0.6}\text{N}$ . This allowed for the classification of the differences between these two dopants in terms of incorporation and major compensating defect formation.

The  $\text{V}_{\text{III}}\text{-nSi}_{\text{III}}$  and  $\text{V}_{\text{III}}\text{-nGe}_{\text{III}}$  complexes were identified as the primary defects responsible for the doping limits in  $\text{Al}_{0.4}\text{Ga}_{0.6}\text{N}$  grown by MOCVD on c-plane sapphire substrate. We demonstrate control over the knee behavior (improving the peak carrier concentration) by controlling the III/N chemical potentials and growth temperature. For the case of Ge doped AlGaIn with Al composition of 40%, a plateau with constant carrier concentration ( $1\text{-}2 \times 10^{19} \text{cm}^{-3}$ ) followed by a sharp drop (one order of magnitude to  $10^{18} \text{cm}^{-3}$ ) in carrier concentration is observed which differs from the Si “sharp knee” doping behavior. This behavior corresponds to the formation of different types of complexes during Ge doping in contrast to Si doping. The reduced conductivity ( $8 \Omega^{-1}\text{cm}^{-1}$ ) was increased to  $64 \Omega^{-1}\text{cm}^{-1}$  by decreasing  $\text{NH}_3$  flow rate from 3 slm to 1 slm, which results in a III-rich growth environment and a high formation energy of cation vacancy-related point defects. We also demonstrate a strong increase in vacancy formation with increase in growth temperature and consequently a higher peak conductivity is obtained at lower growth temperatures. Noticeable differences in “knee” behavior of Ge and Si in AlGaIn provides a better platform for self-compensation control in Ge doped AlGaIn via chemical potential control.

1. Reddy, P. *et al.* Improving the Conductivity Limits in Si Doped Al Rich AlGaIn. in *2018 IEEE Research and Applications of Photonics In Defense Conference (RAPID)* 1–4 (IEEE, 2018). doi:10.1109/RAPID.2018.8508932.

#### 4:15 PM KK03

**(Student) Improved Irradiation Hardness of High Aluminum Content AlGaN Polarization Doped Field Effect Transistors** Patrick H. Carey<sup>1</sup>, Fan Ren<sup>1</sup>, Jinho Bae<sup>2</sup>, Jihyun Kim<sup>2</sup> and Stephen J. Pearton<sup>1</sup>; <sup>1</sup>University of Florida, United States; <sup>2</sup>Korea University, Korea (the Republic of)

Spacecraft are subject to significant environmental damage by various fluxes of high energy radiation that make design and implementation more difficult than their permanently terrestrial operating counterparts. One of the most challenging aspects for electronic design is providing sufficient radiation protection to sensitive electronic components at the tradeoff of a higher weight and higher cost for heavier payloads. The strong chemical bonds present in binary and ternary alloys of III-Nitrides make these intrinsically radiation resistant for high dose applications. A measure of this radiation resistance is the mean displacement energy, which for GaN and SiC are approximately 19.8 eV and 21 eV, respectively, significantly higher than that of GaAs, 9.8 eV. To improve even further, a shift to high Aluminum content AlGaN devices may provide superior device longevity in radiative environments. With a polarization doped field effect transistors (POLFETs) there are several key distinctions from High Electron Mobility Transistors (HEMTs), a 2DEG is not formed but rather a 3D electron slab. Additionally, impurity doping is not needed to form quality Ohmic contacts, which removes the effects of impurity scattering, a key improvement for high frequency operation. In this study, High Aluminum content AlGaN POLFETs were irradiated separately with both protons and alpha particles, the two primary components of radiation, to determine the damages induced by each type of radiation. Traditional GaN Si<sub>x</sub> MISHEMT devices were irradiated alongside for comparison of characteristics.

Proton irradiation was performed at an energy of 10 MeV and fluences of  $1 \times 10^{14} \text{ cm}^{-2}$  and  $3 \times 10^{14} \text{ cm}^{-2}$ . The POLFET DC saturation current exhibited a 21 and 36% reduction at fluences of  $1 \times 10^{14} \text{ cm}^{-2}$  and  $3 \times 10^{14} \text{ cm}^{-2}$ , respectively. The carrier removal rates for this energy was  $677 \text{ cm}^{-1}$ . However, switching current at 100 kHz demonstrated near ideal performance by matching the DC output, as opposed to near complete current collapse in irradiated GaN HEMTs. Alpha particle irradiation was performed at 18 MeV with fluences of  $1 \times 10^{13} \text{ cm}^{-2}$  and  $3 \times 10^{13} \text{ cm}^{-2}$ . The POLFETs underwent a reduction in DC saturation current of 23% and 33%, respectively, with a carrier removal rate of  $2520 \text{ cm}^{-1}$ . The same observation was noted in that switching at 100 kHz was near ideal with no degradation, while the GaN devices underwent complete current collapse.

A primary reason for this massive improvement in switching performance is the incorporation of higher amounts of aluminum within the channel layer. Considering the binary bulk case of GaN versus AlN, the electron density ( $N_e Z_p/M$ ) is approximately double. This leads to shorter electronic stopping distance in GaN, e.g. higher energy loss of incident atoms. Another key consideration is that the GaN HEMT contain a 2DEG; therefore, defects are likely to scatter electrons from the channel into the barrier layer or the channel layer, leading to current reduction and quicker formation of a virtual gate from trapped electrons. For the POLFETs, which utilize a 3DES, the likelihood of scattering outside the channel is greatly reduced, as scattering events within the approximately 55 nm thick channel will not necessarily lead to current loss. Trapping events also are less likely to lead to loss of current as the channel has significant depth.

The novel high aluminum content POLFETs have these two distinct advantages over their GaN HEMT competitors and demonstrate significant improvements and potential in medium frequency switching performance for extraterrestrial applications.

#### 4:30 PM KK04

**(Student) Photoluminescence Study of Non-Polar m-Plane InGaN and Near Strain-Balanced AlGaN/InGaN Superlattices** Yang Cao<sup>1</sup>, Brandon Dzuba<sup>1</sup>, Brenden Magill<sup>2</sup>, Alexander Senichev<sup>1</sup>, Trang Nguyen<sup>1</sup>, Rosa Diaz<sup>1</sup>, Michael Manfra<sup>1</sup>, Steve Magill<sup>3</sup>, Carlos Garcia<sup>3</sup>, Giti Khodaparast<sup>2</sup> and Oana Malis<sup>1</sup>; <sup>1</sup>Purdue University, United States; <sup>2</sup>Virginia Tech, United States; <sup>3</sup>National High Magnetic Field Laboratory, United States

We present a detailed study of photoluminescence (PL) as a function of temperature for non-polar bulk In<sub>x</sub>Ga<sub>1-x</sub>N ( $x < 0.22$ ) layers and near strain-balanced In<sub>0.09</sub>Ga<sub>0.91</sub>N/Al<sub>0.15</sub>Ga<sub>0.85</sub>N superlattices grown by plasma-assisted molecular-beam epitaxy (PAMBE) on free standing m-plane GaN substrates. The InGaN thin films were selected to examine the effect of In-composition alone on optical properties. The superlattices were designed primarily to increase the conduction-band offset between the InGaN quantum wells (QW) and AlGaN barriers for applications in novel near-infrared intersubband devices. By tuning the strain between InGaN, AlGaN, and GaN, we are able to design nearly strain-balanced structures for future device fabrication. While the PL characterization of c-plane InGaN thin layers and InGaN/(Al)GaN quantum wells has been reported extensively, there are much fewer published studies of m-plane InGaN or InGaN/(Al)GaN quantum wells. Moreover, most of the published PL investigations of m-plane InGaN or InGaN/(Al)GaN quantum wells to date were done on structures grown by metal-organic chemical-vapor deposition (MOCVD). The PL transition energies were found to be consistently lower than the calculations using structural parameters obtained from high-resolution x-ray diffraction (HRXRD). The discrepancy is stronger for superlattices than for bulk InGaN films. Since exciton localization in high-In regions dominates interband transitions, this discrepancy is very likely due to

inhomogeneous In incorporation. If the effect of strain is ignored, the discrepancy between experiment and calculations is smaller for InGaN layers. Therefore, an overestimation of the effect of strain on the bandgap of InGaN is a possible alternative explanation for this discrepancy. The temperature dependence of PL energies is non-monotonic but similar to that observed for polar c-plane InGaN layers or InGaN/(Al)GaN quantum wells (commonly referred to as "S-shape" curve) and is also attributed to In composition fluctuations. At 80 K, the PL full width of half maximum (FWHM) for the m-plane InGaN layers increases with In composition. The FWHM for an InGaN layer with 11% Indium is close to the theoretical calculation assuming a binomial Indium distribution. The spectral width of the low-temperature PL of our m-plane InGaN/AlGaN superlattices is narrower than previously reported for m-plane InGaN/GaN quantum wells grown by MOCVD. The charge localization depth in our undoped superlattices is evaluated to be  $\sim 13 \text{ meV}$ , much lower than previously reported for single m-plane InGaN/GaN quantum wells. The PL integrated intensity drops rapidly as the temperature is increased to 300 K, indicating strong non-radiative recombination at room temperature, which is likely due to the lower growth temperature in PAMBE than in MOCVD. Time-resolved PL at low temperatures was performed to characterize the relaxation time scales in an undoped as well as a doped superlattice. The time constants are much shorter than the measured values in c-plane quantum wells, indicating more efficient recombination in m-plane structures than in c-plane structures. Intentional doping in the barriers increases the PL peak width significantly for superlattices. Identifying the exact cause of this broadening is of practical interest for devices and will be pursued in future studies. YC, TN, and OM acknowledge partial support from NSF grant ECCS-1253720. AS and BD were supported from NSF award ECCS-1607173. GAK and BAM acknowledge the support from AFOSR under Grant FA9550-17-1-0341. A portion of this work was performed at the National High Magnetic Field Laboratory, which is supported by the National Science Foundation Cooperative Agreement No. DMR-1157490 and the State of Florida.

#### 4:45 PM KK05

**(Student) Electric Field Measurement Using Franz-Keldysh Photocurrent Spectroscopy in GaN Devices** Darpan Verma, Adnan Md Mohsinur Rahman, Mohammad Wahidur Rahman, Siddharth Rajan and Roberto C. Myers; The Ohio State University, United States

GaN power electronics and optoelectronic devices under high field suffer from frequent breakdown due to material inhomogeneity and junction structures that lead to hot spots. Under high bias, semiconductors exhibit the Franz-Keldysh (F-K) effect because of band bending resulting in optical absorption for photon energy below the bandgap. Previously, the impact of the F-K effect in GaN based semiconductor device was modeled using bias dependent photocurrent to calculate the electric field [1, 2]. Here we discuss spectrally-resolved F-K effect measurements in GaN p-n junction diodes revealing the effective absorption edge to be lowered from 3.29 eV to 3.19 eV with increasing applied reverse bias [3]. The F-K effect also causes broadening of the exponential tail in the photocurrent spectra. We show that this bias-dependent photocurrent spectral lineshape can be fit to a model of the F-K effect to determine the local total bias across the p-n junction. While the maximum average electric field across the whole device is in the range 0.6-1.1 MV/cm at the particular measurement position it is 0.2 – 0.5 MV/cm. This indicates the measurement position is an electrostatic cold spot, e.g. fringing field. Since this field measurement relies on fitting the spectra lineshape, it is independent of position-dependent optical reflection changes and other spatial variations in quantum efficiency. Thus, this method could allow mapping of the electric field to pinpoint the breakdown regions (hot spots) and electrostatic cold spots in wide bandgap devices.

**Acknowledgment:** The information, data, or work presented herein was funded in part by the Advanced Research Projects Agency-Energy (ARPA-E), U.S. Department of Energy, under Award Number DE-AR0001036. The views and opinions of authors expressed herein do not necessarily state or reflect those of the United States Government or any agency thereof.

**References:** [1] T Maeda, T Narita, M Kanechika, T Uesugi, T Kachi, T Kimoto, M Horita, and J Suda, Appl. Phys. Lett. **112**, 252104 (2018). [2] T Maeda, M Okada, M Ueno, Y Yamamoto, M Horita, and J Suda, Appl. Phys. Express **9**, 91002 (2016). [3] D Verma, M M R Adnan, M W Rahman, S Rajan, R C Myers, arXiv:2001.03583

SESSION LL: Narrow Bandgap Materials and Devices  
Session Chair: Sanjay Krishna  
Session Hosts: Nicole Pfister and Daniel Wasserman  
Friday Afternoon, June 26, 2020  
Location: ZoomRoom 2

#### 2:00 PM LL01

**(Student) Modeling and Measurement of Impact Ionization in Al<sub>x</sub>In<sub>1-x</sub>As<sub>y</sub>Sb<sub>1-y</sub> Digital Alloys** Stephen D. March<sup>1</sup>, Andrew H. Jones<sup>2</sup>, Joe C. Campbell<sup>2</sup> and Seth R. Bank<sup>1</sup>; <sup>1</sup>The University of Texas at Austin, United States; <sup>2</sup>University of Virginia, United States

Low-noise, high-gain avalanche photodetectors (APDs) for telecommunication-wavelength sensing are difficult to realize due to the stochastic nature of the

impact ionization gain mechanism, which leads to variation in the gain, parameterized by the excess noise factor. Staircase APDs proposed by Capasso [1] mitigate this noise source by localizing impact ionization at deterministic locations within the device and minimizing the gain variation. First attempts to realize the staircase APD using  $\text{Al}_x\text{Ga}_{1-x}\text{As}$  [2, 3] and  $\text{Al}_x\text{Ga}_{1-x}\text{In}_{1-x-y}\text{As}$  [4] suffered from insufficient band offsets to achieve the desired avalanche gain characteristics. We recently demonstrated the successful growth of digital alloy  $\text{Al}_x\text{In}_{1-x}\text{As}_y\text{Sb}_{1-y}$  materials [5] that provide the necessary band offsets and used these materials to realize the first staircase APD, but only with a single step [6]. Scaling to higher staircase step counts to increase amplification requires knowledge of the impact ionization dynamics in these materials. In this work, we used the single-step staircase architecture to explore these dynamics by modifying the band structure profile and studying the resultant gain characteristics via light and dark current-voltage (I-V) measurements. In addition, we complemented these measurements with Monte Carlo and electrostatic modeling to determine the key impact ionization parameters that should be considered when designing multi-step staircase APDs using  $\text{Al}_x\text{In}_{1-x}\text{As}_y\text{Sb}_{1-y}$  digital alloys. Single-step staircase APD structures were grown using molecular beam epitaxy on (001)-oriented GaSb substrates with varied conduction band profiles to modulate the relevant transport parameters, namely: field drift energy, step scattering loss, ionization mean free path length, and relative ionization threshold energy. Photo-gain obtained from I-V measurements were paired with Monte Carlo simulations that track carrier transport phenomena. Staircase results were compared against traditional p-i-n APD architecture at similar gain conditions and exhibited a much tighter spread in impact ionization location and significantly broader impact ionization energy threshold distribution. Step efficiency, parameterized by the probability of impact ionization at the step edge [7], was calculated from I-V and Monte Carlo to highlight the optimal design parameters that should be considered when developing APDs that use the  $\text{Al}_x\text{In}_{1-x}\text{As}_y\text{Sb}_{1-y}$  digital alloy material system. Additional temperature-dependent tests are in progress to further qualify and quantify scattering mechanisms, as well as their impact on impact ionization performance. This work was supported by the Army Research Office (W911NF-17-1-0065) and DARPA. References: [1] F. Capasso, IEEE Trans. Nucl. Sci. 30, 424 (1983). [2] G. Ripamonti, et al., *Nucl. Instrum. Methods Phys. Res., Sect. A*, vol. 288, no. 99 (1990). [3] M. Toivonen, et al., *Electron. Lett.* vol. 28, no. 32 (1992). [4] M. Tsuji, et al., *Jpn. J. App. Phys.*, vol 33 (1994). [5] S.J. Maddox, et al., *57<sup>th</sup> Electronic Materials Conf. (EMC)*, Columbus, OH (2015). [6] M. Ren, et al., *73<sup>rd</sup> Device Research Conf. (DRC)*, Columbus, OH (2015). [7] K. Matsuo, et al., *J. Lightwave Tech.*, vol 3, no. 6 (1985)

## 2:15 PM LL02

**(Student) Temperature Stability of III-V Digital Alloy Bandgaps** Ann K. Rockwell<sup>1</sup>, Andrew H. Jones<sup>2</sup>, Yuan Yuan<sup>2</sup>, Xingjun Xue<sup>2</sup>, Stephen D. March<sup>1</sup>, Joe C. Campbell<sup>2</sup> and Seth R. Bank<sup>1</sup>; <sup>1</sup>The University of Texas at Austin, United States; <sup>2</sup>University of Virginia, United States

We recently demonstrated the successful growth of low-noise,  $k \sim 0.01$  to 0.05,  $\text{Al}_x\text{In}_{1-x}\text{As}_y\text{Sb}_{1-y}$  on GaSb and  $\text{In}_{0.52}\text{Al}_{0.48}\text{As}$  on InP avalanche photodiodes (APDs), comparable to that of current state-of-the-art silicon detectors, by utilizing the digital alloying growth technique [1, 2]. In addition to the excess noise factor, the temperature stability of APDs is incredibly important in applications, including single photon detectors operating in the Geiger-mode. An APD exhibits a proportional relationship between temperature and the bias required to maintain breakdown, with typical levels necessitating temperature regulation. This is parameterized by the breakdown voltage temperature coefficient,  $\Delta V_{\text{bd}}/\Delta T$ , with a smaller value being preferred. Interestingly, we have seen that the  $\text{Al}_x\text{In}_{1-x}\text{As}_y\text{Sb}_{1-y}$  digital alloys exhibit a significantly reduced value of  $\Delta V_{\text{bd}}/\Delta T$ ,  $\sim 5\text{mV/K}$ , compared with most APD materials, including Si, InP, and random InAlAs [3]. We have found that  $\text{Al}_x\text{In}_{1-x}\text{As}_y\text{Sb}_{1-y}$  and  $\text{In}_{0.52}\text{Al}_{0.48}\text{As}$  digital alloys exhibit reduced bandgap temperature dependence, which could explain the anomalously low  $\Delta V_{\text{bd}}/\Delta T$  values observed in Ref. 3. This work seeks to understand how the digital alloying technique increases APD temperature stability.

All samples in this work were grown on either GaSb, InP, or InAs substrates by solid-source molecular beam epitaxy. In each sample, the digital alloy was strain-balanced to the corresponding substrate by varying the relative thicknesses of the individual constituent binary or ternary layers. The temperature stability of the bandgap was measured with both photoluminescence (PL) and spectrally-resolved photocurrent, in which the sample or device was placed in a nitrogen-cooled cryogenic chamber for precise temperature control. With temperature dependent PL, we observed a weaker bandgap temperature dependence of InAlAs digital alloys than their random alloy counterpart, and a decrease in bandgap temperature dependence with increasing period thickness. Photocurrent results were consistent with the PL experiments; we found that InAlAs random alloy PIN diodes showed a bandgap temperature dependence of about  $-0.59\text{meV/K}$  while a comparable digital alloy InAlAs PINs showed a much smaller temperature dependence of only  $-0.34\text{meV/K}$ . In order to more fully characterize the temperature dependence of the digital alloys, experiments on a wider range of period thickness APDs are ongoing and will be reported at the conference. This work was supported by the Army Research Office (W911NF-17-1-0065) and DARPA (GG11972.153060).

[1] S.J. Maddox, et al., *57<sup>th</sup> Electronic Materials Conf. (EMC)*, Columbus, OH (2015).

[2] A.K. Rockwell, et al., *Appl. Phys. Lett.*, 113, 102106 (2018).

[3] A.H. Jones, et al., *Optics Express*, 25, 24340 (2017).

## 2:30 PM LL03

**(Student) Characterizing the Optical and Electrical Properties of Al<sub>x</sub>In<sub>1-x</sub>As<sub>y</sub>Sb<sub>1-y</sub> Digital Alloys** Joshua A. McArthur, Stephen D. March, Ann K. Rockwell, Andrew F. Briggs and Seth R. Bank; The University of Texas at Austin, United States

$\text{Al}_x\text{In}_{1-x}\text{As}_y\text{Sb}_{1-y}$  grown as a lattice-matched digital alloy on GaSb substrates (henceforth referred to as AlInAsSb) recently emerged as a promising material system for avalanche photodetectors (APD) operating at near- to mid-IR wavelengths. In particular, AlInAsSb possesses a broadly tunable bandgap over a wide alloy composition range, as well as favorable band offsets that lead to excess low-noise avalanche multiplication gain. [1] This makes them favorable compared to bulk APDs, like Si, which lack the bandgap flexibility for spectral response at telecom and mid-IR wavelengths [2]. Unfortunately, many of the AlInAsSb optical and electrical properties remain relatively unknown. Specifically, absorption coefficients and background carrier concentrations must be determined to advance AlInAsSb detector design and performance. A few key challenges prevent collecting electrical and optical data on samples as grown. For example, transmission-type measurements to determine absorption spectra are obscured by the bandedge of GaSb at  $\sim 1.7\ \mu\text{m}$  and free carrier absorption at longer wavelengths. This obstruction coincides with the  $\text{Al}_x\text{In}_{1-x}\text{As}_y\text{Sb}_{1-y}$  direct bandgap range (0.25-1.24 eV) for aluminum concentrations of  $x > 0.4$ . Furthermore, direct carrier concentrations are challenging to measure because of the conductive GaSb substrates [3] with background carrier concentrations of  $\sim 10^{17}\text{cm}^{-3}$  [4]. In order to avoid parallel conductive channels through the GaSb substrate, more complex and less desirable CV measurements are currently required to accurately determine carrier concentrations in AlInAsSb, involving the growth of thick i-region PIN diodes. Transfer to an insulating and transparent platform would greatly simplify both optical and electrical measurements of key fundamental material properties. Here we present the transfer of epi-films to transparent, insulating substrates to directly measure the optical and electrical properties of AlInAsSb digital alloys. First grown by MBE, the samples were then adhered epi-side-down to a glass slide or sapphire wafer. Then, using an etch process described by Grzesik [5], the substrate and etch-release layers were selectively removed, leaving the digital alloy region on the new target substrate. Transmission and reflection spectra were measured using a Fourier transform infrared spectroscopy microscope from which absorption spectra were calculated accounting for multiple internal reflections [6]. Preliminary data suggests that this method was successful in isolating AlInAsSb from the GaSb substrate. Band edge absorption from AlInAsSb was observed for aluminum concentrations near  $x=0.2$ , which was previously obscured by GaSb absorption. The absorption coefficient,  $\alpha$ , for this concentration was measured to be  $\sim 10^4\text{cm}^{-1}$ . Different aluminum concentration samples are being prepared to examine the compositional dependence of absorption. In addition, Hall measurements to determine background carrier concentrations are in progress and will be presented at the conference. This work was supported by the National Science Foundation (DMR-1839175 and CCF-1838435). References: [1] S.J. Maddox, et al. *Crystal Growth Des.* 2016. [2] S.J. Maddox, et al. *SPIE Vol.* 9854. 2016 [3] Virkkala, et al. *Phys Rev B.* 2012 [4] WaferTech GaSb Wafer Datasheet [5] Grzesik, et al. *J Electron Mater.* 2013 [6] Look, et al. *J Vacuum Science and Tech.* 2016

## 2:45 PM LL04

**Leveraging Air-Bridge Architectures for Enhanced Spectral Utilization and Thermophotovoltaic Conversion Efficiency with In<sub>0.53</sub>Ga<sub>0.47</sub>As Cells** Tobias Burger, Dejiu Fan, Sean McSherry, Byungjun Lee, Stephen R. Forrest and Andrej Lenert; University of Michigan, United States

Thermophotovoltaic (TPV) converters offer a solid-state approach for conversion of locally emitted thermal radiation to electrical power. Given current performance standards and module costs (i.e.,  $\$/W$ ), TPVs may be suitable for certain niche applications, such as extraterrestrial power generation for deep space exploration or remote power generation. However, development of highly efficient TPV cells would enable widespread application in grid-scale energy storage, distributed co-generation, and direct solar energy conversion. TPV converters rely on wavelength-selective transport to facilitate high-efficiency operation. While absorption of above-bandgap (in-band) photons is necessary for achieving the technology's characteristically high power densities, suppression of low energy (out-of-band) photons is necessary to eliminate parasitic loss pathways and enable efficient operation. Utilization of TPV cells with high out-of-band reflectance for recycle of unusable radiation back to the emitter has enabled superior spectral utilization compared to competing approaches, including use of wavelength-selective thermal emitters. However, cell features currently utilized to promote out-of-band reflectance (metallic back surface reflectors, Bragg/plasma filters, and photonic crystals) suffer from considerable parasitic absorption and have yet to surpass 95% out-of-band reflectance. Here, we report the development of a thin-film  $\text{In}_{0.53}\text{Ga}_{0.47}\text{As}$  TPV cell with an air-bridge architecture, exhibiting  $>98\%$  reflectance of out-of-band power, enabled by lossless Fresnel reflection at the  $\text{In}_{0.53}\text{Ga}_{0.47}\text{As}$ -air interface and  $<2\%$  loss at the air-Au interface. These properties represent the best spectral control among TPV converters to date and enable record-high conversion efficiency, as characterized under illumination by a  $1200^\circ\text{C}$  blackbody emitter. Further, we demonstrate that the quality of

spectral utilization becomes less sensitive to cell bandgap in this high reflectance regime, which relaxes the otherwise strict requirement for matching emitter temperature to cell bandgap. This approach may enable use of more affordable PV materials, like Si, for TPV converters and facilitate commercialization.

### 3:00 PM LL05

#### MBE Growth of Doped Bi<sub>2</sub>Se<sub>3</sub>—Toward True Topological

**Insulators** Patrick Taylor<sup>1</sup>, Siddharth Tyagi<sup>2</sup>, Isaak Mayergoyz<sup>2</sup>, Greg Stephen<sup>2</sup>, Adam Friedman<sup>2</sup>, Michael Dreyer<sup>2</sup>, David Bowen<sup>2</sup>, Dan Hinkel<sup>2</sup>, Robert Butera<sup>2</sup>, Charles Krafft<sup>2</sup>, Brandi Wooten<sup>3</sup>, Joseph P. Heremans<sup>3</sup>, Peter Litwin<sup>4</sup>, Jiwei Lu<sup>4</sup> and Stephen McDonnell<sup>4</sup>; <sup>1</sup>U.S. Army Research Laboratory, United States; <sup>2</sup>University of Maryland, United States; <sup>3</sup>The Ohio State University, United States; <sup>4</sup>University of Virginia, United States

Topological Insulator (TI) materials promise a wide variety of fascinating new integrated device technologies that could leverage the unique spin-polarized surface currents coupled with the complete absence of bulk transport. In practice, however, achieving true bulk insulation in common TI materials remains a significant challenge. Bismuth selenide, Bi<sub>2</sub>Se<sub>3</sub>, is an interesting topological material because 1) it offers one of largest bulk band gap<sup>1</sup> values of known TIs such that bulk intrinsic carriers can be small, 2) the Dirac bands appear separated from bulk bands to minimize scattering<sup>1</sup>, and 3) spin-orbit torque efficiency values are among the highest in the literature.<sup>2,3</sup> However, Bi<sub>2</sub>Se<sub>3</sub> typically displays near degenerate n-type bulk carriers<sup>4</sup> caused by the appearance of selenium vacancies within the crystal structure. This remains a challenge towards efficient devices. In this work, we present results from efforts to reduce the background n-type carriers in MBE-grown Bi<sub>2</sub>Se<sub>3</sub> through the use of dopants including Sn, Pb, and Sr. We will present results from transport measurements, thermal measurements, and scanning tunneling spectroscopy (STS) (Fig. 1) to show that the Fermi level may be positioned closer to the mid-gap Dirac states and approach true bulk insulator behavior by suitable choice of dopants.

1. H. Zhang, C. Liu, X. Qi, X. Dai, Z. Fang, S.-C. Zhang, *Nature Physics*, Vol. 5, p.438 (2009); 2. Y. Wang, D. Zhu, Y. Wu, Y. Yang, J. Yu, R. Ramaswamy, R. Mishra, S. Shi, M. Elyasi, K. Teo, Y. Wu, H. Yang, *Nature Communications*, Vol. 8, Article number: 1364 (2017) 3. J. Han, A. Richardella, S. Siddiqui, J. Finley, N. Samarth, L. Liu, *Phys. Rev. Lett.* 119, 077702 (2017); 4. A. Mellnik, J. Lee, A. Richardella, J. Grab, P. Mintun, M. Fischer, A. Vaezi, A. Manchon, E.-A. Kim, N. Samarth, D. C. Ralph, *Nature*, Vol 511, p. 449 (2014)

### 3:15 PM BREAK

### 3:45 PM LL06

#### Metamorphic InAs on InP with Low Threading Dislocation

**Density** Brendan Eng<sup>1</sup>, Ryan D. Hool<sup>1</sup>, Pankul Dhingra<sup>1</sup>, Yukun Sun<sup>2</sup> and Minjoo L. Lee<sup>1</sup>; <sup>1</sup>University of Illinois at Urbana-Champaign, United States; <sup>2</sup>Yale University, United States

The properties of InAs, such as its narrow bandgap, high electron mobility, and ability to form heterostructures with nearly lattice-matched GaSb and AlSb, make it desirable for applications including mid-infrared detectors/emitters, transistors, and plasmonics. Nonetheless, InAs-based technologies are constrained by high cost, limited substrate dimensions, and low processing maturity. To overcome this industrial challenge, metamorphic graded buffers can be grown on lower-cost substrates to reach the InAs lattice constant. Owing to the moderate misfit between InAs (3.1%) and extensive manufacturing infrastructure, InP is a natural choice for metamorphic InAs growth. While mixed-cation alloys like InGaAs or InAlAs can be used to bridge the 3.1% lattice constant difference between InP and InAs, mixed-anion InAsP graded buffers are preferred due to their smoother surface morphology, lack of phase separation, and independent control of growth rate and composition. In this work, we demonstrate metamorphic growth of InAs on InP using InAsP step-graded buffers with threading dislocation density (TDD) as low as  $3.9 \times 10^6 \text{ cm}^{-2}$ , which is the lowest value to our knowledge and comparable to the best values for metamorphic buffers grown on GaAs with similar misfit.

We grew InAs<sub>0.5</sub>P<sub>0.5</sub> graded buffers on InP at a substrate temperature ( $T_{\text{sub}}$ ) of 420, 450, and 480°C with a grading rate of 1.06%/μm to determine the optimal growth window for InAsP alloys using solid source molecular beam epitaxy (MBE). High- $T_{\text{sub}}$  growth reduced the rms roughness measured from atomic force microscopy (AFM) from 2.7 nm at 420°C to 1.8 nm at 480°C but led to the nucleation of pyramid and hillock defects seen in Nomarski microscopy. At  $T_{\text{sub}}=480^\circ\text{C}$ , crosshatch lines were barely visible in comparison to lower  $T_{\text{sub}}$  growths which retained superior crosshatch morphology with long crosshatch lines and clear surface undulations along [110] and [1-10] directions. The intermediate  $T_{\text{sub}}$  of 450°C led to the lowest TDD value of  $4.3 \times 10^6 \text{ cm}^{-2}$  measured by electron channeling contrast imaging (ECCI), which was 2 and 2.5 times lower than 420 and 480°C growth respectively. We determined that 450°C was the optimal  $T_{\text{sub}}$  for InAsP alloys based on low TDD and rms roughness (2.1 nm).

To investigate the effects of composition on surface morphology and TDD, we grew InAsP graded buffers with terminal As compositions of 25, 50, 80, and 100% (i.e. pure InAs). All buffers were grown at  $T_{\text{sub}}=450^\circ\text{C}$ , while the InAs cap for the 100% sample was grown at 480°C based on a review of MBE growth literature for InAs. Rms roughness increased from 1.9 nm to 5.4 nm as As% was increased from 25 to 80%, likely due to accumulating crosshatch

roughness from the increased graded buffer thickness at higher As%. A further increase of As% from 80 to 100% reduced the rms roughness from 5.4 to 3.9 nm due to the enhanced In surface diffusion at the 480°C InAs cap layer growth. TDD increased from  $4.3 \times 10^6 \text{ cm}^{-2}$  to  $7.8 \times 10^6 \text{ cm}^{-2}$  when As% increased from 50 to 100% for graded buffers with similar grading rates, indicating reduced dislocation glide velocities for higher As% InAsP alloys.

Finally, we grew InAsP metamorphic buffers all the way to pure InAs with grading rates of 0.51%-4.0%/μm. TDD showed a linear dependence on grading rate for all samples with a value as low as  $3.9 \times 10^6 \text{ cm}^{-2}$  obtained for a 5.95 μm graded buffer, roughly a one order of magnitude TDD reduction in comparison to InAs grown on a thin, 750 nm graded buffer. The surface of all samples showed clear crosshatch morphologies with rms roughness ranging from 3.2-3.9 nm. All samples exhibited room-temperature photoluminescence (RT-PL), and the InAs grown on InP with TDD of  $3.9 \times 10^6 \text{ cm}^{-2}$  yielded an integrated PL intensity only ~1.55x lower than an InAs homoepitaxial sample. MBE growth of low-TDD InAs on InP has the potential to enable monolithic integration of high-performance InAs-based mid-infrared optoelectronic devices on a commercially mature InP platform.

### 4:00 PM LL07

#### Interfacial Misfit Dislocation Array Based Metamorphic Antimonide

**Buffers for Long-Wave IR Detectors** Ahmad Mansoori, Sadhvikas J. Addamane, Darryl Shima, Thomas Rotter and Ganesh Balakrishnan; The University of New Mexico, United States

While III-V alloys such as InAsSb have the potential to achieve long wavelength IR detectors, the access to high crystal-quality narrow bandgap III-Vs for such applications has been challenging. The complete lack of a viable substrate with a lattice constant between GaSb and InSb has resulted in a situation where a significant swath of bandgaps for long-wave IR detectors with excellent band-offset options based on combinations of alloys such as AlInSb, AlGaInSb, GaInSb, and InAsSb are yet to be fully exploited. In the absence of a naturally occurring binary substrate akin to InP for the III-As material system, the only other option to access lattice constants  $> 6.1 \text{ \AA}$  is to use metamorphic growth modes. Achieving a low threading dislocation density ( $10^6 \text{ defect/cm}^2$ ) metamorphic buffers with a fully relaxed lattice constant around 6.3 Å on commercially available large format substrates such as InP and GaAs is the goal of this study.

The growth of GaSb on GaAs substrates has been demonstrated through the use of a growth mode based on inducing 90 interfacial misfit dislocation arrays (IMF) between the GaSb epilayer and the GaAs substrate. The characterizing feature of this growth mode is the immediate strain relief at the highly mismatched interface via the formation of periodic 90° misfit dislocations. This array allows the growth of fully relaxed and low-defect density GaSb on GaAs ( $3 \times 10^7 \text{ defect/cm}^2$ ) within 500 nm of growth. While this growth process has resulted in the demonstration of both III-Sb lasers and detectors on GaAs substrates, a similar buffer has not been demonstrated in other material systems. To realize a metamorphic buffer with a lattice constant of ~6.3 Å, we make use of In<sub>0.53</sub>Ga<sub>0.47</sub>Sb layers grown on In<sub>0.53</sub>Ga<sub>0.47</sub>As/InP. The idea is to form the IMF array by replacing the Arsenic sub-lattice in InGaAs on InP with an antimony layer. This is very similar to how GaSb is grown on GaAs and a successful demonstration could lead to a high-quality metamorphic buffer for lattice constants in the 6.25 – 6.3 Å range.

To achieve such an interface, 500 nm In<sub>0.53</sub>Ga<sub>0.47</sub>Sb is grown on In<sub>0.53</sub>Ga<sub>0.47</sub>As/InP. To achieve a low threading dislocation density, the growth temperatures were varied between (460 and 360 °C). XRD and TEM were used to measure threading dislocation density and layer relaxation as an indicator of metamorphic layer quality. XRD of InGaSb layers confirmed the relaxation of >99.5% in all samples. High-resolution cross-section TEM images showed the formation of misfit dislocation arrays at the interface of InGaAs and InGaSb layer. The threading dislocation density was measured from TEM images and for all samples is around  $10^{10} \text{ cm}^{-2}$ . An InAlSb quantum well structure is added on the top of the InGaSb buffer to study photoluminescence (PL). Room and low-temperature PL can be used to evaluate the quality of the buffer layer. The presentation will detail our efforts to reduce the threading dislocations through optimization of the mismatched interface and also through the inclusion of dislocation filter layers.

### 4:15 PM LL08

#### (Student) High-Speed Mid-Infrared Detection Using InSb-Pixel-Loaded

**Microwave Resonators** Yinan Wang<sup>1</sup>, Sukrith Dev<sup>1</sup>, Frank Yang<sup>2</sup>, Leland J. Nordin<sup>1</sup>, Yimeng Wang<sup>1</sup>, Monica Allen<sup>2</sup>, Jeffery Allen<sup>2</sup>, Emanuel Tutuc<sup>1</sup> and Daniel Wasserman<sup>1</sup>; <sup>1</sup>The University of Texas at Austin, United States; <sup>2</sup>Rice University, United States; <sup>3</sup>Air Force Research Laboratory, United States

There has been significant recent interest in developing high-speed mid-infrared detectors for emerging applications such as infrared LIDAR, free-space optical communication, and dual-comb spectroscopy (DCS). In DCS, two optical frequency combs with slightly different frequency spacing are combined at the detector element, generating a new comb of radiofrequency (RF) beatnotes<sup>1</sup>. By putting samples under investigation (most often molecules with distinct and narrow absorption features) in the path of one or both sources, the optical absorption spectrum of the sample can be effectively mapped to the RF spectrum, allowing for broadband spectroscopy with high sensitivity. The principle of DCS requires high-speed detectors with bandwidths greater than the RF beatnote frequencies generated by the dual combs, which has been

difficult to achieve in the mid-wave infrared (MWIR) range with conventional detector architectures such as photodiodes and photoconductors due to the intrinsic tradeoff between speed and sensitivity.

Here, we demonstrate a MWIR detector using a microwave resonator circuit loaded with an InSb pixel. The microwave resonator is a split-ring resonator (SRR) coupled to a microstrip busline, terminated with coplanar contact pads. The SRR is fabricated on a 500  $\mu\text{m}$  thick 99.6% aluminum oxide substrate using a standard photolithography, metallization (10 nm Ti/ 500 nm Au) and lift-off process. The 600 nm thick InSb absorber is grown on a 200 nm thick AlSb sacrificial layer, on a GaAs substrate by molecule beam epitaxy. Lattice-mismatched InSb is chosen intentionally to reduce carrier lifetime through the introduction of additional defects while still maintaining strong infrared absorption. Pixels are fabricated through the following steps. First, a photoresist etch mask is defined using photolithography. The sample is then etched down to the substrate with inductively-coupled plasma etching using  $\text{BCl}_3/\text{Cl}_2/\text{Ar}$  gases. After cleaning the photoresist, a diluted HF bath is used to selectively etch away the sacrificial AlSb layer, leaving InSb pixels on AlSb pillars<sup>2</sup>. Finally, a polydimethylsiloxane (PDMS) polymer stamp is used to peel off the pixels from the original substrate. The individual pixel is transferred to the gap of the SRR using a dry transfer technique<sup>3</sup>.

The circuit is then driven at the resonant RF frequency of the SRR. When light is absorbed by the pixel, photogenerated carriers change the InSb conductivity which alters the RF response of the microwave circuit, and thus the signal transmitted to the RF detector. The change in the detected RF signal serves as the readout mechanism for the incident IR light. The time response of the detector is characterized with a 1550 nm 100 fs pulsed laser by measuring the temporal decay in the RF signal following an optical pulse. We measure temperature- and power-dependent time response of the detector, showing sub-nanosecond carrier lifetime for all temperatures and pump powers. A lumped element circuit time-domain simulation is developed and shows excellent agreement with our experimental results, allowing us to understand the detector time response as resulting from both the circuit and material responses. Furthermore, we excite our detectors with a high frequency modulated laser signal to test the detector's achievable bandwidth. We demonstrate the detection of frequency components as high as 2 GHz at room temperature. The results from this work demonstrate the potential of the hybrid RF/optoelectronic detector architecture for applications requiring high-bandwidth mid-infrared detection. The authors would like to acknowledge funding support through the AFOSR Lab Tasks 19RWCOR015, 20RWCOR090 (PO: Drs. B. Pokines and M. Schmidt). [1] Coddington, I., Newbury, N., & Swann, W. (2016). *Optica*, 3(4), 414-426. [2] Zamiri, M. et al. (2016). *Applied Physics Letters*, 108(9), 091110. [3] Kim, K. et al. (2016). *Nano Letters*, 16(3), 1989-1995.

#### 4:30 PM LL09

**(Student) Highly Strained, High Indium Content III-V Materials toward 4-Micron Type-I Emitters** Scott D. Sifferman<sup>1</sup>, Andrew F. Briggs<sup>1</sup>, Scott J. Maddox<sup>1</sup>, Hari P. Nair<sup>2</sup> and Seth R. Bank<sup>1</sup>; <sup>1</sup>The University of Texas at Austin, United States; <sup>2</sup>Cornell University, United States

Type-I diode lasers are an appealing approach for mid-infrared (2-5 microns) coherent light sources since they offer potential performance advantages such as low threshold power consumption, stable temperature-stable operation, and comparatively simple growth. Below 3 microns, high-performing GaInAsSb/(Al)Ga(As)Sb laser devices have been demonstrated with low threshold currents and high wallplug efficiencies. Emission can be extended to longer wavelengths by increasing the indium content in the quantum well emitters, while simultaneously increasing the arsenic content to mitigate the onset of strain-related defect formation that degrades luminescence performance. The increased arsenic content, however, compromises the valence band offset for hole confinement, resulting in severe performance degradation beyond ~3.4 microns. Retaining compressive strain in the quantum well alloy improves hole confinement, but in most cases strains have typically been limited to less than ~1.8 percent, limiting the achievable valence band offsets at longer wavelengths. Even with engineered barriers containing both aluminum and indium, GaSb-based type-I diode lasers have been limited to a maximum emission wavelength of 3.73 microns with QWs strained to 1.5% [1]. We examined the effect of indium content and quantum-well strain on the emission wavelength of GaSb-based quantum wells. We demonstrate that by increasing the indium fraction of GaInAsSb QWs to >0.7 and the compressive strain to ~2.4%, the emission wavelength of type-I GaSb-based emitters can be extended past 4 microns. GaInAsSb quantum well test structures were grown on (001)-oriented GaSb substrates in a Varian Gen. II solid-source molecular beam epitaxy system. The indium fraction of the quantum wells was varied from 0.43 to 0.73, with compressive strains ranging from 1.1% to 2.6%. The peak photoluminescence wavelength of these structures increased with increasing indium content, with strains >2.3% needed to maintain type-I alignments at the longer wavelengths. At the highest indium fractions, lattice-matched AlGaAsSb (Al=0.3) barriers enabled type-I photoluminescence emission out to 4.1  $\mu\text{m}$  with increased efficiency and reduced linewidth. This work was supported by the Army Research Office (W911NF-15-1-0612).

[1] K. Vizbaras and M.C. Amann, *Semicond. Sci. Technol.* 27, 032001 (2012).

#### 4:45 PM LL10

**Comparison of Auger Recombination Across Material Systems with Externally Applied Biaxial Strain** Andrew F. Briggs<sup>1</sup>, Kenneth Underwood<sup>2</sup>, Scott D. Sifferman<sup>1</sup>, Juliet Gopinath<sup>2,3</sup> and Seth R. Bank<sup>1</sup>; <sup>1</sup>The University of Texas at Austin, United States; <sup>2</sup>University of Colorado Boulder, United States

Conventional semiconductor laser diodes are challenging to operate at high-carrier density due to loss from the non-radiative Auger process. This process has been implicated as a cause of high threshold currents and increased temperature sensitivity of lasers and droop in light-emitting diodes.<sup>[1],[2]</sup> Auger recombination constrains radiative efficiency at higher carrier population, increased temperature, and in small bandgap materials. Early work to reduce Auger recombination suggests epitaxial strain can be used to mitigate the process.<sup>[3],[4]</sup> However, it is not clear if the reduction in Auger recombination is due to the epitaxial strain itself or the compositional change of alloy necessary to induce the epitaxial strain. Because of their narrow bandgap, mid-infrared (mid-IR) materials such as GaInAsSb quantum wells experience significant Auger recombination that compromises device performance, presenting an ideal testbed for fundamental studies of Auger recombination.

Our initial work has focused on biaxial strain applied to GaInAsSb quantum well membranes to directly mirror the strain introduced with heteroepitaxy. The biaxial application of strain with a two-dimensional stretcher allows us to characterize the strain-dependence of any material system that can be made sufficiently thin.<sup>[5]</sup> Membranes were bonded to flexible PTFE substrates using a Au-Au cold welding approach. Samples were then mounted onto a biaxial sample stretcher and were characterized with X-ray diffraction, photoluminescence, and Raman under different applied strains. We find evidence that the reduction in the Auger coefficient in the GaInAsSb quantum wells appears to be due to the compositional changes to the alloy, rather than the concomitant mechanical deformation. We are currently working to generalize our findings by repeating these experiments on near-IR InGaAs quantum wells grown on GaAs and InP substrates; results will be reported at the conference.

This work was supported by the National Science Foundation (Award No. DMR-1508603 and DMR-1508783).

[1] Silver, et al., *IEEE Journal Of Quantum Electronics* vol. 33 (1997).

[2] N.K. Dutta, *Journal Of Applied Physics*, vol. 54 (1983).

[3] A. R. Adams, *Electron. Lett.*, vol. 22, 249 (1986).

[4] E. Yablonoitch and E. O. Kane, *J. Lightwave Technol.*, vol. 4, 504 (1986).

[5] A.F. Briggs et al., *60<sup>th</sup> Electronic Materials Conf.*, June 2019

#### SESSION MM: III-Nitrides—Tunnel Junctions and InGaN Growth

Session Chair: Theeradetch Detchprohm

Session Hosts: Matt Brubaker and Srabanti Chowdhury

Friday Afternoon, June 26, 2020

Location: ZoomRoom 3

#### 2:00 PM MM01

**(Student) Monolithic MOCVD-Grown III-Nitride Tunnel Junctions with Ultra-Low Resistance** Syed Mohammad Najib Hasan<sup>1</sup>, Zane A. Jamal-Eddine<sup>1</sup>, Brendan P. Gunning<sup>2</sup>, Hareesh Chandrasekar<sup>1</sup>, Mary H. Crawford<sup>2</sup>, Andrew M. Armstrong<sup>2</sup>, Siddharth Rajan<sup>1</sup> and Shamsul Arafin<sup>1</sup>; <sup>1</sup>The Ohio State University, United States; <sup>2</sup>Sandia National Laboratories, United States

In this work, we report on the effect of activation annealing and doping on GaN-based interband tunnel junctions (TJs) grown by metal organic chemical vapor deposition (MOCVD). We demonstrate state-of-art low-resistance and voltage loss TJs, and lateral activation of buried p-layers for layer area diodes to enable future high power density multiple active region III-nitride light emitting diodes. III-nitride light emitting diodes are very successful for a broad range of lighting applications, but the long-standing challenge of efficiency droop at high current densities remains unsolved. A proposed solution to this is to use multiple active region structures with interband TJs in between [1]. Such a topology allows achieving higher power density at lower currents. While excellent TJ resistance values have been reported before by MBE or hybrid MBE/MOCVD approaches [2], all-MOCVD based TJs still show an excess voltage and resistance compared to the current state-of-the-art results. In this work, we report our experimental results on reduction of the voltage losses through optimizing Mg activation for buried p-GaN layer and engineering of the p-doping. The p-n diode samples used in this study were grown on GaN/sapphire templates by MOCVD. The TJs, consisting of p- and n-doped GaN layers with a high concentration of Mg and Si respectively, were grown above the p-n junction. In the first experiment reported here, we investigated the effect of high temperature annealing for Mg activation in the p-GaN layer through its sidewalls. The sidewall activation process have historically showed a dependence of turn-on voltage and resistance on device area due to challenges related to lateral activation. Devices with a larger dimension (>50  $\mu\text{m}$  sides) have suffered from higher voltage penalty, resulting in non-uniform illumination from LEDs due to the insufficient activation. In this work, we processed square mesas with 54, 74 and 105  $\mu\text{m}$  sides and the activation anneal was performed using a rapid thermal annealing system in N<sub>2</sub> atmosphere. Remarkably, the devices with Mg activation at an annealing temperature of  $\geq 900^\circ\text{C}$  (significantly higher than typical activation

temperatures) exhibit flat voltage-drop characteristics with no dependence on the device areas indicative of complete Mg-activation in the active area. The devices show reasonably low leakage current with 9 orders of rectification between -4 to 4 V. The diodes also show an ideality factor of  $\eta = 2$  in the ON-state with a series resistance of 2.7 m $\Omega$ -cm<sup>2</sup> indicative of electron-hole recombination. Using the optimized activation conditions, we investigated the effect of the p-doping turn-on profile on the TJ resistance. Due to the time required to turn-on and turn-off the doping while growing the p-doped layers of the TJs, the doping profiles spread out at a few-nanometers scale. Therefore, the thickness of the  $p^+$  layer was varied (6/9/12/18 nm) to understand the compensation effect of the  $p$ -dopants. The expected depletion width for the nominal doping concentration of  $2e20$  cm<sup>-3</sup> is expected to be 12 nm. Remarkably, it is observed that the TJ-associated voltage drop decreases monotonically as the p-doping thickness is increased, suggesting that the Mg doping concentration has not reached its maximum value in the samples with the thinner p-doped layers. In this work, with respect to the reference  $p$ - $n$  diode with metal ohmic contacts, the voltage penalties as low as 0.14 V (1 A/cm<sup>2</sup>) and 0.47 V (100 A/cm<sup>2</sup>) are achieved, which is also among some of the lowest ever reported for the monolithic MOCVD-grown for GaN homojunction TJs. In conclusion, we have shown the feasibility of an all-MOCVD approach to realize large area lateral activation as well as excellent voltage losses in GaN PN tunnel junctions. The reported work shows the promise of tunneling based multiple active region LEDs. [1] Akyol et al., *Appl. Phys. Lett.* 103, 081107, 2013 [2] Alhassandull et al., *Appl. Phys. Express* 11.4, 042101, 2018

## 2:15 PM MM02

**(Student) Design of Fully Transparent Tunnel Junctions for Application in III-Nitride Optoelectronics** Zane A. Jamal-Eddine<sup>1</sup>, Syed M. Hassan<sup>1</sup>, Brendan P. Gunning<sup>2</sup>, Hareesh Chandrasekar<sup>1</sup>, Mary H. Crawford<sup>2</sup>, Andrew M. Armstrong<sup>2</sup>, Shamsul Arafin<sup>1</sup> and Siddharth Rajan<sup>1</sup>; <sup>1</sup>The Ohio State University, United States; <sup>2</sup>Sandia National Laboratories, United States

Recently there has been much interest generated around tunnel junctions (TJs) for applications in III-Nitride optoelectronics. TJs could enable multiple active region emitters that provide a promising solution to realize high power density without efficiency droop[1]. There has not been a detailed physics-based understanding of tunneling physics in III-Nitride LEDs and key questions must be answered. Our work aims to answer key design questions related to voltage and resistance losses in GaN tunnel junctions, especially under design constraints set by MOCVD growth limitations. We use simulations to design and engineer transparent graded InGa<sub>x</sub>N tunnel junctions, and demonstrate that these simulations can predict experimentally observed resistance and voltage penalty. We also use simulations to design graded InGa<sub>x</sub>N TJs with state-of-art low voltage penalty of 0.19 V at 100 A/cm<sup>2</sup>, the lowest measured value for an all-MOCVD approach. **Modeling:** We use a standard device simulator (Silvaco Atlas) with a nonlocal band to band tunneling model to gain physical insight into the design tunnel junctions. By considering the origin of the voltage drop in III-Nitride TJs it is possible to identify design parameters which can be manipulated to achieve the required low  $V_{TJ}$  for a cascaded LED. Starting with the GaN homojunction TJ, which consists of a simple heavily doped  $p^{++}/n^{++}$  junction, we identify depletion width and the Fermi level position in the  $p$ -type GaN as key design parameter. The use of graded InGa<sub>x</sub>N interlayers near the tunnel junction interface enables us to achieve higher Mg activation, which enable higher tunneling rates between the heavily doped  $p^{++}$ GaN and  $n^{++}$ GaN. Simulations help to understand the effect of the non-degeneracy in  $p^{++}$ GaN which leads a large energy difference between the Fermi level and valence band. This leads to a voltage drop required to align the valence band states on the  $p$ -side of the tunnel junction with the conduction band states on the  $n$ -side. In contrast, electrostatic ionization of graded  $p$ -InGa<sub>x</sub>N leads to near-degenerate  $p$ -InGa<sub>x</sub>N, which enables a reduced voltage for onset of tunneling. Simulations directly provide quantitative comparison of tunneling rates, both as a function of design and as a function of applied voltage. As the operating voltage of the TJ increases, the tunneling distance decreases and the band to band tunneling rates increase. We show how the thickness of the graded InGa<sub>x</sub>N interlayer impacts the  $V_{TJ}$ . **Experiment:** We compare the models developed here with experimental results. We have used a simulation-driven approach to design experiments for monolithic growth by MOCVD. Tunnel junctions were grown on top of a standard pn-diode containing a thick  $n^+$ GaN template, a 200nm  $n$ -GaN layer with  $[Si]=2 \times 10^{16}$  cm<sup>-3</sup>, and a 90nm  $p^+$ GaN layer with  $[Mg]=3 \times 10^{19}$  cm<sup>-3</sup>. The GaN homojunction TJ contains a 12nm  $p^{++}$ GaN layer with  $[Mg]=2 \times 10^{20}$ cm<sup>-3</sup> followed by a 10nm  $n^{++}$ GaN layer with  $[Si]=3 \times 10^{20}$ cm<sup>-3</sup>, and finally a 500nm  $n^+$ GaN contact layer. The graded InGa<sub>x</sub>N interlayer TJs contain a 12nm (or 6nm)  $p^{++}$ GaN layer with  $[Mg]=2 \times 10^{20}$  cm<sup>-3</sup> followed by a  $p^{++}$ InGa<sub>x</sub>N layer graded from 0% to 10% In mole fraction and  $[Mg]=4 \times 10^{20}$ cm<sup>-3</sup>. Next a  $n^{++}$ InGa<sub>x</sub>N layer graded from 10% to 0% In mole fraction and  $[Si]=4 \times 10^{20}$ cm<sup>-3</sup> followed by a  $n^{++}$ GaN layer with  $[Si]=3 \times 10^{20}$  cm<sup>-3</sup> and finally a 500nm  $n^+$ GaN contact layer. The devices were compared to a control pn-diode to extract  $V_{TJ}$ . These TJs were measured to have  $V_{TJ} = 0.19$ V and  $V_{TJ} = 0.47$ V at current density of 100 A/cm<sup>2</sup> for the graded InGa<sub>x</sub>N interlayer TJ and the GaN homojunction TJ, respectively. In comparison, the expected values from modeling are  $V_{TJ} = 0.26$ V for InGa<sub>x</sub>N interlayer TJ and  $V_{TJ} = 0.56$ V for GaN homojunction TJ. This shows that standard device models give key insight into the ultimate limits of tunnel junctions, and can provide a powerful way to design and predict the performance of tunnel junctions. [1] Akyol, F., Krishnamoorthy, S., Rajan, S. (2013). *Applied Physics Letters*, 103(8), 081107.

## 2:30 PM MM03

**(Student) Carrier Localization and Dynamics of Nonpolar  $m$ -Plane InGa<sub>x</sub>N/GaN MQWs at Elevated Temperatures** Xuanqi Huang<sup>1</sup>, Dongying Li<sup>1</sup>, Po-Yi Su<sup>1</sup>, Houqiang Fu<sup>1</sup>, Hong Chen<sup>1</sup>, Kai Fu<sup>1</sup>, Steven DenBaars<sup>2</sup>, Shuji Nakamura<sup>2</sup>, Tsung-Han Yang<sup>1</sup>, Jossue Montes<sup>1</sup>, Chen Yang<sup>1</sup>, Jingan Zhou<sup>1</sup>, Xin Qi<sup>1</sup>, Fernando A. Ponce<sup>1</sup>, Cun-Zheng Ning<sup>1</sup> and Yuji Zhao<sup>1</sup>; <sup>1</sup>Arizona State University, United States; <sup>2</sup>University of California, Santa Barbara, United States

III-nitride optoelectronic devices have been widely commercially deployed nowadays. The nonpolar InGa<sub>x</sub>N/GaN multiple-quantum-wells (MQWs) are favored due to the eliminated intrinsic electrical fields in comparison to their polar  $c$ -plane counterparts. This enables the enhanced radiative capability of InGa<sub>x</sub>N/GaN QWs. In addition, there exist many optoelectronic applications for III-nitrides that operate at a much higher temperature rather than room temperature (RT). To explore the fundamental underlying physical mechanisms on optical properties from RT to high temperatures of nonpolar InGa<sub>x</sub>N/GaN MQWs, we studied the temperature-dependent optical properties and carrier dynamics for 2 nonpolar ( $m$ -plane) InGa<sub>x</sub>N MQW samples with different thickness of InGa<sub>x</sub>N QW using photoluminescence (PL) and time-resolved photoluminescence (TRPL) from RT to 400 °C and streak camera spectroscopy measurements at RT and employed scanning transmission electron microscopy (STEM) to investigate In atom distribution and structural uniformity across MQWs. The first sample with 6-nm InGa<sub>x</sub>N QW is denoted as  $m6$  and the second one with 3-nm InGa<sub>x</sub>N QW is  $m3$ . Temperature-dependent PL results show that both nonpolar  $m$ -plane InGa<sub>x</sub>N MQW samples are capable of emitting relatively strong light at 400 °C. The peak intensity of  $m6$  at 400 °C is only  $\sim 7$  times lower than itself at room temperature while it's  $\sim 16$  times lower for  $m3$ , at an excitation laser power of 50  $\mu$ W. In contrast, the peak intensity of  $c$ -plane InGa<sub>x</sub>N MQW sample decreases  $\sim 1000$  times from RT to 400 °C (not shown here). Furthermore, we extracted temperature-dependent carrier lifetimes from TRPL results from RT to 400 °C and adopted a theoretical lifetime model that accounts for carrier localization. There are five main parameters for fitting:  $\tau_{loc}$ ,  $E_{loc}$ ,  $N_{pp}$ ,  $\tau_{nr}$  and  $E_A$ . The solid lines in Fig.3(a) and (c) exhibit the fitting results for 2 samples under 3 excitation powers. The grey dashed lines in Fig. 3(a) and (c) represent the nonradiative recombination lifetime. Moreover, the ratio of free and localized carrier densities can be also estimated from this model and plotted in Fig. 3(b) and (d). Considering the STEM studies in Fig.1, we can then propose that the fundamental difference in carrier dynamics of both samples lies in disparate potential confinement of carriers. For  $m3$ , the significant Indium fluctuation across barrier layers contributes to obscure interface between QWs and barriers, diminishing carrier confinement in QWs. This effect further populates carriers more spatially in both QW and barrier regions and more energetically into higher energy levels, which in turn makes carriers susceptible to nonradiative centers. Therefore this accounts for larger  $n_{free}/n_{oc}$  ratio and the decreasing lifetime after 400K observed in  $m3$ . In comparison,  $m6$  acquires explicit and uniform QW/barrier interface and hence better carrier confinement. Therefore carriers stay at localization centers and is able to maintain strong radiative capability, especially considering exciton radius is much smaller than QW width. In addition, streak camera spectroscopy at RT clearly that  $m6$  has a much broader emission spectrum and there is an energy transfer process/kinetic from QW to the low energy states with increasing time delay. While in  $m3$ , we observe the progressive narrowing of the emission line from QW and no sign of low energy states. For  $m3$ , no sign of carrier redistribution indicates that photoexcited carriers populate into higher energy states and tend to follow a global Fermi distribution and carrier localization is negligible. In conclusion, we analyze optical properties and carrier dynamics of nonpolar ( $m$ -plane) InGa<sub>x</sub>N MQW samples from RT to 400 °C using PL and TRPL. Carrier dynamics exhibit divergent behaviors due to different localization effects and QW structural homogeneity. These results offer new insights and strategies for further development of InGa<sub>x</sub>N-based emitters toward the theoretical limit of their efficiency.

## 2:45 PM MM04

**(Student) Growth, Characterization and Relaxation of In<sub>x</sub>Ga<sub>1-x</sub>N Templates and Their Impact on Multiple Quantum Wells** Mostafa Abdelhamid, Tim B. Eldred, Evyn L. Routh, Nadia El-Masry, James LeBeau and Salah Bedair; North Carolina State University, United States

Nitride based Light Emitting Diodes (LEDs) with In<sub>x</sub>Ga<sub>1-x</sub>N/GaN multiple Quantum Wells (MQWs) show a deterioration in Quantum efficiency as the emission wavelength is shifted from Blue towards Green or longer wavelength emission. This is referred to as the "green gap" and it originates from the large lattice mismatch between the In<sub>x</sub>Ga<sub>1-x</sub>N well and the underlying GaN template specifically for high indium content required for long wavelength emission and the accompanied piezoelectric field in the strained wells. A good quality relaxed In<sub>x</sub>Ga<sub>1-x</sub>N template can address this green gap by reducing the mismatch between the In<sub>x</sub>Ga<sub>1-x</sub>N MQWs and the underlying In<sub>x</sub>Ga<sub>1-x</sub>N template. In this work, device quality In<sub>x</sub>Ga<sub>1-x</sub>N templates are grown by Metal Organic chemical vapor deposition (MOCVD) using the semibulk (SB) approach and characterized for use as templates for MQWs. The approach is based on periodically growing an In<sub>x</sub>Ga<sub>1-x</sub>N layer of thickness  $\sim 25$  nm then capping it with a thin 1-2 nm GaN layer. This In<sub>x</sub>Ga<sub>1-x</sub>N/GaN period is repeated multiple times ( $\sim 20$  periods) to achieve the desired template thickness. The insertion of thin In<sub>x</sub>Ga<sub>1-x</sub>N interlayers between each two successive In<sub>x</sub>Ga<sub>1-x</sub>N layers helps in preserving the smoothness of the surface by getting rid of excess indium

inclusions and by backfilling some of the V-pits that are formed as the film gradually relaxes. Different characterization techniques were used to evaluate the quality of the grown templates and the strain relaxation processes. Secondary Ion Mass Spectrometry (SIMS) reveals that increasing the degree of relaxation in the template by increasing the number of periods is accompanied by a gradual increase in indium content. This variation in indium content along with the variation in lattice parameters with gradual relaxation makes it challenging to apply standard X-Ray diffraction (XRD) and Reciprocal Space mapping (RSM) techniques to estimate the degree of relaxation of the top layers. High-resolution High-angle annular dark-field scanning transmission electron microscopy (HAADF-STEM) and Energy-dispersive X-ray spectroscopy (EDS) were used to evaluate the variation in the indium content, the lattice constant 'a', and the degree of relaxation across the template. HAADF-STEM shows the abrupt interfaces for the SB with backfilling of some V-pits. Degree of relaxation estimated from measured lattice parameters and indium content is shown to increase gradually with increasing number of periods and it reaches a degree of relaxation greater than 70% for the topmost layer with an indium content of  $x \sim 0.08$ . Atomic force microscopy (AFM) of this 20-period  $\text{In}_{0.08}\text{Ga}_{0.92}\text{N}$  SB template shows an RMS roughness of  $\sim 1.3$  nm. Photoluminescence (PL) was used to evaluate the optical properties of the grown  $\text{In}_x\text{Ga}_{1-x}\text{N}$  templates. A model was also developed to estimate the degree of the relaxation of the  $\text{In}_x\text{Ga}_{1-x}\text{N}$  template using the PL emission wavelength and the indium content at the top layer as deduced from SIMS. Several test structures of  $\text{In}_x\text{Ga}_{1-x}\text{N}$  MQWs were grown under the same conditions on GaN and on the  $\text{In}_x\text{Ga}_{1-x}\text{N}$  template to investigate the effect of the underlying template on the MQW emission. A consistent red shift in PL emission has been observed for MQWs grown on the SB template as compared to identical MQWs grown on GaN. This red shift can be attributed to the decrease in bandgap of  $\text{In}_x\text{Ga}_{1-x}\text{N}$  MQWs as the compressive strain is reduced along with an increase in indium content that is accompanied by the reduced strain. This shows the potential of using relaxed  $\text{In}_x\text{Ga}_{1-x}\text{N}$  SB templates for long wavelength LEDs.

### 3:00 PM MM05

**$\text{Al}_x\text{Ga}_{1-x}\text{N}$  Homo Junction Tunnel Diodes with  $0 \leq x \leq 58\%$  — First Demonstration of Negative Differential Resistance in  $\text{Al}_x\text{Ga}_{1-x}\text{N}$  Homo Junction Tunnel Diodes and 110% Improvement in 275 nm UV-LED Output Power** Evan Clinton<sup>1</sup>, Zachary Engel<sup>1</sup>, Ehsan Vadiée<sup>1</sup>, Christopher M. Matthews<sup>1</sup>, Richard Floyd<sup>2</sup>, Mohammad K. Hussain<sup>2</sup>, Mikhail Gaevskii<sup>2</sup>, Abdullah Mamun<sup>2</sup>, Asif Khan<sup>2</sup> and W. Alan Doolittle<sup>1</sup>; <sup>1</sup>Georgia Tech, United States; <sup>2</sup>University of South Carolina, United States

$\text{Al}_x\text{Ga}_{1-x}\text{N}$  ( $0 < x < 0.6$ ) homo junction tunnel diodes are fabricated and demonstrate the first ever demonstrated negative differential resistance (NDR) at  $\sim 1.4$  V and  $\sim 2.4$  V for GaN and  $\text{Al}_{0.19}\text{Ga}_{0.81}\text{N}$  respectively with high reverse bias current densities necessary for tandem series connected devices and tunnel contacts. NDR was found in the  $\text{Al}_x\text{Ga}_{1-x}\text{N}$  p+/n+ diodes up to 19% Al with current depressions but no NDR up to 42% Al. Additionally, an  $\text{Al}_x\text{Ga}_{1-x}\text{N}$  tunnel diode with 9% Al results in a peak-to-valley current ratio (PVCR) of  $\sim 1.1$ , similar to the NDR found in GaN.

Tunnel junctions for the III-nitrides are heavily investigated to increase design freedom and realize tandem series connected devices, simplify fabrication with less metallization and lithography, and enable substantially better contact resistances to n-type material. In some applications, the use of heterojunction interlayer-based tunnel contacts introduces unwanted absorption and/or introduces defects due to the inherent lattice mismatch and possible parasitic light absorption. Thus, when possible, tunnel homo junctions are often preferred. Utilizing an n-type tunnel contact to a p-type layer is especially beneficial for high Al content  $\text{Al}_x\text{Ga}_{1-x}\text{N}$  films where ohmic contacts to p-layers are difficult as well as hole activation and injection to active layers are problematic. Most importantly, an ohmic n- $\text{Al}_x\text{Ga}_{1-x}\text{N}$  tunnel contact can replace the often used detrimental absorbing p-GaN layers that are grown on top of p- $\text{Al}_x\text{Ga}_{1-x}\text{N}$  layers to enable a more ohmic contact.

The metal modulated epitaxy (MME) growth technique performed in an MBE system enables high hole concentrations for  $\text{Al}_x\text{Ga}_{1-x}\text{N}$  and the abrupt interfaces required to form tunnel junctions without polarization engineered interlayers which can limit optoelectronic device performance. Furthermore, widening the bandgap energy of  $\text{Al}_x\text{Ga}_{1-x}\text{N}$  for higher Al content tunnel contacts can allow for deep UV optoelectronics with less optical absorption loss.

MME conditions for  $\text{Al}_x\text{Ga}_{1-x}\text{N}$  that limit phase separation are presented, and varied Mg and Si doping of  $\text{Al}_x\text{Ga}_{1-x}\text{N}$  ( $0 < x < 0.6$ ) materials is compared. We demonstrate  $\text{Al}_x\text{Ga}_{1-x}\text{N}$  homo junction tunnel p+/n+ diodes and tunnel contacted n+/p+/i/n devices with silicon doped n-type layers exhibiting silicon concentrations of up to  $5 \times 10^{20} \text{ cm}^{-3}$  and magnesium doped p-type layers with Mg concentrations above  $7 \times 10^{20} \text{ cm}^{-3}$ . Reverse bias tunneling is observed for all  $\text{Al}_x\text{Ga}_{1-x}\text{N}$  devices and decreases with increasing Al content in the tunnel diodes as the bandgap increases.

An n++ $\text{Al}_{0.25}\text{Ga}_{0.75}\text{N}$ /p++ $\text{Al}_{0.25}\text{Ga}_{0.75}\text{N}$  Homo junction tunnel contacted AlGaN UV LED operating at 273 nm yielded an increase in power of 110% at 7.5mA over the same structure with a p++ GaN contacted 275 nm UV-LED. These results are promising for improving performance of a wide array of ultraviolet and visible wavelength III-nitride devices including light emitting diodes (LEDs), lasers, and solar cells.

### 3:15 PM BREAK

SESSION NN: AlN and AlGaN Growth  
Session Chair: Russell Dupuis  
Session Hosts: Matt Brubaker and Srabanti Chowdhury  
Friday Afternoon, June 26, 2020  
Location: ZoomRoom 3

### 3:45 PM NN01

**(Student) Controlling Defect Formation of AlN Nanostructures—Path towards Efficient Current Conduction of Ultrawide Bandgap Semiconductors** Yuanpeng Wu, David A. Laleyan, Zihao Deng, Chihyo Ahn, Anthony Aiello, Ayush Pandey, Xianhe Liu, Ping Wang, Kai Sun, Elaheh Ahmadi, Yi Sun, Mackillo Kira, Pallab Bhattacharya, Emmanouil Kioupakis and Zetian Mi; University of Michigan—Ann Arbor, United States

Ultrawide bandgap semiconductors, including AlN, BN,  $\text{Ga}_2\text{O}_3$ , and diamond, are critical for applications in next generation high power, high frequency electronics, ultraviolet optoelectronics, high power photonics and quantum devices.[1] Progress in these fields, however, has been severely limited by the lack of scalable substrate, large densities of defects, and extremely poor current conduction. Mg, the most commonly used p-type dopant in AlN, has a prohibitively large activation energy  $E_A \sim 630$  meV, which is significantly larger than room-temperature thermal energy and, consequently, results in virtually negligible doping efficiency. Moreover, during the epitaxy of Mg-doped AlN, the Fermi level is shifted towards the valence band edge, significantly reducing the formation energy for nitrogen-vacancies as well as other point defects and impurity incorporation, which compensates the presence of free holes and further introduces various defects emissions. Here we show, both theoretically and experimentally, that such fundamental material issues of AlN can be potentially addressed through nonequilibrium epitaxy of nanostructures.

N-rich conditions are used during epitaxy of AlN nanostructures. The formation energy of N-vacancy related defects in AlN nanostructures can be enhanced by nearly 3 eV under N-rich epitaxy condition, compared to conventional N-poor condition. Moreover, the formation energy for Al-substitutional Mg-dopant incorporation is decreased by  $\sim 2$  eV under N-rich epitaxy. In this work, AlN nanostructures were grown on n-type Si wafer using a Veeco GEN II molecular beam epitaxy. We have first investigated the effect of growth temperature and  $\text{N}_2$  flow rate on the formation of Al-vacancies for undoped AlN nanostructures. It is seen that, when grown under a  $\text{N}_2$  flow rate of 1 sccm and temperature of 965 °C, a single peak excitonic emission of 5.93 eV (labelled as  $I_1$ ) was obtained, which is in agreement with excitonic emission of strain-free AlN. An additional Al vacancy related peak of 5.2 eV (labelled as  $I_2$ ) was observed when the growth temperature was reduced to 810 °C. Moreover, when a relatively low  $\text{N}_2$  flow rate of 0.33 sccm was used, defect-free emission can be obtained despite low growth temperature. Mg-related impurity peak  $I_3$  was observed from the spectrum of Mg-doped AlN sample grown at a  $\text{N}_2$  flow rate of 0.33 sccm. With increasing  $\text{N}_2$  flow rate, the intensity ratio of  $I_2$  to  $I_1$  decreases by two orders of magnitude. The decay-shapes of  $I_2$  and  $I_3$  follow exponential law with fitted short lifetimes of 140 ps and 360 ps, respectively. Such a fast decay, compared to  $\mu\text{s}$  decay time reported previously for donor acceptor pair related transitions in Mg-doped AlN epilayers, suggests both  $I_2$  and  $I_3$  originate from the transitions involving conduction band and impurity energy level inside the bandgap, which further proves that growth of Mg-doped AlN nanowires under nitrogen rich condition can efficiently suppress compensating defect formation, e.g., N-related vacancies. Under optimized growth conditions, AlN nanowire LEDs exhibit excellent current-voltage characteristics, including a turn-on voltage  $\sim 6$  V and negligible reverse leakage current. The current-voltage measurements showed a minimum ideality factor of 4.6 at around 2.4 V, after which the ideality factor increases drastically to values  $> 20$  with increasing voltage. The slopes of temperature-dependent I-V are largely invariant from room temperature to 200 °C and hence the ideality factor shows a strong temperature dependency, suggesting a strong carrier tunneling effect. Work is currently in progress to achieve deep UV LEDs with high power operation by enhancing the light extraction efficiency utilizing AlGaIn photonic nanocrystals and by optimizing the device fabrication process.

[1] Y. Wu, et al. *Appl. Phys. Lett.* **116**, 013101 (2020)

### 4:00 PM NN02

**(Student) Growth of High Quality Crack-Free Partially Relaxed Thick  $\text{Al}_{0.24}\text{Ga}_{0.76}\text{N}$  on Porous GaN Based Compliant GaN Pseudo-Substrates** Shubhra S. Pasayat, Nirupam Hatui, Weiyi Li, Chirag Gupta, Steven DenBaars, Shuji Nakamura, Stacia Keller and Umesh Mishra; University of California, Santa Barbara, United States

The (Al,Ga)-N alloy system is very attractive for ultraviolet (UV) optoelectronic devices and high-power, high-frequency electronic devices, owing to its ultra-wide bandgap (3.4eV to 6eV). One critical problem, however, is the lack of large area lattice matched substrates. When  $\text{Al}_x\text{Ga}_{1-x}\text{N}$  is grown on readily available substrates such as sapphire or silicon, the high dislocation density of the (Al,Ga)N material degrades the device performance. Low dislocation density AlN bulk substrates, on the other hand, are very expensive and not available in large diameters. When grown on GaN, the tensile strain induced by the lattice mismatch between GaN and  $\text{Al}_x\text{Ga}_{1-x}\text{N}$  leads to the cracking of thicker AlGaIn layers [1]. Hence, high quality,  $\text{Al}_x\text{Ga}_{1-x}\text{N}$  pseudo-

substrates are highly desired. Recently, we demonstrated relaxed InGaN films grown on compliant GaN-on-porous-GaN tile arrays, wherein the strain was released elastically by the mechanically flexible porous GaN under-layers[2]. *In this work, we demonstrate relaxed AlGaIn films using the same technique, enabling the fabrication of AlGaIn pseudo-substrates with arbitrary Al composition.*

For the fabrication of the compliant GaN-tile arrays, a thin UID GaN layer was grown on 800-nm-thick GaN:Si ( $\text{Si} = 5 \times 10^{18} \text{ cm}^{-3}$ ) on UID GaN-on-sapphire layers by MOCVD. The samples were then patterned into  $10 \mu\text{m} \times 10 \mu\text{m}$  tile arrays using a  $\text{BCl}_3/\text{Cl}_2$  dry etch chemistry. A doping selective electrochemical (EC) etch was performed as reported in ref. [2-4], which led to the porosification of the GaN:Si layer resulting in compliant GaN-tile arrays. On these samples, first a 200nm thick graded  $\text{Al}_{1-x}\text{Ga}_x\text{N}$  ( $x = 0$  to 0.16) was grown at 1080 °C, with a co-loaded GaN-on-sapphire template as reference. Cracks were seen on the reference sample as expected due to AlGaIn thickness exceeding the critical layer limit, but not on the  $\text{Al}_{1-x}\text{Ga}_x\text{N}$  grown on the GaN-on-porous GaN tiles [1]. Via high-resolution X-ray diffraction ( $\omega$ -2 $\theta$ - $\omega$ ) reciprocal space maps (RSMs) around the GaN (-1-124) reflection, the relaxation of the graded AlGaIn layer was found to be ~13%. Further regrowth of nominally 300nm  $\text{Al}_{0.16}\text{Ga}_{0.84}\text{N}$ , resulted in a smooth, 1 nm surface roughness, crack-free AlGaIn stack. While the nominal  $x_{\text{Al}}$  for the 300nm  $\text{Al}_{1-x}\text{Ga}_x\text{N}$  stack was 0.16 when grown strained to GaN, an enhanced aluminum uptake of 0.24 was observed due to composition pulling effect from the partially relaxed graded  $\text{Al}_{1-x}\text{Ga}_x\text{N}$  underlayer. Due to the presence of the flexible porous GaN layer underneath the AlGaIn layer stack, the  $\text{Al}_{0.24}\text{Ga}_{0.76}\text{N}$  top layer was now 63% elastically relaxed. Thus the a-lattice constant of the AlGaIn top layer corresponded to that of a fully relaxed  $\text{Al}_{0.15}\text{Ga}_{0.85}\text{N}$  film. The study on the impact of the thickness and the composition of the AlGaIn layers on the degree of relaxation is currently underway and will be discussed in detail at the conference.

These results represent the first demonstration of relaxed AlGaIn on GaN films. With the base layers being grown homo-epitaxially, this method enables the fabrication of crack-free AlGaIn layer stacks with a dislocation density similar to the base layers [2]. In conclusion, thick ~63% relaxed crack-free  $\text{Al}_{0.24}\text{Ga}_{0.76}\text{N}$  layers were achieved using GaN-on-porous GaN base layers, which are attractive as base layers for UV LEDs and ultra-wide bandgap electronic devices.

References : [1] K. Itoh *et al.* J. Cryst. Growth, vol. 104, No. 2 (1990) [2] S. S. Pasayat *et al.* Appl. Phys. Lett. (under review), [3] Y. Zhang *et al.*, *Phys. Status Solidi B* **247**, No. 7, 1713–1716 (2010), [4] S. S. Pasayat *et al.*, *Semicond. Sci. Technol.*, vol. **34**, 115020 (2019), [5] J. M. Bethoux *et al.* App. Phys. Lett. **94**, 6499(2003), [6] S. S. Pasayat *et al.*, *Material*, vol. 13, 213 (2020)

#### 4:15 PM NN03

**(Student) Plastic Strain Relaxation of Ga-Rich AlGaIn on AlN Single Crystal Substrates** Yan Guan<sup>1</sup>, Shun Washiyama<sup>1</sup>, James Tweedie<sup>2</sup>, Tim B. Eldred<sup>1</sup>, Seiji Mita<sup>2</sup>, Pegah Bagheri<sup>1</sup>, Dennis Szymanski<sup>1</sup>, Ramón Collazo<sup>1</sup> and Zlatko Sitar<sup>1</sup>; <sup>1</sup>North Carolina State University, United States; <sup>2</sup>Adroit Materials Inc, United States

High crystal quality AlGaIn epitaxial films are highly desirable for near to deep UV optoelectronics applications due to a tunable wide bandgap ranging from 3.4 eV for GaN to 6.0 eV for AlN. The use of foreign substrates for AlGaIn epitaxy resulted in highly-mismatched heterostructures with high dislocation densities. The use of recently available AlN single crystals leads to high crystalline quality epitaxial films due to close matching to AlGaIn lattice parameters and thermal expansion coefficients. However, the lattice mismatch between AlGaIn and AlN results in compressively strained alloy films, varying in strain magnitude with composition. This compressive misfit strain can consequentially affect the properties of AlGaIn-based devices leading to undesirable compositional non-uniformities or unreliable performance. Nevertheless, there are no current models to describe AlGaIn relaxation mechanisms on c-plane AlN as it is expected that these films are pseudomorphic on these substrates. This is expected as there is no resolved shear stress to activate the primary slip systems in hexagonal wurtzite structure under biaxial strain. As such, in this work, the strain relaxation of AlGaIn on AlN single crystal substrate with relatively large lattice misfit is investigated. Mismatch strain relaxation could happened by dislocation nucleation, dislocation bending, crystallographic tilting or surface roughening. In the case of preexisting dislocations in the substrate, their propagation through the film would play an important role in strain relaxation through dislocation bending.  $\text{Al}_{1-x}\text{Ga}_x\text{N}$  layers were grown by MOCVD either on a c-plane AlN substrate or an AlN template on sapphire substrate to elucidate the role of these preexisting dislocations. The dislocation density in an AlN substrate is below  $10^3 \text{ cm}^{-2}$ , whereas that in an AlN layer grown on sapphire is  $\approx 2 \times 10^{10} \text{ cm}^{-2}$ . Al mole fraction was varied from 25% to 90% by varying metalorganic precursor flow rates. High resolution X-ray diffraction (HRXRD) was employed to determine the composition and strain relaxation. Atomic force microscopy (AFM) and transmission electron microscopy (TEM) were carried out to characterize the surface morphology and defect structures.

HRXRD symmetric (002) and asymmetric (105) reciprocal space mappings (RSMs) revealed that  $\text{Al}_{1-x}\text{Ga}_x\text{N}$  layers grown on AlN substrate were pseudomorphic, regardless of alloy composition ( $0.5 < x < 0.9$ ). Instead of plastic relaxation, the AlGaIn films exhibited so-called “epilayer tilt”. In contrast, full relaxation of the in-plane lattice parameter was observed in Ga-rich 1  $\mu\text{m}$  thick  $\text{Al}_{0.25}\text{Ga}_{0.75}\text{N}$  layers grown on AlN substrates. The relaxed  $\text{Al}_{0.3}\text{Ga}_{0.7}\text{N}$  layer did

not show a strain gradient. This is in contrast to the strain gradient that was observed in AlGaIn on AlN/sapphire, which is believed to result from dislocation inclination. This difference indicates that  $\text{Al}_{0.25}\text{Ga}_{0.75}\text{N}$  layer was abruptly relaxed due to a lack of the preexisting dislocations in AlN substrate. In addition, AFM revealed high density of growth spirals on the relaxed  $\text{Al}_{0.25}\text{Ga}_{0.75}\text{N}$  layer. X-ray rocking curve measurement also showed much broader AlGaIn peaks compared the AlN bulk crystal. Therefore, Ga-rich AlGaIn is plastically relaxed on AlN by generating dislocations seemingly contradicting the hypothesis that there is no resolved shear stress activating the primary slip system due to the expected biaxial strain. The dislocation structure in the relaxed AlGaIn layer will be presented as well as possible relaxation mechanism including the resulting critical layer thickness.

#### 4:30 PM NN04

**Low Temperature Hydride Assisted HVPE Growth of Single Crystal AlN Films** Kevin Udway, Jacob Leach and Gregg Dodson; Kyma Technologies, United States

High quality aluminum nitride layers grown by hydride vapor phase epitaxy (HVPE) methods have classically needed growth temperatures well in excess of 1100°C with many of the best results being grown in the range of 1400°C. These high temperatures are used in order to promote the surface migration of Al adatoms, allowing for smooth morphologies and high crystalline quality. However, these elevated temperatures make the use of quartz reactor chambers difficult, as quartz begins to soften at 1200°C, and requires specially designed reactors. This study examined the use of hydrochloric gas, injected directly into the growth surface, to create an etching effect on the growing AlN film, and increase the mobility of Al adatoms at the crystal surface, allowing for high quality, single crystal AlN layers with a growth temperature of just 1000°C. With this method, AlN layers of 5  $\mu\text{m}$  thickness were grown on c-plane (0 0 0 1) sapphire, with a growth rate of 20  $\mu\text{m}/\text{hour}$ , and a resulting full-width at half-maximum (FWHM) of symmetric (0 0 2) rocking curve reflection of 343 arcsec and asymmetric (1 0 -1 2) reflection of 942 arcsec. Growth rates of single crystal AlN layers above 100  $\mu\text{m}/\text{hour}$  were also achievable, although crystalline quality suffered.

#### 4:45 PM NN05

**Crack and Strain Free 16- $\mu\text{m}$  Thick AlN on Sapphire for the Thermal Management of III-N Electronics** Abdullah Mamun, Mohammad K. Hussain, Joshua Letton, Shahab Mollah, Iftikhar Ahmad, Mikhail Gaevski, MVS Chandrashekar, Grigory Simin and Asif Khan; University of South Carolina, United States

We report MOCVD growth and characterization of 3 to 16  $\mu\text{m}$  thick, crack-free, low-dislocation density AlN template layers on basal plane sapphire substrates. X-ray diffraction, Raman, Cathodoluminescence (CL) imaging, and transmission electron microscopy were used to establish the presence of intentionally created microscopic voids for strain-management at the AlN/Sapphire interface. This led to unstrained, smooth (rms roughness < 0.2 nm) crack-free growth on 2-inch diameter wafers. Dislocation annihilation due to these voids was observed, with total dislocation densities (from etch pit density) decreasing with increasing AlN thickness from  $5.9 \times 10^8$  down to  $2.0 \times 10^8 \text{ cm}^{-2}$ . The in-plane mosaicity of these films was inferred to be due to vacancies/point defects rather than from extended defects such as dislocations. The thermal conductivity of the thickest AlN layers as measured by the time-domain thermoreflectance (TDTR) was 30% higher at 120 K, despite the higher dislocation densities in our MOCVD grown layers. This demonstrates that the limiting factor in the use of AlN for thermal management of ultra-wide bandgap power and opto-electronics is not threading dislocations. The thick AlN epitaxial layers enable an easier transfer from the sapphire substrates to higher thermal conductivity materials and they are ideal for applications requiring increased light extraction from optoelectronic devices. This underscores their high value for next-generation ultra-wide bandgap III-N devices.

SESSION OO: Spintronic and Magnetic Materials and Devices

Session Chair: Songrui Zhao

Session Hosts: Kasey Hogan and Benjamin McEwen

Friday Afternoon, June 26, 2020

Location: ZoomRoom 4

#### 2:15 PM OO01

**(Student) High-Temperature Probe of Coherent Evolution in Isolated Near-Surface Spin Centers through Resonance in Low-Field DC Magnetoresistance** Stephen R. McMillan<sup>1</sup>, Nicholas J. Harmon<sup>2</sup> and Michael Flatté<sup>1,3</sup>; <sup>1</sup>University of Iowa, United States; <sup>2</sup>University of Evansville, United States; <sup>3</sup>Technische Universiteit Eindhoven, Netherlands

Components for quantum information processing and quantum sensing require localized spin-coherent states. These states can be realized in isolated magnetic dopants embedded in a non-magnetic semiconducting host. A critical requirement for utilizing a dopant-based system is an understanding of how the complex host environment influences the coherent spin dynamics at an individual site. The energy scales of these interactions can be many orders of

magnitude smaller than the thermal energy in the system challenging the resolution of high-temperature spectroscopy. By coupling the coherent dynamics of the spin center with the correlated transport through a spin-polarized nano-contact, resonances in the dc magnetoresistance provide a dynamic means of resolving these low energy interactions even at high temperatures. As an initial proposal we calculate the current through a spin-1/2 dopant that is addressed by a spin-polarized scanning tunneling microscope (SP-STM) and exchange coupled to an occupationally stable spin-1/2 center [1]. The stochastic Liouville formalism is employed to calculate the current through the individual dopant and we predict a substantial increase in resistance at mT scale applied magnetic fields due to the formation of a non-trivial bottleneck. Resonance between the Zeeman and exchange coupling leads to restricted coherent evolution of the dopant spin resulting in an on-site polarization opposing that of the SP-STM. This feature provides a precise method for measuring the dopant exchange coupling to a nearby electronic spin and by direct analog hyperfine coupling in the presence of a nuclear spin without the use of ac electric or ac magnetic fields. While spin-1/2 centers are excellent candidates for magnetic field sensing, they are insensitive to local electric fields. In addition to the spin-1/2 centers we consider transport mediated by a single spin-1 center, such as a divacancy in SiC, addressed by an SP-STM opening the coherence-correlation method to resolution of local electric and strain fields. This material is based on work supported by the U.S. Department of Energy, Office of Science, Office of Basic Energy Sciences, under Award Number DE-SC0016447 and its renewal DE-SC0016379. [1] S.R. McMillan, N.J. Harmon, M.E. Flatté, [https://arxiv.org/abs/1907.05509] [cond-mat.mes-hall]

### 2:30 PM 0002

**Ferromagnetic Behavior in Rare Earth-Doped III-Nitride Semiconductors Grown by Molecular Beam Epitaxy** Javier Wu<sup>1</sup>, Kiran Dasari<sup>1</sup>, Wojciech M. Jadwisieniczak<sup>2</sup> and Ratnakar Palai<sup>1</sup>; <sup>1</sup>University of Puerto Rico at Río Piedras, United States; <sup>2</sup>Ohio University, United States

III-Nitride semiconductors and their alloys (InN, GaN, AlN, and InGaN) are promising materials for applications in electronics. Currently a great deal of attention is being focused on adding spin degree-of-freedom into semiconductor to create a new area of solid-state electronics, called spintronics. In spintronics not only the current but also its spin state is controlled. Such materials need to be good semiconductors for easy integration in typical integrated circuits with high sensitivity to the spin orientation. In the past, most of the attention on ferromagnetic semiconductor has focused on the GaMnAs and InMnAs. Despite of many years of intense research the highest Curie temperatures ( $T_c$ ) reported were far below the room temperature, about 185K for GaMnAs and ~35 K for InMnAs. The major material challenge is to magnetize and stabilize semiconductors with room temperature ferromagnetic ordering without significantly affecting the physical properties of semiconductors.

Rare-earth (RE) elements play an important role in many functional materials and exhibit interesting magnetic and optoelectronic properties. Due to their highly localized 4f electrons, the direct f-f interactions between the neighboring rare-earth atoms are very weak. This produces larger magnetic moments in 4f REs than 3d transition metals. Most of the earlier works on dilute magnetic semiconductor (DMS) were focused on TM doped GaN and ZnO and weak magnetization has been reported with few percentage (< 5%) of doping. In order to enhance the magnetization, higher percentage of TM doping in ZnO and GaN was investigated but it was found that the magnetization related to the clustering or precipitation of TM ions. Since REs have higher magnetic moment than TMs, we expect to achieve higher magnetization with a few percentages of RE doping. In the present work, thin films and nanorods of Yb and Er-doped GaN and InGaN were grown using molecular beam epitaxy (MBE). Yb-doped GaN and InGaN thin films and nanorods show room temperature ferromagnetism with enhanced luminescent properties. The paper will discuss the origin of room temperature behavior in RE-doped III-nitride nanostructures [1-2].

References:

K. Dasari, J. Wang, M. J-F Guinel, W.M. Jadwisieniczak, H. Huhtinen, R. Mundle, A.K. Pradhan, **R. Palai**, "Growth, microstructural, Optical, and magnetic properties of the high In-content InGaN:Yb nanorods grown by molecular beam epitaxy", Journal Applied Physics. **118**, 125707 (2015).

K. Dasari, J. Wu, H. Huhtinen, W.M. Jadwisieniczak, **R. Palai**, "Growth, luminescence and magnetic properties of GaN:Er semiconductor thin films grown by molecular beam epitaxy" Journal of Physics D: Applied Physics, **50** (17), 175104 (2017).

### 2:45 PM 0003

**Temperature-Dependent Magnetic Transitions of a CoCrPt-Ru-CoCrPt Synthetic Ferrimagnet** Bradlee K. Beauchamp and Ernesto E. Marinero; Purdue University, United States

The magnetic orientations and switching fields of a CoCrPt-Ru-CoCrPt synthetic ferrimagnet with perpendicular anisotropy have been studied at temperatures 2-370 K. It was found that two sets of allowed transitions occur in the CoCrPt-Ru-CoCrPt system, with the transitions between these two regimes being around 2-50 K. The hysteresis curves of the synthetic ferrimagnet are assessed using the energy diagram technique which accurately describes the

competition between exchange energy, Zeeman energy, and anisotropy energy in the system. This energy diagram technique is then used to predict the change in hysteresis curve properties of the synthetic ferrimagnet at 220 K and 370 K which represent potential operation temperature extrema that the synthetic ferrimagnet could be expected to operate at, were it to be utilized as a free layer in a memory spintronic device.

### 3:00 PM 0004

**(Student) Low-Damping Ferromagnetic Resonance in Electron-Beam Patterned, High-Q Vanadium Tetracyanoethylene Magnon Cavities** Andrew J. Franson<sup>1</sup>, Na Zhu<sup>2</sup>, Seth Kurfman<sup>1</sup>, Michael Chilcote<sup>1</sup>, Denis R. Candido<sup>3,4</sup>, Kristen Buchanan<sup>5</sup>, Michael Flatté<sup>3,4</sup>, Hong Tang<sup>2</sup> and Ezekiel Johnston-Halperin<sup>1</sup>; <sup>1</sup>The Ohio State University, United States; <sup>2</sup>Yale University, United States; <sup>3</sup>The University of Iowa, United States; <sup>4</sup>The University of Chicago, United States; <sup>5</sup>Colorado State University, United States

Integrating patterned, low-loss magnetic materials into microwave devices and circuits presents many challenges due to the specific conditions that are required to grow ferrite materials, driving the need for flip-chip and other indirect fabrication techniques. For example, coupling magnons to qubits has seen either low-loss magnons in yttrium iron garnet (YIG) coupled to qubits through an intermediary microwave cavity mode, or relatively high-loss magnons in permalloy coupled directly to qubits. The low-loss ( $\alpha=3.98 \times 10^{-5}$ ), room-temperature ferromagnetic coordination compound vanadium tetracyanoethylene (V[TCNE]<sub>x</sub>) is a promising new material for these applications that is potentially compatible with traditional semiconductor processing techniques. Here we present the deposition, patterning, and characterization of V[TCNE]<sub>x</sub> thin films with lateral dimensions ranging from 1 micron to several millimeters. Growth occurs in an argon atmosphere at 30 mTorr and 50 °C. We employ electron-beam lithography and liftoff using an aluminum encapsulated PMMA/P(MMA-MAA) copolymer bilayer on sapphire. This process can be trivially extended to other common semiconductor substrates. Films patterned via this method maintain low-loss characteristics down to 25 μm with only a factor of 2 increase down to 5 μm, as characterized through scanning electron microscopy, cavity ferromagnetic resonance, and broadband ferromagnetic resonance. A manifold of thickness and radial confined spin wave modes reveals the quality of the patterned films. Further fitting, simulation, and analytic analysis provide an exchange stiffness,  $A_{ex} = (2.2 \pm 0.5) \times 10^{-10}$  erg/cm, as well as insights into the mode character and surface-spin pinning. Below a micron, the deposition is nonconformal, which leads to interesting and potentially useful changes in morphology. This work establishes the versatility of V[TCNE]<sub>x</sub> for applications requiring highly coherent magnetic excitations ranging from microwave communication to quantum information.

### 3:15 PM BREAK

### 3:45 PM 0005

**(Student) Tailoring Magnons for Applications in Quantum Information Science** Huma Yusuf<sup>1</sup>, Michael Chilcote<sup>2</sup>, Hil Fung H. Cheung<sup>2</sup>, Donley Cormode<sup>1</sup>, Andrew J. Franson<sup>1</sup>, Seth Kurfman<sup>1</sup>, Ezekiel Johnston-Halperin<sup>1</sup> and Gregory D. Fuchs<sup>2</sup>; <sup>1</sup>The Ohio State University, United States; <sup>2</sup>Cornell University, United States

The ability to move beyond the study of isolated qubits to explore hybrid systems, i.e. where two or more component qubits coherently couple to yield new functionality, and to transduce and transmit quantum information is a key challenge for the emerging field of quantum information science and technology (QIST). Magnons (or spin-waves) provide an appealing avenue toward realizing this functionality as they can couple to a wide variety of spin-qubits using either exchange or dipole coupling, have coherence lengths from microns to millimeters, and can coherently transduce between spins, microwave photons, and phonons.

However, in order to fulfill this potential, materials with high quality-factor (high-Q), or low-loss, magnons are required. For almost half a century, we have been limited to yttrium iron garnet (YIG) despite substantial efforts to identify alternative materials. The molecule-based ferrimagnet vanadium tetracyanoethylene (V[TCNE]<sub>x</sub>;  $x \sim 2$ ) has recently emerged as a compelling alternative to YIG. In contrast to other molecule-based materials, V[TCNE]<sub>x</sub> has a single-peaked, narrow magnetic resonance feature (less than 1 G at 10 GHz) and has a Curie temperature of over 600 K with sharp hysteresis switching to full saturation at room temperature. In addition to being magnetically robust, V[TCNE]<sub>x</sub> is a promising material for integration into solid-state quantum information systems due to its low damping ( $\alpha = (3.98 \pm 0.22) \times 10^{-5}$ ), high quality factor (Q up to 8,000) microwave resonance, ease of patterning, and compatibility with a wide variety of substrates.

Here we will discuss how V[TCNE]<sub>x</sub> can be exploited for applications in quantum information science. We report anomalous temperature dependent anisotropy in V[TCNE]<sub>x</sub> thin films, where we observe switching of magnetic easy-axis from in-plane at 300 K to out of plane at 25 K with a clear absence of anisotropy at 100 K. This observation reveals the ability to employ temperature dependent strain-tuning for engineering magnon modes and validates the utility of V[TCNE]<sub>x</sub> at low temperatures, where many quantum systems operate. Furthermore, we will discuss applications of patterned V[TCNE]<sub>x</sub> magnon-resonators in a hybrid quantum device.

#### 4:00 PM OO06

**(Student) First Principles Calculation of the Electronic Structure of V(TCNE)<sub>2</sub>** Yueguang Shi and Michael Flatté; The University of Iowa, United States

Over the past two decades there has been growing interest in organic magnetic materials, due to their potential applications in the field of magnonics and spintronics.[1,2,3,4] Vanadium tetracyanoethylene, V(TCNE)<sub>2</sub>, is a room temperature ferrimagnetic semiconductor with a  $T_c \sim 600$  K [5] which has very low loss ferromagnetic resonance and spin-wave propagation [1, 2]. Previous first principles calculations of the electronic structure have indicated a substantially larger band gap (0.8 eV) than experimentally inferred (0.5 eV) [6,7], and that the band gap itself is an indirect gap with the valence maximum located at the (0,0,0.5) point and the conduction minimum at the (0,0.5,0) point. Our crystal axes are defined so that an equatorial TCNE ligand lies in the plane (0 0 1) and an apical ligand lies in the plane (1 1 0) in a unit cell. The study of Ref. 6 used a local-orbital basis with B3LYP hybrid functional. Here we explore the electronic structure using a plane-wave code VASP[8,9,10]. We have tried the following functionals: Perdew-Burke-Ernzerhof (PBE), PBE0, Becke, 3-parameter, Lee-Yang-Parr (B3LYP), Heyd-Scuseria-Ernzerhof (HSE06). The ferrimagnetic structure is studied using both collinear magnetic structure calculations and non-collinear calculations. We confirm that the structure of VTCNE has a triclinic unit cell with each V atom surrounded by 6 organic ligands, as found in Ref. 6. However, in contrast to the previous study we find a direct band gap of 0.4 eV located at the (0,0.5,0.5) point. This band gap better agrees with the experimental inference from the conductivity activation energy [7]. Further studies will explore the optical properties of this material as well as its magnetic dynamics.

We acknowledge funding from NSF-DMR1808704.

[1] H. Yu, M. Harberts, R. Adur, Y. Lu, P. C. Hammel, E. Johnston-Halperin, and A. J. Epstein, *Appl. Phys. Lett.* **105**, 012407 (2014). [2] N. Zhu, X. Zhang, I. H. Fröning, M. E. Flatté, E. Johnston-Halperin, and H. X. Tang, *Appl. Phys. Lett.* **109**, 082402 (2016). [3] H. Liu, C. Zhang, H. Malissa, M. Groesbeck, M. Kavand, R. McLaughlin, S. Jamali, J. Hao, D. Sun, R. A. Davidson, L. Wojcik, J. S. Miller, C. Boehme, and X. V. Vardeny, *Nat. Mater.* **17**, 308–312 (2018). [4] A. Franson, N. Zhu, S. Kurfman, M. Chilcote, D. R. Candido, K. S. Buchanan, M. E. Flatte, H. X. Tang, and E. Johnston-Halperin, *APL Materials* **7**, 121113 (2019). [5] J. M. Manriquez, G. T. Yee, R. S. McLean, A. J. Epstein, and J. S. Miller, *Science* **252**, 1415 (1991). [6] G. C. De Fusco, L. Pisani, B. Montanari, and N. M. Harrison, *Phys. Rev. B* **79**, 085201 (2009). [7] V. N. Prigodin, P. R. Nandyala, K. I. Pokhodnya, J. S. Miller, and A. J. Epstein, *Adv. Mater.* **14**, 1230 (2002). [8] G. Kresse and J. Hafner, *Phys. Rev. B* **47**, 558 (1993); *ibid.* **49**, 14 251 (1994). [9] G. Kresse and J. Furthmüller, *Comput. Mat. Sci.* **6**, 15 (1996). [10] G. Kresse and J. Furthmüller, *Phys. Rev. B* **54**, 11 169 (1996).

#### 4:15 PM OO07

**Analytical Calculation of Fringe Fields and Magnetization Profiles in V[TCNE]<sub>x-2</sub> Cylindrical Disks** Denis R. Candido<sup>1,2</sup> and Michael Flatté<sup>1,2</sup>; <sup>1</sup>University of Iowa, United States; <sup>2</sup>The University of Chicago, United States

Magnons or spin waves [1,2] are collective excitations in magnetic materials that can be created through the application of alternating magnetic fields. They have been extensively investigated due to their long spin coherence times and their potential applications. In this work we solved Maxwell's and the Landau-Lifshitz-Gilbert equations for a ferrimagnetic V[TCNE]<sub>x-2</sub> disk [3,4] on top of a diamond substrate. More specifically, with complete pinning at both the bottom and top surfaces we obtained analytical expressions for the magnon dispersion, magnetization profile and fringe fields [4,5]. We also relax the pinning condition and investigated the effect on fringe fields, dispersion and magnetization. We calculated these quantities for out of plane magnetic fields. The material is based on work supported by the U.S. Department of Energy, Office of Basic Energy Sciences, under Award Number DE-SC0019250.

[1] R. W. Damon and J. R. Eshbach, *J. Phys. Chem. Solids* **19**, 308 (1961). [2] R. W. Damon and H. van de Vaart, *Journal of Applied Physics* **36**, 11 (1965) [3] Na Zhu, Xufeng Zhang, I. H. Fröning, Michael E. Flatté, E. Johnston-Halperin and Hong X. Tang., *Applied Physics Letters* **109**, 082402 (2016) [4] Andrew Franson, Na Zhu, Seth Kurfman, Michael Chilcote, Denis R. Candido, Kristen S. Buchanan, Michael E. Flatté, Hong X. Tang, and Ezekiel Johnston-Halperin, *APL Mater.* **7**, 121113 (2019). [5] Denis R. Candido, Gregory D. Fuchs, Ezekiel Johnston-Halperin, Michael E. Flatté, in preparation

#### 4:30 PM OO08

**(Student) Magnon Modes of V[TCNE]<sub>x-2</sub> Magnonic Crystals** Kwangyul Hu<sup>1</sup> and Michael Flatté<sup>1,2,3</sup>; <sup>1</sup>University of Iowa, United States; <sup>2</sup>The University of Chicago, United States; <sup>3</sup>Eindhoven University of Technology, Netherlands

In magnonics, Yttrium iron garnet (YIG) has been long considered as an ideal magnetic material for its low damping, narrow FMR linewidth[2] and long spin lifetime[3]. However, deposition of high quality YIG requires a specific substrate superlattice, gadolinium gallium garnet (GGG) with high temperature. In addition, recent studies revealed that the linewidth of YIG greatly increases in low temperature regime[5]. These disadvantages limit the integration of YIG such as with silicon or with superconductors. Recently, an organic semiconducting ferrimagnet, vanadium tetracyanoethylene

(V[TCNE]<sub>x-2</sub>) is receiving strong interest as a magnonic media to replace YIG. Compared to YIG, high quality V[TCNE]<sub>x-2</sub> can be grown on various substrates such as quartz and silicon using the low temperature chemical vapor deposition[6]. Furthermore, narrow FMR linewidth of V[TCNE]<sub>x-2</sub> is stable even in the cryogenic condition. With the same advantages of YIG[7-8], these results show the potential of V[TCNE]<sub>x-2</sub> in construction of magnonic devices. Here, we investigate and present dispersion relations and linewidths of magnonic crystals based on V[TCNE]<sub>x-2</sub>. We used the Landau-Lifshitz-Gilbert (LLG) formalism to calculate magnetization in the magnonic crystals. The plane wave method and linear approximations are employed to simplify the LLG equation[9-10]. To model the magnonic crystals, we consider both quasi one-dimensional and two-dimensional infinitely periodic heterostructures of V[TCNE]<sub>x-2</sub> and YIG. We also analyze surface modulated magnonic crystals (SMMC) of bulk V[TCNE]<sub>x-2</sub>. Our results offer understanding of spin wave properties in V[TCNE]<sub>x-2</sub> and suggest how to design viable magnonic devices using V[TCNE]<sub>x-2</sub>. We Acknowledge support from NSF EFRI NewLAW under Award No. EFMA-1741666.

[1] C. Hauser, *et al. Sci. Rep.* **6**, 20827 (2016). [2] E. G. Spencer, R. C. LeCraw and R. C. Linares Jr, *Phys. Rev.* **123** 1937 (1961). [3] Y. Y. Sun, Y. Y. Song and M. Z. Wu, *Appl. Phys. Lett.* **101**, 082405 (2012). [4] C. L. Jermain, S. V. Aradhya, N. D. Reynolds and R. A. Buhrman *Phys. Rev. B* **95**, 174411 (2017). [5] H. Yu, *et al. Appl. Phys. Lett.* **105**, 012407 (2014). [6] N. Zhu, *et al. Appl. Phys. Lett.* **109**, 082402 (2016). [7] H. Liu, *et al. Nat. Mater.* **17**, 308-311 (2018). [8] G. Sietsema, T. Liu and M. E. Flatté, *SPIN*, **7**, 1740012 (2017). [9] M. L. Sokolovskyy and M. Krawczk, *J. Nanopart. Res.* **13**, 6083 (2011). [10] R. A. Gallardo *et al. Phys. Rev. B*, **97**, 144405 (2018).

#### 4:45 PM OO09

**(Student) 3D Mode Engineering in Magnon Microresonators** Huma Yusuf<sup>1</sup>, Donley Cormode<sup>1</sup>, Hil Fung H. Cheung<sup>2</sup>, Seth Kurfman<sup>1</sup>, Andrew J. Franson<sup>1</sup>, Michael Chilcote<sup>2</sup>, Gregory D. Fuchs<sup>2</sup> and Ezekiel Johnston-Halperin<sup>1</sup>; <sup>1</sup>The Ohio State University, United States; <sup>2</sup>Cornell University, United States

Magnons (quantized spin wave excitations in magnetic materials) are central to the operation of many microwave electronic devices and show additional potential for use in quantum information science and technology (QIST). Magnons can be used to store and transmit information, coherently couple to microwave photons, phonons, and spins, and have coherence lengths of microns to millimeters. Vanadium tetracyanoethylene (V[TCNE]<sub>x</sub>) is a molecule-based, room-temperature, low-loss ferrimagnet. Its low loss is quantified by the ultra-low Gilbert damping of its magnonic excitations ( $\alpha = (3.98 \pm 0.22) \times 10^{-5}$ ) and high quality-factor (Q up to 8,000), comparable to or better than inorganic yttrium iron garnet (YIG) thin films. Here, we discuss strategies that exploit the low temperature (50 C) and conformal deposition of V[TCNE]<sub>x</sub> films via chemical vapor deposition (CVD) to realize 3D nano- and micro-structures that act as resonant magnon cavities. We focus on the use of pre-patterned substrates etched with grooves [1] and patterned with posts to generate structures that provide 1D and 0D magnon confinement, respectively. The shape of these magnetic structures controls both their magnetic anisotropy (via strain) and the mode shape of confined magnons. We demonstrate the ability to quantitatively model these confined magnons, revealing excellent agreement with experimentally measured spectra. This result establishes our ability to engineer 3D mode confinement for high-Q (low loss) magnons for applications in microwave electronics and QIST. [1] M. Chilcote, M. Harberts, B. Fuhrmann, K. Lehmann, Y. Lu, A. Franson, H. Yu, N. Zhu, H. Tang, G. Schmidt, and E. Johnston-Halperin, "Spin-wave confinement and coupling in organic-based magnetic nanostructures," *APL Mater.* **7**, 111108 (2019) doi: 10.1063/1.5119077

SESSION PP: Novel Materials  
Session Chair: Kyle McNicholas  
Session Hosts: Kurt Eyink and Kunyao Jiang  
Friday Afternoon, June 26, 2020  
Location: ZoomRoom 5

#### 2:00 PM PP01

**Enabling Low-Temperature Epitaxy of Functional Complex Oxides** Henrik Sonstebj and Ola Nilsen; University of Oslo, Norway

Complex oxide electronics are attracting increasing attention due to the possibility of constructing devices with fundamentally different behavior than what is found in traditional Si-based materials systems. This is a welcome development at a time where Si-based architectures are close to reaching its fundamental inherent size and effect limitations. A detrimental challenge for the implementation of oxide electronics has been the lack of applicable deposition techniques that work under conditions that can facilitate monolithic device integration.

High quality epitaxial complex oxides systems are typically deposited by physical techniques such as pulsed laser deposition (PLD) or molecular beam epitaxy (MBE). While these techniques offer extremely high quality epitaxy and sharp interfaces, they typically operate at high temperatures and high vacuum, and on limited substrate areas. Chemical vapor deposition (CVD) and

chemical solution deposition (CSD) are also employed, but the resulting films are typically in need of post deposition annealing to facilitate solid phase epitaxy.

This has traditionally also been the case for atomic layer deposition (ALD), but with new insight in growth we have been able to find routes for direct epitaxy of a range of nickelates and ferrites at temperatures as low as 225 °C. ALD offers straightforward upscaling on large area wafers with already existing deposition technology. Furthermore, the technique does not require line of sight, and can be used to deposit films on substrates with complex geometries. In this talk, we present a facile route for ALD of the important metallic complex oxide LaNiO<sub>3</sub> at 225 °C. The resulting thin films are highly epitaxial as deposited on LaAlO<sub>3</sub> (100/110/111) and SrTiO<sub>3</sub> (100/110/111), with no post-deposition annealing required to obtain the attractive functional properties. The interface towards the substrates are near defect free, and extremely sharp. Thickness can be varied between sub-nanometer to approximately 100 nm without loss of epitaxy or functionality. Hall measurements reveal resistivities in the 100 μΩ cm range, with carrier concentrations >10<sup>22</sup> cm<sup>-3</sup>. The LaNiO<sub>3</sub> films remain metallic at all temperatures.

We go on to show how ALD can further be used to cation substitute the host LaNiO<sub>3</sub>-material with Cu<sup>2+</sup> on Ni-site to tune the electronic properties. Films remain crystalline as deposited up to substitution levels of 50 %, after which post-deposition annealing is necessary to obtain epitaxy. Substitution is attainable from 0 to 100 %, with large variation in electronic properties. We show that electronic resistivity can be tuned smoothly over 6 orders of magnitude from 100 μΩ cm to 100 Ω cm, with temperature dependent resistivities showing increasing metal-insulator transition (MIT) temperatures. MIT temperatures can be tuned from 0 K to above RT.

This new development in the possibility of low-temperature direct epitaxy of important functional materials open up for facile monolithic device integration of complex oxides, which will become important in novel oxide electronic devices.

## 2:15 PM PP02

### (Student) Magnetic and Electronic Characterization of Magnetic

**Topological Insulator MnBi<sub>2</sub>Se<sub>4</sub>**, Alexander J. Bishop<sup>1</sup>, Tiacong Zhu<sup>1</sup>, Tong Zhou<sup>2</sup>, Menglin Zhu<sup>1</sup>, Dante O'Hara<sup>1,3</sup>, Alexander Baker<sup>4</sup>, Shuyu Cheng<sup>1</sup>, Robert Walko<sup>1</sup>, Jacob Repicky<sup>1</sup>, Jay Gupta<sup>1</sup>, Chris Jozwiak<sup>5</sup>, Eli Rotenberg<sup>5</sup>, Jinwoo Hwang<sup>1</sup>, Igor Zutic<sup>2</sup> and Roland Kawakami<sup>1</sup>; <sup>1</sup>The Ohio State University, United States; <sup>2</sup>University at Buffalo, The State University of New York, United States; <sup>3</sup>University of California, Riverside, United States; <sup>4</sup>Lawrence Livermore National Laboratory, United States; <sup>5</sup>Lawrence Berkeley National Laboratory, United States

The intrinsic magnetic topological insulators MnBi<sub>2</sub>X<sub>4</sub> (X = Se, Te) are promising candidates in realizing various novel topological states related to symmetry breaking by magnetic order. Although much progress had been made in MnBi<sub>2</sub>Te<sub>4</sub>, the study of MnBi<sub>2</sub>Se<sub>4</sub> has been lacking due to the difficulty of material synthesis of the desired trigonal phase. Here, we report the synthesis of multilayer trigonal MnBi<sub>2</sub>Se<sub>4</sub> with alternating-layer molecular beam epitaxy. Atomic-resolution scanning transmission electron microscopy (STEM) and scanning tunneling microscopy (STM) identify a well-ordered multilayer vdW crystal with septuple-layer base units in agreement with the trigonal structure. Systematic thickness dependent magnetometry study confirms the layered antiferromagnetic ordering as predicted by theory. Angle resolved photoemission spectroscopy (ARPES) reveals the gapless Dirac-like surface state of MnBi<sub>2</sub>Se<sub>4</sub>, which demonstrates that MnBi<sub>2</sub>Se<sub>4</sub> is a topological insulator above the magnetic ordering temperature. These systematic studies show that MnBi<sub>2</sub>Se<sub>4</sub> is a promising candidate for exploring the rich topological phases of layered antiferromagnetic topological insulators.

## 2:30 PM PP03

**MOCVD Growth and Characterization of ZnSnN<sub>2</sub>**, Benthara H. Jayatunga<sup>1</sup>, Md Rezaul Karim<sup>2</sup>, Menglin Zhu<sup>2</sup>, Jinwoo Hwang<sup>2</sup>, Hongping Zhao<sup>2</sup> and Kathleen Kash<sup>1</sup>; <sup>1</sup>Case Western Reserve University, United States; <sup>2</sup>The Ohio State University, United States

Since the first reports of its synthesis in 2011 and 2012<sup>1,3</sup>, interest in ZnSnN<sub>2</sub> for diverse applications, including photovoltaics<sup>1,3,4</sup>, visible light photocatalysis<sup>5</sup>, and optoelectronics<sup>6</sup>, has been growing. Novel nitride-based LED device designs promise high gains in efficiency at emission wavelengths into the green, amber and even red.<sup>6,8</sup> Their realization requires the precise insertion of an ultrathin layer of ZnGeN<sub>2</sub> or ZnSnN<sub>2</sub> into the active region of an InGaAs-GaAs LED structure. While thin films of ZnSnN<sub>2</sub> have been synthesized by RF sputtering<sup>1,9</sup> and by MBE<sup>2,10,11</sup>, and thin films of ZnGeN<sub>2</sub>, ZnSiN<sub>2</sub> and their alloys by MOCVD, the synthesis of ZnSnN<sub>2</sub> thin films by MOCVD has not yet been reported. It is a challenging goal, given the narrow temperature window between efficient activation of ammonia and the thermal decomposition of ZnSnN<sub>2</sub> at near-atmospheric pressures. We report here the results of studies of ZnSnN<sub>2</sub> films grown on r- and c-plane sapphire substrates, GaN templates on sapphire, and In<sub>0.15</sub>Ga<sub>0.85</sub>N templates on GaN-on-sapphire, at temperatures from 500 °C to 560 °C, using tetramethyltin (TMSn), diethylzinc (DEZn), germane and ammonia. Chamber pressures were varied between 200 and 500 torr. In addition, the ratios of the cation precursors and the total cation-to-anion precursor ratios were varied. Single crystal growth, as evidenced by 2θ-ω x-ray diffraction scans, was achieved on all of these substrates. Wurtzitic (0002) ZnSnN<sub>2</sub> diffraction were observed at 2θ ~ 32.9° for the samples grown on

c-sapphire, GaN (0001) and InGaN (0001) templates, and wurtzitic (11-20) peak at 2θ ~ 54.8° for the films grown on r-sapphire. Higher pressures and higher temperatures promoted better crystallinity and more continuous films, as revealed by scanning electron microscopy (SEM) images and 2θ-ω x-ray diffraction peak widths and intensities. Crystal quality was observed to be highly dependent on growth temperature. For example, in one series a 10 °C change in growth temperature resulting in a factor of 15 increase in diffraction peak intensity. SEM images show that films grown on the GaN templates had better uniformity in nucleation than those grown on sapphire. The presence of satellite peaks around the Bragg peak in the XRD 2θ-ω scan for a film grown on a GaN template, and the absence of satellite peaks for the films grown simultaneously on c- and r-sapphire, also indicate superior quality for the film grown on GaN. HAADF-STEM images of films grown on these templates showed smooth interfaces at the film-substrate boundary and show growth rates as high as 167 nm/h, considerably higher than reported previously for MBE growth.<sup>9,10</sup> Electron diffraction patterns show single crystallinity. Rocking curves show FWHM as low as 0.10°. RMS surface roughnesses, measured by atomic force microscopy, are of the order of 3 nm for 1 μm x 1 μm areas. Current work is focusing on optimizing growth on InGaN templates. These templates are promising for their relatively lower lattice mismatch with ZnSnN<sub>2</sub>. Their use is a next step toward producing LED device structures. This work was supported by the National Science Foundation under grant no. DMREF: SusChem: 1533957 and by the U.S. Department of Energy under grant no. DOE SSL: DE-EE0008718. <sup>1</sup>Coronel, N.C. et al., Proc. 38<sup>th</sup> IEEE Photovoltaic Specialists Conf., 2524 (2012). <sup>2</sup>Feldberg, N. et al., Proc. 38<sup>th</sup> IEEE Photovoltaic Specialists Conf., 2527(2012). <sup>3</sup>Quayle, P. et al., MRS Communications 3, 135 (2013). <sup>4</sup>Cao, X. et al., Scientific Reports 7, 14987 (2017). <sup>5</sup>Bai, Y. et al., Phys. Chem. Chem. Phys. 20, 14619 (2018). <sup>6</sup>Han, L.; Kash, K.; Zhao, H., J. Appl. Phys. 120, 103102 (2016). <sup>7</sup>Karim, M.R. and Zhao, H., J. Apply. Phys. 14, 034303 (2018). <sup>8</sup>Hyt, B.; Rollès, M.; Miska, P., Phys. Status Solidi RRL 13, 1900170 (2019). <sup>9</sup>Fioretti, A. et al., J. Mater. Chem. C 3, 11017 (2015). <sup>10</sup>Le, D.D. et al., Cryst. Growth Des. 18, 1385 (2018). <sup>11</sup>Makin, R.A. et al., J. Vac. Sci. Tech. B35, 02B116-1 (2017).

## 2:45 PM PP04

### (Student) Metalorganic Chemical Vapor Deposition of ZnGeN<sub>2</sub> Films on

**GaN—Effects of Cation Stoichiometry on Surface Morphology and Crystallinity** Md Rezaul Karim<sup>1</sup>, Benthara H. Jayatunga<sup>2</sup>, Menglin Zhu<sup>1</sup>, Rebecca A. Lalk<sup>2</sup>, Olivia Licata<sup>3</sup>, Baishakhi Mazumder<sup>3</sup>, Jinwoo Hwang<sup>1</sup>, Kathleen Kash<sup>2</sup> and Hongping Zhao<sup>1,1</sup>; <sup>1</sup>The Ohio State University, United States; <sup>2</sup>Case Western Reserve University, United States; <sup>3</sup>University at Buffalo, The State University of New York, United States

Novel optoelectronic device designs based on the heterostructures of III-N and II-IV-N<sub>2</sub> are promising to advance device performance significantly. For example, by utilizing InGaN-ZnGeN<sub>2</sub> quantum well (QW) [1] structures instead of pure InGaN, the band structure engineering in the QW active region can lead to improved electron-hole wavefunction overlap, and thus enhance the radiative efficiency for photon generation. These novel heterostructures have great potential to address the current challenge of low quantum efficiency in InGaN QW based light emitting diodes emitting in green and beyond. The materials development of ZnGeN<sub>2</sub> is still at an early stage as compared to the much matured GaN material system. In an ideal octet rule preserving ordered structure of ZnGeN<sub>2</sub>, every N atom is coordinated by exactly two Zn and two Ge atoms. However, local violation of octet rule can be caused by non-ideal coordination of N by the cations. The disordered structure is thermodynamically less favorable but can still be achieved, for example, in kinetics-limited growth regime [2]. The ordered ZnGeN<sub>2</sub> has a bandgap very close to that of GaN (~3.4 eV) and a lattice mismatch of <0.1% with GaN. Interestingly, the valence band of ZnGeN<sub>2</sub> has been predicted to be ~1 eV above that of GaN [3], which has inspired novel designs for high efficiency light emitters. In this work, we investigated the metalorganic chemical vapor deposition (MOCVD) of ZnGeN<sub>2</sub> films on GaN/c-sapphire templates. Diethylzinc (DEZn), germane (GeH<sub>4</sub>) and ammonia were used as the precursors for Zn, Ge and N, respectively. A systematic study was conducted to investigate the cation stoichiometry as a function of growth temperature (T<sub>g</sub>), total reactor pressure (P) and DEZn/GeH<sub>4</sub> molar flow rate ratio (R<sub>II/IV</sub>). Under the investigated growth window, the Zn/(Zn+Ge) composition in the films, determined from energy dispersive X-ray spectroscopy, decreased monotonically with increase in T<sub>g</sub> but increased with increase in P and R<sub>II/IV</sub>. Atom probe tomography data did not indicate the presence of any secondary phases such as Zn<sub>3</sub>N<sub>2</sub> or Ge<sub>3</sub>N<sub>4</sub>. The surface morphology and crystallinity of the grown films had strong correlation with the Zn/(Zn+Ge) composition. The scanning electron microscopy images showed that the near-stoichiometric films have planar surfaces whereas Zn-rich films had crystallites on their surface and the Zn-poor films had faceted surface. Scanning transmission electron microscopy (STEM) imaging revealed that the Zn-rich and Zn-poor films have columnar and filament-like morphology, respectively, whereas the near-stoichiometric films have continuous film-like cross-sectional morphology. TEM nano-diffraction patterns as well as X-ray diffraction 2θ-ω scan profiles indicate that the near stoichiometric films are single crystalline. Nano-diffraction pattern of the stoichiometric films resembled that of a disordered ZnGeN<sub>2</sub> structure. Room temperature Raman spectra of near-stoichiometric films showed only the phonon density of states like features of a cation disordered ZnGeN<sub>2</sub>. Cathodoluminescence and photoluminescence spectra measured at different temperatures had similar features with peak emission

wavelength at ~ 2 eV. In conclusion, the stoichiometry of ZnGeN<sub>2</sub> films can be widely tuned by tuning the MOCVD growth parameters. The surface morphology and the crystallinity of the films were found to have strong correlation with the Zn/(Zn+Ge) composition. The stoichiometric ZnGeN<sub>2</sub> films grown on GaN were demonstrated with uniform surface morphology and high crystalline quality. The results from this work will provide pathway to implement ZnGeN<sub>2</sub> in device structures. This work is supported by NSF (DMREF: SusChem: 1533957) and U.S. DOE (DOE SSL: DE-EE0008718). **References** 1. L. Han, et al., *J. Appl. Phys.*, 120, 103102 (2016). 2. P. C. Quayle, et al., *Phys. Rev. B.*, 91, 205207 (2015). 3. A. P. Jaroentjitchai, et al., *Phys. Rev. B.*, 96, 079907(E) (2017).

### 3:00 PM PP05

**(Student) Nucleation of IV-VI Rocksalt PbSe and PbSnSe on (001) and (111) Oriented III-V Zincblende Substrates** Brian B. Haidet<sup>1</sup>, Eamonn T. Hughes<sup>1</sup>, Leland J. Nordin<sup>2</sup>, Kevin Vallejo<sup>3</sup>, Paul Simmonds<sup>3</sup>, Daniel Wasserman<sup>2</sup> and Kunal Mukherjee<sup>1</sup>; <sup>1</sup>University of California, Santa Barbara, United States; <sup>2</sup>University of Texas, Austin, United States; <sup>3</sup>Boise State University, United States

The IV-VI rocksalt semiconductors have a number of unique properties stemming from their unique bonding, with a mix of ionic, covalent, and metallic character[1]. This allows them to diverge from many of the trends set by conventional covalently bonded III-V semiconductors where material parameters scale closely with bandgap. Pb-rich PbSnSe has an extremely narrow direct bandgap ranging from 0.3–0 eV, but despite this, it has abnormally high carrier mass, low Auger recombination, and a high dielectric constant. Additionally, for alloy compositions > 30% Sn, PbSnSe becomes a topological crystalline insulator with an inverted gap[2]. With this range of peculiarities, we believe the IV-VI system is not only technologically interesting, but provides the opportunity to probe how mixed bonding affects minority carrier properties, notably non-radiative recombination in the mid-infrared.

Previously, IV-VI growth has been dependent on fluorite substrates and buffer layers[2,3], but in this work, we explore PbSe growth on more conventional III-V substrates. This IV-VI/III-V interface incorporates a change in valency, surface charge, and crystal structure. Readily available GaSb and InAs are both nearly-lattice-matched to PbSe, but present chemically different surfaces, making this a model system for an investigation of cross-system heteroepitaxial growth. Uncontrolled nucleation of PbSe on III-V surfaces results in a temperature- and substrate-dependent mixture of grain orientations. Here, we demonstrate that the nucleation behavior of PbSe can be controlled by modifying the III-V surface reconstruction and chemistry prior to growth. Specifically, by exposing arsenide surfaces to PbSe flux at high temperature, we can convert the surface into a suitable template for single-orientation nucleation of PbSe, resulting in cube-on-cube (001) growth, and consistently 180° rotated (111) growth. Preliminary XPS results show the presence of both lead and selenium on such a treated surface. The growth mode of PbSe appears insensitive to lattice mismatch, with substrates ranging from significantly mismatched GaAs to nearly matched InAsSb. Interestingly, the effectiveness of this pre-treatment does not extend to antimonide surfaces. These results highlight the importance of surface chemistry over lattice mismatch as a dominant factor in this heteroepitaxial system.

With this method, we have produced (001)-oriented PbSe films with 369 and 185 arcseconds of tilt about the and [110] directions, respectively, in films only 80 nm thick. This result is on par with multi-micron-thick films from other studies[4]. We also report strong 4 μm photoluminescence at room temperature for PbSe grown on highly lattice-mismatched GaAs. With particular interest to novel interface states, we also directly observe a symmetry-breaking structural distortion in PbSe localized near the heterovalent interface using atomic resolution STEM.

[1] J. Raty, M. Schumacher, P. Golub, V.L. Deringer, C. Gatti, M. Wuttig, *Adv. Mater.* 31 (2019); [2] G. Springholz, G. Bauer. *Semiconductors, IV-VI*, in: *Wiley Encycl. Electr. Electron. Eng.* (2014); [3] P. Müller, A. Fach, J. John, A. N. Tiwari, H. Zogg, and G. Kosterz. *J. Appl. Phys.* 79 (1996); [4] X.J. Wang, Y.B. Hou, Y. Chang, C.R. Becker, R.F. Klie, T.W. Kang, R. Sporcken, and S. Sivananthan. *J. Cryst. Growth* 311 (2009)

### 3:15 PM BREAK

SESSION QQ: Fundamental Issues in Epitaxy  
Session Chair: Kyle McNicholas  
Session Hosts: Kurt Eyink and Kunyao Jiang  
Friday Afternoon, June 26, 2020  
Location: ZoomRoom 5

### 3:45 PM QQ01

**(Student) Optimization of All-MBE Selective Area Epitaxial Overgrowth Method** Ashlee Garcia, Alec M. Skipper, Daniel Ironside and Seth R. Bank; The University of Texas at Austin, United States

An all-molecular beam epitaxy (MBE) approach to selective area epitaxy (SAE) of III-V semiconductors is a promising method to enable the seamless

integration of metals, dielectrics and high-quality crystalline semiconductors. This technique enables the development of novel optoelectronic structures, such as high-contrast photonics, site-controlled quantum emitters, stacked pixel detectors, and photonic integrated circuits. By utilizing patterned dielectrics and metals to define crystal seeding regions, SAE can be performed to embed patterned amorphous microstructures into crystalline semiconductors<sup>1</sup>. While SAE by metal organic chemical vapor deposition has been widely successful for these applications due to its high material deposition selectivity, a SAE MBE method enables further advances in this space due to its high layer precision and highly non-equilibrium growth conditions<sup>1,2</sup>. SAE through conventional continuous MBE growth is difficult to achieve due to III-V polycrystalline formation on the amorphous mask even at growth temperatures as high as 700 °C. Nishinaga et al. developed periodic supply epitaxy (PSE) as a method to inhibit polycrystalline deposition by employing cycles of group III deposition and interruption periods under a constant group V flux<sup>3,3</sup>. SAE was achieved using a high temperature, low growth rate PSE process that decreased nucleation of polycrystalline GaAs on the amorphous mask as a result of increased Ga adatom diffusion to seeding windows and desorption of remaining Ga adatoms<sup>3</sup>. Recently, we have incorporated this method into a two-stage growth approach to demonstrate high-quality GaAs planar coalescence over patterned SiO<sub>2</sub> and Tungsten microstructures<sup>1,2,4</sup>.

While the demonstrated all-MBE approach is ideal due to its precision and ability to perform growth under non-equilibrium conditions, applications requiring larger features are limited by nucleation of polycrystalline semiconductor on the amorphous surface as a result of low deposition selectivity and low Ga adatom surface diffusion length, L<sub>d</sub><sup>1,3,4</sup>. Surface diffusion lengths of Ga on SiO<sub>2</sub> at the processing temperature of 630-640 °C have been reported to be ~56 μm in proximity of a 5 μm stripe window, theoretically-limiting mask features to ~112 μm, or 2L<sub>d</sub><sup>3</sup>. This work explores the feature limitations of the current all-MBE approach developed by Ironside et al.<sup>1</sup> and optimizes the periodic supply epitaxial growth method<sup>3</sup> to mitigate deposition of polycrystalline semiconductor on amorphous metals and dielectrics, thereby allowing for regrowth over features on the order of 100s of microns. By increasing L<sub>d</sub> and promoting desorption of the remaining group III adatoms off of the mask, deposition selectivity over large features can be attained. Increasing substrate temperature has demonstrated an increase in selectivity due to increased desorption and diffusion length, however increased surface roughness has been observed at higher temperatures. High As/Ga flux ratios have been employed to counteract the roughness resulting from kinetic roughening<sup>1,4</sup>. We report systematic studies of substrate temperature, As/Ga flux, and As species that identify a growth window that enhances PSE-MBE growth selectivity, while simultaneously inhibiting kinetic roughening. [1] D. J. Ironside et al., *ACS J. Crystal Growth and Design* (2019). [2] A. M. Skipper et al., 2019 MRS Electronic Materials Conf. [3] F. E. Allegretti and T. Nishinaga, *Journal of Crystal Growth* (1995). [4] D. J. Ironside et al., 2018 MRS Electronic Materials Conf.

This research was primarily supported by the National Science Foundation through the Center for Dynamics and Control of Materials: an NSF MRSEC under Cooperative Agreement No. DMR-1720595, as well as DMR-1839175.

### 4:00 PM QQ02

**(Student) Monolithic Integration of Patterned Metal-Dielectric Stacks Overgrown with III-V Semiconductors by Molecular Beam Epitaxy** Alec M. Skipper<sup>1</sup>, Yihao Fang<sup>2</sup>, Feng He<sup>1</sup>, Aaron J. Muhowski<sup>1</sup>, Daniel Ironside<sup>1</sup>, Daniel Wasserman<sup>1</sup>, Yaguo Wang<sup>1</sup>, Mark J. Rodwell<sup>2</sup> and Seth R. Bank<sup>1</sup>; <sup>1</sup>The University of Texas at Austin, United States; <sup>2</sup>University of California, Santa Barbara, United States

Metals and dielectrics have historically been relegated to the periphery of conventional III-V devices due to the challenges associated with integrating amorphous/polycrystalline material with crystalline semiconductor growth. Epitaxially-embedded patterned metals and dielectrics could be useful in a wide variety of photonic and electronic devices to introduce both passive (e.g. polarizers, mirrors, or waveguides), and active (e.g. buried Ohmic contacts and enhanced optical emission) functionality. Monolithic integration of semiconductors, dielectrics, and metals would allow for 3D integration of optoelectronic devices and photonic integrated circuits. This necessitates the study of epitaxial lateral overgrowth processes that allow arbitrarily patterned metal and dielectric structures to be buried within III-V layer stacks. However, during semiconductor overgrowth, the growth parameters must be carefully tailored to prevent the formation of polycrystalline deposits, voids, and dislocations. Such imperfections could introduce optical scattering and recombination sites that reduce the efficiency of devices. Furthermore, at the elevated temperatures necessary for III-V crystal growth, metals can diffuse into the semiconductor, distorting the crystal structure and forming unintentional contact spikes.

To date, the most successful approach to integrate metals into epitaxial layer stacks has focused on crystalline metals, such as rare earth pnictide (e.g. ErAs) films [1] and nanostructures [2]. However, the self-assembled growth of rare earth pnictides makes the integration of arbitrary shaped metals challenging. Prior work on the integration of patterned metals focused primarily on applications to electronic devices, such as metal base transistors [3]. Work on the epitaxial lateral overgrowth of dielectrics has progressed independently from metals, with recent efforts focusing on using buried dielectrics to block the propagation of dislocations in metamorphic heteroepitaxy [4]. This leaves the direct, simultaneous, incorporation of buried metals and dielectrics into

III-V materials largely unexplored. We present patterned tungsten on SiO<sub>2</sub> gratings embedded in molecular beam epitaxy (MBE) grown GaAs to study metal, dielectric, and semiconductor epitaxial integration for device applications. Tungsten and SiO<sub>2</sub> were chosen as they are largely nonreactive with GaAs and stable to the high temperatures necessary for epitaxial growth [5, 6]. Lateral overgrowth of patterned features was achieved by using III-flux modulated periodic supply epitaxy to seed selective growth from a GaAs (001) substrate. Tailoring the crystal plane orientation of the patterned metal stacks results in lateral epitaxial overgrowth that can be integrated into III-V layer structures. Successful lateral epitaxial overgrowth was confirmed by scanning electron microscopy (SEM) and atomic force microscopy (AFM). Fourier transform infrared (FTIR) spectroscopy was used to observe the strong diffraction effects expected from embedded tungsten/SiO<sub>2</sub> grating structures. Further characterization of the optical, electrical, and thermal properties will be presented at the conference. This research was partially supported by the National Science Foundation through the Center for Dynamics and Control of Materials: an NSF MRSEC under Cooperative Agreement No. DMR-1720595, as well as CCF-1838435. [1] C.J. Palmstrom et al., Appl. Phys. Lett., 53, 2608-2610 (1988) [2] C. Kadow et al., Appl. Phys. Lett. 75, 3548-3550 (1999) [3] M.A. Hollis et al., Advanced Processing of Semiconductor Devices, 797, 335-347 (1987) [4] J.-S. Park et al., Appl. Phys. Lett., 90, 052113 (2007) [5] P. Vohl et al., J. of Crystal Growth, 56, 410-422 (1982) [6] J.P. Harbison et al., Appl. Phys. Lett., 47, 11, 1187-1189 (1985)

#### 4:15 PM QQ03

**(Student) Tuning Band Gap Energy through Controlled Disorder in Ternary Heterovalent Compounds** Krystal R. York<sup>1</sup>, Robert Makin<sup>1</sup>, Steve Durbin<sup>1</sup>, James Mathis<sup>2</sup>, Nancy Senabulya<sup>2</sup>, Roy Clarke<sup>2</sup> and Roger Reeves<sup>3</sup>; <sup>1</sup>Western Michigan University, United States; <sup>2</sup>University of Michigan, United States; <sup>3</sup>University of Canterbury, New Zealand

Although silicon remains the leading material for many electronic applications, its low absorption coefficient reduces its competitiveness in the high efficiency solar cell arena and its indirect band gap is a poor match for light emitting diode (LED) and solid-state lighting applications. Therefore, alternative materials have been investigated and commercialized, many of which are comprised of gallium and indium - two elements which are heavily mined, low in earth abundance, and challenging to recycle. Thus, there is a need to explore materials that are less harmful to the environment. Such unexplored materials include MgSnN<sub>2</sub> and ZnSnN<sub>2</sub>, which are comprised of earth abundant elements that have a mature recycling infrastructure. It has previously been reported that ZnSnN<sub>2</sub> has a predicted band gap of around 2 eV and MgSnN<sub>2</sub> has a predicted band gap of 3.43 eV. However, it has more recently been reported that ZnSnN<sub>2</sub> actually has a range of optical band gaps from 1.12-1.98 eV, and MgSnN<sub>2</sub> has a range of optical band gaps from 1.87-3.43 eV. This indicates that these materials could be a viable substitute for InGaN alloys (band gaps ranging from 0.7-3.4 eV), which are commonly used in LEDs, photovoltaics, and other devices.

ZnSnN<sub>2</sub> and MgSnN<sub>2</sub> are able to have this large range of band gaps through the exploitation of the disorder in the cation sublattice. The long-range order parameter S is used to quantify the cation sublattice disorder. This parameter has been determined using x-ray diffraction (XRD), Raman spectroscopy, and in-situ reflection high-energy electron diffraction (RHEED), with excellent agreement among the three techniques. This is accomplished by calculating the ratio of the integrated intensities of an identified ordered peak, to that of an identified disordered peak. These heterovalent ternary materials demonstrate a clear relationship between the optical band gap energy and S. Moreover, when looking at data extracted from the literature, we were able to see this same trend in other related, heterovalent ternary materials (i.e. ZnGeN<sub>2</sub>, ZnSnP<sub>2</sub>, and CuInS<sub>2</sub>). Specifically, the relationship between the optical band gap energy and S<sup>2</sup> is linear. Recent experiments have confirmed we are able to reproducibly achieve target values of S<sup>2</sup> to within a few percent. S<sup>2</sup> can range from 0 (completely disordered) to 1 (completely ordered) and is directly related to the fraction of cation atoms on the correct site. Systematic variation of process parameters has led to the realization that the lattice structure of heterovalent ternary materials can be controlled, switching between structures that are orthorhombic (fully ordered sublattice) in nature and wurtzitic. This new approach to quantifying the relationship between band gap energy and disorder in semiconductors is based on structural motifs in the context of an Ising model. The motif distribution in the semiconductor's lattice is the predominant reason for the range of band gaps. Using the Ising model, we assign one cation as spin up (e.g. Zn) and the other cation as a spin down (e.g. Sn). While demonstrated in the example materials of ZnSnN<sub>2</sub> and MgSnN<sub>2</sub>, we have evidence that the basic approach applies to a much broader range of materials, as we will discuss.

#### 4:30 PM QQ04

**Phase Separation and Surface Diffusion in InGaAs** Mark E. Twigg, Nadeemullah Mahadik, Nicole Kotulak, Stephanie Tomasulo and Michael Yakes; U.S. Naval Research Laboratory, United States

Phase separation in III-V semiconductor alloys remains a problem that limits the performance of electronic materials. As the first stage in a comprehensive program addressing this issue, we have begun investigating an alloy system in which only the group III elements differ: InGaAs. Lattice-matched InGaAs alloy films were deposited at three temperatures (400, 450, and 500C) by

molecular beam epitaxy on a (001) InP substrate. According to kinetic instability theory, the critical temperature for spinodal phase separation in InGaAs is 814C, a temperature well above the growth temperatures used in this study [1,2]. Dark-field (DF) cross-sectional transmission electron microscopy (XTEM), using the composition sensitive g=002 reflection, was used to determine the amplitude of composition modulations averaged over the thickness of the XTEM sample. The amplitude of composition modulation was found to decrease with increasing growth temperature, yielding values of 0.6, 0.4, and 0.3 atomic percent for the growth temperatures 400, 450, and 500C, respectively, a trend in accord with kinetic instability theory. X-ray reflectivity and 2-dimensional small angle x-ray measurements also indicate that the 400C growth shows significantly greater phase separation than the 450 and 500C growths. Atom probe tomography indicates that the amplitude of composition modulation for the 400C growth is approximately 1 atomic percent, a value that compares favorably with the 0.6 atomic percent measured by DF XTEM. The range of wavelengths for lateral composition modulation is found to extend from approximately 3 to 30 nm. According to the literature, such wavelengths have been found to depend on growth temperature for a number of III-V semiconductor alloys, in agreement with predictions based on surface diffusion. Measurements of the composition modulation wavelength as a function of temperature have been performed by analyzing DF XTEM images recorded using the g=220 diffraction vector, from XTEM samples with the glue line along the rapidly-diffusing [110] direction. Diffraction-contrast TEM imaging is known to be particularly sensitive to lattice parameter undulations, such as those associated with phase separation in compound semiconductors [3]. Fast Fourier Transform (FFT) power spectra recorded from each image allowed the dominant composition modulation wavelengths to be determined. Analyzing these wavelengths as a function of temperature yields the same activation energy (0.55 eV) as that found in surface diffusion of In droplets on the (001) InGaAs surface [4]; thereby confirming the role of surface diffusion in phase separation driven composition modulations. The close correspondence between the activation energy measured by surface diffusion of In adatoms, and that measured by analysis of XTEM images, is consistent with the possibility that In adatoms play the primary role in surface diffusion for InGaAs. The leading role of In adatoms in surface diffusion is also suggested by the morphology of In droplets on the InGaAs surface, as compared to Ga droplets on the InGaAs surface. That is, In droplet diffusion results in the formation of a uniform halo consisting of In incorporated into the InGaAs lattice, while Ga droplet diffusion results in pits marking the InGaAs surface. The difference between the diffusion of Ga adatoms compared to In adatoms on the (001) InGaAs surface suggests an avenue for both a more complete understanding of the role of surface diffusion in phase separation in compound semiconductor alloys, as well as suggesting the possibility that surface diffusivity and the resulting phase separation could be controlled and limited. [1] F. Glas, Phys. Rev.B, 62, 7393 (2000). [2] I. P. Ipatova, V. G. Malyshekin, and V. A. Shchukin, J. Appl. Phys. 7198 (1993). [3] M. M. J. Treacy, J. M. Gibson, and A. Howie, Philos. Mag. A51, 389 (1985). [4] M. A. Stevens et al., J. Appl. Phys. 121, 195302 (2017).

#### 4:45 PM QQ05

**(Student) A Refined Model for Epitaxial Tilt of Epilayers Grown on Miscut Substrates** Michael E. Liao and Mark Goorsky; University of California, Los Angeles, United States

Crystal modeling and reciprocal space analysis were employed to develop a refined understanding of the origin of tilt in epitaxial layers grown on miscut substrates. In the current literature, the Nagai tilt model<sup>1</sup> is often cited to explain tilt of epitaxial lattice planes compared to the substrate lattice planes. The basis of this model is that both the steps on a miscut substrate surface and lattice parameter mismatch result in a tilted epitaxial layer with respect to the substrate. However, this model incorrectly describes how the substrate applies biaxial stress onto the epitaxial layer. The substrate applies biaxial stress parallel to the surface of the substrate.<sup>2,3</sup> To realize the correct directions of the applied stress, the surface plane should first be identified. (1) For an on-axis substrate, this is trivial since the orientation plane associated with the substrate is the true surface plane, e.g., (001). (2) On the other hand, the orientation plane associated with a miscut substrate is not the actual surface plane. For instance, the surface plane of a cubic substrate with a miscut of 10° away from the (001) along [110] is the (118) plane and not the (001) plane. Thus, the in-plane directions for the applied biaxial stress are parallel to the (118) in this example. Moreover, reciprocal space was used to further realize that the {00l} reflections would be symmetric reflections for on-axis (001) substrates but would be asymmetric reflections for miscut (001) substrates. The insight gained from reciprocal space illustrates why epitaxial tilt is observed for epitaxial layers grown on miscut substrates for any crystal system. We present our method for calculating the amount of tilt expected for cubic epitaxial layers on cubic substrates and compare it with predictions from the Nagai model. The equation that arises from our model is:

$$t = \tan^{-1} \left\{ \frac{[d_{e,0}(\mathbf{a}\cdot\mathbf{b})(d_{c,i} + d_{c,i}v - 2vd_{c,i}')] / [d_{c,i}d_{c,i}'](\mathbf{a}\cdot\mathbf{c})(1-v)]}{m} \right\}$$

where t is the relative tilt of the epitaxial layer plane of interest; d<sub>e,0</sub> and d<sub>c,i</sub> are the relaxed out-of-plane and in-plane epitaxial layer d-spacing, respectively; d<sub>c,i</sub>' is the strained in-plane epitaxial layer d-spacing; v is the epitaxial layer Poisson's ratio; m is the miscut angle of the substrate; **a** is the direction parallel to the associated orientation plane along the miscut direction; **b** is the direction perpendicular to the substrate's true surface; and **c** is the direction parallel to the substrate's true surface along the miscut direction. For a (001) cubic substrate miscut 10° towards the [110] that has a lattice mismatch with the

epitaxial layer of ~20%, the (001) epitaxial layer planes are expected to tilt ~4°. (A Poisson's ratio of 0.36 was used for the epitaxial layer). On-axis substrates were also examined, such as the expected tilt for the (224) plane of the epitaxial layer grown on a (001) substrate. Using the same lattice parameters and Poisson's ratio from the previous example, the expected tilt of the (112) plane is ~9.7°. While this type of scenario is understood as the cubic epitaxial layer being tetragonally distorted, this could also be interpreted as a (112) oriented substrate miscut 35.3° towards the [110], making the true surface (001). We find that while the equation associated with the Nagai model may give acceptable quantitative predictions, especially for low lattice-mismatch and low miscut scenarios, the Nagai model does not provide an accurate description of the physics for the commonly observed epitaxial tilt. Examples for group IV, III-V, and II-VI systems will be presented.

References: 1. H. Nagai, J. of Appl. Phys., **45**, 3789 (1974). 2. K.-N. Tu, et al., *Electronic Thin Film Science for Electrical Engineers and Materials Scientists*, in: *Stress in Thin Films*, Macmillan Publishing Co., New York, (1992). 3. J. Y. Tsao, *Materials Fundamentals of Molecular Beam Epitaxy, Coherency and Semi-coherency*, Academic Press, Inc., California, (1993).

SESSION RR: Flexible, Printed and/or Dissolvable  
Thin Films or Nanomembranes  
Session Chair: Andre Zeumault  
Session Hosts: Jae-Hyun Ryou and William Wong  
Friday Afternoon, June 26, 2020  
Location: ZoomRoom 6

## 2:00 PM RR01

**Scalable Normal and Shear Force Sensing Active-Matrix ZnO Thin-Film Transistors Array on Flexible Substrates for Slip and Grip Feedback in Closed-Loop Robotics** Hongseok Oh<sup>1</sup>, Gyuchul Yi<sup>2</sup>, Michael Yip<sup>1</sup> and Shadi Dayeh<sup>1,2</sup>; <sup>1</sup>University of California, San Diego, United States; <sup>2</sup>Seoul National University, Korea (the Republic of)

Mechanoreceptors on the human hand allow us to perform sophisticated manipulations of objects, such as sewing using needles, flipping pages, grasping an egg or opening a door. These mechanoreceptors provide high resolution, wide dynamic range tactile feedback on a variety of physical parameters such as shear force, which can be accordingly manipulated to form a closed-loop network to correct any errors. Similarly, for robotics and neuroprosthetic applications, versatile manipulations of objects can only be achieved through high resolution spatiotemporal tactile sensing. However, multiple modalities which have been used so far to indirectly infer tactile information do not meet the requirements for high fidelity and feasibility. While direct tactile sensors are considered to satisfy all the requirements, it is still challenging to simultaneously achieve high spatiotemporal resolutions and shear force sensing ability using these. The difficulties can however be overcome by developing tactile sensors which can simultaneously sense the tactile forces and multiplex signals.<sup>[1]</sup> With no need for additional driving elements, this approach can circumvent the tradeoffs for density and performance. Engineering these sensors to sense shear forces at the required spatiotemporal resolution will allow human-like tactile perception for robots. Still, manufacturing challenges need to be addressed before implementing multi-functional tactile sensors on flexible substrates with the desired density and shear-force sensing ability in a scalable way. In this work, we report the fabrication of such a tactile sensor array on flexible substrates with millimeter scale spatial resolution, millisecond scale temporal resolution, and sensation of shear force distribution, which enables grip adjustment for robotic and/or fingers by using closed-loop control.<sup>[2]</sup> We leveraged the advanced piezoelectric zinc oxide (ZnO) thin-film transistors (TFTs) with dual gate structure fabricated on flexible polyimide substrates by scalable manufacturing processes. The device recorded broad ranges of normal (50 – 250 mN) and shear forces (5 – 20 mN) with high sensitivity, which can help replicate the sense of touch. The individual piezoelectric ZnO TFTs perform force sensing, signal amplification and multiplexing. The construction of an active matrix of ZnO TFTs allowed fast signal multiplexing from hundreds of elements. As a result, the TFT array was able to capture the three-dimensional information of a tactile input. For closed-loop robotic applications, the arrays were mounted on a robotic gripper to generate a tactile feedback. The continuous feedback from the sensor array enabled a secure grip of fragile objects such as a raw egg, without the need for visual information or human intervention. Furthermore, by introducing shear forces into the closed-loop control algorithm, the gripper can adjust the gripping force for heavy objects to prevent slipping, even though no information about the weight of the object was provided. The achievements in this work will enable human-like sense of touch in robotics, which can allow advanced applications such as slip-force control for robotic surgery that would not be possible otherwise. [1] S. Iarhevi Vishniakou, Renjie Chen, Yun Goo Ro, Christopher J. Brennan, Cooper Levy, Edward T. Yu, and Shadi A. Dayeh. "Improved performance of zinc oxide thin film transistor pressure sensors and demonstration of a commercial chip compatibility with the new force sensing technology." *Advanced Materials Technologies* 3, no. 3 (2018): 1700279. [2] Hongseok Oh, Gyuchul Yi, Michael Yip and Shadi A. Dayeh. "Scalable Tactile Sensor Arrays on Flexible Substrates with High Spatiotemporal Resolution Enabling Slip and Grip for Closed-Loop Robotics", *submitted*.

## 2:15 PM RR02

**(Student) MoS<sub>2</sub> Suspended in Polythiophene Semiconductor Solutions for Inkjet-Printed Thin-Film Transistor Device Fabrication** Hyunwoo Choi, Wontae Park, Naeun Kim and William Wong; University of Waterloo, Canada

Printing technologies have led to the development of low-cost, rapid and large-area fabrication of next-generation electronic systems. While promising for its capability for large-area scaling and low-cost processing, the quality of solution-based electronic inks inhibit the device performance of these materials compared to its Si-based counterparts. The relatively low carrier mobility of organic semiconductors (OSCs) limits its use in high-performance integrated circuit applications. In contrast, crystalline inorganic semiconductor materials have high charge-carrier mobility but are difficult to process using printing approaches. Low-dimensional materials, such as graphene or molybdenum disulfide (MoS<sub>2</sub>), in combination with polymeric semiconducting inks may potentially help to alleviate this performance deficiency. A suspension of transition metal dichalcogenide (TMD) flakes or particles within a polymeric semiconductor solution may be a unique approach for developing high-performance electronic inks for printed electronics. The integration of the TMD materials within a polymeric film could provide "islands" of single crystalline high transport materials within a disordered polymeric thin-film matrix. A mixture of MoS<sub>2</sub> suspended in a polymeric semiconductor, Poly(3-hexylthiophene-2,5-diyl) (P3HT), was used to form a nano-composite hybrid ink formulation. The ink was made using bulk MoS<sub>2</sub> structures exfoliated within the P3HT solution. The ink consisted of different concentrations of MoS<sub>2</sub> in 10 mg/ml P3HT in a dichlorobenzene solution; the MoS<sub>2</sub> was exfoliated and dispersed in the P3HT using a sonication process. The hybrid MoS<sub>2</sub>/P3HT ink was first spin-coated on a heavily-doped Si wafer having a 100 nm thermal-oxide dielectric layer and patterned gold source and drain electrodes. The resulting reference bottom-gate TFTs had current-voltage characteristics with an extracted threshold voltage of 1 V, a saturation field-effect mobility of  $1.3 \times 10^{-3}$  V/cm<sup>2</sup>-s and a current on/off ratio of  $> 10^5$ . The field-effect mobility of these devices were found to be an order of magnitude higher and having a lower threshold voltage compared to the P3HT-only TFTs, suggesting the MoS<sub>2</sub> structures in the P3HT were effective in enhancing the transport properties of the polymeric semiconducting film.

Separate from the spin-coated TFTs, the electrical characteristics of the printed devices were found to be dependent on the assembly of the MoS<sub>2</sub> within the P3HT film. The assembly process was controlled using surface energy modulation of the thermal oxide to change the wetting and drying characteristics of the printed ink. Hexamethyldisilazane (HMDS) was used to functionalize the oxide surface. Contact angle measurements were used to characterize the relative change of the surface energy as a function of HMDS exposure time to the surface in order to optimize the oxide surface conditions for MoS<sub>2</sub> assembly in the films. A contact angle of ~90°, indicating a hydrophobic surface, resulted in a uniform distribution of MoS<sub>2</sub> within the P3HT film. The resulting TFTs fabricated using the printed hybrid inks were found to have extracted parameters for threshold voltage and field-effect mobility similar to those of the spin-coated reference devices and significantly improved performance compared to the P3HT-only devices. Finally, the effect of the surface functionalization to control the assembly of the MoS<sub>2</sub> and their effect on device performance will be presented.

## 2:30 PM RR03

**(Student) Leveraging Display IGZO TFT Technologies for High Definition Brain Mapping** Andrew Bourhis, Hongseok Oh, Ritwik Vatsyayan, Shadi Dayeh and Ian Galton; University of California, San Diego, United States

The human brain contains hundreds of billions of neurons that connect with one another to form complex networks and feedback systems that encode and process information. This stunning complexity is a double-edged sword, however, because it makes diagnosing and treating ailments such as epilepsy or neurodegenerative diseases incredibly difficult. Thus, to gain insight into how the brain functions, we must investigate the spatiotemporal dynamics of the generation and propagation of broadband brain activity (from local field potentials to cellular action potentials) in as fine detail as possible and with large cortical coverage. Our group and others have demonstrated that electrocorticography (ECoG) microelectrode array recordings from the cortical surface can resolve a significant repertoire of brain activity in animals<sup>1-3</sup> including humans.<sup>2</sup> But scaling ECoG devices for large cortical coverage is hampered by two main bottlenecks: 1. The impedance of the electrodes increases with smaller geometries, so the achievable signal to noise ratio of measurements decreases as the size of the electrode contacts is reduced, and 2. The physical routing of interconnects becomes extremely challenging for passive electrode arrays with over hundreds of electrodes. Thus, there is a pressing need for a new bio-compatible measurement system that is capable of scaling towards ultra-high spatiotemporal resolution. Toward this end, we have taken inspiration from high-definition flexible displays and have developed a novel neural interface that uses dual-gate indium gallium zinc-oxide thin-film transistors (TFT) incorporated into the microelectrode arrays to form an on-site time-multiplexing acquisition circuit. These TFTs are fabricated at low temperature so they are compatible with flexible bio-compatible polymer substrates with low glass-transition temperatures, such as polyimide. This is crucially important because it allows conformity of the electrode to the brain curvilinear structure and mechanical compliance to its movement. We have optimized the device architecture and fabrication process for use in biological

acquisition, to achieve low ohmic contact resistance, high intrinsic gain, relatively high electron mobility (10cm<sup>2</sup>/Vs), a high cut-off frequency (~150MHz for 5μm channel length), a high on/off current ratio, and tunable negative threshold voltages. We have also developed a hermetic encapsulation strategy using multiple polymer layers and alumina passivation of metal leads and devices. We have shown that this strategy can effectively passivate and protect metal leads when immersed in saline even when driving these leads with large square wave bias voltages for 24 hours. We have fabricated and tested 256-channel multiplexing circuits with low-impedance platinum nanorod sensing microelectrodes, and have developed custom acquisition circuits and firmware to perform benchtop characterization in saline. We will soon test these systems in-vivo in a rat model and compare the recordings with those captured from a passive sensing strategy. 1. Ganji, M. et al. Selective Formation of Porous Pt Nanorods for Highly Electrochemically Efficient Neural Electrode Interfaces. *Nano letters* **19**, 6244-6254 (2019). 2. Paulk, A. C. et al. Microscale physiological events on the human cortical surface detected with PEDOT: PSS Electrodes. *bioRxiv*, 770743 (2019). 3. Khodagholy, D. et al. NeuroGrid: recording action potentials from the surface of the brain. *Nature neuroscience* **18**, 310 (2015).

#### 2:45 PM RR04

**(Student) Single-Crystalline III-N Thin-Film Piezoelectric Sensors for Various Applications** Nam-In Kim, Jie Chen, Weijie Wang and Jae-Hyun Ryou; University of Houston, United States

Piezoelectric-type of sensors are very promising for various pressure and motion-sensing applications due to their advantages of high sensitivity, rapid response time, simple structure, reliable operation, light weight, and low power consumption. Lead zirconate titanate (PZT) is the most dominant piezoelectric material by its high piezoelectric coefficients. However, PZT is limited in several applications such as health-care monitoring system and high-temperature conditions by its toxicity for environments and human bodies and limited operation temperature (~200 °C) by piezoelectric characteristics loss related to Curie temperature ( $T_c$ ). Recently, III-N thin film material has been proposed as a piezoelectric sensing material. Especially, single-crystalline gallium nitride (GaN) piezoelectric thin film has been reported to show excellent output voltage, indicating outstanding sensitivity, rapid response time by a high electromechanical coupling factor, chemical and mechanical long-term stability, high thermal resistance, and excellent biocompatibility. In the present study, we developed and demonstrated flexible GaN sensors for three different applications: (1) human body pulse sensor, (2) high-pressure sensor in harsh environments, and (3) eye-lid motion sensor. A III-N thin film on silicon substrate was transferred on a flexible substrate. X-ray diffraction analysis was conducted to confirm the single-crystalline quality of the GaN film without defect. First, flexible piezoelectric pulse sensor (PPS) based on single-crystalline III-N thin film meets sensitivity and durability requirements for flexible pulse sensor applications by demonstrating its ability to generate an electrical response from small deflections, down to the micrometer scale, and withstand the cyclic forces of an over 13 000 cycles test. Therefore, the robust F-PPS is sensitive enough to measure the pulse waveforms from the most widely used artery pulse sites, with no signs of degradation. Important information can be obtained from the measured pulse waveforms, such as the pulse rate, augmentation index (Aix), and pulse wave velocity (PWV). This robust, biocompatible flexible pulse sensor is a promising candidate for health monitoring flexible electronics. Second, a flexible GaN piezoelectric pressure sensor attached on a diaphragm that is connected to high pressure high-temperature work space. The generated output potentials from the piezoelectric sensor were measured and compared with theoretical and simulated voltage values, showing a close match between the experimental data and the simulated values. The piezoelectric GaN sensor was demonstrated to function properly up to ~350 °C. Above 350 °C, a reduction in piezoelectric output voltage was observed due to the increasing intrinsic carrier concentration in the transducer material. The measurement reliability and stability of the sensor was also demonstrated with several pressure levels and elevated temperatures. Constant voltage output values were found even for extended time durations. The results from measurements obtained at high temperatures and long-time periods show that the piezoelectric flexible GaN pressure sensor is very promising for high pressure and high temperature applications. Third, the sensor was attached on human face and the response signal was collected for eye blinking and eyeball movement. The flexible III-N piezoelectric sensors can be applied in several applications such as wearable electronics and health care devices.

#### 3:00 PM RR05

**(Student) Flexible Solar-Blind Photodetector Based on b-Ga2O3 Nanomembranes** Junyu Lai, Md N. Hassan, Edward Swinnich and Jung-Hun Seo; University at Buffalo, The State University of New York, United States

Flexible photodetectors are one of the indispensable components in the upcoming internet of things era due to their mechanical versatility to be attached on any surfaces and the ability to convert light signals into electrical signals. Most popular materials for flexible photodetectors are low-dimensional semiconductors such as quantum dots, nanowires, two-dimensional materials because of their excellent mechanical and electrical properties. These low-dimensional materials typically have the bandgap ranging from 0.5eV to 3eV and exhibit good photo-sensitivity due to their large surface-to-volume ratio, which satisfies most of visible light detection purposes. However, the photo-

sensitivity of these flexible photodetectors severely degraded under the visible light illumination, (namely, sunlight or room light) due to unwanted photocurrent associated with their small bandgap, thus it is required to have additional components for the light filtering or signal modulation. On the other hand, there are wider spectrum of photodetector applications that simultaneously require good flexibility and high photo-sensitivity regardless of the environmental condition. Photodetectors based on ultra-wide bandgap (UWBG) semiconductors, which have an optical bandgap greater than 4eV such as AlGaIn and diamond, affect less in visible light due to their large bandgap. The high rejection ratio between visible light and UV light, also called a solar-blind property, enables UWBG based photodetectors to operate at any environmental conditions. However, several technical challenges need to be solved in order to realize a flexible form of solar-blind photodetectors. The most critical requirement for the realization of flexible solar-blind photodetectors is to create UWBG semiconductor in a free-standing form so as to transfer-print it onto the flexible substrate.

Beta phase gallium oxide (b-Ga<sub>2</sub>O<sub>3</sub>) as an emerging UWBG semiconductor, not only have large bandgap (E<sub>g</sub>=4.9eV) with moderate carrier mobility but also can be easily exfoliated from the bulk due to a monoclinic structure. Therefore, it is possible to create high-quality single-crystalline b-Ga<sub>2</sub>O<sub>3</sub> nanomembranes (NMs) that are exfoliated from the bulk substrate using a well-known scotch tape method, thus b-Ga<sub>2</sub>O<sub>3</sub> NMs can be transfer-printed onto the desired substrate.

In this presentation, we will present our recent development in b-Ga<sub>2</sub>O<sub>3</sub> NMs based flexible solar-blind photodetectors. As shown in Figure 1(a)-(d), we will discuss the details of the fabrication process including a creation of b-Ga<sub>2</sub>O<sub>3</sub> NMs and photodetectors based on b-Ga<sub>2</sub>O<sub>3</sub> NMs. To understand changes in the mechanical property of b-Ga<sub>2</sub>O<sub>3</sub> NMs by the bending, we will show Raman spectroscopy and three-dimensional atomic probe tomography of b-Ga<sub>2</sub>O<sub>3</sub> NMs (Figure 1(g)). As seen in Figure x, b-Ga<sub>2</sub>O<sub>3</sub> NM based flexible solar-blind photodetectors showed a stable electrical performance under the bending and illumination condition. Interestingly, as shown in Figure 1(e) and (f), the peak position of the photo-current vs. wavelength graph measured at a flat condition and under the bending condition was slightly shifted from 252nm for a flat condition to 260nm for the bending condition. To investigate the reason for the peak shifting, we will discuss the structural property using SEM, AFM results and the optical property of b-Ga<sub>2</sub>O<sub>3</sub> NMs which reveal slight changes in n, k values to due nano-size cracks in b-Ga<sub>2</sub>O<sub>3</sub> NMs. (Figure 1(h) and (i)) Finally, we will discuss the plasma treatment method to restore the cracked b-Ga<sub>2</sub>O<sub>3</sub> NMs which chemically bridges disconnected grains in b-Ga<sub>2</sub>O<sub>3</sub> NMs.

In summary, we have successfully demonstrated b-Ga<sub>2</sub>O<sub>3</sub> NMs based flexible solar-blind photodetectors which show good solar-blind characteristics with stable electrical performance under the bending condition. Our research provides a viable route in the realization of high performance flexible solar-blind photo-detection systems.

#### 3:15 PM BREAK

#### 3:45 PM RR06

**(Student) Thermal Conductivity of b-Ga2O3 Nanomembranes Using a Modified Micro-Raman Spectroscopy** Yixiong Zheng, Edward Swinnich and Jung-Hun Seo; University at Buffalo, The State University of New York, United States

In recent years, b-Ga<sub>2</sub>O<sub>3</sub> has recently seen significant attention as the next generation ultra wide-bandgap semiconductor, due to exceptional material properties including the wide bandgap (~4.9eV), the large electrical breakdown voltage (~8 MV/cm), lattice compatibility with other wide bandgap semiconductors, large area affordable substrates grown from the melt. All of these properties lead to b-Ga<sub>2</sub>O<sub>3</sub> can be potentially applied for high-frequency devices, deep-ultraviolet optoelectronics, and high-power applications, where the thermal properties play a critical role in their operation. However, the thermal conductivity of b-Ga<sub>2</sub>O<sub>3</sub> is substantially lower than other wide bandgap semiconductors; namely, the thermal conductivity of bulk b-Ga<sub>2</sub>O<sub>3</sub> is 20~30 W/m K versus AlN(200W/m K), SiC(370W/m K), GaN(230W/m K), and diamond(>2000W/m K). Furthermore, unlike most of the other wide bandgap semiconductors, the thermal conductivity of b-Ga<sub>2</sub>O<sub>3</sub> varies ~30% depending on the crystal orientation due to the anisotropic property from the monoclinic lattice structure. Therefore, accurate characterization of the thermal conductivity of b-Ga<sub>2</sub>O<sub>3</sub> is critical to design the aforementioned future applications. Conventionally, there are several characterization methods to measure the thermal conductivity of materials. For example, the laser flash technique uses the thermal diffusivity of the materials, and the three-omega (3ω) method converts the thermal conductivity from the temperature-dependent electrical conductivity. These methods, however, have large measurement errors or require additional microfabrication to measure it. Particularly, the 3ω method is mainly focusing on the cross-plane direction thermal conductivity, which is not applied for anisotropic materials. Recently, the Time-domain thermoreflectance (TDTR) method which uses the thermoreflectance decay of a pulsed laser has been used to measure the thermal conductivity of b-Ga<sub>2</sub>O<sub>3</sub>. While this method offers the in-plane thermal conductivity, the heat transfer of the TDTR method is sensitive to the thickness of the metal film which needs to cover the entire surface. In this presentation, we will introduce the modified micro-Raman spectroscopy and the working principle of the system which captures a subtle thermal vibration as a form of the Raman shift (Figure 1(b)).

This method offers several advantages over existing techniques; namely, in-plane and direct thermal conductivity measurement. Thus, this method does not require any additional patterning or thin-film for the thermal conductivity measurement, and also can capture the thermal conductivity of the desired location/plane without being restricted by the surface type/orientation. To characterize the thermal conductivity of b-Ga<sub>2</sub>O<sub>3</sub>, we have created three types of free-standing b-Ga<sub>2</sub>O<sub>3</sub> nanomembranes (namely thicknesses of 4000 nm, 1000 nm, and 100 nm, respectively) from the bulk b-Ga<sub>2</sub>O<sub>3</sub> (Figure 1(a)). b-Ga<sub>2</sub>O<sub>3</sub> nanomembranes were transfer-printed on the diamond substrate using a well-known scotch tape method. A series of Raman spectroscopy was performed under different temperature conditions (from 100K to 500K with a 40 K interval) under different laser power intensities (from 0.5mW to 10mW) using 5× and 20× objective lenses to apply different heat flux (Figure 1(c)-(j)). Finally, the thermal conductivity of 4 W/m K, 16 W/m K and 27 W/m K for 100nm, 1000nm, and 4000nm b-Ga<sub>2</sub>O<sub>3</sub> nanomembranes were measured using modified micro-Raman spectroscopy (Figure 1(j)) and compared our values with other previous values (Figure 1(k)). We also revealed the temperature-dependent thermal conductivity b-Ga<sub>2</sub>O<sub>3</sub> nanomembranes. We believe this method not only provides accurate thermal conductivity of b-Ga<sub>2</sub>O<sub>3</sub> which is the crucial information for b-Ga<sub>2</sub>O<sub>3</sub>-based future applications, but also implements the thermal conductivity characterization of other low dimensional materials.

4:00 PM RR07

**Scalable Strategies for Fabricating Ultrathin Metal Oxides—Synergistic Improvements to Performance and Reliability of Perovskites Solar Cells and Transparent Transistors** William J. Scheideler; Dartmouth College, United States

Inorganic metal oxides are critical optoelectronic materials that promise to drive new energy, sensing, and switching devices based on their extreme transparency and exceptional electronic transport (electron mobility,  $\mu_e \sim 10$ -100 cm<sup>2</sup>/Vs). Solution-processing and printing-based fabrication methods have the potential to deliver these unique properties of metal oxides in flexible electronics and low cost-per-area energy technologies such as perovskite solar cells. However, *scalable fabrication* of metal oxide devices first requires deeper understanding of how the *optoelectronic* functionality of metal oxide films synthesized directly from solution derives from their precursor ink chemistry. Implementation in high-efficiency solar cells and high-mobility thin film transistors demands control of the detailed bulk and surface chemistry of these materials to maximize performance and alleviate operational stability issues. This talk will present generalizable strategies for synthesis of high-performance metal oxides at low-process temperatures using scalable, aqueous processing and printing methods suited for R2R fabrication. We explore the generality of aqueous chemistries for fabricating ultrathin (5-25 nm) films of both p-type and n-type metal oxides (NiO<sub>x</sub>, InO<sub>x</sub>, etc.) at low temperatures (200 – 300 °C). Detailed XPS analysis of these films show commonalities in their low-temperature transformations from M-OH bonding to M-O-M, strongly correlated with optoelectronic functionality in thin film transistors and perovskite solar cells. Applications to both of these classes of devices are enhanced by the elimination of organic residues and metal hydroxide phases, both of which can be addressed by aqueous processing strategies. Interestingly, the chemical and optoelectronic properties of these metal oxides are coupled to their *thermomechanical reliability*. We specifically observe that mechanical fracture energy of these materials scales with their precursor chemistry analogously to electronic properties such as mobility and conductivity. Application of ultrathin oxides in transistors and solar cells illustrate the impact of enhanced low-temperature processing on device physics and performance. Aqueous conductors (CdO<sub>x</sub>) and semiconductors (InO<sub>x</sub>) exhibit greater conductivity and electron mobility than organic inks, resulting in high performing thin film transistors with exceptional mobility (> 20 cm<sup>2</sup>/Vs) and subthreshold slope (< 100 mV/dec) processed by scalable printing methods. Similarly, both the performance and stability of planar double-cation (CsFA) perovskite solar cells can be enhanced by aqueous p-type NiO<sub>x</sub> charge transport layers, exhibiting stabilized photovoltaic conversion efficiency (PCE) > 17 % with fill factors > 80%. These cases illustrate the power of these synthetic strategies as generalizable to a variety of transparent metal oxides.

4:15 PM RR08

**Nanomaterial Based Transparent and Flexible Gas Barrier Film Fabrication by Solution Process** Sejung Kim<sup>1,2</sup>, Byeong-Kwon Ju<sup>3</sup>, Donghwan Kim<sup>2</sup> and Jung-Hun Seo<sup>1</sup>; <sup>1</sup>University at Buffalo, The State University of New York, United States; <sup>2</sup>Sungkyunkwan University, Korea (the Republic of); <sup>3</sup>Korea University, Korea (the Republic of)

As the demand for flexible and wearable electronics devices increases, flexible and transparent gas barrier films are becoming an important issue to prevent water and vapor from entering the device to increase the lifetime and stability of devices such as electronic or display devices. Conventional gas barrier films consist of an inorganic/organic multilayer structure. These films are produced using vacuum based processes such as atomic layer deposition (ALD), chemical vapor deposition (CVD) and sputtering. However, vacuum based processing has disadvantages of low production efficiency, high production cost and flexibility. In addition, inorganic layers also frequently crack under bending stresses, which permits H<sub>2</sub>O and O<sub>2</sub> to flow through flexible electronic devices. To solve this problem, we fabricated a gas barrier film using nano materials and

polymers. Instead of a vacuum process for depositing film layers, a passivation layer was deposited using a layer-by-layer assembly method based on solution processing via electrostatic attraction. As nano materials to lengthen the moisture permeation path of water, graphene oxide (GO) and montmorillonite (MMT) were used. Since GO exhibits a large aspect ratio and MMT is a plate-like material, they were suitable for gas barrier films. In addition, polydiallyldimethylammonium chloride (PDDA) and poly(vinyl alcohol) (PVA) were used as suitable polymers to be mixed with GO and MMT. A zeta-potential analysis was used to characterize the electrostatic attraction between the PDDA(GO) solution and PVA(MMT) solution. The GO solution exhibited a zeta potential value of negative charge before mixing with PDDA, but after mixing with PDDA, the PDDA(GO) solution has a positive charge. Oppositely the zeta-potential value of the PVA(MMT) solution has a negative surface charge. The fabricated flexible gas-barrier films have good transparency and improved WVTR characteristics. When GO and MMT are alternately laminated, compared to when each is used alone extending the diffusion path length for gas molecules by inserting GO into the PDDA. When PDDA(GO) and PVA(MMT) are alternately laminated, they nano materials are stably bonded by hydrogen bonding or crosslinking effects between GO and MMT. That each layers PDDA(GO) and PVA(MMT) are well aligned. Thus filling the vacancies formed when the layers are laminated individually and blocking pathways for water vapor permeation. Hence, water vapor transmission rate (WVTR) value of the PDDA(GO)/PVA(MMT) films was greatly reduced. The water vapor transmission properties of the flexible gas-barrier thin films were analyzed by Ca-test. Calcium (Ca) is highly sensitive to water and water vapor when it reacts with water vapor passing through a gas-barrier film, calcium oxide is formed. This oxidizes the Ca therefore, an insulating film experiences an increase in resistance value under an applied constant voltage, which can be observed by monitoring the decrease in current through the film. We are comparing of the WVTR values measured before and after the bending testing of the PDDA(GO)/PVA(MMT) gas-barrier film. The WVTR value is changed from  $5.0 \times 10^{-3}$  g/m<sup>2</sup>/day before testing to  $3.1 \times 10^{-3}$  g/m<sup>2</sup>/day afterward. This result shows that no significant change occurs in the WVTR value, even after repeated bending. Therefore, this flexible gas barrier film is applicable to an electronic device which requires transparency and flexibility.

# EMC INDEX

This index lists session chairs, presenters and co-authors.

- Session chairs will have the session letter code. (eg: A)
- The plenary speaker will have two \*(asterisks) before the session letter code and paper number in bold type. (eg: \*\*A01)  
Invited speakers will have one \* (asterisks) before the session letter code and paper number in bold type. (eg: \*E01)
- All other Presenters will have the session letter code followed by the paper number in bold type. (eg: B02)
- Co-authors will have the session letter code followed by the paper number in regular type. (eg: B02)

## A

Abate, Yohannes, H08, EE02  
Abdelhamid, Mostafa, **MM04**, PS1.10  
Abdullaev, Azat, DD04  
Abrand, Alireza, **B02**, O02, PS1.24  
Abuzaid, Hattan, D02  
Adams, Rachel, V09  
Addamane, Sadvikas, LL07  
Adnan, Md Mohsinur Rahman, **N06**  
Agarwal, Anant, L06, L07  
Aghamiri, Neda Alsadat, **H08**  
Ahmad, Habib, **X01**, X02, **PS1.07**, **PS2.05**  
Ahmad, Iftikhar, NN05  
Ahmad, Shahzad, **R03**  
Ahmadi, Elaheh, N, X05, Y02, Y04, NN01  
Ahmed, Fiaz, **PS1.11**  
Ahmed, Taimur, R06  
Ahn, Chiho, NN01  
Ahn, Heebeom, **II03**  
Ahn, Kyle, **J01**, J02  
Ahn, Minhyung, **A04**  
Ahn, Yongmo, A04  
Ahoujja, Mohamed, PS2.07  
Ahyi, Ayayi, L09  
Aiello, Anthony, NN01, PS1.08  
Ailihumaer, Tuerxun, I03, **AA02**, AA04, PS1.04  
Akazawa, Masamichi, **PS2.09**  
Akbar, Sheikh, W06, GG03, HH03  
Akinwande, Deji, K06, R06  
Allemang, Christopher, C, **HH07**  
Allen, Jeffery, LL08  
Allen, Martin, CC08  
Allen, Monica, LL08  
Aller, Henry, **AA10**, **DD06**  
Allerman, Andrew, JJ04  
Al Mueeed, Syed Ahmed, M03  
Alquier, Daniel, B04  
Anaya, Julian, AA06  
Anderson, Travis, C05, G09, I02, P04, PS1.07  
Ang, Kah-Wee, R03  
Aonuki, Sho, **DD01**  
Arafin, Shamsul, MM01, MM02  
Arehart, Aaron, I04, U07, V05, V09, V10, CC03  
Arif, Muhammad, II01  
Armstrong, Andrew, MM01, MM02  
Arnold, Corey, **R04**, **PS2.19**  
Arpiainen, Sanna, D01  
Asel, Thaddeus, K05, **V03**, BB06  
Ashraf, Chowdhury, R09  
Ashton, James, **L05**  
Austin, Drake, **PS2.23**  
Avash, Ihteyaz, **R10**

## B

Babcock, Sean, U09  
Baboli, Mohadeseh A., B02, O02, PS1.24  
Back, Tyson, EE06  
Bae, Jinho, CC02, KK03  
Bagheri, Pegah, **KK02**, NN03  
Bahoura, Messaoud, PS2.24  
Bai, Tingyu, G05, **AA06**  
Bajaj, Sanyam, Y01  
Baker, Alexander, PP02  
Bakhtary-Noodeh, Marzieh, **C06**, Q03, **Q05**

Balakrishnan, Ganesh, O09, LL07  
Banerjee, Sanjay, R07  
Bank, Seth, M, M06, M07, M08, Z, Z02, Z03, LL01, LL02, LL03, LL09, LL10, QQ01, QQ02  
Bansal, Anushka, **EE05**  
Barman, Sajib, G04  
Barnum, Aldriel, K05  
Barone, Veronica, PS1.06  
Barrow, Michael, **O03**, **PS1.13**  
Bassim, Nabil, EE10  
Bayram, Ferhat, K01, K02  
Beagle, Lucas, **K03**  
Beauchamp, Bradlee, **OO03**, PS1.12  
Beck, Megan, A01  
Beckmann, Karsten, A02  
Bedair, Salah, MM04, PS1.10  
Behera, Makhesh, **PS2.24**  
Bell, L. Douglas, Q04  
Ben-Haim, Sharona, T04  
Bennett, Brian R., PS1.18  
Berger, Paul, G06, HH05  
Berquist, Zachary, Z08  
Bertani, Paul, **T02**  
Bertness, Kris, B01, PL  
Berweger, Samuel, **R08**  
Bhalerao, Sagar, **G06**, **HH05**  
Bhattacharya, Pallab, NN01, PS1.08  
Bhattacharyya, Arkka, **N08**, V02, V04, V06, CC04  
Bhuiyan, A F M Anhar Uddin, H05, **V01**, V05, V09, V10, BB01, CC03, CC05  
Binder, Andrew, **C01**, P, Q  
Birdwell, A., **AA08**  
Bishop, Alexander, **PP02**, PS2.11  
Bisig, Samuel, O04  
Biswas, Mahitosh, X05  
Blaauw, David, O03  
Blackburn, Jeffrey, R08  
Blair, Steve, G08  
Blumer, Ari, U04  
Blumer, Zak, G07, U04  
Boltasseva, Alexandar, PS1.12  
Bonanno, Peter, L02, **AA03**  
Bonaf, Bastien, H04  
Booth, Kristen, L06, L07  
Borovac, Damir, M03, P01  
Bourhis, Andrew, T03, T04, HH06, **RR03**  
Bowen, David, LL05  
Bowen, Timothy, EE10  
Bowers, John, M05  
Boyadzhiev, Alexandra, **PS2.11**  
Boyer, Bryce, PS2.23  
Boyer, Jacob, G07, **U04**  
Briggs, Andrew, Z02, LL03, LL09, **LL10**  
Briggs, Natalie, EE10  
Brillson, Leonard, K05, N02, BB06, BB07, GG01, HH, HH04  
Brooks, Christopher, W01  
Brown, Elliott, Z10  
Brubaker, Matt, **B01**, MM, NN  
Bryan, Isaac, KK01  
Bryan, Zachary, KK01  
Buchanan, Kristen, OO04  
Burger, Tobias, LL04  
Butera, Robert, LL05

## C

Cady, Nathaniel, A02  
Cagin, Emine, **O04**  
Calderon Ortiz, Gabriel, **H02**  
Caldwell, Joshua, EE02  
Campbell, Joe, LL01, LL02  
Candido, Denis, OO04, **OO07**  
Canova, Marcello, W01  
Cao, Linyou, D02  
Cao, Yang, **KK04**  
Carey, Patrick, **KK03**  
Carpena-Nunez, Jennifer, EE06  
Caruntu, Gabriel, PS1.16  
Cassuto, Guy, R10  
Cavallo, Francesca, Z05  
Cazalas, Edward, U08  
Cetnar, John, **X04**  
Cha, Jung Suk, **PS2.16**  
Chae, Sicun, **GG04**  
Chan, Silvia, P02  
Chanana, Ashish, G08  
Chandan, Greeshma, Z01  
Chandrasekar, Hareesh, P05, Y01, MM01, MM02  
Chandrashekhar, MVS, L, AA05, CC, NN05, PS1.11  
Chang, Alexander, **C02**  
Chang, Ching-Wen, HH01  
Chatratin, Intuon, **N04**  
Chauhan, Ankur, AA05  
Chauhan, Vinay, DD04  
Chavan, Prasad, G01  
Cheek, Quintin, **B03**  
Chen, Di, HH01  
Chen, Eric, **U09**  
Chen, Hong, C03, J03, V08, MM03, PS1.09  
Chen, Jiazhen, K04  
Chen, Jie, U05, Y03, RR04  
Chen, Quark, **HH01**, PS2.15  
Chen, Zeyu, AA04  
Chen, Zhaoying, I04  
Cheng, Qianyu, **AA04**  
Cheng, Shuyu, PP02  
Cheng, Zhihui, **D02**  
Cheung, Hil Fung, OO05, OO09  
Chiang, Ivan, EE03  
Chiaramonti, Ann, H03  
Chien, Szu-Chia, G02, **K05**  
Chilcote, Michael, OO04, OO05, OO09  
Cho, Cheolhee, **CC02**  
Cho, Hanna, W01, W02  
Cho, Hans, S03  
Cho, Kyungjune, EE01, FF01  
Cho, Minkyu, C06, Q03, Q05  
Cho, Tae, HH07  
Choi, Hyunwoo, **RR02**  
Choi, Ilgyu, **PS2.08**  
Choi, Sukwon, Y03  
Choi, U Hyeok, PS2.01  
Chou, Harry, R07  
Chou, Hsuing, PS2.15  
Choudhury, Tanushree H., **R09**  
Chowdhury, Sayema, **R07**  
Chowdhury, Srabanti, MM, NN  
Christodoulides, Joseph A., PS1.18  
Chu, Alan, **PS1.12**  
Chu, Rongming, P03

Chu, Wei-Kan, HH01  
Ciacci, Joseph, T04  
Cimatu, Katherine Leslee A., M04  
Cimpoiasu, Elena, **PS1.18**  
Cinquanta, Eugenio, K05  
Ciszek, Jacob, **F03**  
Clarke, Roy, QQ03  
Cleary, Daniel, T03, T04  
Clevenger, Michael, II09, PS1.05  
Clinton, Evan, X01, X02, MM05, PS1.07, PS2.05  
Cohn, Rachael, **H06**  
Collazo, Ramón, H, X, Y, KK01, KK02, NN03  
Cooke, Jacqueline, N05, **V04**  
Cooley, Kayla, **A03**  
Coridan, Robert, **O05**  
Cormode, Donley, OO05, **OO09**  
Cornuelle, Evan, **CC05**  
Cowsky, Jade, **GG01**  
Crawford, Kevin, AA08  
Crawford, Mary, MM01, MM02  
Cui, Peng, HH08  
Cui, Zhenjun, EE03

## D

Dang, Giang, N05  
Daniels, Kevin, D, K, K01, K02, R, R10  
Das, Hrishikesh, L01  
Das, Kumar, CC10  
Dasari, Kiran, OO02  
Dasgupta, Neil, HH07  
Daughton, David, V05  
Davis, Benjamin, **PS1.22**, PS1.23  
Davis, Robert, PS2.18  
Dayeh, Shadi, O10, T01, T03, T04, HH06, RR01, RR03  
Debesay, Thomas, **PS1.20**  
Deitz, Julia, G02  
De La Rosa, Angel, PS1.19  
DenBaars, Steven, MM03, NN02  
Deng, Xuguang, C03, V08  
Deng, Zihao, NN01  
Deng, Ziling, **BB03**  
Derege, Michael, C04  
Detchprohm, Theeradetch, C06, Q, Q03, Q05, MM  
Dev, Sukrith, LL08  
Devor, Anna, T01  
Dey, Tuhin, M08  
Dhar, Sarit, L08, L09  
Dhingra, Pankul, M06, M07, LL06  
Diaz, Rosa, KK04  
Dibaji, Hassan, **Z05**  
Dickens, Dickens, N03  
Dickerson, Jeramy, C01  
Diez Pinzon, Sandra, **Y02**, Y04  
Dix, Connor, O09  
Dockins, Maddox, PS2.19  
Dodson, Gregg, NN04  
Donald, Scott, JJ02  
Dong, Zuoming, **Z02**  
Doolittle, W. Alan, A06, S02, X01, X02, MM05, PS1.07, PS2.05  
Dou, Letian, H02  
Dreyer, Michael, LL05  
Dudley, Michael, I03, AA02, AA04, PS1.04  
Dunphy, Benjamin R., PS1.18  
Dupuis, Russell, C06, Q03, Q05, X, Y, NN  
Durbin, Steve, QQ03  
Dutta, Aveek, PS1.12  
Dutta, Soumya, II04  
Dwyer, Matthew, Z05  
Dzuba, Brandon, KK04  
D'Andrea, Cosimo, K05

## E

Ebrish, Mona, **C05**, G09, I02, K, P04, U  
Eisner, Brian, **V02**

Eldred, Tim, MM04, NN03  
El-Jaroudi, Rasha, **M06**, M07, M08  
El-Masry, Nadia, MM04, PS1.10  
Elsharif, Hesham, EE10  
Eng, Brendan, U01, LL06  
Engel, Zachary, X01, **X02**, **MM05**, PS1.07, PS2.05  
Engel-Herbert, Roman, EE05  
Eo, Jung Sun, II02  
Eom, Chang-Beom, BB06  
Ertekin, Elif, EE07  
Ewing, Daniel, I, J, O  
Eyink, Kurt, **Z07**, PP, QQ

## F

Fahrenkrug, Eli, B03  
Fali, Alireza, EE02  
Fan, Dejiu, LL04  
Fan, Wei, **AA01**  
Fan, Zongjian, **PS1.03**  
Fang, Jen-Chun, **PS1.17**  
Fang, Yihao, QQ02  
Fares, Chaker, **CC07**, CC09  
Farshchi, Rouin, U07  
Favela, Carlos, U05  
Favela, Elizabeth, CC10  
Fedorenko, Anastasiia, PS1.24  
Feezell, Daniel, J01, J02, CC04  
Feigelson, Boris, C05  
Feng, Zixuan, H05, V01, **V05**, V09, V10, BB01, CC03, CC05  
Feygelson, Tatyana, AA06, DD06  
Fisher, Timothy, PS2.23  
Flatté, Michael, OO01, OO04, OO06, OO07, OO08  
Floyd, Richard, MM05  
Folland, Thomas, EE02  
Forrest, Stephen, LL04  
Foster, Geoffrey, **P04**  
Fox, Matthew J., PS1.18  
Franklin, Aaron, D02  
Franson, Andrew, **OO04**, OO05, OO09, PS1.14  
Friedl, Martin, BB02  
Friedman, Adam, LL05  
Frye, Clint, **JJ02**  
Fu, Houqiang, C03, J03, V08, MM03, PS1.09  
Fu, Kai, **C03**, J03, MM03, PS1.09  
Fuchs, Gregory, OO05, OO09  
Fujii, Kazuhito, CC01

## G

Gadenne, Virginie, F04  
Gaevski, Mikhail, MM05, NN05, PS1.11  
Gajdardziska-Josifovska, Marija, GG02  
Galazka, Zbigniew, CC10  
Gallagher, James, G09, **I02**, PS1.07  
Gallagher, Joshua, J01  
Gallegos, Aryn, O03  
Gallis, Spyros, K07  
Galton, Ian, RR03  
Gao, Hantian, N02, **BB07**, GG01, HH04  
Garcia, Ashlee, Z03, **QQ01**  
Garcia, Carlos, KK04  
Garland, Ben, **PS1.23**  
Gazda, Eliza, Q03  
Ge, Ruijing, K06  
Gebriel, Wafaa, **PS1.21**  
Gellman, Andrew, AA10, DD06  
Genov, Dentcho, Z02  
Georgieva, Jana, P02  
Gerngross, Maik, O04  
Gerton, Jordan, B05  
Gertsch, Jeffrey, T04  
Ghadbeigi, Leila, **N05**, V04  
Ghadi, Hemant, **V09**, V10  
Ghazisaedi, Maryam, BB04  
Ghosh, Aheli, A06, **S02**

Ghosh, Rudeesh, R07  
Gim, Jiseok, PS1.08  
Ginley, Theresa, Z01  
Glavin, Nicholas, K03, PS2.19, PS2.23  
Gliebe, Kimberly, PS2.23  
Goldberger, Joshua, K05  
Goldman, Rachel, BB  
Golio, Nick, DD06  
Gonzalez-Serrano, Karla, **II06**  
Goorsky, Mark, C05, G05, AA06, JJ, KK, QQ05  
Gopalan, Prashanth, **G08**  
Gopinath, Juliet, LL10  
Gotoh, Jun, II01  
Gouma, Perena, H01  
Graham, Samuel, AA06, PS2.17  
Grasser, Tibor, D01, D04  
Grassman, Tyler, G02, G07, U02, U04  
Greytak, Andrew, PS1.11  
Grieco, Christopher, **W07**  
Groome, Chloe, **W05**  
Grundmann, Marius, CC07, HH04  
Gu, Yuqian, R06  
Guan, Rian, P03  
Guan, Yan, KK02, **NN03**  
Guerboukha, Mohamed-amine, **F04**  
Guiney, Ivor, N01  
Gulyas, Istvan, M08  
Gunning, Brendan, I02, P04, X, Y, JJ04, MM01, MM02  
Guo, Qiang, D  
Gupta, Chirag, NN02  
Gupta, Jay, BB03, PP02

## H

Haglund, Richard, EE02  
Haidet, Brian, **PP05**  
Hall, Doug, C, O, O08, JJ, KK  
Han, Jung, C02  
Han, Sangmoon, PS2.08  
Han, Sang-Woo, **P03**  
Haque, Aman, CC07, CC09  
Hardy, Matthew, P, Q  
Harmon, Nicholas, OO01  
Harrison, Sara, JJ02  
Harvey, Todd, B01  
Hasan, Syed Mohammad Najib, **MM01**  
Haseman, Micah, N02, **HH04**  
Hassan, Md, RR05  
Hassan, Syed, MM02  
Hatem, Christopher, M01  
Hatui, Nirupam, JJ03, NN02  
Haug, William, W03  
Hazra, Jubin, **A02**  
He, Feng, QQ02  
He, Yanwei, **EE03**  
Hecht, Adam, O09  
Hemker, Kevin, AA05  
Hendricks, Jessica, V03, **PS2.07**  
Heremans, Joseph, E03, DD05, LL05  
Hernandez, Joel, U06  
Heron, John, A04, GG04  
Herrera-Fierro, Pilar, O03  
Herrick, Robert, M05  
Hersam, Mark, A01  
Hery, Travis, A05  
Hettiaratchy, Elline, G02, **G03**  
Higashiwaki, Masataka, CC  
Hill, Madelyn, Z07  
Hill, Megan, BB02  
Hilse, Maria, EE05  
Hines, Nicholas, AA06  
Hinkel, Dan, LL05  
Hite, Jennifer, C05, I02, AA  
Hobart, Karl, C05, G09, I02, P04, AA06, DD06  
Hodges, Deidra, **PS1.19**  
Hoffman, Anthony, Z, Z09  
Hogan, Kasey, C04, Q04, **DD07**, OO

Holoviak, Stephen, EE10  
 Holzner, Felix, O04  
 Hong, Dajung, II07  
 Hool, Ryan, U01, U03, LL06  
 Hoshikawa, Keigo, CC01  
 Hosokura, Tadasu, H07  
 Hossain, Lorraine, T01  
 Hou, Caixia, **CC08**  
 Hovden, Robert, PS1.08  
 Howell, Caroline, Z09  
 Howell, Robert, AA10  
 Hruska, Martin, F04  
 Hsain, Hanan, S01  
 Hu, Jun, PS2.04  
 Hu, Kwangyul, **OO08**  
 Huang, Chunyi, **BB02**  
 Huang, Hsien-Lien, V01, **BB01**, CC05  
 Huang, Xuanqi, C03, J03, V08, MM03, PS1.09  
 Hubbard, Seth, PS1.24  
 Huda, Muhammad, **G04**  
 Huey, Bryan, H07  
 Huey, Warren, K05  
 Hughes, Eamonn, **H04**, M05, PP05  
 Hughes, Lillian, **AA07**  
 Humphreys, C J, N01  
 Hussain, Mohammad, Y01, MM05, NN05  
 Hwang, Jinwoo, H02, V01, BB01, CC05, PP02, PP03, PP04

**I**  
 Iheomamere, Chukwudi, R04  
 Illarionov, Yury, **D01**, D04  
 Imroze, Fiheon, **II04**  
 Inbanathan, Flavia P.N., **M04**  
 Ingram, David C., M04  
 Ironside, Daniel, Z03, QQ01, QQ02  
 Irvin, Nicholas, U09  
 Irving, Doug, KK01  
 Isaacs-Smith, Tamara, L09  
 Islam, Ahmad, EE06  
 Islam, Zahabul, CC07, CC09  
 Istrate, Cosmin, S01  
 Ivanov, Tony, AA08

**J**  
 Jackson, Thomas, O07  
 Jacobs, Alan, C05, G09  
 Jadwisieniczak, Wojciech, M04, OO02, PS2.21  
 Jalil, Osama, R03  
 Jamal-Eddine, Zane, MM01, **MM02**  
 Jamison, John, **G02**, G03  
 Janes, David, II  
 Jang, Der-Jun, PS2.15  
 Jang, Yeonsik, II02  
 Janotti, Anderson, N04, V  
 Jaramillo, Rafael, **S04**  
 Jayan, Reeja, BB05  
 Jayatunga, Benthara, **PP03**, PP04  
 Jayawardhena, Isanka Udayani, **L09**  
 Jayich, Ania, AA07  
 Jean-Remy, Philip, **PS2.18**  
 Jena, Debdeep, CC06  
 Jeon, Ju-Won, II07  
 Jeon, Seokmin, B05  
 Jeong, Hoon, **Q03**, Q05  
 Ji, Mi-Hee, C06, Q03  
 Jia, Meng, HH08  
 Jian, Zhe (Ashley), Y04  
 Jiang, Jie, EE06  
 Jiang, Kunyao, R, CC10, PP, QQ  
 Jiang, Shishi, K05  
 Jiao, Xinwei, **PS1.02**  
 Jin, Tian, PS2.04  
 Jinschek, Joerg, H01  
 Johnson, Harley, EE07  
 Johnson, Jared, V01, BB01, CC05

Johnston-Halperin, Ezekiel, OO04, OO05, OO09, PS1.14  
 Jones, Andrew, LL01, LL02  
 Jones, Jacob, S01  
 Jones, Kenneth, C04  
 Jones, Kevin, M01, JJ04  
 Jozwiak, Chris, PP02  
 Ju, Byeong-Kwon, RR08  
 Jung, Daehwan, M05  
 Justeau, Camille, B04  
 Justice, Joshua, **L01**

**K**  
 K. Sood, Ashok, Q05  
 Kabos, Pavel, R08  
 Kachi, Tetsu, PS2.09  
 Kaehr, Bryan, **F02**  
 Kajikura, Atsushi, CC01  
 Kakabalo, Moarabi, F01  
 Kalarickal, Nidhin Kurian, N06, **CC03**  
 Kaloyeros, Alex, K07  
 Kalra, Anisha, **I01**, **Q01**, Q02  
 Kamoshida, Ryo, PS2.09  
 Kang, Keehoon, EE01, FF01, II03  
 Kang, Minseok, **L06**, L07  
 Kang, Sang-Woo, K02  
 Kang, Seonkyeong, PS2.13  
 Kapadia, Rehan, M09  
 Kaplar, Robert, C01, I02, P04  
 Karim, Md Rezaul, I04, V01, PP03, **PP04**  
 Karnati, Priyanka, **HH03**  
 Karpov, Victor, S05  
 Kash, Kathleen, PP03, PP04  
 Kasher, Tal, **G07**, U02  
 Kavey, Benard, **PS1.16**  
 Kawaharamura, Toshiyuki, N05  
 Kawakami, Roland, PP02, PS2.11  
 Kayede, Emmanuel, **JJ03**  
 Kazanowska, Barbara, **JJ04**  
 Kecskes, Ian, O02  
 Kei, Chi-Chung, HH01  
 Keller, Stacia, P02, JJ03, NN02  
 Kelson, Chabak, AA10  
 Keskinen, Jari, HH05  
 Khafizov, Marat, **DD04**  
 Khan, Asif, Y01, MM05, NN05, PS1.11  
 Khan, Digangana, K01, K02  
 Khan, Irfan, **Z09**  
 Khan, Kamruzzaman, **X05**  
 Kheirandish, Elaheh, **GG02**  
 Khodaparast, Giti, KK04  
 Kim, Donghwan, RR08  
 Kim, Dongyoung, L04  
 Kim, Jae Jin, O06  
 Kim, Jae-Keun, **EE01**, FF01  
 Kim, Jaekyun, PS2.01, PS2.12, PS2.13  
 Kim, Jaeyoung, EE01, **FF01**  
 Kim, Janghyuk, CC02  
 Kim, Jihyun, CC02, KK03  
 Kim, Ji Hyun, **KK01**, KK02  
 Kim, Jin Soo, PS2.08  
 Kim, Jung Hyun, W01, W02, PS1.02  
 Kim, Junwoo, II03  
 Kim, Mijung, **U01**  
 Kim, Naemun, RR02  
 Kim, Nam-In, **RR04**  
 Kim, Samuel, **PS2.17**  
 Kim, Sejung, **RR08**  
 Kim, Soaram, K01, **K02**, R  
 Kim, Tae-Wook, II02  
 Kim, Wonjae, D01  
 Kim, Youngkyun, PS2.01, **PS2.12**  
 Kim, Youngrok, EE01, II03  
 King, Richard, U09  
 Kioupakis, Emmanouil, FF, GG, GG04, NN01, PS1.08  
 Kira, Mackillo, NN01  
 Kirste, Ronny, KK01, KK02  
 Klein, Benjamin, H03

Klein, Brianna, O09  
 Klem, John, O09  
 Klump, Andrew, KK02  
 Kneiß, Max, CC07  
 Knobloch, Theresia, D01, **D04**  
 Kobayashi, Masakazu, **PS2.06**  
 Koehler, Andrew, G09, I02, P04  
 Kohl, Forrest, W07  
 Kohler, Bern, W07  
 Koishikawa, Yuki, CC01  
 Koley, Goutam, K01, K02  
 Korzun, Barys, **U06**  
 Koshi, Kimiyoshi, CC01  
 Kotha, Mounika, **K07**  
 Kotulak, Nicole, QQ04  
 Kouklin, Nikolai, GG02  
 Kozak, Brian, AA01  
 Kozen, Alexander, S03  
 Krafft, Charles, LL05  
 Krishna, Sanjay, K02, LL  
 Krishnamoorthy, Sriram, G, G08, N05, N08, V02, V04, V06, CC04  
 Krishnamurthy, Mahalingam, Z07  
 Kronz, Jeffrey, **EE04**  
 Krupanidhi, Saluru, PS2.03  
 Ksari, Younal, F04  
 Kub, Fritz, I02, P04  
 Kuball, Martin, AA06  
 Kuciauskas, Darius, U07  
 Kulmala, Tero, O04  
 Kumar, Viswanathan, PS1.09  
 Kumawat, Kishan, **PS2.03**  
 Kuo, Chien Cheng, PS2.15  
 Kuo, Yu-Ling, HH01  
 Kupp, Benjamin, R08  
 Kuramata, Akitō, G09, CC01  
 Kurdak, Cagliyan, Y02  
 Kurfman, Seth, OO04, OO05, OO09, **PS1.14**  
 Kuroda, Marcelo, L08

**L**  
 Lagally, Max, Z05  
 Lai, Junyu, **RR05**  
 Laleyan, David, X03, NN01  
 Lalk, Rebecca, PP04  
 Landi, Brian, O02  
 Lauhon, Lincoln, A, C02, **K04**, BB02  
 Law, Stephanie, E, Z01, Z04, Z06  
 Leach, Jacob, P03, **JJ05**, NN04  
 LeBeau, James, MM04  
 Lee, Byungjun, LL04  
 Lee, Chul-Ho, II02  
 Lee, Daesu, BB06  
 Lee, Dawoon, **PS2.01**, PS2.12, PS2.13  
 Lee, Dongyun, PS2.13  
 Lee, Hong-Sub, A01  
 Lee, Hyunseok, PS2.13  
 Lee, Jack, K06  
 Lee, Jihan, A04  
 Lee, Jihwan, **O10**, T01  
 Lee, Jiyoung, T02  
 Lee, Jung-woo, BB06  
 Lee, Keundong, **T01**  
 Lee, Michael, **W02**  
 Lee, Ming-Hsun, **N07**  
 Lee, Minjoo, M06, M07, U, U01, U03, **LL06**  
 Lee, Sang Heon, T01, T04  
 Lee, Seung, A04  
 Lee, Seunghyun, K02  
 Lee, Seungjun, T02  
 Lee, Seung Min, Y03  
 Lee, Sora, **O07**  
 Lee, Sunghwan, **II09**, **PS1.05**  
 Lee, Takhee, EE01, FF01, II02, II03  
 Lee, Woocheol, FF01, II03  
 Leedy, Kevin, GG01  
 Lelis, Aivars, L05  
 Lemme, Max, D04  
 Lenahan, Patrick, L03, L05

Lenert, Andrej, **Z08, LL04**  
 Lepkowski, Daniel, G07, **U02, U04**  
 Lernnartz, Jeffery, AA01  
 Letton, Joshua, NN05, PS1.11  
 Lewis, Daniel, K01, K02  
 Li, Bingjun, C02  
 Li, Brian, **U03**  
 Li, Connie, E  
 Li, Dongying, MM03  
 Li, Siming, U07  
 Li, Weiyi, NN02  
 Li, Wenbo, I04  
 Li, Wenshen, **CC06**  
 Li, Xiuling, **O01**  
 Li, Yuan, EE03  
 Liao, Chih-Hsiung, HH01  
 Liao, Michael, **G05, QQ05**  
 Licata, Olivia, PP04  
 Lichtenwalner, Daniel, L02, L05  
 Liehr, Maximilian, A02  
 Lin, C.M., HH01  
 Lin, Chia-Hung, **CC01**  
 Lin, Guangyang, HH08  
 Lin, Tai-Siang, HH01  
 Lin, Tianxiang, CC10  
 Lintereur, Azaree, J01  
 Little, Charles, B01  
 Litwin, Peter, LL05  
 Liu, Chison, R07  
 Liu, Hanxiao, PS1.09  
 Liu, Jian, **PS1.01**  
 Liu, Jianlin, EE03  
 Liu, Shiyi, II05  
 Liu, Tianshi, L06, L07  
 Liu, Wenjian, **P02**  
 Liu, Xiang, AA01  
 Liu, Xianhe, NN01  
 Llu, Xinke, R03  
 Liu, Yafei, **I03, AA02, AA04, PS1.04**  
 Liu, Yuanyue, **W04**  
 Logesh, Karunakaran, II04  
 Long, Yaoyao, CC06  
 Look, David, N02, X04, GG01  
 Look, Paige, PS2.23  
 Lu, Jiwei, LL05  
 Lu, Ping, M01  
 Lu, Wei, A04  
 Lu, Wu, T02, Y01  
 Lu, Yanfu, EE10  
 Lu, Yang, II07  
 Lucian, Pintilie, S01  
 Lund, Matthew, U08  
 Lundh, James, Y03  
 Lupo, Donald, G06, HH05  
 Lussem, Bjorn, II05  
 Lyle, Luke, **CC10**  
 Lynn, Kelvin, N03, V06

## M

Mace, Emily, J01  
 Mack, Shawn, PS1.18  
 Maddox, Scott, LL09  
 Maeng, Seohyun, **PS2.13**  
 Magginetti, David, **B05, U08**  
 Magill, Brenden, KK04  
 Magill, Steve, KK04  
 Mahadik, Nadeemullah, **L02, AA, AA03, QQ04**  
 Mahapatro, Ajit, PS2.10  
 Mahoney, Monica, J02  
 Majumdar, Sayani, D01  
 Makarov, Vladimir I., M04, PS2.21  
 Makin, Robert, QQ03  
 Maldonado, Stephen, B03  
 Malen, Jonathan, AA10, DD06  
 Malis, Oana, KK04  
 Mamun, Abdullah, MM05, **NN05**  
 Manasreh, Omar, PS1.21

Manda, P.K., II04  
 Mane, Anil, **R01**  
 Manfra, Michael, KK04  
 Manning, Brian, **L03**  
 Mansoori, Ahmad, O09, **LL07**  
 Mäntysalo, Matti, HH05  
 March, Stephen, **LL01, LL02, LL03**  
 Marinero, Ernesto, OO03, PS1.12  
 Marks, Tobin, K04  
 Marohn, John, H06  
 Martin, Joel, T04  
 Martin, Michael, H07  
 Maruyama, Benji, EE06  
 Mastro, Michael, C05, I02  
 Mates, Tom, AA07  
 Mathis, James, QQ03  
 Matthews, Christopher, X01, X02, MM05, PS1.07, PS2.05  
 May, Brelon, G02, **O06**  
 May, Steven, **\*E02**  
 Mayergoyz, Isaak, LL05  
 Mazumder, Baishakhi, H05, V01, PP04  
 McArthur, Joshua, **LL03**  
 McCabe, Lauren, **M02**  
 McClellan, Claire, AA07  
 McComb, David, G02, G03  
 McCrone, Timothy, **A06, S02**  
 McCrory, Duane, L03  
 McDonnell, Stephen, LL05  
 McEwen, Benjamin, C04, Q04, DD07, II, OO  
 McGaughey, Alan, AA10, BB05, DD06  
 McGinnity, Tracie, Z09  
 McGlone, Joe, V05, V09, **V10, Y01, CC03**  
 McGrier, Psaras, W03  
 McLoughlin, Lauren, II07  
 McMillan, Stephen, **OO01**  
 McNicholas, Kyle, M06, PP, QQ  
 McPherson, Chris, K05  
 McSherry, Sean, LL04  
 Mech, Roop K, R05  
 Medvedeva, Julia, BB09  
 Mehmood, Furqan, **S01**  
 Meng, Qian, M06, M07, **M08**  
 Mengle, Kelsey, GG04  
 Meyers, Vincent, **C04, H, Q04, AA, DD07, FF, GG**  
 Meynell, Simon, AA07  
 Mi, Zetian, W, X03, NN01, PS1.08  
 Mikolajick, Thomas, S01  
 Miller, Elisa, R08  
 Miller, Michael, **U07**  
 Mirin, Richard, Z10  
 Mirkhosravi, Farnood, J01, J02  
 Mishra, Umesh, P02, JJ03, NN02  
 Mita, Seiji, NN03  
 Mithun, C.A., II04  
 Mock, Alyssa L., G09  
 Mody, Jay, H  
 Mohan, Sivasakthya, R06  
 Mohanty, Subhjit, **Y04**  
 Mohny, Suzanne, A03, O07  
 Mohseni, Parsian, B, B02, **O02, Z, PL, PS1.24**  
 Mohta, Neha, **R02, R05**  
 Mollah, Shahab, NN05, PS1.11  
 Molotokaite, Egle, K05  
 Montes, Jossue, C03, J03, **V08, MM03, PS1.09**  
 Moody, Diamond, CC10  
 Moody, Michael, K04  
 Moon, Eunseong, O03  
 Moore, David, PS2.23  
 Moore, Wyatt, CC03  
 Moran, Thomas, **H07**  
 Morell, Gerardo, M04, PS2.21  
 Morisette, Dallas, L09  
 Morral, Anna, BB02  
 Morris, Patricia, GG03, HH03

Moses, Isaiah, **PS1.06**  
 Motoki, Keisuke, X01, PS2.05  
 Mou, Shin, N, V03, PS2.07  
 Muazzam, Usman, **G01**  
 Mueller, Sara, BB03  
 Mueller, Thomas, D01  
 Muhowski, Aaron, Z03, QQ02  
 Mukherjee, Kunal, H04, M05, AA07, PP05  
 Mukherjee, Madhubanti, **DD02, DD03**  
 Mukhopadhyay, Souvik, **A05**  
 Murai, Shunta, PS2.09  
 Muralidharan, Bhaskaran, EE08  
 Muratore, Christopher, K03, PS2.19, PS2.23  
 Muratore, Tobin, X04  
 Murayama, Koji, H07  
 Myers, Roberto, G02, G03, N06, V07, KK05  
 Myers-Ward, Rachel, K01

## N

Nadaud, Kevin, B04  
 Nair, Hari, LL09  
 Nakamura, Shuji, MM03, NN02  
 Nanayakkara, Sanjini, R08  
 Nanda, Karuna, PS2.03  
 Narang, Prineha, **\*E01**  
 Nath, Dignijoy, G01, I01, N01, Q01, Q02, R02, R05, JJ01  
 Neal, Adam, V03, PS2.07  
 Neumaier, Daniel, D04  
 Neupane, Mahesh, AA08  
 Newburger, Michael, PS2.11  
 Nguyen, Trang, KK04  
 Ni, Chaoying, Z01  
 Nilsen, Ola, PP01  
 Ning, Cun-Zheng, MM03  
 Noesges, Brenton, K05, **BB06**  
 Noh, Siyun, PS2.08  
 Nomoto, Kazuki, CC06  
 Nordin, Leland, LL08, PP05  
 Norman, Justin, M05  
 Nouri, Mohammad, **D03**

## O

O'Hara, Dante, PP02  
 Oberdorfer, Christian, V07  
 Odoeze, Jidefor, **O08**  
 Oh, Hongseok, HH06, **RR01, RR03**  
 Oh, Jungwoo, Y03  
 Onwona-Agyeman, Boateng, **HH02**  
 Ooi, Yu Kee, J01, **J02, N03, V06, CC04**  
 Otsuka, Fumio, CC01  
 Otte, Nepomuk, Q03

## P

Pachter, Ruth, EE06  
 Page, Michael, PS1.14  
 Paik, Hanjong, GG04  
 Pak, Jinsu, FF01  
 Palai, Ratnakar, **OO02**  
 Palmese, Elia, **P01**  
 Pan, Fenghongkang, **PS2.04**  
 Pan, Jinbo, BB06  
 Pandey, Ayush, X03, NN01, **PS1.08**  
 Park, Jaeseo, K02  
 Park, Wonta, RR02  
 Pasayat, Shubhra, **NN02**  
 Patmiou, Maria, **S05**  
 Patrone, Lionel, F04  
 Paul, Pran, U07  
 Peart, Matthew, P01  
 Pearton, Stephen, CC07, CC09, KK03  
 Pedowitz, Michael, **K01, K02, R10**  
 Peng, Hongyu, I03, AA02, AA04, **PS1.04**  
 Perez, Phoebe, PS2.15  
 Peterson, Rebecca, N, N07, V, HH, HH07  
 Petluru, Priyanka, Z03  
 Pfister, Nicole, LL  
 Phelan, W. Adam, AA05  
 Phillips, Jamie, A04, K, O03, HH, PS1.13

Pierce, Michael, O02  
Piper, Louis, W  
Pochet, Pascal, EE07  
Polat Genlik, Sevim, **BB04**  
Polly, Stephen, PS1.24  
Polyushkin, Dmitry, D01  
Ponce, Fernando, MM03, PS1.09  
Popp, Andreas, CC10  
Porter, Lisa, CC10, PL  
Pouladi, Sara, **U05**, Y03  
Poulin-Vittrant, Guylaine, B04  
Powell, Kaden, **U08**  
Pradhan, Sangram, PS2.24  
Prakash, Divya, Z05  
Premadasa, Uvinduni I., M04  
Premysl, Fitol, F04  
Prokes, Sharka, S03  
Prunnila, Mika, D01  
Ptak, Aaron, O06  
Puchades, Ivan, O02  
Puri, Nidhi, **PS2.10**  
Pushkarev, Anatoly, U06  
Puzycki, Sarah, PS1.13

## Q

Qi, Xin, C03, J03, V08, **MM03**  
Qian, Yang, B05, U08  
Qiu, Zanlin, **H01**  
Qu, Hao, AA01

## R

R, Muralidharan, G01, I01, N01, Q01, Q02, R02, R05, JJ01  
Radha Krishnan, Raj Kishen, **I105**  
Raghavan, Srinivasan, G01, I01, Q01, Q02, JJ01  
Raghothamachar, Balaji, I03, AA02, AA04, PS1.04  
Rahman, Adnan Md Mohsinur, KK05  
Rahman, Mohammad Wahidur, **P05**, Y01, KK05  
Railanmaa, Anna, HH05  
Raimundo, Jean-Manuel, F04  
Rajabpour, Siavash, **EE10**  
Rajan, Siddharth, N06, P05, V05, Y01, CC, CC03, KK05, MM01, MM02  
Rakib, Tawfiqur, **EE07**  
Ramadoss, Koushik, L09  
Ramamurthy, Rahul, L09  
Ramanathan, Shriram, H08, BB08, PS2.20  
Ramdin, Daram, **N02**, GG01, HH04  
Randall, Clive, BB07  
Ranga, Praneeth, G08, N08, V02, **CC04**  
Rao, Lalith, **W01**, PS1.02  
Rao, Rahul, EE06  
Rao, V Ramgopal, EE08  
Raslan, Ahmed, T03  
Rathi, Monika, U05  
Rathkanthiwar, Shashwat, I, I01, J, Q01, **Q02**  
Rathod, Urmilaben, R04  
Ravan, Shantam, HH07  
Razzak, Towhidur, P05, **Y01**  
Reczek, Joseph, F02, **I108**  
Reddy, Pramod, KK01, KK02  
Redwing, Joan, R09, EE04, EE05, **\*\*PL01**  
Reed, Amber, X04  
Reese, Matthew, U08  
Reeves, Roger, QQ03  
Reid, Obadiah, R08  
Reinhardt, Catherine, JJ02  
Ren, Fan, CC07, CC09, KK03  
Renteria, Emma, **O09**  
Repicky, Jacob, PP02  
Reunchan, Pakpoom, N04  
Rice, Anthony, O09  
Richter, Curt, D02, S, T  
Ringel, Steven, G07, I04, U02, U04, V05, V09, V10, Y01, CC03  
Ro, Yun Goo, T01

Robinson, Joshua, R09, EE10  
Rocco, Emma, C04, **Q04**, BB, DD07, FF, GG  
Rockwell, Ann, **LL02**, LL03  
Rodriguez, Francisco, U04  
Rodriguez, Miguel, DD07  
Rodwell, Mark, QQ02  
Roeder, Ryan, Z09  
Romanczyk, Brian, JJ03  
Roshko, Alexana, B01  
Rotenberg, Eli, PP02  
Rotter, Thomas, O09, LL07  
Routh, Evyn, MM04, **PS1.10**  
Roy, Anupam, R07  
Roy, Saurav, N08, CC04  
Ruiz, Isaac, EE  
Rumsey, Jaime, P03, JJ05  
Ruppalt, Laura, S03  
Russman, Samantha, **T04**  
Ruzmetov, Dmitry, AA08  
Ryou, Jae-Hyun, U05, Y03, RR, RR04  
Ryu, Mee-Yi, PS2.08

## S

S, Niranjan, **N01**  
Sabio, Fernando, N04  
Sadaf, Sharif, O, BB  
Sahoo, Prasana, R08  
Sahu, Sulata, BB07  
Saleh, Muad, V06  
Salemi, Arash, L06, L07  
Sanford, Norman, H03  
Sangwan, Vinod, **A01**  
Sanjay, Sooraj, R05  
Sapkota, Keshab, M01, JJ04  
Saraswat, Devansh, CC06  
Sarkar, Debarghya, M09  
Sarker, Jith, **H05**, V01  
Sasaki, Kohei, G09, CC01  
Sasaki, Nobuo, **I101**  
Sato, Takuma, DD01  
Sayed, Islam, P02, JJ03  
Sayre, Jay, W01  
Scarpulla, Michael, J01, J02, N03, N05, V02, V04, V06, CC04  
Scheideler, William, **RR07**  
Schirmer, Matthias, O04  
Schkeryantz, Luke, W03  
Schmidt-Sane, Peter, AA01  
Schofield, Marvin, GG02  
Schroeder, Uwe, S01  
Scott, Shelley, Z05  
Seabaugh, Alan, II06  
Segovia, Dinorah, B05  
Selvamanickam, Venkat, U05  
Selvidge, Jennifer, **M05**  
Sen, Prosenjit, N01  
Senabulya, Nancy, QQ03  
Senichev, Alexander, KK04  
Sensale Rodriguez, Berardi, G, G08, N05, V04  
Seo, Jung-Hun, AA09, JJ, KK, RR05, RR06, RR08  
Seo, Junseok, EE01  
Seong, Tae-Yeon, PS2.16  
Serna, Martha, **R06**  
Serpen, Gursel, S05  
Seth, Subhashree, O09  
Shaffer, Gregory, AA01  
Shah, Deesha, PS1.12  
Shah, Pankaj, AA08  
Shah, Piyush, PS1.14  
Shah, Rushabh, H04  
Shahedipour-Sandvik, Fatemeh (Shadi), C, C04, P, Q04, DD07  
Shalaev, Vlad, PS1.12  
Shang, Chen, M05  
Shang, Ju Ying, K04  
Sharifi Abdar, Payman, M04  
Sharma, Abhishek, EE08  
Sharma, Kapil, **BB09**  
Sharps, Paul, O09  
Shea, Patrick, L  
Shen, Shyh-Chiang, C06, Q03, Q05  
Shepherd, Nigel, R04, PS2.19  
Shervin, Shahab, Y03  
Shevelev, Mike, C04  
Shi, Wenhao, EE03  
Shi, Yueguang, **OO06**  
Shields, Seth, K05  
Shima, Darryl, LL07  
Shin, Jaeho, **I102**  
Shin, Jiwon, EE01, FF01  
Shvydka, Diana, S05  
Sifferman, Scott, **LL09**, LL10  
Simin, Grigory, NN05  
Simmonds, Paul, PP05  
Singh, Abhishek, DD02, DD03  
Singh, Deependra, PS2.03  
Singh, Manjri, **PS2.14**  
Singh, Shreya, D02  
Singh, Surinder, PS2.14  
Singh, Vinamrita, **PS2.02**  
Sinha, Abhinaba, **EE08**  
Sinha, Mekhola, AA05  
Sinnott, Susan, EE10  
Sitar, Zlatko, KK01, KK02, NN03  
Sjoden, Glenn, U08  
Skipper, Alec, **Z03**, QQ01, **QQ02**  
Sklyar, Vlad, C04  
Slimani Tlemceni, Taoufik, **B04**  
Snyder, David, EE04  
Sohel, Shahadat, P05, Y01  
Sohn, Jung Joo, PS1.05  
Soikkeli, Miika, D01  
Song, Jianan, P03  
Song, Jingfeng, H07  
Song, Renbo, M03, P01  
Spencer, Michael, D, L, **AA05**  
Srinivasan, Gopalan, PS1.14  
Stahlbush, Robert, L02, AA03  
Steinbrunner, Erich, V03  
Stephen, Greg, LL05  
Stiff-Roberts, Adrienne, F, F01  
Stockert, Edward, **PS2.15**  
Straker, Michael, AA05  
Strandwitz, Nicholas, PS1.22, PS1.23, PS2.22  
Su, Po-Yi, MM03  
Subramanian, Shruti, R09  
Suemasu, Takashi, DD01  
Sugimoto, Shigetou, II01  
Sultan, Muhammad Shehzad, M04, **PS2.21**  
Sun, Kai, NN01  
Sun, Rujun, **N03**, V04, **V06**  
Sun, Sam-Shajing, PS1.20  
Sun, Yi, X03, NN01  
Sun, Yifei, H08  
Sun, Yukun, U01, U03, LL06  
Sung, Woongje, L04  
Sunkari, Swapna, L01  
Susner, Michael, **EE06**, **EE09**  
Suzuki, Keigo, H07  
Swinnich, Edward, **AA09**, RR05, RR06  
Szymanski, Dennis, NN03  
Sønsteby, Henrik, **PP01**

## T

Tadjar, Marko, **G09**, AA06, CC02, CC07, CC09  
Tandon, Ram, PS2.10  
Tang, Hong, OO04  
Tansu, Nelson, M03, P01  
Tao, Jun, **M09**  
Taylor, Aidan, M05  
Taylor, Patrick, E03, **LL05**  
Tchoe, Youngbin, T01, **T03**, T04  
Terai, Yoshikazu, DD01  
Terry, Fred, PS1.13

Thangaraja, Amutha, CC01  
Thieu, Quang Tu, CC01  
Thunemann, Martin, T01  
Tian, Hao, EE03  
Tian, Yuan, O08  
Tiras, Kevser, **PS1.15**  
Toko, Kaoru, DD01  
Tomasulo, Stephanie, QQ04  
Tomecek, David, F04  
Tomek, Creighton, AA01  
Tomkins, Randy, C04  
Tong, Xiao, PS1.19  
Trajo, Orlando, HH07  
Tsou, Chuan-Wei, C06, Q05  
Tu, Li Wei, HH01, PS2.15  
Tulapurkar, Ashwin, EE08  
Turaczy, Kevin, Z08  
Turner, Emily, **M01**  
Tutuc, Emanuel, LL08  
Tweedie, James, NN03  
Twigg, Mark, **S03, QQ04**  
Tyagi, Siddharth, LL05

## U

Uchida, Yuki, CC01  
Udwary, Kevin, NN04  
Um, Jung Hwan, Y03  
Underwood, Kenneth, LL10  
Uppalapati, Balaadithya, K01, K02  
Uraoka, Yukiharu, II01  
Urwin, Brittany, Z07  
Usami, Noritaka, DD01  
Utegulov, Zhandos, DD04  
Uzlu, Burkay, D04

## V

Vadiee, Ehsan, MM05  
Vaeth, Alexander, **W06**  
Valerio Frias, Luis, PS1.19  
Vallejo, Kevin, PP05  
van der Weide, Danier, Z05  
van Duin, Adri, R09, EE10  
Vanjari, Sai Charan, **JJ01**  
Vasileska, Dragica, PS1.09  
Vatsyayan, Ritwik, **HH06, RR03**  
Vemuri, Vamseedhara, **PS2.22**  
Venkatakrishnan, P., II04  
Vera, Alexander, EE10  
Vergés, Jonas, O04  
Verma, Darpan, N06, **KK05**  
Vinnakota, Raj, Z02  
Vishnu, Sundaresan, A05  
Voevodin, Andrey, R04, PS2.19  
Voronine, Dmitri, R08  
Voss, Lars, JJ02  
Vu, Dung, DD, **DD05**  
Vu, Nguyen, GG04  
Vura, Sandeep, JJ01

## W

Wachter, Stefan, D01  
Wada, Hirofumi, CC01  
Wadekar, Paritosh, HH01, PS2.15  
Wagner, Guenter, CC10  
Wakimoto, Daiki, G09  
Walker, Janine, **GG03**  
Walko, Robert, PP02  
Wallis, Thomas, R08  
Walter, Timothy, O07  
Waltl, Michael, D01, D04  
Wang, Binbin, G02, G03  
Wang, Buguo, N02  
Wang, George, M01, JJ04  
Wang, Gunuk, II02  
Wang, Hongwei, BB06  
Wang, Lu, **L08**  
Wang, Maoji, B05  
Wang, Meng-Jen, U08  
Wang, Ping, **X03, NN01**

Wang, Qi, H08, **PS2.20**  
Wang, Sivakumar, Z01  
Wang, Tianyang, PS1.02  
Wang, Weijie, U05, **Y03, RR04**  
Wang, Yaguo, QQ02  
Wang, Yaxian, K05  
Wang, Yekan, C05, G05, AA06  
Wang, Yimeng, LL08  
Wang, Yinan, **LL08**  
Wang, Yong, **Z04**  
Wang, Yuejing, **Z06**  
Wang, Zhengtianyue, **Z01**  
Washiyama, Shun, KK02, NN03  
Waskiewicz, Ryan, L03  
Wasserman, Daniel, E, Z02, Z03, LL, LL08, PL, PP05, QQ02  
Watanabe, Shinya, CC01  
Webler, Bryan, PS2.18  
Wei, Xiongliang, **M03, P01**  
Weidenbach, Alex, A06, S02  
Weil, James, AA08  
Weiner, Brad, M04, PS2.21  
Weiss, Elan, **V07**  
Wenckstern, Holger, CC07, HH04  
Wetzel, Christian, I, J, JJ, KK  
White, Marvin, L06, L07  
White, Rachel, M06, **M07, M08**  
White, Samuel, **EE02**  
Wierer, Jonathan, M, M03, P01  
Wilhelm, Thomas, B02, O02, PS1.24  
Williams, Leslie, PS2.24  
Windl, Wolfgang, G02, K05, V07, BB03  
Wise, Adam, AA10  
Wistey, Mark, M06, M07, M08, U  
Withrow, Travis, V07  
Wolfson, Eric, **W03**  
Wong, William, D03, F, RR, RR02  
Wood, Michael, F02  
Woodall, Jerry, **DD08, PS1.03**  
Wooten, Brandi, **E03, LL05**  
Wright, Shawn, PS1.13  
Wu, Encheng, PS2.09  
Wu, Javier, OO02  
Wu, Xiaohan, **K06**  
Wu, Xifan, BB06  
Wu, Yuanpeng, **NN01**  
Wujcik, Evan, **II07**

## X

Xia, Zhanbo, V05  
Xian, Minghan, **CC09**  
Xiao, Neng, W03  
Xing, Diang, L06, L07  
Xing, Huili Grace, CC06, EE  
Xu, Ke, A, S, T  
Xu, Long, EE03  
Xu, Zhihao, DD01  
Xue, Hao, Y01  
Xue, Xingjun, LL02

## Y

Yakes, Michael, QQ04  
Yamaoka, Yu, CC01  
Yamashita, Yudai, DD01  
Yan, Qimin, BB06  
Yang, Chen, C03, J03, V08, MM03, **PS1.09**  
Yang, Frank, LL08  
Yang, Hao, T02  
Yang, Hohyun, PS2.08  
Yang, Seunghoon, II02  
Yang, Tsung-Han, C03, **J03, V08, MM03, PS1.09**  
Yanguas-Gil, Angel, A, S  
Yasuoka, Tatsuya, N05  
Yates, Luke, AA06  
Yeh, Sung-Wei, HH01  
Yi, Gyuchul, T01, RR01  
Yim, Sang Gyu, II07  
Yip, Michael, RR01

Yokoo, Masanori, CC01  
Yoo, Daekyoung, II03  
Yoon, Heayoung, B05, S, T, U08, II  
Yoon, Yohan, B05  
York, Krystal, **QQ03**  
You, Wei, F  
Young, David, O06  
Younis, Usman, **R03**  
Yu, Edward, W  
Yu, Susanna, L06, L07  
Yu, Xiaoxiao, AA10  
Yu, Yifei, D02  
Yuan, Yuan, LL02  
Yumnam, George, DD02  
Yun, Nick, **L04**  
Yusuf, Huma, **OO05, OO09**

## Z

Zeng, Yuping, HH08  
Zeumault, Andre, DD, RR  
Zhaludkevich, Aliaksandr, U06  
Zhanbo, Xia, N06, CC03  
Zhang, Buang, **F01**  
Zhang, Hanyu, R08  
Zhang, Jie, **HH08**  
Zhang, Qihua, **H03**  
Zhang, Shuyan, **BB05**  
Zhang, W-D., **ZB01**  
Zhang, Yuanchang, Z07  
Zhang, Yuxuan, **I04**  
Zhang, Yuying, Z01  
Zhang, Zhen, H08, **BB08**  
Zhao, Hongping, G, H05, I04, V, V01, V05, V09, V10, BB01, CC03, CC05, EE, PP03, PP04  
Zhao, Songrui, B, OO  
Zhao, Yuji, C03, V08, MM03, PS1.09  
Zheng, Yixiong, **RR06**  
Zhou, Jingan, C03, J03, V08, MM03, PS1.09  
Zhou, Tong, PP02  
Zhu, Menglin, H02, V01, PP02, PP03, PP04  
Zhu, Na, OO04  
Zhu, Shengnan, L06, **L07**  
Zhu, Tiacong, PP02  
Zhukovskiy, Maksym, O08  
Zide, Joshua, M, M02, Z06, DD  
Zivasatienraj, Bill, A06, S02  
Zubair, Muhammad, R03  
Zutic, Igor, PP02